



Indira Gandhi Centre for Atomic Research



Annual Report 2022



Government of India
Department of Atomic Energy
Indira Gandhi Centre for Atomic Research
Kalpakkam - 603 102

IGCAR

2022

INDIRA GANDHI CENTRE
FOR ATOMIC RESEARCH

ANNUAL
REPORT



Government of India
Department of Atomic Energy
Indira Gandhi Centre for
Atomic Research
Kalpakkam 603 102

Editorial Committee**Chairman**

Ms. S. Rajeswari

Members

Dr. John Philip

Dr. T. R. Ravindran

Dr. C. V. S. Brahmananda Rao

Shri A. Suriyanarayanan

Shri M. S. Bhagat

Shri G. Venkat Kishore

Ms. Sujatha P N

Shri M. Rajendra Kumar

Shri S. Kishore

Shri Biswanath Sen

Dr. N. Desigan

Shri K. Varathan

Member-Secretary

Shri P. Vijaya Gopal

CONTENTS

Foreword

Editorial

Articles at a Glance

I. Fast Breeder Test Reactor	01
II. Prototype Fast Breeder Reactor	11
III. R&D for Fast Breeder Reactors	31
IV. Fuel Cycle	75
V. Basic Research	91
VI. Infrastructure, Resource Management & Biodiversity	175
VII. Awards/Publications/ Events/Organisation	197

Address for Correspondence

Ms. S. Rajeswari

Chairman, Editorial Committee

Head, Scientific Information Resource Division

Indira Gandhi Centre for Atomic Research

Kalpakkam - 603 102

Phone : +91-44-27480281

Email : raj@igcar.gov.in

e-Copy available at: <http://www.igcar.gov.in>

Published by

Scientific Information Resource Division, SQ&RMG,
Indira Gandhi Centre for Atomic Research, Kalpakkam - 603 102

Foreword



Dear Colleagues,

I am delighted to release the IGCAR Annual report of 2022. The report highlights accomplishments in R&D pertaining to fast reactor and associated fuel cycle technologies as well as in the frontier areas of basic and applied research.

The Fast Breeder Test Reactor (FBTR) was raised to its rated design power level of 40 MWt for the first time on 7th March 2022. The reactor has operated for more than 128 days and generated more than 23.5 million Units during 2022. The U-233 based Kalpakkam Mini Reactor (KAMINI) continued to operate up to 30 kWt for neutron radiography of irradiated fuel pins, activation analysis of samples from AMD-Hyderabad, ASI, Institutions and testing of neutron detector etc.

As you would be aware, the Prototype Fast Breeder Reactor (PFBR) at BHAVINI is in an advanced stage of integrated commissioning. The entire Design and also the Electronics and Instrumentation group is fully working with BHAVINI team for the various issues and activities. Focused support from other groups such as ESG and SQ&RMG is also being provided. Three major activities that have been successfully accomplished include (a) Baselineing of more than 250 documents pertaining to V&V of I & C – pre requisite for Main Vessel Sodium Filling (b) rectification of 741 dummy subassemblies and (c) Successful demonstration of ISI vehicle DISHA.

Compact Reprocessing facility for Advanced fuels in Lead shielded cells (CORAL), facility has successfully completed its 63rd campaign and is continuing to function normally well beyond its design intent. Demonstration fast reactor Fuel Reprocessing Plant (DFRP), has reached an advanced stage with the cold commissioning being successfully completed.

In our endeavour towards indigenous development of improved materials and processes, phase-pure, high-density (~99.8%) tungsten carbide pellets of diameter

13.4mm and height 9.1mm have been fabricated in-house using a spark plasma sintering facility, for use as lower axial shielding in FBTR fuel sub-assemblies. Post-Irradiation Examination through NDE of irradiated fuel pins from a FBTR Mark-I sub-assembly operated at a linear heat rate of 400 W/cm was completed. A multiple specimen test facility has been developed to study the crack growth behaviour of small-sized pipe bends. First phase of testing on specimens has been carried out.

Cadmium Zinc Telluride single crystals of size 5×5×5 mm have been grown in-house and also incorporated in to a gamma radiation detector and found to have adequate gamma ray spectral resolution and stability. Larger (~25mm) crystals have been grown and are undergoing tests. A high-resolution RBS system with depth resolution of 0.2-0.3nm has been applied to thickness and stoichiometry of ultra-thin film multilayers. This has enabled correlation of interface features in Ni/Si/Ni/Si and Ni/Graphene/Ni/SiC with magneto-resistance measurements to demonstrate ferromagnetic coupling across silicon layers in the former case and antiferromagnetic coupling across graphene layers in the latter case.

As part of metal fuel development activities, U-6 wt. % Zr blanket slugs were fabricated using the upgraded injection casting system (10 kg) inside inert atmosphere glove box and was qualified for its functionality. Prior to electro-refining irradiated U-Zr alloy fuel, all the optimization process parameters were carried out utilizing virgin U-Zr alloy in molten salt medium at Hot-cells. Subsequently, uranium metal deposition was successfully demonstrated by electro-refining irradiated U-6Zr. In addition, an engineering scale pyroprocessing facility with remote handling has been established and electro-refining of 10 kg uranium metal was demonstrated in this facility.

An Integrated Radiation Monitoring Facility (IRMF) was commissioned at Anupuram Township and inaugurated by the then Chairman AERB Shri Nageswara Rao. A team from National Disaster Management Authority (NDMA) also visited the facility and appreciated it. First responder training course on Nuclear & Radiological Emergencies was conducted at IGCAR for 244 personnel from National Disaster Responses Force. More than 600 radiation monitoring equipments from various DAE units, hospitals, industries were calibrated at the NABL accredited Calibration facility.

During this period, two technologies developed under “Atma Nirbhar Bharat” programmes of IGCAR have been successfully transferred to industry through the Incubation Centre. Two Indian patents were granted. A collaborative incubation agreement was also signed with a Mumbai based private manufacturer to complete development of the technology “Replaceable Feed-through connectors for Glove Boxes” and Chennai based firm for developing “Hydrogen Sensor” technology.

Towards human resources development, twenty young trained scientists and engineers (OCES-2021, 16th Batch) have successfully completed their orientation programme at BARC Training School at IGCAR. Our Centre has been providing projects/internship opportunity to Postgraduate students for completing their academic programme and thereby aids to kindle the interest in students to pursue research in frontier areas of science and technology.

As part of Azadi Ka Amrit Mahotsav celebrations a program an ‘Anu Awareness’ programme was organized. An exhibition depicting the role of nuclear

energy, applications of radiation and DAE based technologies for society, quiz and other competitions were organized. More than 2000 students participated in the competitions and around 20,000 students, teachers and researchers visited the exhibition. ‘Grand Iconic Week’ was celebrated from August 22-28, 2022 as part of the ‘Azadi Ka Amrit Mahotsav’ on the theme ‘Atoms in the Service of the Nation’. Generation of 750 Magic Squares” by 75 students from eight neighbourhood Government Higher Secondary Schools using 75 important dates of milestone activities of DAE, ‘Sand art sculpture’ to create awareness on the societal applications of various technologies developed by DAE and ‘Anu Walkathon’ for Atoms in the Service of the Nation at Elliot’s beach, Chennai were some of the highlights of the celebration.

This year, apart from the other R & D and regular activities at the various groups of IGCAR and GSO, our focus would continue to be on supporting the activities of PFBR towards Main Vessel Sodium Filling and subsequent First Approach to Criticality, hot commissioning of DFRP, continuing to run FBTR at 40 MWt for more than 100 days, Commissioning of Metal Fuel Laboratory and commissioning and dedication of Doppler Weather Radar Facility.



(B. Venkatraman)
Distinguished Scientist &
Director, IGCAR

Our Primary Mission

To conduct a broad based multidisciplinary programme of scientific research and advanced engineering development, directed towards the establishment of the technology of Sodium Cooled Fast Breeder Reactors (FBR) and associated fuel cycle facilities in the Country. The mission includes the development and applications of new and improved materials, techniques, equipment and systems for FBRs, pursue basic research to achieve breakthroughs in Fast Reactor technology.

Editor's Desk



Dear Reader,

I am pleased to present the Annual Report of IGCAR for 2022 as the Editorial Committee Chairman.

This year, the annual report has 158 technical articles. A significant portion of this report reflects the progress in mission-specific activities of IGCAR concerning FBTR, PFBR, R&D on future Fast Reactors, and the Fuel Cycle. The rest of the chapters indicate the basic research essential for sustained growth in research and development, technology transfers and societal benefit programs. Other supporting development activities are part of the chapter on infrastructure, resource management and biodiversity.

The articles have gone through multiple editing stages to ensure accuracy and readability. I convey my sincere thanks to the Editorial Committee for their dedicated efforts in successfully bringing out the Annual Report.

Chapter-I on Fast Breeder Test Reactor has an article on sustained operation of FBTR at 40 MWt.

Another important article on non-destructive examinations on FBTR Mark-1 fuel sub-assembly irradiated at high linear heat rating and sodium inlet temperature is discussed.

Chapter-II on Prototype Fast Breeder Reactor highlights the status of PFBR. The articles on design and development of a Magnetostriction Transducer for Couplant free Ultrasonic guided wave based inspection of steam generator tubes of PFBR is also discussed.

Chapter-III on R&D for FBR has articles about the Centre's efforts to develop indigenous technology for future nuclear reactor programs. There are various articles on the non-destructive determination of Pu-isotopic composition in MOX pellets using high resolution gamma spectrometry, indigenous design and

development of radar level probe for liquid sodium level measurement etc.

Chapter-IV on Fuel Cycle including studies related to commissioning of various sub-systems in DFRP, development of improvised neoprene gauntlet through indigenous manufacturing, radiofrequency induction heating system for fixing the nuclear material on a planchet for radiometric analysis and other developments.

Chapter-V on Basic Research has the highest number of articles, and this chapter articles covering the CdZnTe-based gamma spectrometer, developments of NDE tools, physical characterization techniques and analysis. Chapter-VI on Infrastructure, Resource Management, and Biodiversity is a chapter that highlights the efforts & augmentation of essential services, public awareness, biodiversity documentation, and infrastructure management. Chapter-VII has details on the publications, the events, awards, organization, and a summary of the activities of the various groups.

We welcome feedback from readers concerning the quality of the presentation and the technical content therein. We thank the Group Directors for their support and the enthusiastic authors for providing quality articles in the stipulated time.

The committee sincerely thanks Dr. B. Venkatraman, Director, IGCAR, for his keen interest, continued guidance and support towards bringing out the publication in its present form.

S. Rajeswari
Chairman, Editorial Committee &
Head, Scientific Information Resource Division

I. Fast Breeder Test Reactor		
Sl.No	Title	Page No
1.01	Sustained Operation of Fast Breeder Test Reactor at 40 MWt	02
1.02	Non-destructive examinations on FBTR Mark-I fuel sub-assembly irradiated at high linear heat rating and sodium inlet temperature	03
1.03	Upgradation of Computerized Online Work Permit Management System of FBTR	06
1.04	Installation and Commissioning of Portal Monitor for Active areas of FBTR	07
1.05	Replacement of Water Sub-headers of Steam Generators of FBTR	08
1.06	Manufacture Of Inlet Water Sub-Headers For FBTR Steam Generator Module	09

II. Prototype Fast Breeder Reactor		
2.01	PFBR Commissioning Status	12
2.02	Assessment of Irradiation Damage of MAPS-1 End Shield using Surveillance Specimens	13
2.03	Design and Development of a Magnetostriction Transducer for Couplant Free Ultrasonic Guided Wave Based Inspection of Steam Generator Tubes of PFBR	15
2.04	Modification of Application software for Sodium Instrumentation systems of PFBR	17
2.05	Qualification and Deployment of Dissimilar Weld Inspection Device (DISHA) in PFBR	18
2.06	Technology Development for Real Time Temperature Sensing of PFBR Periscope Xenon Lamp at High Voltage and High Temperature Environment	19
2.07	Seismic Qualification Test on Distributed Digital Control System Server and Data Exchange and Processing Unit for PFBR	20
2.08	Effect of Radial Clearance at Discriminator Guide Location during Axial Flow Vibration of Core Subassembly in PFBR	21
2.09	Root Cause Analysis of Scoring on SA hexcan & Higher Extraction Load Observed with Certain SAs in PFBR Dummy Core and Implementation of Solutions	22
2.10	Estimation of Stability Domain in PFBR using Lyapunov Exponent Method	23
2.11	Sodium Calibration of Eddy Current Sensor for Core Flow Monitoring of Blanket & Storage Subassemblies	24
2.12	High Temperature Testing of Dismountable Type Ultrasonic Transducer	25
2.13	Analysis of Pressure Transient in Secondary Sodium Circuit due to Pump Seizure in PFBR	26
2.14	Performance evaluation of Flow Distribution Device for 170 m ³ /h Capacity ALIP	27
2.15	Performance Evaluation of Decay Heat Removal System for The Sodium to Sodium Decay Heat Exchanger Type-B	29

III. R&D for Fast Breeder Reactors		
3.01	High temperature Oxidation Behaviour of T91 Alloy	32
3.02	Fabrication and Characterization of 170 nos. of U-6 wt. % Zr Slugs for DND Application	33
3.03	Commencement of Engineering Scale U Metal Electrorefining in PPRDF	34
3.04	Engineering Challenges in Establishing Pyroprocess R&D Facility (PPRDF)	36
3.05	Studies on the Conversion of UO ₂ to UCl ₃ using AlCl ₃ in LiCl-KCl Melt and the Effect of Lanthanide (Ln: Nd, Pr, La and Ce) Oxides on the Conversion Efficiency of UO ₂	38
3.06	Preparation and Analysis of Li-Cd Alloys with Different Concentrations for Studies on Reductive Extraction of Actinides Related to Pyrochemical Reprocessing	39
3.07	Measurement of Phase Transformation Temperatures of Metallic Fuel	40
3.08	Non-Destructive Determination of Pu - Isotopic Composition in MOX Pellets using High Resolution Gamma Spectrometry	41
3.09	Development of green separation techniques for extraction and recovery of actinides using supercritical carbon dioxide modified with Tris (2-methylbutyl) phosphate	43
3.10	Manufacture of Compressed Air Receiver Tanks and Soft Water Storage Tank for Steam Generator Test Facility	44

III. R&D for Fast Breeder Reactors		
3.11	Indigenous Design and Development of Radar Level Probe for Liquid Sodium Level Measurement	46
3.12	Performance Evaluation of 8051 Microcontroller under Gamma Radiation Environment for Severe Accident Monitoring System	47
3.13	Deployment of Indigenous Wireless Sensor Network for the Assessment of Slope Stability at Avalanche Site	48
3.14	Design and Development of Wireless Sensor Network based Acoustic Emission System	49
3.15	Establishment of Licensed Certifying Authority (CA) Facility for DAE at IGCAR	50
3.16	Deployment of Critical Intranet services in IGCAR Private Cloud	51
3.17	CCTV Surveillance System for DAE Residential Township SISD/EIG	52
3.18	Turbulent Natural Convection and Aerosol distribution studies for sodium pool fire in a confined environment	53
3.19	Thermal transient measurements of optical periscope lamp assembly for different flow rates using thermal imaging	55
3.20	In-sodium visualization of Molten Fuel sodium interaction using X- ray radiography	57
3.21	Development of carbonate based powder for Sodium fire extinguishment	58
3.22	Disposal of sodium using controlled mist technique	59
3.23	Corrosion Behaviour of Ceramic Composite Coated and Uncoated P-91 steel and Type 316 LN Stainless Steel in Lead with Oxygen at 550°C	60
3.24	Plasma-sprayed Lanthanum Zirconate and Yttrium Aluminum Monoclinic coatings its Performance in Molten liquid-sodium	61
3.25	Durability of Plasma Sprayed Alumina Coating on Inconel 600 with Different Bond Coats for Neutron Detector Application	62
3.26	Polymer-Silane Based Superhydrophobic Coatings on Carbon Steel with Enhanced Corrosion Resistance and Self-cleaning Property	63
3.27	Microstructural characterization of Laser Rapid Manufactured Hard-facing Alloy Bushes for FBR application	64
3.28	High Temperature Thermophysical Properties of Spark Plasma Sintered Tungsten Carbide	65
3.29	Understanding formation of borides in concentrated P91-B alloys	66
3.30	Effect of Zr addition on microstructure and Nano-mechanical Properties of P9 steel	67
3.31	Use of Dynamic Transformation to Enhance Thermo-mechanical Processing of Gr. 92 Heat-resistant Steel	68
3.32	Role of Nitrogen on Fracture and Fatigue Crack Growth Behaviour of SS316L	69
3.33	Manufacturing of Alloy 625 Bush by Wire Arc Additive Manufacturing (WAAM) Process	70
3.34	Non-Destructive Inspection of Dissimilar Weld between Main Vessel and Roof Slab at 152° ISI port, PFBR	71
3.35	Design and Development of remote Field Eddy Current Array Probe for Imaging of Defects in Steam Generator Tubes of PFBR	72
3.36	Enhancement in Creep Strength of Grade 91 Steel by Addition of Boron	73
3.37	Creep-fatigue interaction Behavior of Simulated Microstructures and the Actual Weldment of P91 steel	74

IV. Fuel Cycle		
4.01	Study on Corrosion Rates of Abut Surfaces in Huey test	76
4.02	Design and Installation of Lightning Protection System for the Buildings in DFRP and CORAL at RpG	78
4.03	Designing the Flow Sheet for Fast Reactor Fuel Reprocessing by using Advanced Computer Codes	80
4.04	Development of Glove Box Adaptable Plutonium Oxalate Precipitator for Continuous Operation	81
4.05	Development of a Jack System for Positioning and Replacement of Lighting Plugs for Lead Cells	82
4.06	Development of improvised Neoprene Gauntlet Through Indigenous Manufacturing	83
4.07	Development of Silicon Photo-multiplier (SiPM) and Fibre Optics based Radioactive Contamination Monitor	84
4.08	Development of Special Fixtures and Tools for Fast reactor Fuel Reprocessing	85
4.09	Kinematic Analysis and Evaluation of Swept Areas of An Articulated Manipulator Used in Hot Cells of DFRP	87
4.10	Online Detection of Plant Abnormalities using Machine Learning Based Data Analytics	88
4.11	Radiofrequency Induction Heating System for Fixing the Nuclear Material on A Planchet for Radiometric Analysis	90

V. Basic Research		
5.01	Evaluation of residual stress in polycrystalline-Ge thin film grown on glass via Au-induced crystallization using GIXRD	92
5.02	Portable and wireless CdZnTe-based gamma spectrometer (C-VEGAS) with 5.5 % resolution at 662 keV of ¹³⁷ Cs	93
5.03	Tuning Electronic Structure of Diamond by Surface Functionalization	94
5.04	Synthesis of Diamond / Vertical Graphene Hybrid Structures for Tribological and Electronic Applications	95
5.05	Enhanced Photoluminescence Quantum Efficiency in Large Area Monolayer MoS ₂	96
5.06	Deterioration of the system performance due to the unidentified reverse current flow in the transmitter loop in SQUID based TDEM system	97
5.07	PZN-PT Single Crystal Based Surface Acoustic Wave Transducer	98
5.08	Achieving optimal classification in the machine learning approach by performing effective feature reduction	99
5.09	Functional anatomical imaging using magnetocardiography (MCG)	100
5.10	Chloride Enhanced Seed-Mediated Gold Nanorods for Superior Surface Enhanced Raman Spectroscopic (SERS) Activity	101
5.11	IV Characteristics of Si PIN Diodes under Controlled Humid Conditions and Integrity of Surface Passivation Layer	102
5.12	Structural stability of CoB at high pressures and compressibility trends among group VIII 3d transition metal monoborides	103
5.13	Temperature dependence of elastic constants and phonon modes in the energetic material TEX	105
5.14	Experimental evidences for a Quantum Spin Liquid ground state in Y ₂ CuTiO ₆ , a double perovskite compound	106
5.15	Studies of intrinsic and ion-irradiation induced vacancy defects in Zr/Al containing ODS alloys	107
5.16	Enhancement of Photoluminescence due to NV centres in nanodiamond films formed by ion implantation	108

V. Basic Research		
5.17	Electron correlation & different predicted structures of U_2Mo	109
5.18	Molecular Dynamics (MD) study of Iron Phosphate Glass	110
5.19	Ion beam evaluation and characterization of TiO_2 based ultraviolet and ionizing radiation detectors	111
5.20	Development of Chemical Emergency Response System	112
5.21	A study on radon and thoron measurements in Glass Fiber Reinforced Gypsum (GFRG) buildings at Kalpakkam	113
5.22	Lithium formate – A Tissue equivalent high level dosimeter based on Electron Paramagnetic resonance	114
5.23	Site specific transfer factor of ^{210}Po from soil to rice crop in the experimental field at DAE site IGCAR	115
5.24	Development of Linear Kalman-Filter Technique for Source Term and Dose Rate Estimation	116
5.25	Cytokinesis block micronucleus assay (CBMN) in gamma irradiated blood samples for radiation dose assessment	117
5.26	Analysis of extreme values of meteorological parameters at Kalpakkam site	118
5.27	Determination of angular dependence factor for gamma radiation monitoring instruments	119
5.28	Effective sampling for radiocarbon measurement in the atmosphere	120
5.29	A comparative study on Residual stress of SS 304L Welds using X-ray Diffraction Technique (XRD)	121
5.30	Application of machine learning in ultrasonics for classification of annealing conditions in austenitic stainless steel	123
5.31	Numerical estimation of efficiency of HPGe based actinide monitor for various radionuclides present in lungs	124
5.32	Dimensional Measurement in Gamma Ray CT imaging using the Shape phantom	125
5.33	Studies on characteristic limits for measuring ionizing radiation	126
5.34	Tribocorrosion Behavior and its Mechanisms of Type 304L Stainless Steel in Nitric Acid Media	127
5.35	An AFM based study on the effect of X-ray exposure on adhesion properties of multi-walled carbon nanotube incorporated silicone polymer nanocomposites	128
5.36	Effect of Zn substitution on the AC magnetic heating properties of Zn-Mn mixed ferrite nanoparticles prepared using microwave assisted synthesis	129
5.37	Effect of aging heat treatment on Microstructure, Mechanical Properties, and Lattice Strain of Alloy 61	130
5.38	Molecular dynamics simulations on mechanical properties and associated deformation mechanisms of model materials	132
5.39	Electrochemical Preparation of Th_7Ni_3 Intermetallic in $CaCl_2$ melt by FFC Cambridge Process	133
5.40	Li Intercalation in Graphite and Formation of Li_2C_2 in LiCl-KCl Eutectic Melts	135
5.41	Coupled heat and mass transfer simulation of melt crystallization of LiCl-KCl-CsCl mixture	136
5.42	Automatic droplet dispensing system for producing uniform size of microspheres using sol-gel method	137
5.43	Commissioning of high purity argon glove box facility with process equipment for DOER studies	139
5.44	Design and development of power supply for electron bombardment furnace of KEMS	141
5.45	Removal of Cs^+ and Sr^{2+} ions from simulated radioactive waste solutions using zeolites-A synthesized from kaolin	142

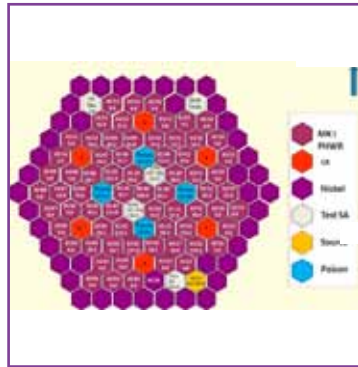
V. Basic Research		
5.46	Electrochemical studies on hydride ion conducting $\text{CaBr}_2\text{-CaHBr}$ solid electrolyte	143
5.47	Unraveling the Extraction and Coordination Behavior of U(VI) in Sulphuric Acid Medium by Bi-functional Dialkyl-H-Phosphonates	144
5.48	Vaporisation studies over $\langle \text{UAl}_2(\text{cr})+\text{U}(\text{cr}) \rangle$ two phase region of U-Al system	145
5.49	Development of an indigenous ion exchange based radioactive radionuclides removal method from the routine laboratory organic liquid waste	146
5.50	In-house Developed Small Volume Calorimeter for Non-Destructive Assay of Plutonium based nuclear fuels	147
5.51	Highly efficient functionalized Metal Organic Frameworks for the Extraction of Pd(II) from Aqueous Solution	149
5.52	Studies Related to the Aqueous Reprocessing of Metallic Alloy Fuels using Phosphonate based solvents	150
5.53	Pyro-processing of irradiated U-6Zr in hot cells	151
5.54	Novel Pulsed Laser Deposition Sampling Methodology for ICPMS Chemical Analysis towards Burn-up Measurements	152
5.55	Indium Tin Oxide thin-film as Sensor cum Heater Material	153
5.56	Experimental setup for Fatigue life Testing of Bellows	154
5.57	Testing of Ferro-Magnetic Particle Collector In Water	155
5.58	Design, Development and Deployment of Mobile Robotic System for the Pre-Service Inspection (PSI) of DFRP Waste Vault	156
5.59	Decay power measurements from P91, SS316L, SS304L and D9 steels: Irradiation experiment in KAMINI	157
5.60	Development of a Test facility for the multi-specimen prototype pipe bends for LBB studies	158
5.61	Numerical Simulation of Operational Transients of FBR1&2	159
5.62	Towards accurate computation of corium thermal hydraulics during fast reactor severe accident	160
5.63	Numerical analysis of sodium pool spreading on the sloped floor in SFR cell by developing multidimensional model	161
5.64	Numerical analysis of sodium flow boiling in narrow sub-channels of SFR by developing CFD based multiphase flow model	162
5.65	Analysis of the criticality behaviour of FBR core debris bed on the core catcher by developing 2D diffusion based model	163
5.66	Development of Sensor for Direct Sodium Pressure Measurement	164
5.67	Qualification of Inconel-625H bellows for Sodium Service Valves	165
5.68	Design optimization of Core Flow Monitoring Mechanism for Blanket and Storage Subassemblies	166
5.69	Development of Compact hydrogen meter for Steam generator leak detection system	167
5.70	Optimized procedure for Regeneration of Secondary Cold Trap	168
5.71	Hydraulic Validation of Hydraulic Suspended Absorber Rods for Future FBRs	170
5.72	Development of a novel ultrasonic bath for centrifugal extractor bowl dechoking	171
5.73	Uranium extraction and stripping experiments with TiAP solvent in multistage Annular Centrifugal Extractor	173

VI. Infrastructure, Resource Management & Biodiversity

6.01	Commissioning of an Emergency Backup Evacuation System in RML	176
6.02	Restoration of RML high bay 20/5T EOT crane clutch plate.	178
6.03	Operating Performance and Sustained Quality of Permeate at 2 MIGD Desalination Plant at IGCAR	179
6.04	Restoration of an Aged Building Through Strategic Repair	180
6.05	Formation of 33 kV Ring Main system for improved reliability	181
6.06	Increased reliability of central chilled water supply and revamping of air handling units for ACV services of IGCAR	182
6.07	Commissioning of 11 kV PDC XI substation	183
6.08	Building for Development & Testing Facility for Advance Study on High Temperature Material	184
6.09	Establishment of Hydraulic Pressure test facility for portable fire extinguishers and Self Contained Breathing Apparatus (SCBA) filling facility in IGCAR	186
6.10	Industrial, Fire and First Aid Training program to meet AERB Regulation	187
6.11	Human Resource Management – Induction of Junior Research Fellows in IGCAR	188
6.12	Development of Budget Automation System (DAEBAS) v2.0 for DAE Units	189
6.13	Aazadi ka Amrit Mahotsav and DAE Iconic Week	191
6.14	Incubation and Transfer of IGCAR Technologies	193
6.15	Advanced Digital Library & Services	194
6.16	Biodiversity at DAE Kalpakkam complex	195

VII. Awards/Publications/Events/Organisation

	Awards & Honours	198
	Seminars, Workshops, Webinars and Meetings	199
	Publications	201
	Events	202
	IGC Council	218
	Organisation and Activities of Various Groups	222
	Organisation Chart - IGCAR	235
	List of Important Abbreviations	241
	Annual Report Editorial Team	244



CHAPTER I

Fast Breeder Test Reactor

I.01 Sustained Operation of Fast Breeder Test Reactor at 40 MWt

Fast Breeder Test Reactor (FBTR) is a loop type, sodium cooled experimental fast reactor with design power of 40 MWt (13.2 MWe) and has been in operation since 1985 at various power levels upto 32 MWt till 29th irradiation campaign. Power could not be raised to rated power of 40 MWt by adding MK-I carbide fuel sub-assembly (FSA) alone due to minimum shutdown margin (SDM) criterion. Hence a novel idea was implemented to introduce four boron carbide (50% enriched in B-10) poison SAs in the second ring to increase the core size beyond 56 FSAs after getting safety clearance from AERB. Accordingly, transition to 30th irradiation campaign core was completed in six fuel handling steps. After each fuel handling step, physics parameters like SDM, control rod (CR) worth and critical heights were measured and ensured to be within limits.

Out of 68 MK-I FSAs required for operation at 40 MWt, 27 are fresh and among these, 8 were loaded in the 4th ring and 19 in the 5th ring. Between step 2 and step 5, 4 poison SAs were loaded in second ring at 02-01, 02-04, 02-07 and 02-10 locations. (Fig. 1)

Major missions of the 30th irradiation campaign at 40 MWt were as follows:

Continuing irradiation of the sodium bonded metallic fuel pins Ternary fuel-1 (23% Pu-19% EU-6%Zr), Ternary fuel-2 (19%Pu-U-6%Zr), Binary fuel (14.8% EU-6%Zr) and Natural U-6%Zr metallic fuel, continuing long term

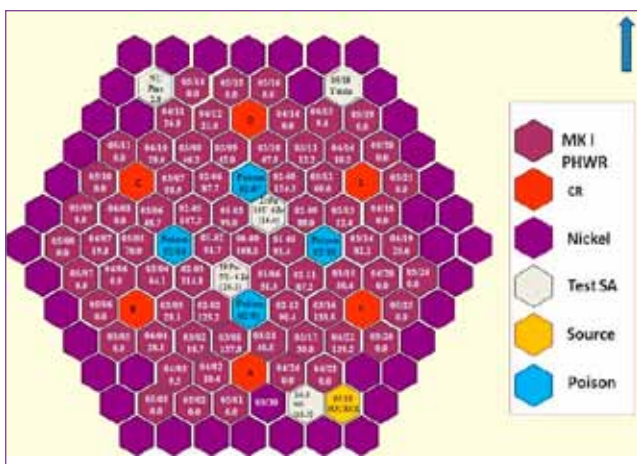


Fig. 1: Core configuration with 68 MK-I FSA

irradiation of D9 structural material and irradiation of yttria special subassembly for production of Strontium-89 isotope for medical application

30th irradiation campaign was initiated with criticality of reactor on 22nd February 2022. The measured shutdown margin was 4485 pcm which is above the Technical Specification limit of 4200 pcm. Measured CR worth was 9685.7 pcm as against the estimated value of 9411.3 pcm. Measured value of isothermal temperature and power coefficients were -3.47 ± 0.17 pcm/°C and -7.06 pcm/MWt respectively. The measured value of temperature and power coefficients are well above the estimated values adhering to Technical Specification limits. Hence, operation programme of Reactor was continued and power raised to design power of 40 MWt on 7th March, 2022 at 17:30 h.

Total duration of the 30th irradiation campaign was 45 effective full power days (EFPD) at 40 MWt. The campaign came to an end when the Mark-I FSA at 03-16 location attained its permitted burnup limit of 140 GWd/t. Prior to the controlled shutdown of the reactor, house load operation test and load throw-off test for turbo-generator (TG) were carried out to demonstrate the capability of the plant to withstand transients such as grid disturbances.

31st irradiation campaign at 40 MWt

After getting clearance from AERB, fuel handling operations for the 31st irradiation campaign were carried out in a single step involving change of reactivity worth of ~ 800 pcm. Three burnt MK-I FSAs were shifted to periphery and three fresh MK-I FSAs were loaded in the core. The yttria capsule SA from 05-18 location was discharged from the core for recovering strontium-89 isotope for medical application and a fresh yttria capsule loaded in the same location.

The 31st irradiation campaign with 68 FSAs (MK-I) in the core commenced on 7th June 2022 with startup criticality. After completing low power physics experiments such as control rod calibration and isothermal temperature coefficient of reactivity measurement and ensuring

Salient Features of 30 th irradiation Campaign at 40 MWt	
Start of the campaign at 40 MWt	7 th March 2022
End of the campaign	7 th May 2022
Reactor Power/ TG Power	40 MWt/~10 MWe
Reactor inlet /outlet sodium temperature	382°C/492°C
Central SA outlet temperature	518°C
Primary sodium loop flow	640 m ³ /h
Secondary sodium loop flow	330 m ³ /h
Feed water / steam temperature	192°C / 425°C
Feed water flow	77 m ³ /h
Feed water / steam pressure	132/120 kg/cm ²
Operating time of reactor	1240 h
Thermal energy produced	41453.4 MWh
TG synchronization time	1080 h
Electrical energy generated	8.5 Million Units

adherence to Technical Specifications, reactor power was gradually increased to 40 MWt and TG synchronized to grid delivering ~10 MWe .

In the year 2022, FBTR was operated cumulatively for 130 EFPD at 40 MWt with TG generating 24.6 million units of electricity.

I.02 Non-destructive examinations on FBTR Mark-I fuel sub-assembly irradiated at high linear heat rating and sodium inlet temperature

The burnup limit for Mk-I carbide fuel sub-assembly (FSA) irradiated in FBTR at a high linear heat rating (LHR) of 400 W/cm and high sodium inlet temperature from the beginning of life, is around 100 GWd/t, based on thermo-mechanical modeling. To explore the feasibility of extending the burn-up, one FSA of 105 GWd/t burnup was taken for detailed Post-Irradiation Examinations (PIE) in hot cells of Radio Metallurgy laboratory. This article highlights the salient results of the non-destructive examinations carried out on the FSA and fuel pins.

Metrology of FSA

After sodium cleaning, the FSA was subjected to dimensional measurements using a remotely operable profilometer called Dimensional measurement-cum-Laser Dismantling (DMLD) machine fitted with an omni-directional induction type touch trigger sensor. The dimensions measured were (i) width-across-flats (WAF) shown in Fig.1, (ii) corner-to-corner distances (CCD), and (iii) head-to-foot misalignment (HFM). The increase in WAF (1.23% strain) has contributions from

both void swelling and irradiation creep, while increase in CCD (0.89%) is predominantly due to void swelling, since irradiation creep is negligible at corners.

The FSA was dismantled using lasers and the fuel pin bundle was extracted. A set of representative fuel pins located diagonally across the hexagon was selected for detailed non-destructive examinations. The diameter of the fuel pins were measured using a LVDT based profilometer, while the length of the pins was measured using a dial gage setup.

The dilation profiles axially along the fuel pins (Fig. 2) followed the dpa profile peaking around the core mid-plane. The diameter profiles in two orthogonal orientations showed signatures of ovality, with maximum difference of ~0.050 mm. The length increase in the fuel pins, caused by void swelling strains, was measured on all 61 pins to identify the maximally swelled pin. The same pin also exhibited higher diametrical strain of 3.9%, indicating that void swelling could be the major contributor to fuel pin dilation.

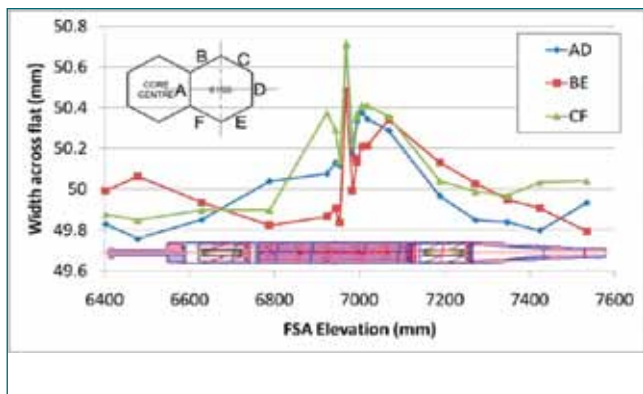


Fig. 1: Typical axial profile of width across flat of hexagonal wrapper of 105 GWd/t FSA

Radiography, Gamma scanning and Eddy Current testing of fuel pins

Non-destructive examinations (NDE) such as X-radiography, neutron radiography, gamma scanning (GS) and Eddy Current Testing (ECT) were carried out on selected fuel pins.

X-radiography was remotely carried out using a 420 kV industrial X-ray machine. A stainless steel (SS) pre-filter was used to reduce gamma fogging in radiographs, thickness of which was arrived from CIVA X-ray simulation model. This along with optimized exposure parameters resulted in an optical density of ~0.5 and good contrast delineating the internal details of fuel pins (Fig. 3).

The pellet to pellet gap and pellet to clad gap could be observed in some locations in the fuel column. Stack length increase varied from 2 - 4%.

Neutron Radiography was carried out at the south beam port of KAMINI reactor using indirect technique with dysprosium and indium converter screens at a reactor power of 20 kW and exposure time of 20 min. The fuel

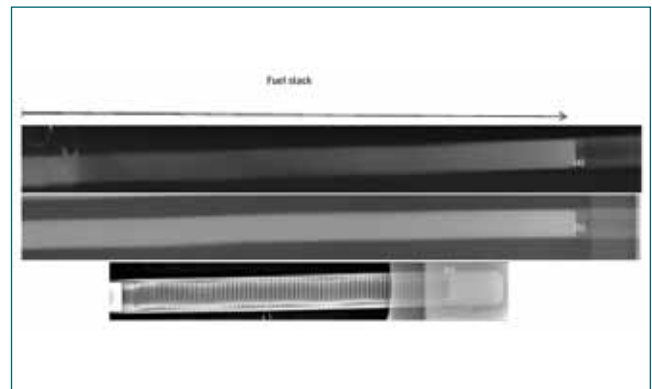


Fig. 3: X-Ray images of a typical irradiated fuel pin exposed (a) without and (b) with SS pre-filter and (c) The enlarged image of spring region in.

stack length measured from raw radiographs was in the range of 2-4% (Fig. 4). Image processing was carried out to reveal features of fuel pellets. Inter-pellet gap was observed in a few fuel pins at the top of the fuel columns. Axial gamma scanning was carried out to study the axial distribution of gamma emitting fission products (FP) using a fuel pin scanning bench inside the hot cell. Gamma spectrum was acquired at 0.5 mm interval using a HPGe based gamma spectrometry system through the collimator in the hot cell wall. Segregation of cesium was observed at the ends of fuel columns in a few pins. Some pins showed presence of ¹³⁷Cs in plenum regions. ¹⁰⁶Ru distribution followed axial flux profile (Fig.5). Stack length measured by GS compares well with radiography results. Eddy current testing of fuel pins was carried out using a newly developed high sensitive segmented coil probe and the conventional encircling differential probes. Seven indications were observed in the fuel column regions of four fuel pins which were characterized as ID indications based on phase angle parameter. The circumferential locations of the indications were identified

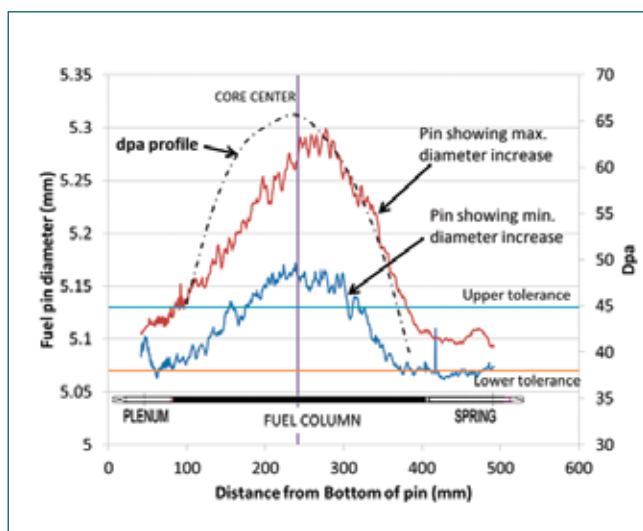


Fig. 2: Typical diameter profiles along the fuel pins

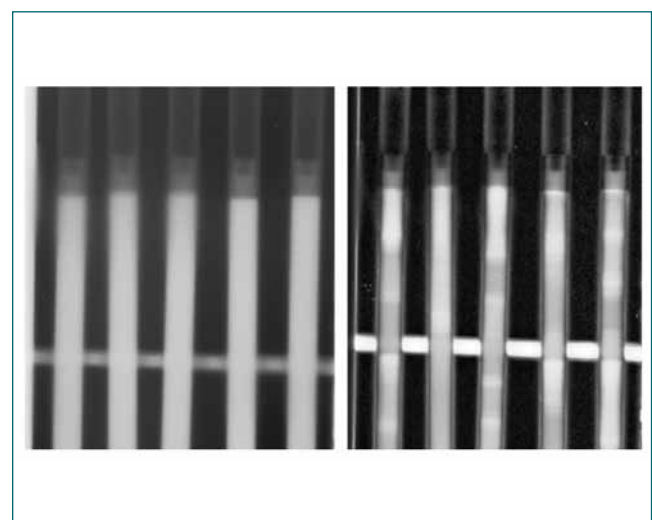


Fig. 4: Neutron radiographs of fuel pin below core mid-plane, Raw image (left), Processed image (right)

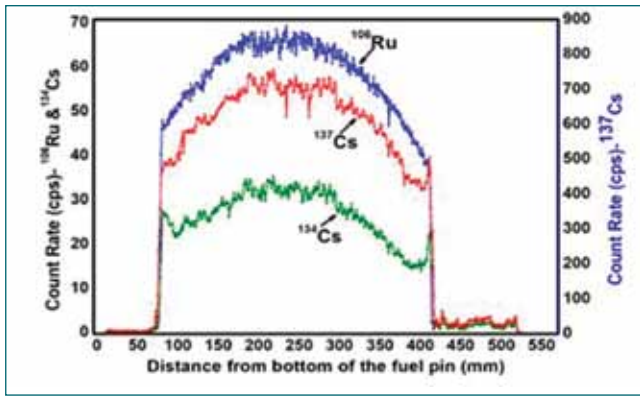


Fig. 5: Typical gamma profile of a fuel pin

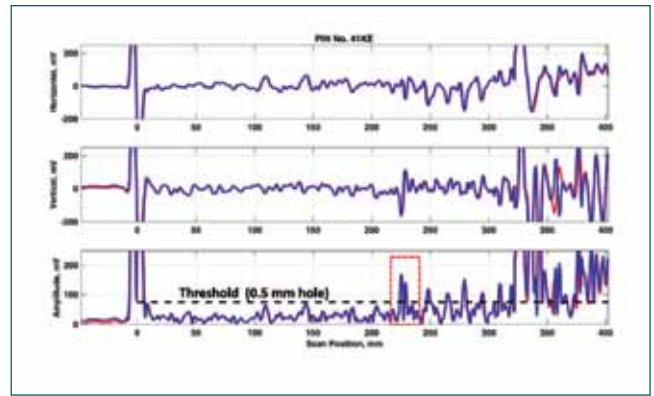


Fig. 6: Horizontal, vertical and amplitude EC signals of a fuel pin.

Table.1 Comparison of PIE results of 105 GWd/t with previous FSAs operated at lower LHR

Measured parameter (with nominal pre-irradiation values in parenthesis wherever applicable)	PIE data (Max values)		
	105 GWd/t	100 GWd/t	155 GWd/t
LHR (W/cm)	400	320	320
Na T (in/out)°C	380/485	350/445	
Head to foot misalignment of FSA (mm) (< 1.5 mm)	3.95	4.3	7.5
Increase in width across flat of wrapper (49.80 +0.2/-0 mm)	1.23 %	0.7 %	1.3 %
Increase in Corner to Corner distance (57 mm)	0.89 %	0.5 %	1.18%
Increase in fuel pin diameter (5.10 ± 0.03mm)	3.9 %	1.6 %	5 %
Increase in fuel pin length (531.5 +0.4/-0.6mm)	1%	0.4 %	1.1%
Increase in fuel stack length (320 ± 1.5 mm)	4 %	2.6 %	3.7 %

using the segmented coil output. Typical horizontal, vertical and amplitude EC signals of a fuel pin which showed distinct ID indication at around 231 mm of the fuel column is shown in Fig. 6.

Stack length estimation was done for the first time from EC signals and the same were benchmarked with radiography results.

Comparison with previous PIE data

The dimensional changes in the wrapper, fuel pin and the fuel stack length of the 105 GWd/t burnup are compared with the previous PIE data obtained for 100 GWd/t and 155 GWd/t FSAs (Table 1). In the earlier irradiation campaigns, the carbide FSAs were operated at a lower LHR of 320 W/cm (peak) with sodium inlet/outlet temperatures of 350/445°C for most part of their residence time. The higher LHR (400 W/cm) of 105 GWd/t FSA led to higher center line temperatures resulting in higher fuel swelling and this corroborates well with the higher stack length increase at comparable

burnup. With increase in the sodium inlet/outlet temperatures to 380/485°C, the mid-wall temperatures of clad and wrapper seen by 105 GWd/t FSA is 25-30°C higher compared to the earlier irradiations. The closeness of the operating temperatures to peak swelling temperature of SS316 has resulted in higher levels of dilations in wrapper and fuel pins of 105 GWd/t FSA, compared to those measured for earlier FSAs at similar burnup/dpa levels.

It can also be seen from Table 1 that the dimensional changes in the fuel, clad and wrapper of 105 GWd/t (400 W/cm) are very close to that of 155 GWd/t (320 W/cm) data, signifying higher levels of damage in the 105 GWd/t FSA.

The results of NDE on wrapper and fuel pins enabled the selection of fuel pins and wrapper locations for detailed destructive examinations viz. swelling measurements, fission gas release, microstructural examinations and mechanical property evaluation.

I.03 Upgradation of Computerized Online Work Permit Management System of FBTR

Computerized Work Permit Management System (CWPMS) is an online plant management system. CWPMS streamlines the operation and maintenance, health physics and industrial safety activities of FBTR. This system is used to control and execute any work to be performed in FBTR and designed to ensure that work is accomplished as per FBTR protection code safely and efficiently. In FBTR, activities like preventive maintenance, breakdown maintenance and surveillance checks on various safety systems are carried out as per AERB guidelines. CWPMS is used to execute plant maintenance activities with clear authorization and enable the user agencies to plan and execute the works in a safe manner. The salient features of the system are:

- i. Provides information about the ongoing jobs to the authorized persons.
- ii. Ensures that standard and approved safe practices are followed at various stages of work execution.
- iii. Maintains history of the maintenance works carried out on any equipment.
- iv. Enables planning periodic maintenance programs in an effective manner.
- v. Features a single source of reliable maintenance information, improved decision making, better resource utilization and reduction of paperwork.
- vi. Generates daily, weekly, monthly, quarterly and yearly reports as per user's request.

Upgradation of this system has been carried out by Central Data Processing Section (CDPS) to replace the current working system mainly to improve the features based on experience feedback and eliminate bugs and deficiencies noticed in the existing system. CWPMS is a client server based online web application system. It

has been built with Apache, Jboss and MySQL server (Fig.1). The Model View Controller software design approach has been used for the development. The web development tools like Java servlet, JSP, Jscript and Spring framework were used.

It has a main server with Network Attached Storage for data archival with an offline backup server (Fig.2). The client software being browser-based, any user on the FBTR LAN having valid username and password can use the system. Client system in FBTR Main Control Room is facilitated with Red Label Tag and Jumper Tag printer to enable control room personnel to take printout similar to the earlier paper-based work permit system. Following are the major modifications carried out:

- i. New sections are introduced in report page for Industrial Safety Permit, Expiry Permit and Welding and Cutting Permit.
 - ii. Auto logout and prevention of multiple logins into the system is introduced.
 - iii. Permit log and validity check for permit is implemented.
 - iv. Approval for applying the permit for preventive maintenance/surveillance works, breakdown maintenance works and system deficiencies.
 - v. Features like inter-agency transfer with mail communication, export reports in excel format, expiry and renewal of permit, comment box for mentioning reason for surrendering and suspending a permit are provided.
- After upgradation and testing in lab, a working group was constituted involving all the agencies for rigorous testing of the system by creating dummy permits from raising to clearing involving all combinations and ensured that it has been implemented as per the FBTR protection code. After getting clearance from the working group, CWPMS 2.0 was deployed in FBTR for regular use and the performance was found to be satisfactory.

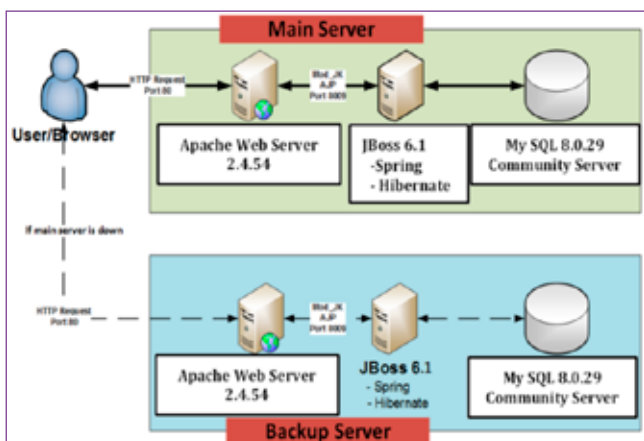


Fig.1: CWPMS Architecture

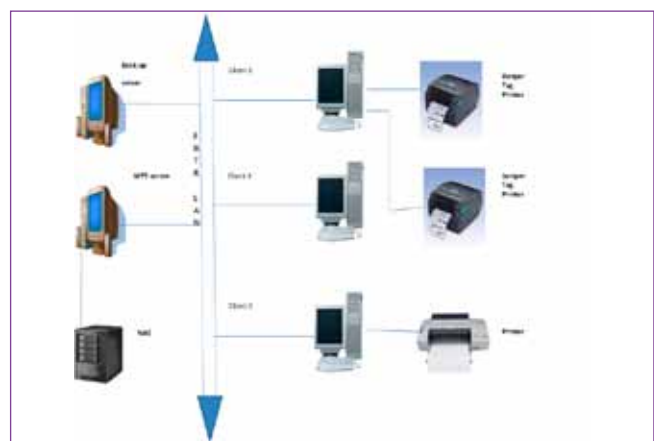


Fig.2: CWPMS with Clients PC

I.04 Installation and Commissioning of Portal Monitor for Active Areas of FBTR

Portal monitors are instruments used for measurement of external personal contamination. A portal monitor was installed for monitoring personal contamination at the exit of active areas in FBTR. This monitor helps to prevent the spread of contamination as per radiological protection procedure of FBTR.

Portal monitor is capable of simultaneously measuring beta and gamma contamination. The total whole body surface including hands, head and feet is measured with 25 segments of large plastic scintillation detectors. It has salient features like (1) Large area scintillation proportional counter with mylar film and protective grille is used as detector (2) Automatically adjustable overhead detector from 160 cm to 210 cm. (3) Quick Scan technology to reduce counting time (4) Measurement of calculation time as per ISO 11929 (5) Negligible dead zones between individual detectors (6) Detection coverage area of 21500 cm² (7) Robust stainless-steel housing (8) It has user screens and voice prompts (9) Easy maintenance with sophisticated detectors plug-in system and (10) Complies with the requirement of international standard IEC 61098.

For effective control of spreading of contamination from active areas to inactive areas in FBTR, structural layout of active building change room was altered. Turnstile gate was installed at the entry point of the active areas of FBTR as shown in Fig.1. All plant personnel going to

active area shall go through a turnstile gate which has one-way entry. Portal monitor was installed at the exit of active areas as shown in Fig. 2. All personnel coming out of active areas shall pass through the portal monitor. Entry to portal monitor is always open. Once a person enters inside and positioned properly, the monitor scans the whole body of the person automatically in front side. A voice message will guide the person to turn to backside for further counting. If counts are within limits, exit door will open automatically with a voice message, else the exit door will not open and person has to report to Shift Health Physicist for further assistance.

Detectors are provided with thin layer of Mylar film which is prone for damage. Hence, an additional protective polythene layer over the Mylar film was attached to prevent damage to the film and detector. The presence of additional protective layer will slightly increase the minimum detectable level (MDL). The attenuation of beta contamination due to the polythene sheet has been studied using beta source Pb210-Bi210 in a GM counting system. Maximum reduction in efficiency is 49%. With the additional protective layer, estimated MDL value for the counting duration of 10 s is 0.34 Bq/cm² which is 4.4 times lower than the minimum AERB-Derived Working Level of 1.5 Bq/cm². All the functional checks on the portal monitor were completed and the monitor was put in service for regular use. Performance of the portal monitor has been found to be satisfactory.



Fig.1: One way entry through turnstile gate to active areas of FBTR



Fig.2: One way exit through portal whole body contamination monitor from active areas of FBTR

I. 05 Replacement of Water Sub-headers of Steam Generators of FBTR

Steam Generator (SG) of FBTR is once through shell and tube type counter flow heat exchanger that generates superheated steam at 125 kg/cm² and 480°C. There are two SG modules in each east and west secondary sodium loops. Out of the total four modules, three modules are made of 2.25Cr-1Mo-Nb stabilized ferritic steel and one module is made of 9Cr-1Mo-Nb stabilized ferritic steel. In each SG module, sodium flows through shell and water/steam flows through the tube.

During 25th irradiation campaign, it was observed that orifice assembly of Tube-E in one east SG module (SGna 500B) had fallen due to stress corrosion cracking (SCC). SCC occurred because of residual tensile stresses developed due to geometrical constraint against thermal shrinkage during welding of orifice holder tube and orifice assembly. The existing water sub-headers of three SG modules have welded type orifice assemblies made up of SS 316 and are susceptible for premature failure due to SCC. The SG module made up of 9Cr-1Mo-Nb stabilized ferritic steel has bayonet type orifice assembly which is also likely to dislocate from its position due to depressurization cycles. Hence, it was decided to replace all existing water sub-headers with newly fabricated water sub-headers made up of Alloy 800 as it is a superior material compared to SS 316. All works related to water sub-header replacement was carried out inside SG casing itself. This work was taken up prior to 31st irradiation campaign.

Before starting the replacement work, welding procedure sequence and welder performance qualification were carried out for meeting FBTR specifications. As FBTR steam generator modules were fabricated with different materials for steam header and water

header of individual modules, separate procedure and performance qualifications were carried out.

After successfully completing the qualification requirement, mock-up trials were conducted for weld configurations simulating the congested locations to obtain experience by the working personnel.

After successful completion of mock-up trials, cutting locations were marked in the water sub-headers and tubes and then they were cut (Fig. 1) after obtaining clearance from Quality Assurance authorities. Water sub-headers of all the four SG modules were cut and replaced one after another.

Gas Tungsten Arc Welding (GTAW) process with argon gas purging was used for welding. Every day, before commencing the actual job, trial pieces were welded to establish consistent performance of welders. Tube internal areas were inspected visually with videoscope before fit-up and weld edges were also inspected visually to avoid any abnormalities before fit-up. Liquid Penetrant Test (LPT) was carried out on weld edges to detect any surface defect.

In SGna 500B, the blanked Tube-D was made through at both water and steam headers and expansion bend segment of Tube-E at water header was also normalized. After successful completion of all the welding works (Fig.2&3), Post Weld Heat Treatment (PWHT), LPT, Radiography Test (RT) and Helium Leak Test (HLT) were carried out for all the weld joints. Finally, hydro testing of SG at 135 bar was carried out and all weld joints were qualified successfully.

After replacement of SG water headers, reactor was operated at 40 MWt in 31st irradiation campaign.



Fig. 1: Cut and Removed Water Sub-headers

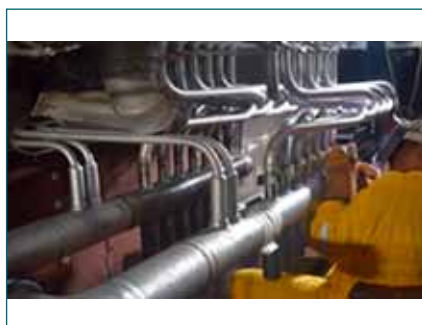


Fig.2: Fit-up and Welding of Water Sub-headers



Fig.3: After replacement of Water Sub-headers

I.06 Manufacture of Inlet Water Sub-Headers for FBTR Steam Generator Module

Central Workshop Division (CWD) was entrusted to manufacture modified inlet water sub-header of the steam generator module of Fast Breeder Test Reactor [FBTR] to replace the existing water sub headers with modified ones having integrated type orifice assembly made of Alloy 800 which is having better resistance to stress corrosion cracking (SCC). The existing water sub headers of SG modules in FBTR have welded type orifice assembly made of SS316 and are susceptible for premature failure due to SCC. The overall size of the inlet water sub- header is outside diameter 114.3 mm x length 981.2 mm. Carbon steel pipe (SA106 Gr.B) is used for sub-header and each sub-header houses seven numbers of orifice assemblies (Alloy 800) connected to the steam generator module to facilitate the controlled flow of water at the inlet.

Precision Machining of Orifice Assembly Components

Pre-machining of the orifice assembly components (Ni-Fe-Cr alloy 800), keeping allowance for final machining was done in the CNC lathe to achieve the specified dimensional and surface roughness tolerances in accordance with IS:2102 (Fig.1). Cubic Boron Nitride (CBN) cutting tool inserts were used for machining the super alloy parts with average cutting speed limited to 250m/min, feed rate 0.2mm/rev and dept of cut 1mm in order to prevent the early tool failure and work hardening tendency. Fig. 2 shows all machined parts for 7 sub-headers.

The propensity of potential adhesion between the cutting tool and alloy 800 was decreased by ensuring the supply of copious amount of coolant at the cutting tool-job interface. Also the built up edge tendency was



Fig.1: Precisely machined components of modified orifice assemblies



Fig.2: Gas tungsten arc welding of orifice assemblies

tackled using chip breakers. Geometrical tolerances, which are critical to maintain the concentricity during fit-up, were maintained.

Assembly, Welding and Final Machining of Orifice Assembly

The orifice assembly consists of orifice holder, flow breaker, orifice and porous end cap. These precisely machined components were butt welded using gas tungsten arc welding (GTAW) process with inconel 82 filler wire and were subjected to Liquid Penetrant Testing (LPT) at root and final passes. Thermal straightening / heat correction, an established distortion correction technique, was done to control/correct the inevitable geometrical deviations caused due to the concentrated heat of multiple welds. The normal elastic spring-back would allow the component to assume its correct geometrical shape. The stresses generated thereby will pull the component into the required shape. Local heating is, therefore, a relatively simple but effective means of correcting welding distortion. Shrinkage level is determined by size, number, location and temperature of the heated zones.

This technique needs considerable skill to avoid damaging the component. All the butt weld joints



Fig. 3: DMW joint (Carbon Steel and Alloy 800)



Fig. 4: Bandsaw cutting of DMW joint



Fig. 5: Sectioned view of DMW joint



Fig.6: Hydro testing (at 250 kg/cm²) of fabricated inlet water sub-header

were subjected to 100% radiography testing. Final machining of orifice assemblies was carried out in the CNC machining centres. Fig. 3 shows the welded orifice assemblies.

Qualification of Dissimilar Weld (DMW) at Nozzle joint

Mock-up welding of the final weld joint simulating the actual weld configuration was carried out and examined by sectioning the welded components. To qualify the dissimilar fillet weld between the alloy 800 orifice assembly and the inlet water sub-header pipe (ASTM A106 Gr.B), a mock-up welding of orifice assembly to a short length sub-header pipe was carried out followed by band-saw cutting of a 90° segment to inspect/visualize the weld joint penetration and thus qualified the dissimilar fillet weld joint. Figures 4 and 5 show the band-saw cutting process and sectioned view of DMW joint respectively.

Helium Leak Testing

The fabricated sub-header with modified nickel base super alloy 600 orifice assemblies were subjected to helium leak testing prior to hydro testing to overcome the issue of complete draining of water residues which will hinder the HLT process, if present. HLT was conducted under vacuum as per ASME section V article 10, and the leak rate was less than 6.6x10⁻⁸ std cc/s.

Hydro Testing

Hydro testing of the fabricated inlet water sub-header

to the test pressure of 250 kg/cm² (1.25 times of design pressure multiplied by least stress ratio) was carried out as per the approved procedure in accordance with UG-99 of ASME Section VIII Division 1 to validate the integrity of weld joints. De-mineralized water is filled in the sub-header and pressurized using a single acting reciprocating type hand pump. Two calibrated pressure gauges were used (Fig. 6,7).

inlet water sub-header

Finished and integrated water sub-headers of FBTR steam generator are shown in Fig. 8 and Fig. 9 respectively.

WPS, PQR & WPQ were developed for the similar and dissimilar welding of sub-header to ensure sound weld joints and also for the increased productivity. The sub-header was successfully fabricated meeting all the manufacturing and NDT specifications. All the weld joints were subjected each pass liquid penetrant inspection. A close control of overall dimensions and minimum distortion was achieved by proper adoption of weld joint design, joint edge preparation and the application of appropriate welding technique. It is imperative to mention that this challenging orifice assemblies modification work carried out with the approval of various high level monitoring committees aided in the operation of FBTR at its design power of 40 MWt. These inlet-water sub-headers are fabricated in accordance with ASME Code section VIII Division 1.



Fig.7: Nitrogen Gas Filling in fabricated sub-header

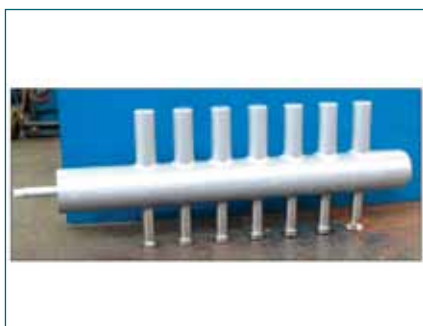
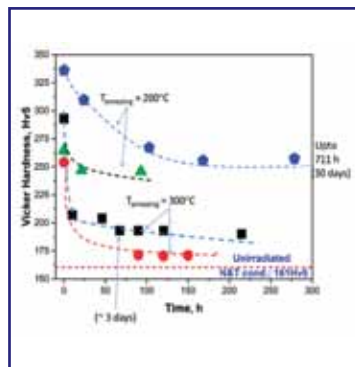
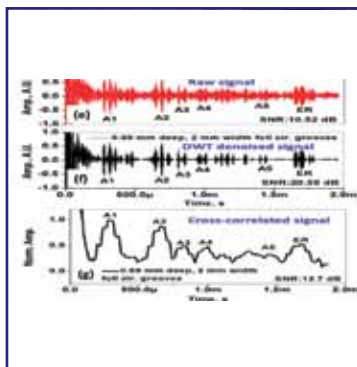
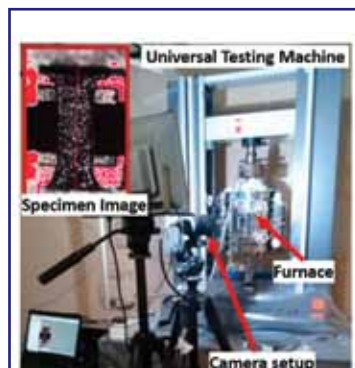


Fig. 8: Inlet water sub-header with modified orifice assemblies



Fig. 9: Inlet water sub-header welded to FBTR SG module



CHAPTER II

Prototype Fast Breeder Reactor

II.01 PFBR Commissioning Status

Prototype Fast Breeder Reactor (PFBR) at Kalpakkam is a 500 MWe (1250 MWt) liquid sodium cooled, pool type fast reactor using mixed oxide of uranium and plutonium as fuel. The plant is located 500 m south of the existing Madras Atomic Power Station. After completion of manufacture, construction, & erection of all the structures, systems & components of PFBR, commissioning of the individual systems and the integrated commissioning is in progress. Figure 1 shows the overall view of PFBR. The major works that have been completed during the year 2022 are as follows:

The design modification of Dummy Subassemblies and buffing of 7 Nos of grid plate sleeves had been done. Guide machining, sharp edge correction, boroscope inspection and dummy foot gauge checking were completed for ~724 subassemblies in a phased manner. The sub-assemblies were reloaded back in respective core positions after Quality Assurance checks.

High temperature testing (~120 deg C) of In-Service Inspection (DISHA) vehicle with all Ultrasonic Examination & Eddy Current Testing probes at Site Assembly Shop was completed. Demonstration of handling DISHA in emergency conditions has been completed.

Demonstration of deployment of ISI vehicle (DISHA), in the interspace region between SV & MV, Movement of DISHA in the clockwise and counter clockwise direction in the interspace region, auto scanning for Eddy Current Test & Ultrasonic Test were carried out on the dissimilar weld joint in the roof slab.

Refurbishment works on Control Safety Rod Drive Mechanism (CSRDM) were completed and further testing and Qualification were completed.

Site validation as part of Independent Verification & Validation has been completed for sodium system and safety related auxiliary systems

Design improvements and Flow balancing were completed for wall penetration cooling system in SGB-1 and 2.

Fissile Zone Identification Detector (FIZID) commissioning with new Cadmium Zinc Telluride (CZT) detector was completed and its performance tested successfully.

The final phase of cleaning of the main vessel hot pool was carried out.

During cold pool inspection, a breach in integrity of IHX-1 (NE) was identified and IHX-1 replacement is in progress.



Fig. 1: Overall view of Nuclear Island and Site Assembly Shop

II.02 Assessment of irradiation Damage of MAPS-1 End Shield using Surveillance Specimens

ASTMA203D (Fe-3.5%Ni ferritic steel) is the material of Calandria Side Tube Sheet (CSTS) of end shield assembly of Madras Atomic Power Station-1 (MAPS-1), Kalpakkam. Towards monitoring the changes in the mechanical properties of the end shield material caused by neutron irradiation, surveillance coupons in the form of pre-fabricated half size Charpy V Notch specimens (HCVN: 55 mm x 10 mm x 5 mm) of the steel irradiated in optical sight plugs of MAPS-1 reactor were retrieved and tested. The surveillance specimens were exposed to a cumulative neutron fluence of 2.49×10^{19} n/cm² (E > 1 MeV) over a period of 18 effective full power years at a temperature of ~70°C.

Instrumented impact testing was carried out as per ASTM E23 on six nos, of HCVN specimens at temperatures of 50-175°C to evaluate the shift in ductile-to-brittle transition temperature (DBTT). Post test shear lip measurements using a dial gage setup and % shear area measurement using an optical camera were carried out. As the surveillance specimens were radioactive, the impact tests were conducted remotely with local lead shielding and by employing multiple enclosures with dynamic ventilation around the machine to minimize the dose to operators and avoid spread of contamination.

The measurements of impact energy, % shear area and lateral expansion revealed brittle mode of failure for temperatures of 50-100°C, and ductile failure mode at 175°C. The results of impact test indicated shift of DBTT of the steel in between 100-175°C from the un-irradiated value of -86°C (Fig.1).

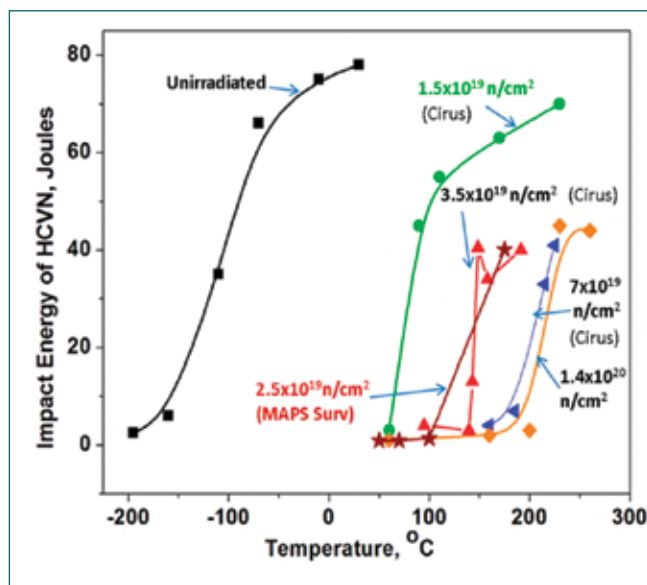


Fig. 1: Impact test results of MAPS surveillance coupons plotted along with previous results from accelerated irradiations performed in Cirrus.

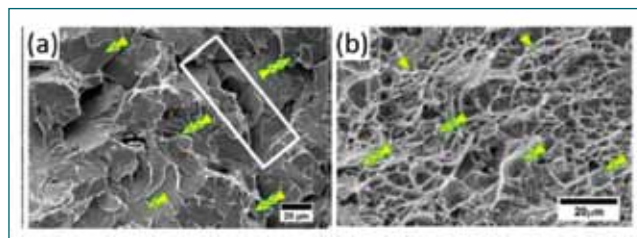


Fig. 2 SEM fractographs of Charpy specimens tested at (a) 100°C and (b) 175°C *Ductile regime/tearing, cleavage facets, and microcrack are marked in figure as single, double and triple arrow respectively. Region inside rectangular box shows secondary crack

Fracture surface features examined and quantified in Scanning Electron Microscope (SEM) revealed brittle features with estimated ductile to brittle ratio of 5:95 for test temperature of 100°C and ductile fracture mode (90-10 ratio of ductile-brittle) at 175°C, in line with the impact test results (Fig. 2).

With the objective of determining the tensile properties viz. yield strength, ultimate tensile strength and elongation of the irradiated steel, miniature tensile specimens were fabricated from broken CVN specimens by slicing 12x5x1 mm³ blank using diamond wire saw and then punching out a tensile profile having 3.0 mm gage length, 1.5 mm gage width and 1.0 mm thickness. The tensile testing of this miniature specimen geometry

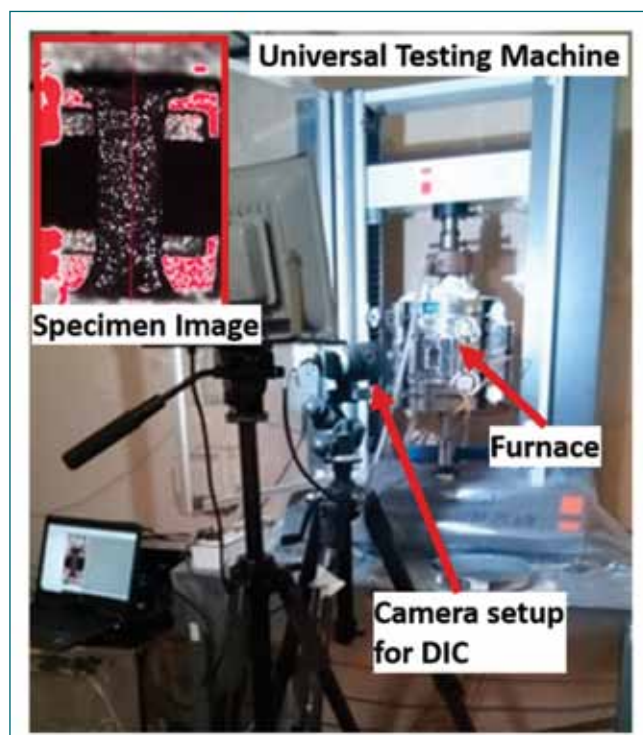


Fig. 3 : A view of the universal testing machine with DIC setup (inset shows the speckled image of specimen captured by camera for strain measurement by DIC)

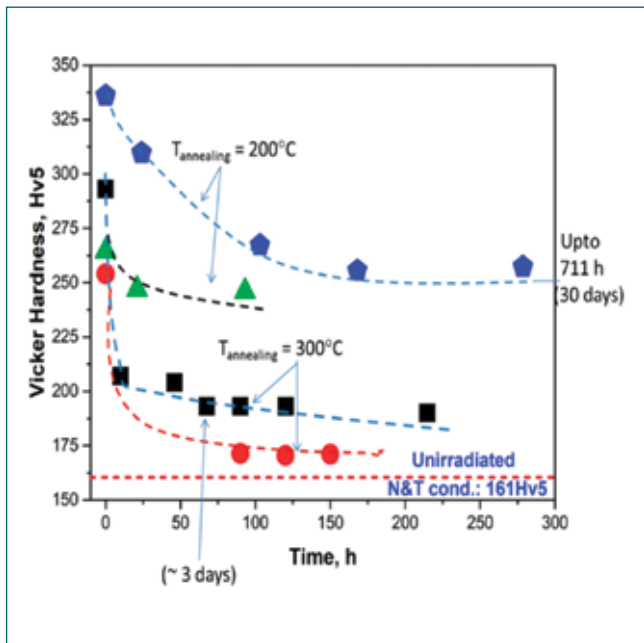


Fig. 4: Reduction of hardness of irradiated Fe-3.5% Ni steel after annealing treatments

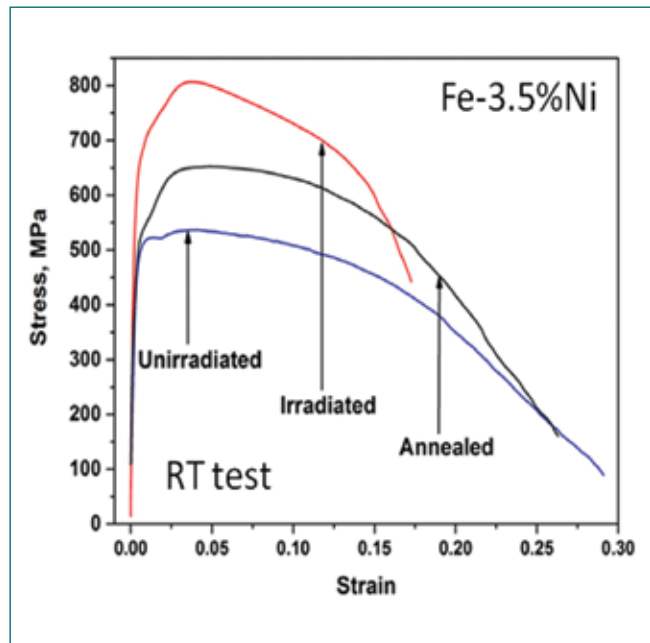


Fig. 5: Reduction of hardness of irradiated Fe-3.5% Ni steel after annealing treatments

has been standardized and benchmarked with ASTM standard specimen tests. Tensile tests were carried out at ambient, 50°C, 70°C, and 175°C in a universal testing machine fitted with a resistance heating furnace. Digital Image correlation (DIC) was employed at ambient as well as high temperature for accurate strain measurement owing to the small size of the tensile specimen (Fig. 2). Tensile properties indicated significant hardening of irradiated steel at all test temperatures, the extent of hardening decreasing with increasing test temperature. The uniform elongation had almost dropped by 70-90% of the unirradiated value, caused by the loss of work hardening capability of the steel.

One way to reverse the embrittling effects of neutron irradiation is to anneal the steel to restore the toughness properties. Small specimens of the irradiated steel were subjected to annealing treatments at 200°C and 300°C using an electric resistance furnace.

The annealing treatments were interrupted at regular intervals, for hardness measurement, followed by reloading and continuation of the annealing. The

recovery in mechanical properties were analysed by Vickers hardness at 5kg load. On annealing at 200°C, the reduction of the hardening saturates at 40% after 168hrs, while annealing at 300°C resulted in almost 90% reduction of hardening after 70hrs (Fig. 4).

Tensile test performed using miniature specimens prepared from annealed condition (300°C for 70 hours) revealed reduction of irradiation induced hardening and recovery of ductility to almost 95% of the unirradiated condition (Fig. 5).

The fractographs of tensile fracture surfaces examined under SEM revealed ductile features post annealing, similar to that of unirradiated condition corroborating the results of hardness measurements and tensile test (Fig. 6). Based on these results, the feasibility of in-situ annealing of the MAPS-1 end shield is being explored by NPCIL. The results of various investigations performed on irradiated surveillance coupons of Fe-3.5%Ni end shield material will serve towards life extension of MAPS-1 and RAPS-2 reactors of the stage 1 of Indian nuclear programme.

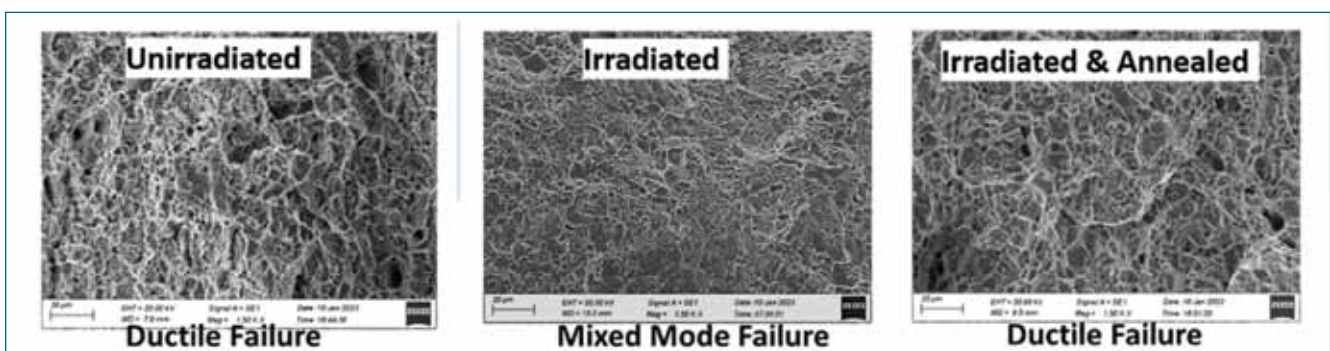


Fig. 6: SEM images of tensile tested fracture surfaces of different conditions of Fe-3.5%Ni steel

II.03 Design and Development of a Magnetostriction Transducer for Couplant Free Ultrasonic Guided Wave Based Inspection of Steam Generator Tubes of PFBR

Steam generator (SG) tubes are one of the critical components in PFBR and are made of Mod. 9Cr-1Mo ferritic steel. Hot liquid sodium flows on the outside while water flows inside the SG tubes for steam generation. Compromise on the integrity of the tubes

might lead to highly exothermic sodium-water reaction. As a result, high pressure waves and corrosive products are formed from this reaction, which may pose a threat to the structural integrity of the entire component. Hence, it is vital to ensure that the tubes are defect-free. To this

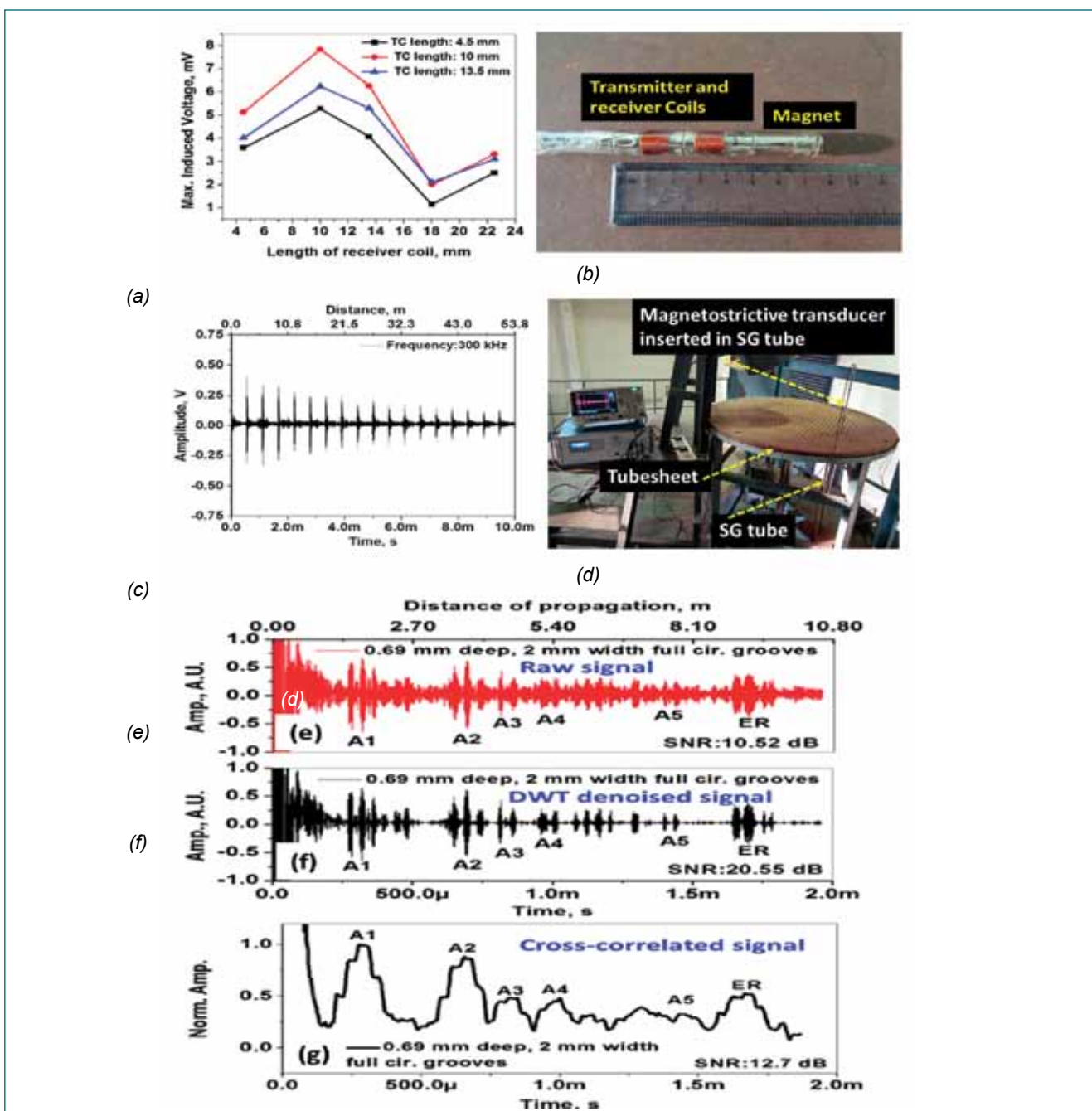


Fig. 1: (a) Maximum induced voltage in the receiver coil for different transmitter and receiver coil lengths obtained in FE model, (b) Photograph of the developed in-bore magnetostrictive transducer, (c) Experimental signal, showing multiple end reflections, obtained in a 1.5 m long tube at 300 kHz, (d) Photograph of experimental setup at RHS SG test facility, (e) Raw experimental signal obtained in a 5.5 m long SG tube welded to tubesheet with circumferential defects (A1-A5) of depth 0.69 mm (30% wall thickness), (f) DWT de-noised signal and (g) Cross-correlated signal

aim, Remote Field Eddy Current Testing (RFECT) has been identified for the evaluation of the integrity of SG tubes. However, RFEC inspection is time consuming, as it demands scanning point-by-point across the entire tube length of 23 m using an RFECT probe (from tube ID).

To overcome this limitation, an in-bore magnetostrictive transducer was developed for the couplant-free inspection of SG tubes using longitudinal ultrasonic guided waves (L(0,2) mode). The inspection requires the transducer to be placed at one location on the ID of the tube to get complete information of the tube in a very short time. The transduction and reception involve coils wound over rod shaped permanent magnets. In order to optimize the coil parameters, axi-symmetric finite element models were developed in finite element (FE) simulation software COMSOL. The optimized length of the transmitter and the receiver coils was found out to be 10 mm (~half the wavelength) for the frequency of 300 kHz (Fig. 1a). FE models also revealed the generation, propagation and reception of L (0,2) modes in the frequency range of 250 kHz to 350 kHz. Based on this, an in-bore magnetostrictive transducer was developed (Fig. 1b). To ascertain the utility of the transducer in steam generator tubes for the long range testing, L(0,2)

mode at 300 kHz frequency is propagated in a 1.5 m long tube by inserting the transducer in the tube (Fig. 1c). The resulted multiple end reflections indicate that 23 m length of an SG tube can be inspected. Further to check the capability of defect detection, SG tube segments welded to a tubesheet were tested at SG test facility. The tubes are 5.5 m long with a thermal expansion bend. One of the tubes has five full circumferential defects (A1-A5) of depth 0.69 mm (30% of 2.3 mm wall thickness). Figure 1e shows the experimental raw signal obtained in the tube with the defects (A1-A5). Although all five defects are detected, there is a lot noise in the signal. In order to remove the noise, Discrete Wavelet Transform (DWT) was applied. Figure 1f shows the de-noised signal. In the de-noised signal, there is an improvement in the SNR of about 10 dB. Further, multiple echoes (Fig. 1e&f) caused by bidirectional propagation of guided waves may cause confusion in interpretation. In order to clear this, cross-correlation technique was applied to the signal. Figure 1g shows the cross-correlated signal in which there are only five peaks indicating five defects. The developed ultrasonic guided wave inspection methodology is fast and reliable in detecting defects with the required sensitivity and has potential to be deployed in actual SG tube inspection.

II.04 Modification of Application Software for Sodium Instrumentation Systems of PFBR

The Sodium instrumentation systems of PFBR comprising of Continuous Level Probe electronics (CLPE), Discrete Level Probe Electronics (DLPE), Sodium Aerosol Detector Electronics (SADE) and Mutual Inductance type Leak Detector Electronics (MILDE) are Computer based systems. The sodium electronics are stand alone system but MILDE is interfaced with Distributed Digital Control System (DDCS). This technology was developed in-house at IGCAR and the supply, installation and commissioning were originally carried out by M/s. ECIL. In order to meet the SG D-25 guidelines, the installed application software of all sodium systems have to be modified to incorporate Self-diagnosis features, such as Input signal validation, Output signal validation, Cyclic Redundancy check (CRC), Software hang detection by Watch Dog Timer (WDT), etc.

In this regard, the application softwares for sodium systems were modified to implement input signal validation (input open / short / out of range detection) before performing data processing, so that the microcontroller performs its intended functions on valid inputs only. Output signal validation (output open / short detection) was incorporated in all sodium systems to monitor the accuracy of the driven outputs, such as primary excitation current, high excitation voltage, etc. CRC and WDT features were introduced in the

application softwares for sodium systems to periodically monitor the system integrity of program and data memories, and to detect software hang conditions respectively. These features are demonstrated using instrumented code.

Additional improvements were made in CLPE and DLPE softwares to improve the Master-Slave communication protocol, so that errors due to disruption of ongoing communication by any new interrupt is avoided. Relevant changes in HMI menus and level processing functions were made in the application software of CLPE and DLPE to accommodate categorization of level measuring systems as Fill type and Drain type system. Increased testability range for In-situ testing and driving of failsafe outputs on failure of a leak detector module were also incorporated in the application software of MILDE units.

The modified softwares were tested on sample sodium electronics units in Lab and validated by the Independent Validation and Verification team. These units were installed in the sodium facility at Hall-III and in Sodium Facility for Component Testing (SFCT) for Burn-in stability testing for a period of 168 h and its performance was found to be very good. Modification of application software of all 182 nos. of sodium electronics units of PFBR was completed. Fig. 1 shows the test setup for validation testing of CLPE and MILDE.



Fig. 1: Validation testing of comprising of Continuous Level Probe electronics (CLPE) and Mutual Inductance type Leak Detector Electronics (MILDE) at Lab

II.05 Qualification and Deployment of Dissimilar Weld Inspection Device (DISHA) in PFBR

In-Service Inspection (ISI) of PFBR reactor vessel is essential to assure its integrity throughout the lifetime of the reactor. One of the critical welds – the dissimilar weld between roof slab shell and main vessel is mandatory to be inspected periodically as part of ISI. Its inaccessibility and operation in high temperature environment required development of a remotely controlled robotic vehicle - DISHA to perform the inspection. DISHA is designed to move around the roof slab on the anti-convection barrier (ACB) and is equipped with Visual Inspection (VI) camera, Ultrasonic Testing (UT) and Eddy Current Testing (ECT) transducers for inspection of the dissimilar weld. DISHA is deployed by a cable take-up/release system (CTS) from the operating floor. DISHA is designed to be deployed through each of the six ISI ports to complete the inspection of the entire circumference of the dissimilar weld.

Testing and Qualification of DISHA with high sensitivity UT probes was done initially at room temperature in the mock-up test facility. Following the room temperature tests, DISHA with high sensitivity UT probes was tested at 120°C continuously for 24 hours and performance of the device was demonstrated with the functioning of visual inspection and UT systems. Further, handling of DISHA under a set of anticipated emergency scenarios such as traction motor failure, lighting failure and pneumatic line failure, was tested and demonstrated in the mock-up. In addition, a new ACB plug amenable for DISHA movement on ACB was fabricated and tested for remote handling using a special-purpose gripper. The remote handling of the ACB plug was also qualified in the dedicated mock-up.

Following the successful RT & HT qualification, DISHA



Fig.2 DISHA with CTS at 152° ISI port location in reactor

with CTS and control panel were installed at EL 38 m in reactor. Firstly, the new ACB plug (Fig.1) was inserted through the 152° ISI duct / port from EL 31.5 m in to the ACB port using the special-purpose gripper.

After, pre-deployment checks and UT calibration, DISHA was successfully deployed for the first time in the reactor vault through the 152° ISI port (Fig.2) at room temperature and air atmosphere and placed over the newly installed ACB plug. After HOMING operation, DISHA was steered / controlled 1.2 m clockwise from the ACB port and 1.7 m counter clockwise from the ACB port. The video from the on-board cameras was continuously recorded in the digital video recorder (DVR) in the control panel. Fig. 3 shows the dissimilar weld seen by VI camera. The performance of DISHA has been satisfactory and very good as per the design intent. For the first time, remote ultrasonic testing of the dissimilar weld was conducted with UT couplant circulation system, in reactor and inspection data have been acquired successfully. DISHA was then successfully retrieved safely back. Deployment, landing over ACB plug, wheel open/close, curvilinear traction, visual inspection, navigation functions, ultrasonic testing and retrieval have been performed satisfactorily as per the design intent.



Fig.1: New ACB Plug Deployed in the 152° ACB port seen by the on-board camera



Fig.3: Dissimilar weld seen by visual inspection camera (VIC)

II.06 Technology Development for Real Time Temperature Sensing of PFBR Periscope Xenon Lamp at High Voltage and High Temperature Environment

PFBR periscope as shown in Fig.1 is one of the vital ISI devices to be installed in the In-Vessel Transfer Port (IVTP) for viewing the reactor cover gas region. Two nos of xenon lamps are housed at the bottom of the periscope system and the argon supply lines are routed from the top to cool the lamp. The design limit of surface temperature of Xenon lamp is 150°C. It was required to enhance the life of the Xenon lamp by improving the cooling geometry.

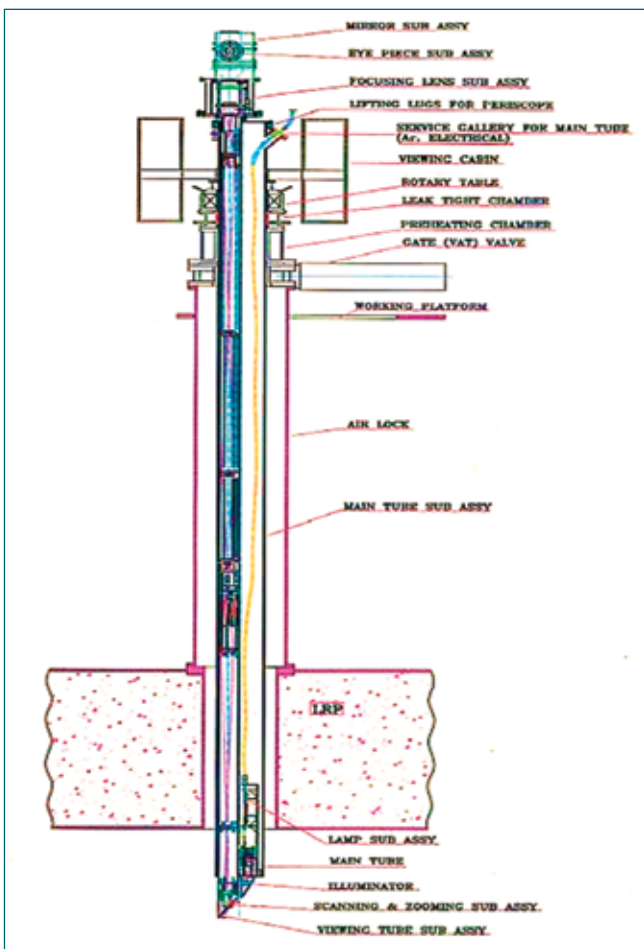


Fig. 1: Periscope layout

Further, it is most essential to accurately measure the lamp temperature in order to protect the lamp from failures. Technology development has been done to fix the RTD temperature sensor very close to the lamp by embedding the same into the heat fin as shown in Fig.2. However, the heat fin sees high temperature of the order of 120 to 150°C during operation and also very high voltage (24kV) during start up of the lamp. Hence the research focus is with the objective to have material of high electrical dielectric strength and very high thermal conductivity to encapsulate the sensor. The thickness of the encapsulating sheath was designed with a factor of safety by considering 30kV as the fin voltage during startup. Fig.3 and Fig.4 shows the test setup to qualify these sheath material for dielectric strength. Hence, initially encapsulated sheath was made of teflon material and later by improving on the machining process MACOR material (Machinable Ceramic Glass Rod) was used. This gives good thermal conductivity for enhancing the temperature sensitivity and good dielectric as well. Table.1 shows the properties of both the material. The sensor application is validated in a test set up as shown in Fig.5.

Table.1 Properties of Sheath material used for RTD		
Parameter	Teflon	MACOR
Thermal conductivity (W/m k)	0.25	1.4
Dielectric strength (kV/mm)	60	40
Machinability	Good	Poor
Radiation resistance	Poor	Good
Required Sheath thickness (based on temperature sensitivity)	0.25	0.75

Finally the developed temperature sensing is validated in the overall lamp test facility where the real time lamp temperature is plotted on a HMI screen.

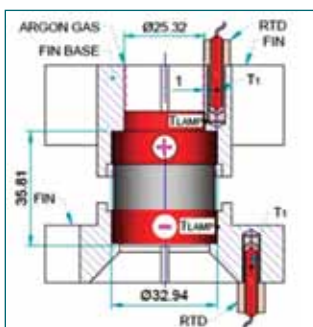


Fig. 2: RTD in Fin



Fig. 3: Testing of RTD sheath

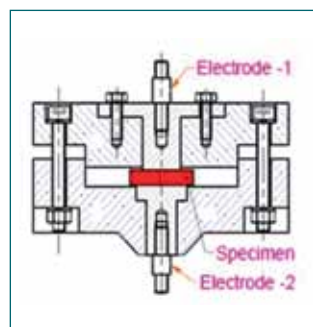


Fig. 4: Dielectric test setup



Fig. 5: Qualification setup

II.07 Seismic Qualification Test on Distributed Digital Control System Server and Data Exchange and Processing Unit for PFBR

Seismic qualification tests have been carried out for Distributed Digital Control System (DDCS) server and Data Exchange & Processing Unit (DEPU) housed individually in a cabinet along with dummy loads using 100 t shake table as shown in Fig-1. Even though both of these systems are classified as seismic category-2, it has been subjected to five Operating Basis Earthquake (OBE) and one Safe Shutdown Earthquake (SSE) for future reference. The Floor Response Spectra (FRS) corresponding to 38m Elevation of PFBR Control Building has been taken as Required Response Spectrum (RRS). Test Response Spectra (TRS) are generated such that

the TRS envelops the RRS in each direction for OBE and SSE. The assembled cabinet was mounted on the shake table and tested for design basis earthquake conditions as per IEEE-344 standard. Accelerometers and strain gauges are mounted at different locations to assess the dynamic amplification and structural integrity of the test equipment. Based on the observations from pre-test, intermediate-test and post-test inspections carried out, it can be stated that DDCS server and DEPU have met not only the required seismic criteria (SC-2) but also criteria for Seismic Category-1 components.

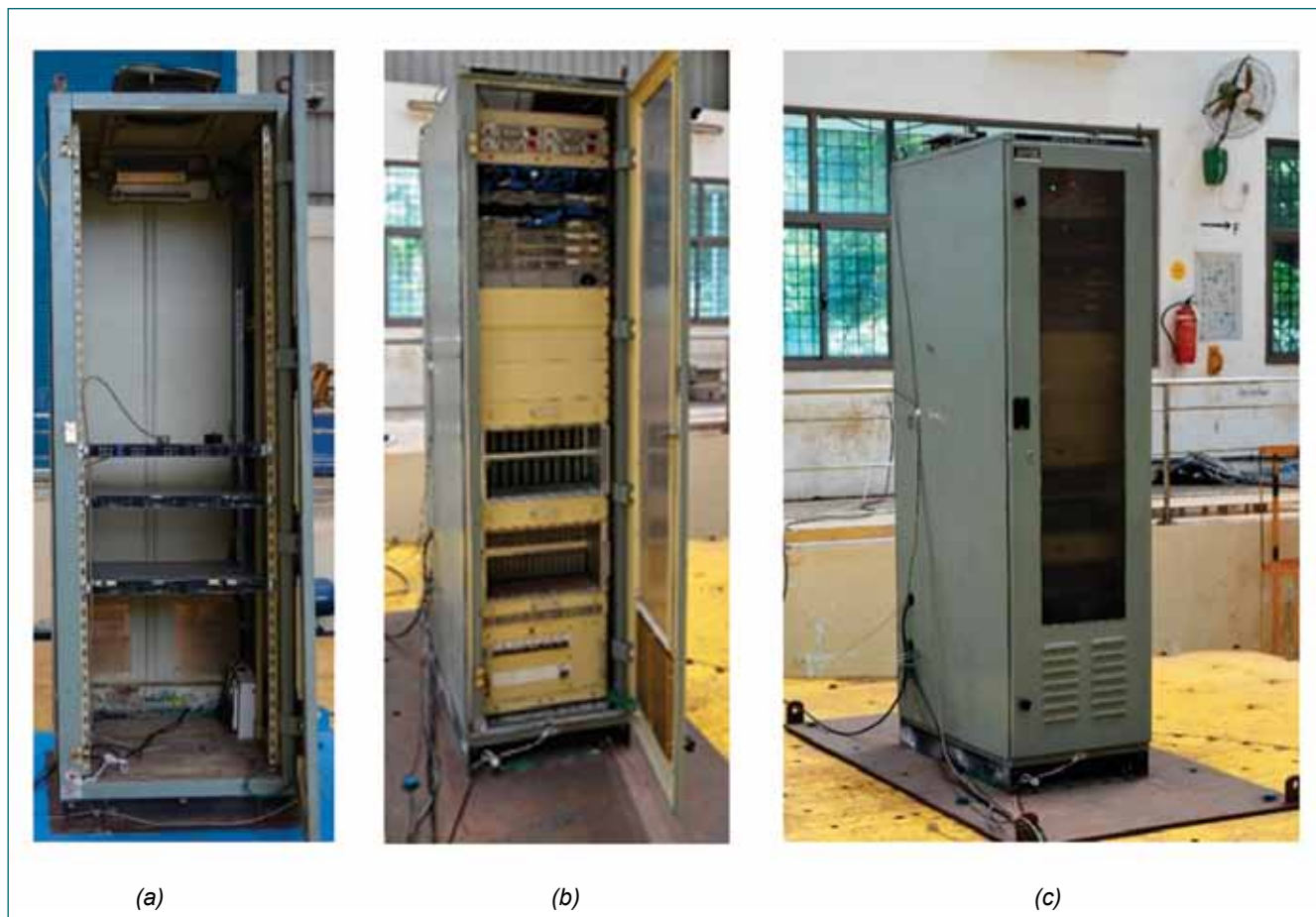


Fig 1: Cabinet mounted on the shake table (a) DDCS mounted inside cabinet , (b) DEPU mounted inside cabinet and (c) Cabinet mounted on the shake table

II.08 Effect of Radial Clearance at Discriminator Guide Location During Axial Flow Vibration of Core Subassembly in PFBR

The PFBR core comprises 1757 subassemblies (SA) of different kinds, such as fuel, blanket, and neutronic shielding. These SAs are free-standing hexagonal wrapper tubes containing tightly packed fuel pins. The internal coolant flows (~36 kg/s) from the bottom of the SA to the top, form a turbulent regime that may induce flow-induced vibrations (FIV). In this work, the axial flow-induced FIV with special emphasis on the influence of radial clearance on the dynamic behaviour of SA is studied. In the core, the SA rests on the grid plate sleeve at the top and is guided at the discriminator guide diameter at the bottom. The support at the top of the sleeve forms a line contact between SA and the sleeve. Then at the discriminator location, the radial clearance between the sleeve and SA varies between 30 μm minimum to 60 μm maximum, as per the original design. This clearance is proposed to be increased by 50-75 μm to improve the functional requirement of SA insertion. Hence two cases of radial clearances of 60 μm and 120 μm are studied.

This work aims to perform the transient dynamic analysis for SA under an equivalent load of internal axial flow. The effect of the radial clearance at the discriminator location is to be studied for its impacts on the dynamic behaviour of SA under resonance conditions. Since maintaining a precise clearance in the experimental setup (Fig.1) is challenging, the full-scale axial flow experiment is conducted with zero clearance conditions. Then the equivalent force from the experiment is applied

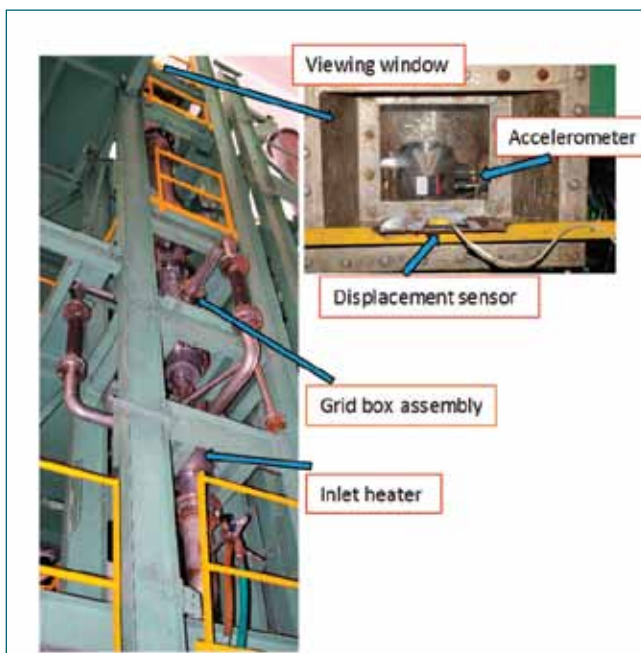


Fig. 1: Experimental setup

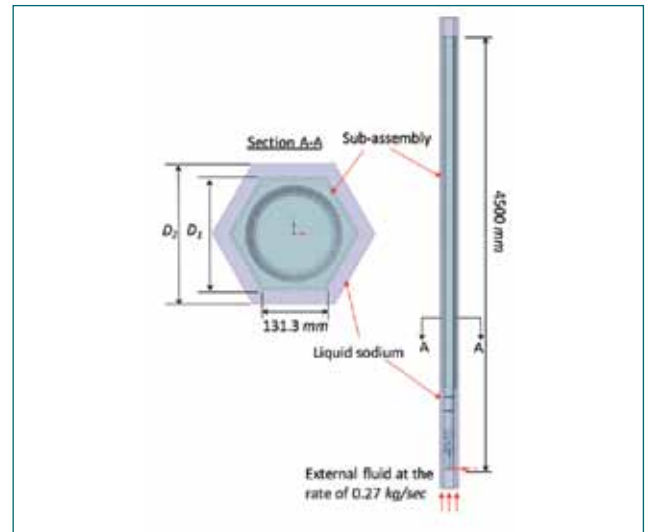


Fig. 2: Fluid-structure coupled model for FSI study

to the numerical model to study the clearance effect. In the axial flow experiment, the SA top displacement amplitudes are measured using a laser sensor and an accelerometer. The maximum displacement of SA with clearance is 0.38 mm for flow rate (Fr)=100% from the axial flow experiment. Furthermore, it is found that the displacement increases with the increasing flow rate. The dominant frequency during axial flow is found as 2.9 Hz.

After SA experiment, a numerical analysis of two-way coupled fluid-structure interaction (FSI) is performed to estimate the added mass and added damping properties for the immersed SA. As shown in Fig.2, a simplified SA model is used, and it is ensured that the SA model used is dynamically similar to the actual reactor SA, which means the mode number and mode shapes are similar to the actual SA for the first few modes. The added mass and added damping are calculated as 23 kg/m (or 103.74 kg) and 10.4%, respectively. And then, a numerical model is made with a nonlinear spring with a gap element to study the effect of clearance on the dynamic behaviour of SA for various damping ratios. The equivalent force from the experiment is applied to the numerical model to study the clearance effect. The SA is excited in its first mode fundamental frequency to obtain the maximum vibration. For full flow rate (i.e., 100% flow) and 60 μm radial clearance at the discriminator, it is seen that the top and bottom displacement of SA is 0.477 mm and 12.7 μm , respectively. It is found that the displacement response of SA increases with increasing radial clearance up to a few microns corresponding to the given force. Further increasing radial clearance is not affecting the response of SA.

II.09 Root Cause Analysis of Scoring on SA Hexcan & Higher Extraction Load Observed with Certain SAs in PFBR Dummy Core and Implementation of Solutions

During handling of dummy Subassemblies (SA) using Transfer Arm (TA) in PFBR core, it was observed that some of the SAs needed higher extraction loads to be removed from the core. Also, during the in-core inspection, scoring lines were observed on the SA hexcan surface. Hence, it was proposed to find the root cause for the occurrence of scoring on the SA hexcan faces and also for the higher extraction load on certain SAs in the core and to find the solutions to avoid it.

Root cause analysis for scratch/scoring marks on the SAs

Towards the root cause analysis of scoring marks on SAs, based on several studies & out-pile tests, it was concluded that the marks observed were caused due to interaction between the SAs, predominantly due to the offset handling nature of SA by TA and due to the presence of sharp corners & edges in the self-orientation features and in the guide lugs of the SA (Fig. 1). As a solution, it was recommended to smoothen the sharp corners/edges (in self-orientation feature of SA).

Root cause analysis of Higher Extraction Loads (HEL) in certain SAs

Visual examination of HEL SAs showed few scoring marks in the discriminator guide. Internal surface inspections of sleeves at HEL SAs using boroscope revealed few scoring marks in the hard-faced region. From inspection, it is evident that interactions between the foot and sleeve guides caused scoring on the foot. As the radial gaps are only ~ 30 microns, the scored

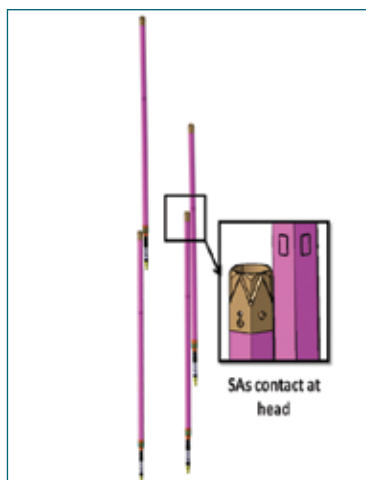


Fig. 1: SA interactions at the self-orientation features when handled by TA

material gets lodged in the radial gaps which causes further increase in extraction loads (Fig. 2). As a solution, it was recommended to increase the radial gap by 50 microns by machining of the guide portion of the foot and also to smoothen the vertical sharp edges

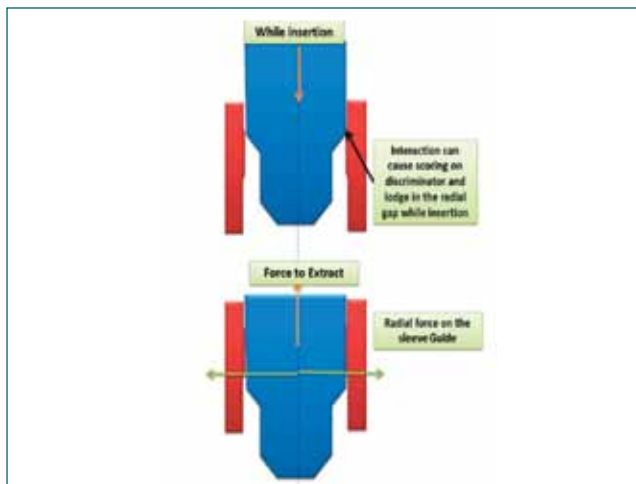


Fig. 2: Scenario of HEL in case of lower radial gaps

of the discriminator guide to R8 mm which will ensure smooth insertion and extraction of the SA.

Testing to confirm the modifications

In order to confirm the root causes, few SAs were smoothened i.e. sharp edges in the self-orientation features were smoothened and discriminator guide diameter was reduced by from 78.8e7 to 78.64 (0/+0.03) mm along with the smoothening of the six vertical edges (to radius R8 mm) in the guide and SA handling trails using transfer arm were carried out. Testing revealed that scoring has substantially reduced with modifications and also repeated handling of the SAs with modified guide diameter did not show any increase in the handling load, which confirms the effectiveness of the modifications.

Modification of all the dummy core SAs

The procedure for smoothening and guide machining was arrived at after several trials at IGCAR. After obtaining AERB clearance, modification works on all the dummy core SAs (724 nos.) were taken-up at PFBR site. The extraction of SAs, execution of modification works, inspection and re-installation were successfully completed with the total co-ordination among site execution team, QA, CWD and design team. In order to check the effectiveness of the modifications, several in-pile tests were carried out after completion of all the modifications on the SAs. The successful completion of tests also gave confidence that SA stuck conditions will not be repeated.

II.10 Estimation of Stability Domain in PFBR using Lyapunov Exponent Method

Lyapunov exponents (λ) are very useful tool for nonlinear stability assessment in a dynamical system. It characterizes the rate of separation of infinitesimally close trajectories and it can be estimated as

$$\lambda = \lim_{t \rightarrow \infty} \lim_{\delta Z_0 \rightarrow 0} \frac{1}{t} \ln \frac{|\delta Z(t)|}{|\delta Z_0|}$$

Here, δZ_0 is the difference between the two infinitely close initial points considered at time $t=0$ and $\delta Z(t)$ is the difference between the time evolved values of the dynamical variable after time t .

The Lyapunov exponent method is used to study the stability domains of PFBR in terms of reactivity feedback coefficients. The neutron dynamics in a fast reactor like PFBR can be represented with point kinetics equations along with reactivity feedback models. Doppler feedback, fuel axial expansion, core radial expansion and coolant expansion are the feedback effects considered in the analysis. These feedbacks are calculated using change in temperature of fuel, steel and sodium and the corresponding feedback coefficients. The heat transfer equations are solved to estimate the change in temperatures of fuel, clad and coolant. The numerical

solution of the governing equations is achieved using a computer program written in Python.

Two infinitely close points (reactor power) are taken as the initial points and the dynamical system is allowed to evolve in time. After a sufficiently long time the difference in the power corresponding to both the initial points are found out. Lyapunov exponent is calculated using the difference in power values at the beginning and end of time t . If the estimated value is negative, then the dynamical system is said to be a stable system. The stability domain plots are generated by varying any two reactivity coefficients simultaneously keeping other reactivity coefficients unchanged. The stability domain is estimated with respect to Doppler and fuel axial expansion coefficients and plotted in Fig. 1. The calculated values for PFBR (denoted as red dot in figure) is well within the stable domain. Figure 2 shows the domain of stability with respect to coolant expansion and core radial expansion feedback. Similar plots are made for other combinations of coefficients too. The analysis results show that the domain of stability for PFBR is vast and the operating point is well within the stable region. The margin to instability is minimum in case of Doppler, feedback coefficient which has to be negative all the time.

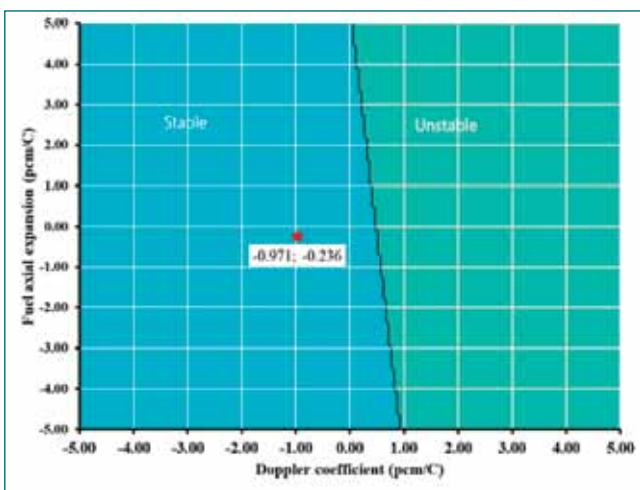


Fig. 1: Domain of stability with respect to Doppler and fuel axial expansion feedback coefficients

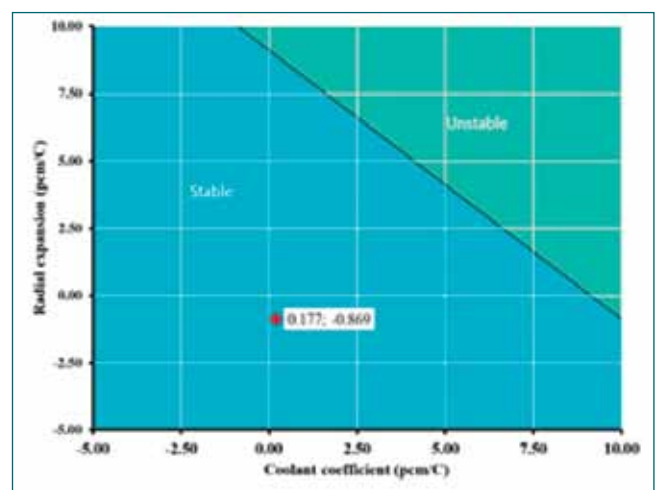


Fig. 2: Domain of stability with respect to coolant expansion and core radial expansion feedback coefficients

II.11 Sodium Calibration of Eddy Current Sensor for Core Flow Monitoring of Blanket & Storage Subassemblies

Core flow monitoring mechanism (CFMM) is used for measuring the sodium flow exiting from the core subassemblies (SA) during initial commissioning at selected locations and at selected blanket subassembly locations during refuelling shutdown. An Eddy Current Flow Sensor (ECFS) is used for measuring the sodium flow. Fig. 1 shows the photograph of ECFS used in CFMM. The operating range of the ECFS for CFMM is 0-5 m³/h. at 200°C. The ECFS was calibrated in sodium before assembling with CFMM. However, it was found that the ECFS was calibrated in higher flow range corresponding to fuel subassembly locations which is quite high compared to flow through blanket and storage subassemblies of PFBR. Hence, the flow sensor was re-calibrated for low flows, corresponding to its operating flow range of blanket and storage subassemblies.

The required low flow rates could not be achieved in the existing ECFS calibration loop of Steam generator test facility (SGTF) and hence a new sodium test section was added to Large components test rig (LCTR). The test section has provision for introduction of sensors with minor intervention and the geometric features identical to CFMM were simulated. Necessary features were added for preventing sodium leakage from the test section. The test section inlet is connected to the LCTR common outlet header and the outlet to LCTR common return line.



Fig. 1: Photograph of ECFS along with cable

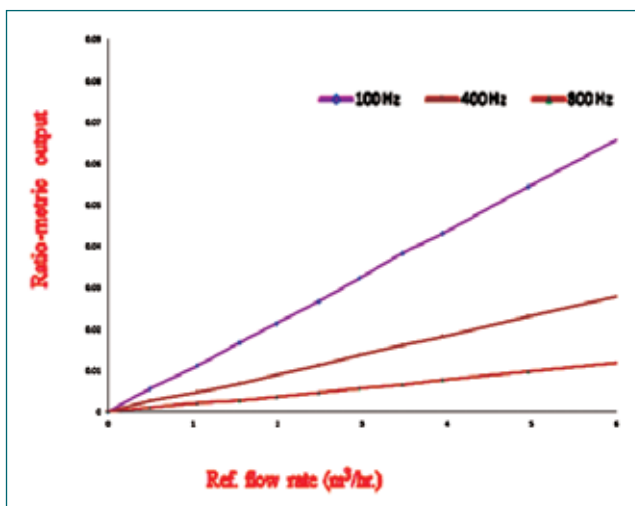


Fig. 2: Ratio-metric output of the sensor

Heaters and sodium leak detectors were provided on the pipe lines of the test section. A permanent magnet flow meter (PMFM) is provided and is used as reference flow meter for calibrating the CFMM. The reference PMFM was calibrated in Thermal shock test facility. Provisions were made for continuous monitoring of temperature and sodium flow rate in the test section.

Calibration was carried out for sodium flow rates from (0–7.6) m³/h. for three different frequencies (100 Hz, 400 Hz and 800 Hz) at sodium temperature of 200°C. The ratio-metric output of the sensor for different flow rates are shown in Fig. 2. It is seen that the sensor output is linear in the tested range of flow rates for the three frequencies. The sensitivity is found to be 0.011, 0.005 and 0.002 (mV/m³/h) at 100 Hz, 400 Hz and 800 Hz respectively.

The CFMM sensor is calibrated in sodium for the flow rates at blanket and storage subassemblies and the sensor output is found to be linear. The calibration has demonstrated the use of the ECFS for low flow rates in PFBR. Also, the testing demonstrated that CFMM can be used for measuring Blanket SA / Storage SA flow in PFBR, without any new modifications.

II.12 High Temperature Testing of Dismountable Type Ultrasonic Transducer

In PFBR, Under Sodium Ultrasonic Scanner (USUSS) is used prior to every fuel handling campaign to scan the core plenum region between control plug and core top to ensure that there is no protrusion of core subassemblies or any other items that hinders the plug rotation. The ultrasonic transducers (UT) of USUSS are welded with its transducer holder and Dismountable type UT was conceived to facilitate in-situ replacement of transducers used. Fig. 1 shows the assembly of dismountable type UT.

The dismountable type UT consists of two parts, namely - male part and female part as shown in Fig. 2. The male part comprises of MI cable, male lemo connector and their mounting arrangement. The female part comprises of UT (1MHz), female lemo connector and their mounting arrangement. One such dismountable type UT was fabricated, assembled and tested to study its feasibility of implementation in USUSS. After qualification of all weld joints of the fabricated transducer, the qualified transducer was put to test in water. Echo signal received during water experiment was found to be satisfactory. Later, high temperature testing of the transducer was conducted in silicone oil up to 225 °C in steps of 25 °C. Echo signal received during silicone oil experiment was found to be satisfactory.

Suitable sodium test vessel with required instrumentation was fabricated and qualified. UT along with SS target was

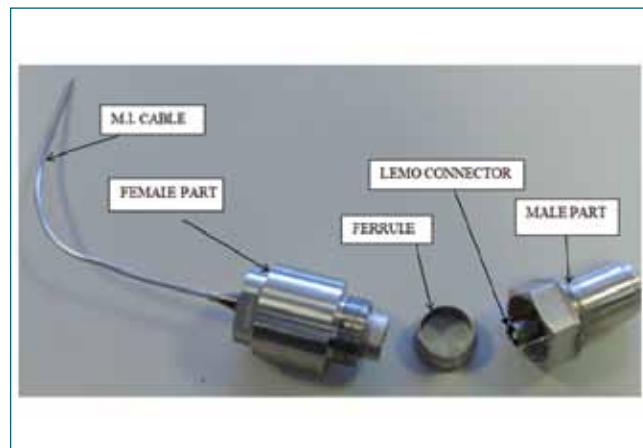


Fig. 2: Parts of Dismountable type ultrasonic transducers (UT)

installed in the vessel and Sodium at 120 °C was filled such that the UT was fully immersed in sodium. The temperature was raised in steps of 25 °C from 120 °C up to 225 °C, and echo signal at various intermediate sodium temperatures was monitored and recorded. The sodium temperature was maintained at 225 °C for a week to check the integrity of UT and healthy echo signal was observed throughout the experiment.

After sodium testing, the transducer was retrieved from the test vessel, cleaned and observed that there was no ingress of sodium in to the transducer assembly. The dismountable type transducer was tested and qualified in sodium up to temperatures of 225 °C.



Fig. 1: Dismountable type ultrasonic transducers (UT) assembly

II.13 Analysis of Pressure Transient in Secondary Sodium Circuit due to Pump Seizure in PFBR

Secondary sodium circuit in fast reactor transfers heat from reactor core to steam generator. Secondary sodium pump delivers the required flow in the circuit. During a pump seizure event, pump speed reduces sharply resulting in water hammer type pressure transient scenario in the circuit. Since, this is a design basis event, the circuit should withstand the peak pressures developed during the event. Further, this event should not lead to the opening of rupture discs provided in the circuit, which caters to the safety requirement during sodium-water reaction in steam generator.

Analysis is carried out in system dynamics code Flownex. A model is developed using various component models

available in the code. The model is validated against published experimental and theoretical benchmark results. Following the event, inlet pressure at pump increases and outlet pressure decreases (Fig. 1). Maximum pressures at the pump inlet is 546.6 kPa (abs). Maximum pressures at rupture disc location is 592 kPa (abs) which is well below the set pressure of rupture disc 1.1 MPa (abs). Thus, there is no risk of rupture disc breaking during the event. Maximum pressures estimated in the pipelines are within the design limit. A parametric study is carried out by varying the pump seizure time in the range of 1 to 0.1 s and it is seen that the maximum pressures are within the acceptable limits.

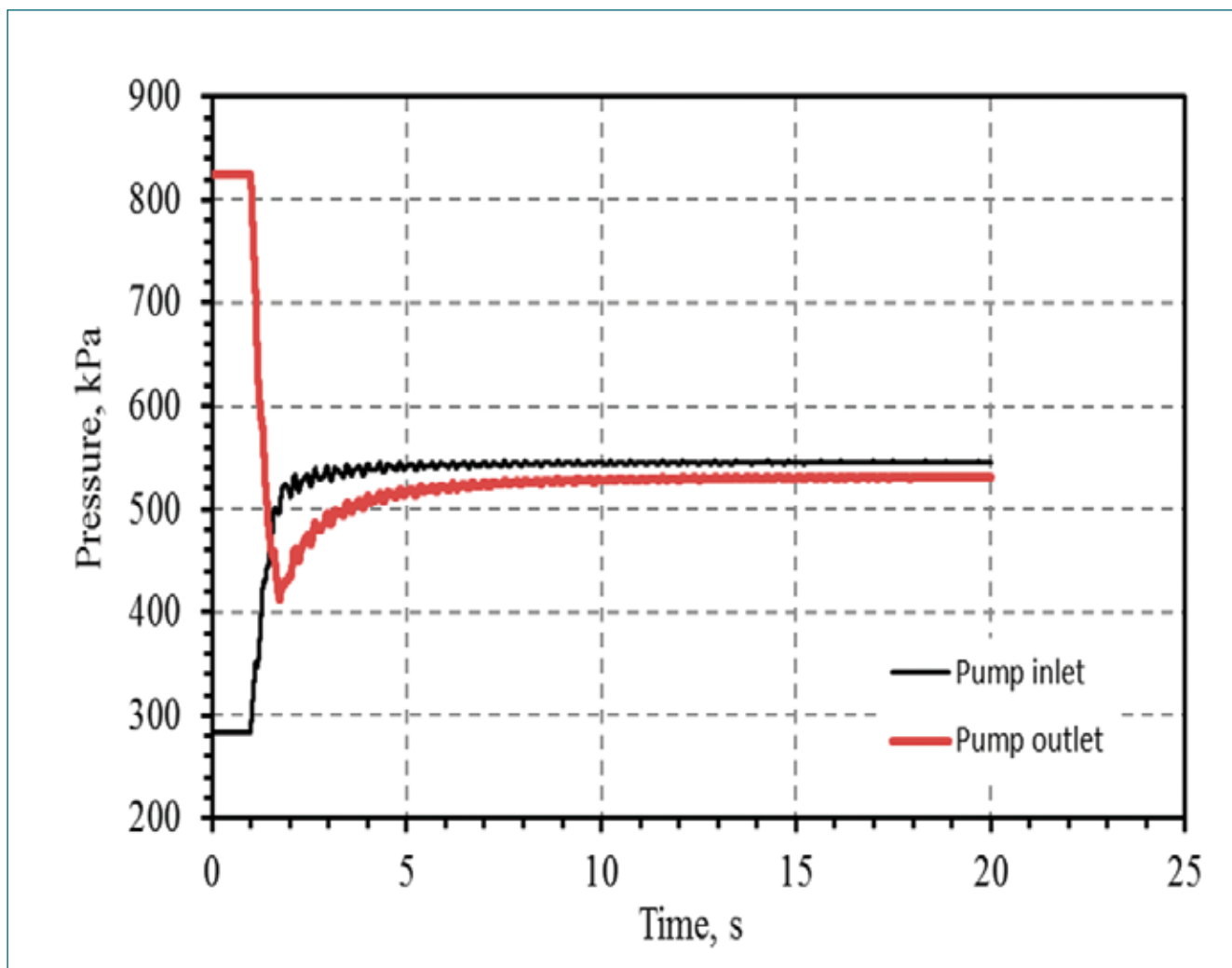


Fig. 1: Evolution of pump inlet and outlet pressure following pump seizure

II.14 Performance Evaluation of Flow Distribution Device for 170 m³/h Capacity ALIP

An annular Linear Induction Pump (ALIP) with 170 m³/h capacity is provided in secondary sodium circuit of PFBR. A Flow Distribution Device (FDD) has been designed to be inserted at the entry of ALIP in order to have uniform velocity distribution in the annular space. The non uniformity in velocity distribution may cause operational problems of ALIP. Accordingly, the FDD was designed and experimental study was carried out to evaluate the performance of FDD.

Experimental set up details:

Experimental studies are conducted in a full scale model of ALIP with water as stimulant in Engineering Hall II. The FDD was installed at the specified location inside ALIP. FDD is 45° conical porous shell. It consists of 88 numbers of holes of diameter 10 mm. Holes are positioned in such a way that uniform velocity is achieved in the annular zone. Details of the flow distribution device and schematic of FDD installation position in the EM pump is shown in Fig. 1.

Miniature size pitot tube developed for velocity measurement in the small annular zone is utilized for this experimental study. Three measurement planes are identified for velocity measurement in annular zone as shown in Fig. 1. In each plane, pitot tubes are installed at 6 positions along the circumferential direction at equal angular distance. Separate static tapping is provided for each plane in the set up. Differential pressure across pitot tube position and static tapping is measured

simultaneously for all 6 pitot tubes in each plane. Pressure drop across the model is also measured to understand pressure drop offered by the FDD.

Experimental study:

During experimental study, reading for each plane is measured separately i.e. initially at all 6 locations in Plane 1 are recorded simultaneously by isolating Plane 2 and Plane 3 tapings. Subsequently reading for Plane 2 and Plane 3 are acquired for each flow rate setting. Experimental studies are conducted at different flow rates (80-170 m³/h). Velocity measured by the pitot tube is normalized with respect to average velocity in the respective row. Maximum and minimum deviation from normalized velocity is tabulated in Table 1. Normalized velocity distribution is plotted against angular position of the duct in Fig. 2 and compared against measurement obtained without FDD. It is found that due to insertion of FDD, there is a good improvement in the uniformity of velocity distribution in the first row. However, there is marginal improvement in second row and almost no improvement in the third row. The pressure drop in ALIP suction (ALIP inlet – Annular inlet) increased by 18.65% at 120 m³/h flow rate due to FDD (i.e. from 35.13 KPa to 41.68 KPa). It is concluded that the present design of FDD is useful in order to have uniform velocity distribution in the entry region of the annular space of ALIP without much increase in pressure drop.

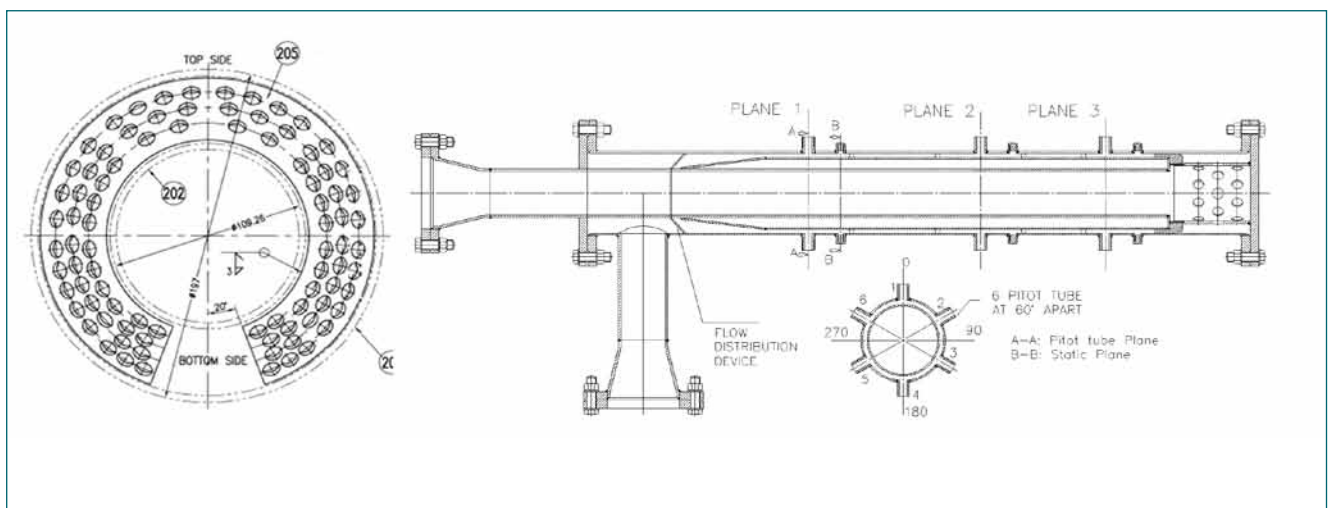


Fig. 1: ALIP test model with flow distribution device

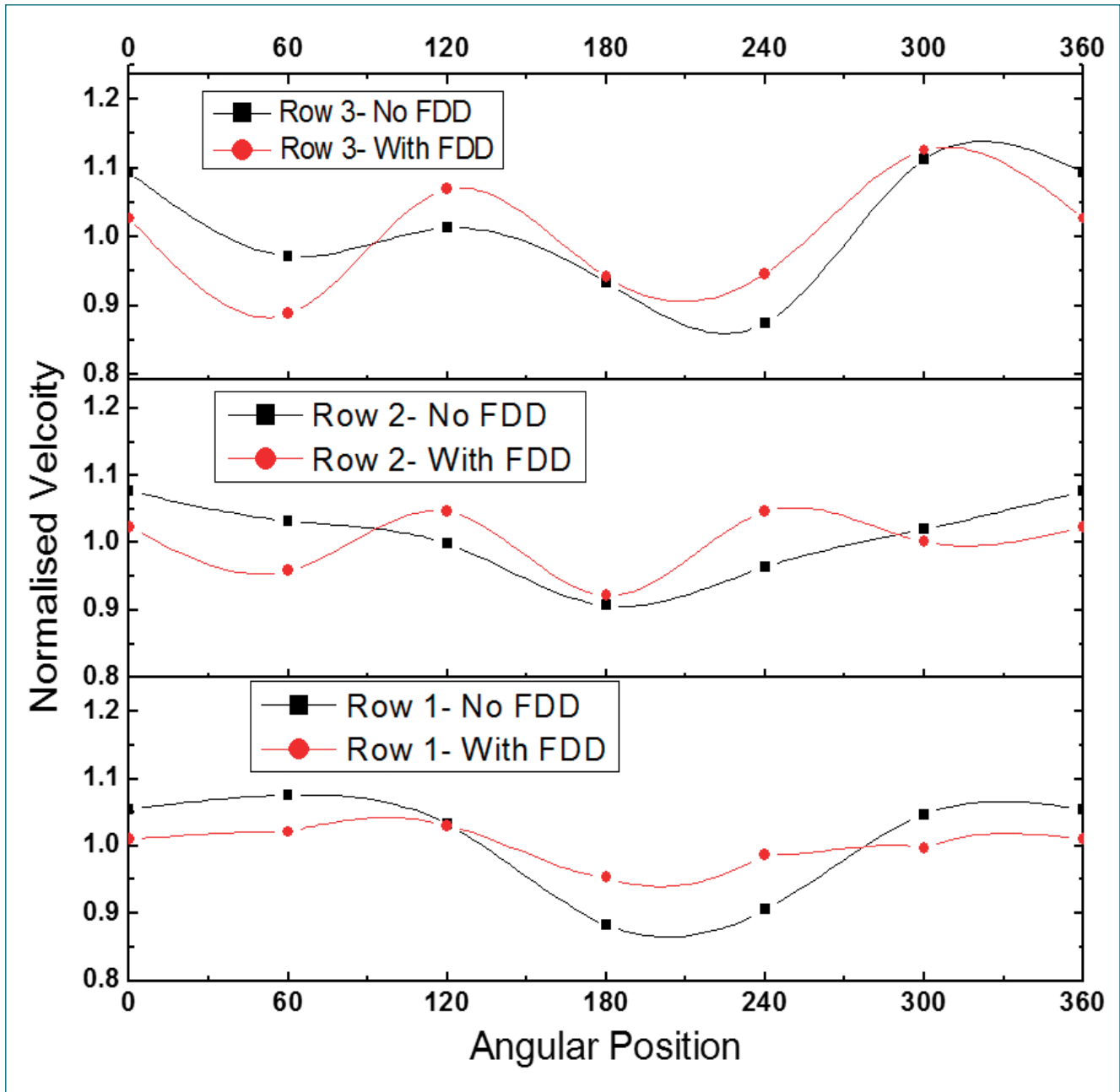


Fig. 2: Normalised velocity distribution Vs Pitot tube angular position at 120 m³/h flow rate.

Table 1: Deviation from mean at 120 m ³ /h flow rate							
Flow rate (m ³ /h)	Row	Without FDD (normalized velocity)			With FDD (Normalized velocity)		
		Max	Min	Total variation	Min	Max	Total variation
120	1	1.08	0.88	20%	1.03	0.95	8%
120	2	1.08	0.91	17%	1.05	0.92	13%
120	3	1.11	0.87	24%	1.13	0.89	24%

II.15 Performance Evaluation of Decay Heat Removal System for the Sodium to Sodium Decay Heat Exchanger Type-B

In PFBR, Safety Grade Decay Heat Removal system (SGDHR) is employed as a safety feature for removal of post shutdown decay in the case of non availability of Operational Grade Decay Heat Removal System (OGDHR). SGDHR system consists of four independent loops of 8 MWt individual heat removal capacities. Each loop consists of a sodium to sodium heat exchanger (DHX) immersed in the hot pool of reactor, secondary sodium loop, sodium to air heat exchanger (AHX), chimney which generates required air flow across the AHX tubes and air side isolation dampers. DHX picks up the decay heat from hot pool and transfer to secondary sodium loop which transfers the heat to AHX. The secondary sodium gets circulated by natural convection in loop due to the temperature difference in hot and cold legs of the loop. From AHX, the decay heat is released to atmospheric air as the ultimate heat sink. This system will be in poised state during nominal operating condition and it will be put on action against demand by opening air dampers.

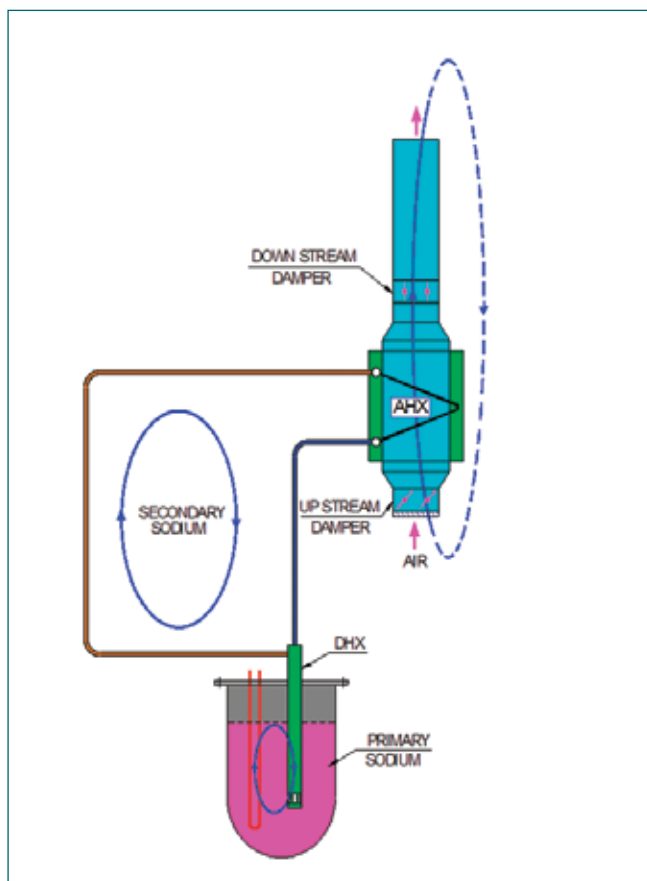


Fig. 1: Schematic of SADHANA facility

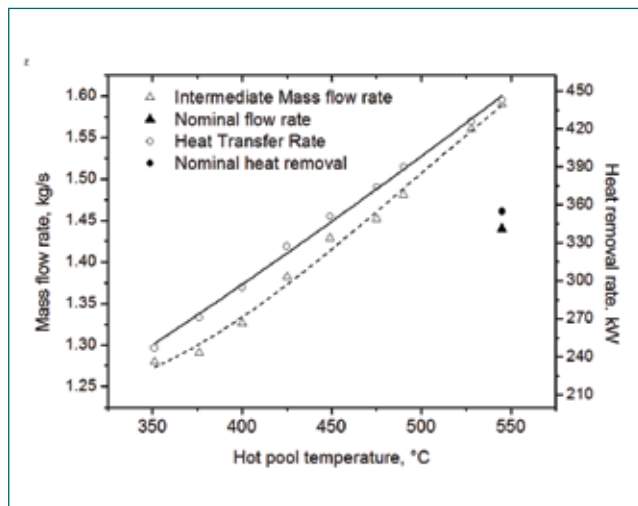


Fig. 2: Results of steady state experiments

Out of four independent loops of SGDHR system, two loops are of type A design and other two are of type B design. DHX type A is vertical counter-flow shell and tube heat exchanger consisting of straight tubes. DHX type B is vertical, U- tube shell and tube heat exchanger. AHX type A has sodium inlet and outlet headers which are connected by serpentine shaped finned tube bundle with four passes. AHX type B has ring type sodium headers which are connected by straight vertical finned tube bundle. The difference in design imparts diversity in the SGDHR system and avoids common cause failure.

To study the thermal hydraulic behavior of SGDHR of PFBR, a 1: 22 scaled down model in power by simulating Richardson number, SADHANA (SAfety Decay Heat removAl loop in NAtrium) was established in Engineering Hall-III, IGCAR. The schematic of the facility is shown in Fig 1. The nominal heat removal capacity of SADHANA loop is 355 kW. In SADHANA loop, hot pool is simulated by a test vessel. Sodium in the test vessel is heated by immersion electrical heaters. Various experiments were planned in the loop with different combination of DHX (type A & type B) and AHX (type A & type B). All experiments planned with combination of DHX type A and AHX type A were successfully carried out and the design of heat exchangers and loops were demonstrated and validated. Now the performance of DHX type B with combination of AHX type A in SADHANA has been experimentally demonstrated. This report brings out the results of the experiments conducted with DHX type B and AHX type A combination.

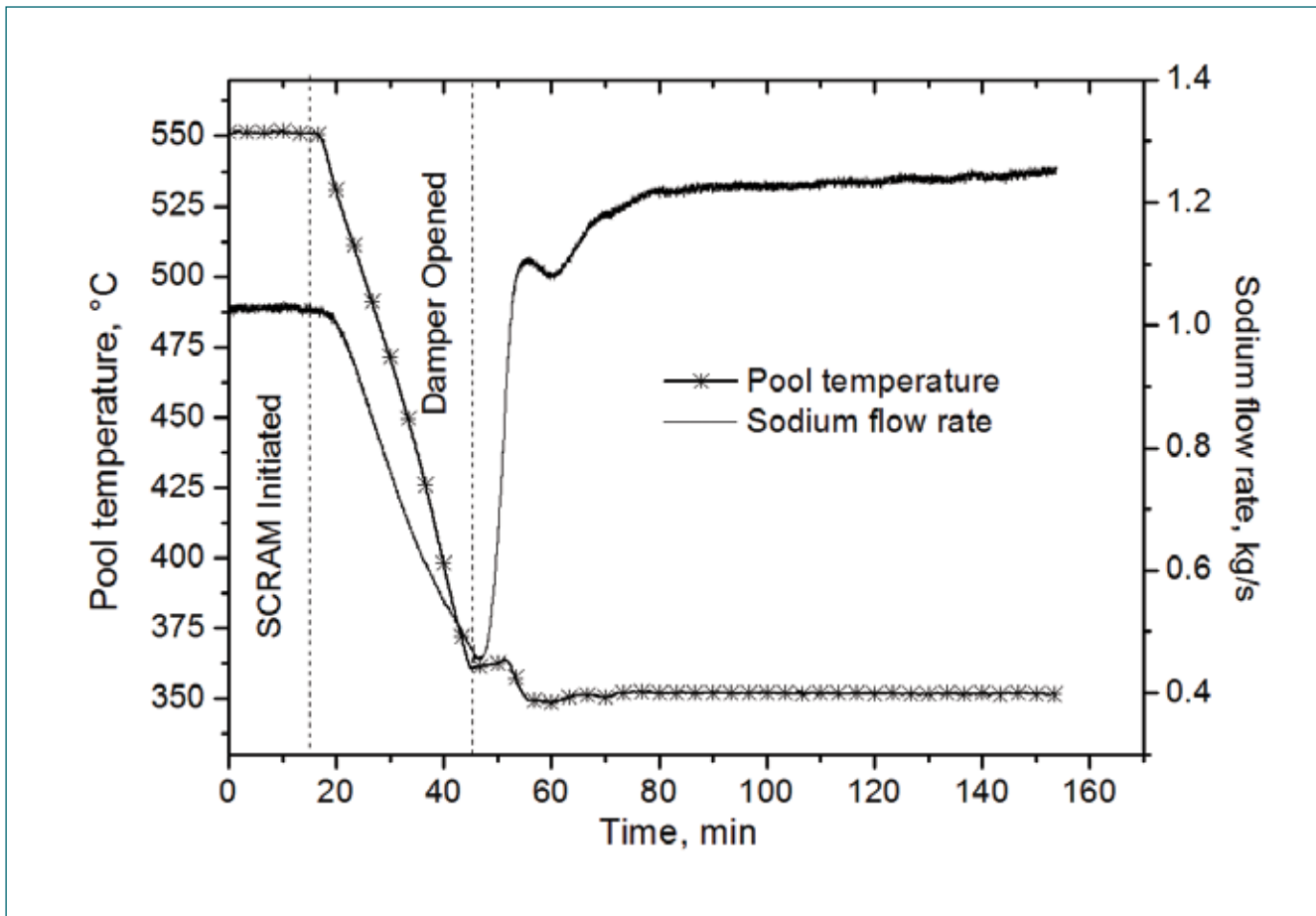


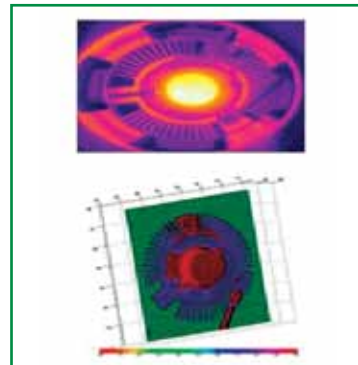
Fig. 3: Results of spurious SCRAM with delay of dampers opened

From the steady state experiments for various pool temperatures from 350°C to 547°C, the performance of the loop has been evaluated. The results of the steady state performance are shown in figure 2. At nominal operating condition, the loop could remove 443kW heat from the hot pool which is 24.7% higher than the design requirement (i.e 355 kW). The sodium flow in the secondary circuit is 1.59 kg/s which is 10.4% higher than design basis flow rate (i.e 1.44 kg/s). The higher heat transfer performance of the loop is due to margins provided in the design calculation. Thus design of heat exchangers and correlation used in heat transfer and pressure drop calculation are evaluated.

Among the plant transients in PFBR, Spurious SCRAM with both OGDHR and SGDHR functional event, gives maximum cooling rate to the hot pool. During this scenario, the hot pool temperature falls below the cold leg of the secondary circuit and hence there exists a possibility of reversal of the sodium flow direction in the secondary circuit which will affect the heat transfer performance of the system. The performance of

SADHANA facility with reversed flow condition also was studied for various hot pool temperatures. In reversed flow condition at nominal operating condition of hot pool, the loop could remove 250kW heat from the hot pool which is 43.6% lesser than the actual capacity. The sodium flow in the secondary circuit was 1.24 kg/s which is 22% lesser than actual flow rate.

Since the facility is not capable of exact simulation of reactor transients, the results of transient experiments will be used for validating the design tools used for SGDHR system of PFBR. The result of the spurious SCRAM experiment with delay of 30 minute damper opening is shown in Fig 3. During sudden fall of hot pool temperature, the secondary flow starts to reduce due to reduction of hot pool temperature and once the air dampers are opened, the flow rises and settles corresponding to pool temperature without any flow reversal and oscillation. Thus the stability of the SGDHR system for its heat transfer capability is established with these experiments.



CHAPTER III

R&D for Fast Breeder Reactors

III.01 High Temperature Oxidation Behavior of T91 Alloy

Ferritic-martensitic steels are extensively used in thermal and nuclear power plants due to their higher thermal conductivity and lesser thermal expansion coefficient. These alloys are used in high temperature environment prevailing in a nuclear reactor due to their excellent combination of strength, toughness, processability, heat transfer properties, high temperature creep resistance, and stress corrosion cracking resistance. T91 alloy (Ferritic-martensitic steel) is proposed as material of clad for metal fuel fast breeder reactors. The choice is based on the fact that it shows very low swelling (BCC structure) and minimum DBTT (Ductile Brittle Transition Temperature) shift. The possibility of oxidation of this alloy under the influence of high temperature and exposure time cannot be ruled out. The formation of oxide scale may increase the metal temperature and may lead to failure of tubes due to corrosion and creep. The study on the high temperature oxidation of this steel is useful in understanding the underlying mechanism of oxidation and for further improvement in the oxidation resistance of these materials.

The high temperature oxidation of T91 alloy was studied using thermogravimetry and differential thermal analyses technique in a TGA/ DSC 3+ thermogravimetric analyzer supplied by M/s. Mettler Toledo, Switzerland. The equipment had a mass sensitivity of 0.1 μ g and a temperature sensitivity of 0.01 K. It was calibrated using ICTAC recommended standards (In, Au & Pd). To carry out high temperature oxidation studies, oxidizing atmosphere was maintained during heating by a constant supply of oxygen gas (50 ml / min) in the close vicinity of the sample, the flow of the gas was controlled by mass flow controller. For a typical experiment ~ 5 mg of T91 alloy of 1 x 1 mm size was heated from 1073

to 1673 K by varying heating rate rates viz. 1, 3, 5 and 10K min⁻¹ in an alumina crucible of 70 μ l capacity. The thermogravimetry curve obtained for oxidation of T91 alloy is shown in Fig. 1. No significant mass change was observed upto 1123 K. Beyond this temperature slow oxidation was observed upto 1250 K. Rapid oxidation started after this temperature and it completed at 1650 K. The total mass gain during this oxidation reaction was found to be ~47%. Change in slope of the curve in temperature interval (1073 – 1673 K) showed the simultaneous oxidation of individual components of alloy T91. Alloy T91 (Fe-9Cr-MoVNb) contains 9% of chromium with major alloying elements Mo, V, and Nb. The change in slope of the curve is due to difference in the tendency of constituent elements to form oxide, which is decided by the standard Gibbs energy of formation of respective oxide and kinetics of the reaction.

The x-ray diffraction pattern of T91 alloy and the product of oxidation is shown in Fig. 2. Most of the peaks corresponds to the oxides of major constituents of the alloy T91 (Fe and Cr). Peaks pertaining to constituent elements were not observed in the oxidized product.

Isothermal experiments were carried out at four different temperatures viz. 1173, 1373, 1573 and 1773 K for 6 h. The percent mass gain during the isothermal experiment is given in Table 1. The extent of oxidation is a function of temperature and time of exposure.

Table 1: Mass (%) gain during isothermal experiments				
T/ K	1173 K	1373 K	1573 K	1773 K
Mass(%)	6.7	11.5	25.3	35.1

Further work to study the kinetics and mechanism of the reaction, and to study the variation of extent of reaction w.r.t. effective activation energy is in progress.

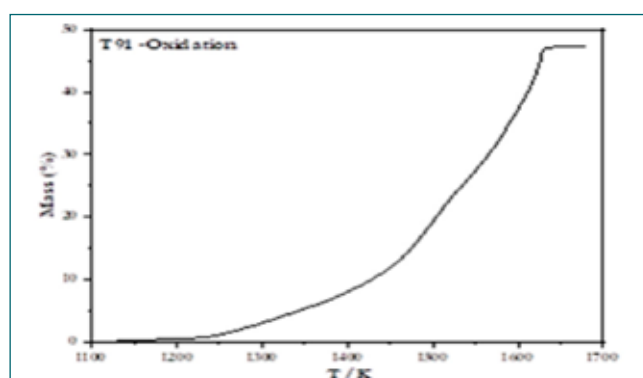


Fig. 1: Mass % vs. T oxidation of T91

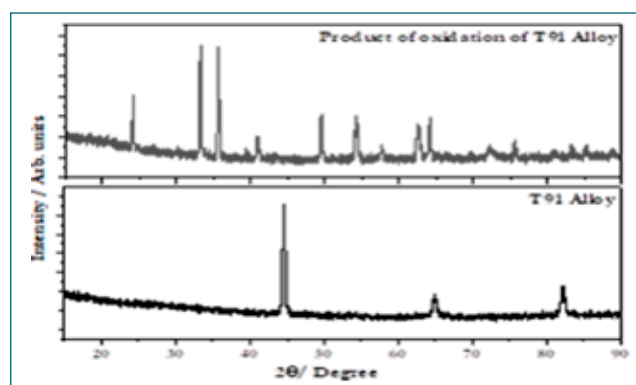


Fig. 2: Product of oxidation of T91 alloy (Top) & x-ray diffraction pattern of T91 alloy (Bottom)

III.02 Fabrication and Characterization of 170 nos. of U-6 wt. % Zr Slugs for DND Application

Calibrate the bulk DND system of PFBR, it was proposed to fabricate a DND SA (Mk-2) subassembly with 19 pins. Each pin will have 640 mm length of U-6wt.%Zr alloy slug. The total 640 mm length will be achieved by introducing 8 nos. of 80 mm length and 4.94 mm dia slugs. An engineering scale facility for the optimization of process parameters for preparation of UZr slugs by injection casting method was established in MC&MFCG (Fig. 1). The 10 kg capacity injection casting system was qualified for its functionality by casting copper slugs. Various process parameters viz. power of the induction heater, heating rate, purity of the glove box, vacuum inside the casting chamber, temperature of melting / casting, dwell time for molten alloy, casting pressure and time of casting were optimized in various campaigns to arrive at defect free U-Zr slugs.

Quartz tubes (500 mm length) coated (inner surface) with yttria (Fig. 2) were used as mould for injection casting. The process for coating inner surface of the quartz tube was developed and standardized. The in-house coated quartz tubes were used for casting of U-Zr slugs. Graphite crucible was used as container material for molten alloy. To avoid contamination of alloy with carbon these crucibles were also coated with yttria. The optimization of process parameters to get thin adherent coating on the inner surface of the graphite crucible was done by CSTD, MMG.

Casting of U-Zr slugs involved the following procedure: Blank experiments with yttria coated graphite crucible, i.e.



Fig. 3 Uranium metal after cleaning

without charge. Uranium metal was cleaned to remove oxide coating. The uranium metal pieces and zirconium metal sponge was used to prepare alloy. The procedure to clean uranium metal was standardized. A photo of cleaned uranium metal is shown in Fig. 3. Accurately weighed quantities of uranium and zirconium were taken in the coated graphite crucible and loaded in the injection casting chamber. To achieve the homogeneous mixing, melting was carried out at 1723 K. After completion of first melting the molten alloy was cooled and re-melted at the same temperature. Quartz moulds were lowered in the melt, the system was pressurized with UHP argon gas and slugs were cast. The cast U-6 wt.%Zr slug with coated quartz mould is shown in Fig. 4 and 5. Physical and chemical characterization of the U-6 wt.%Zr slugs was carried out to qualify the slugs. The dimensions and the weight of the slugs are given in the Table 1.



Fig. 1: Casting facility 10 kg capacity



Fig. 2: Quartz tube coated by newly developed and conventional study technique.



Fig. 4: Cast UZr alloy in Coated quartz mould

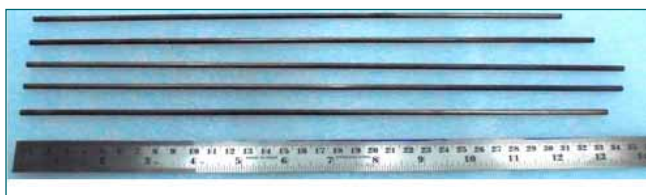


Fig. 5 Photograph of qualified U 6 Wt.% Zr alloy slug with coated mould.

Table 1: Characteristics of the injection cast slugs

Slug no.	Mass (g)	Length (mm)	Dia. (mm)	Density (g/cc)
1	101.63	309	4.97	16.8
2	73.20	227	4.91	16.9
3	113.06	345	4.94	17.0
4	118.69	360	4.94	17.1

The desired density of the slug was achieved in this process. The slugs were also characterized for their

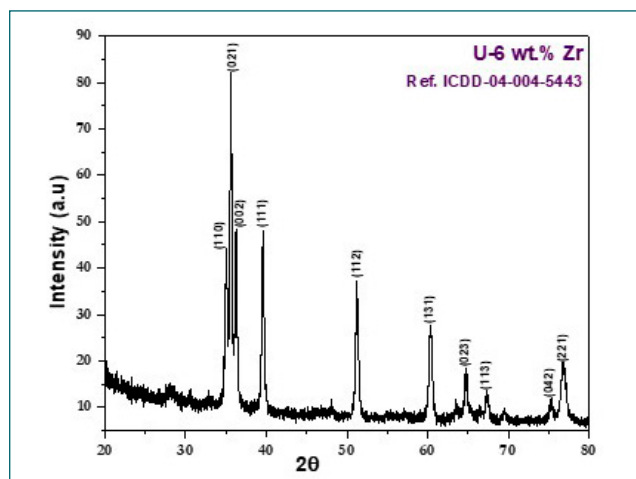


Fig. 6: X-ray diffraction pattern of the U-6 wt% Zr cast slug.

chemical composition (U, Zr, C, O, N) and phase (Fig. 6). The desired chemical composition, phase and microstructure was achieved for the cast alloy.

III.03 Commencement of Engineering Scale U Metal Electrorefining in PPRDF

Pyroprocess R&D Facility (PPRDF) has been set-up for scaled up studies on alloys of natural uranium at 10 kg per batch scale, so that experience will be generated for designing a Pyroprocess plant for spent metal fuel. In respect to this a major milestone on commencement of first engineering scale U metal electrorefining in PPRDF has been successfully completed with 4.6 kg Uranium deposit on solid cathode. The execution of first U-Electrorefining experiment was carried out in a planned manner with several major accomplishment of intermediate activities, such as, achieving leak tightness (0.1 vol% per h) and purity (O_2 & $H_2O < 50ppm$ each) in $500m^3$ containment box (CB) containing argon, transfer of 900kg of molten salt from

salt storage vessel to High Temperature ElectroRefiner (HTER) vessel & maintaining its temperature at $450^\circ C$, in-situ preparation of 2 wt% UCl_3 in molten salt, loading of 10 kg U metal into anode basket & remotely transferring it along with solid cathode into HTER vessel, commencement of electrorefining operation, remotely taking out of solid cathode with U metal deposits & scraping U deposit from solid cathode in scraping station & collecting it in graphite crucible, remote removal of un-oxidized U metal from anode basket, recovery of fallen U metal from cadmium pool, remote sampling of molten salt & cadmium from HTER vessel and finally remote movement of all the scraped U product & un-oxidized U



Fig. 1: PPRDF $500 m^3$ Containment Box



Fig. 2: Salt storage vessel with transfer line



Fig. 3: Anode basket & solid cathode



Fig. 4: Anode & cathode assembly located over HTER vessel



Fig. 5: U deposit in the solid cathode with occluded salt



Fig. 6: Scraping station and graphite crucible with scraped uranium

metal into inert glove box attached to containment box.

Containment box and argon system

In PPRDF all the pyroprocessing equipments are housed inside the 500 m³ CB containing argon. The leak tightness of CB was first achieved to below 0.1 vol% at both positive (+100mmWC) and negative (-100mmWC) pressure. The CB was then converted into argon from air in a systematic manner to conserve argon. It took around 1 month to convert containment box from air to argon and to get required purity (O₂ & H₂O < 50ppm and N₂ < 5%). The argon and nitrogen requirement for this facility was met with the help liquid argon Cryogenic system and Nitrogen generation system. After converting the CB to argon environment the argon purity (O₂ & H₂O < 50ppm), temperature (<40°C) and Pressure (-20 to -40mmWC) was maintained throughout the operation using Argon Recirculation and Purification System (ARPS) and Argon Pressure Control System (APCS). Fig.1 shows the photograph of the CB.

Transfer of molten salt into HTER

Transfer of molten salt into HTER starts with melting (m.p 365°C) of 1000Kg of purified molten salt (44.2wt%LiCl-55.8wt%KCl eutectic) kept in the leak tight salt storage vessel outside the CB. The time required for melting the salt was around 2 weeks. After that the salt line along with HTER vessel was cold & hot (200°C) purged with ultra pure argon. After hot purging, salt line and HTER vessel temperature was slowly raised to 400°C. During this time 427 Kg of Cd metal present in the HTER vessel was melted and the trapped moisture present inside the Cd rod was released. Hot purging of ultra pure argon was continued again for 6 hr to drive out the moisture released from Cd rod. After this, the temperature of salt storage vessel, salt line and HTER vessel was raised and maintained at around 450°C. The salt was then transferred to HTER vessel by slowly raising the cover gas pressure of salt storage vessel from 0.1 to 0.5 bar. The salt transfer was monitored by monitoring the level

drop in the salt transfer vessel using back pressure method. After salt transfer, the temperature of molten salt inside the HTER vessel was maintained at 450°C throughout the operation. Fig.2 shows the photograph of the Salt storage vessel with transfer line.

In-situ preparation of UCl₃ in HTER

Presence of uranium ions in the molten salt electrolyte is necessary for starting of electrorefining operation. In HTER it was decided to start with 1.5wt% of uranium ions in the electrolyte (equivalent to 2wt% of UCl₃). The UCl₃ in HTER was prepared by in-situ reaction of Uranium metal and CdCl₂ in molten salt.



15 kg of CdCl₂ was first vacuum dried before addition of it into HTER vessel remotely using CdCl₂ transfer vessel. The 15 kg of uranium required for UCl₃ preparation was then placed into the cruciform shaped anode basket in rodlet form and transferred remotely into HTER vessel. In HTER vessel the CdCl₂ present in the salt react with U metal at anode basket to produce UCl₃ & Cd metal as per reaction (1). To increase the reaction kinetics stirrer and anode basket was also made to rotate continuously at 50 rpm.

Transfer of Anode and solid cathode into HTER

After getting the required U-ion concentration in the molten salt, 10 kg of U metal was loaded in the anode basket and then attached to the anode assembly. Similarly, solid cathode where U will get deposited was attached to the cathode assembly. Weights of both assemblies were taken using load cell and then transferred to HTER vessel using 5 ton in-cell crane. Fig. 3 shows the photograph of anode basket & solid SS cathode. Fig. 4 shows the photograph of HTER with vessel anode and cathode assembly.

Commencement of U Electrorefining

U-electrorefining operation was carried on Galvanostatic mode (constant current). It starts with measurement of open circuit potential (OCV) of cathode and anode



Fig. 7: Anode tilting mechanism

with respect to reference electrode. After that the cell current was slowly raised and the potential of anode was monitored w.r.t reference electrode. The cut-off voltage for the anode was set between 0.45-0.5V to prevent oxidation of other metals in anode (in actual case Zr). The maximum cell current achieved was 30A. Total 8827410 Coulombs of charge was passed, which corresponds to 7.25 kg of U metal deposits, but the recovered U in solid cathode was 4.6 kg, where as the remaining 2.65 kg of U deposit has fallen down in liquid Cd pool due to the larger diameter of deposit in solid cathode. The fallen U in liquid Cd pool was later recovered by anodizing the Cd pool. Fig.5 shows the photograph of the U deposit in the solid cathode with occluded salt.

Recovery of U deposit from solid cathode

The U deposit in solid cathode was remotely moved from HTER vessel to scraping station, where the solid cathode was rotated and U deposit on solid cathode was removed using vertical lathe type mechanism. The scraped U along with occluded salt was collected in the graphite crucible which will later go to Automatic Vacuum Distillation and Melting System (AVDMS) for salt distillation and U consolidation. Fig.6 shows the photograph of the scraping station and graphite crucible with scrapped U.

Recovery of un-oxidized U metal from anode

The anode basket containing un-oxidized U metal was detached from anode assembly in assembly station and remotely taken to anode tilting mechanism using gripper tool and crane. In anode tilting mechanism the anode basket was heated to 400°C and tilted upside down to remove the un-oxidized U metal into collection vessel. Fig. 7 shows the photograph of the anode tilting mechanism.

Salt and cadmium sample from HTER was also remotely taken at various stages of the operation for material balance and U- accounting.

With these activities the first U- electrorefining campaign has been completed. As a next step the scrapped U occluded with salt will be processed in AVDMS to obtain pure U ingot.

III.04 Engineering Challenges in Establishing Pyroprocess R&D Facility (PPRDF)

Pyroprocess R&D facility (PPRDF) was set-up with an objective of demonstrating High temperature electrorefining and cathode deposit consolidation in a 500m³ argon atmosphere containment box. High temperature electrorefining was carried out using 10 kg natural uranium slugs in molten salt electrolyte (LiCl-KCl eutectic mixture) at 500°C. About 1000 kg of eutectic salt mixture was purified and stored in a storage vessel. This salt was then transferred to the electrorefiner vessel housed in the containment box by pressurizing with Ultra High Pure (UHP) argon.

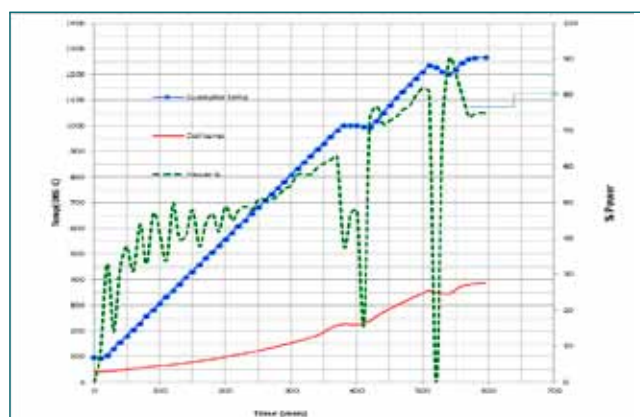


Fig. 1: Transient temperature and power profile

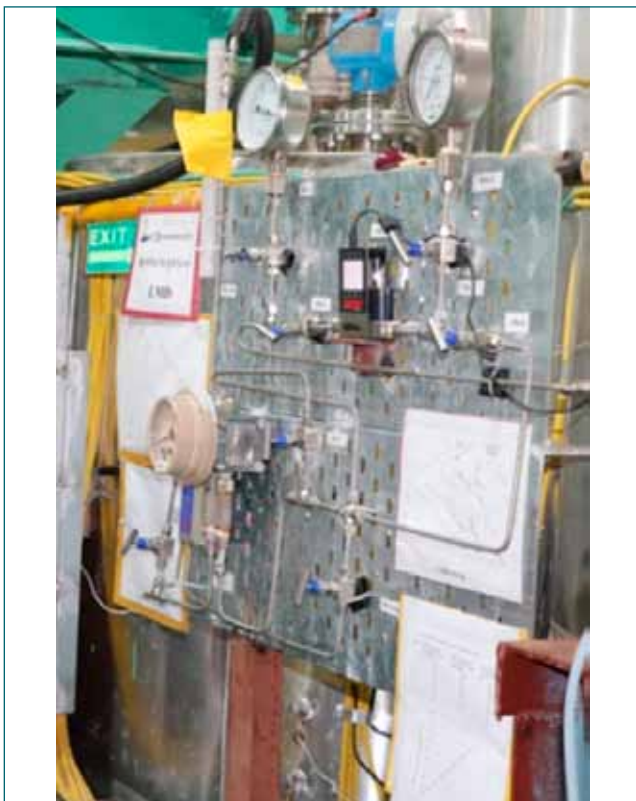


Fig. 2: Salt level measurement system

Development of level probe for molten salt using back pressure method

Development of continuous molten salt level measurement probe is an important requirement during salt transfer operation. In this regard conventional level measurement technique using back pressure method used in aqueous reprocessing was developed for level measurement of high temperature molten salt system. The main challenges faced in development of high temperature based level measurement using back pressure was clogging of gas bubbler tube due to solidification of molten salt caused by the sudden change in the cover gas pressure over salt level. This challenge was overcome by providing equalizer valve connecting



Fig. 3: Heat sink for bus bar

the cover gas and the bubbler tube inlet. The back pressure based continuous level measurement has been installed in the salt storage vessel of PPRDF and was used very successfully during salt transfer operation for monitoring the drop in salt level with time. Fig. 2 shows the photograph of the salt level measurement system installed in the salt storage vessel of PPRDF.

Automated operation of Distillation and melting system

During pyrochemical reprocessing, the cathode deposit consolidation has to be carried out by a water-less induction heating upto 1250°C. A blank heating run was conducted in the containment box to generate the blank heating curve during distillation and melting. The entire operation is split in four steps. In the first step, temperature is ramped from 30 to 1000°C at 150°C/h. In the second step, the system is maintained at this temperature for 30 minutes to ensure completion of salt distillation. In the third step, the temperature is ramped up to 1250°C at 400 torr (abs) pressure. In the fourth step, the temperature was maintained at 1250°C for 30 minutes to ensure completion of melting. All the four process steps of the heating cycle were automated by programming in PLC. Temperature feedback was taken from an R-type thermocouple placed on the susceptor. The temperature of the susceptor, induction coil and the various power levels during operation is plotted and shown in Fig. 1. The maximum temperature attained in the induction coil during the process was 360°C.

Design and fabrication of heat sink for AVDMS power feedthrough

During the metal melting step at 1250°C in the crucible, the copper coil and the connecting bus bars of the power feedthrough also gets heated. The power feedthrough on the vacuum chamber is sealed by viton O-ring and it would attain a maximum temperature of 285°C. This resulted in O-ring failure and hence leak tightness was lost. A heat sink made of copper was therefore designed by carrying out thermal analysis using Comsol 5.3a. Optimization of the number of fins was done so as to maintain the temperature of the O-ring area below 200°C. A finned heat sink of 100mm x 100mm x 30mm consisting of 20 fins of 1mm thickness and 4 mm pitch was arrived after several iterations in Comsol. This final fin configuration can maintain the temperature of the O-ring at 187°C. The heat sinks were subsequently fabricated by machining and wire cutting of solid copper blocks. The copper heat sink installed at site is shown in Figure 3.

III.05 Studies on the Conversion of UO_2 to UCl_3 using AlCl_3 in LiCl-KCl Melt and the Effect of Lanthanide (Ln: Nd, Pr, La and Ce) Oxides on the Conversion Efficiency of UO_2

Molten salt based ElectroRefining (ER) process for recovery of actinides is the main step of pyrochemical reprocessing of spent metallic fuels. Conventionally, LiCl-KCl salt loaded with ~6 wt.% UCl_3 is used as electrolyte in ER process for electro-transport. Keeping in view of O_2 and moisture sensitive nature of the LiCl-KCl salt, actinide metals and chlorides, the process is carried out under inert Ar atmosphere. O_2 impurities convert the actinide chlorides to actinide oxides, which are insoluble and electrochemically inactive species in LiCl-KCl melt. As a result, the efficiency of the ER process decreases, leading to poor separation factors for actinides in pyro-reprocessing. Hence, the conversion of actinide oxides to their chlorides and use them as electrolyte is an important step in pyrochemical reprocessing. Present work describes about the conversion of UO_2 to UCl_3 in the presence of lanthanide oxides.

Conversion of UO_2 to UCl_3

Conversion of UO_2 to UCl_3 was carried out using AlCl_3 and Al metal in LiCl-KCl melt at 773 K. The conversion efficiency was analyzed using UV-Vis spectroscopy

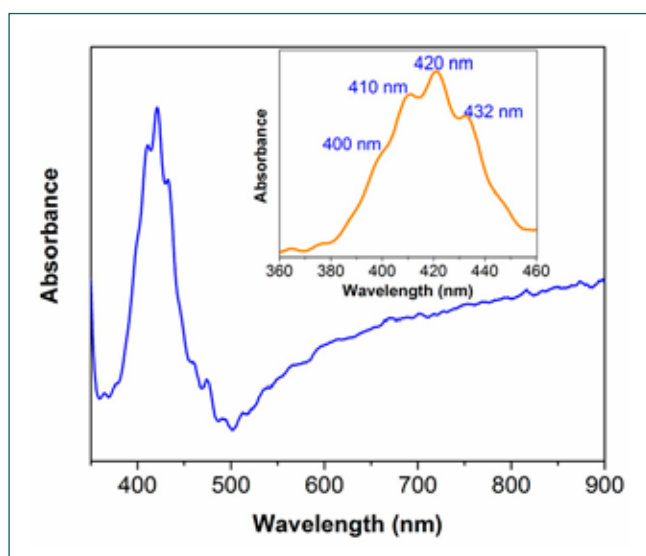


Fig. 1: UV-Vis spectra of the equilibrated product of $\text{UO}_2 + \text{AlCl}_3 + \text{Al}$ in LiCl-KCl

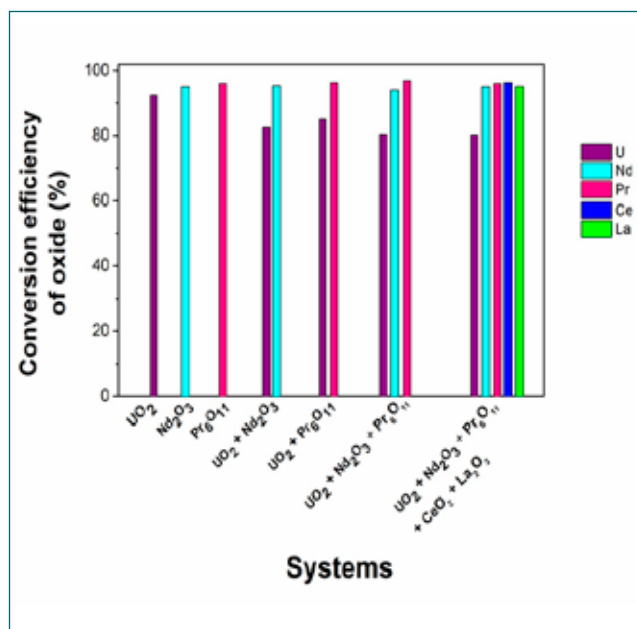


Fig. 2: Conversion efficiency of oxides

by measuring the absorbance of U(VI) at 420 nm in 1M $\text{HNO}_3 + 1 \text{ M H}_3\text{PO}_4$ medium (Fig. 1). The conversion process was optimized by varying concentrations of AlCl_3 (stoichiometric $\times 1$ to 4) and the duration of reactions (45 min to 5 h). About 93% conversion of UO_2 to UCl_3 was achieved by doubling the stoichiometric requirement of AlCl_3 in 50 g of LiCl-KCl salt in 2.5 h.

The effect of lanthanide oxides on the conversion of UO_2 to UCl_3

The chlorination of UO_2 in presence of Nd_2O_3 , Pr_6O_{11} , CeO_2 and La_2O_3 in LiCl-KCl melt was carried out using AlCl_3 and Al metal at 773 K. U, Nd and Pr were estimated using UV-Vis spectroscopy whereas La and Ce were estimated using ICP-OES. Conversion of ~95% for lanthanide oxides were achieved when they were chlorinated independently. About 8% decrease in conversion efficiency of UO_2 was observed in presence of a single lanthanide oxide when compared to chlorination of UO_2 alone was carried out (Fig. 2). The conversion efficiency of UO_2 in presence of mixture of lanthanide oxides was decreased by nearly 12%.

III.06 Preparation and Analysis of Li-Cd Alloys with Different Concentrations for Studies on Reductive Extraction of Actinides Related to Pyrochemical Reprocessing

Lithium cadmium (Li-Cd) alloys are relevant to pyrochemical reprocessing flow-sheet and being used in reductive extraction of actinides by Actinide Draw Down Process (ADDP).

Lithium (Li) is highly reactive with oxygen and moisture at room temperature. Apart from recirculating argon gas through standard gas purification towers for removal of oxygen and moisture, necessary provisions were made to remove nitrogen from argon atmosphere glove box. Argon gas of the glove box was passed through zirconium getter at 1223K to remove nitrogen. Around 10 ppm oxygen was measured in glove box during preparation of Li-Cd alloys. Three different concentrations (I) 25 at.% (II) 50 at.% and (III) 75 at.% of Li in Li-Cd alloys having length and diameter of 15-22 mm and 8-10 mm respectively were prepared (Fig. 1a, 1b and 1c) by melting and equilibrating Cd and Li metal in argon atmosphere glove box in the temperature

range of 673 K - 873K. After 30 minutes of equilibration, molten alloys were poured into pure iron moulds which are kept at room temperature. (I) 25 at.% (II) 50 at.% and (III) 75 at.% of Li in Li-Cd alloys were annealed for about 65 hours in argon atmosphere glove box at 500 K (Fig. 2a, 2b and 2c). Li-Cd alloys have different colors with different concentrations of Li. Samples were prepared by cutting top and bottom ends of each alloy, dissolved in dil. nitric acid and analyzed. Concentration of Li in Li-Cd alloys were back calculated by analyzing Cd concentration by EDTA titration. Table 1 shows the Li concentration obtained by taking the average of the analysis results of the top and bottom ends of Li-Cd alloys. Two different phases with separate phase boundaries were observed in optical microscope image (Fig. 3) for 75 at.% Li in Li-Cd alloy exhibiting that alloy is not homogenous.

Present study suggests that distribution of Li in Li-Cd alloys is not uniform.

Table. 1. Li concentration (in at.%) in Li-Cd alloys

S. No.	Li concentration in Li-Cd alloy	Li concentration in Li-Cd alloy before annealing	Li concentration in Li-Cd alloy after annealing
1.	25	30	36
2.	50	50	56
3.	75	72	76

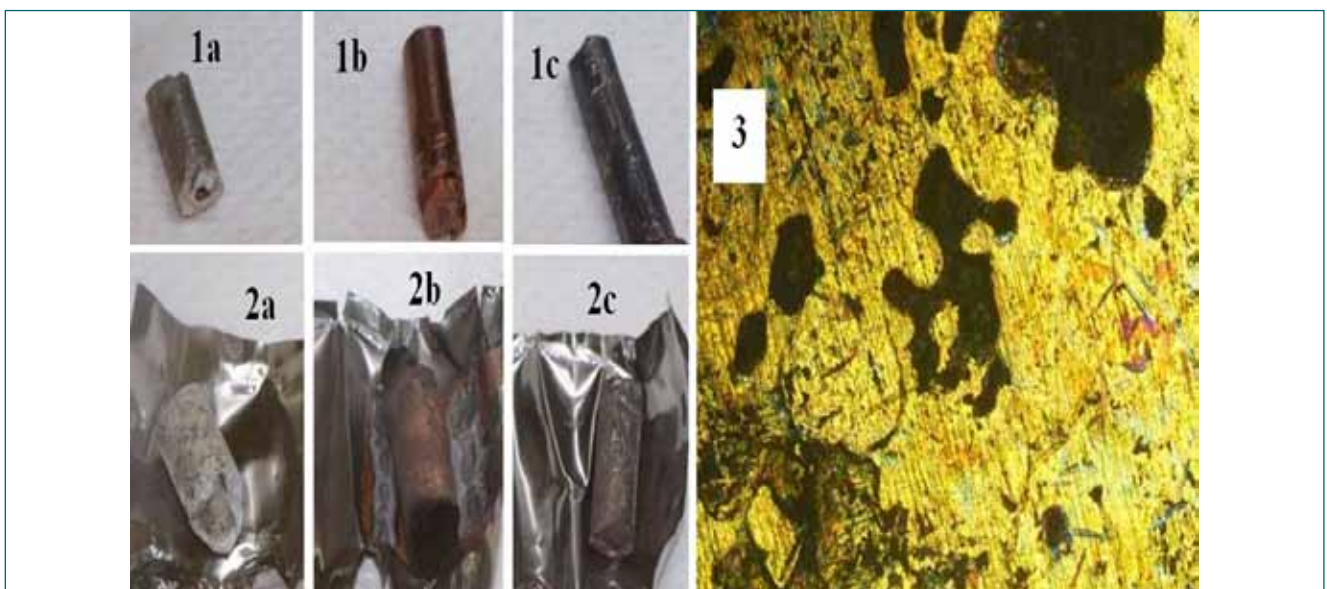


Fig. : 1a. 25 at.%, 1b. 50 at.%, 1c. 75 at.%, Li in Li-Cd alloy before annealing, Fig. 2a. 25 at.%, 2b. 50 at.%, 2c. 75 at.%, Li in Li-Cd alloy after annealing, Fig. 3. Optical microscope image - 75 at.%Li in Li-Cd alloy.

III.07 Measurement of Phase Transformation Temperatures of Metallic Fuel

Use of metallic fuel in fast reactor is advantageous in several aspects. Complete characterization of metallic fuel is an essential prerequisite before its use. Hence as a part of characterization, studies on the thermal stability of the fuel viz., temperature at which the solid state transformation and melting occurs was taken up. A glove box experimental facility with Thermo Gravimetry-cum-Differential Thermal Analysis (TGDTA) was built and qualified for handling plutonium samples recently. The solid state transformation temperature of U-19Pu-6Zr was measured successfully by using this facility. The phase transformation temperatures of U-6Zr were also measured prior to the measurements on Pu bearing alloys.

The TGDTA system was functionally tested outside the glove box and temperature calibrated by measuring the melting points of high purity metal standards (In, Sn, Zn, Al, Ag & Au). The measured values were satisfactory and agree within ± 0.5 K with the standards.

Commissioning of the glove box facility involved design & fabrication of several components including the feedthroughs for signal and electrical cables. In addition, all the PVC connections in the instrument for gas and

water service were replaced into metal connections. All these were tested & qualified after installation. The instrument was calibrated again. For the first time in IGCAR, an auto-recirculation-cum-purification system was commissioned and qualified for radioactive glove box work. The glove box leak rate was within the permissible limit for handling the radioactivity.

Measurements on injection cast U-6Zr alloys were carried out in TGDTA inside the glove box. The measured solid state transformation temperatures, the solidus and the liquidus temperatures matched well with the literature. Figure 1 shows the thermogram of U-6Zr. The following phase transformation temperatures were identified at a heating rate of 5 K/min i.e., i) at 808 K ($\delta \rightarrow \gamma$ transition), ii) at 850 K ($\alpha \rightarrow \beta$ transition), iii) at 948 K ($\gamma \rightarrow \gamma'$ transition), iv) solidus temperature at 1439 K and v) liquidus temperature at 1505 K.

Similarly, measurements were carried out on the metallic fuel, U-19Pu-6Zr at a heating rate of 10 K/min under flowing ultra high purity argon. Figure 2 shows the thermogram of U-19Pu-6Zr metallic fuel and the observed solid state transformation temperature at 927 K.

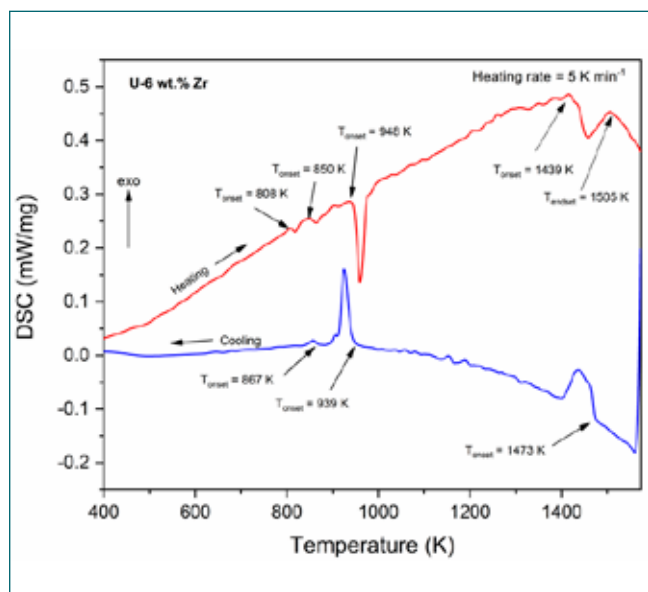


Fig. 1: Thermogram of U-6 wt% Zr alloy measured by using TGDTA in the glove box

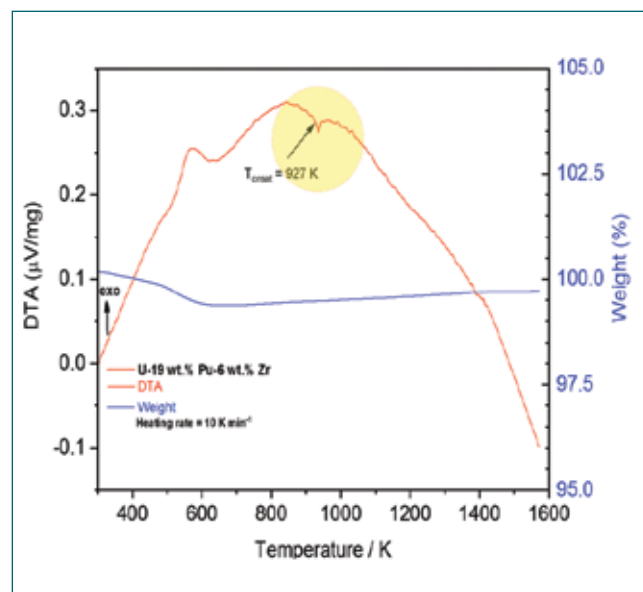


Fig. 2: Thermogram of U-19wt.%Pu-6wt.%Zr alloy measured by using TGDTA in the glove box

III.08 Non-Destructive Determination of Pu - Isotopic Composition in MOX Pellets using High Resolution Gamma Spectrometry

Isotopic composition (IC) of Pu is a mandatory requirement to determine the fissile worth of MOX [(U,Pu)O₂] pellets which are to be used as fuel in fast reactors. Thermal Ionization Mass Spectrometry (TIMS) is the most reliable technique which provides accurate data on Pu-IC with high precision. However, it involves use of chemical methods (dissolution, dilution, separation, etc.) which generate radioactive waste for further processing and also needed planchetting for ²³⁸Pu assay by α -spectrometry. Non-destructive assay of Pu-IC using High Resolution Gamma Spectrometry (HRGS) has several advantages over conventional technique i.e. TIMS in terms of easy sample preparation, rapid analysis and applicability on final products irrespective of their physical or chemical state. The present work describes the gamma spectrometric analysis of solid Pu samples of MOX pellets to obtain Pu-IC by HRGS. 20 MOX pellets were transferred to individual polypropylene vials and doubly sealed in a glove-box.

A planar High Purity Germanium (HPGe) detector having a resolution of 600 eV at 122 keV with thin Be window was used for recording the gamma spectra. The detector was coupled with an associated PC based 8 k multichannel analyzer (MCA) ISA card of Aptec along with acquisition software. These sealed MOX pellets were directly counted in front of the detector at a distance of 5 cm. Cd sheets of 1.5 mm thickness were placed as a filter in between the samples and the detector to minimize the intense 59.5 keV photo peak of ²⁴¹Am and the acquisition was carried out for about 8 h. Typical of gamma spectrum of MOX pellet is shown in Fig. 1.

The acquired gamma spectra were analyzed for peak areas (P) using peak fitting software PHAST. Full energy peak efficiency is a strong function of gamma ray energy and counting geometry and needs to be determined experimentally by using standard sources.

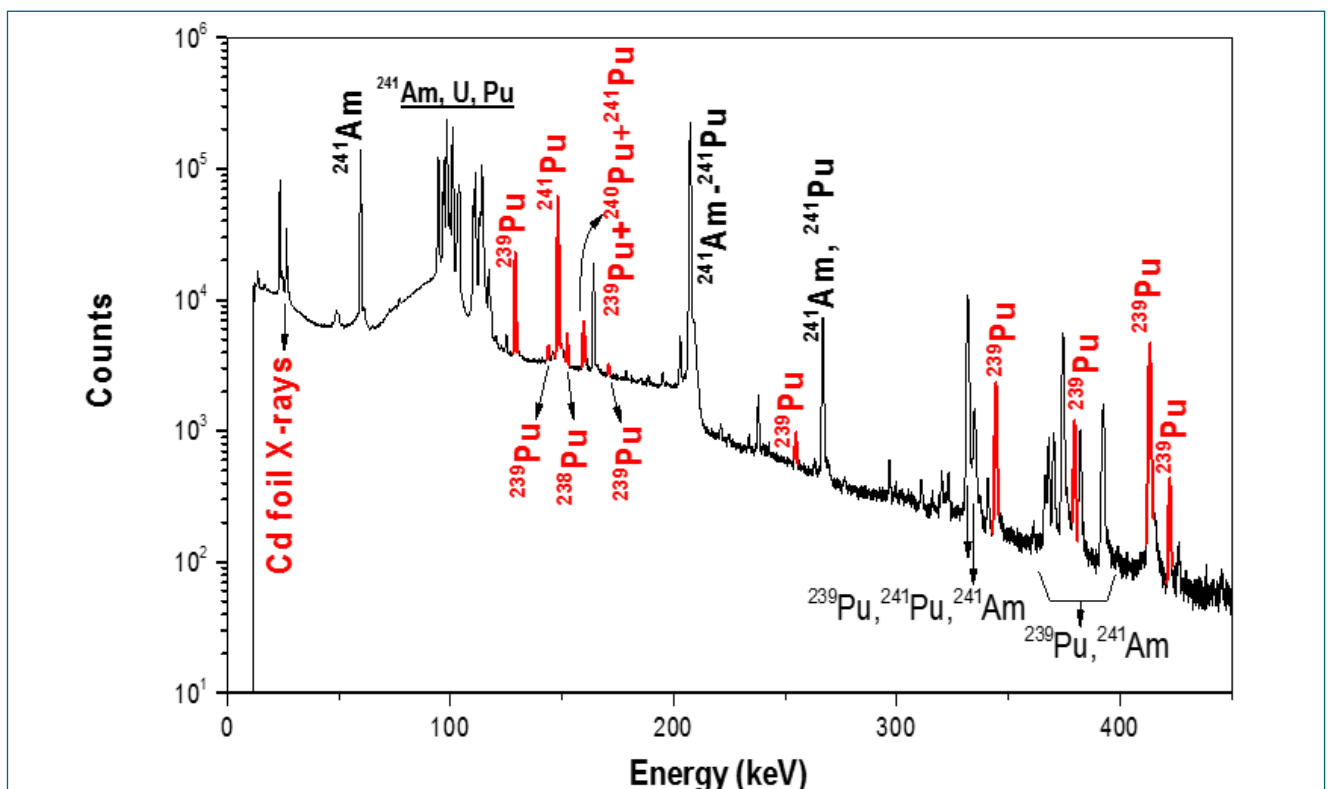


Fig. 1: Typical gamma spectrum of one of the MOX pellets measured using HPGe detector

Table 1 Comparison of Pu-IC in MOX pellet between HRGS and the established TIMS method

Sample ID / Pu isotope	B-1259_P-2		B-1261_P-18		B-1264_P-10		B-1268_P-9		B-1269_P-20	
	HRGS	TIMS	HRGS	TIMS	HRGS	TIMS	HRGS	TIMS	HRGS	TIMS
²³⁸ Pu	0.168	0.151	0.170	0.151	0.163	0.15	0.162	0.146	0.158	0.141
²³⁹ Pu	69.3	68.997	67.9	69.052	68.2	69.213	69.6	69.03	69.9	68.966
²⁴⁰ Pu	25.1	25.665	26.1	25.648	26.1	25.636	25.1	25.618	24.9	25.59
²⁴¹ Pu	3.81	3.365	4.02	3.356	3.70	3.232	3.59	3.443	3.59	3.542
²⁴² Pu	1.59	1.823	1.80	1.792	1.79	1.768	1.57	1.764	1.53	1.76
HRGS/TIMS (²³⁹ Pu+ ²⁴¹ Pu)	1.010		0.993		0.992		1.010		1.013	

Efficiency calibration is not carried out as the standard of similar matrix and geometry (MOX pellet) is not available. However, relative in-situ efficiency ratios are adequate to determine the Pu isotopic ratios. The relative efficiency ratios are advantageous as they are independent of counting geometry. In the present study, gamma energies (E) of ²³⁹Pu were used in the energy range of 120-420 keV to construct the in-situ relative efficiency calibration plot. Logarithmic polynomial with 3rd order was used to fit each experimentally obtained ratios (eq. 1) and determined the fitting parameters to calculate the relative efficiencies for isotopes of Pu using the eq. 2.

$$\frac{\varepsilon(E_x)}{\varepsilon(E_y)} = \frac{N_B P_A(E_x) T_{1/2}^A I_y^B}{N_A P_B(E_y) T_{1/2}^B I_x^A} \quad (1)$$

$$\ln[\varepsilon(E)] = \sum_{i=0}^3 a_i (\ln E)^i \quad (2)$$

where N_A is number of atoms of the isotope A, I is abundance of gamma energy and T_{1/2} is half-life. For the two isotopes of Pu, 'A' and 'B', the atom ratio (N_A/N_B) can be determined using eq 3.

$$\frac{N_A}{N_B} = \left[\frac{P_A(E_x) \varepsilon(E_y)}{P_B(E_y) \varepsilon(E_x)} \right] \frac{T_{1/2}^A I_y^B}{T_{1/2}^B I_x^A} \quad (3)$$

The atom ratios were used to calculate the atom % abundances of different Pu isotopes using eq. 4 and 5.

$$f_{241} = \frac{100}{1 + \frac{N_{238}}{N_{241}} + \frac{N_{239}}{N_{241}} + \frac{N_{240}}{N_{241}} + \frac{N_{242}}{N_{241}}} \quad (4)$$

$$f_i = \frac{N_i}{N_{241}} \times f_{241} \quad (5)$$

(where i = 238, 239, 240 & 242)

However, owing to the complex nature of gamma spectra of Pu isotopes, the respective photo peaks are needed corrections for spectral interferences. 152.68, 171.39 and 148.56 keV photo peaks of ²³⁸Pu, ²³⁹Pu and ²⁴¹Pu respectively were used to determine the atom ratios of ²³⁸Pu/²⁴¹Pu and ²³⁹Pu/²⁴¹Pu. The 160 keV photo peak is a combination of 159.96 keV (²⁴¹Pu), 160.19 keV (²³⁹Pu) and 160.31 keV (²⁴⁰Pu). Appropriate corrections were given to obtain the peak area of 160.31 keV (²⁴⁰Pu) and used for atom ratio (²⁴⁰Pu/²⁴¹Pu) calculations.

In the case of ²⁴²Pu, isotopic correlations reported for PHWR grade Pu was used to calculate the atom ratio of ²⁴²Pu/²⁴¹Pu. All the atom ratios were converted in to their respective weight ratios and compared with the results of the same obtained using TIMS for five pellets are presented in table 1. The relative precision values of 0.5-5% were obtained for ^{239,240,241}Pu isotopes and about 10% for ^{238,242}Pu. Total fissile content (²³⁹Pu+²⁴¹Pu) in MOX pellets was compared and showed a very good agreement with a maximum deviation of around 1%.

III.09 Development of green Separation Techniques for Extraction and Recovery of Actinides using Supercritical Carbon Dioxide Modified with TRIS (2-Methylbutyl) Phosphate

Extraction and recovery of actinides from different process steps of nuclear fuel cycle operations is an important task. The extraction is generally carried out using well established techniques such as solvent extraction, ion-exchange, solid-phase extraction and chromatographic techniques. However, these conventional methods result in the generation of secondary liquid waste, which requires further, waste management.

In the recent past supercritical fluid extraction (SFE) based methods are successfully employed for extraction and recovery of organic and inorganic compounds. SFE has several advantages over conventional separation techniques such as i) reduction in the generation of toxic organic waste, ii) direct recovery of compounds from solid matrices, iii) fine-tuning the extraction behavior using experimental parameters.

The development of an SFE process for the recovery of metal ions involves the following: (a) identification of metal-ion-specific ligands; (b) selection of ligand based on the nature of matrix; (c) measurement of solubility of specific-ligands in supercritical carbon dioxide (SCCO₂) medium; (d) use of SCCO₂ containing ligands for recovery of metal ions and (e) optimization of experimental parameters such as temperature, pressure and co-solvent composition.

The solubility of tris(2-methylbutyl) phosphate (T2MBP) in SCCO₂ medium was experimentally determined using a flow saturation technique. The solubility was found to be high and ranges in the order of 10⁻¹ mol/mol, hence can be employed in SCCO₂ medium. The solubility increases with pressure and decreases with temperature.

The experimental solubility data is correlated with different semi-empirical models for their predictions. Based on the solubility data SFE method was developed for the extraction of uranium from U-Zr alloy as well as from U-Zr feed solution using SCCO₂ modified with T2MBP. The effect of temperature, pressure and flow rate of SCCO₂ was investigated and the parameters are optimized for efficient extraction. Complete extraction of U from U-Zr feed solution (4M HNO₃) and the extraction profile is depicted in Figure 1, under similar conditions, Zr extraction was found to be 3%.

The recovery of U from U-Zr alloy (3g chunk) is carried out acid equilibrated T2MBP and extraction profile is shown in Figure 1. Complete extraction is not achieved and the extraction was found to be diffusion controlled. The complete recovery can be achieved with U-Zr in powder form.

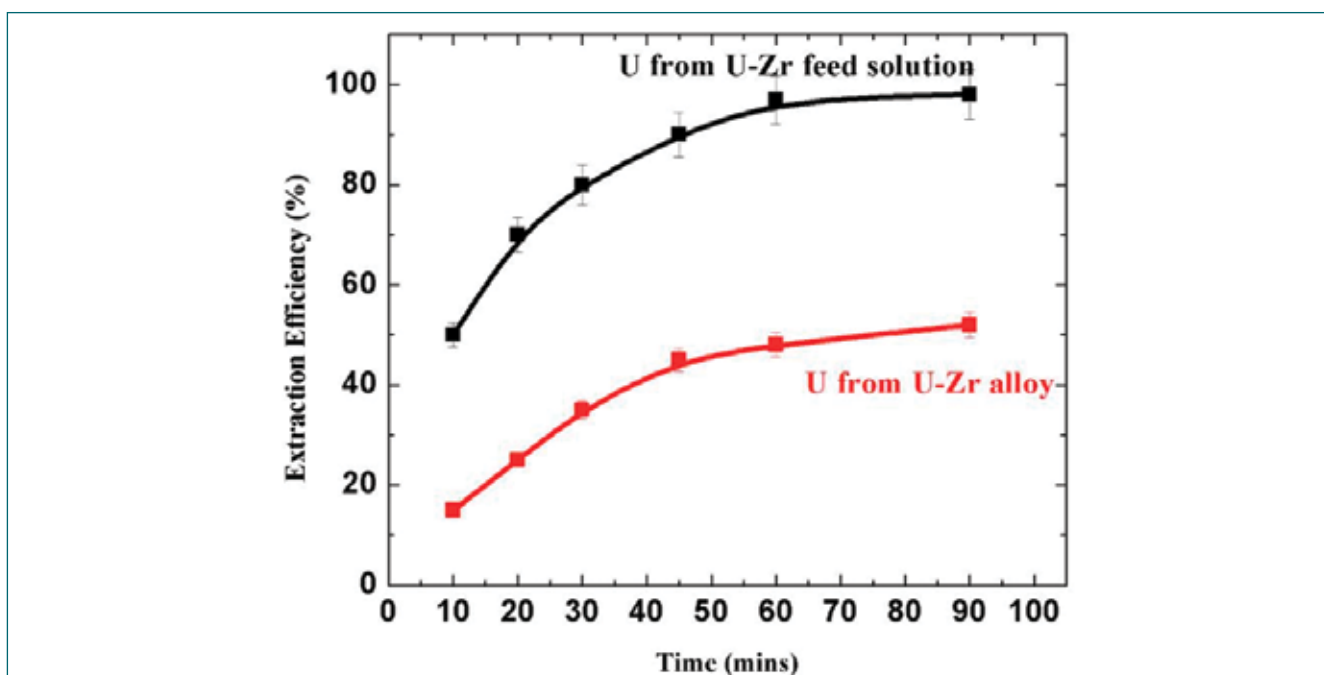


Fig. 1: Supercritical fluid extraction of uranium from U-Zr using SCCO₂ modified with tris(2-methylbutyl) phosphate

III.10 Manufacture of Compressed Air Receiver Tanks and Soft Water Storage Tank for Steam Generator Test Facility

Central Workshop Division (CWD), IGCAR was entrusted with manufacturing of two compressed air receiver tanks (Fig.1) and one soft water storage tank for the Steam Generator Test Facility (SGTF). This article highlights these two manufacturing activities in the following sections.

COMPRESSED AIR RECEIVER TANKS

Welding and Fabrication

The horizontal type cylindrical tanks have either ends closed with torispherical dished ends and are meant for receiving/storing compressed air used for pneumatic actuation of valves in various sodium test loops in the SGTF. The overall size of the tank is outside diameter 406 mm x length 1611 mm and the material of construction is 8mm thick mild steel plates in killed condition. Volume of each fabricated compressed air receiver tank is 150 Litres.

The plates were subjected to non-destructive testing viz. UT to determine soundness, followed by oxy-acetylene gas cutting, manual grinding of cut edges and bevelling to 37 ½ deg. using plate bevelling machine.

The tori-spherical dished ends were cold formed to required dimensions and the 390mm ID x 1255mm long shells was fabricated in conformity with the dimensions of the formed dished ends. The shell plates were pre-pinned at both the edges and formed using pyramid type Himalaya plate bending machine followed by template checking of the formed profile. During fit-up, the root side mismatch was controlled and ensured within 0.2mm. Manual GTAW process was used for the longitudinal seam welds (root and hot pass), while SMAW welding process was used for the subsequent capping passes in 1G position. Copper coated solid AWS A5.18, ER 70S-2 filler wires of 1.2 mm diameter rods were used during GTAW root pass, while low hydrogen long baked AWS A5.18, E 7018 electrodes of 3.15 mm diameter x 350mm length were used for filling/capping passes. Specially designed mechanical spiders were effectively utilized during welding to control the ovality and mismatch. The welds were subjected to liquid penetrant inspection (LPI) during root & final pass welding.



Fig. 1: Major parts of the compressed air receiver tanks

Nozzle locations were marked at appropriate orientations on the formed and L-seam welded cylindrical shells as per the drawing specifications. Further, seven numbers of internal threaded nozzles of ½" BSP x 14TPI, ¼" BSP x 19TPI, ¾" BSP x 14TPI and 3/8" BSP x 19TPI were set-in type fillet welded on the fabricated tank and all the welds were subjected to root and final pass LPI. Anticipating contraction of internal threaded nozzles, respective threaded end plugs were fastened during welding. Since, the internal threaded nozzles supplied were of cast products, which have high crack propensity, welding of these nozzles to the air receiver tank were carried out using Inconel 82 nickel alloy filler wires to avoid cracking. Pre-formed brackets were also welded to the tank to fix the pressure gauges, pressure relief valve, instruments, filter, regulator and lubricator (FRL) unit etc. Drain Nozzle welded at bottom of the receiver tank and the weld was subjected to LPI. The formed torispherical dished ends were welded to either ends of the shell.

Hydro and Pneumatic testing

The fabricated tanks were subjected to Hydro testing to a test pressure (Fig.2) of 15kg/cm² (g) as per the approved procedure in accordance with UG-99 of ASME Section VIII Division 1 using two calibrated pressure gauges to validate the integrity of weld joints. Dimensional measurement were carried out after Hydro Testing.

Pneumatic testing of the fabricated tanks were carried out as per the approved procedure in accordance with UG-100 of ASME Section VIII Division 1. Compressed nitrogen gas (Fig.3) was used as a medium and tested at a pressure of 15 kg/cm² (g) with two calibrated pressure gauges along with a safety pressure relief valve. Soap solution was applied over the weld joints to identify



Fig. 2: Hydrostatic and Pneumatic Testing of Compressed Air Receiver Tank



Fig. 3: Fabricated Compressed Air Receiver Tanks

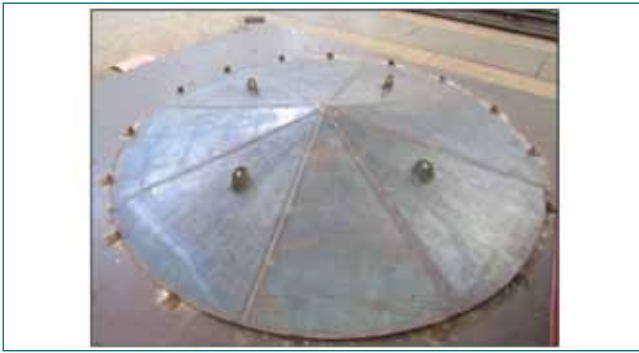


Fig. 4: Segmental conical roof

leakage, if any, and the weld joints were found to be sound. Dimensional measurement were carried out after Pneumatic testing too.

Fig. 2 shows Hydro and Pneumatic testing of the fabricated tanks. Fig. 3 shows final fabricated tanks ready for filling with compressed air.

SOFT WATER STORAGE TANK

The overall size of the tank is Diameter 2500 mm x Height 1500mm and the material of construction is 8mm thickness mild steel plate in killed condition. Volume of the fabricated tank with conical roof is 7.854 m³ with storage capacity of 6 m³.

Forming and welding of Shell

The shell plates were pre-pinched at both the edges along the height direction and then rolled using pyramid type Himalaya plate bending machine followed by template checking of the formed shell profiles. After fit-up, longitudinal seam welding was done using special mechanical spiders to control the ovality and mismatch. All the welds were subjected to LPI during root & final pass welding.

Forming and welding of Conical Roof

The conical Roof was formed into 8 segments of petal construction. These formed segments were aligned and welded together by SMAW process, followed by LPI at root & final pass. Four lifting lugs were fillet welded on the top of the conical roof at specified locations to facilitate lifting while assembling.

Forming of circular rings

For rigidity, 6 mm thick plates were rolled and welded inside the tank at bottom and the base plate was welded at the bottom of the tank. At top of the tank 6 mm thick plate was rolled and welded outside the tank. All Nozzle

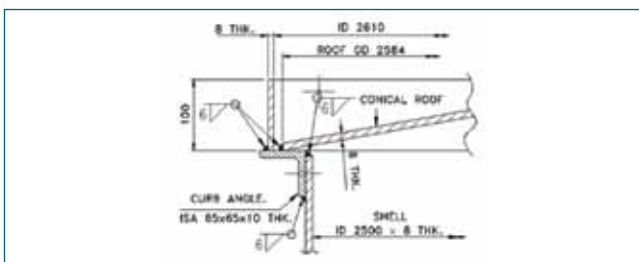


Fig 5: Fillet welding details of Curb Angle



Fig. 6: Formed curb angle

openings and man hole opening were cut by oxy-acetylene process and edge preparation was carried out to facilitate welding.

Fabrication of the Tank

The Fabricated conical roof was assembled and welded with the main shell. This fillet weld was subjected to LPI. Top circular plate (ID 2610 X 8mm thick x 100mm height) was welded at roof. Drain Nozzle were welded at bottom of the shell and these welds were also subjected to LPI. The manhole shell was assembled with the main shell using circumferential seam welds.

Development of procedure for forming the Curb angle and welding

A procedure was developed for formation of curb angle in the plate bending machine through mockup trials with special grooved rollers. These formed top and bottom curb angles were fillet welded in 2F position to the outer and inner periphery of the shell respectively. They serve as attachments or seats for the conical tank roof and provide stiffening for the tank shell. Total weld length was 8.28 m. To control weld distortion, spiders were mounted inside the shell beneath the weld joints while fit up as well as welding. Figs.3 and 4 show the fillet welding details of the curb angle and the final formed curb angle respectively.

The soft water storage tank for SGTF was successfully fabricated meeting all the manufacturing & NDT specifications. All the weld joints were subjected LPI during each pass. A close control of overall dimensions, minimum distortion was achieved by proper adoption of joint design, joint preparation and welding technique.



Fig 7: Fabricated and Installed Soft Water Tank

III.11 Indigenous Design and Development of Radar Level Probe for Liquid Sodium Level Measurement

RADAR Level Probe (RLP) for liquid Sodium level measurement [Fig.1] of Fast Breeder Reactors is indigenously designed and developed by IGCAR in collaboration with SAMEER, Mumbai. RLP is based on the transmission of a continuous wave of a RF energy which is frequency modulated. A portion of the transmitted signal is diverted to the receiver to act as the frequency reference. The frequency modulation of the continuous wave acts as the timing mark which is changing at a known modulation rate. Mixer at the receiver end produces the beat of transmitted and received signals. Level information can be inferred by processing the beat frequency signal.

Bench Level functional testing of RLP was performed using dihedral corner reflector [Fig.1], to check the functionality of RLP. To check the maximum design range (20 m) of RLP, range experiments were carried out with discrete lengths of RF cables from 0.5 m to 20 m using a reference horn antenna.

A test setup was made at Electronics Division(ED) laboratory for water level measurement. A Mild Steel cylindrical tank with dimension of 2 m height and 1.2 m diameter is fabricated at Central Workshop of IGCAR and installed at ED. A reference tubular level gauge

is mounted along the length of the tank. The RLP has flange type of arrangement to mount on the top of the tank. Level measurements were carried out by filling water from empty tank to full level of the tank [Fig.1].

After the satisfactory performance of level measurement in water tank, indigenously developed Radar Level Probe was installed at Test vessel 2 of Large Component Testing Rig in Hall-3 of RDTG for liquid sodium level measurement. Test Vessel 2 is of 13 m depth and 2.08 m diameter stainless steel sodium tank. RLP was installed through a nozzle with mating flange [Fig.1]. Sodium level was measured by RLP and recorded up to the range of 13 m. The level measurements were repeated at process temperature of 200°C, 225°C, 250°C and 300°C. The performance was found consistent during filling & draining for the entire period of operation.

The indigenously developed RLP was tested for environmental conditions [Fig. 2] also as per IS 9000 standard. It was tested for Dry Heat Test, Dry Cold test, Temperature Cycle Test and Damp Heat Test. It was tested for Electromagnetic interference and Electromagnetic Compatibility as per IEC 61000 standard for pre-compliance at EMI/EMC lab of ED.



Fig. 1: Functional Testing at Bench Level, for Water Level Measurement and Liquid Sodium Level Measurement



Fig. 2: EMI/EMC and Environmental Testing facilities of Radar Level Probe

III.12 Performance Evaluation of 8051 Microcontroller under Gamma Radiation Environment for Severe Accident Monitoring System

Electronics & Instrumentation is an essential and integral part of nuclear power plants that facilitate to monitor, control and operate the plant from a centralized control room. Remote Terminal Units (RTU) are used in the field environment of PFBR for acquiring sodium leak information, measurement of surface temperature of sodium pipelines and status of various digital/analog inputs from field. RTU is a general-purpose 8051 microcontroller based single board, data acquisition & control card for real-time monitoring of plant parameters and control action via commands received from a remote control room operator. However, the functionality of the 8051 microcontroller gets affected due to the harsh environment associated with the potential risk of release of radioactive substances, especially during the accident scenario.

A study was conducted to investigate the effect of gamma radiation on the performance of the Atmel make 8-bit high-performance flash 8051 microcontroller as shown in Fig. 1. The custom PCBs were designed to house the microcontroller, which included circuitry for biasing the device during irradiation and in-situ measurement of various parameters inside Gamma Chamber. A regulated supply voltage of 5V was supplied for the operation of the microcontroller at the input device current of ~25 mA. The microcontroller was programmed for specific application code to provide an output with a series of digital HIGH and LOW signals that drives the associated LEDs of the PCB as well as sending the output data to

the PC through a serial communication port. A GC-5000 self-shielded gamma irradiation chamber was used for the irradiation experiments. The radiation source was ^{60}Co isotope and the dose rate inside the chamber was 1.9 kGy/h. The microcontroller was irradiated and examined for the programmed sequence, current, pin output voltage and its performance verification. It was observed that the output data display was stopped after certain dose rate. The board was then removed from the radiation chamber for functional evaluation and the error in the memory array was recorded. The test aims to assess the ability to reprogram the microcontroller and analyze its functionality after exposure to a specific dose of radiation.

It was observed that the microcontroller can operate up to a dose of 0.6 kGy without affecting its performance. Although, beyond this dose, the gamma radiation degrades the functionality of the device and a dose rate of more than 1 kGy can lead to a permanent failure where the microcontroller can no longer be reprogrammed. Their ability to blink the LEDs and send data over the serial port were affected by radiation effects. There was a decrease in pin output voltage up to 3.5 V and an increase in device input current of ~300 mA with the increase in total absorbed dose. However, the overall radiation tolerance limit is satisfactory to design a robust I&C system for Severe Accident Monitoring of NPP. In addition, the tolerance limit can be improved by suitable radiation shielding.

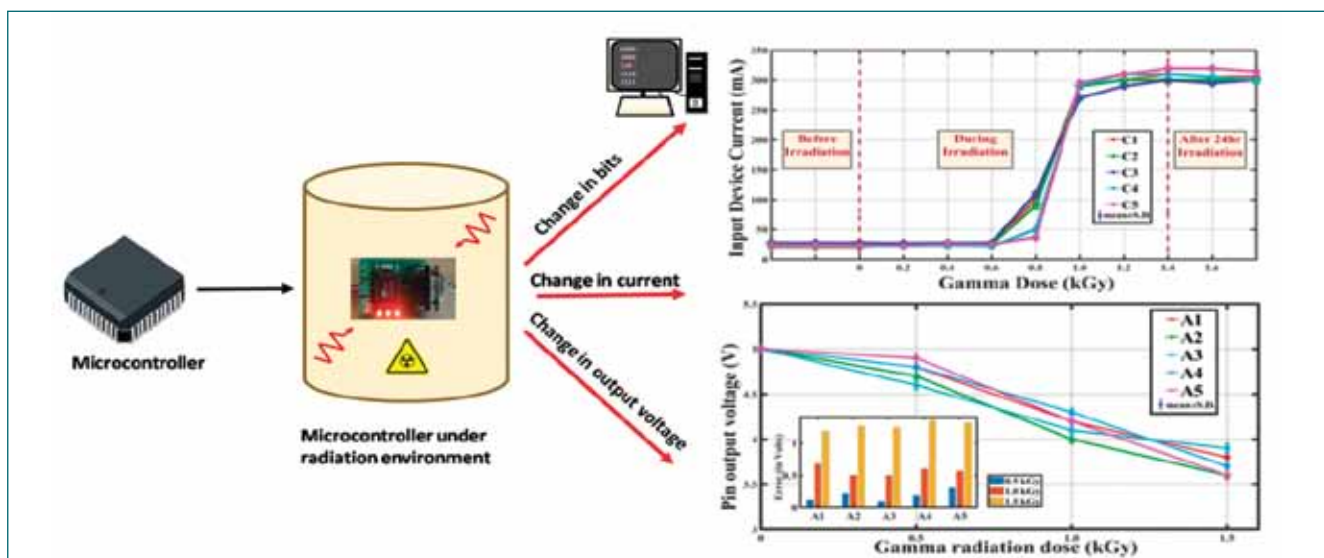


Fig. 1: Effects of gamma radiation on 8051 microcontroller

III.13 Deployment of Indigenous Wireless Sensor Network for the Assessment of Slope Stability at Avalanche Site

Snow Avalanche is a rapid flow of snow down a mountain slope. This is a well-known natural hazard, which can result in loss of property & life. Avalanche forecasting is carried out using snow slope stability assessment in a given area by professional forecasters.

Office of Principal Scientific Advisor to the Government of India (OoPSA-Gol) has sponsored a collaborative project between Indira Gandhi Centre for Atomic Research (IGCAR) and Defence Geoinformatics Research Establishment (DGRE), Chandigarh. The objective is to develop technology to enhance the avalanche forecasting capability through systematic data collection of snow and meteorological parameters from a mountain slope using Wireless Sensor Networks (WSN).

WSN Node for Meteorological Sensors

WSN comprises of small, low-power, distributed devices, called as WSN nodes for processing the collected data and communicating wirelessly. The in-house developed IP rated WSN Nodes that are qualified to withstand harsh winter conditions (as per IS 9000 std. & up to -40°C), can be powered by solar panels and backed up by batteries. These nodes measure snow-metrological data from an avalanche slope and transmit wirelessly to a nearby Basestation(BS). The following are the sensors used for this project: (a) Ambient Temperature Sensor, (b) Relative Humidity Sensor, (c) Wind Speed Sensor, (d) Wind Direction Sensor, (e) Atmospheric Pressure Sensor, (f) Snow Depth Sensor, (g) Snow Surface Temperature Sensor, (h) Shortwave & Longwave Radiation Sensor, (i) Snow & Rain Precipitation Sensor, (j) Temperature Profiler and (k) Soil Water Content Sensor. In addition, special WSN nodes for Acoustic Emission Sensing and Digital Image Capturing have also been developed.

Site Deployment for Meteorological Sensors

A mountain slope at Dhundi, Himachal Pradesh has been identified as deployment site. The project is executed in two phases. In Phase-I deployment during winter 2019-2020, WSN nodes were deployed at five locations for monitoring a single mountain slope. In each location,

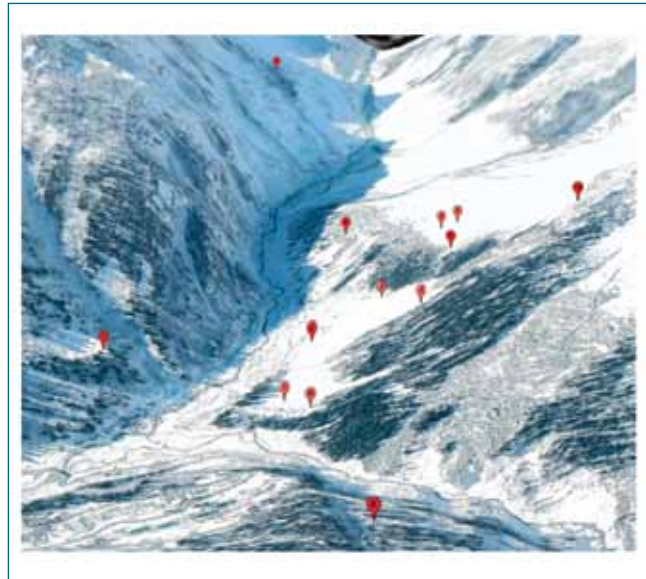


Fig. 1: Locations of WSN nodes deployed at Dhundi, HP to monitor 4 mountain slopes

3 nodes were deployed. They were programmed to collect data in every half an hour interval and transmit wirelessly in 2.4GHz using ZigBee protocol. BS node was connected to BS Server that has Wireless Network Management Station(WNMS) software, which received and stored data periodically for off-line processing.

Based on experience gained from Phase-I deployment, general purpose Signal Conditioning Boards to cater different types of sensors have been developed. In Phase-II deployment during winter 2021-2022, WSN has been redeployed & extended further to 9 locations to monitor 4 mountain slopes. An additional site with digital camera & WSN wake-up node for mountain slope monitoring has also been deployed. To detect and capture the acoustic events created due to snow instability, specialized WSN node has been developed and deployed in winter 2022-2023. To study the behavior of wireless signal over seasonal variations, specially designed Network Analyzer Node has been deployed at all locations and the data is logged in WNMS. The schematic of WSN deployed at the site is depicted in Fig.1. The deployed WSN is working smoothly, the metrological data is received by the BS and it is being monitored remotely from IGCAR and DGRE.

III.14 Design and Development of Wireless Sensor Network Based Acoustic Emission System

Acoustic Emission (AE) is a phenomenon of radiation of acoustic waves by materials and structures as result of sudden change or movement. This is usually due to defects such as crack formation or plastic deformation. The acoustic waves can be analyzed for detection and localization of these defects. In applications where remote detection of AE is required, Wireless Sensor Networks (WSN) can play a major role to acquire & process AE signals and for further transmission towards Base Station (BS).

To capture AE events in remote areas, Wireless Sensor Network based Acoustic Emission analyzer system (AE-WSN) has been designed and developed in-house [Fig. 1]. It captures AE signal using PK6I sensor, which is working at the resonant frequency of 55 KHZ, processes the signal on-board with limited memory and processing capability of WSN node. This system consists of four modules which are Sensor Excitation



Fig. 1: In-house developed Acoustic Emission WSN Node

Board (SEB), Signal Conditioning Circuit, Processing unit and Transceiver. The PK6I sensor is a medium frequency, resonant, AE sensor with an integral, ultra-low noise, 26dB preamplifier. SEB provides power to sensor and also act as a passive band pass filter with lower and upper cut off frequency of ~25 KHZ and ~100 KHZ respectively. Single ended output from SEB is converted to differential ended and fed to AD7380, a Successive Approximation Register (SAR) type ADC. Received acoustic signals are sampled @ 500KSPS and converted to 16bit/sample digital data.

Based on the processing requirement, Arm Cortex-M7 based microcontroller has been selected. Firmware has been developed to calculate acoustic related parameters such as Count, Amplitude, Absolute Energy, Duration, Rise-time and Measured Area of the Rectified Signal Envelop (MARSE) in hit driven mode. For MARSE calculation Hilbert Transform using CMSIS library & Approximate Method using polynomial curve fitting have been implemented on node. Performance and timing analysis were compared. Provision is incorporated to remotely configure control parameters such as Threshold, Hit Definition Time, Peak Definition Time and Hit Lockout Time. Remote supervision and diagnostic provisions has been incorporated into the system firmware such as Watch dog reset, Remote node hard reset, Remote node soft reset & Remote destination address change with unicast packet. The developed system has been validated using FieldCal AE Signal Generator and pencil lead break test. The block diagram of the system is shown in Fig. 2.

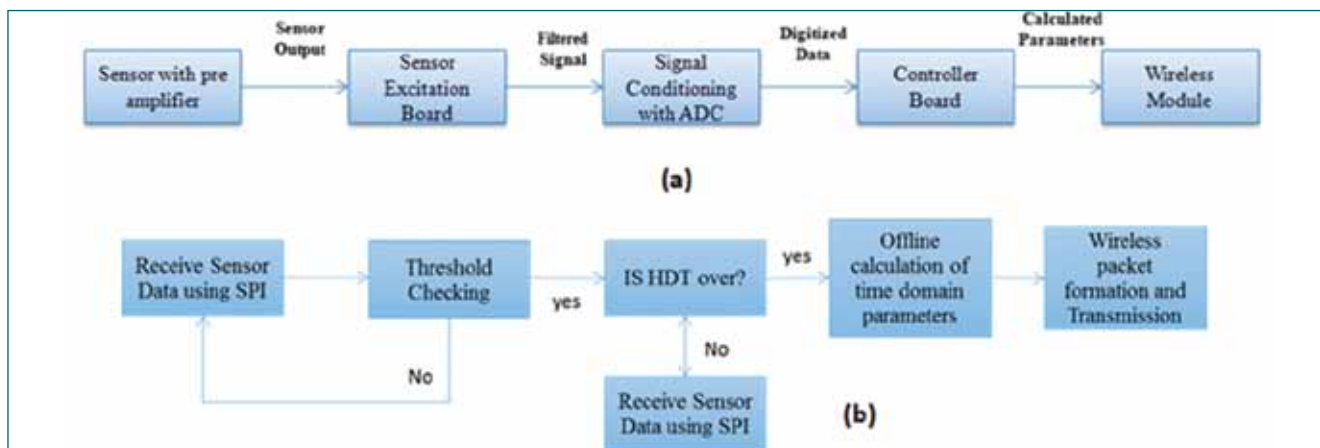


Fig. 2: (a) Hardware Block Diagram of AE-WSN & (b) Simplified Software Flow of AE-WSN

III.15 Establishment of Licensed Certifying Authority (CA) Facility for DAE at IGCAR

Certifying Authority (CA) is an electronic entity that issues, stores and revokes digital signature certificates (DSC) to individuals or electronic services, such as a web-service, to reliably identify them in digital space. The identity established through a DSC issued by a licensed CA is legally valid as per the Indian IT ACT 2000 and a digital signature created using these DSCs are treated on par with hand written signature. Hence, to accelerate the digitization of file processing and workflows using digital signatures across DAE, Computer Division, IGCAR has established a Certifying Authority facility to issue DSCs to the employees and electronic services of DAE. Besides the CA service that issues/revokes DSCs, the CA facility, also, hosts OCSP and Time-stamping services.

The Controller of Certifying Authority (CCA), Meity licenses the working of Certifying Authorities in India and provides necessary guidelines that are required to be met by the CAs. These guidelines were followed to establish IGCAR CA facility

Infrastructure

Two identical sites (Primary & DR) were commissioned with metal barriers, biometric access control, 24x7 CCTV monitoring, DG backed power supply, water logging sensors and a 3-tier security.

Hardware

FIPS 140-2 Level 3 certified Hardware Security Modules (HSMs) were procured, configured and commissioned to carry out the cryptographic operations in a secured and tamper-evident environment.

Software

IGCAR CA services and network security mechanisms

were developed using open-source Linux based operating system and software. Additional modules required were developed using Shell script and MySQL DB. All the software components such as operating system, web services, database etc are hardened.

Security: Defense-in-depth strategy was followed for holistic protection of CA facility. Both Primary and DA sites are protected by a perimeter firewall. The firewall allows only necessary HTTP traffic to provide OCSP and Time-stamp services. Behind perimeter firewall, an application level firewall is configured to filter out the unwanted HTTP request types. All the system admin operations of CA service are restricted offline. IDS service is configured on all the servers in CA facility (Fig.1 & 2).

Authentication & Authorization

The CA facility is designed to be accessed following the two-person control mechanism to achieve a high level of security for carrying out critical operations. The control mechanism was implemented using bio-metric access and physical access keys. The bio-metric access is restricted only to the authorized CA personnel.

Audit

All the systems were subjected to internal security audit to identify the vulnerabilities. Both primary and DA setups were then audited by third party auditors empanelled by the CCA as part of pre-operative audit to verify the compliance. Security recommendations suggested by the auditors were implemented.

In-principle approval to operate IGCAR CA was received from the CCA. The Key-ceremony was conducted to generate public-private key pair of IGCAR CA and Certificate Signing Request was submitted to the CCA for issuing the CA certificate

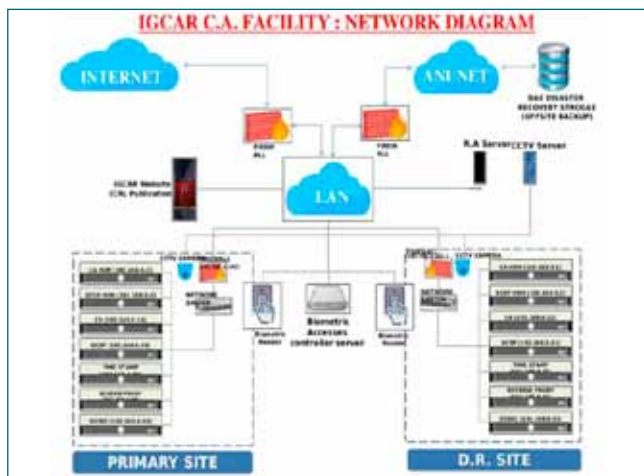


Fig. 1: IGCAR CA Facility Network



Fig. 2: IGCAR CA Primary Site, Annex Building

III.16 Deployment of Critical Intranet Services in IGCAR Private Cloud

A private cloud solution is deployed for IGCAR to provide a reliable, flexible and secure hosting platform for providing service delivery models of Infrastructure as Service (IaaS) and Platform as Service (PaaS) using open source tools, Openstack and Ceph. Openstack is a collection of open source tools that controls large pools of compute, storage and networking resources. Ceph is an open source software defined storage platform that is deployed to achieve a high-performance, reliable and scalable storage of 200 TB.

Currently, more than 30 servers offering crucial Intranet / Anunet services which include Email servers, Archive servers and Web servers for Workflow management, budget management, E-procurement, PC AMC management and various other activities are hosted on the cloud (Table 1). These servers are deployed with different operating systems such as CentOS 7/8/9, Ubuntu 20.04/22.04, Rocky Linux 8/9, Debian 10, Windows 10 and Windows Server 2016/2019. The cloud

supports deployment of servers with Legacy OS like Windows XP / RHEL 5 and porting of physical servers to overcome hardware obsolescence.

The cloud facilitates live migration of virtual servers at times of server maintenance or breakdown. The

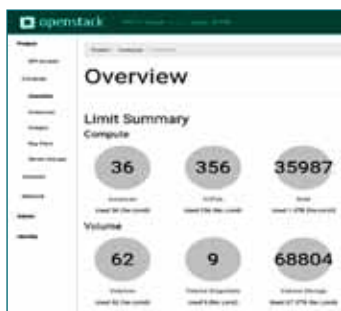


Fig. 1: Dashboard showing cloud servers (instances) and usage



Fig. 2: Dashboard of Zabbix Tool for Monitoring Cloud servers

hardware resources (CPU/ Memory/ Disk Space) allocated to a server can be resized as per user’s demands and requirements. Snapshots of servers can be taken at regular intervals, so that in case of an unexpected system error, a working version of the server can be redeployed. The persistent block device storage attached to a virtual server can be reattached to another server in case of server upgradation or recovery. All these features have significantly increased the availability of the servers hosted on the cloud.

A dashboard depicting the current status of the cloud environment that includes server instances and resource allocation is shown in Figure 1. An open-source monitoring tool, Zabbix is installed and configured to monitor the entire cloud infrastructure including servers, virtual machines, services and databases. Figure 2 shows the Zabbix monitoring tool’s dashboard. A web portal for the cloud is developed in house to add, edit and view details of cloud users and resources allocated to them.

Table1: Details of Servers deployed in the Private Cloud			
	Server	OS	Resources
Web Servers	Work Flow Management - ATOMS, ATOMS2	CentOS 8	16 Cores 128GB RAM 2 TB Disk
	E-Procurement Server	CentOS 8	24 Cores 128 GB RAM 2 TB Disk
	Utility Servers –PC AMC Mgmt, CSPORT, Earth Quake Notification, Water Quality Monitoring, Plan Server, DAE Budget & Accounting Server	Ubuntu 20, Ubuntu 22	4 - 24 Cores, 8 - 128 GB RAM, 100GB - 2 TB Disk
	Knowledge Mgmt Servers - EIG , RDG, CG	Rocky 8	4 Cores, 8GB RAM, 330 GB
Security , Auditing & N/W Related Servers	Central Authentication Server, Anti Virus Server, Security Audit Server, Centralized End Point Monitoring, CCA compliance Mgmt, Intranet VC compression	Win Ser 2016, CentOS 8, Rocky 8, Debian 10	4- 16 Cores, 8 - 32 GB RAM. 300 GB - 1 TB Disk
Storage Servers	IGC Workspace, Centralized Log Server, Storage Servers for Accounts, PHRMD	Rocky 8 Ubuntu 22	4 -8Cores, 8 - 24GB RAM 330 GB – 10 TB Disk
Email Servers	Email Ldap Server, Email Archive Server, IGCAR Mail Backup, BARCF Email Server	CentOS 8 CentOS 7	4 -8 Cores 8 - 32G RAM , 1 – 21TB Disk

III.17 CCTV Surveillance System for the Residential Township (DAE Anupuram Township)

DAE Anupuram Township is provided with CCTV Surveillance system comprising 120 nos. of IP cameras and 23 field network switches spread across various streets and road junctions of the Township. The cameras include 2 MP IP cameras, 5MPIP cameras at various gates and important locations, Automatic Number Plate Recognition (ANPR) cameras at the gates to capture the number plate of the incoming/outgoing vevhicles. The cameras are installed on 5 meter pole and positioned at optimum height so as to get the clear view of the street. The signals from these cameras are processed at the field switches first; get converted into optical signals using optical transceivers and reach Control room in optical form through the single mode fiberoptic cables. The length of the fiber cable installed in the whole township is around 14 Kms.

The township area is divided into two segments, forming two optical loops (rings) covering the entire township. Field switches placed in the junction box, takes the signals from the cameras installed in the nearby streets. CAT 6 cable is used when the cable length is less than 80 meters and optical cables are used when the cable length is more than 80 meters. All these field switches are connected via backbone optical cables. These camera signals in optical form are converted back into electrical form at the core switches installed at control room. Core switches are configured in redundant mode so that the system will continue to function even if one core switch fails. Live view of these cameras, installed

at various places of the township is obtained through 2 nos. of work stations and displayed in 4 nos. of CCTV monitors installed at the control room.3 nos. of monitors are allocated for displaying the live view of cameras in 3 different areas of the township and the fourth monitor is being used to display the live view of important cameras especially various gates. ANPR software is configured to store the vehicle entry/exit images captured by the ANPR cameras as well as the text from the license plate.

Moreover, the system is provided with Video Management Server, Video Recording Server and 5 nos. of storages of 18 TB capacity (each) in control room, facilitating to provide a retention time of one month. One CISF official is deployed on round the clock shift basis in the CCTV Control room. 2 x 3 KVA UPS systems are provided to feed power to the computer systems in the control room during power failure.

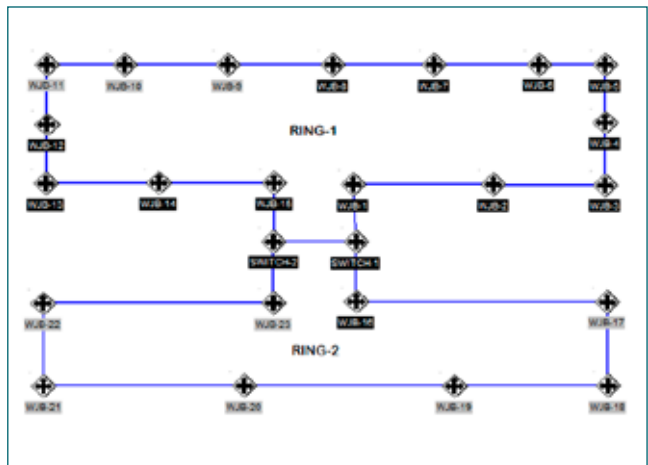


Fig. 2: Network Architecture of CCTV System



Fig.1: View of Junction box MHC Earth pit and pole in the field



Fig.3: CISF CCTV control room at Anupuram

III.18 Turbulent Natural Convection and Aerosol Distribution Studies for Sodium Pool Fire in A Confined Environment

In case of a Core Disruptive Accident in a sodium-cooled fast reactor, sodium will be ejected from the reactor vessel into the Reactor Containment Building (RCB) which results in sodium fire. Liquid sodium combustion generates aerosols, which get dispersed and remain suspended in RCB based on their size, degree of turbulence and other factors, before a major fraction gets deposited within RCB. The Environment Source Term (EST) primarily depends on the dynamics of sodium aerosols inside the containment followed by leakage through containment wall. SFR containments being large, experiments at prototype scale are not possible. Hence, a combination of small scale experiments and computational tools are essential to carry out safety analysis of SFRs. The models shall be validated with data from experimental facilities which are smaller in size than the RCB and then employed to predict prototype behaviour. In existing containment codes, the evolution of suspended aerosol concentration has been predicted, assuming uniform aerosol concentration in large containment buildings. However, in actual case a non-uniform concentration profile exists, which leads to stratification of aerosol concentration inside the containment. Towards assessment of aerosol dynamics in a realistic scenario, sodium pool fire experiments were conducted in a chamber of volume 140 m³ and spatio-temporal characteristics of sodium aerosol, temperature distribution and convective velocity were measured experimentally. A 0-D numerical model was applied for

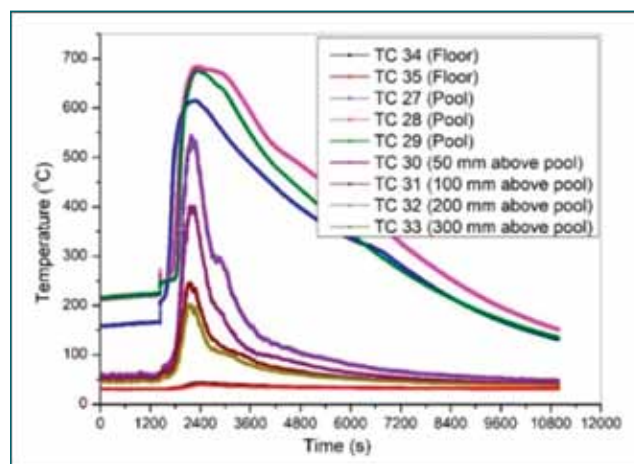


Fig. 2: Evolution of temperature during sodium pool fire.

the evolution of aerosol characteristics and results are compared with measured concentration values and a 2D CFD model was developed to get the temperature and velocity fields due to sodium fire inside the chamber.

Experimental Facility

The facility consists of a closed rectangular steel chamber of size 5.6 m x 5.4 m x 4.6 m with a volume of 140 m³ designed to withstand an internal pressure of 1 bar at 40 °C. The facility has dedicated real-time and offline aerosol metrological devices, sodium system and instrumentation, an array of thermocouples for temperature monitoring along with data acquisition and a high-speed video imaging system. The sodium fire experiments were carried out by using 2.0 kg of sodium spreading to form a pool area of ~ 0.25 m² on a tray. Sodium combustion aerosol was sampled in 12 locations at three elevations viz. 1.2 m, 3.0 m and 3.85 m from the

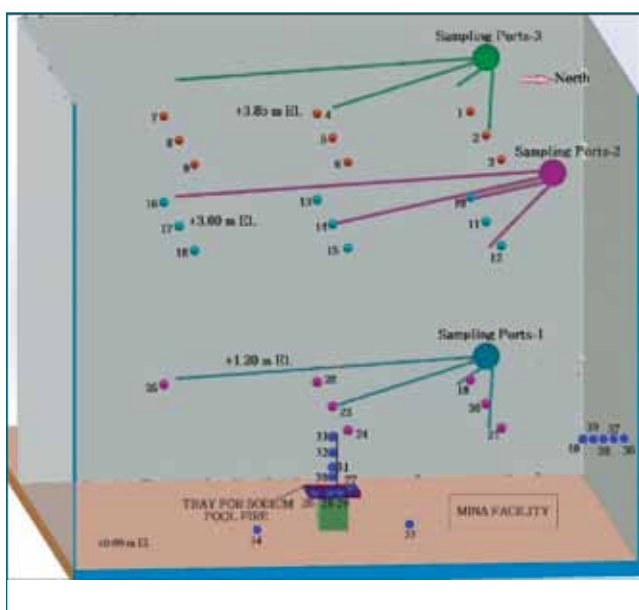


Fig.1: A schematic 3-D view of the test chamber.

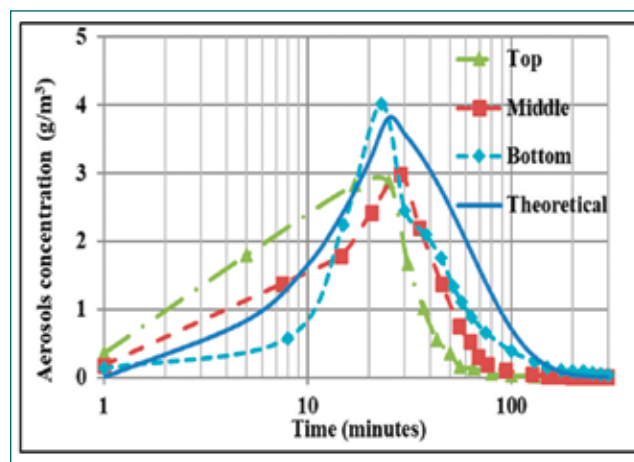


Fig. 3: Evolution of aerosol concentration.

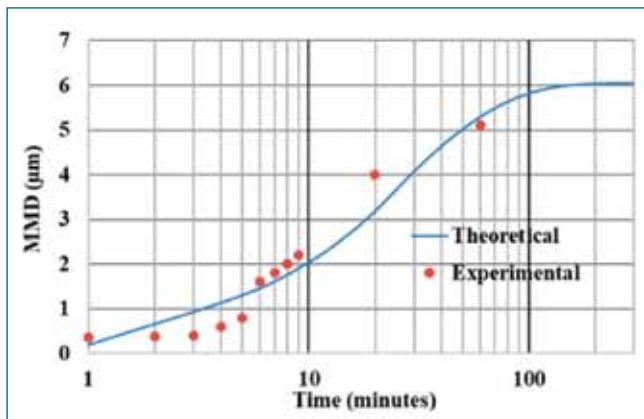


Fig. 4: Evolution of median size growth of aerosol

chamber floor and at four azimuthal locations on each elevation to obtain the spatial distribution of aerosol. The three-dimensional isometric view of the sampling positions and temperature monitoring locations are shown in Fig.1.

Temperature Rise in the Sodium Pool

The rise in pool temperature in and around the sodium pool was recorded using k type thermocouples. Sodium pool temperature in the tray was increased to a maximum of 685°C in ~ 10 minutes and remained at ~ 660°C until the completion of sodium combustion (~25 minutes from the T0) (Fig. 2).

Sodium Burning Characteristics

After 24 hours of the experiment, a sample was taken from the residue in the tray for determining un-burnt sodium. From the burnt sodium mass and duration of the fire, the average burning, and aerosol release rates are calculated and found to be 17.3 kg/m²hr and 0.24 g/s respectively.

Concentration and Size of Sodium Aerosols

The measured and predicted sodium aerosol concentration as a function of time is given in Fig. 3.

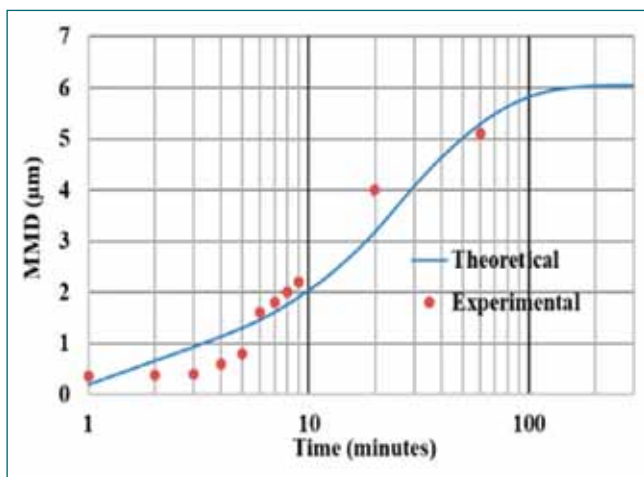


Fig. 5: Velocity profile and temperature contour

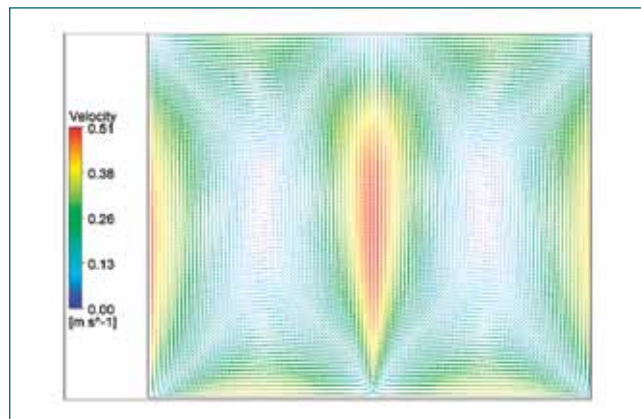


Fig. 6: Peak velocity observed in the rising plume

The maximum average aerosol concentration at the bottom, middle, and top elevations are 4.0, 2.4 and 2.8 g/m³ respectively. The suspended aerosol concentration is higher at top elevation than the middle and bottom (up to 10 minutes). After sodium fire when aerosol generation ceases (after 25 minutes), the concentration decreased more rapidly at the top elevation than at middle and bottom. After about 100 minutes, the suspended aerosol concentration is ~ 2%, 4% and 10% of maximum concentration at top, middle and bottom elevation, respectively, while it is 18% as per the prediction. The evolution of aerosol mass concentration needs to be addressed by 3D Fluid modeling (Fig. 3).

The initial aerosol median size is 0.2 µm, and the size enlarges one order higher (up to 2 µm) within 10 minutes (Fig. 4). After that, the size growth is relatively slower and increased by 5.0 µm in about 60 minutes. The size evolution of aerosol by theoretical simulation captures the overall trend reasonably well.

The fraction of total deposited aerosol mass is dominant on the floor (91.96 %) than the side walls (6.70 %) and downward facing surface (1.35%).

CFD prediction of Temperature and Velocity Field

A 2D CFD model is developed to predict the temperature and velocity fields due to sodium pool fire. The buoyancy driven convective flow along with radiative heat transfer is analyzed by assuming the sodium pool to be at a constant temperature of 950 K. Turbulence is modelled using k-ε model. The chamber is assumed to contain sodium hydroxide aerosol which is an absorbing medium. The velocity profile and temperature contour obtained inside the chamber are illustrated in Fig. 5 and Fig 6 respectively. Temperature field range is limited to 30°C to 60°C for better representation in Fig 5. Temperature in the vicinity of sodium pool is high. The peak velocity observed in the rising plume above the pool is around 0.5 m/s as seen in Fig. 6.

III.19 Thermal Transient Measurements of Optical Periscope Lamp Assembly for Different Flow Rates using Thermal Imaging

An optical periscope is an instrument used for visual inspection, if any obstacles are present in the direct line of sight of the observer. In a nuclear reactor where many factors limit the visual inspection, periscopes are vital for in-service inspections. The Prototype Fast Breeder Reactor (PFBR) Periscope is used to inspect reactor internals at the cover gas region above the liquid Sodium level. It is 400 mm in diameter and 10 m in length, housing an image channel and two Xenon lamps to illuminate the inspection region. The lamps operate at high voltage, 24 kV, and switch to 14 V during regular operation. Fig. 1 represents the schematic diagram of the PFBR Periscope.

The periscope's xenon lamp had frequent failures even at room temperature operations. Hence, Remote Handling and Irradiation Experiments Division (RHIED) have taken up to study the system and to carry out the design modifications to make the lamp holder assembly and to ensure the successful working of the lamp. The pulse voltage for starting the lamp has changed from 24 kV to 15 kV and then switches back to 14 V during regular operation. A technology modification has been done by placing a Resistance Temperature Detector (RTD) temperature sensor close to the lamp terminal. The design modification was validated through

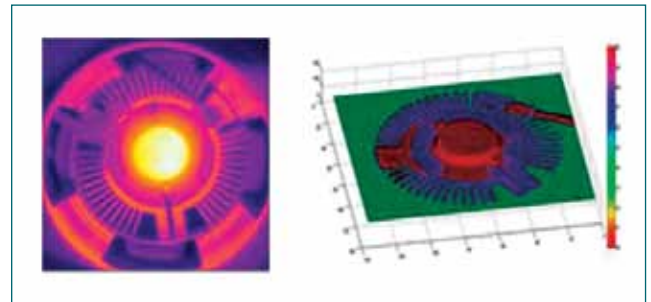


Fig. 2: (a) Close up view of the Fin Region of a typical IR Thermal image. (b) 3D surface plot of the thermal image taken during the operation of the lamp.

comprehensive temperature profiling of the system using infrared thermal imaging.

Passive thermal mapping was carried out using FLIR T400 Infrared Camera, which has an uncooled microbolometer detector. The spectral range of the system is 7-13 μm in wavelength. The system was mounted on a tripod stand having a distance of 50 cm from the sample. Factors like emissivity, relative humidity, and ambient temperature influencing temperature measurement are considered while obtaining images. The thermograms were obtained at regular intervals, which were later analyzed using FLIR Tools software.

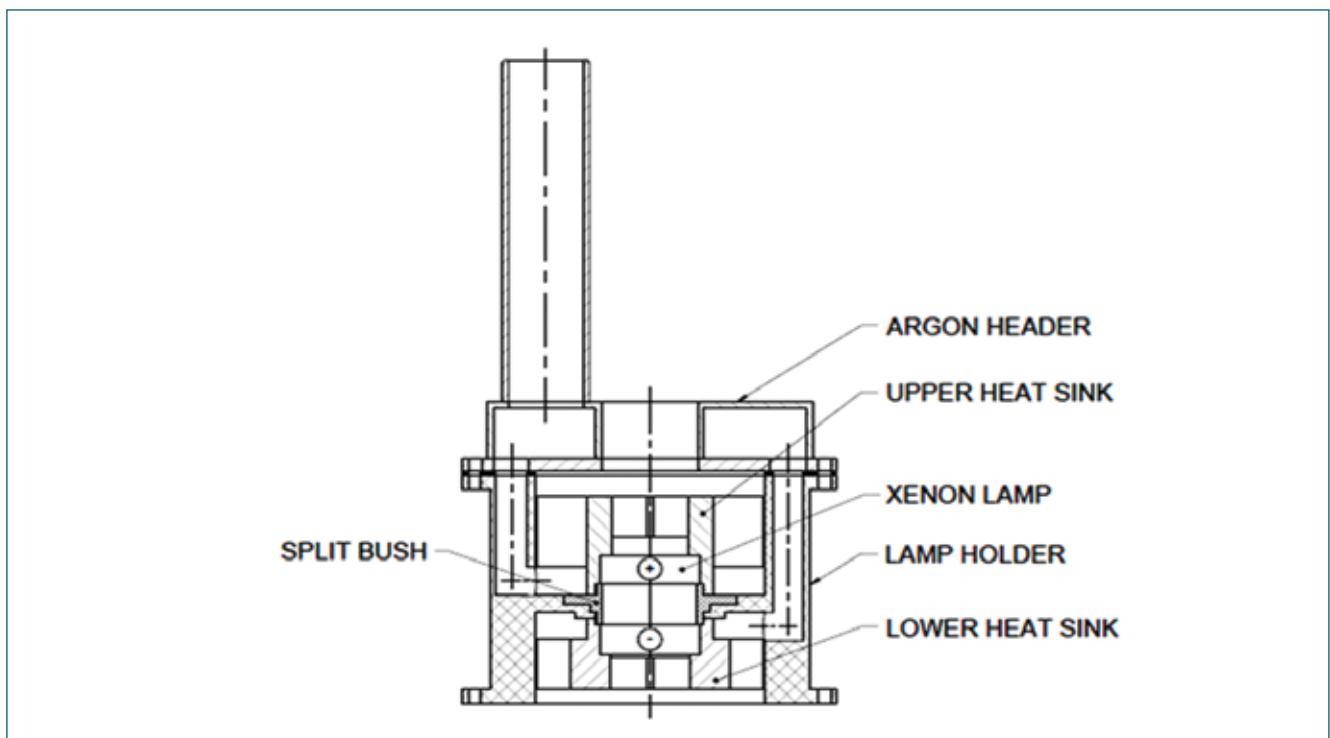


Fig. 1: Lamp assembly with cooling arrangement

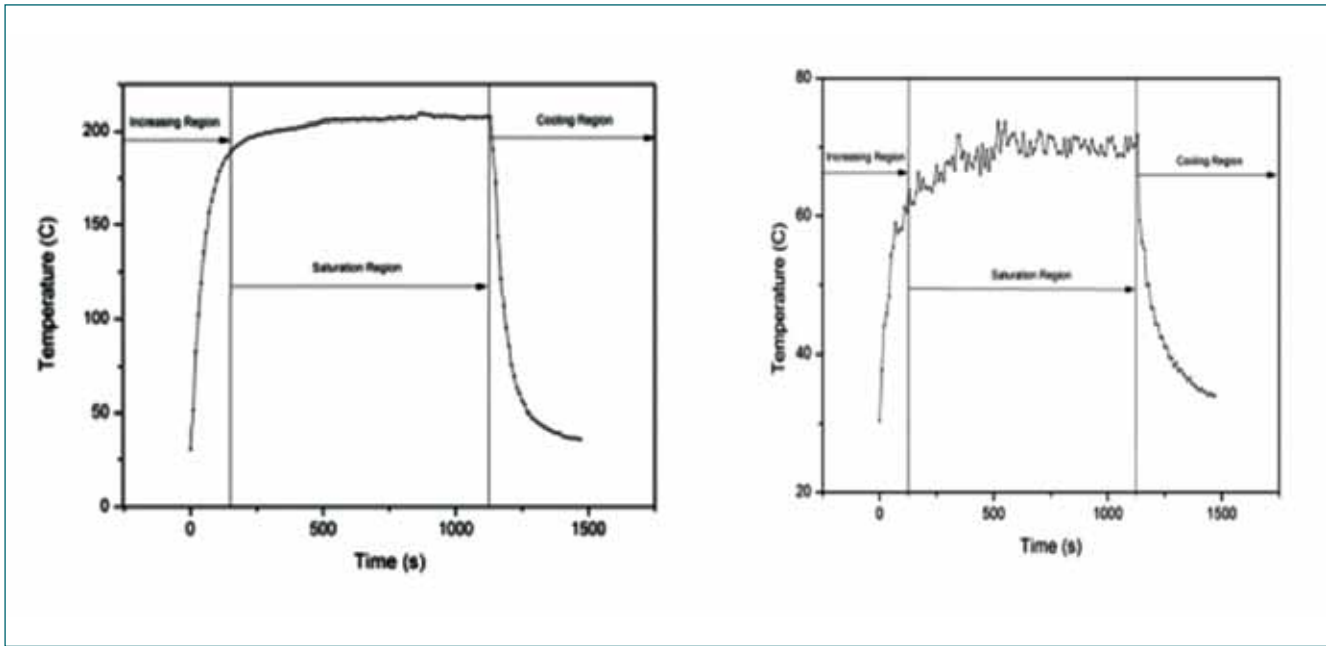


Fig. 3: Plot of maximum temperature at (a) the lamp surface and (b) the Fin during the operation of the lamp and switch off state with respect to time at a flow rate of 1000 lpm

A total of three experiments were carried out for the non-contact temperature mapping of the surface of the Xenon flash lamp and the fin region at three different flow rates- 800 lpm, 1000 lpm, and 1200 lpm. The measurement tools, such as area profiling- circle or rectangle, and line profiling, were chosen for the analysis. Temperature values extracted from the thermal images were plotted and analyzed.

Fig. 2 shows the 3D surface plot of the lamp assembly with the fin region. It can be observed from the image that the maximum temperature recorded is on the lamp compared to the fin region.

The maximum temperatures mapped on the outer glass surface of the lamp and the fin region during the operation and during the cooling phase at each flow rate are plotted against time (Fig. 3). It was observed from the plot the increase in temperature was high for the initial few minutes (heating region). After the initial rise in temperature, a saturation region was observed in which there was no significant temperature rise. During the cooling phase (cooling part), temperature fall has been observed to have a steep slope.

The overall temperature profile of the lamp with respect to time is the same for all three flow rates- 800 lpm, 1000 lpm, and 1200 lpm. The temperature profile of the fin region for different flow rates revealed that the maximum

temperature attained was above 80°C for 800 lpm. In contrast, the temperature rise was 70°C and less than 70 °C for 1000 lpm and 1200 lpm, respectively. The temperature difference on the cooling phase for a timed lap of 50 s for 1000 lpm and 1200 lpm is given below in the table, and this data indicates that the cooling is more efficient with a higher flow rate.

Table 1: Drop in temperature during cooling phase for the time of 50 s.

Flow rate (lpm)	Temperature Drop (deg C)
1000	21.7
1200	28.0

The temperature measurement indicates that the maximum temperature recorded was on the lamp region, and uniform temperature distribution was exhibited in the Fin Region with no significant hot spot. The effect of flow rate in the heat dissipation of the Fin Region by forced convection was also clearly indicated by the comparison of surface temperature mapping of the Fin Region in all three flow rates- 800 lpm, 1000 lpm, and 1200 lpm. Cooling is more efficient for 1200 lpm and 1000 lpm and comparatively less for 800 lpm. The trend in temperature profile recorded during the operation and lamp assembly and cooling phase has been brought by the study.

III.20 In-sodium Visualization of Molten Fuel Sodium Interaction using X- ray Radiography

In case of a hypothetical core melt accident in Sodium Cooled Fast Reactor (SFR), the molten fuel comes in contact with cold pool sodium leading to Molten Fuel Coolant Interaction (MFCI). During MFCI, the melt will undergo fragmentation due to various hydrodynamic and thermal instabilities at the melt-sodium interface. The interaction can also result in rapid pressure rise due to generation and expansion of sodium vapor. The fragmented debris settle as a bed on core catcher provided at the bottom of the reactor vessel. The debris bed continues to generate heat due to radioactive decay. Coolability of the debris has to be ensured for safe retention of the degraded core and protecting the reactor vessel. Heat transfer from the debris bed strongly depends on the size, shape and porosity of the bed. Hence, in depth knowledge of melt fragmentation phenomena during MFCI is very important.

An experimental study has been taken up at SED, SQRMG to investigate MFCI using simulated corium (melt mixture of alumina and Iron) and sodium. An experimental setup consisting of a melt generation system by aluminothermy reaction and an interaction vessel of 100 mm diameter and 600 mm length for holding sodium column was installed and integrated to an X-ray imaging system (Fig. 1). An X-ray source (Varian 451-Be X-ray tube & Gulmay generator) and a Digital Flat Panel Detector (XRD 1621AN14ES) are used for X-ray imaging. The main objective is to capture attributes of MFCI viz., melt fragmentation, debris formation, velocity and settling behavior of debris and dynamics of sodium bubbles generated.

Two experiments were conducted by releasing simulated melt (30 g and 500 g respectively) at ~ 2400 °C into 3 kg of sodium maintained at ~ 400 °C. The melt fragmentation was captured using radiosopic imaging

with 450 kV, 10 mA X-ray sources and DFPD. K-type thermocouples along with GP 10 Yokogawa make data logger & PC is used for acquisition of temperature data. Prior to experiments, the X-ray imaging system was calibrated using standard phantoms of steel and HDPE for melt jet and voids respectively.

The X-ray images were acquired at 30 frames per second. In the first experiment, sodium vapor pocket and fragmentation of the melt droplet was observed at sodium interface. The images were processed using flat field technique and sequence of fragmentation at 33 ms interval is shown in Fig. 2. Size of the fragmented particles during first fragmentation is $\sim 0.8 - 21$ mm. Temperature rise in sodium was ~ 100 °C.

In the second experiment with 500 g melt, the fragmentation was found to be more vigorous with instantaneous melt fragmentation. Intense mixing of the melt droplets and sodium vapor was noticed near the sodium-argon interface. Processed images of melt fragmentation at 33 ms interval in 2nd experiment is shown in Fig 3. Temperature rise in sodium was ~ 209 °C. During the first fragmentation, the fragmented particles were found to be in range of 0.66 -12 mm. The particles were observed to fragment further. However, no sodium vapor bubbles were noticed from the bottom part of the interaction vessel, indicating temperatures of the particles to be below the boiling point of sodium and hence completely solidified. The average velocity of the fragmented debris is deduced to be 0.37 m/s.

Post experiment, the sodium was drained and the fragmented debris was retrieved by vacuum evaporation method. The particle size distribution indicated log normal distribution with a mass median diameter of 0.3 mm. Further experiments are planned on large scale fuel sodium interactions.



Fig. 1: Experimental set up

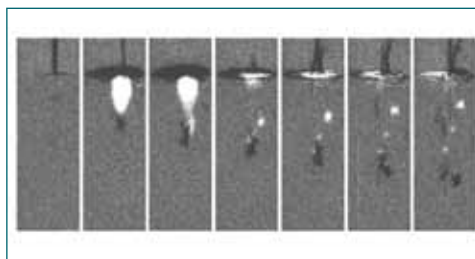


Fig. 2: Fragmentation of a melt droplet in sodium (Processed X-ray images at 33 ms interval)

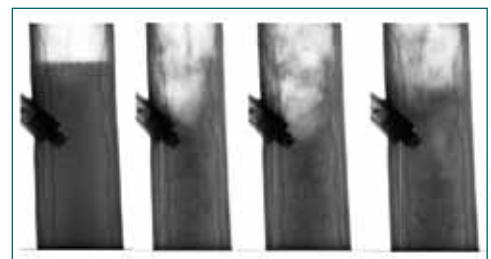


Fig. 3: Fragmentation of melt stream in sodium (Processed X-ray images at 33 ms interval)

III.21 Development of Carbonate Based Powder for Sodium Fire Extinguishment

In sodium cooled fast reactors and process loops, sodium fire is one of important safety concern due to its highly reactive nature. When sodium leaks accidentally, it can react spontaneously with air leading to sodium fire. Sodium fire management is challenging as it produces white dense smoke with toxic as well as corrosive aerosols. Hence, highly efficient fire suppressants must be developed for rapid extinguishment of sodium fire. Several extinguishants have been used throughout the world like Met-L-X in USA and MARCALINA in France. Currently, bicarbonate based dry chemical powder (B and C class type) is used in INDIA for such application. Eutectic Carbonate powder (Met-C) is being developed and tested (Fig. 1) in different scales of sodium fire for performance evaluation at SQRMG-IGCAR. Powder effectiveness is also compared with currently used powders during these tests.

Met-C Powder has been tested for apparent density, moisture content, hygroscopic nature, free flow, particle size distribution, water repellency as per recommended IS 4308:2019, before taking up the fire extinguishment

tests. During the series of tests, pool area and depth were varying parameters starting from lab scale to 8.5 kg inventory of sodium. Powder is observed to form protective crust over sodium fire and extinguish successfully. Typical performance comparison test results for 1.5 kg sodium fire are shown in Table 1. Met-C powder is found to be relatively efficient and promising as compared to currently used bicarbonate DCP. Qualification tests are planned with higher inventory up to 50 kg, surface area and pool depth to ascertain its efficiency on practical site application purpose.

Table.1 Performance comparison tests		
Parameter	Bicarbonate based DCP	Met-C powder
Density(g/cc)	1.071	0.807
Qty. of powder Used(Kg)	4.383	0.736
Q powder / Q Na ratio	3.1	0.545
Qty. of Powder used (g/ cm ² Na pool)	7.93	1.33
Na Fire extinction Time	6.5 min	31 sec



Fig. 1: Photographs of Sodium fire extinguishment

III.22 Disposal of Sodium using Controlled mist Technique

Sodium is used for various safety experiments at IGCAR. After the tests, waste sodium need to be disposed in safe and eco-friendly manner considering the permissible limits of generated sodium combustion aerosols, hydrogen management and required neutralization before release to environment. Towards this, disposal process is being developed using controlled water mist injection, associated with exhaust gas treatment system (EGTS). The supporting test facility for optimization of this process in batch mode consists of a combustion chamber equipped with mist nozzle distribution system and cameras for process visualization as shown in Fig. 1. The stainless steel disposal tray is kept below the multi nozzle assembly to accommodate waste solid sodium, for controlled combustion and disposal. The chamber is connected to EGTS for aerosol management.

Three tests were carried out to study the feasibility of using the technique for sodium disposal and optimize the process operating conditions. The test conditions were varied for sodium quantity (~ 1 kg), mist injection rates (23 - 183 ml/min), distance between nozzle to disposal tray (570 - 1000 mm), number of sodium blocks and nozzles. Typical experiment of 1 kg sodium disposal test with four nozzle spider configuration is shown in Fig. 2, with a mist injection rate of 183 ml/min and nozzle to sodium distance of 1000 mm.

During the disposal process, controlled sodium



Fig.1: Combustion chamber with multi-nozzle injection system and disposal tray

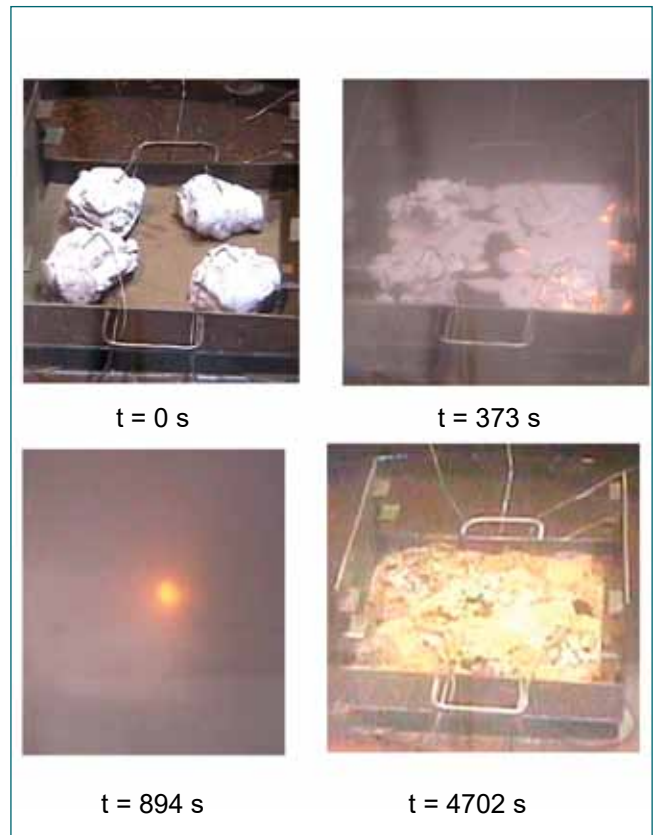


Fig. 2: Stages of 1 kg sodium disposal

combustion could be achieved without any localized explosion. Using this process, sodium was disposed within a period of 16 minutes, consuming 3 L of water through mist nozzles followed by sodium combustion for a period of 9 minutes. The maximum temperatures recorded on the sodium brick during the disposal process was 897 °C during combustion. The left over residues on disposal tray was neutralised and disposed off after the tests.

The results indicated optimum disposal rate of 2.4 kg/h with the present test configuration. The requirement of a minimum separation distances of 570 mm or higher between the nozzle and disposal tray was also confirmed for safe solid sodium disposal. The tests indicated that with higher sodium inventory, the effectiveness of multi nozzle mist injection system will be higher for effective solid sodium disposal. This preliminary series of tests confirmed applicability of controlled mist technique for waste sodium disposal through optimized design and process parameters. Experiments are planned with additional nozzles and large size disposal tray for relatively large quantity of waste sodium, for faster disposal rate.

III.23 Corrosion Behaviour of Ceramic Composite Coated and Uncoated P-91 steel and Type 316 LN Stainless Steel in Lead with Oxygen at 550°C

Heavy liquid-metal (HLM) coolants based on lead (Pb), lead-bismuth eutectic (LBE) and lead-lithium eutectics (LLE) gained more interest in recent years for the future advanced fast spectrum nuclear reactors of Generation - IV type. Corrosion issues of structural materials in a molten lead environment are the major problem for the heavy liquid metal coolants based future advanced nuclear reactors. The present study focused on understanding the corrosion mechanisms of P-91 steel and type 316LN SS in as received and 50% Al₂O₃ - 50% Y₂O₃ Atmospheric Plasma Spray (APS) coated conditions in the molten lead with 10-5 wt.% oxygen at 550 °C for different exposure durations.

The SEM analysis of the 500 h molten lead exposed P-91 steel exhibited dissolution corrosion attack along with oxide enrichment (Fig. 1 (a) and (b)). The penetration of lead was not observed in the molten lead attacked regions. The cross-section corrosion morphology of 1500 h molten lead exposed 316LN SS showed intergranular dissolution attack (Fig. 1c). The detailed SEM-EDS point analysis at different depth of the sample revealed that the concentrations of 316LN SS constituent elements (Fe, Cr, Ni, Mo) varied and penetration of Pb (Fig. 1d). The Ni content had decreased significantly in the lead attacked region than the unaffected region. The higher depletion of Ni is due to higher solubility of Ni in molten lead than other elements. This high solubility of certain steel elements (especially Ni) in the liquid Pb results in the destabilisation of the austenitic phase close to the

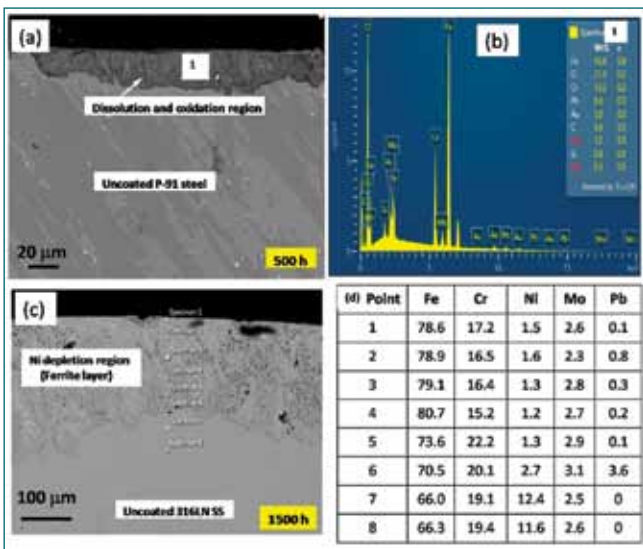


Fig. 1: BSE cross-section image of molten Pb exposed uncoated samples (a) P-91 steel-500 h (b) EDS spectrum of 1 as indicated in 1(a), (c) 316LN SS-1500 h and (d) EDS analysis at different points as indicated in 1(c).

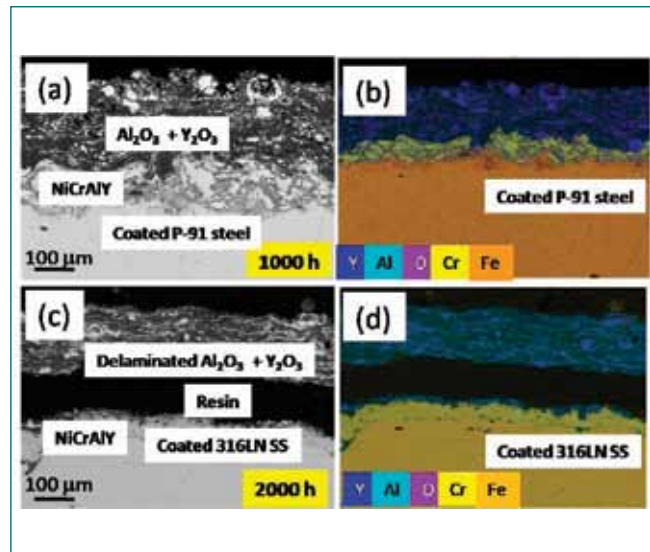


Fig. 2: BSE cross-section image of molten Pb exposed coated samples (a) P-91 steel-1000 h image, (b) corresponding EDS map of 2(a), (c) 316LN SS-2000 h image, and (d) corresponding EDS map of 2(c)

steel surface and its transformation into ferrite phase. Thus, the post molten lead exposure characterization revealed the dominant corrosion mechanism as dissolution and oxidation without phase transformation for P-91 steel, whereas the dissolution mechanism led to phase transformation in 316LN SS. The development of innovative protection ceramic composite coatings on P-91 steel and 316 LN SS steel is an important area of research to overcome the issues of structural materials in molten lead conditions.

Both P-91 and 316LN SS, are coated with a mixture of 50% Al₂O₃ – 50% Y₂O₃, as top coat and NiCrAlY as bond coat. Fig. 2 presents the BSE-EDS mapping of coated P-91 and 316LN SS. The results (Fig. 2 (a) and (b)) indicated that the composite ceramic coating had impeded the P-91 surface dissolution and oxidation by hindering the molten lead interaction with the surface. The ceramic composite coat on 316LN SS exhibited cracking and delamination after exposure to molten lead at 550 °C (Fig. 2(c) and (d)). High CTE of 316LN SS induces high thermal expansion mismatch stresses between the coating and substrate while exposed to molten lead at 550 °C. Therefore, the top ceramic coat of 316LN SS is cracked and delaminated in molten lead environment. Further, the low CTE of P-91 steel favored the stability of ceramic composite coating during testing at 550 °C in molten lead environment. However, no lead ingress into the surface was found for both coated P-91 steel and 316LN SS.

III.24 Plasma-sprayed Lanthanum Zirconate and Yttrium Aluminum Monoclinic Coatings Its Performance in Molten Liquid-sodium

Air plasma-sprayed (APS) ceramic coatings are being explored as chemical, environmental, electrical, and thermal barrier systems for components employed in sodium-cooled fast-spectrum nuclear reactors (SFRs). The design and constructional requirements of several components demand the APS coatings in continuous contact with the aggressive and corrosive liquid-sodium (coolant) environments. Conventional APS coatings were found to be susceptible to liquid-metal corrosion in high-temperature liquid-sodium environments. Towards this, emerging thermal barrier ceramics such as Lanthanum Zirconate (LZ) and Yttrium Aluminum Monoclinic (YAM) are investigated by exposing APS deposited ceramic coatings in liquid-sodium at 400 °C for 500 h and 1000 h.

As-coated pristine LZ coatings showed a white-colored topcoat. After 500 h of sodium exposure, several sublayers were found to be exfoliated, leaving behind some remnant parts of the topcoat surface. 1000 h sodium-exposed LZ coatings showed complete exfoliation of the previously seen remnant sublayers. However, several layers of the topcoat were still found to be intact and properly adhered to the bondcoat as noted in Fig. 1. APS-coated pristine YAM coatings were found to appear in a creamy texture. The 500 h and 1000 h sodium-exposed coatings were observed to be undamaged and free of any visible deterioration. Nevertheless, the exposed coatings were discolored after cleaning, and the degree of discoloration was found to increase with increasing exposure time.

LZ shows phase stability (cubic phase) from room temperature until it reaches its melting point (~2300 °C). APS-deposited pristine LZ coatings retained the same phase as that of the LZ powder but showed much more crystalline peaks when contrasted to the feedstock (Fig. 2). Phase analysis of sodium-exposed coatings exhibited

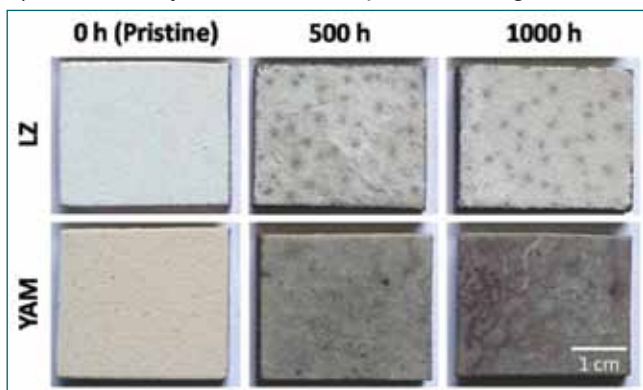


Fig. 1: Photographs of APS coatings LZ & YAM

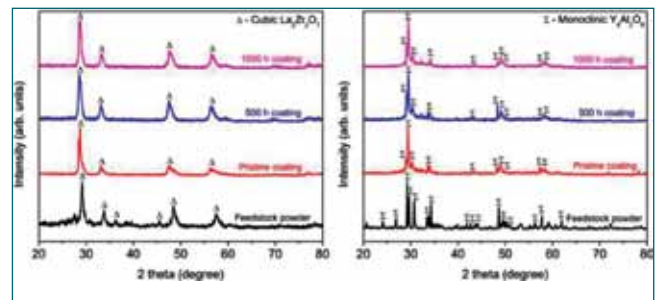


Fig. 2: Diffractograms of LZ and YAM coatings

neither phase changes nor the formation of any corrosion products. Pristine YAM coatings also retained the same phase as that of its feedstock powder but with improved crystallinity. Additional peaks corresponding to reaction byproducts or phase instability were not seen in the diffractograms as shown in Fig. 2.

From the SEM analysis (Fig. 3), LZ coatings were found to be degraded due to the combined effects of erosion of topcoat layers and spallation due to the development of parallel delamination cracks in the topcoat. Formation of the delamination cracks may be accredited to the coalition of microdefects due to the infiltration of liquid-sodium into the deep sublayers of the topcoat. However, YAM coatings exhibited superior performance in liquid-sodium as compared to LZ, which can be attributed to the resistance to grain boundary attack and the better cohesive bonding between the adjacent splat boundaries. Moreover, YAM coatings showed phase stability, structural integrity, and chemical inertness in liquid sodium environments. Except for some mild surface attacks in the form of pinholes, amplified roughness, and augmented porosity, YAM coatings performed well in liquid-sodium. Considering the research outcomes, APS coated YAM is a promising candidate to be used as protective coatings over replaceable components of SFR.

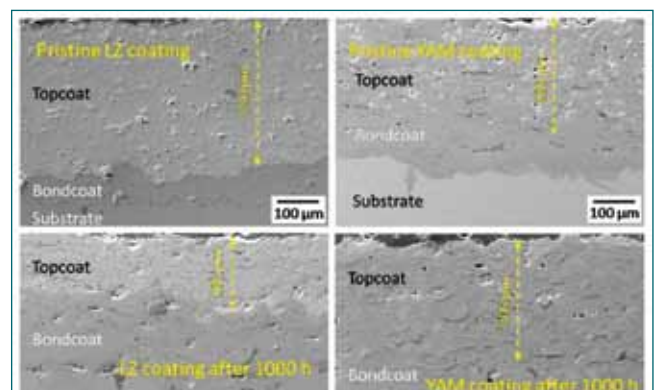


Fig. 3: SEM images of LZ Coatings

III.25 Durability of Plasma Sprayed Alumina Coating on Inconel 600 with Different Bond Coats for Neutron Detector Application

Thermally sprayed alumina coatings are widely used in electrical and electronic industries because of its dielectric properties and are proposed as a candidate coating material for high temperature fission chamber neutron detectors in PFBR. Inconel 600 samples with and without alumina top coat and two different bond coats (Ni-50Cr and NiCrAlY) deposited by plasma spray process was evaluated. NiCrAlY bond coat with and without alumina top coat subjected to isothermal aging at 923 K for 1000 h experienced lower percentage weight gain compared to alumina top coat with Ni-50Cr bond coat (Fig 1). Figure 2a shows the surface morphology of Ni-50Cr bond coat after isothermal aging at 923 K for 1000 h. The formation of faceted single crystal oxide formed on the surface of Ni-50Cr bond coat after isothermal aging is clearly evident in Fig 2a. XRD and EDS results showed that the formed single crystal oxide is Cr_2O_3 . The single crystal chromia has grown relatively rapidly and the formation of such bulky single crystals growing in preferential directions with protrusions on one end is detrimental to the integrity of the bond coat and alumina top coat. High resolution SEM micrograph of NiCrAlY bond coat after isothermal aging exhibited fine disc shaped oxide morphology (peg-like protrusions)

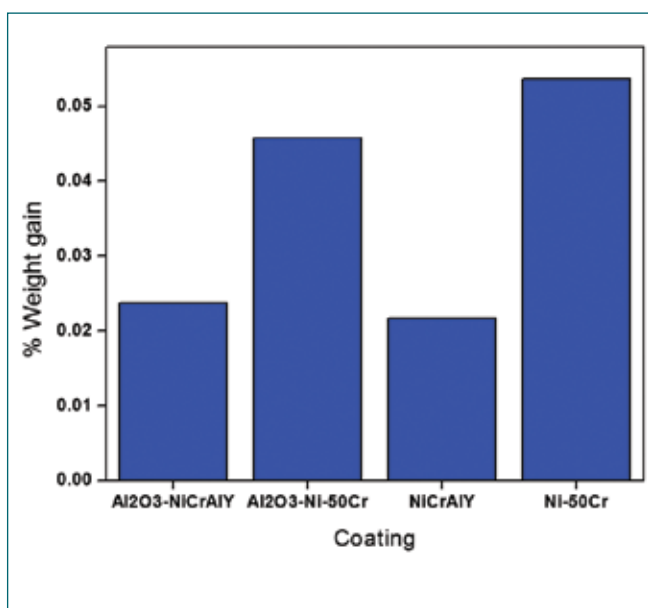


Fig. 1: Percentage weight gain of plasma sprayed Ni-50Cr, NiCrAlY bond coat and alumina top coat with Ni-50Cr & NiCrAlY bond coat over Inconel 600.

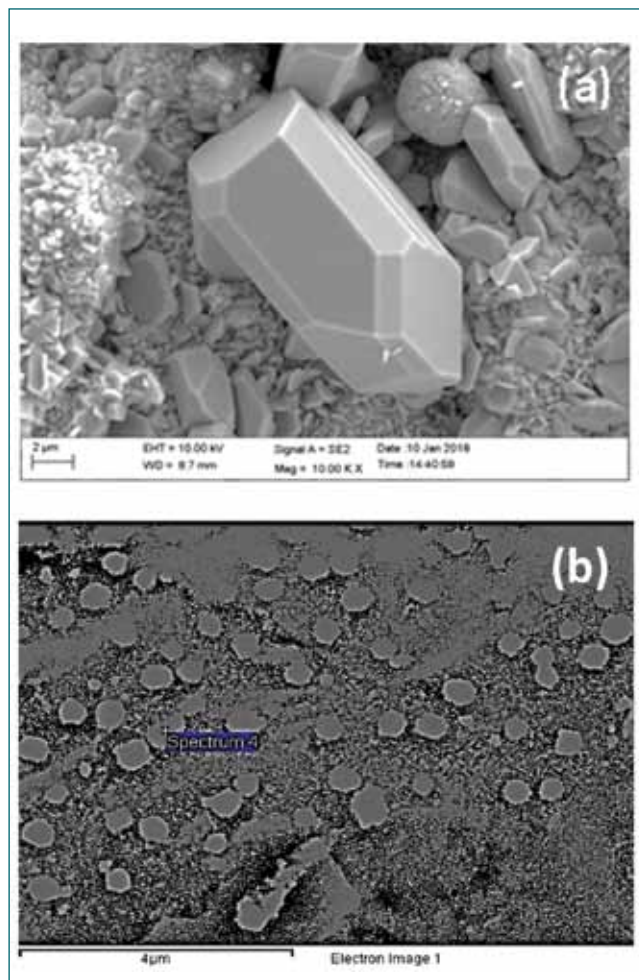


Fig. 2: SEM micrograph of (a) Ni-50%Cr bond coat & (b) NiCrAlY bond coat after isothermal aging.

(Fig 2b). These fine peg-like protrusions evident in the present study are reported to enhance scale adherence by mechanical keying mechanism. The isothermally aged Ni-50Cr bond coat showed undesirable epitaxial growth with protruding Cr_2O_3 crystals ($13.5\ \mu\text{m}$) while the NiCrAlY bond coat showed uniform thermally grown oxide (TGO) of $1\ \mu\text{m}$ with fine disc-shaped pegs. Thus, alumina coated Inconel 600 sample with NiCrAlY bond coat exhibits relatively better performance because of lower oxidation rate and mechanical keying mechanism. From these studies, it is clear that NiCrAlY bond coated alumina sample with formation of an oxidation resistant, yttria enriched, homogeneous and uniform TGO layer of $\alpha\text{-Al}_2\text{O}_3$ of $\sim 1\ \mu\text{m}$ thickness provides better performance compared to Ni-50Cr bond coat

III.26 Polymer-Silane Based Superhydrophobic Coatings on Carbon Steel with Enhanced Corrosion Resistance and Self-cleaning Property

Carbon steels are the materials of choice for structures and pipelines in marine, chemical, oil and construction industries mainly because of their mechanical strength, ease in production and cost effectiveness. It is well known that carbon steels undergo severe corrosion in aggressive conditions compared to stainless steels limiting their use in marine and humid environments. Protective coatings, including superhydrophobic (SHP) coatings were attempted to improve the corrosion resistance of carbon steel.

A novel polyvinylidene fluoride (PVDF)-SiO₂-Silane-based superhydrophobic (SHP) coating was fabricated on carbon steel samples with enhanced corrosion resistance and self-cleaning properties. The coating was fabricated by incorporating hydrophobic SiO₂ nanoparticles into the PVDF matrix first and then coating with a silane based low surface energy material. Perfluoro octyl triethoxy silane (PFOTES) and hexadecyl trimethoxy silane (HDTMS) were the low surface energy materials used. PVDF-SiO₂ was coated on carbon steel samples resulting in a water contact angle (WCA) of $155.6 \pm 1.3^\circ$.

The SHP property was further enhanced ($WCA > 170^\circ$) by modifying the PVDF-SiO₂ coating by PFOTES / HDTMS silanes. Field emission scanning electron microscopy (FESEM) images showed the aggregation of silica nanoparticles resulting in a typical cauliflower like morphology on the SHP coated carbon steel surface. Atomic force microscopy (AFM) analysis also confirmed the micro-nano hierarchical structure and the root mean square roughness was 250 nm. Attenuated

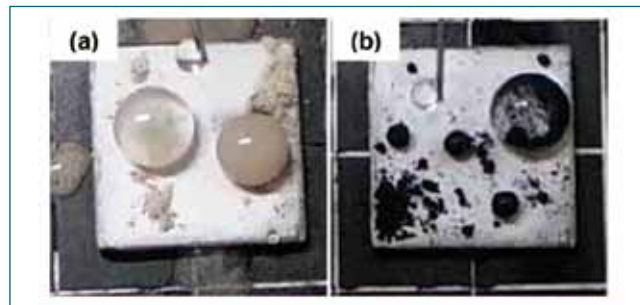


Fig. 2: Photographs showing self-cleaning property of PVDF+SiO₂+Silane coated SHP carbon steel surface contaminated with (a) chalk powder and (b) graphite, respectively.

total reflectance–Fourier transform infrared (ATR-FTIR) spectroscopy and x ray photoelectron spectroscopy (XPS) results showed the bonding between SiO₂ nanoparticles and silane in the SHP coating. Further, SHP coating on carbon steel samples showed excellent self-cleaning property and effectively removed hydrophobic as well as hydrophilic contaminants. The samples remained superhydrophobic with $WCA > 150^\circ$ with an increase in the ionic strength of NaCl solution from 1 to 5 M. SHP coating was intact after complete immersion in water and effectively repelled acidic solutions and retained its superhydrophobic property. Besides, electrochemical studies in 3.5 wt.% NaCl confirmed the superior corrosion resistance provided by PVDF based SHP coating in aggressive chloride conditions. This study would open up possibilities for further research on polymer based SHP coatings on carbon steel / other metals or alloys with long term chemical stability and mechanical durability for addressing corrosion issues in industrial applications.

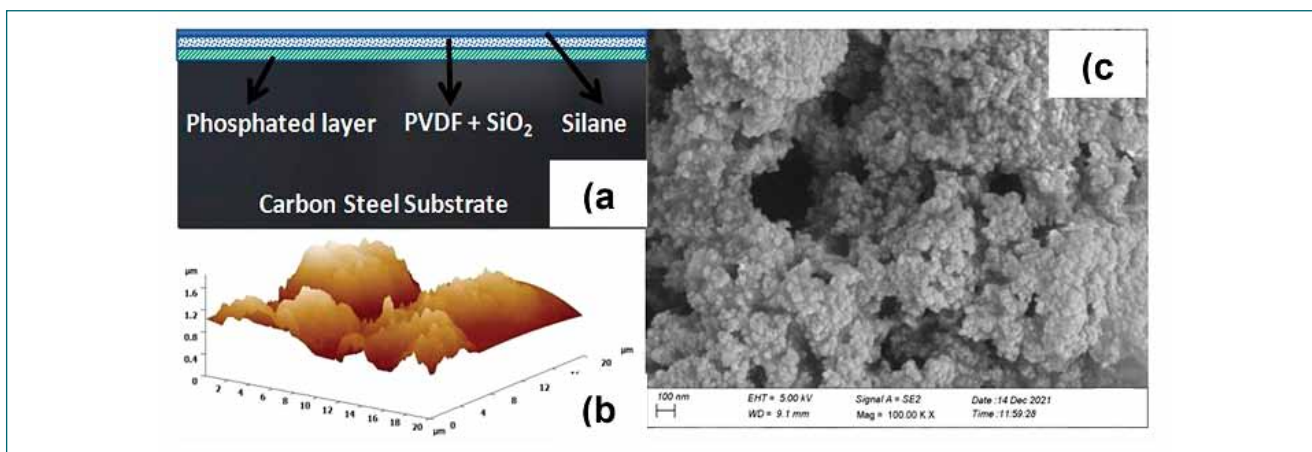


Fig. 1: (a) Schematic showing the PVDF+SiO₂+Silane coating on carbon steel substrate, (b & c) AFM and FESEM images of PVDF+SiO₂+Silane coated carbon steel substrate.

III.27 Microstructural Characterization of Laser Rapid Manufactured Hard-facing Alloy Bushes for FBR Application

High temperature wear resistant Ni-based hard facing alloy bushes are required in dynamic moving components of FBRs. Due to the difficulties faced (cracking, dilution) during casting and weld deposition, the bushes were fabricated through a novel laser rapid manufacturing (LRM) technique at RRCAT Indore. Microstructure and phase stability of the LRM bushes was investigated at IGCAR using variety of experimental techniques, equilibrium and Scheil's non-equilibrium simulations. Observed microstructure was understood based on non-equilibrium eutectic solidification reaction in Ni-Cr-B-Si-C multicomponent system.

The bushes (inset Fig. 1(a)) were manufactured through LRM using Ni-13.5Cr-0.5C-2.4B-3.7Si-4.1Fe (wt%) powder with average particle size of 100 μm. SS 304L build plate was maintained at 400 °C during deposition and the component was cooled in a sand bath for 8 h post deposition. As fabricated bushes met the design specifications as given in Table 1.

Fig. 1(a) shows the layered morphology of the bush along the build direction and Fig. 1(b) is the corresponding XRD pattern showing the presence of Ni₃B, Ni₃Si, CrB, Cr₅B₃, Cr₃C₂, Cr₇C₃ and Cr₂₃C₆ phases. LRM bushes had a defect free uniform fine dendritic solidification structure. Microstructural heterogeneity observed was only between layer overlap region (LOR) (marked as A in Fig. 1(a)) and layer interiors. In the LOR the primary γ-Ni dendrites and precipitates were coarser than in layer interiors.

Table 1 Comparison of the desired and actual parameters for the LRM bushes		
Measured parameter (Unit)	Desired Value	Actual Value
Length (mm)	20.2 ± 0.1	20.26 ± 0.02
Outer diameter (mm)	18.0 ± 0.1	18.0 ± 0.01
Inner diameter (mm)	15.0 ± 0.1	14.97 ± 0.06
Roughness (mm)	0.8 × 10 ⁻²	(0.2 ± 0.02) × 10 ⁻³
Density (g/cc)	Min 95% of theoretical Density(8.14)	7.917 ± 0.008 (97% of theoretical Density)
Hardness (HV0.1)	595 (min)	720 ± 40

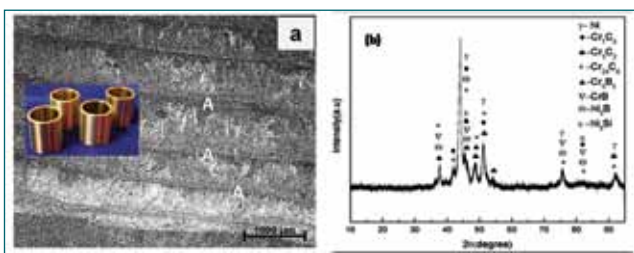


Fig. 1: (a) Layered structure along the build direction (inset shows the as-deposited bushes) (b) XRD pattern obtained from LRM bushes

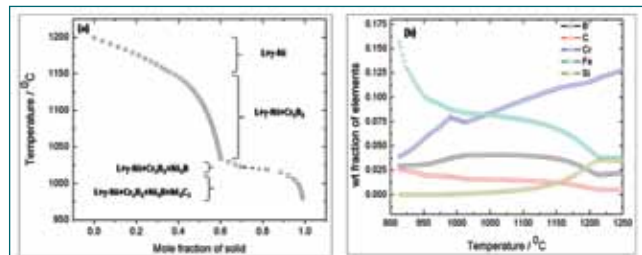


Fig. 2: Scheil's simulation showing (a) solidification sequence and (b) elemental redistribution in the liquid phase under non-equilibrium conditions

According to equilibrium solidification simulations nickel borides, silicides and chromium borides are not stable at room temperature. Scheil's non-equilibrium simulations (Fig. 2(a)) predicted the following solidification sequence: L → L+γ-Ni → L+γ-Ni+Cr boride → L+γ-Ni+Cr boride+proeutectic Ni₃B → L+γ-Ni+Cr boride+Ni₃B+eutectic(Ni₃B+M₃C₂). When the solidification rate was fast enough to prevent the formation of Cr borides, the terminal liquid solidified as a Ni-B-Si eutectic due to segregation of Si to the interdendritic regions (Fig. 2(b)).

Based on detailed investigation it was concluded that microstructure of LRM bushes (Fig. 3) is dominated by γ-Ni+Ni₃B anomalous and lamellar eutectic constituents. In addition low volume fractions of γ-Ni+Ni₃B+Cr₃C₂ and Ni-B-Si eutectics are present in the interdendritic regions. Though the solidification starts with precipitation of Cr borides, they are extremely small due to insufficient time spent in their solidification range. Precipitation of nickel silicides was observed within secondary γ-Ni dendrites. Such a combination of phases with unique morphology and distribution resulted in enhanced hardness of the LRM bushes compared to weld deposited ones.

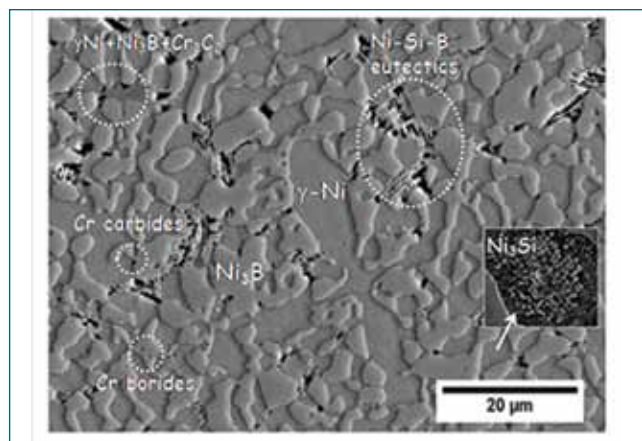


Fig. 3: Microstructure of LRM Ni-based hardfacing alloy bushes

III.28 High Temperature Thermophysical Properties of Spark Plasma Sintered Tungsten Carbide

In the Fast breeder Test reactor (FBTR), grid plate is a permanent support structure made of type 316 SS (FBTR quality). Due to fast neutron irradiation over a period of 30 years, the mechanical properties of structural materials including that of the grid plate has degraded leading to serious concerns on the reactor operation beyond its design life. Therefore adequate lower axial shielding of the grid plate was considered with utmost priority as a part of the life extension activity of FBTR.

Tungsten carbide (WC) turned out to be the optimum choice for shielding material owing to its high density, structural stability, efficient neutron attenuation, lower reactivity change in addition to its compatibility with liquid Na and austenitic steels. In order to meet the requirement, WC pellets were fabricated in-house using spark plasma sintering (SPS) technique. Optimized process parameters for SPS to achieve WC pellets of 99.5% theoretical density are: Pressing stress - 35 MPa, Temperature - 2098 K, Holding time - 15 min. To qualify the material behavior under reactor operating conditions, high temperature thermophysical properties were measured from room temperature up to 1273 K. Measurements of temperature induced dilation $\Delta l(T)$

(i.e. l_T - l_{298}) and thermal diffusivity (λ_T) were carried out as a function of temperature using push rod dilatometry and laser flash method respectively. The temperature dependence of thermal expansion (%) and mean coefficient of bulk thermal expansion (CTE) i.e. α_{mean} was estimated from measured $\Delta l(T)$ and the bulk density (ρ_T) was calculated from α_{mean} assuming isotropic expansion for polycrystalline WC. Measured bulk expansion was in good agreement with reported values of lattice expansion. The dynamic Young's modulus (E) was measured using impulse excitation method and the Debye temperature (θ_D) was estimated as a function of temperature from the sound velocities. The heat capacity (C_v , C_p) was estimated using quasiharmonic approach and used further to calculate the temperature dependence of thermal conductivity $k = \lambda_T \rho_T C_p$. The k values thus estimated were found to be in close agreement with the measured values reported for the hot pressed WC. The phonon contribution to k was also estimated from Slack's model which revealed that the Slack's approach can only be validated at room temperature. Figure 1(a)-(d) shows the measured values of Thermal expansion, heat capacity (C_v , C_p), thermal diffusivity (λ_T) with density (ρ_T), as well as thermal conductivity (k) of SPS-WC respectively.

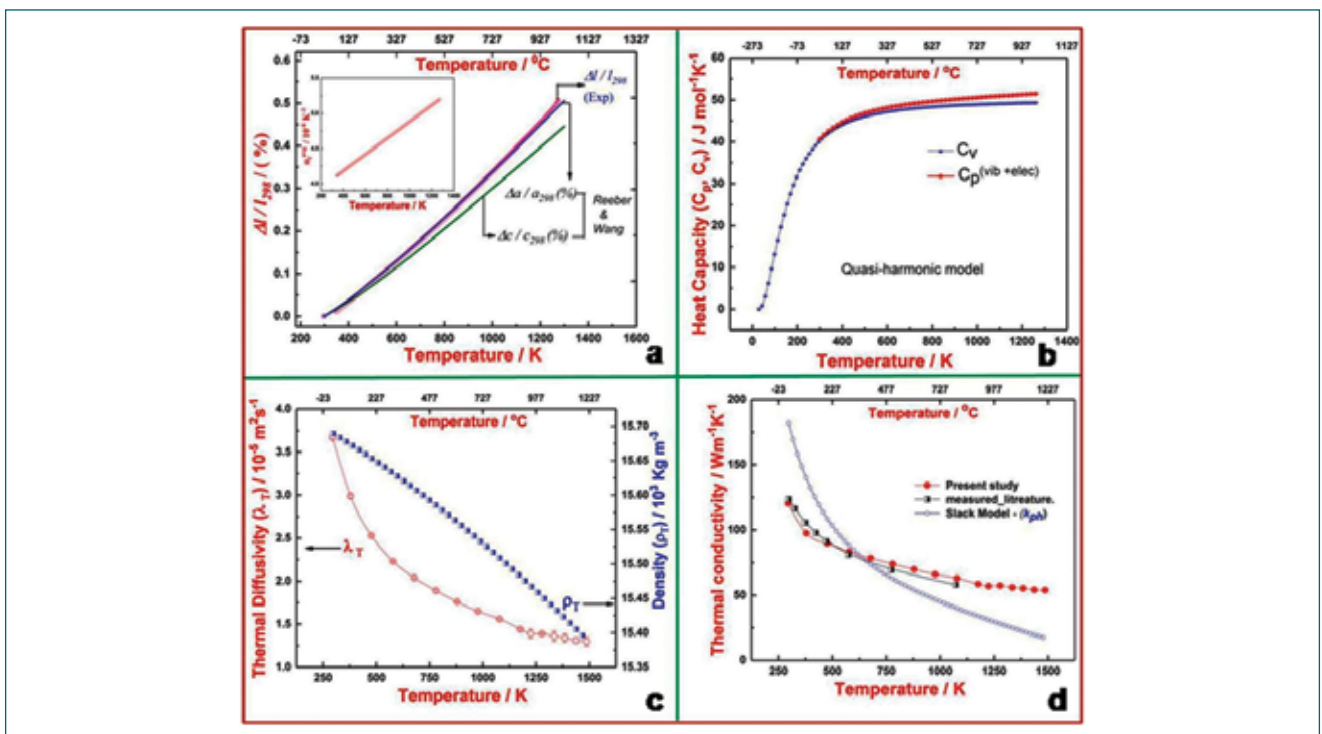


Fig. 1: Temperature dependence of (a) Thermal expansion; (b) heat capacity (C_v , C_p); (c) thermal diffusivity (λ_T) and density (ρ_T) (d) thermal conductivity (k) for SPS-WC

III.29 Understanding Formation of Borides in Concentrated P91-B Alloys

Metal borides are an interesting class of materials that offer excellent wear resistance, oxidation resistance and excellent heat resistant material besides being of relatively low cost. More recently, medium-high B steel (HBS) have gained attention from nuclear scientists as a candidate material for the hexahedral tubes of spent nuclear fuel storage applications due to the high neutron absorption cross-section of B. Another significant property of the material is its large saturation magnetization, which makes it suitable for magnetic recording, magnetic refrigeration, and application in magnetic cores. Fe_2B is brittle but alloying with Cr has been demonstrated to be a good method for improving fracture toughness.

In this study, Thermo-Calc has been used to calculate the equilibrium phase diagrams for B-added P91 steel, as well as for estimating the variation of the amount of phases and Gibbs free energy for the different compounds with temperature. Alloys with three different compositions were prepared by arc melting Mod. 9Cr1Mo steel with 5wt.%, 2.5wt.% and 0.5wt.% of B. The samples were normalized and tempered (N&T) at 1080°C and 760°C, respectively, for 1 hour each. Microstructure of N&T steels was examined by SEM-EBSD and XEDS. Phase identification in B-added P91 steels was carried out using XRD.

Fig. 1 shows that the phase fraction of Fe_2B increases with the increase in B concentration during its nucleation. In 5wt.% B-added P91, Fe_2B phase nucleates before the Fe-bcc phase, and ~62% of the material is Fe_2B replacing Fe-bcc as the matrix phase. Fig. 2 shows the SEM-XEDS maps, revealing that Fe in Fe_2B is substituted by Cr to form $(Fe,Cr)_2B$. The grain size of $(Fe,Cr)_2B$ ranges from 46µm to 2µm. Segregation of this intermetallic phase along the Prior Austenite Grain Boundaries (PAGBs) is prominent in 0.5wt% boron added P91 steel.

N&T steels with 0.5wt.% B-added P91 showed $M_{23}C_6$

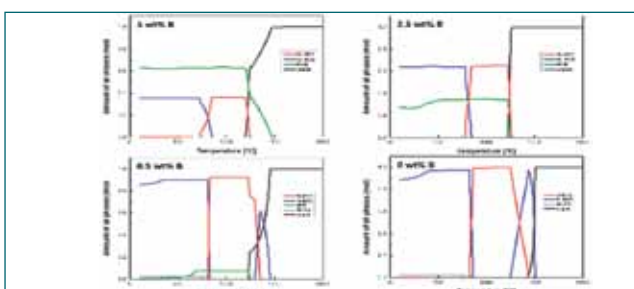


Fig. 1: Calculation using Thermo-Calc showing the amount of phases formed in different composition of B-added P91 steel.

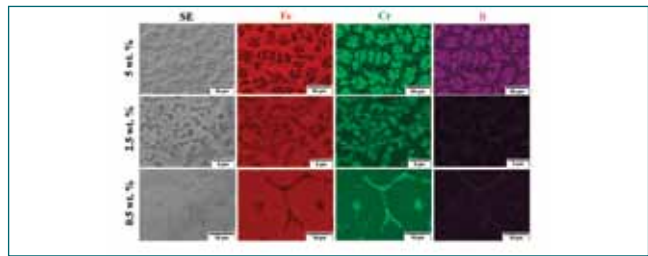


Fig. 2: SEM-XEDS maps showing microstructural and microchemical changes in P91 steel with different concentrations of B showing Cr enrichment along with Fe and B in Fe_2B phase

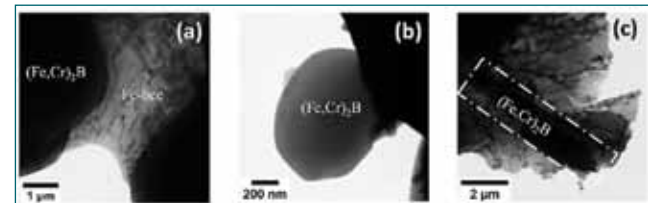


Fig.3: BF-TEM micrographs showing the microstructure in (a) 5wt.%, (b) 2.5wt.%, and (c) 0.5wt.% B-added P91 steel

and MC kind of precipitates along the laths, while $(Fe,Cr)_2B$ forms along the GB in all steels with different B content as shown in the bright-field TEM micrographs in Fig. 3. The borides are observed to nucleate along the periphery of the Cr-rich carbides. The 5wt% B-added P91 behaved like a composite material forming $(Fe,Cr)_2B$ phase reinforcement in α -Fe phases with distinct hardness values. 5wt% B-added P91 steel in as-cast and N&T sample condition showed a Rockwell hardness of 69 and 56 HRC, respectively. Fig. 4 shows the indentation marks in as-cast and N&T steels. Even though the hardness for the boride phase (well outside the HRC scale, ~19 GPa) was expected to be high and brittle, significant fracture toughness was observed even with 150 kgf load. Superior toughness properties were attributed to the dissolution of Cr in the Fe_2B phase which makes the bond less covalent and stiffens the B-B bond.

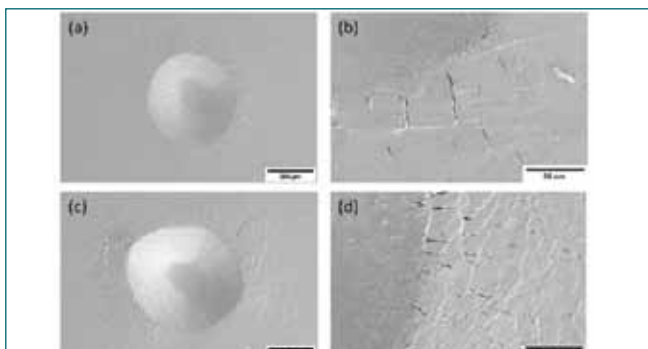


Fig. 4: Indentation marks from Rockwell hardness test of 5wt. % B-added P91 steel in (a-b) as-cast, and (c-d) N&T condition.

III.30 Effect of Zr Addition on Microstructure and Nano-mechanical Properties of P9 steel

To understand the interaction between ferritic/martensitic steel clad and Zr liner in the Metal Fast Breeder Reactors (MFBR), a systematic study has been initiated to analyze the effect of zirconium addition to P9 steel on microstructure and nanomechanical properties. Thermodynamic equilibrium calculations were carried out using ThermoCalc software and steels with Zr concentration up to 2 wt% were synthesized by vacuum arc melting. These steels were then hot rolled at 1000°C and further cold rolled up to 30-35%. After the thermo-mechanical treatments the steels were homogenized at 1000°C for 2h and water quenched.

XRD analysis of the homogenized steels showed BCC (α), which confirms that the alloys are ferritic in nature (Fig.1). Minor additional peaks were also observed suggesting secondary phases present in addition to the BCC (α) phase in high Zr concentrations, which were identified to be ZrC in addition to $Fe_{23}Zr_6$ in steels with Zr >1%. Homogenized steels showed a microstructure of predominantly martensite up to 0.25% Zr with low amounts of ferrite. However, the ferrite volume fraction increased with Zr concentration. The grain size decreased with increased grain boundary precipitation as the Zr concentration of the steels increased. Figure 2(a) shows the TEM micrograph of 0.25ZrP9 steel

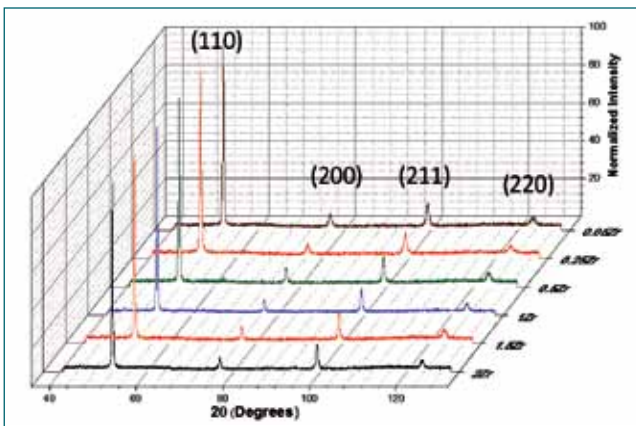


Fig. 1 XRD patterns of the Zr added P9 steel homogenized at 1000°C showing major ferrite phase

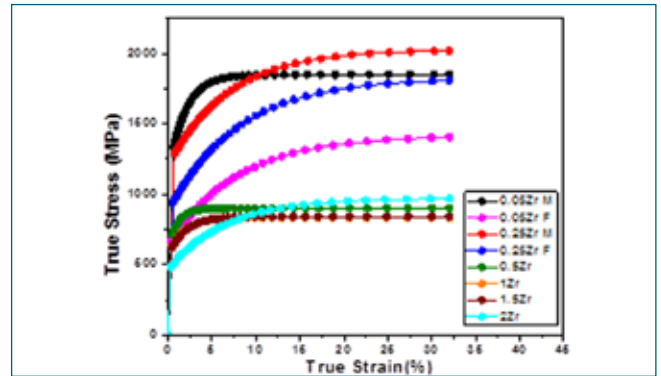


Fig. 3: True Stress – true strain plot of Zr added P9 steel shomogenized at 1000°C using IIT

with ferrite + martensite along with precipitation of ZrC (circled). Figure 2(b) shows the high angle annular dark field (HAADF) image of 2ZrP9 steel with both inter and intragranular precipitates, the former one as networks along grain boundaries. EDX analysis showed that the inter granular precipitates are enriched with Fe and Zr, while the intragranular phase was rich w.r.t Zr. Selected area diffraction (SAD) patterns confirmed that Zr rich precipitates are ZrC phase (fig. 2(c)) while the Fe, Zr rich precipitates are $Fe_{23}Zr_6$ phase (fig 2(d)). Thus based on XRD and TEM analysis, it can be concluded that the microstructure of the homogenized steels is $\alpha + ZrC$ up to 1%Zr and $\alpha + ZrC + Fe_{23}Zr_6$ for steels with Zr >1%.

Hardness, yield strength and elastic modulus are determined for all the homogenized steels using the instrumented indentation test (IIT) at room temperature with a spherical indenter of tip radius 7.65 μm . Figure 3 shows the true stress – true strain plot for both martensite and ferrite phases in the homogenized steels. It can be observed that yield strength of martensite is higher than ferrite in steels up to 0.25% Zr, though the work hardening rate is higher for ferrite as expected. The yield strength of both martensite as well as ferrite decreases with increase in Zr concentration. This can be attributed to the coarse inter and intragranular precipitation, whose volume fraction increased with Zr concentration of the steel.

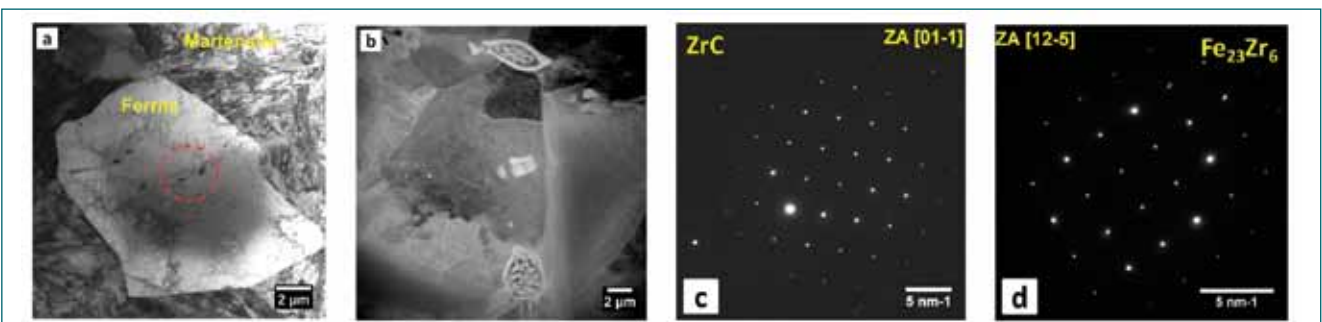


Fig. 2: (a) Bright field image of P9 steel with 0.25Zr showing ferrite and martensite with precipitation of ZrC (Circled), (b) HAADF image of P9 steel with 2Zr showing ferrite with inter and intragranular precipitates.(c) and (d) Selected area diffraction patterns of ZrC and $Fe_{23}Zr_6$ respectively from 2ZrP9 steel shown in (b).

III.31 Use of dynamic transformation to Enhance Thermo-mechanical processing of Gr. 92 Heat-resistant Steel

Stabilization of softer ferrite phase in a hard and brittle martensitic phase may alter the strength and toughness of the steel during manufacturing and service. The present investigation reveals the occurrence of dynamic transformation (DT) in a boiler steel, 'Gr. 92' (Fe-9Cr-1.8W-0.5Mo-0.4Mn-0.06Nb-0.027V-0.12C - in wt%), observed for the first time and shows how DT can control microstructural and mechanical properties of the steel.

Thermomechanical treatment

A plate of Gr. 92 steel was used to make cylindrical compression specimens of dimensions 6.0mm diameter x 9.0mm height. These specimens were compressed to 50% strain at 1173K (with strain rates of 0.001s⁻¹, 0.1s⁻¹, 1s⁻¹ and 10s⁻¹). The deformation temperatures were chosen to be around the expected A₃ temperature of 1170K-1180K. After deformation, the specimens were immediately (< 2s) quenched in water to minimise any

static/meta-dynamic processes that may initiate during cooling. The stress-strain curves, as shown in Fig. 1, were used to numerically calculate the derivatives for analysing work-hardening behaviour. In the current study, the double-derivative curves ($\partial\theta/\partial\sigma$ vs σ) generated at all conditions were found to exhibit double minima, signifying occurrence of DT.

Microstructural Analysis of DT-ferrite

The microstructure was investigated in greater detail using a scanning electron microscope (SEM) and the crystallographic orientation was measured using electron back-scatter diffraction (EBSD). EBSD band contrast (BC) map containing DT-ferrite is shown in Fig. 2(a). At low magnifications, the DT-ferrite appears to form several large islands (one encircled in Fig. 2 (a)). The volume fraction of ferrite increases with an increase in strain rate, as shown in Fig. 2(b). With an increase in strain rate, more defects accumulate in the austenite grains. This leads to the nucleation of more ferrite grains. Variation of hardness with strain rate is also shown in Fig. 2(b). The plot shows that the hardness of the steel is sensitive to the volume fraction of ferrite present in the steel. By controlling the volume fraction of ferrite, mechanical properties of the steel can be controlled.

To summarize, ferrite islands in martensitic matrix can be produced by exploiting the phenomenon of dynamic transformation in Gr.92 steel. The ferrite formed can be continuous or discontinuous and could be ultrafine grained. Judicious use of this treatment can improve workability during the manufacturing process. The possibility of improving toughness through DT is currently being investigated.

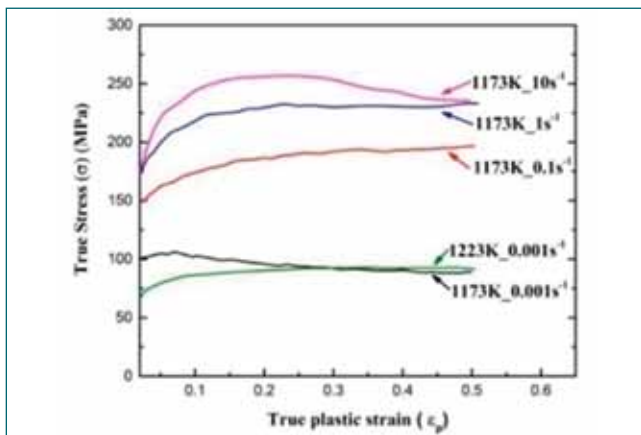


Fig. 1: True stress (σ) -true plastic strain curves at different conditions.

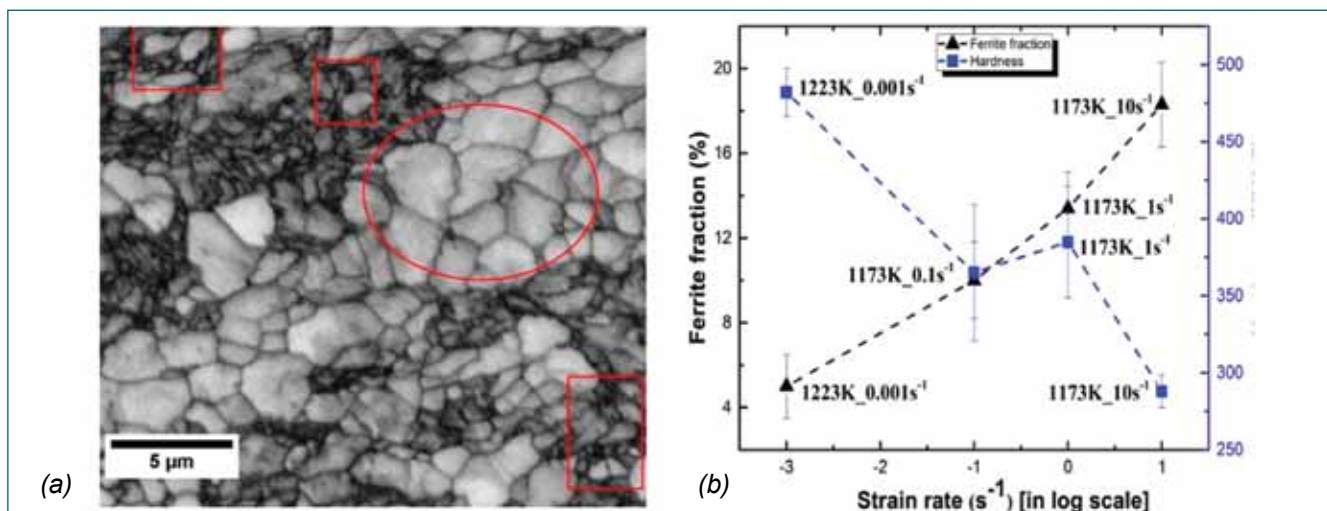


Fig. 2: (a) EBSD BC map following deformation at 1173K with 10s⁻¹ strain rate (Ferrite grains are encircled), (b) hardness and ferrite fraction Vs strain rate.

III.32 Role of Nitrogen on Fracture and Fatigue Crack Growth Behaviour of SS316L

Nitrogen alloyed low carbon austenitic stainless steel (SS316L(N)) is used for the main vessel, inner vessel, and IHX components of the Prototype Fast Breeder Reactor (PFBR). Increasing the current reactor life from 40 years to 60–100 years by enhancing the creep rupture life of SS 316L with increasing Nitrogen level is envisaged. It is known that Nitrogen addition in 316L stabilizes the austenite phase, increases the yield strength by refining the grain size, affects the stacking fault energy, and modifies the dislocation structure during deformation. Previous studies have shown increase in tensile and creep properties along with the corrosion resistance with enhancing Nitrogen concentration. Further, evaluation of fracture and fatigue crack growth (FCG) is essential to ensure the structural integrity of reactor components. Thus the fracture and FCG properties of SS316L(N) with varying Nitrogen have been investigated to understand the role of Nitrogen content. For this purpose, SS316L with varying Nitrogen in the range 0.07 to 0.22 wt% has been subjected to fracture test as per ASTM E1820. FCG tests have been carried out at different load ratios (R) in the range of 0.1 to 0.7 as per ASTM E647 standard.

Fracture results in Fig 1 indicated the better fracture resistance of 0.14 wt % Nitrogen at all temperatures. Generally known that the initiation of a crack ahead of a large stretch zone during sharp crack growth is an indication of higher fracture energy, the characteristic parameter stretch zone width (δ) measured under the

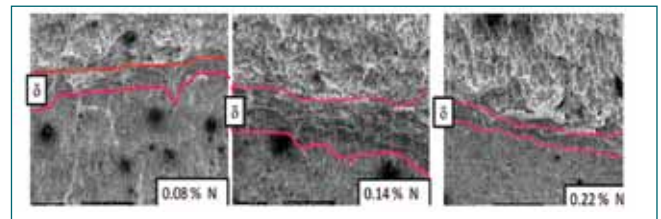


Fig. 2 : Stretch zone width (δ) with nitrogen level by SEM

scanning electron microscope (SEM) in Fig 2 and it has been found to be significant for 0.14wt% compared to other nitrogen variants and hence possess better fracture resistance.

Figure 3 shows the threshold stress (ΔK_{th}) variation with Nitrogen at different load ratios. This variation of ΔK_{th} data is shown with stacking fault energy (SFE) in Fig 4, indicating that the 0.14 wt% Nitrogen found to be have the lowest SFE. This has resulted in a better slip planarity and slip reversibility and led to better FCG resistance in the threshold regime. The interesting point here is that the beneficial role of Nitrogen in tensile properties and creep life increases with Nitrogen monotonically. On the other hand role of Nitrogen has been found to be optimum at 0.14 wt % for a better fracture and FCG resistance. This is attributed to the local change in the slip character during the fatigue crack initiation. The crack tip stress and strain fields, in combination with Nitrogen have altered the crack tip slip character from wavy to planner, thus affecting the strain localization characteristics giving rise to higher fracture toughness and ΔK_{th} .

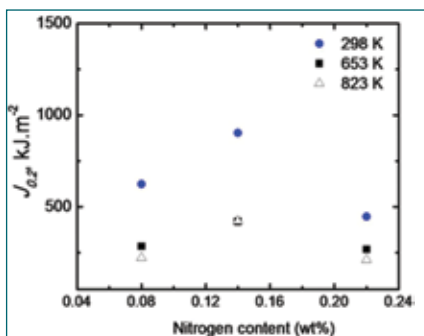


Fig. 1: Fracture ($J_{0.2}$) with varying nitrogen shows the maximum fracture toughness at 0.14 N.

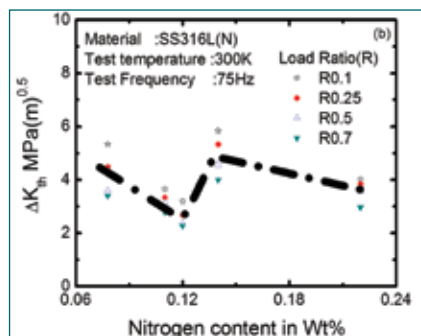


Fig. 3: Variation in ΔK_{th} with nitrogen level in 316L

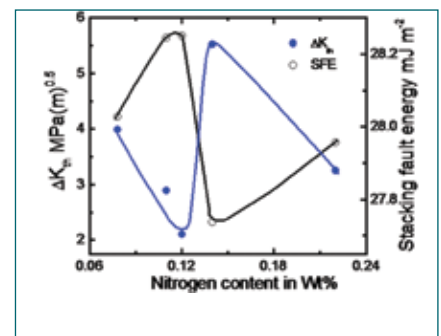


Fig. 4: ΔK_{th} with nitrogen and comparison with stacking fault energy of 316L

III.33 Manufacturing of Alloy 625 Bush by Wire Arc Additive Manufacturing (WAAM) Process

Additive manufacturing is considered as a near net-shape forming technology. It is widely used in the fabrication of parts, which in general difficult to produce through conventional processes. Wire arc additive manufacturing (WAAM) uses arc as the heat source and wire as the feedstock material. Compared with the laser additive manufacturing and electron beam additive manufacturing, WAAM has the advantages of fabricating large structural components because of its higher deposition rate, higher material utilization rate, and lower cost. In this direction, an attempt has been made to manufacture Alloy 625 cylindrical bush by WAAM technique using Integrated Robotic Cold Metal Transfer (CMT) system developed in-house.

Prior to fabrication of actual component, an optimization experiments were performed to achieve defect-free and homogeneous single weld bead using continuous synergic CMT parameters. Subsequently, multi-layer build-ups were made one over another onto 12 mm thick AISI 316L(N) stainless steel plate. Figure 1 shows the WAAM Alloy 625 part in progression with the set-up details. The WAAM built part of Alloy 625 is also shown in Figure 2. Microstructure, hardness and tensile property of the multi-layer builds-up were performed after radiographic examination.

Microstructure of the WAAM built Alloy 625 reveals finer dendritic-cellular solidified structure. The columnar grains/dendritic-cellular structure was oriented along the built direction opposite to heat flow. Hardness measurements taken along the WAAM built direction

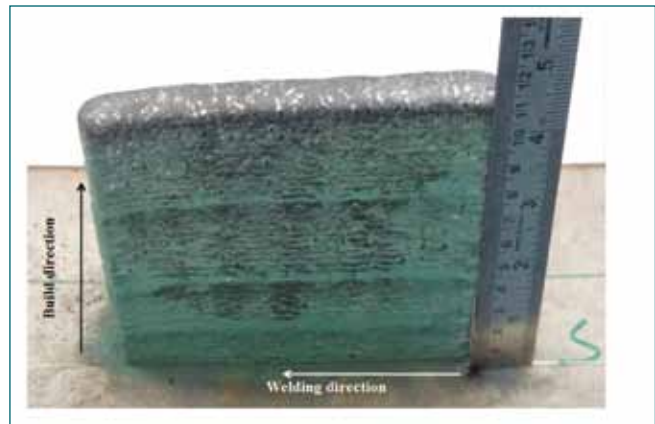


Fig 2: WAAM built part of Alloy 625

revealed hardness values between 350 to 480 HV0.2. The variation in hardness could be due to formation of secondary precipitates during multi-pass deposition process. Room temperature tensile tests were carried out at a strain rate of $1 \times 10^{-3} \text{ S}^{-1}$ using miniature specimens which were extracted from bottom, middle and top of the built part. Engineering stress-strain plots are shown in Fig. 3. Yield strength of the material remains 300 MPa whereas ultimate tensile strength varied between 450 to 500 MPa. The ductility and YS values obtained from the tensile tests are comparable with the values reported in the literature. This suggests the suitability of WAAM process for producing Alloy 625 product for use with comparable mechanical properties.

Based on the results obtained from the multi-layer deposit, a defect free cylindrical bush of height 120 mm with 80 mm outer diameter and 6 mm wall thickness has been successfully demonstrated using CMT based WAAM process (Fig. 4).

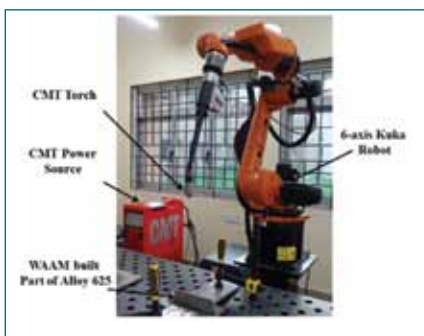


Fig 1: WAAM set-up used for building Alloy 625 part

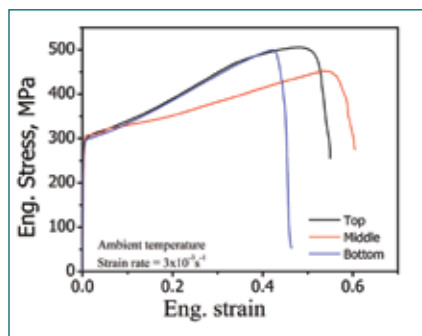


Fig 3: Tensile stress-strain curves for WAAM Alloy 625

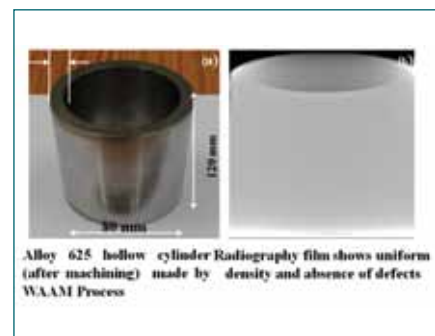


Fig 4: (a) Cylindrical hollow bush of Alloy 625 and (b) radiographed image of the bush showing no defect

III.34 Non-Destructive Inspection of Dissimilar Weld between Main Vessel and Roof Slab at 152° ISI Port, PFBR

The PFBR primary containment structure is made up of a main vessel (316 LN SS) and a reactor roof slab (RS) structure (A48P2 carbon steel), which is essentially a box filled with concrete. The main vessel (MV) is a large single vessel (12.8 m in height and 12.9 m in diameter) made of thick (25 to 40 mm) stainless steel plates. A circumferential dissimilar weld (316 LN stainless steel to A48P2 carbon steel) connects the upper end of the MV to the RS. The structural integrity of the circumferential dissimilar weld between MV and RS is very critical as it withstands full load of the MV. Nondestructive in-service inspection (ISI) of this critical weld is envisaged during reactor shutdown. For this a Dissimilar Metal Weld Inspection Device, or “DISHA,” was developed which carries non-destructive testing (NDT) modules for remote visual testing (VT), eddy current testing (ECT) and ultrasonic testing (UT) at 120 °C. The DISHA vehicle was qualified for deployment in PFBR after extensive systematic nondestructive studies on the 1:1 mockup facility available at SAS, BHAVINI. These studies included a successful demonstration of the performance of the UT and the ECT modules of DISHA for 24 h continuous operation at (i) room temperature and (ii) 120°C.

Deployment of DISHA vehicle from the 152° ISI port, PFBR (EI 38m) was performed to inspect the dissimilar weld between the main vessel and the roof slab. In this campaign, the dissimilar weld inspection (25 scans) for a length of 3 m, i.e. from ~134.5° to ~162.5° orientation is successfully completed.

Inspection was automated to acquire and save the UT and ECT data during each scan. In-house developed IGUANI-DISHA software was used to analyze the ultrasonic and eddy current data. Figures (1a-1d) show the ultrasonic C-scan images (plan view) generated using the data obtained by the right side integrated probe (beam propagation from MV side to RS side) for all angles (0°, 45° and 70°) and 45° of individual transducer (beam propagation parallel to the weld axis). Figure 1e shows the eddy current C-scan image. The analysis of the ultrasonic inspection data acquired from the dissimilar weld confirms that the weld is free from any major indications. On the RS side perpendicular to the dissimilar weld, a geometric indication is observed at -520 mm from the center of the 152° ISI port (i.e. at ~156.5°) which corresponds to the cooling box “J” vertically welded on the ID side of the RS structure at this orientation (Fig. 1d). This confirms that the ultrasonic inspection is conducted with a sufficient couplant between the ultrasonic transducers and the dissimilar weld and that the inspection data acquired at the 152° ISI port is valid. It is also found that due to undulations near the dissimilar weld, loss of normal beam back wall echo is observed at some locations on the main vessel ID especially on the SS side. The dissimilar weld interfaces are clearly distinguished in the eddy current C-scan image (Fig 1e) and the weld centerline is 10 mm below the center of the NDE probe holder (scan axis). The inspection results demonstrated a successful non-destructive inspection of the dissimilar weld for a length of 3m using DISHA vehicle at 152° ISI port, PFBR.

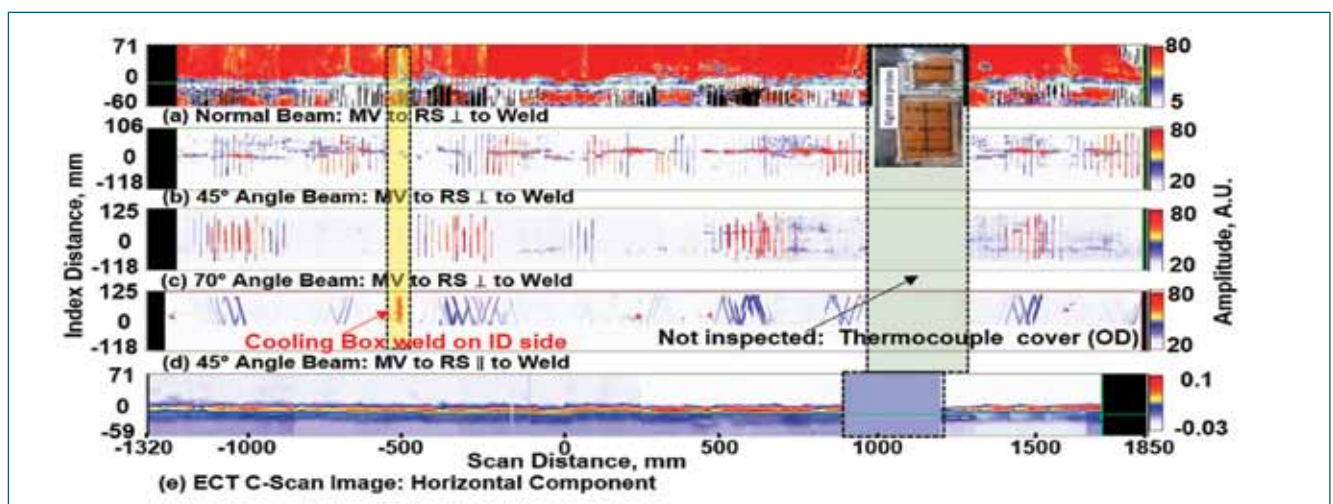


Fig. 1: (a-d) Ultrasonic and (d) eddy current C-scan images for about 3 m length of the dissimilar weld (the complete inspection range) at the 152° orientation of the ISI port, PFBR

III.35 Design and Development of Remote Field Eddy Current Array Probe for Imaging of Defects in Steam Generator Tubes of PFBR

Remote Field Eddy Current (RFEC) non-destructive testing technique was specifically developed for in-service inspection of PFBR steam generator (SG) tubes made of mod. 9Cr-1Mo ferritic steel. It employs a circumferentially wound, cylindrical exciter and receiver coils which are axially separated by a characteristic distance. The technique in its present form is efficient in reliably detecting 20% wall loss defects with volumetric size equivalent to that of a 2.3 mm diameter through hole. Development of an array probe having multiple segmented receiver coils was envisaged, in order to further improve the sensitivity and defect localization capability of the technique.

Extensive finite element modelling studies were carried out in this regard to understand the magnetic field distribution inside the tube and the tube wall. Based on the studies, a radial type receiver coil was found to be efficient in detecting defects. Further, RFEC probe having a single segmented radial type receiver coil of 4 mm diameter was optimised and fabricated to evaluate the performance and experimentally study and optimise the number of receiver coils which can be arranged along the circumference for reliable detection of defects. For this study, an SG tube having through holes of 5.0 mm, 2.3 mm and 1.2 mm diameter was used. RFEC signal was acquired while the receiver is placed at defect location for varying probe orientations in circumferential direction. The RFEC phase angle change observed for all the three defects for various orientations is shown in Fig. 1. It can be seen that the phase angle change is highest when the probe is located exactly below the defect (at 0°) and decreases on either side in a Gaussian fashion. The amplitude falls to a defect free value at

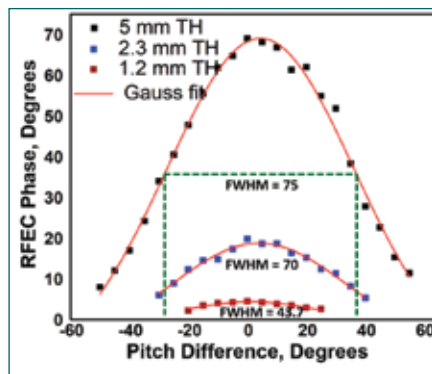


Fig. 1: Measured phase variations for 5 mm, 2.3 mm and 1.2 mm diameter through holes along the circumferential direction.

approximately 20° on either side for 1.2 mm hole. In order to accurately estimate the probe response in the circumferential direction, the full width at half maximum (FWHM) was computed by fitting the

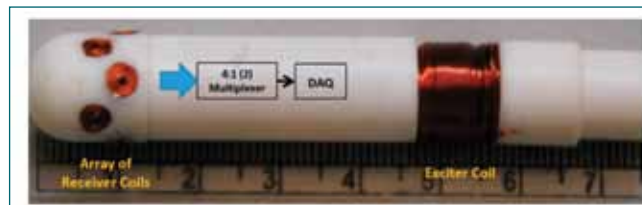


Fig. 2: Photograph of the in-house developed 8-Coil RFEC array probe.

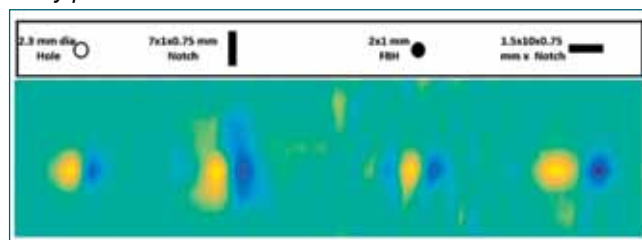


Fig. 3: RFEC phase image of different types of defects in a mod. 9Cr-1Mo SG tube.

response to a Gaussian function. The FWHM for the 1.2 mm diameter hole was found to be 43.7°. Considering the coil diameter, the extent of the coil response was found to be approximately 45°. Thus an array probe having 8 numbers of radial type receiver coils spaced at 45° apart would be optimum for reliable detection of defects. However, the OD of the probe was kept at 11.4 mm to inspect the SG tubes having an ID of 12.2 mm. A staggered arrangement was opted to accommodate 8 coils in this 11.4 mm OD surface. Figure 2 shows the photograph of the developed RFEC array probe having 8 number of receiver coils. Further, to minimise cabling for data acquisition from the receiver coils a multiplexer unit was used which time slice receiver coil data acquisition as schematically shown in Fig. 2. This design has significantly reduced the cabling requirement and resulted in ease of fabrication of the probe.

The performance of the probe was validated by imaging different types of defects such as holes, notches and flat bottom holes present in an SG tube. Fig. 3 Shows the RFEC phase image of these defects obtained by the array probe. As can be seen the developed array probe could reliably image all the defects with an SNR greater than 10 dB. The developed RFEC array probe showed enhanced defect detection and localization capabilities and can be used for rapid imaging of defects in PFBR SG tubes. Further, the array probe can also be used for mapping of SG tube wall thickness by acquiring images over a band of excitation frequencies. Hence, the developed RFEC array probe has great potential in future PFBR SG tube inspection campaigns.

III.36 Enhancement in Creep Strength of Grade 91 Steel by Addition of Boron

The modified 9Cr-1Mo steel (9Cr-1Mo-VNbCN alloy), referred as Grade 91 steel (Gr.91), is being used for steam generator components of fast breeder reactor (FBR). The Gr.91 steel derives its strength from a high dislocation density, $M_{23}C_6$ and MX precipitates, grain and sub-grain boundaries and solid solution strengthening. Coarsening of $M_{23}C_6$ is inevitable under creep exposure which would eventually cause recovery of martensitic lath boundaries originally pinned by fine $M_{23}C_6$ precipitates. In order to increase the stability of the microstructural constituents during long-term creep exposure, modification in the conventional heat treatment conditions and addition of solute elements (such as boron, nitrogen) are being explored. Boron added Gr.91 steel (Gr.91BN) was developed with controlled nitrogen content (to avoid the formation of boron nitride).

The Gr.91 and Gr.91BN (0.006 wt.% B and 0.011 wt.% N) steel plates were normalized at 1373 K for 30 minutes and tempered at 1033 K for 3 hours followed by air cooling. Creep tests were performed at 823, 873 and 923 K over the stress range of 100-340 MPa. Tempered martensitic microstructure was observed in both the steels. Finer $M_{23}C_6$ and MX precipitates, and lath structure having higher dislocation density were present in Gr.91BN steel as compared to Gr.91 steel. The size of $M_{23}C_6$, MX precipitates, and lath width were respectively 140, 30 and 700 nm in Gr.91 steel while in Gr.91BN steel these were 100, 25 and 500 nm respectively. Finer precipitates pin the dislocation structure and boundaries more effectively, which delays the recovery of dislocation structure and migration of lath boundaries against deformation. The creep curves of

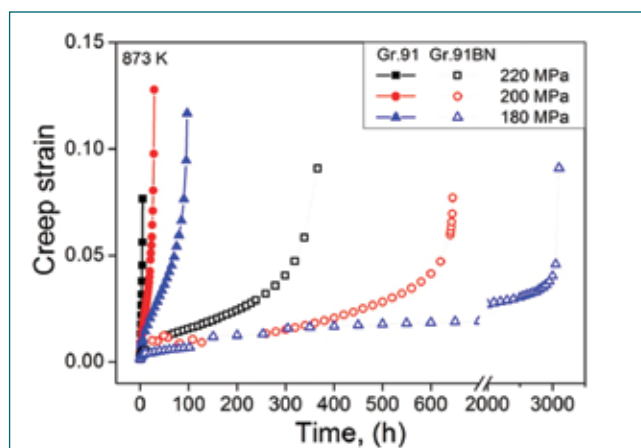


Fig. 1: Creep curves of (a) Gr.91 and (b) Gr.91BN steels at 873 K

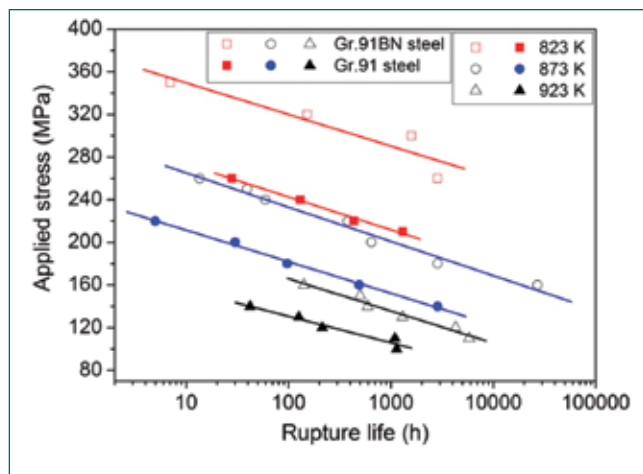


Fig. 2: Rupture life with applied stress of Gr.91 and Gr.91BN steels

Gr.91 and Gr.91BN steels at 873 K are shown in Fig. 1. Gr.91BN steel showed higher creep rupture lives compared to the boron-free steel under similar test conditions. Significant decrement in creep rate occurred in the transient and secondary creep regimes in Gr.91BN steel. The secondary creep rate in Gr.91BN steel was lower by about two orders of magnitude at 823 and 873 K and one order at 923 K, as compared to the Gr.91 steel. The delay in the onset of tertiary creep deformation in Gr.91BN steel is attributed to the stabilization of various boundaries predominantly by finer $M_{23}C_6$ precipitates. Gr.91BN steel possessed higher creep rupture life in comparison with Gr.91 steel over the investigated temperature and stress range (Fig. 2). Addition of boron with controlled nitrogen content led to an increase in the creep strength by about 70, 40 and 20 MPa corresponding to a rupture life of 10^4 h in the case of Gr.91BN steel at 823, 873 and 923 K respectively as compared to Gr.91 steel (Fig. 1). The creep strength evaluated using the Larson-Miller parametric method at 873 K for 10^5 h rupture life was observed to be higher by about 33% in the case of Gr.91BN steel compared to the Gr.91 steel. Further, the coarsening of $M_{23}C_6$ precipitates was found to be reduced in Gr.91BN steel in comparison with the Gr.91 steel. In the case of Gr.91 steel, boundaries were almost parallel to the stress direction near the fracture region, while in the case of Gr.91BN steel distinct pinning of boundaries by fine precipitates was noticed. The present study demonstrated the beneficial role of boron addition to grade 91 steel (Gr.91BN) in enhancing the stability of microstructural constituents and associated significant enhancement of the creep rupture strength.

III.37 Creep-fatigue Interaction Behavior of Simulated Microstructures and the Actual Weldment of P91 Steel

P91 ferritic/martensitic steel finds applications for steam generator (SG) components in the high temperature service loadings owing to an excellent combination of properties such as high creep strength, low coefficient of thermal expansion and good weldability. The high heat input during fabrication of SG components involving fusion welding significantly changes the thermally sensitive microstructure across the heat-affected zone (HAZ) of the P91 steel weldment. This results in the development of microstructurally weak regions in the HAZ such as coarse grain heat-affected zone (CGHAZ), fine grain heat-affected zone (FGHAZ) and inter-critical heat-affected zone (ICHAZ), which often prove to be preferential failure sites. The start-ups and shut-downs and the continuous power generation operation of the power plants leads to damage from low cycle fatigue (LCF) and creep-fatigue interaction (CFI) in the SG components. Thus, LCF and CFI analyses are important in the safe-life design approach of steam generator components of power plants. The present work aims to understand the influence of individual constituent regions of the P91 weldment at elevated temperature under CFI loading condition.

Three principal microstructures of the HAZ, viz., CGHAZ, FGHAZ and ICHAZ were simulated through isothermal furnace heat treatments at 1200°C, 935°C and 865°C respectively. All simulated microstructures predominantly developed tempered martensite after oil quenching followed by tempering (760°C/3 h). Grain and precipitate sizes and microhardness for each microstructural constituent were determined and compared with those of the actual weldment to confirm the accuracy of the simulation through heat treatments. LCF & CFI tests



Fig. 2: P91 actual weldment failure location under CFI condition at 550 °C.

were carried out on each microstructure and the actual weldment at a strain amplitude of $\pm 0.6\%$ using triangular & trapezoidal waveforms with a nominal strain rate of $3 \times 10^{-3} \text{ s}^{-1}$ and a temperature of 550 °C. The chemical compositions of the P91 steel base metal and weld metal filler wire are given in Table 1.

The cyclic stress response (CSR) of the different regions are seen to shift downwards under CFI condition compared to LCF on account of the additional creep damage due to the application of hold at the peak tensile strain (Fig. 1(a)). Coarsening of precipitates and substructures eases the deformation process, resulting in higher cyclic softening under CFI than LCF. The ICHAZ exhibited a higher dwell sensitivity (defined as the ratio of the number of cycles to failure under CFI loading to the number of cycles to failure under LCF), as shown in Fig. 1(b). The actual weldment failed in the interface between the FGHAZ and the ICHAZ under C-F loading (Fig. 2). The mode of failure was found to be largely governed by Type IV cracking. The shifting of strain localization due to the initial hardening behavior of the softest ICHAZ and deformation constraint from the surrounding stronger weld metal, CGHAZ and base metal caused the interface failure under the CFI condition. The fatigue lives of homogenous microstructures

such as the base metal, CGHAZ and FGHAZ are directly proportional to the extent of recrystallization and inversely proportional to the degree of recovery under CFI loading (Fig. 3).

Table 1: Chemical composition of P91 Steel

Element (wt.%)	C	Cr	Mo	V	Nb	Ni	Mn	N	Fe
Base metal	0.11	9.3	0.99	0.25	0.1	0.14	0.46	0.068	Bal.
Filler wire	0.082	9.0	1.0	0.24	0.055	0.70	0.55	0.055	Bal.

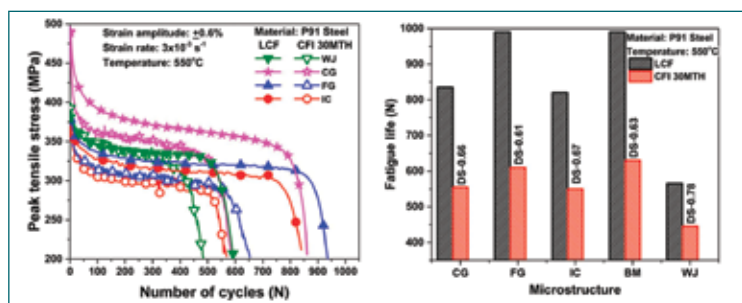


Fig. 1: Comparison of (a) CSRs and (b) fatigue lives of different constituent regions and the actual P91 WJ under LCF and CFI loadings at the strain amplitude of $\pm 0.6\%$. DS – Dwell Sensitivity.

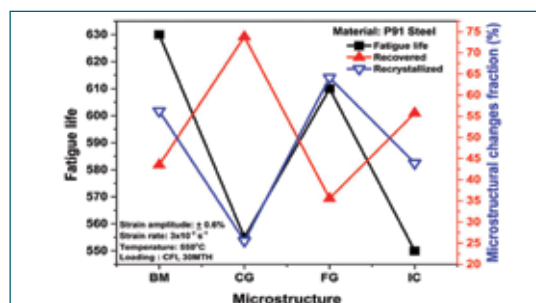
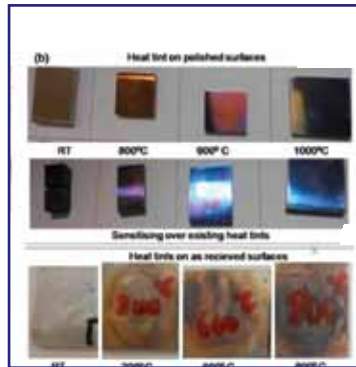


Fig. 3: Fatigue life Vs. microstructural changes in the CGHAZ, FGHAZ, ICHAZ and base metal under CFI loading at 550 °C



CHAPTER IV

Fuel Cycle

IV.01 Study on Corrosion Rates of abut Surfaces in Huey Test

Nitric acid grade (NAG) SS304L steels are opted as structural material in reprocessing application due to their superior corrosion resistance in nitric acid and others. The allowable corrosion rate of the structural material permitted for this application should be 15 mils/yr on average for 5 cycles and 18 mils/yr maximum in any cycle of test ie practice C of ASTMA 262. The same is confirmed through test results of base, undiluted filler material and welding procedure specification. However, the results obtained from standard corrosion tests may not be always true representations for all types of welded configurations, such as locations where post weld cleaning and visual examination is not feasible for example unfused abut surfaces in root side of fillet or partial penetration weld joints.

Experiments

The corrosion testing has been carried out as per plan given in Fig.1. The drawing and actual samples are shown in Fig. 2 and Fig. 3 respectively.

Results and discussion

No sign of weld metal oxidation at root side is seen during examination of root bend samples from fillet welds (Figure. 4a). The heat tints of red to blue and violet colour in appearance are observed on the root side abutting faying surfaces of fillet weld, in which back purging was not provided during the welding, similar to colour of heat

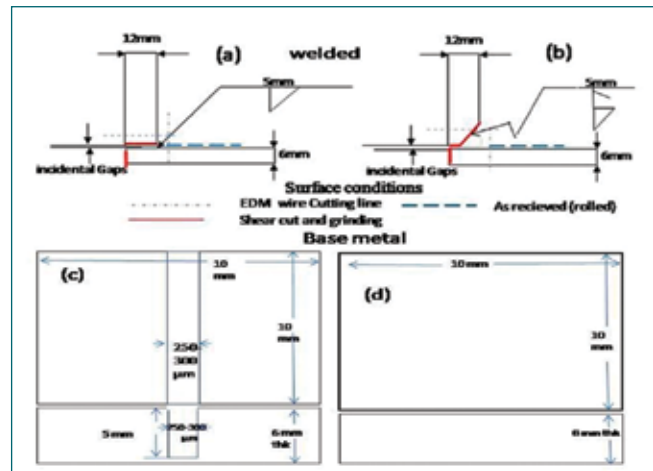


Fig. 2: Drawing of samples for corrosion testing (a) fillet weld joint, (b) groove fillet, (c) base metal with groove (c), & without groove(d)

tints as shown in Fig. 4b. No heat tints are observed wherever purging is provided during welding.

The average corrosion rates for all types of samples are observed within acceptable range, except for the fillet weld joint made without back purging as shown in Fig 5. Similarly, higher average corrosion rates are observed for grooved base metal samples with heat tints as compared to standard test specimen, specified in ASTMA 262. The presence of groove and heat tints in base metal contributes individually for higher rates of corrosion as seen from Fig 6.

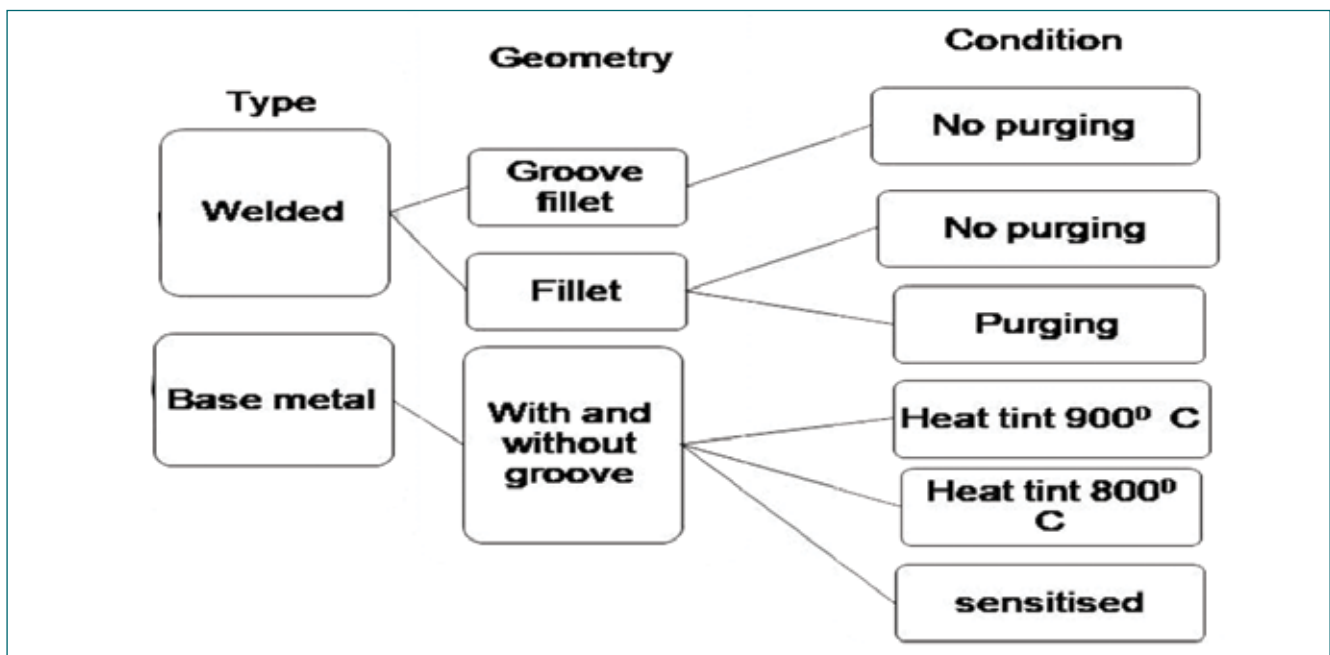


Fig. 1: Sample plan for corrosion testing.

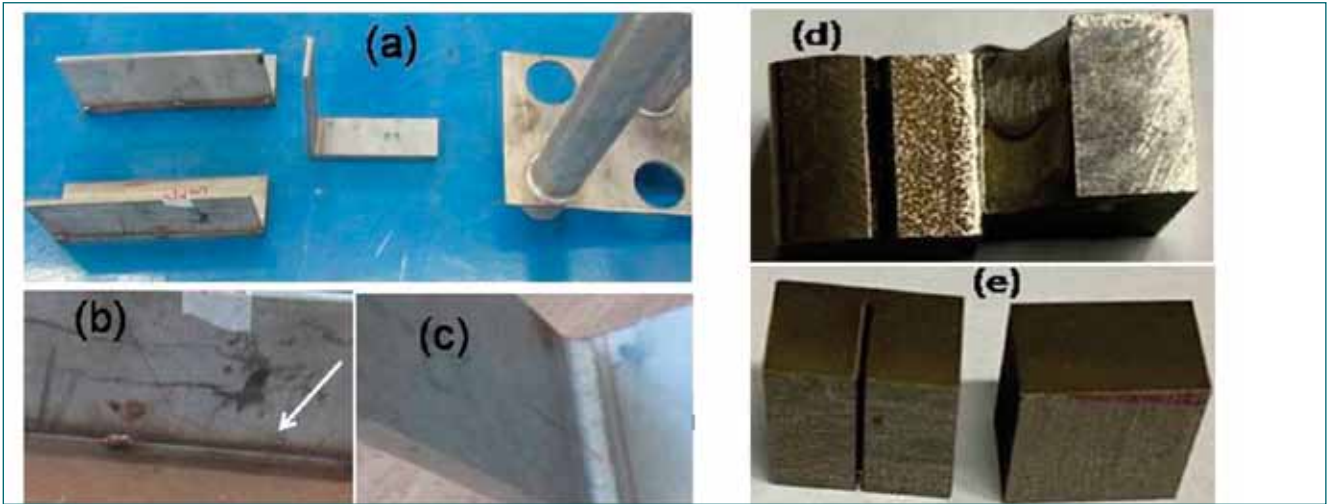


Fig. 3: Welded coupons (a) all types, (b) root of fillet with arrow showing incidental gap and (c) face of fillet weld (d) welded and (e) base metal.

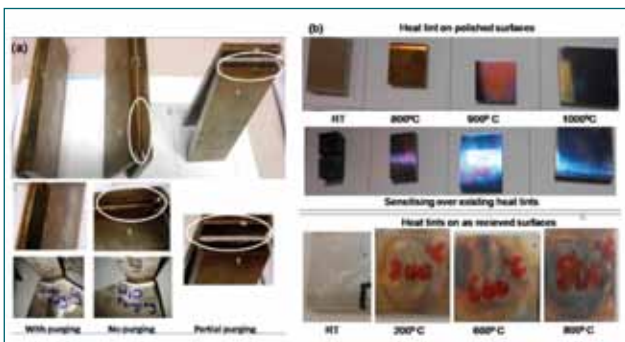


Fig. 4: Heat tints (a) on abutted surfaces in the root side of fillet weld joints, in which no purging or partial purging provided during welding, (b) created on base metal with polished and as received surfaces.

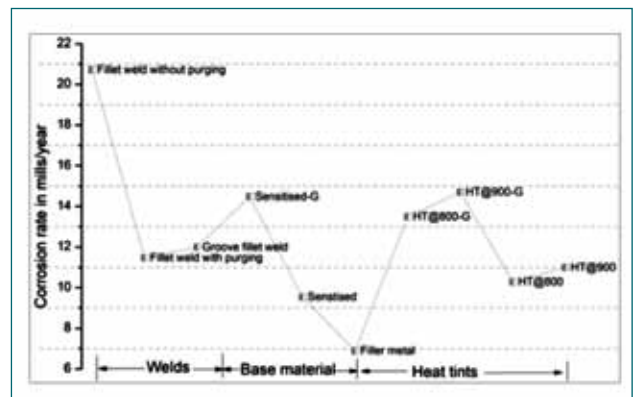


Fig. 5: Average corrosion rate of all the samples after corrosion tests.

The heat tints developed at higher temperature show higher corrosion rates. The corrosion rates for fillet weld with purging are reducing with each cycle as compared

with standard groove fillet welded sample, that show slightly increasing trend with each cycle.

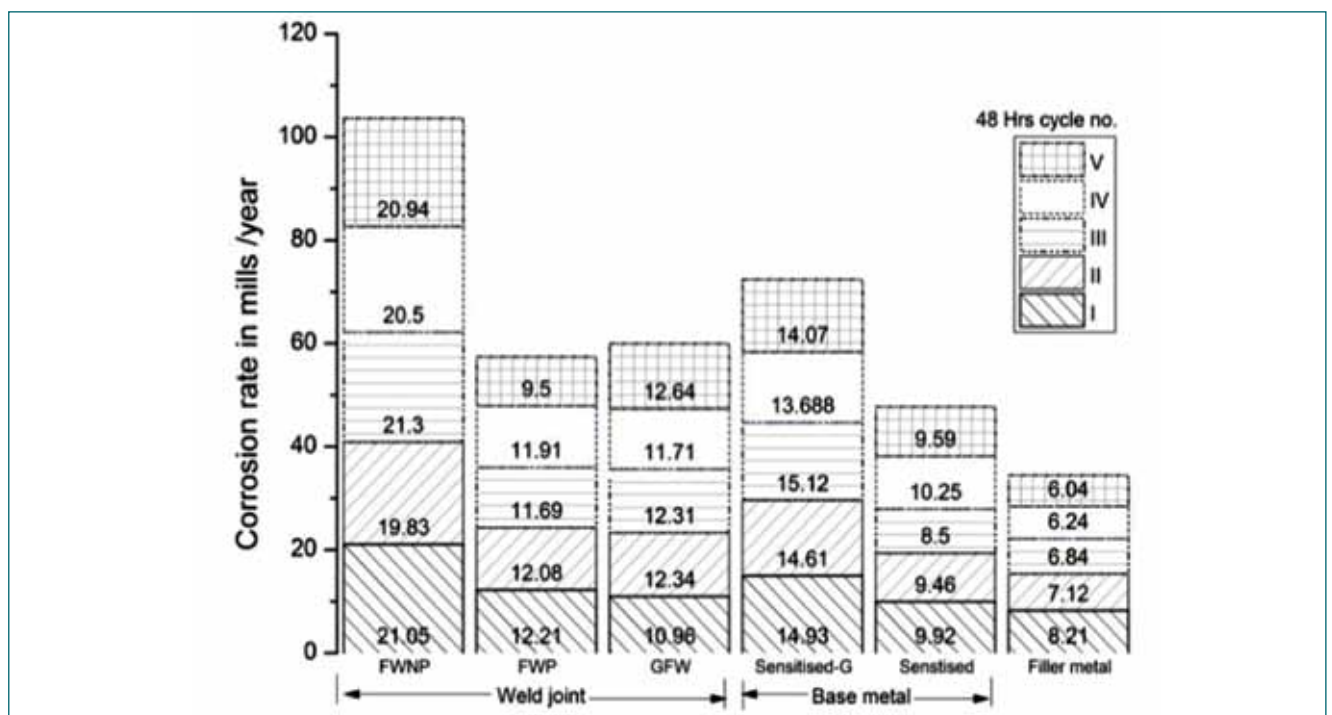


Fig. 6: Comparison of corrosion rate for base material, weld joint and un-diluted filler metal

IV.02 Design and installation of Lightning Protection System for the Buildings in DFRP and CORAL at RpG

An external lightning protection system (LPS) has been designed and installed on different buildings in DFRP and CORAL plants as per latest IS/IEC 62305 guidelines.

Problem description and risk assessment

Lightning strikes can cause serious damage to buildings and structures, as well as pose danger to the people inside. To protect against these potential hazards, it is important to have a lightning protection system in place. The first step in installing a lightning protection system is to conduct a risk assessment. This involves identifying the potential risks to the building or structure as well as the areas that are most likely to be struck by lightning.

Design of LPS

The design of a LPS will vary depending on the type of building or structure, as well as the Class (or Level) of protection that is needed. As per IS/IEC 62305 there are 4 Levels of lightning protection. The Level-1 LPS provides the maximum possible protection which is recommended for the radioactive nuclear facilities. Hence, the Level-1 LPS is considered for both DFRP & CORAL.

The LPS consists of series of components that work together to divert the electrical energy from a lightning strike away from a building or structure. These components include horizontal & vertical air terminals, down conductors and earthing systems.

The air terminal is one of the key components of a lightning protection system. The optimum location of the air terminals on the building structures was evaluated by the “Rolling sphere” method. This is the universal method of design particularly recommended for geometrically complicated applications. Here, a sphere of radius 20 m (for

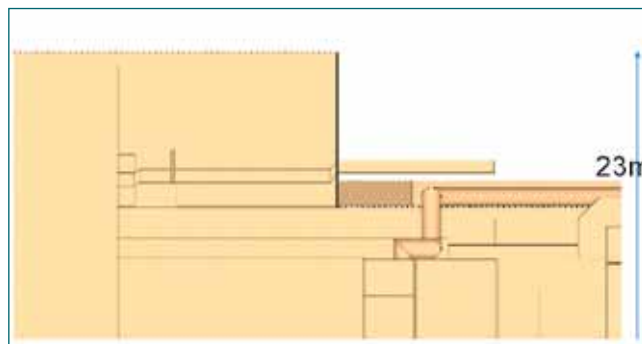


Fig. 2: DFRP PPF and HEF building structures.

Level-1 protection) is rolled around & over the building under evaluation (for which LPS is to be provided) in all the directions. The contact points between the sphere and the buildings are the potential points of lightning strike. All possible points of strike are thus shown on the model (Figure 1). The naturally protected volumes resulting from the geometry of the building and its surroundings are also clearly shown in the figure-1. The air terminals are not required inside the protected volume.

Both DFRP and CORAL plants have complex building structures and are large in size. Hence the rolling sphere method has been implemented by the use of open-source computer programs and CAD software. Figure – 2 shows a 2D model of a portion of the PPF and HEF buildings of the DFRP plant and Figure – 3 shows the same portion of the building as evaluated by the rolling sphere method.

The Figure 3 shows the unprotected potential points of lightning strike in Orange colour and the protected portion (under the Blue colour veil) as evaluated by Rolling Sphere method. The Figure – 4 below shows installed air terminals on unprotected/striking surface of the building.

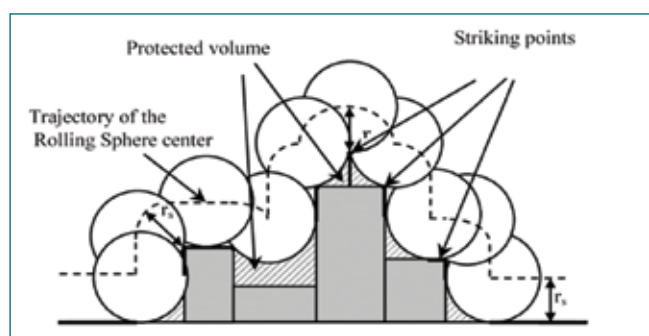


Fig. 1: Illustration of the Rolling Sphere Method.

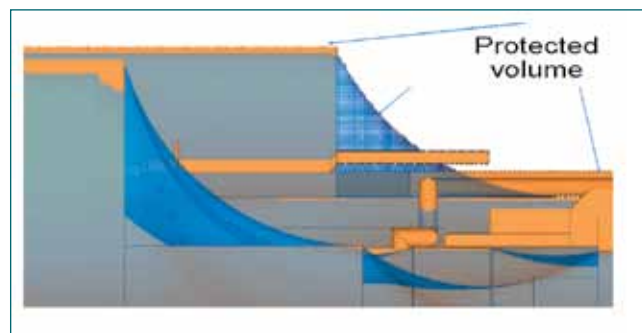


Fig. 3: Exposed structure evaluated by Rolling Sphere method.

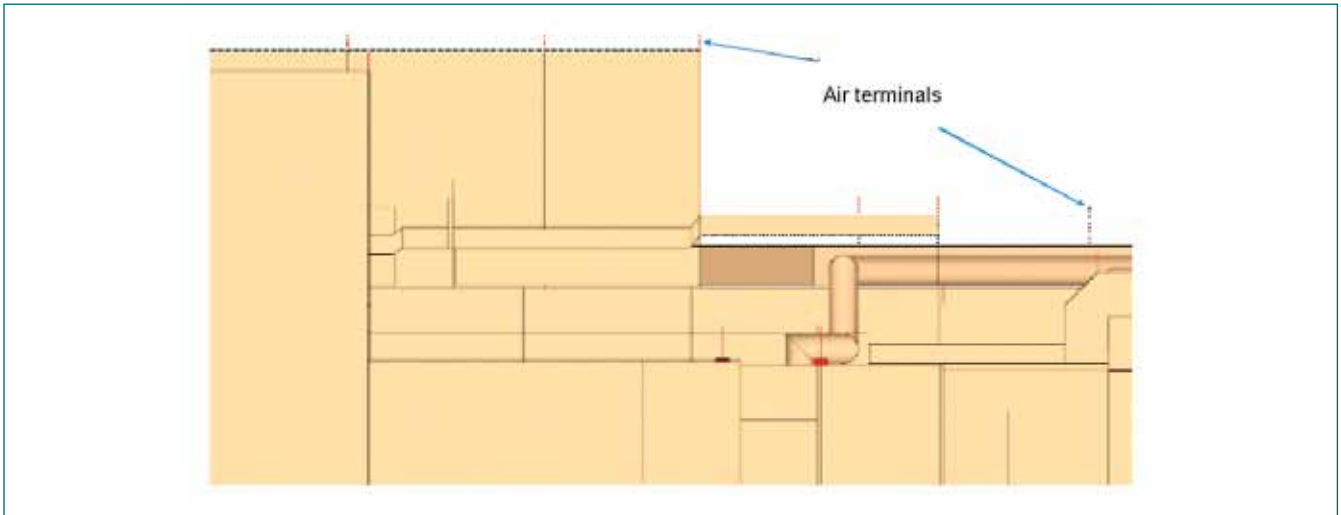


Fig. 4: Installed air terminals on the top of buildings

The protected volume after installation of air terminals on the unprotected portion (potential points for lightning strike) of the building as evaluated by rolling sphere method is shown in Figure-5.

The above figure-6 shows a comparison of the protected volume of the entire DFRP facility before and after installation of lightning protection system.

The air termination network of the LPS has been installed in potential striking points of lightning at DFRP & CORAL in confirmation to IS/IEC 62305.

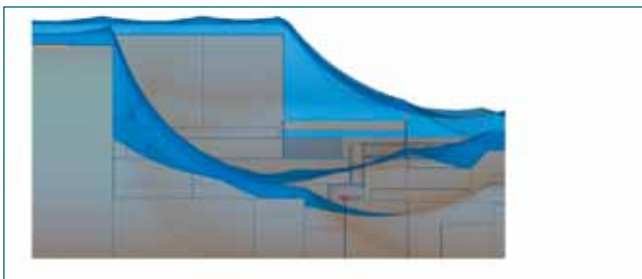


Fig. 5: The exposed structures are fully cover under protection volume.

The air-terminal is then connected to a grounding system through down conductors laid on the wall, which carry the electrical energy from the lightning strike to the earthing system.

Another important component of a lightning protection system is the earthing system. Each down conductor has been provided with an individual earth pit and all the earth pits were connected together to form a single earth network.

Considering the corrosive nature of the saline environment and acid handlings, SS304 conductors have been used in this LPS except the copper bonded steel earth electrodes which are buried in the earth.

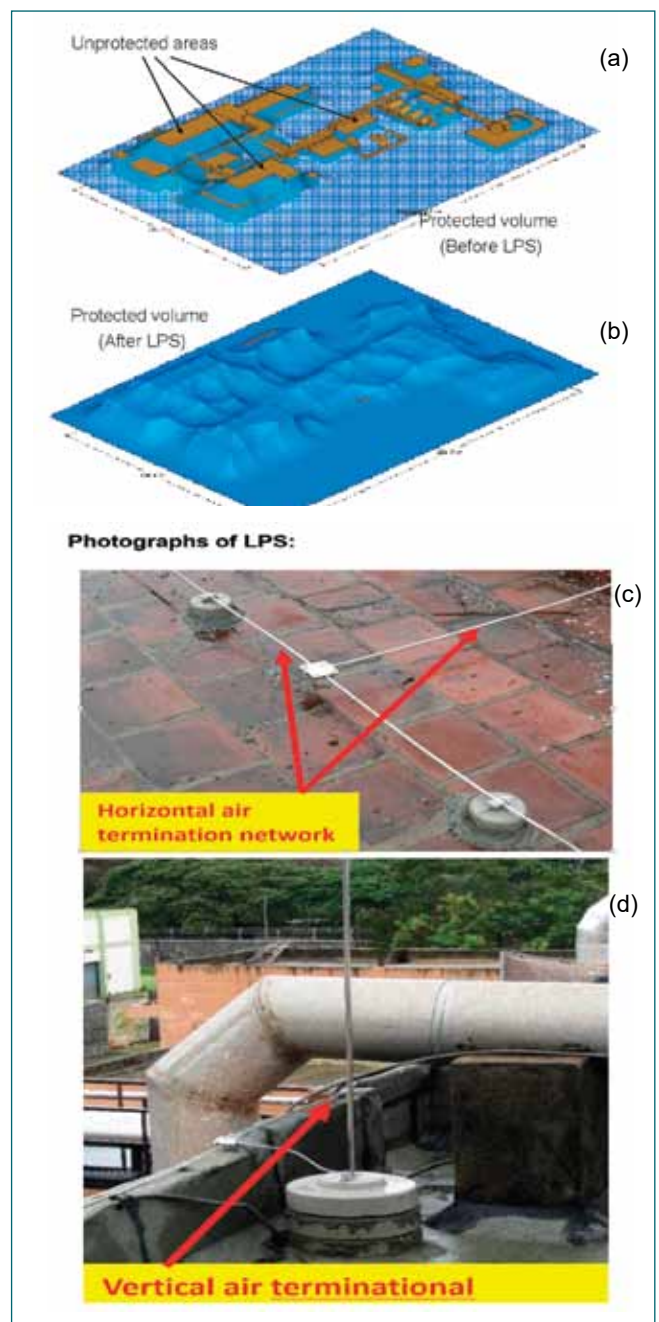


Fig. 6: 3D model of protected volume of entire DFRP before and after LPS.

IV.03 Designing the Flow Sheet for Fast Reactor Fuel Reprocessing using Advanced Computer Codes

The spent nuclear fuel is reprocessed for the recovery of uranium and plutonium by a liquid-liquid extraction procedure, known as the PUREX process. The fissile and fertile elements such as uranium and plutonium present in the dissolver solution are extracted into the organic solvent phase composed of 1.1M tri-n-butyl phosphate (TBP) in n-dodecane (n-DD). The driving force for the extraction of U(VI) and Pu(IV) in organic phase is due to the differences in the chemical potential of these elements in organic and aqueous phases. The distribution coefficient is one of the important parameters that is studied in liquid-liquid extractions in order to understand the degree of mass transfer, solvent requirement, and thermodynamic stability of the extracted species in organic phase. The distribution coefficient is defined as the ratio of the concentration of solute in organic to aqueous phases that are in equilibrium. In order to reduce the solvent requirement which depends on the value of the distribution coefficient of the solutes, the aqueous phase is contacted multiple times with organic phase to quantitatively extract the solute. The optimization of such multi-stage extraction process, known as the solvent extraction flow-sheet, as well as the process design of multi-stage solvent extraction is often analyzed with the help of computer simulation. In order to accomplish the latter, a reliable model for the estimation of the distribution coefficient of the solute is required. Therefore an advanced computer code namely "Solvent Extraction Equilibrium Speciation Calculation" (SEESPEC) has been developed at Reprocessing Group, IGCAR. The SEESPEC code is based on a thermodynamic approach for estimating the distribution coefficients of U(VI), Pu(IV) and HNO₃ in TBP. In this SEESPEC, the partial dissociation of nitric acid and different plutonium species in the nitrate solution such as the mono, di, tetra and hexa nitrate species were included in order to make the model closer to the real time system in terms of the distribution coefficient. The deviation between the experimental and estimated values of the distribution

coefficients, pertaining to Pu(IV) was almost reduced by half as compared to those predicted by another model SEPHIS reported in literature. The SEESPEC code has been employed for the simulation of a proposed solvent extraction flow-sheet. This simulation includes the design of solvent extraction flow-sheet, optimization of various process parameters in the stripping steps, estimation of the safe operating envelope of the process for process control applications. In the first co-decontamination (HA) cycle, the number of stages required for the extraction of uranium & plutonium and scrub stages needed to achieve the required decontamination from the fission products was estimated using SEESPEC code and is shown in fig 1. From this figure it is evident that a minimum of 6 stages are required for the extraction of U(VI) and Pu(IV) with an organic to aqueous phase ratio of one. The radiolytic degradation of the organic phase is more in fast reactor fuel reprocessing systems. Among the various degradation products, the di butyl phosphate (HDBP) forms a strong complex with Pu(IV) and U(VI) at lower acidities. Therefore stripping of Pu(IV) complexed with DBP is difficult. Hence it is proposed to reduce the strongly complexing Pu(IV) (with TBP) in to a weakly complexing Pu(III) by using U(IV) as a reducing agent and to recover plutonium in the form of Pu(III) in the HC(1st stripping) cycle. Hence the optimum feed location of U(IV) and the flow-rate of U(IV) solution for achieving nearly complete stripping of Pu(IV) could be estimated by this simulation. Also the desired operating envelope for the aqueous strip-1 flow-rate for different loaded organic feed-flow rates has been estimated by using the SEESPEC code. The dynamic simulation of the HC bank has been carried out in order to study the effect of flow-rate variation in the stripping of actinides. From these simulation results, such effects in HC cycle could be predicted easily and accordingly the process could be fine tuned in the plant in order to optimize the flow rate to enable minimum retention of the heavy metals in the lean organic phase issuing out of the HC cycle.

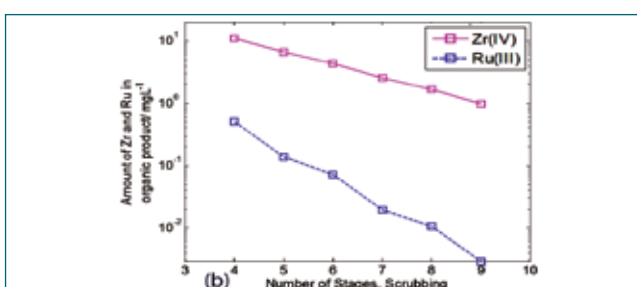
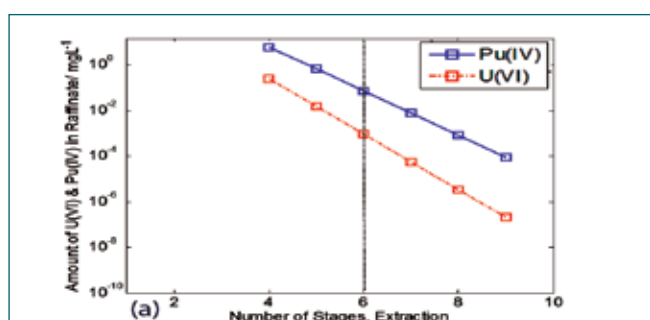


Fig. 1: The concentration of solutes and fission products in raffinate and organic product stream estimated by SEESPEC
a) U(VI) & Pu(IV) b) Zr(IV) & Ru(II&III)

IV.04 Development of Glove Box Adaptable Plutonium Oxalate Precipitator for Continuous Operation

The reconversion process is an essential step in spent nuclear fuel reprocessing in which the decontaminated uranium and plutonium nitrate solutions are converted in to solid forms suitable for fuel fabrication. There are various methods reported for the conversion of plutonium from its nitrate solution form to plutonium oxide. Reactive crystallization or fast crystallization, or simply precipitation, is one of the most important chemical engineering applications widely used in various industries for several decades. As per the current practice in nuclear-spent fuel reprocessing plants, plutonium is precipitated as plutonium (IV) oxalate from the nitrate solution by using oxalic acid in a batch or semi-continuous precipitator, followed by filtration and washing of the oxalate precipitate which is further calcined to obtain plutonium oxide powder. Due to the radioactive nature of plutonium, developmental work in this regard can be conveniently carried out by using non-radioactive lanthanides. Cerium is a common surrogate for plutonium, often used for equipment testing and development. A glove box adaptable continuous precipitator-thickener-clarifier as shown in Figure 1 was

developed for the plutonium oxalate precipitation and for concentrating the plutonium oxalate slurry. This equipment consists of two vertical glass columns with a 3 L operating volume for each. To evaluate the performance of the equipment, experimental runs were carried out by using cerium nitrate and oxalic acid. The effect of agitator speed and residence time on the distribution of the cerium oxalate at the different compartments of the equipment and the supernatant carryover has been investigated. For residence times beyond 15 minutes, 99 percent of the solid recovery was observed in the first column, while the supernatant loss was observed to be less than 0.5%. Solid recovery in column 1 reduced from 99% to 11.8% as the agitator speed was increased 500 to 1000 rpm, even then the overall solid recovery in the system was more than 99%. The new equipment could process the metal nitrate solution up to a throughput of 38 L h⁻¹ with less than 1% solid carryover to supernatant by maintaining the agitator speed in the range of 500 to 1000 rpm.

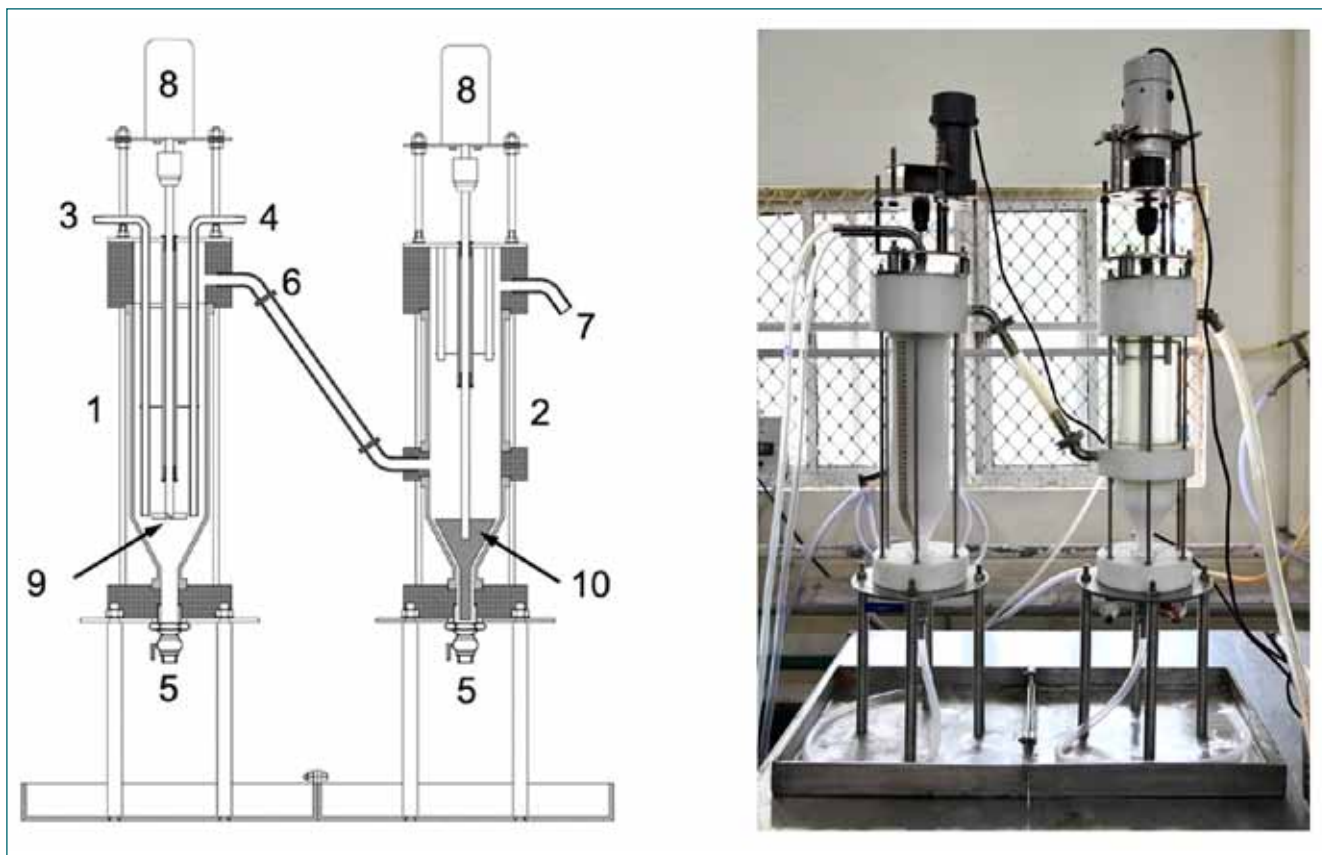


Fig. 1: Schematic and photograph of plutonium oxalate precipitator and slurry thickener for continuous operation: 1 - column 1; 2 - column 2; 3 - feed; 4 - precipitant; 5 - slurry drain; 6 - suspension or clear liquid overflow; 7 - clear liquid overflow; 8 - impeller/rake drives; 9 - pitched blade impeller; 10 - rake;

IV.05 Development of a Jack System for Positioning and Replacement of Lighting Plugs for Lead Cells

Demonstration Fast reactor fuel Reprocessing Plant (DFRP) have many hot cells housing multiple equipments. They are operated and maintained remotely with the aid of manipulators, in-cell cranes and are monitored by surveillance camera, in-service inspection vehicle, etc. For carrying out the above operations optimally, proper illumination is required. Based on the area and the operations envisaged, different types of lighting arrangements need to be designed. The contactor cells and sampling cells are comprised of 250mm thick lead walls right in front of their operating area. These cells have been provided with a first of its kind heat pipe cooled LED light. The lighting fixture is in turn attached to a removable lead plug weighing approximately 40 kg. Further, this lighting fixture is attached to a slender and long structural member to suit the cell layout. Additionally, the 250 mm long lead plug is having two different diameters and is designed to fit with close tolerance with the cell wall port radiation streaming. In addition to all these factors, heavy plugs need to be inserted or withdrawn during routine maintenance. This requirement is further exacerbated by the different locations and elevations at which these operations have to be performed.

In all, there are about 100 lighting fixtures distributed over two floors. The typical construction of this jack includes a clamping arrangement for holding the light plug, translating it up and down as well as back and forth to achieve the desired positioning.



Fig. 1: Heat pipe cooled LED light with Lead shielded Plug



Fig. 2: TDFRP Contactor cell lighting arrangement

The concentricity of this fixture with the port in which it has to be positioned is ensured with the help of a laser guide. Appropriate fixtures have also been provided at the site in front of the wall to ensure that the entire machine gets physically locked at an appropriate position. The final placement is through a self-guided translation of the plug, once the concentric positioning is achieved. There are two motors to effect the up-down and back-forth motion of these plugs which enable both positioning and removal of the latter, smooth movement has been facilitated by deploying ball screws. The entire equipment has been constructed with light weight aluminium structure to enable easy transportation & handling.



Fig. 3: Lighting Plug Jack

IV.06 Development of Improvised Neoprene Gauntlet Through Indigenous Manufacturing

Gauntlets are used for handling radioactive solution in glove boxes. Often these need to be imported. Those manufactured indigenously have very short service lives especially when they are used for handling 30% TBP in NPH or 4 to 6 M nitric acid or both. These chemicals are used in the aqueous reprocessing of spent reactor fuels by the PUREX process. Hence, a two stage developmental work was initiated to fabricate an indigenous product with better performance and longer service life. In the first stage, a rubber compound based on neoprene was developed. In the second stage, gauntlet samples were fabricated by dip coating method using this rubber compound. The dip coating method was chosen since the gauntlets manufactured by moulding technique were found to be less flexible.

For the development of the rubber compound, poly chloroprene rubber and other appropriate chemicals were used as starting materials. The mixing was done as per ASTM D-3182 practice. Test slabs and buttons of these mixed compounds were obtained by compression-moulding technique as per ASTM D-3192 procedure. The rubber compound was sheeted out and the product moulding was carried out at about 450 K for an appropriate curing time. The mechanical properties of the developed rubber compound were determined. Tensile strength, elongation at break and hardness were determined.

The chemical resistance of this rubber compound towards organic solvents and nitric acid was evaluated as per ASTM D-471 procedure. The retention of the properties of the rubber compound after immersion was compared with that of an imported gauntlet and the results are given in table 1. From this table it is evident that the retention of properties in 30% TBP for indigenous rubber compound is better than that of the imported gauntlet and in nitric acid the retention is almost same as that of



Fig. 1: Photograph of neoprene gauntlet

the imported gauntlet. The rubber compound developed in general, was found to be compatible with chemicals, since the changes in tensile strength, elongation at break and hardness were found to be within allowed limits as prescribed by ASTM standards.

In the second stage, based on the rubber compound developed, gauntlet samples were manufactured by dip coating and their photographs are shown in Figure 1. Specimens cut from various locations of this gauntlet were tested for uniformity in mechanical properties and thickness. Visual and physical examination of these gauntlets for permeation and penetration yielded satisfactory results. To check the repeatability of the properties 5 nos. of gauntlets were fabricated and were tested for physical properties. Properties of all these five gauntlets were found to be nearly the same and the properties of the five gauntlets are comparable with that of the imported gauntlet.

For the real time testing of the gauntlets, they were fitted to a glove box of the hot cell and their performance was evaluated. After a period of six months, these gauntlets which were exposed to the vapour of solvent and nitric acid were examined. No appreciable damage has occurred on the gauntlets. For the sake of comparison, a pair of imported gauntlets was also attached to the same glove box. The performance of the indigenously developed gauntlets was found to be equivalent or better than that of imported ones.

Table 1 : Retention in properties of rubber compound and imported gauntlet after immersion				
Time (min)	Bath temp.(°C)	% retention in properties after immersion		
Chemical	Sample	Tensile strength (MPa)	Elongation at break (%)	Hardness Shore A
30% TBP in NPH	imported gauntlet	32	47	72
	Indigenous rubber compound	38	55	82
4 M nitric acid	Imported gauntlet	98	102	104
	Indigenous rubber compound	108	103	102

IV.07 Development of Silicon Photo-multiplier (SiPM) and Fibre Optics based Radioactive

A Radioactive contamination monitor has been developed in a radio-chemical plant for monitoring the alpha-beta radioactive contamination on hand, foot and cloth of the personnel working in the plant. This instrument comprises of seven Alpha-Beta detectors and seven channel electronic module with display unit (Fig. 1). It generates audio-visual alarms on detection of contamination above preset limits. It also alerts the user if the monitoring process is terminated before the preset monitoring time. The detected events are counted over time and displayed digitally in terms of cps or cpm on the display unit. The unit stores measured data and can also communicate with external data acquisition system via ethernet. The monitor performs reliably, round-the-clock, in the nuclear plant environment. These monitoring devices have been installed at the exits of radiation controlled areas in nuclear power plants and other facilities, where radioactive materials are handled.

Along with the conventional radiation detectors, requirement of other type of detectors have been growing for various nuclear applications. Over the last few years,



Fig. 1: Alpha Beta Hand Foot and Cloth Contamination monitor using SiPM and optical fiber.

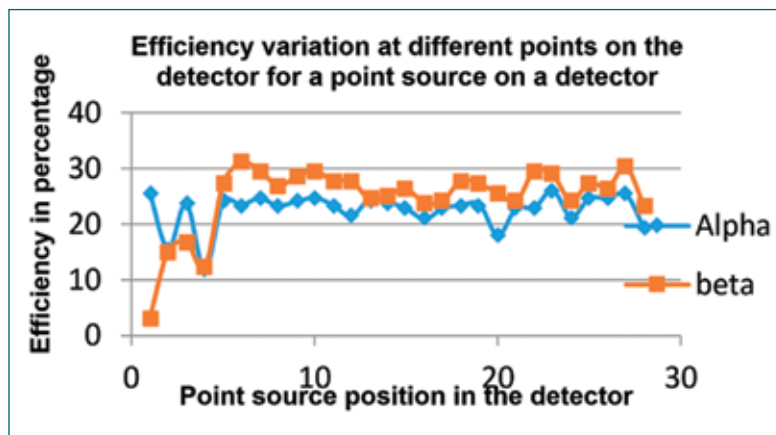


Fig. 2: gives a graphical view of the results obtained

internationally, several scintillation fiber based detectors are developed for hand, foot and clothing contamination monitor. This development introduces latest detector technology to develop compact monitors with improved performance. One such development is the use of dual phosphor detector with SiPM and optical fiber (wavelength shifting fiber for light coupling). The advantages of this detector over the conventional detectors are the following;: 1. single detector for monitoring alpha and beta contamination, 2. SiPM operates at $55\pm 3\text{VDC}$ and hence the use of high voltage in the unit is avoided, 3. detector coupling uses SiPM with wavelength shifting fibers and hence are simpler as compared to conventional Photo Multiplier Tube (PMT) based unit, 4. the efficiency is comparable to that of a PMT based unit, 5. the efficiency does not vary much over the entire surface area of the detector, 6. foot detection of alpha and beta particles is possible whereas the conventional unit uses GM tube for foot detection where only beta detection is possible and 7. it is relatively less expensive and is rugged.

A study was conducted on one particular detector to observe the uniformity of the detector response to a point source. The detector was divided equally into 28 positions with 7 rows and 4 columns to place the source. $^{241}\text{Am} - 1713 \text{ Bq}$ point source was used as an alpha source and $^{90}\text{Sr} - 4869 \text{ Bq}$ point source was used as a beta source for the study. These sources were placed at different positions in the detector and the efficiency of counting was monitored. Figure 2 gives a graphical view of the results obtained. The positions 1 to 4 are in the first row. The first row is near to the SiPM, where the fibers have been grouped together and focused towards the SiPM. The variation in efficiency could be attributed to the bending of fibers, where light collection is not even.

IV.08 Development of Special Fixtures and Tools for Fast Reactor Fuel Reprocessing

Hot cells of Reprocessing plants are equipped with many equipments which need to be compatible for remote operation maintenance using MSM & In-cell crane. It is therefore inevitable to develop the equipments, fixtures & tools indigenously. The following document describes some of the important tools & fixtures developed in-house, deployed at site and tested successfully.

In situ Cable Replacement Mechanism: The hot cells house many electrically operated equipment, which use bunches of data & power cables that are routed through SS pipe embedments fitted with suitable flange at the operator side. Each of these cables is terminated with a male connector (2"x2" (approx.)). For replacement of these cables, both the flange assembly & the pipe embedment need to be replaced (shall feature cable replacement along with the connector) along with the cable and the connector. Conventionally the cable-gasket interface is sealed with an adhesive sealant, alternatively gasket embedded with cables are used, which do not allow replacement of a specific defective cable. Similarly, the EPs won't allow replacement of cable along with the connector.

A Leak Tight Flange and Gasket assembly (LTF) facilitating penetration of cables in a bunch, which had been helium leak tested at a pressure of 1.0 kg/cm²(g) & at a pressure of 3.0 kg/cm²(g) using air-soap solution as testing medium, without the use of sealant adhesive, developed in house has been deployed at many places. Similarly, a special EP, named Twin-EP has been developed to allow loading of a new cable along with the connector inside a feeder pipe and in turn into the main pipe preloaded with bunch of cables. The combination of LTF & Twin- EP will allow in-situ cable replacement



Fig. 1: Adhesive free Leak tight flange

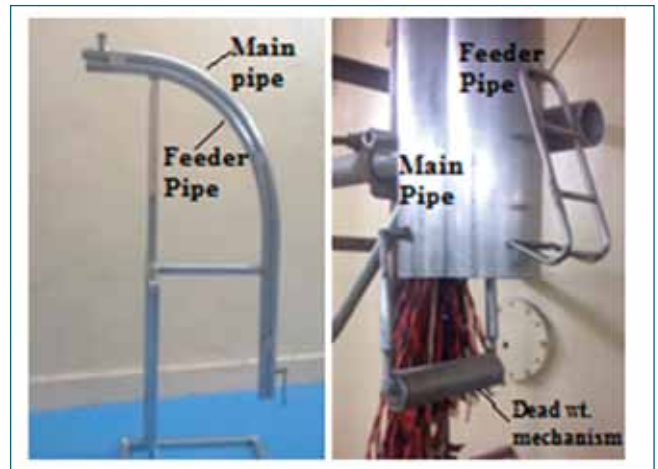


Figure-2: Twin EP

Image of both the flange-gasket assembly & special EP are shown in the Figures.

Remotely Operated Self-Locking Fixture for Wall Mounted Equipment (REMOF): A remotely operable fixture was developed to secure firmly glass dome for electrical bulb to inside the wall of the hot cell vide a wall embedded narrow circular port. The wall thickness is about 2 mtr. and the dome can be fitted blind fold in a couple of minutes and the joint had been qualified with Helium leak tightness at a pressure of 1.0 kg/cm²(g) and at a pneumatic pressure of 3.0 kg/cm²(g). Image of both the flange-gasket assembly & special EP are shown in the Figures.

Modular Remote Sampling System (MORSS): Customized MORSS for the application of collecting samples from nozzles beyond the reach of manipulator was designed, developed, functional tested and installed in sampling cells. These units have been designed with minimum number of maintainable parts & drive units as an alternate to complex Robot, which had the difficulty in accessing most of the parts vulnerable for maintenance and at a cost less than 1/10th of cost of Robot.

The system has been designed in a modular way with passive safety features, enabling replacement of any maintainable parts remotely and in short time and assembly & disassembly of the entire unit in less than an hour. Image of Modular Remote Sampling System is shown in the Figures.

Attachment for the fabrication of pipe bends with minimum inter distance:

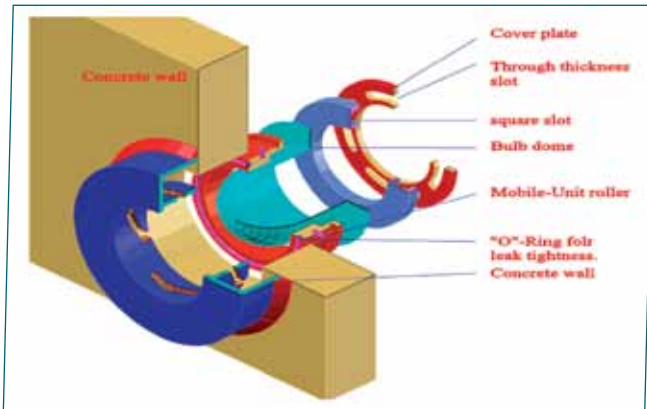


Fig. 3: Conceptual dwg. of REMOF

Process cells of the Reprocessing plants are normally compact, housing high density piping. The pipe spools are to be normally designed with multiple bends and offsets before travelling up to the destined locations which calls for routing of spools with minimum bend to bend distance, which necessitates inevitable introduction of a joint in each case.

A fixture adaptable to the manually operated hydraulic Ram type bending machine has been developed ensur-



Fig. 6: Typical view of Robots

ing fabrication of pipe spools having two successive bends with minimum inter distance without a joint in between. This had brought about a reduction in the total number of weld joints and a concomitant reduction in the associated NDT tests. This further lead to a reduction in cost & time as well as material wastage and also enhanced the overall piping integrity by avoiding joints . Image of Attachment for the fabrication of pipe bends with minimum inter distance is shown in the Figures.



Fig. 4: REMOF Assembly



Fig. 7: Fixture attached to conventional bending machine

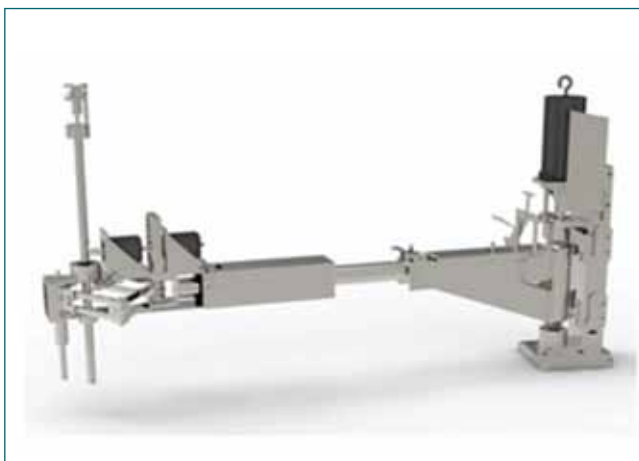


Fig. 5: Indigenous MORSS

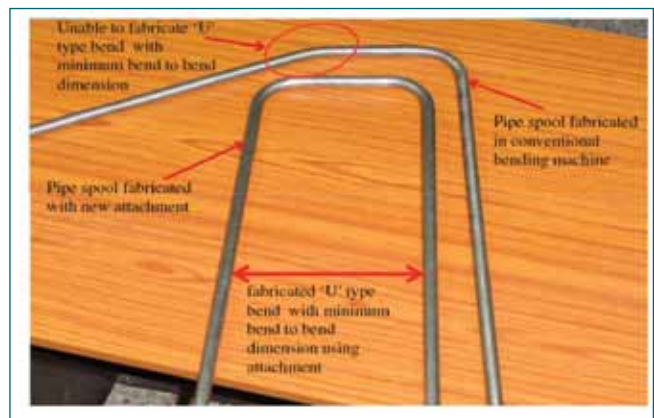


Fig. 8: Spool fabricated with conventional machine Vs one fabricated with the attachment in the same machine

IV.09 Kinematic Analysis and Evaluation of Swept Areas of an Articulated Manipulator used in Hot Cells of DFRP

An articulated master slave manipulator (MSM) is a six degree of freedom MSM, where the master arm and slave arm are coupled to each other through wire ropes and pulleys. The motion of the master arm at cold side is reproduced by the slave arm at hot side with a mechanical advantage of 1:1 as shown in Figure 1(a). Kinematic analysis of manipulators bears extremely useful information about the work volumes and the reach spaces a given manipulator can encompass inside hot cells. Using these, all the in cell critical equipments which require frequent remote maintenance are placed within the reach diagrams of the manipulator.

Work volume and reach diagrams were evaluated by performing direct kinematic studies on an articulated manipulator. From an existing geometrical configuration and motion constraints, kinematic diagram was formulated shown in Figure 1(b) and 1(c) and correspondingly modeled in multi dynamic automated simulation software to obtain motion mapping as shown in Figure 2(a) and 2(b). With the available link lengths of through tube assembly, upper slave arms (650 mm), slave forearm (450 mm) and various joint angle constraints, different motions were generated and the area swept was calculated. Figure 2 gives the 2D workspace and motion map when the through-tube rotation is fixed, shoulder joint (Z motion) is constrained to move from $+52^\circ$ to -70° and elbow joint (Y motion) constraint to move from $+50^\circ$ to -50° . Here the link and the corresponding motion of tongs/end effector has been neglected. The coordinates of the 2D work space are plotted and the swept area is obtained, which works out to be 662188 mm^2 as shown in Figure 2(c). This motion map and area gives important inputs with respect to remote maintenance amenability of different in-cell equipment.

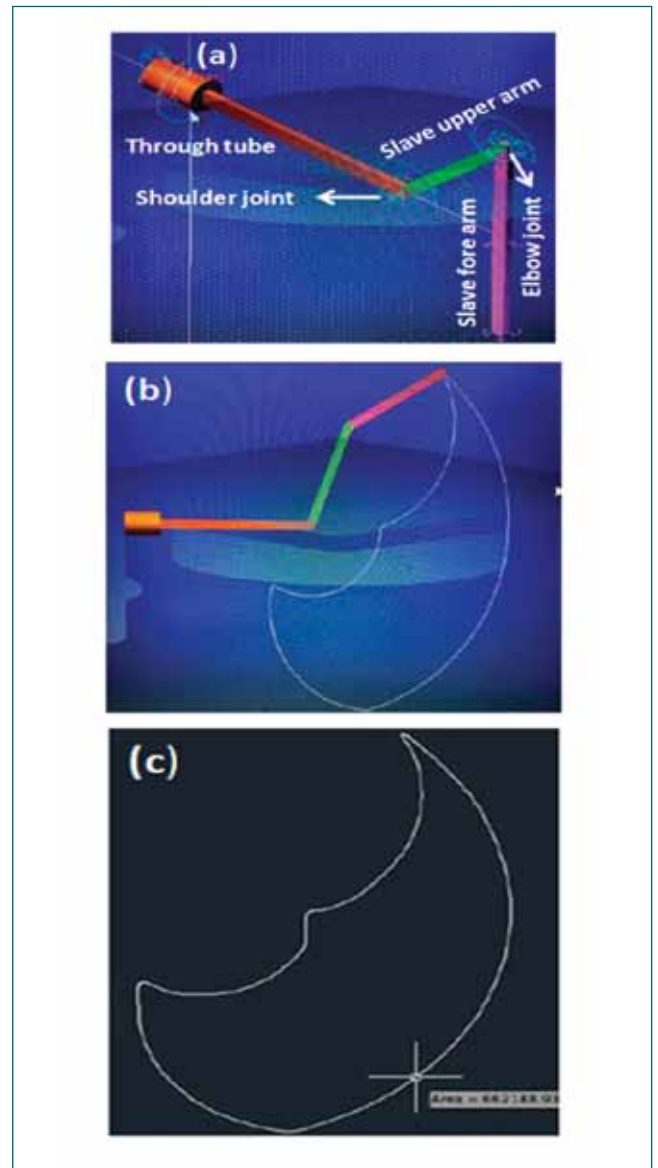


Fig. 2: (a) AMSM simulation Model (b) Motion mapping (c) 2D workspace of AMSM

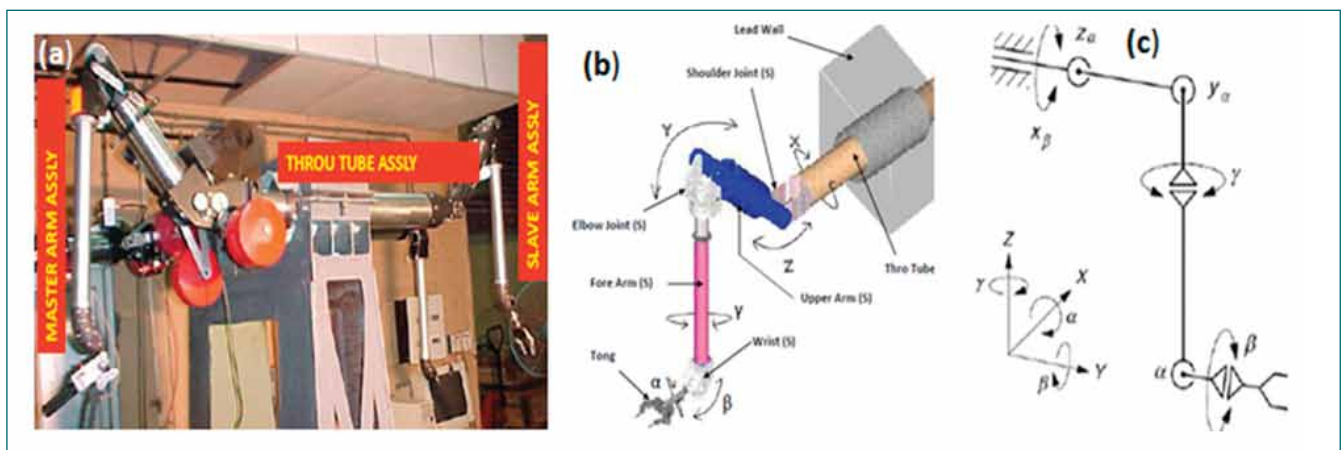


Fig. 1: (a) articulated MSM (b) motions of slave side (c) kinematic representation of articulated MSM.

IV.10 Online Detection of Plant Abnormalities using Machine Learning Based Data Analytics

In DFRP, the control system comprises of PLC and SCADA servers & clients. Typical process parameters like level, density, pressure and temperature are measured by using different indirect measurement techniques. The PLC acts as the controller to scan inputs and control outputs. The supervisory control and data acquisition (SCADA) act as Human Machine Interface (HMI) and communicates with the controller. Operational equipment like evaporator, dissolver, extractors etc are operated from SCADA as per process flow sheet requirements. All interlock conditions have been programmed in the PLC, envisaging all potential failure and alarm conditions. Though these logics ensure smooth plant operation well within safe process limits, a diverse redundant system that can self-learn, predict and alert any possible abnormal event will help the operators to circumspect the area of concern.

To realize the prediction in process behaviour, supervised learning based modelling techniques that simulate or mimic the cognitive processes of a human brain is employed. This not only does the predictive maintenance easily but also helps the designers and plant operators to improve the performance and efficiency of working of any process or equipment. This tool is developed in such a way that it communicates with the existing PLC/SCADA network without disturbing its current functioning. It can also be enhanced into a tool that prescribes corrective

action in automation to ensure safety of plant and plant personnel and improve the quality of final product.

To develop and integrate the prediction tool with the existing system, an open-source Integrated Development Environment (IDE) based on Python as programming language has been chosen. The user interface developed using PyQt can get user inputs & commands and plot/tabulate results using output widgets. Various libraries and packages are used to perform mathematical, logical, statistical computation of multidimensional array objects, which mainly comprise of time stamped process values of various tanks and equipments.

Out of many plant operating scenarios, two real time conditions were taken, to put the machine learning application into use. First requirement is to predict the density of evaporator solution @ room-temperature when evaporation cycle is under operation. During heating of evaporator, due to high temperature of liquid, the measured density using purge method would be an under estimate as compared with the actual concentration due to volume expansion. To know the exact concentration of the evaporator solution, plant operators generally need to wait for the evaporator to cool down that generally takes around 24 hours. This whole process consumes a lot of time to complete each evaporation cycle. To limit this waiting time, the application program is deployed

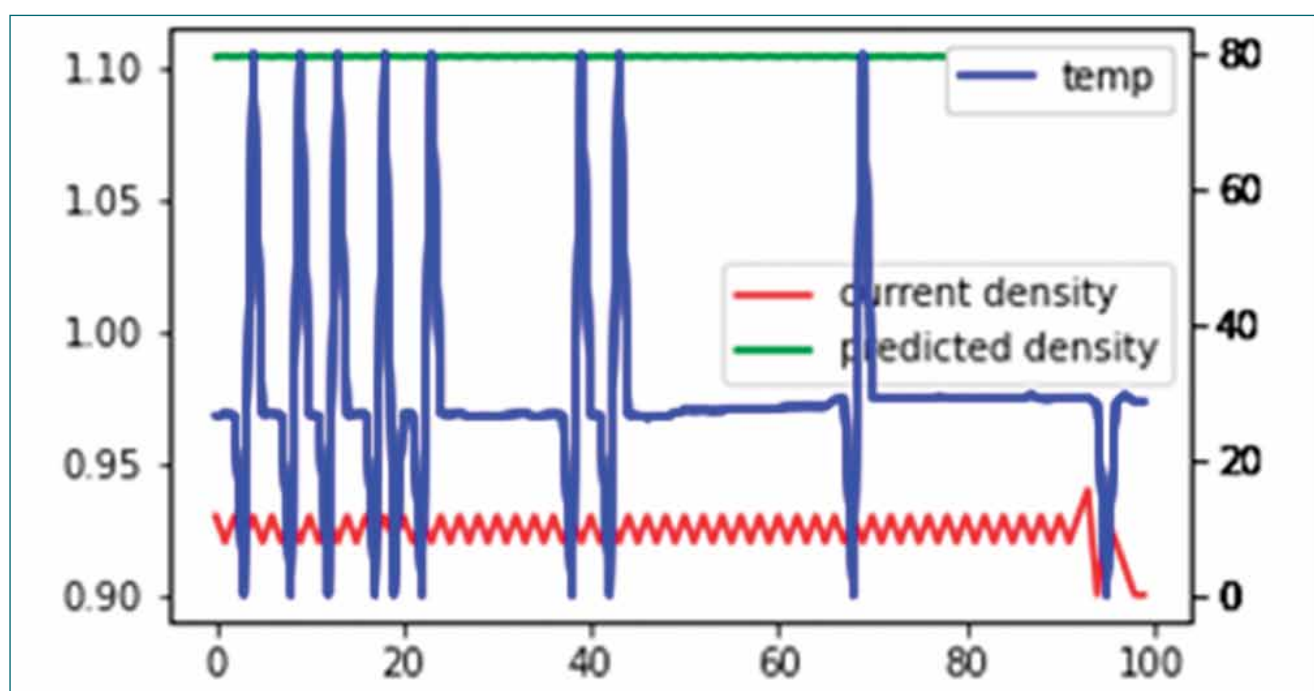


Fig. 1: Application tool predicting actual density of evaporator solution using stored regression model

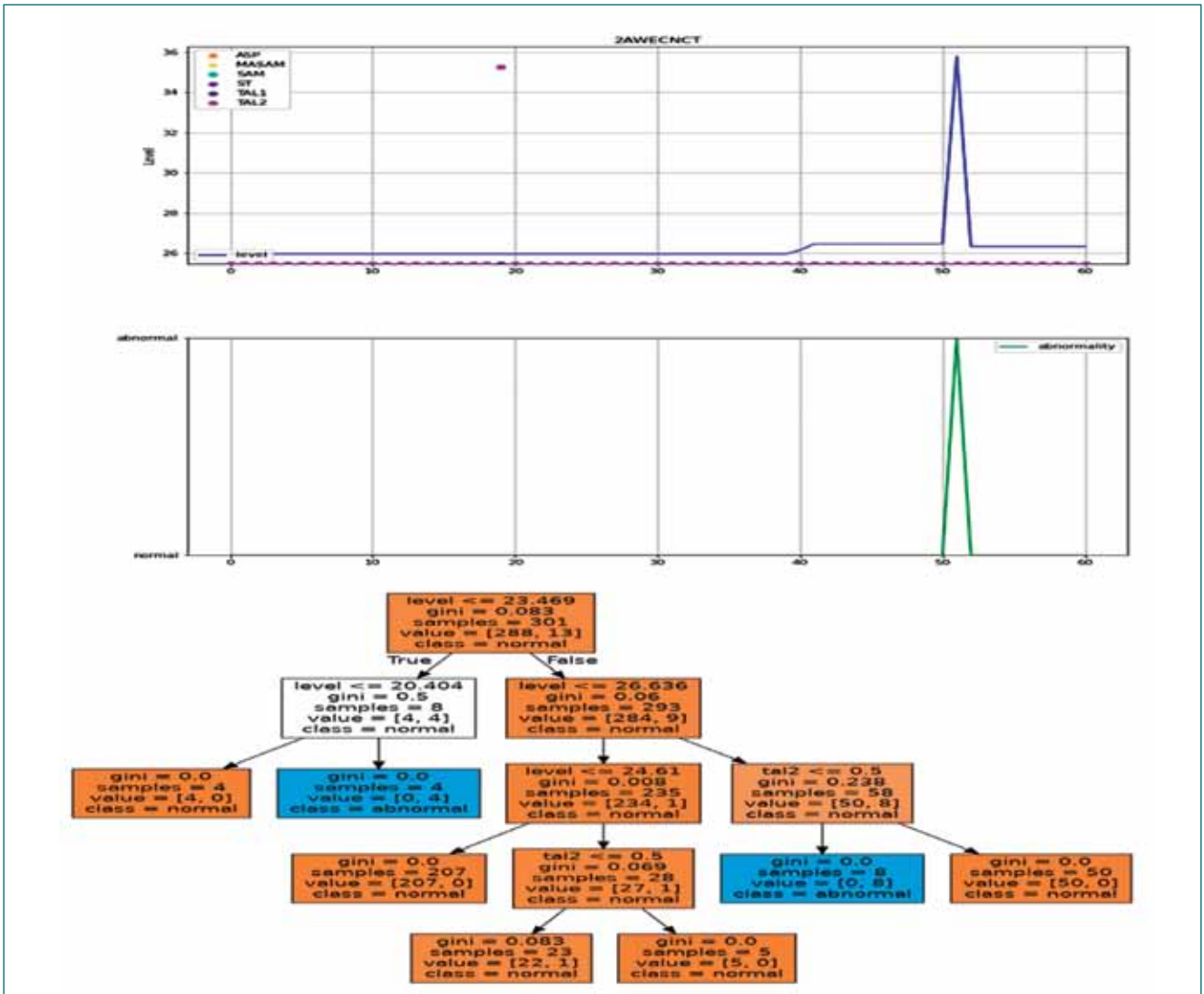


Fig. 2: Application tool predicting abnormality in liquid transfer using decision tree regression model

to predict the actual density even if the temperature is higher. The second requirement is to classify the intended and unintended transfers of solution from any tank.

A supervised learning program is developed that will take current density and temperature values of evaporator solution from the historian server by using SQL queries and would return the value of what the density would be after the equipment has finished its operation and has returned to room temperature by using self-learned model.

It uses the input parameters to determine the concentration of nitric acid in the equipment using linear regression. With that concentration value, densities for various temperatures would then be used as a dataset for training neural networks to do regression and the model thus created is used to predict the density of evaporator solution at room temperature i.e. at 30°C.

After several trials, the optimum number of epochs for which the neural network is most appropriate was found. The neural network regression model was then

employed in this tool. The evaluation of this trained model was carried out by using testing datasets and later deployed for realtime analytics during evaporator operation.

The second scenario is to predict abnormality in the liquid transfer system by using decision tree algorithm. It polls SQL server and obtains data from the historian server. Based on the model obtained from the training data, it can classify whether a transfer involving a given tank is normal or abnormal.

This tool will take in labeled sets of data consisting of level of the tank and on/off status of various inputs and outputs in the tank. The decision tree thus created may be deployed on the data obtained subsequently from the SQL server to classify whether at a given time, a change taking place in the tank is normal or abnormal. The accuracy thus calculated was found to be 0.95604 or 95.6%. Both the tools have been implemented and tested in the plant.

IV.11 Radiofrequency Induction Heating System for Fixing The Nuclear Material on A Planchet for Radiometric Analysis

Alpha particle counting technique is a conventional method employed for the determination of actinides present in process streams and environmental samples in a radiochemical laboratory. This technique is simple, less time consuming and generates minimum amount of waste. In this method, the sample to be analyzed is diluted in such away that solid deposits obtained from typically about 100 μL of sample containing about less than a microgram of alpha emitting nuclides are held onto an SS disc called as planchet. One planchet is prepared by dropping the weighed quantity of sample onto SS plate, dried and heated to red hot using a Bunsen flame to decompose the solvent and fix the nuclear material on the surface of the planchet. In view of this, the planchetting of nuclear materials by this procedure eliminates cross contamination. Nevertheless, the use of LPG cylinder for firing the planchet in this method pose fire hazard. Therefore, safety protocols and utmost precautions are necessary while conducting these measurements.

Alternatively, heating systems based on magnetic induction have been proposed for various heating application. In a radiochemical laboratory, the employment of these systems would help to reduce the potential fire hazard and are best suited for planchetting without cross contamination. Therefore, a commercially available induction heating system has been purchased and

customized to our requirement in order to fix the nuclear material onto a planchet. In this system, the planchet to be heated is placed in a high-frequency electromagnetic field produced by induction coils, which is connected to a 200 kHz radio-frequency generator. The radiofrequency induction coil was placed inside the fume hood. The surface of the coil has been covered with ceramic material. On top of this, a 30 mm quartz disc has been placed. The latter is amenable for decontamination, if required. The major part of the induction heating system namely the RF generator is kept outside the fume hood and therefore, it can be detached at any time and transferred from amber area for maintenance, if required.

The generator unit consists of a single phase AC to DC rectifier unit with smoothing filter section, IGBT/ MOS-FET based inverter for efficient heating. The isolation transformer unit is separated from the main unit by an inter-connecting flexible cable. Both the inverter unit and the isolation transformer unit are air cooled. The operating current of the device was optimized at 3.5 A to reach desired temperature of 1000°C within 20 s. The centerline and peripheral temperature of the planchet were measured with the help of a radiation pyrometer and they were determined to be 1000°C and 1150°C, respectively. Since the performance of the device was verified and found to be satisfactory, it was deployed for alpha planchetting in the active analytical laboratory.

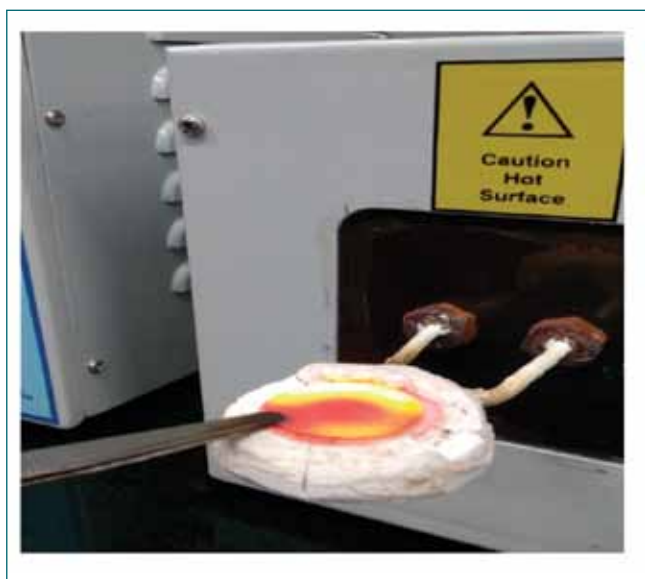
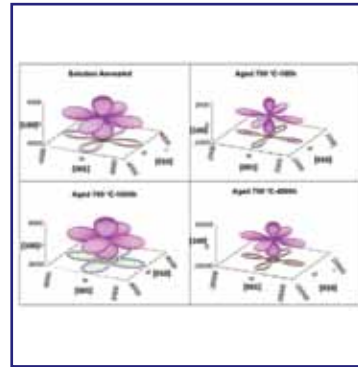
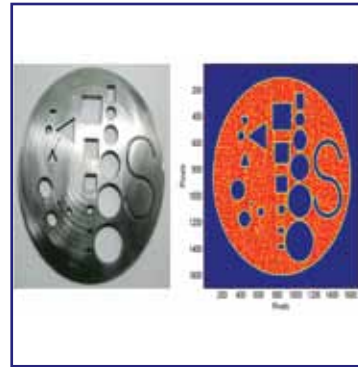
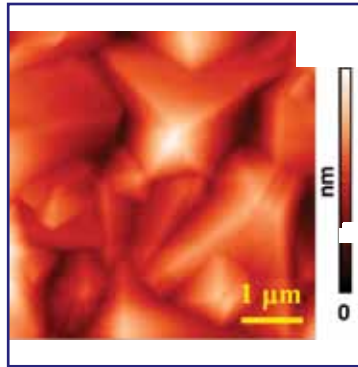


Fig. 1: Induction heating of the planchet



Fig. 2: Temperature measurement of the planchet



CHAPTER V

Basic Research

V.01 Evaluation of Residual Stress in Polycrystalline-Ge Thin Film Grown on Glass Via Au-Induced Crystallization using GIXRD

Polycrystalline (poly)-Ge thin film were grown on glass substrate at $\sim 170^\circ$ using Au-induced layer exchange (AUILE) crystallization of an amorphous-Ge (~ 50 nm)/GeO_x (~ 1 -2 nm)/Au (~ 50 nm)/glass thin film stack. Grazing incidence X-ray diffraction (GIXRD) was employed to ascertain the poly-Ge phase (Figure 1) as well as to evaluate the residual stress endured by the poly-Ge thin film using a modified Sin² ψ technique. In this method, multiple sample tilt angles (ψ) are readily achieved as $\psi = \theta^{\text{hkl}} - \beta$, where θ^{hkl} is the Bragg angle for the hkl-plane and β is the incident angle. Rotational symmetry in the poly-Ge thin film was confirmed by performing GIXRD runs at different azimuth angles (ϕ). The unstrained lattice spacing (a_0) used for calculating the ψ -dependent strain (ϵ_ψ) was determined from the experimentally observed a vs. Sin² ψ plot ($a = d^{\text{hkl}} \times \sqrt{h^2 + k^2 + l^2}$) since Ge has a cubic structure). The in-plane residual stress σ_m was then evaluated by fitting the ϵ_ψ -distribution to the X-ray stress equation (see Figure 2): -

$$\epsilon_\psi = \frac{1 + \nu_{\text{Ge}}}{E_{\text{Ge}}} \sigma_m \sin^2 \psi - \frac{2\nu_{\text{Ge}}}{E_{\text{Ge}}} \sigma_m \quad (1)$$

where $\nu_{\text{Ge}} = 0.21$ and $E_{\text{Ge}} = 132$ GPa. The positive slope (in Fig. 2) shows that σ_m is tensile with a value of ~ 268 MPa. As $\sigma_m = \text{thermal stress } (\sigma_{\text{th}}) + \text{growth stress } (\sigma_g)$, their individual contributions were further accounted.

Thermal or extrinsic stress

Since the poly-Ge thin film have a negligible thickness of ~ 50 nm compared to the considerably thicker glass

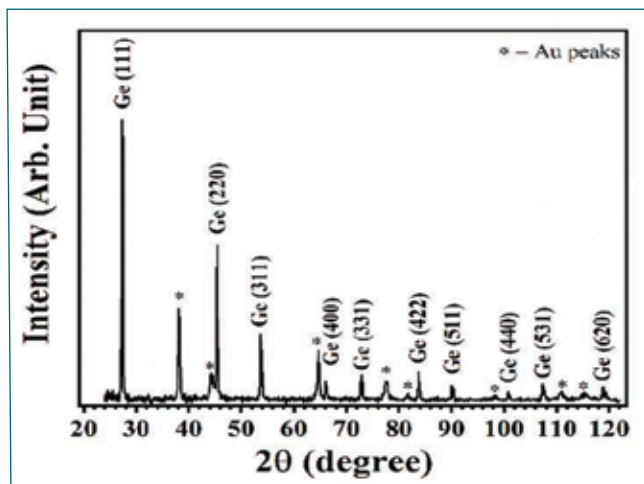


Fig. 1: GIXRD pattern of the poly-Ge thin film

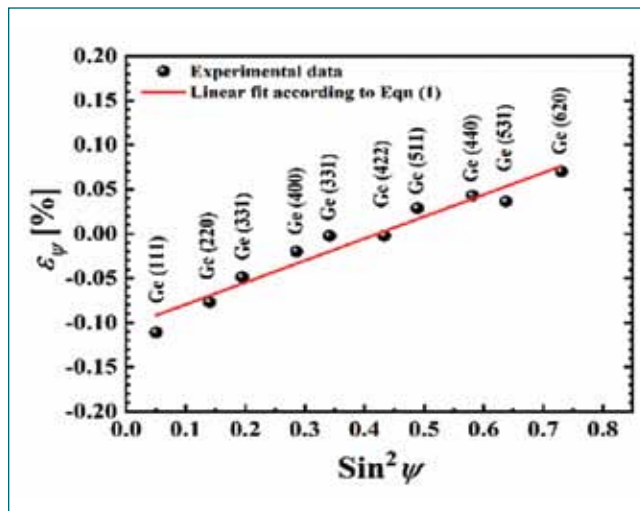


Fig. 2: ϵ_ψ vs. Sin² ψ plot for the poly-Ge thin film

substrate ~ 0.7 mm, the plastic flow in the latter is negligible. In such cases, the σ_{th} in the poly-Ge film is

$$\sigma_{\text{th}} = \frac{E_{\text{Ge}}}{(1 - \nu_{\text{Ge}})} (\alpha_{\text{Ge}} - \alpha_{\text{glass}}) (T_{\text{cryst}} - T_{\text{RT}}) \quad (2)$$

where $T_{\text{cryst}} = 170^\circ\text{C}$; α_{Ge} and α_{glass} are thermal expansion coefficients of Ge and glass, respectively. The expected σ_{th} was tensile ~ 66 MPa, implying that major contribution of ~ 202 MPa to σ_m must stem from σ_g which is also tensile. This is briefly discussed below.

Growth or intrinsic stress

AUILE growth of poly-Ge thin film proceeds via nucleation of crystalline (c)-Ge grain, their lateral growth and coalescence, leading to the formation of grain boundaries (GB). The impinging c-Ge grains in our poly-Ge thin film exhibit a hexagonal distribution. Hence, σ_g have been modelled using the zipping mechanism for tensile stress generation during coalescence of array of islands/grains having a six-fold symmetry. The average stress generated in such cases is given as

$$\langle \sigma_g \rangle = \frac{6}{R} \left(\gamma^{\text{surf}} - \frac{\gamma^{\text{GB}}}{2} \right) \quad (3)$$

where $R \sim 39$ nm, is the average lateral radius of the c-Ge grains measured from EBSD. $(\gamma^{\text{surf}} - \gamma^{\text{GB}/2})$ is the surface energy reduction that drives the zipping process with γ^{surf} and γ^{GB} representing the surface and GB energy of Ge,. The expected value of σ_g from Eqn (3) is ~ 196 MPa, which agrees with our experimental value.

V.02 Portable and wireless CdZnTe-based Gamma Spectrometer (C-VEGAS) with 5.5 % Resolution at 662 keV of ^{137}Cs

The demand for high-performance X-ray and gamma-ray detectors has been continuously growing due to their application in various fields such as national security, nuclear reactors, environmental protection medical imaging, etc. High-purity germanium (HpGe) based detectors with high energy resolution are widely used for radiation monitoring. However, one of the significant drawbacks is the requirement of cryogenics for operation. CdZnTe (CZT) detectors with a wide band gap of ~ 1.57 eV, high atomic number, high resistivity of 10^{10} $\Omega\text{-cm}$, and high electron mobility-lifetime product of $(\mu\tau) \sim 5 \times 10^{-3}$ cm^2/V are the ideal candidate for room temperature radiation detection. However, the growth of high-quality CZT single crystals involves several technological challenges due to inherent material properties.

At MSG, high quality CZT single crystals were successfully grown by systematic optimization of growth parameters using indigenously designed and fabricated crystal growth setups, called traveling heater method (THM). The wafers from the crystal boule were cut, lapped, and polished. Subsequent to specific surface treatments, gold electrodes were deposited on the processed wafer by an electroless process.

The detectors with planar electrodes suffer from the issue of poor hole transport properties. This limitation of the planar detector structure necessitates the usage of other electrode geometries that will compensate for the poor hole transport properties. A detector with a quasi-hemispherical (QH) electrode was prepared by electroding the five sides of the cuboidal CdZnTe crystal of $10 \times 10 \times 5$ mm^3 dimension, as shown in Figure 1 (a). The circular gold electrode on the sixth side constitutes the anode. The electrodes were connected to a BNC connector using gold/copper wire and were housed

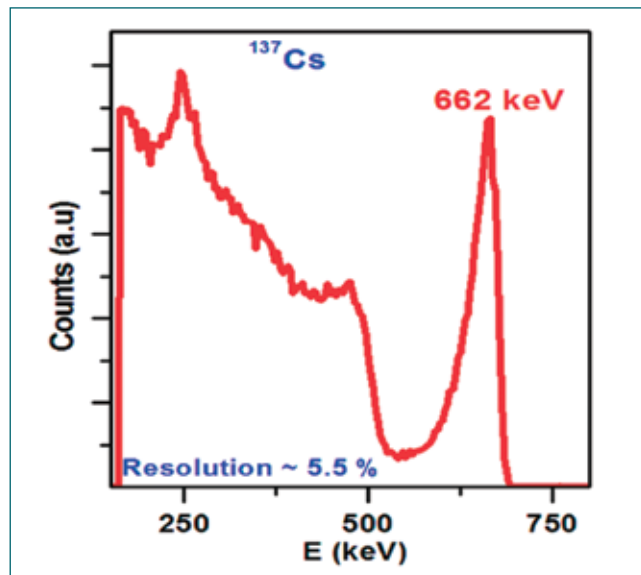


Fig. 2: Gamma spectrum recorded wirelessly from a ^{137}Cs source at an energy resolution of 5.5 %.

in a SS casing with a circular window of 0.1 mm thick aluminum, as shown in Figure 1 (b).

A portable and wireless CdZnTe-Variable Energy GAMMA Spectrometer named C-VEGAS is shown in Figure 1 (c). It houses a commercial battery bank, Wi-Fi tethering device, integrated preamplifier, MCA, and high voltage modules. The crystal housing was connected to C-VEGAS. The spectrum acquisition and control were accomplished using the Wi-Fi connection between the tablet pc and the spectrometer. Figure 2 shows the spectrum recorded using digital signal processing at 1 microsecond shaping time and 0.7 sec flattop time. The detector was positively biased at 1200 V. The photo peak of ^{137}Cs was resolved with an energy resolution of 5.5 %. Further efforts to improve the resolution and efficiency are in progress.

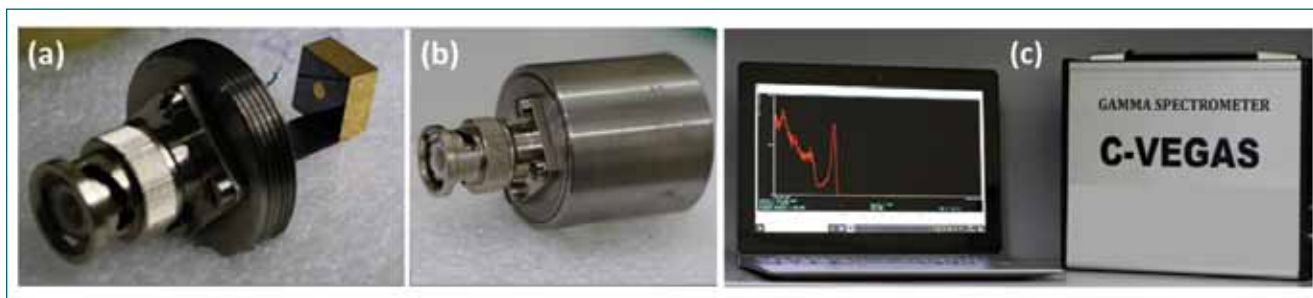


Fig. 1: (a) Gold-coated CZT detector element in quasi-hemispherical electrode geometry mounted on the crystal holder, (b) Detector enclosure with BNC connector, (c) Portable and wireless CdZnTe- Variable Energy GAMMA Spectrometer (C-VEGAS) with a detector and a mini tablet PC.

V.03 Tuning Electronic Structure of Diamond by Surface Functionalization

Ultra-wide bandgap and the absence of shallow dopants are the major challenges in realizing diamond based electronics. However, the surface functionalization offers an excellent alternative to tune electronic structure of diamonds. When the diamond surface is terminated with H-atoms (HD), the C-H bonds create a surface dipole layer which corresponds to an additional potential step that pushes the surface vacuum level below the conduction band minimum of diamond. This results in a surface with negative electron affinity (-1.3 eV) which drives the spontaneous transfer of electrons from valence band of diamond to the adsorbate water layer or other electron accepting molecules, leaving behind the accumulation of two dimensional hole gas at surface and sub-surface. This is the origin of high surface conductivity of HD. Due to this high surface conductivity, HD becomes a potential candidate for various electronic device applications such as field effect transistors, electron field emitters, electrocatalysis, photocatalysis, chemical and bio- sensor applications. In contrast, O-terminated diamond (OD) surface possesses positive electron affinity which leads to an insulating surface with downward band bending. Thus, the HDs and ODs have contrasting electronic properties. Here, we study a systematic variation in structural and electronic properties of polycrystalline H- diamond, in which H is progressively replaced by O through ozone treatment for different duration.

Structural and electrical properties

Figure 1 shows the AFM topography of HD which can be expressed as <110> texture associated with (100) and (111) planes. The water wetting contact angle decreases from 103° down to 33° as a function of ozonation duration of HD surface. The gradual transformation of wettability can be correlated to the systematic

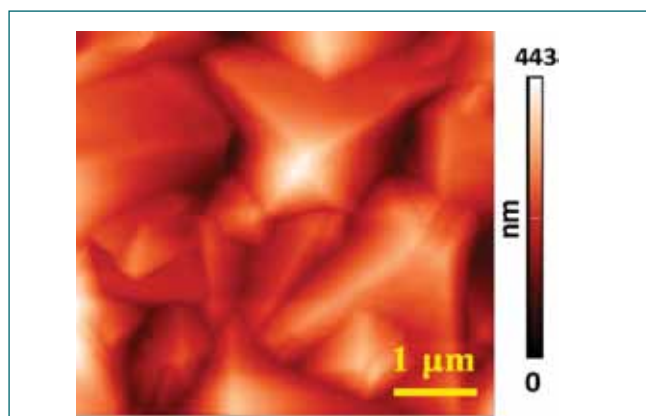


Fig. 1: AFM topography of microcrystalline H-diamond

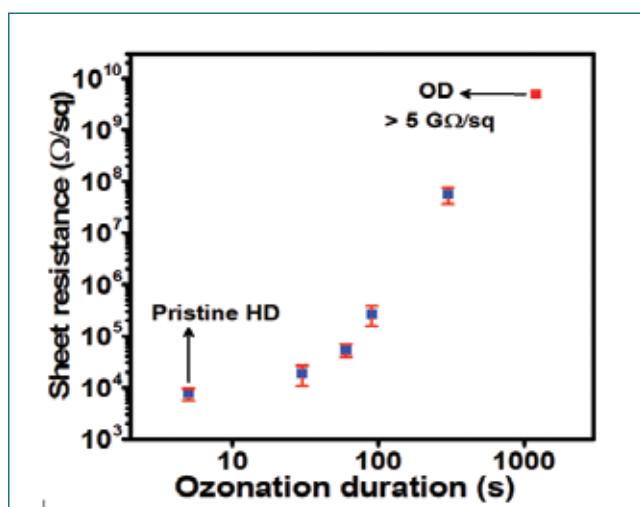


Fig. 2: The sheet resistance of H-diamond vs. ozonation duration

substitution of surface hydrogen by oxygen functional groups during ozonation. The sheet resistance of the as-prepared HD surface increases from ~ 8 kΩ/sq. to over 10 GΩ/sq. with progressive ozonation, as shown in Figure 2. Further, the ozonation of HD films for a short duration of 90 s decreases the surface hole density by two orders from 1.05×10^{13} to $2.49 \times 10^{11} \text{ cm}^{-2}$.

X-ray photoelectron spectroscopy

Figure 3 depicts the X-ray photoelectron spectrum of HD. Detailed XPS studies reveal that a redshift in binding energy (BE) of C1s is observed for pristine and marginally O-terminated HD surfaces (< 90 s) indicating surface band bending due to H-termination whilst the BE shifts to higher energy for ODs.

In summary, the O-substitution at H-site modifies the local electronic structure of the surface. Hence, by controlling the H- and O-concentration on the diamond surface, the surface electronic structure of the functionalized diamond can be tuned from highly conductive to insulating nature.

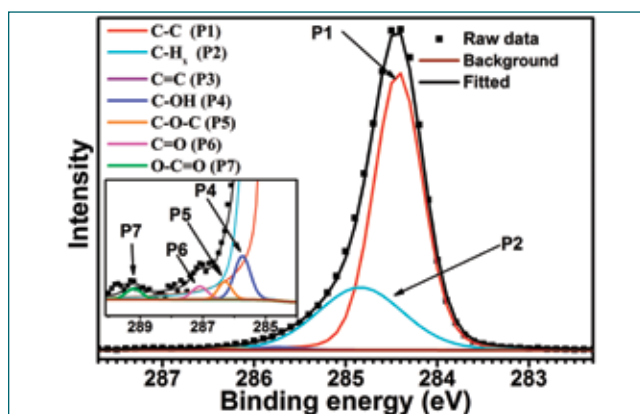


Fig. 3: High resolution XPS C1s spectrum of H-diamond

V.04 Synthesis of Diamond / Vertical Graphene Hybrid Structures for Tribological and Electronic Applications

Diamond and graphene, the two interesting carbon materials, fascinated the scientific world with their unique properties ranging from tribological to electronics to energy storage. If we could combine these two, i.e. Diamond-graphene hybrid structures, it would result in further enhancement of various functional properties. Diamond is well known for its mechanical robustness along with excellent tribological characteristics. While the in-plane C-C bond is stronger in graphitic structures than in diamond, the former is very soft and exhibit ultralow friction due to the weak van der Waals interaction among out-of-plane carbon atoms. The vertical graphene nanosheets (VGNs), covalently bonded to diamond substrate/film, can exhibit ultralow coefficient of friction (CoF) and very high mechanical robustness against scratching, friction, and compression. In addition, the VGNs on diamond can also tune the electronic and optical properties of diamond that offer novel device applications.

Synthesis and Raman spectroscopic study

Microcrystalline diamond (MCD) - VGNs hybrid structures were grown by hot filament chemical vapour deposition. Initially, MCD was grown using methane and hydrogen as feedstocks. Subsequently, the VGNs were grown on diamond using methane and argon feedstock gases. Figure 1 shows the FESEM micrograph of MCD-VGNs hybrid structures and a magnified part is shown as inset. The thickness of the MCD was measured to be $\sim 2 \mu\text{m}$ and the height of VGNs was $\sim 50 \text{ nm}$. Raman spectra of the diamond and MCD-VGNs hybrids are shown in Figure 2. The MCD films displays a sharp Raman band $\sim 1332 \text{ cm}^{-1}$ whilst the MCD-VGNs hybrid structure exhibit a strong signature of a few layer graphene structures displaying D, G and D' bands about 1350, 1585 and 1620 cm^{-1} along with 1332 cm^{-1} band. Tribological analysis

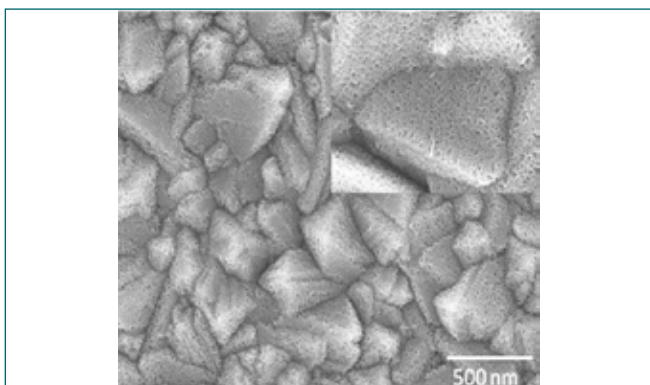


Fig. 1: SEM micrograph of MCD-VGNs hybrid structures

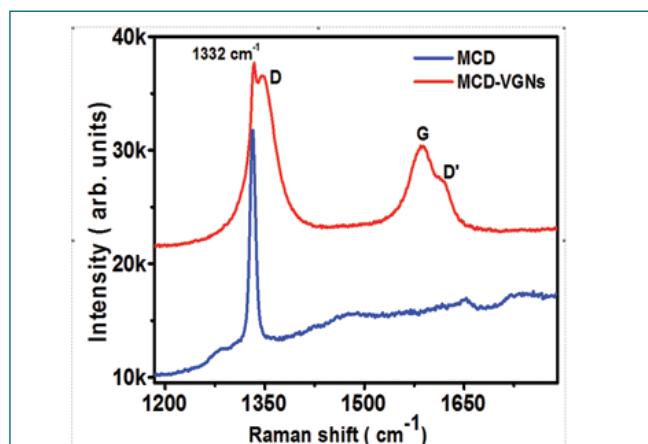


Fig. 2 Raman spectra of MCD and MCD-VGNs hybrid structures

Friction coefficient measurements were carried out by ball on disc reciprocating method at ambient temperature and atmosphere. Alumina ball was used as the counter body. Load applied was 1 N and speed was 3 cm/s with a track length of 4 mm. As shown in Figure 3, the CoF at the beginning was 0.14 and 0.1 for MCD and MCD-VGNs hybrids, respectively. It reached, almost a steady state value of 0.06 and 0.008 towards the end of 40000 cycles. It shows a substantial reduction in friction coefficient for VGNs coated diamond film. This dramatic reduction in friction coefficient is attributed to the realization of three-body abrasion regime by the residual graphene sheets wrapping around the alumina/diamond particles in the sliding interface. Thus, the VGNs act as a solid lubricant which helps in reducing the friction.

The surface conductivity and the fluorescence emission from color centers of diamond are strongly dependent on the surface functionalization or other type of functional coatings. Tuning and evaluation of electronic and optical properties of the diamond-VGNs hybrid structures are under way.

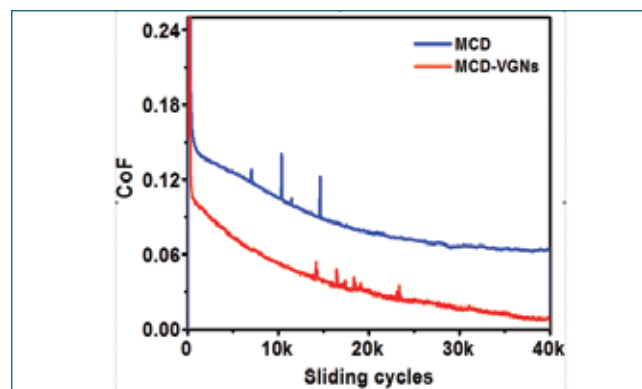


Fig. 3: The co-efficient of friction as a function sliding distance

V.05 Enhanced Photoluminescence Quantum Efficiency in Large Area Monolayer MoS₂

Three atomic thin semiconducting (band gap ~ 1.84 eV) monolayer MoS₂ (1L-MoS₂) attracted a great deal of attention among the research communities because of their fascinating electronic and optical properties, which enable them for use in many optoelectronic applications. Although 1L-MoS₂ is an excellent absorber of visible light, however low photoluminescence (PL) quantum yield (QY) is observed due to the introduction of intrinsic and extrinsic defects. Mostly, the enhancement of PL QY is observed by the physisorption and chemisorption of molecules like O₂, H₂O, and thiols. In addition, local temperature also influences the PL QY. In this context, we manage the laser-generated heat by varying the heat-dissipation area of 1L-MoS₂. In other words, for same laser power density, the large flake-area senses low local temperature compared to the small flake-area due to availability of higher heat dissipating area.

In order to confirm the mentioned effect, we synthesized various flake areas, namely T6 (33 μm^2), T7 (134 μm^2), T8 (248 μm^2), T9 (582 μm^2), T10 (4591 μm^2) and large (~ 4981 μm^2) by a chemical vapour deposition method. Figure 1 shows the typical PL spectra of 1L-MoS₂ flakes of varying sizes (areas) which were collected with a low laser power density, 2.2×10^7 W/m². At room temperature, PL spectra of 1L-MoS₂ is majorly contributed from A-excitons (~ 1.84 eV) and minorly from trions (~ 1.6 eV), and B-excitons (~ 2.0 eV). The

systematic increase in the overall PL intensity with increasing the flake area is observed. The PL intensity of the large-area (4981 μm^2) monolayer was enhanced by ~ 50 times as compared to that for small area flake (33 μm^2). Such observations are also observed in different samples with various flake areas.

Across a triangular flake, the availability of heat-dissipating areas is also different. To validate our claim, we have considered a typical single flake of area, ~ 1000 μm^2 (figure 1a,b inset). The gradual enhancement of PL intensity is observed when moving from the edge region to the central part of the flake. Furthermore, to observe the role of grain boundaries on heat dissipation is also explored. For this study, we have selected the region such that it comprises a large-grain (~ 5000 μm^2) and a small-grain area (~ 500 μm^2) adjacent to it. (fig 1c inset). In this case, PL intensity enhancement was also observed for the large grain as compared to the small grain. The dependence of PL intensity on the grain size indicates that the grain boundaries are acting as a barrier for heat dissipation even though they represent a large area. Figure 2 shows the PL collected from the center (blue circle) and corner (red circle) of a triangular flake (inset of Figure 2). The central region PL shows ~ 10 times higher intensity compared to the corner region. Our results relating PL enhancement with flake areas are also well supported by power-dependent Raman and PL measurements.

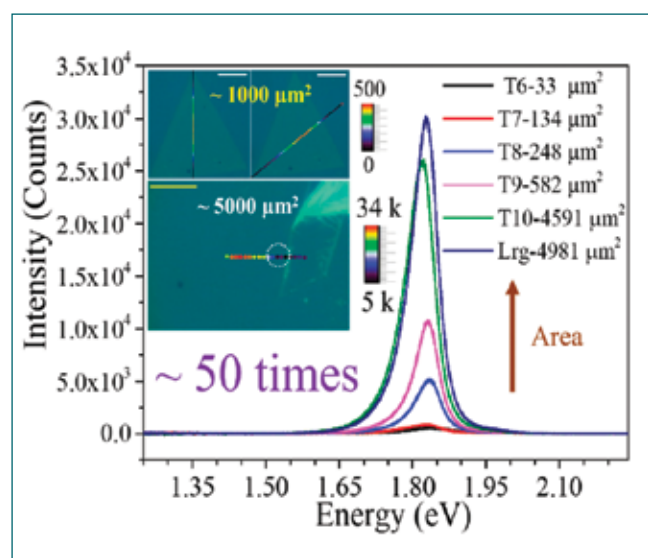


Fig. 1: PL enhancement with increasing flake area. Inset shows PL line imaging. Scale: 10 μm

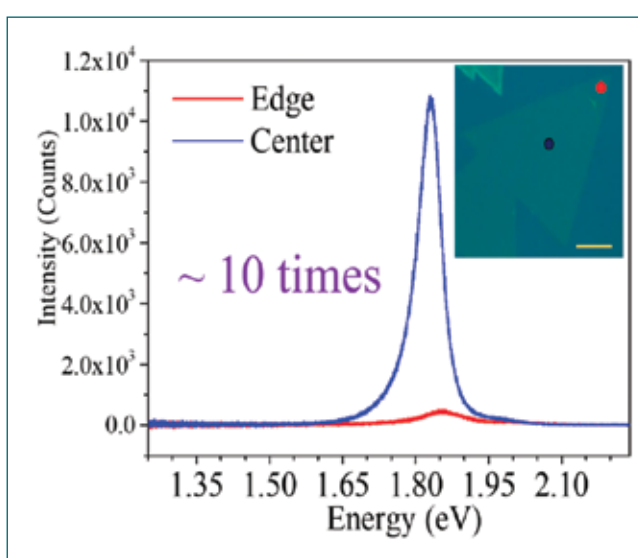


Fig. 2: Variation of PL intensity at center and corner region of a typical flake (inset). Scale: 10 μm

V.06 Deterioration of the System Performance due to the Unidentified Reverse Current Flow in the Transmitter Loop in Squid Based TDEM System

TDEM (Time Domain Electromagnetic) is a widely used technique in geophysical exploration applications and the response of this technique is directly related to the surface and sub-surface properties of the earth. The basic principle of TDEM involves the induction of eddy currents in the ground and subsequent measurement of the decay of these eddy currents using a suitable sensor in time domain. The eddy currents are induced by abrupt switching off of the current passed through a large square loop which is laid on the ground. During the ramp OFF time, emf induced in the ground which drives the eddy currents and the induced eddy currents start decaying and its rate of decay depends on the electrical conductivity of the ground. If the electrical conductivity of the ground is high there will be a slow decay, otherwise, the induced eddy currents decays rapidly. The decay of the induced eddy currents produce secondary magnetic field which is measured by suitable sensors such as induction coil or magnetometer. The induction coil measures the rate of change of magnetic field ($V \propto dB/dt$), whereas the magnetometer measures the magnetic field ($V \propto B$) directly. Therefore, the decay of secondary magnetic field measured by the magnetometer is proportional to $t^{-3/2}$, whereas the same measured by the induction coil is proportional to $t^{-5/2}$. While recording the secondary magnetic field with respect to time in TDEM measurements, the output of the induction coil decays much faster than the output of the magnetometer. Therefore, one can measure the secondary magnetic field even at a later decay time with magnetometer and hence the investigation depth is high. In recent days, SQUID (Super conducting Quantum Interference Device) is used to measure the decay of the secondary magnetic field due to its extremely high sensitivity for the detection of tiny changes of magnetic field, and this high sensitivity is almost unaffected even at very low frequencies.

Very recently, IGCAR has developed a SQUID based TDEM system and tested at MC Palle, AMD camp, Cuddappa (dt), AP. In this field test, it is found that the decay of the secondary magnetic field is rapid at earlier decay time and reaches negative at later decay time. In literatures, these negative decay transients

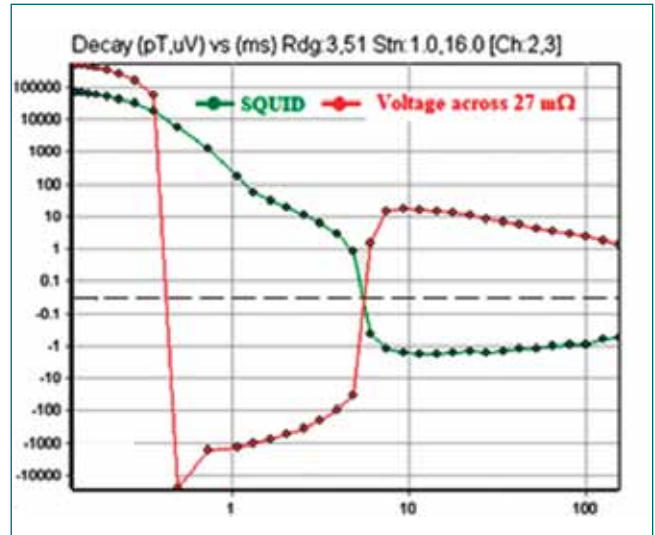


Fig. 1: Magnetic field measured by the SQUID located at the centre of the transmitter loop and the voltage measured across the resistor

are attributed to induced polarization effects by the international researchers for more than two decades with SQUID systems and five decades with the induction coil including Heliborne systems. In our second field test, a small resistor (27 m Ω) has been connected in series with the transmitter loop in order to measure any flow of reverse current in the transmitter loop after the current applied to the transmitter loop (400 m x 400 m) is completely switched off (ramp OFF time \sim 1.4 ms). The simultaneous recorded output of the SQUID located at the centre of the transmitter loop and voltage measured across the resistor are shown in Figure 1. This experimental data clearly indicates that the SQUID is sensing the ground response in addition to the reverse current flow in the transmitter loop. This unwanted reverse current flow destroying the late signal coming from the deep layers of the ground. Nevertheless, SQUID is sensing a conducting layer with a thickness of 10 to 15 m located at depth of 600 m below the surface. These negative decay transients occurred in either SQUID or induction coil based TDEM measurements have been verified in laboratory experimental simulations and a novel hypothesis has been proposed to explain this peculiar phenomena.

V.07 PZN-PT Single Crystal Based Surface Acoustic Wave Transducer

Surface Acoustic Wave (SAW) transducers generate mechanical waves which travel along the surface of the device under test to study the physical phenomena. These transducers can be used for under liquid structural change monitoring, where extreme operation condition deter use of conventional transducers. The surface waves can be transmitted into the liquid environment through waveguides where the transducer is placed at safe operating condition attached to the waveguide. Lead zinc niobate-lead titanate (PZN-PT) relaxor materials have superior piezo electric properties with large strain response to applied electric field $d_{33} = 2000$ to 3000 pC/N and high electromechanical coupling factor with mechanical conversion efficiency of 80-90%. They can remain piezo active above room temperature as their ferroelectric transition is at 160°C . SAW transducers have been fabricated with home grown PZN-PT single crystal

SAW Device

The SAW transducer is designed using an $5\text{mm} \times 5\text{mm} \times 0.6\text{mm}$ gold electrode PZN-PT single crystal mounted on to a Prespex block with a silver based epoxy such that it generates surface acoustic waves on the device under test. The thickness of the crystal is chosen such that it has an operating frequency in the range of 2 MHz to 3



Fig. 1: SAW transducer fabricated with home grown PZN-PT single crystal

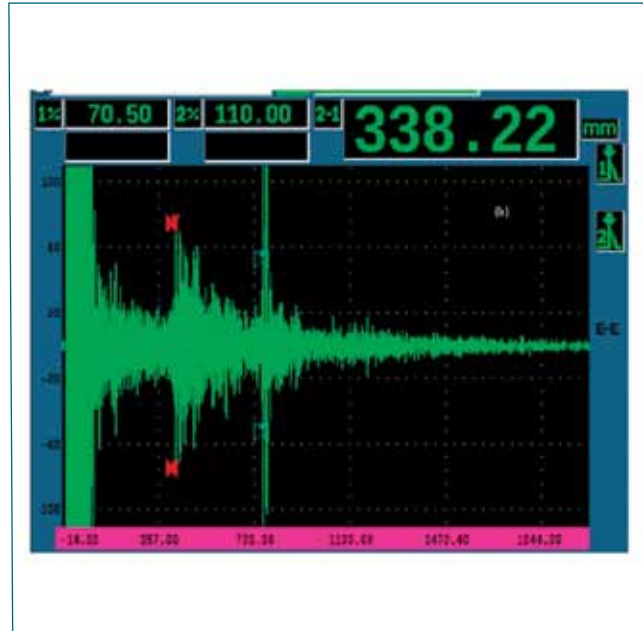


Fig. 2: Acoustic echo spectrum produced by fabricated SAW transducer

MHz. The silver-based epoxy acts both as a matching layer as well as conducting ground electrode. Electrical connections are made on the top of the PZN-PT single crystal and ground electrode with a miniature coaxial cable for better noise cancellation. The SAW device is attached with a BNC connector to a commercially available ultrasonic piezo based flaw detector. The fabricated SAW transducer is shown in Figure 1.

SAW transducer testing

The transducer was tested at room temperature attached to a one-meter-long metal wave guide dipped in water that simulates a similar fluid environment under which the transducer has to work. The electro-acoustic parameters of the transducer were tested using Olympus Epoch 650 flaw detector at a frequency of 2.8 MHz with an applied voltage of 400 V. The transducer was able to produce two echoes, one corresponding to the weldment of the waveguide to the metal base dipped inside the water and the other corresponding to the length of the water vessel in the direction of propagation of the wave. The spectrum produced by the home built SAW device is shown Figure 2. The spectrum produced by the in-house developed SAW device matches well with the spectrum produced by the commercially available probe.

V.08 Achieving Optimal Classification in the Machine Learning Approach by Performing Effective Feature Reduction

Recent reported significant breakthroughs have been achieved through the use of artificial intelligence (AI) in many fields, especially in the problems related to signal de-noising, image processing, and classification tasks. AI enables algorithms to mimic human intelligence. AI is further classified into machine learning and deep learning. Deep learning is used where a large amount of data is available for learning the relation between input and output, whereas machine learning is preferred for a relatively smaller dataset.

Machine learning (ML) enables algorithms to perform the task of learning based on the features extracted from the input data. However, one of the significant challenges in machine learning models is the curse of dimensionality; as the size of the features grows with data, severely affecting the performance of machine learning models due to the redundancy/noise present in the feature set. This problem is resolved conventionally using feature reduction techniques like principal component analysis (PCA) and the correlation approach. Both of these approaches work on the assumption of the linearity of the input feature set which would sometime lead to poor performance in classification.

Dimensionality reduction

Dimensionality reduction allows better visualization of the multichannel data and noise suppression, which ultimately improves the classification accuracy for a given problem. PCA can also be represented as a rotation of the coordinate axes in such a way that each Orthogonal axis captures the maximum possible variance, as shown in Figure 1. The implementation of the linear PCA algorithm is preferred for a linearly separable problem, but the application is restricted due to the assumption based on linearity. This issue is

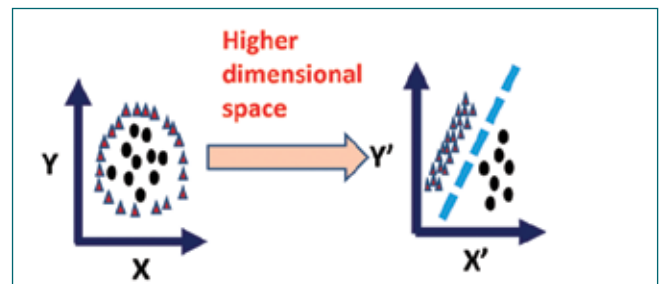


Fig. 2: Mapping of input data to higher dimension space

resolved by kernel PCA (kPCA), where the input data is mapped onto a higher-dimensional feature space using a suitable nonlinear function, as shown in figure 2. After mapping the input data to a higher dimension, PCA is performed in that feature space. Based on this technique, the kernel matrix is computed using the kernel functions in the original input space by avoiding the mapping into the feature space. In kPCA, polynomial kernel and radial basis functions (RBF) have been implemented.

Optimal classification of cognitive tasks in EEG

A study has been carried out related to analyze the cognitive workload by performing an N-back task. Multichannel electroencephalogram (EEG) data is decomposed using a data-driven technique called multivariate empirical mode decomposition (MEMD). Various features have been extracted from the decomposed EEG data to train and test different models of machine learning algorithms. The best possible classification accuracy attained using all features is only 87.13 %, which improved to 92.28% using linear PCA-based feature reduction. By using kPCA, in addition to the feature reduction (up to 50%), a remarkable improvement in the classification accuracy ~ 97.34 % is achieved.

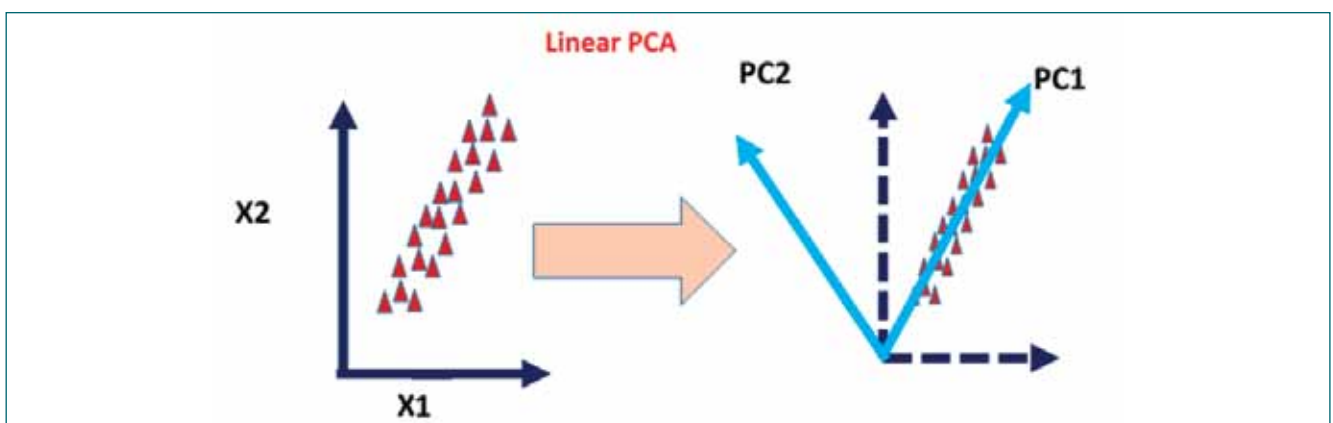


Fig. 1: Dimension reduction by linear principal component analysis(PCA)

V.09 Functional Anatomical Imaging using Magnetocardiography (MCG)

The measurement of weak magnetic fields generated by the electrical activity of the heart in magnetocardiography (MCG) offers unique diagnostic information than the conventional electrocardiogram (ECG). ECG system with its configurations of lead placements on the chest has evolved over a long period of time and has been proven to be indispensable in evaluating cardiac health. However, the electrical conductivity of the human body allows measurement of the cardiac voltage signals at locations which are even far away from the chest (like on the limbs), hence, the ECG is posed with a difficulty in directly inferring the underlying cardiac sources in a precise way. On the other hand, the distribution of cardiac magnetic fields visualized as field maps in multichannel MCG highlight the spatial extent of the cardiac activity closer to its anatomical site and thereby helps to identify cardiac sources. As opposed to the conventional way of interpreting the functioning of the heart with respect to the morphology, timing intervals and rate of occurrence of electrical deflections, the information on the source parameters within the heart opens an avenue to explore the origin of any particular feature of the cardiac cycle. Hence, integration of multi-sensor MCG data with anatomical image of the chest has been attempted. A few subjects who had taken their computed tomogram (CT) image of their chest as a part of the diagnosis of a different medical condition were identified and with their informed consent, MCG was measured using the thirty-seven-channel SQUID sensor-based MCG system

at MSG, IGCAR. As shown in Figure 1 (a), the digital coordinates of the anatomical landmarks such as the edges of the collar bone, the terminal end of the central bone (sternum) of the ribcage, the space in between the fourth and the fifth ribs (fourth intercostal space) etc., are obtained using a 3D digitizer at its stylus tip from the paper grid pasted on the chest of subjects during the MCG measurements. These digital markings had helped to readily map them on the anatomical image of the chest of the same subject as shown in Figure 1(b). The chosen CT slice image showed all these anatomical landmarks along with the silhouette of the heart. Using the digitized points as a guided reference, the edges of the MCG hexagonal sensor array were outlined to its proportionate dimension to fit to the CT image using an image editor tool. Magnetic field contour maps generated from the spatially distributed MCG waveforms of the subject were generated and were co-registered on to the sensor array outlined on the CT image using a standard image registration algorithm. Wavelet transform technique was used to decompose both these images i.e., CT image and the MCG contour map and by choosing the coefficients that contained maximum signal energy in both the figures, the essential features of both the images are retained as shown in Figure 1(c). The resulting fused image served as a functional anatomical image superposing the field distribution pattern of MCG with the anatomy of the heart. It could be expected that such images would be more informative in noninvasive pre and post surgical evaluations using MCG.

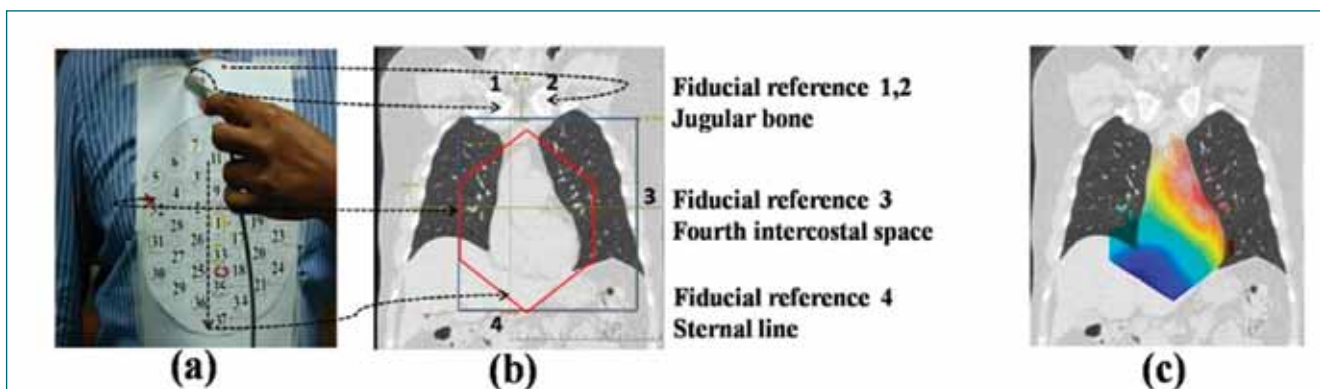


Fig. 1: Functional anatomical imaging using MCG (a) MCG measurement grid pasted on the subject chest shown with fiducial reference points digitized (b) Mapping of these reference points on the chest CT image shown with the outline of the edges of MCG hexagonal array (c) magnetic field map of MCG fused with CT image

V.10 Chloride Enhanced Seed-Mediated Gold Nanorods for Superior Surface Enhanced Raman Spectroscopic (SERS) Activity

The strong light-matter interaction and the coherent oscillation of the conduction electrons at the noble metals (Cu, Ag, Au) dielectric interface have engrossed the field of nanophotonics. Surface Enhanced Raman Spectroscopy (SERS) is a non-destructive, onsite, real-time analytical technique, where noble metals are used for the detection of contaminants. We have developed a modified seed-mediated method for the synthesis of gold nanorods (AuNRs) and demonstrated their improved SERS activity for the detection of a pollutant dye.

Seed-Mediated AuNRs Synthesis

The seed has been prepared by a chemical reduction method of the gold precursor (HAuCl_4) by sodium borohydride (NaBH_4). The growth solution contains the Au precursor, silver nitrate (AgNO_3), hydrochloric acid, ascorbic acid, and the seed solution.

AuNRs and the SERS substrate.

The two optical absorption bands for AuNRs appear from the transverse and longitudinal modes of the electrons. The limitations of the conventional seed-mediated method (plasmonic resonance band position up to 850 nm and the by-product formation) are depicted in the inset of Figure 1.

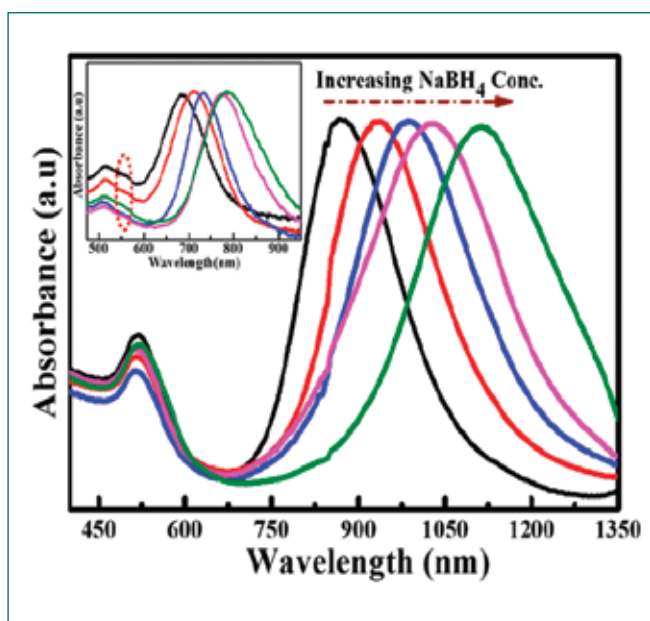


Fig. 1: The UV-Vis optical absorption spectra of AuNRs and insets are described as the structural impurity in the conventional method.

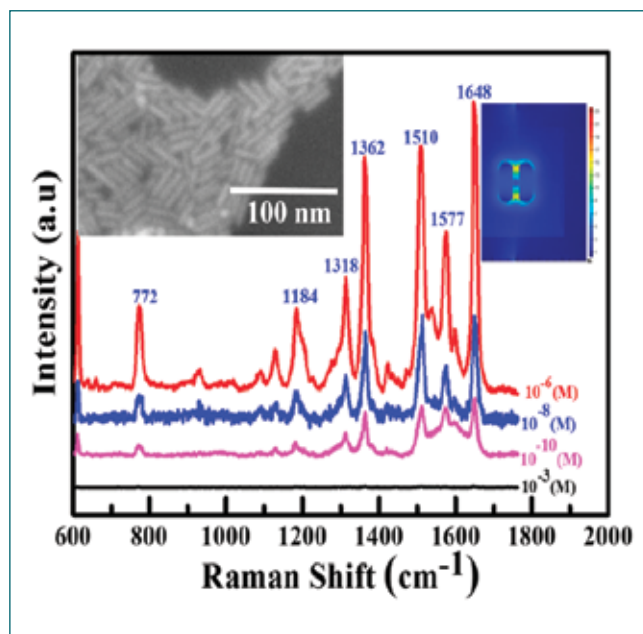


Fig. 2: The SERS spectra of R6G molecule on the AuNRs decorated SERS substrate. Inset depicted the FESEM image and the FDTD calculation of the AuNRs.

The high yield, purity and the resonance spectral limitation are overcome by the addition of the chloride ions in the growth medium. The structural progress in the growth medium has been found to depend strongly on the presence of AgNO_3 and its unidirectional growth is assisted by the chloride ions. AuNRs are drop cast on the thoroughly cleaned Si wafer, followed by IR heating to prepare the SERS substrate.

SERS Experiment and detection activity

The enhanced electric field around the vicinity of the AuNRs increases the Raman scattering cross-section of the analyte molecules. The SERS study has been performed with Rhodamine 6G (R6G) dye. The fingerprint spectral intensity of R6G is enhanced by the plasmonic field at the surface of AuNRs. The thin width and the yield purity of the AuNRs prepared from the chloride-assisted seed-mediated method generate a strong electric field around AuNRs (Inset Figure 2), which enables the detection limit of the R6G molecules better than 10^{-10} (M) level. Such SERS substrate can find application in the real-time evaluation of the heavy metal, food contaminants, etc in water.

V.11 IV Characteristics of Si PIN Diodes under Controlled Humid Conditions and Integrity of Surface Passivation Layer

Silicon PIN diodes are known to find potential applications for a wide range of fields including radiation detection, charged particle spectroscopy, etc. These semiconductor devices are employed for field applications and are subjected to irradiation, temperature, and humidity. It is of both academic and technological interest to understand the integrity of surface passivation layers on the performance of these diodes under controlled humid conditions. Little reports are available on this aspect.

In order to understand the mentioned effect, we have carried out reverse current-voltage (IV) characteristics on two typical commercial planar Si PIN diodes (diodes henceforth referred to as #67 and #77) from 0 to -100 V of reverse bias voltage (V_{RB}) in ambient and controlled humidity conditions (Relative Humidity (RH) range from ~ 16 % to ~ 92 % and are shown in figure 1. It is to be noted that the experiments were repeated three times to check the reproducibility of the IV characteristics. From inset in figure 1, it is observed that IV characteristics are reproducible for diode #77 unlike that of diode #67. From the literature, it is known that such differences in irreproducible behavior could be due to the non-integrity

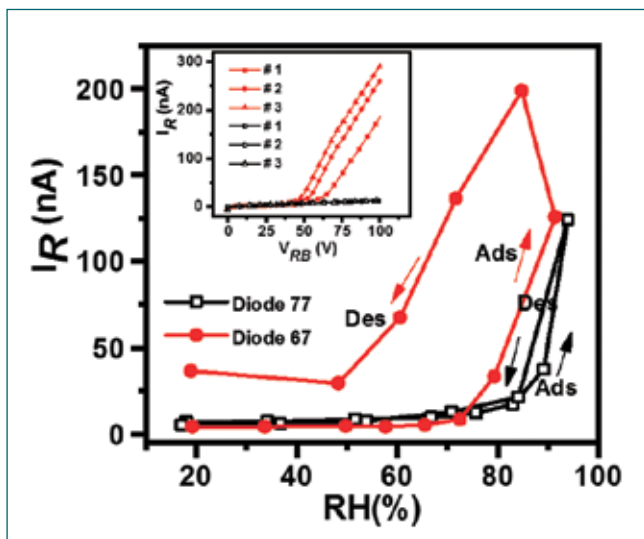


Fig. 1: Variation of I_R as a function of RH during one RH increase and decrease cycle from ~ 16 % to ~ 92 % at V_{RB} of 90 V on diode 67 and 77. Inset shows I_R vs V_{RB} on 2 diodes under ambient conditions. Red and black coloured symbols indicate measurements for diode 67 and 77 respectively. #1, #2, #3 represent measurements repeated 3 times.

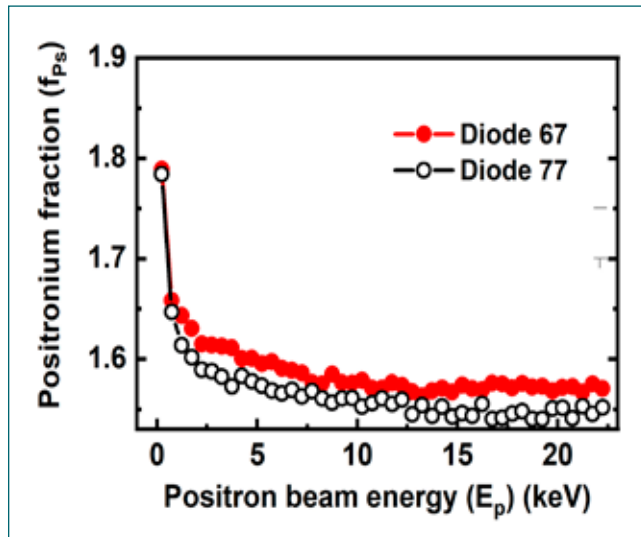


Fig. 2: Positronium fraction as a function of positron beam energy for diodes #67 and #77.

of the surface passivation layer of the diode. Therefore, for further investigations about the differences in the non-reproducibility of the IV characteristics, measurements were performed under controlled RH conditions. The variation of reverse leakage current (I_R) measured for both the diodes at V_{RB} of 90 V for RH values varying from ~ 16 % to ~ 92 % is shown in fig.1 for both adsorption and desorption cycles. For both the diodes, I_R varies from $\sim 10^{-9}$ to 10^{-7} A for both adsorption and desorption cycles, with a magnitude of I_R being marginally larger for #67 than #77. It is very clear from the figure that diode #77 shows a nearly reversible behavior for the adsorption and desorption cycle unlike the stark contrast from diode #67. As little information is available regarding the architecture of the PIN diodes, low-energy positron beam measurements were carried out on the diodes to investigate the integrity of the passivation layer. The variation of the positronium fractions (f_{PS}) with positron beam energy (E_p) is plotted in figure 2 which shows that f_{PS} is high at the surface which then decreases and thereafter saturates at values beyond 4 keV. The saturation value of f_{PS} is higher for diode #67 indicating the presence of more pores/defects. This together with non-reproducibility in RH-driven leakage current measurement (Fig. 1) on diode #67 suggests that more water is present during the desorption cycle. This study illustrates the role of humidity and integrity of surface passivation layer on performance of diodes.

V.12 Structural stability of CoB at high pressures and compressibility trends among group VIII 3d transition metal monoborides

Transition metal borides (TMBs) are hard materials with their Vicker's hardness (Hv) close to 40 GPa taking them into the realm of super hard materials. Cobalt based alloys are widely used as biomaterials in artificial joints due to their high wear and corrosion resistance. However, the fatigue process assisted by corrosion has been reported as the failure mechanism in cobalt–chromium–molybdenum (CoCrMo) orthopedic devices. Boronizing of CoCrMo alloys is shown to improve the wear resistance due to the high surface hardness. The major phases formed during boronization of these alloys are CoB at the surface and Co₂B beneath the surface. The hardness measurements on these boronized alloys yield hardness in the range of 18–21 GPa. It is known that hardness depends on microstructure as well as intrinsic bulk properties such as bulk modulus and shear modulus. Despite wide-ranging relevance, it is surprising that there are no experimental studies on compressibility behaviour of cobalt borides. Structural stability at high pressure and compressibility behavior are probed by High pressure X-ray diffraction (HPXRD) studies. Here we report high pressure X-ray diffraction and first-principles calculations to understand the compressibility behaviour of cobalt monoboride and compare it to other group VIII 3d mono borides.

High-pressure XRD experiments were carried out using a Mao–Bell-type Diamond Anvil Cell (DAC). A stainless-steel gasket of 200- μ m thickness was used to contain the sample between the two opposed diamond anvils. MEW was used as a pressure transmitting medium. Silver was

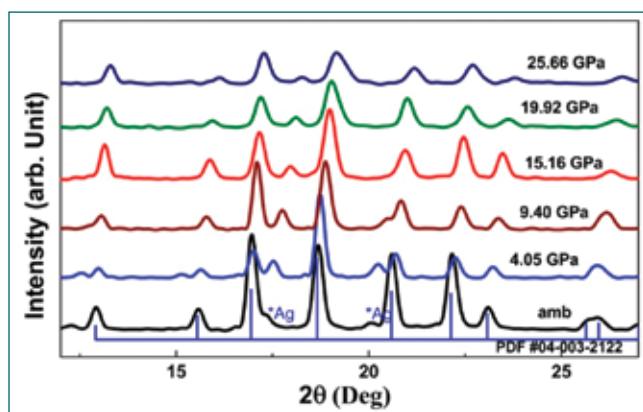


Fig. 1: XRD patterns of CoB at various pressures along with a stick plot of ICDD PDF 04-003-2122

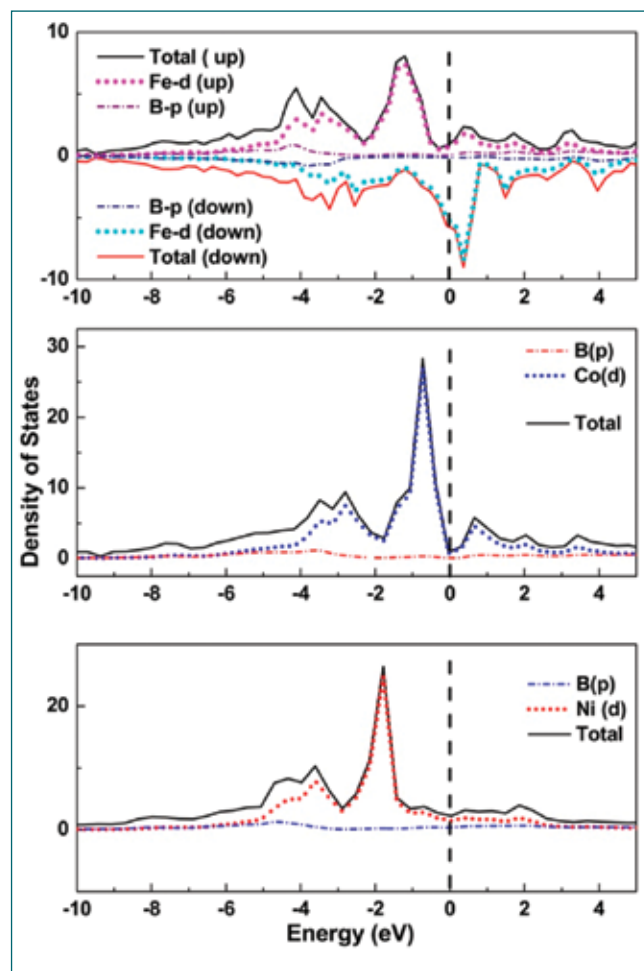


Fig. 2: The calculated electronic density of States of a) FeB, b) CoB, and c) NiB.

loaded along with the sample for pressure calibration inside the DAC. A Genix3D micro X-ray generator with Mo as the target was used for generating X-rays with wavelength 0.711 \AA . The diffracted X-rays were collected onto the image plate of mar345. First-principles calculations were performed as implemented in VASP code on group VIII 3d mono borides. The PAW formalism with the GGA of revPBE to the exchange correlation functional was favoured. The maximum plane wave cut-off energy was set at 550eV.

CoB was synthesized by the arc melting method. In this method, the Co foil and B pieces were taken in 1:1 atomic ratio, and excess boron of 5% by weight was added to account for boron loss during arc melting. The synthesized sample was characterized by XRD and was found to be in a single phase. The refinement

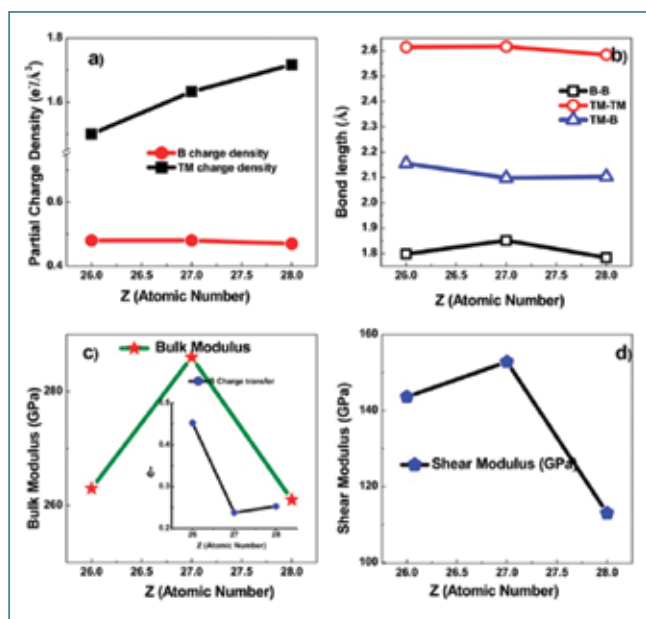


Fig. 3: Properties of Group VIII 3d TMBs: a) charge density on TM and B, b) bond length, c) Bulk modulus and partial charge on B (Inset), d) Shear modulus.

was carried out with FeB-type orthorhombic structure yielding lattice parameters of $a = 5.253(9)$ Å, $b = 3.047(7)$ Å and $c = 3.957(2)$ Å, which are in good agreement with reported values. The refined parameters $W_{rp} = 0.0358$, $R_p = 0.0234$ and reduced $\chi^2 = 0.0556$ are very low indicating good agreement between computed and experimental pattern.

The in-situ HPXRD studies were carried out on CoB up to a pressure of 26 GPa. The collected XRD patterns at various pressures after integration are shown in Fig 1. The silver 2θ peak corresponding to the (200) plane was used to estimate the pressure inside the DAC. The XRD patterns showed no change in the fingerprint, indicating that the orthorhombic structure was stable up to the highest pressure studied. The unit cell volumes were obtained from the HPXRD and fitting the P-V data yielded a bulk modulus of 294 (12) GPa which is in good agreement with 291 GPa obtained from DFT calculations. The bulk modulus of CoB is highest when compared to FeB (263 GPa) and NiB (261 GPa).

Bulk modulus shows an interesting trend that is similar to that of 3d TMs. The bulk modulus in general follows the parabolic trend with its peak near the half filled d-orbital. The bulk modulus in 3d TMs shows markedly different behavior near the half-filled 3d metals i.e. Mn, Fe, and Co with a sharp fall in bulk modulus for Mn and lower bulk modulus for Fe than the expected general trend of 4d and 5d series. A similar trend is also shown in the atomic volumes of these 3d TMs. This marked difference

has been attributed to both spontaneous magnetization and the correlation effect with a strong influence of the later. In the case of monoborides, FeB has a magnetic moment of $1.24 \mu_B$, whereas the monoborides of Co and Ni are not magnetic and the experimental bulk modulus is lower in FeB than that of CoB. Bulk modulus for FeB with spin-polarized and spin-unpolarized calculations yield a value of 263 GPa and 292 GPa respectively. Bulk modulus is reduced in FeB because of the spin-spin interaction leading to a lower bulk modulus than that of CoB. The calculated electronic density of states (DOS) for the monoborides is shown in Fig.2. The density of states reveals two aspects that are common to all of these monoborides. Firstly, it reveals that the DOS at Fermi energy is contributed only by the d states of metal there. Secondly, there is partial hybridization between non-metal p and metal d states. For FeB, the majority spins in the DOS shows a valley at -0.3 eV indicating splitting between bonding and anti-bonding states. The filling of anti-bonding states leads to the weakening of bonds. In the case of minority spin states, the bonding states are only partially filled which also leads to the reduction in the bulk modulus. The density of states in CoB is filled up to Fermi energy and Fermi energy lies exactly in the valley of the density of states and hence has high bulk modulus among the borides considered in this study. The density of states in NiB shows a valley at -1.0 eV below the Fermi energy, also indicating anti-bonding states getting filled. This leads to a lower bulk modulus than that of CoB. Bader charge analysis was carried out on the monoborides to understand the charge distribution. Bader charge analysis carried out on the monoborides reveals (Fig.3a & 3c) that there is a transfer of charge from the metal atom to the boron atom. The charge transfer is higher in FeB than followed by NiB and lowest in CoB. The charge transfer variation is reflected in the bond length of B-B in these systems, where they show an inverse relation to partial charge variation on the boron atom. The B-B bonds are longer in CoB than in FeB and NiB. But the TM-B bond is shorter in CoB than in FeB and NiB, indicating that the charge transfer from Co to B is less and sharing of charge between Co and B is more. Hence in these systems, it is both the B-B and TM-B bonding which is leading to the higher bulk modulus. Apart from the B-B bonds, the partially covalent bonding in Co-B results in higher bulk modulus and higher shear modulus for CoB as compared to that of FeB and NiB.

V.13 Temperature Dependence of Elastic Constants and Phonon Modes in the Energetic Material TEX

An ideal energetic material exhibits high performance, despite having low sensitivity to be handled safely during its use, storage and transport. Sensitivity refers to vulnerability to unintended and undesired detonation initiated by an accidental stimulus of heat, impact or shock. Sensitivity is highly dependent on the molecular arrangements and inter-molecular or lattice interactions. Hence, structural and elastic deformation studies under various stimuli are required to be undertaken for safety analysis. 4,10-Dinitro-2,6,8,12-tetraoxa-4,10-diazatetracyclo [5.5.0.0^{5,9}.0^{3,11}] dodecane (C₆H₆N₄O₈ or TEX) is a candidate material for high performance insensitive explosives. It is a caged polynitramine and is much less sensitive to friction (> 353 N) and impact (23 J) stimuli compared to other high performance explosives, such as, RDX and HMX.

In this work, temperature (T) dependent Brillouin and Raman spectroscopic investigations are carried out on TEX from -196-180°C, to study its elastic and phonon mode behaviours. Ambient values of shear (G) and bulk (K) moduli are obtained from Brillouin modes as G = 5.6 GPa and K = 17.7 GPa. The known lower sensitivity of TEX compared to similar caged secondary explosives as CL-20, RDX, β -HMX is reckoned as due to its inherently high K value. We report direct evidence of rapid reduction in elastic constant of TEX (an elastic

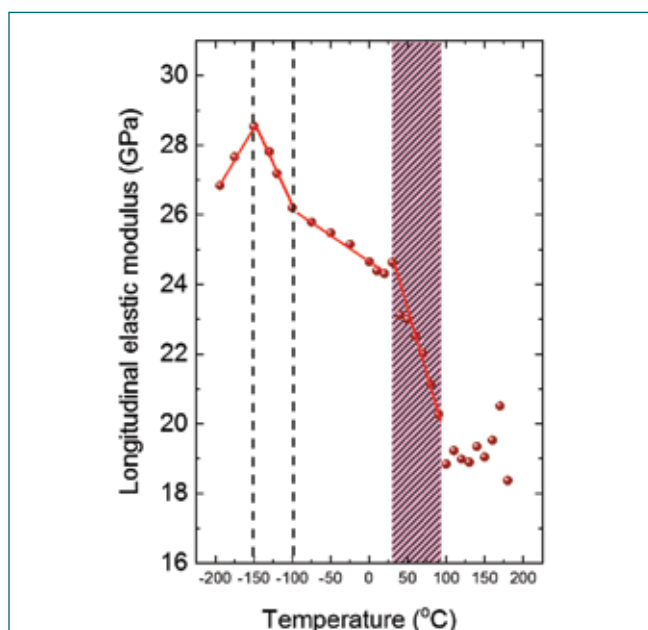


Fig. 1: T-dependence of longitudinal elastic modulus of TEX depicting the steep transition at 20 °C. The shaded region mark the region of abrupt change

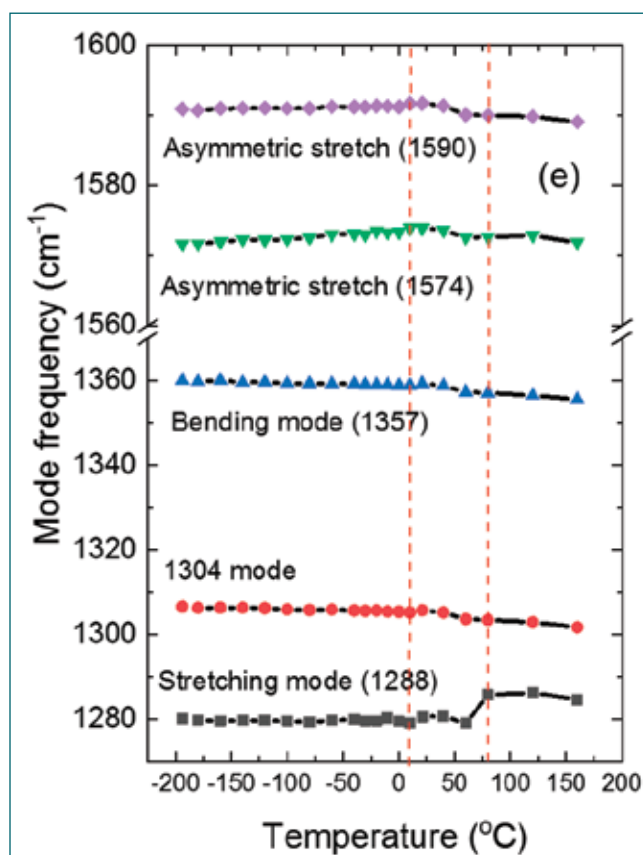


Fig. 2: T-dependence of Raman mode frequencies of some important bands of TEX. The dashed lines depict a region with steeper slope of frequency, the T-range matching the EA. The values in the parenthesis are mode frequencies at ambient

anomaly, EA) from 20-80°C, much before its melting point (Fig. 1). Though there are no phase transitions in this T-span (confirmed using XRD earlier), all Raman bands exhibit softening behaviour around this EA (Fig. 2). Especially, we observe the asymmetric stretching modes of NO at 1574 cm⁻¹ and of NO₂ at 1590 cm⁻¹ exhibit hardening below 20°C but soften after 80°C (Fig. 2). This hardening switching over to softening above EA indicates a release of stiffness manifesting from a conformational change (seen in similar caged materials) and aiding the rising compressibility. Emergence of new diffraction peaks around 50°C and even observed at 150°C (well above EA), suggests that structure at high-T may be isostructural to that at low-T. This study establishes that high K value of TEX contributes to its lower sensitivity however, we also demonstrate reduction in elastic modulus accompanied by anomalies in Raman modes. This decrease in elastic modulus leading to increased compressibility may result in rising sensitivity of TEX just above RT.

V.14 Experimental Evidences for a Quantum Spin Liquid Ground State in Y_2CuTiO_6 , a Double Perovskite Compound

Magnetic materials consisting of spin $\frac{1}{2}$ display exotic properties where triangular or tetrahedral spin arrangement is present. Such materials show some degree of frustration for spin alignment resulting in spin fluctuations. These fluctuations persist down to the lowest temperatures with a Quantum Spin Liquid (QSL) ground state (gs). Materials with QSL gs find applications in quantum computing, understanding of high-temperature superconductivity, data storage & memory. A copper based double perovskite, Y_2CuTiO_6 with hexagonal crystal (space group $P63cm$) structure at room temperature displayed a QSL gs.

Single phase compound of Y_2CuTiO_6 was synthesized by conventional solid state reaction method. Y_2CuTiO_6 (YCTO) crystallizes in hexagonal structure with space group, $P63cm$ (#185).

Temperature variation of molar susceptibility under multiple external magnetic fields shown in figure 1 (main panel) indicated cooperative paramagnetic nature from room temperature down to the lowest temperature measured, 4K. However, a large Curie-Weiss (CW) temperature of -116 K has been estimated from the CW fit (shown in the inset of Fig. 1) to the high temperature data. The large negative value of CW temperature implies antiferromagnetic interactions among Cu spins. The absence of magnetic transition could be understood from the disordered triangular lattice with 50:50 random mixture of spin $\frac{1}{2}$ Cu and non-magnetic Ti ions. The

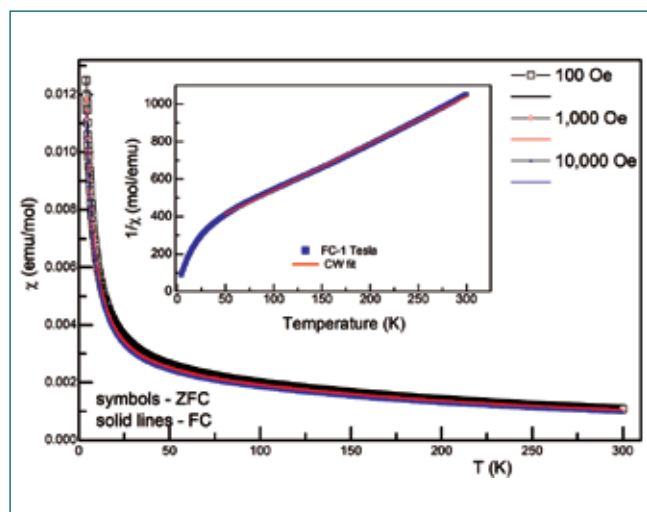


Fig. 1: Temperature dependence of molar susceptibility

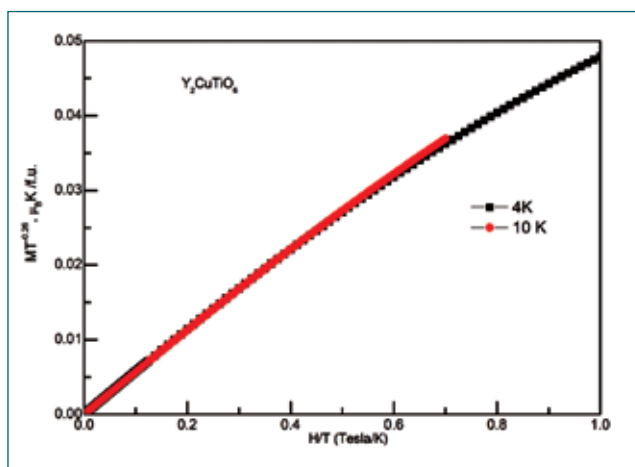


Fig. 2: Scaling behaviour of magnetization

presence of random singlet phase leading to QSL gs has been confirmed from the scaling behaviour of the isothermal magnetization plot, shown in Fig 2.

Temperature dependent magnetic specific heat (Fig. 3 main panel) does not exhibit any anomaly down to lowest temperatures; inset (a) - expanded scale in the low temperature. Thus the specific heat data complemented the magnetization studies. The magnetic response of this material at low temperatures shows scaling behaviour (inset (b)) consistent with random singlet formation on Cu^{2+} sites down to 2 K.

Experimental results confirmed the QSL ground state as the scaling behaviour illustrated the dynamical processes occurring at different magnetic fields and temperatures.

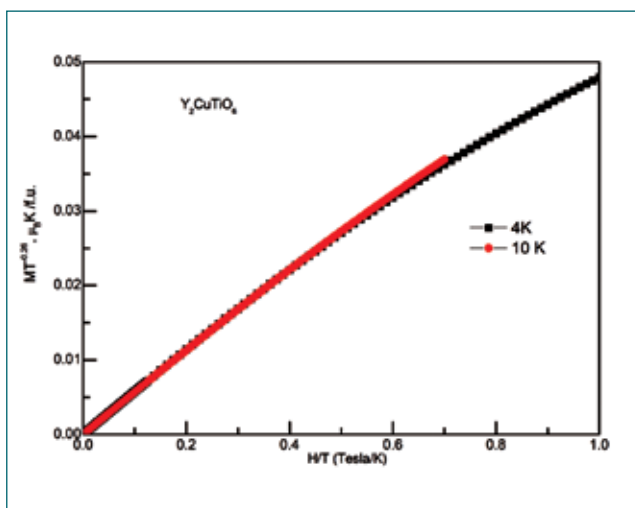


Fig. 3: Evidence for QSL (gs) from specific heat

V.15 Studies of Intrinsic and Ion-irradiation Induced Vacancy Defects in Zr/Al Containing ODS Alloys

Oxide dispersion strengthened (ODS) ferritic steels with thermally stable, nano sized complex oxides homogeneously incorporated into ferrite matrix are one of the most suitable candidate materials for future fast reactor applications. The Zr addition in ODS steels containing Al is found to be beneficial in reducing the void swelling since Y-Zr-O precipitates are finer than Y-Al-O precipitates. In a previous report, it is reported that the as-prepared Al-ODS and Zr-ODS steels have nanometric grains and high density of fine dispersoids, predominantly $Y_4Zr_3O_{12}$. In the present work, positron annihilation spectroscopy is employed to characterize the inherent and irradiation-induced open volume defects in Zr-ODS and Al-ODS steels.

Both Al-ODS and Zr-ODS show two positron lifetime components, as tabulated in the Table 1. These values are consistent with earlier reports on ODS steels. The PALS measurement scan provides information on the nature, size and concentration of the defects. The previous studies have ascribed τ_1 to dislocations in the matrix. The second lifetime component, τ_2 can be arising due to nano-features in the matrix or vacancy clusters resulting from mechanical alloying. If we assume that the second lifetime component is arising from the nano-precipitates, solving two component trapping model yields a number density of $6.7 \times 10^{20}/m^3$ for Zr-ODS and $1.9 \times 10^{21}/m^3$ for Al-ODS. These values are much smaller than the measured particle number density values i.e., $1.7 \times 10^{24}/m^3$ for Zr-ODS and $3.8 \times 10^{23}/m^3$ for Al-ODS. Thus the second longer lifetime components can be attributed only to vacancy clusters. Moreover, the calculated lifetime values of V_6 and V_{15} vacancy clusters in Fe are 304 ps and 386 ps respectively. These values are very similar to the longer lifetime components in this study. Thus, in the present study, τ_2 values of Zr-ODS

can be correlated with V_6 clusters and that of Al-ODS can be attributed to V_{15} clusters.

Table 1. PALS lifetimes and corresponding intensities of Zr-ODS and Al-ODS steels.

Sample	τ_1 (ps)	I_1 (%)	τ_2 (ps)	I_2 (%)	S_b
Zr-ODS	156±8	94	301±12	6	0.54±0.003
Al-ODS	161±7	91	380±18	9	0.56±0.003

The samples are further annealed for 1 h at 800 °C in vacuum (1×10^{-6} mbar) for eliminating pre-existing defects. So the annealed and pristine samples do not show any change in the S-parameter values. Further, the samples are irradiated to a displacement damage of 100 dpa using 1.6 MeV Fe+ ions at room temperature and elevated temperature of 340 °C. The irradiated samples are again characterized by depth-resolved Doppler broadening spectroscopy. Variation of S-parameter for Al-ODS with positron implantation depth is shown in Fig. 1(a) and that of Zr-ODS is shown in Fig. 1(b). For a dose of 100 dpa at room temperature, there is an increase in the S-parameter compared to the un-irradiated bulk, and hence an increase in open volume defects. However, the high-temperature irradiated sample shows a similar S-parameter curve as the unirradiated sample, indicating defect annealing. At 300 °C, in ferritic steel, the concentration of irradiation-induced vacancies is much higher than the thermal vacancies. However, the interstitial mobility is enhanced at this temperature, leading to recombination and annealing of irradiation-induced vacancy defects. This explains the observed trend of decreasing the S-parameters of the 340 °C sample to that of the unirradiated sample.

To summarize, in room-temperature irradiated specimens, Al-ODS showed the presence of open volume defects,

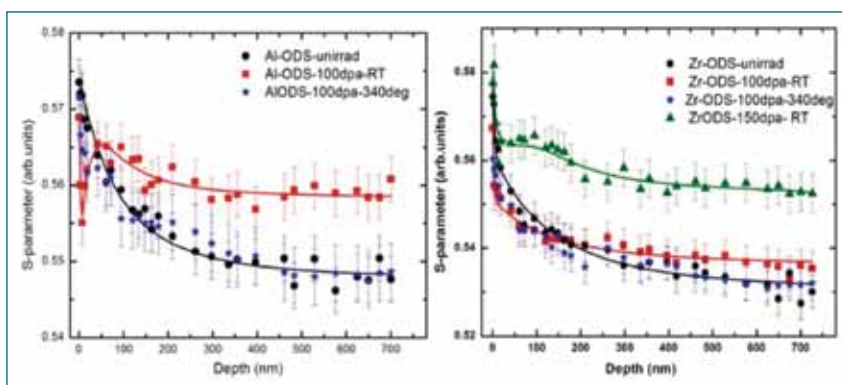


Fig. 1: The S-parameter as a function of positron implantation depth in pristine and self ion-irradiated Al-ODS and Zr-ODS alloys.

and hence an increase in S-parameter for a dose of 100 dpa. But Zr-ODS does not show a significant increment in S-parameter for this dose. So the onset of defect production in Zr-ODS occurs at a higher dose than the Al-ODS. This is the consequence of smaller sized, higher number densities of dispersoids in Zr-ODS, compared to Al-ODS. Both the alloys do not show the presence of open volume defects upon irradiation at 340 °C.

V.16 Enhancement of Photoluminescence due to NV Centres in Nanodiamond Films Formed by Ion Implantation

Single photon sources made up of nitrogen vacancy color centres which can be negatively charged (NV^{-1}) or neutral (NV^0) are most desirable in diamond and is having many applications in the field of quantum information processing, spintronics and photonics. It is possible to tune photoluminescence intensities and lifetime values of N-V centers by varying chemical environment, impurities, grain structure, surface modifications, charge compensation, valence state position etc. Ultrananocrystalline diamond (UNCD) is a distinct form of diamond which has nano size grains, ultra-smooth surfaces, good corrosion resistance, high hardness, high thermal conductivity and bio compatible properties. The grains of UNCD films are sp^3 character while the grain boundaries are a mixture of sp^2 , sp^3 , hydrocarbons and amorphous carbons. Nitrogen atoms are introduced at a depth of 423 nm using 30 keV N^+ ion implantation into UNCD film grown on Silicon substrate without or with Au buffer layer grown using microwave plasma enhanced CVD. The concept of Rp/2 effect is used to overlap vacancy concentration profile over nitrogen concentration depth profile by implanting with 75 keV Ne^+ ions which has twice the projected range of N^+ ions. The samples are annealed using RTA in Ar atmosphere at 500 °C for 2 minutes.

Raman spectroscopy measurements show increase in

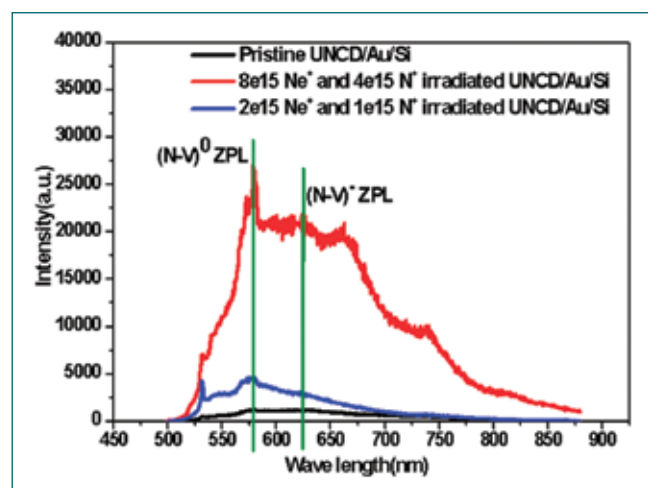


Fig. 1: Enhanced PL observed in N^+ and Ne^+ co-implanted and UNCD/Au/Si samples

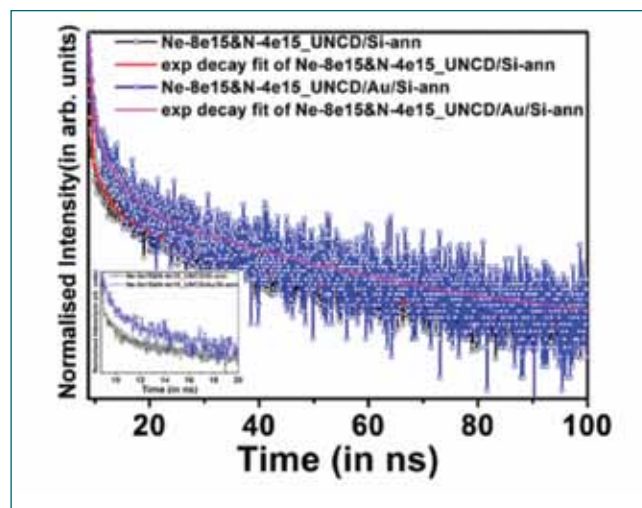


Fig. 2: Time resolved PL observed in N^+ and Ne^+ co-implanted and UNCD/Au/Si samples

defect density (D-peak) and formation of nanographite (G' peak) from I_D/I_G and I_G'/I_D intensity ratios. Relative G' content is more in the co-implanted samples without Au buffer layer. The samples show presence of both NV^{-1} and NV^0 centers from the observed peaks in photoluminescence (PL) spectra at 575 nm and 637 nm (Fig. 1) before implantation itself, due to incorporation of nitrogen during the growth process, but it is dominant in sample without Au buffer layer. Upon implantation and annealing, PL intensity is much enhanced in co-implanted samples with Au buffer layer. Implanted samples also show a little presence of In the case of samples without buffer layer, large nanographite content produced in implantation process acts as an electron depletion/trap layer, thus, reduces the concentration of NV^- centres, which eventually leads to the reduction in PL with low NV^-/NV^0 concentration ratio (0.83) compared to unimplanted samples. In annealed samples with Au buffer layer lower nanographite content and surface plasmon resonances due to Au nanoparticles (observed from XRD) give raise to enhanced PL intensity. The time resolved photoluminescence spectra of these samples which are fitted with constituent lifetimes (τ_1 , τ_2 , τ_3) are shown in Fig. 2. This shows longer lifetime and high quantum efficiency (71%) in annealed samples with Au buffer layer, consistent with the observed PL intensity.

V.17 Electron Correlation & Different Predicted Structures of U₂Mo

Uranium compounds show interesting properties of Mott insulator, ferromagnetic and antiferromagnetic order, heavy fermion and charge density waves etc, owing to the behaviour of U 5f electrons which have different degrees of correlations based on U-U distance and bonding with other atoms. In the case of U₂Mo, the experimental structure is tetragonal at 300 K but the density functional theory (DFT) predicts two more structures, the orthorhombic and hexagonal, to be energetically more stable than the tetragonal structure. The orthorhombic structure is the outcome of Peierls type symmetry breaking of U-U bonds similar to the one observed in case of α -U, but hexagonal structure is a completely different structure which is not observed experimentally. In the present work the tetragonal structure, which is known ground state structure of U₂Mo and the hexagonal structure predicted by DFT calculations are compared. The equation of state (EOS), electronic structure, elastic constants and phonon spectrum are calculated to assess the relative stability. The effect of correlations in 5f electrons of U on the relative stability of these structures is also explored. The calculated EOS parameters for both structures are given in table 1.

Elastic and Dynamical stability

The elastic constants and phonon dispersions are calculated using density functional perturbation theory (DFPT) for both tetragonal and hexagonal structures. The elastic constants meet the Born stability criteria.

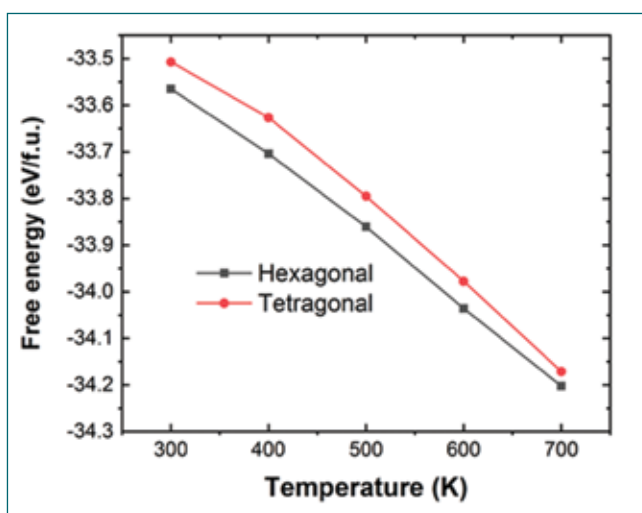


Fig. 1: Free energy of hexagonal and tetragonal structures calculated using DFT.

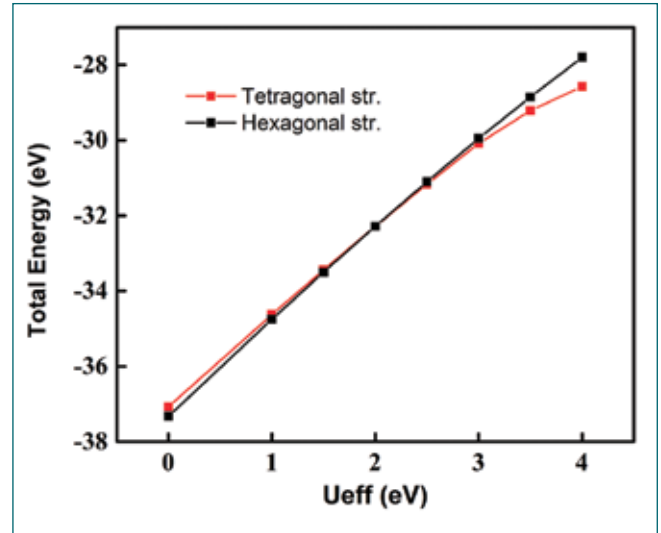


Fig. 2: Total energy of tetragonal and hexagonal structures as a function of Ueff.

Table.1: EOS for different structures of U₂Mo

	E0 (eV/fu)	V0 (Å ³ /fu)	B (GPa)	B'
Tetragonal	-33.29	56.92	177.1	4.7
Hexagonal	-33.42	54.98	174.1	4.8
Expt.		57.74		

But the phonon dispersion for tetragonal structure shows instabilities, whereas hexagonal structure has no unstable phonons. The tetragonal structure is seen to be dynamically unstable at 0 K, but becomes stable when the anharmonic corrections are incorporated in the phonon calculations at 300 K.

Free energy and electron correlations

The free energy calculated for the most stable predicted (hexagonal) and the tetragonal structures as a function of temperature is shown in Fig.1. The hexagonal structure remains more stable than tetragonal structure even at higher temperatures where tetragonal structure is the known ground state. Further, the effect of incorporating electron correlations on the total energy of both structures is calculated as a function of the Hubbard Ueff parameter. As can be seen from fig.2, the tetragonal structure becomes more stable than the predicted hexagonal structure for Ueff > 2 eV & Ueff = 2.5 eV gives the best match for lattice parameters with the experimental data, which signifies the importance of electronic correlations in U₂Mo.

V.18 Molecular Dynamics (MD) study of Iron Phosphate Glass

Iron Phosphate glass (IPG) with Fe/P ratio of 0.67 is proposed as the matrix suitable for immobilization of high-level waste (HLW) due to its properties like high waste loading capacity, chemical durability and high resistance to radiation damage. To understand the origin of these properties from atomistic point of view, it is important to design atomistic models of IPG. Besides, modelling glasses is also an open problem in physics. The research in glass science has been revitalised after the UN declared 2022 as the International Year of Glass.

Modelling the atomistic structure of glasses

An in-house developed Monte-Carlo (MC) Code was used to design randomized configurations of IPG. The general MC scheme is extensible to any glass composition and type. The models developed need only equilibration at specific temperatures for validating the structure and properties, circumventing the computationally intensive melt-quench simulations.

Interatomic potentials for MD studies

Interatomic potential of the form Buckingham + Coulomb for the pair part, and Stillinger-Weber for the three-body part, was splined to ZBL potential for simulating highly energetic processes. The potential was written in table format appropriate for LAMMPS and was suitably modified so that it could be implemented along with Ewald summation. The resultant potential has lower potential energy wells, and is devoid of spurious potential cut offs. Fig.1 shows a comparison of the pair part between the two potentials for Fe^{2+} and O^{2-} ions.

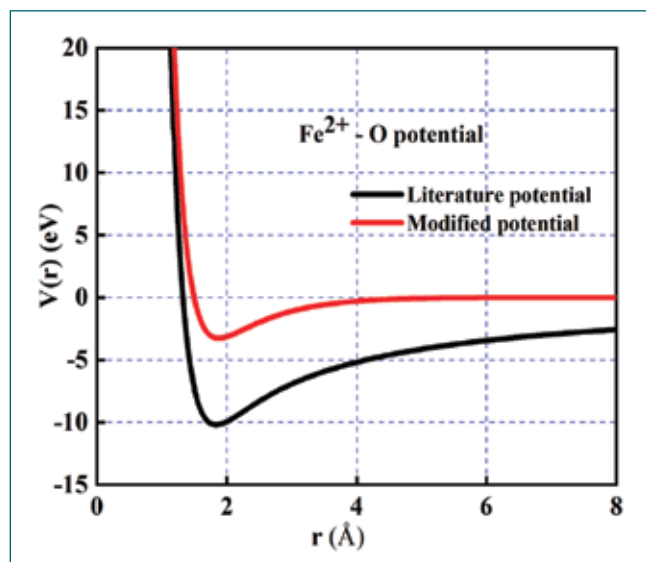


Fig. 1: Interatomic potential developed for MD studies

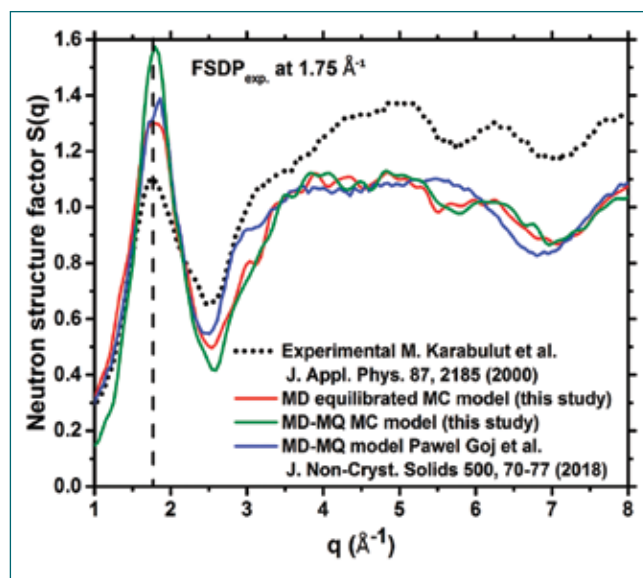


Fig. 2: Neutron structure factor comparison for various models of IPG

Validation of potential and models

The models were validated by comparing the structural properties at various length scales. For short-range, pair correlation functions, coordination numbers, bond-angle distributions were used whereas for medium-range, first sharp diffraction peak (FSDP) in structure factor, rings size distribution and voids size distribution are compared. Fig.2 shows the calculated neutron structure factor compared with existing models and experimental data. Also, models were prepared using melt-quench scheme as well, to test the equivalence of the two methods used for glass modelling i.e. the hybrid scheme involving MD equilibration of randomized MC models and the traditional MD based melt-quench scheme. We found the two schemes produced nearly equivalent structural properties.

Estimating mechanical properties

These models were finally used for estimating the mechanical properties of IPG. The results were found to depend heavily on the thermodynamical ensemble chosen (NVT versus NPT) for equilibration. The results for NVT equilibrated model are: $\langle C_{11} = C_{22} = C_{33} \rangle = 110.9$ GPa, $\langle C_{12} = C_{13} = C_{23} \rangle = 61.7$ GPa, $\langle C_{44} = C_{55} = C_{66} \rangle = 24.6$ GPa, bulk modulus = 78.1 GPa, Young's modulus = 68.2 GPa, shear modulus = 25.3 GPa, and Poisson's ratio = 0.35. This study validates the developed models used against the experimental data.

V.19 Ion Beam Evaluation and Characterization of TiO₂ Based Ultraviolet and Ionizing Radiation Detectors

In particle and nuclear physics, the detection of ionizing radiation emitted by fundamental processes is of prime importance. UV light detection is an important application in various industrial domains spanning optoelectronics, automotive, and astronomy instrumentation. Silicon detectors with doped p and n regions and a depletion zone active area have traditionally been used in these domains. However, harsh temperature conditions and protection from radiation damage necessitate usage of alternative materials. Due to low intrinsic noise and high radiation tolerance, wide-bandgap semiconductors such as GaN, diamond have gained prominence for these applications. The large bandgap significantly suppresses thermal noise generated by intrinsic carriers, giving these devices a simple structure that can be fabricated in one or two lithographic steps compared to the multistep lithography required for doping traditional silicon-based detectors. The high cost and variability of the properties of chemically grown single-crystal diamonds have been a major obstacle in its widespread adoption of diamonds in particle physics. GaN has found wider use for ultraviolet (UV) detection. In this article, results from the fabrication and characterization of a UV and ionizing radiation detector with a novel active material TiO₂ are presented.

For electrical characterization of the detectors, Ti/Au (20/80nm) metal contacts were deposited using a simple shadow mask on the top surface of the prepared detector to ensure good adhesion and a low-resistance Ohmic contact as shown in Fig.1. All electrical characterizations were done in a vacuum chamber probe station at 7×10^{-5} torr. The I–V characteristics of the detectors under dark and UV illuminated conditions are shown in Fig.2. The detectors exhibit Ohmic contacts across the metal–semiconductor junctions with a dark current <0.5 nA up to a bias voltage of ± 100 V. From the dark current and sample dimensions, a sheet resistance $R_s = 5 \times 10^{12} \Omega$

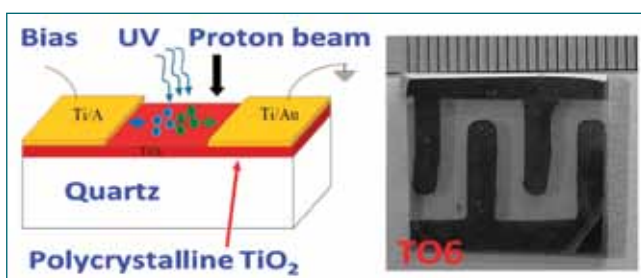


Fig. 1: (a) Schematic of TiO₂ based ionizing detector pristine (b) Detector fabricated for electrical characterisation.

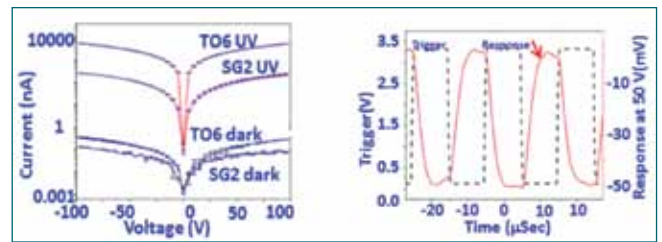


Fig. 2: (a) I–V characteristics of the detector, (b) Detector response as a function of time to UV LED.



Fig. 3: (a) Detectors mounted on the ceramic sample holder (b) vacuum chamber used for H⁺ ion beam irradiation. The ion beam enters from the left.

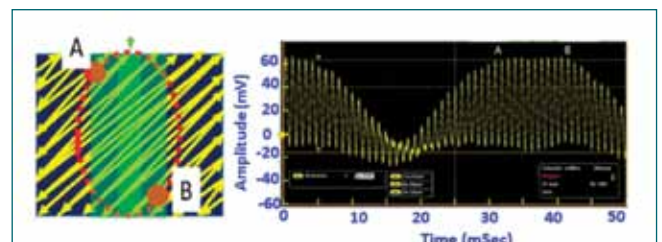


Fig. 4: (a) Illustration of H⁺ ion beam scan over the detector (b) The time-domain response of the detector to the ion beam.

and bulk resistivity $R_b = 1.5 \times 10^8 \Omega \cdot \text{cm}$ are inferred. From the UV photoresponse studies, the responsivity of the detectors was found as 4.8 ± 0.3 mA/W at 30–70 V bias voltages at fast (10- μ s) time scale. The ion beam characterization of the detectors was carried out using 1 MeV, 300 nA H⁺ ion beam from 1.7 MV tandetron accelerator at MSG,IGCAR. The experimental set up used is shown in figure 3.

The ion beam having 10 mm diameter and a scan frequency of 1.015 kHz, scans an area of 30×30 mm at an angle of 45° and the beam scanning cycle repeats every 40 ms. The maximum flux of protons incident on the TiO₂ active area is between A and B and the signal rises to a maximum stable value between the time markers A and B as shown in Fig.4. The signal amplitude increases with bias voltage and reaches a maximum value by 50 V. From the ion beam tests, a charge collection efficiency of $69\% \pm 5\%$ is inferred, comparable to similar measurements for pCVD diamond detectors and GaN PIN alpha radiation detectors.

V.20 Development of Chemical Emergency Response System

Rapid industrial development with increased use of chemical materials in the last few decades has increased the risk and vulnerability for accidents. IGCAR in association with NRSC-ISRO and Factories and Boilers (FAB), Govt of Kerala has developed a Remote Sensing Enabled Online Chemical Emergency Response System (ROCERS) for disaster management of industrial chemical accidents. ROCERS is based on the broad framework of the existing Online Decision Support System (ONERS) which is operational at Kalpakkam site.

Core Elements of ROCERS

ROCERS is designed in a generic framework so that it can be adopted for any industrial site. ROCERS consists of i) chemical sensor network to detect accidents (Fig.1) ii) Chemical dispersion models based on weather prediction and meteorological data to project the chemical concentrations iii) source term model for release rate calculation iv) database of chemical industries, infrastructure and resources along with geographical data of each site v) Web-GIS software for impact analysis providing information on impact zones, affected populations, help line information, protective actions and resources for disaster mitigation. The spatial data is organized into Satellite Remote Sensing imageries, administrative boundaries, land cover, infrastructure (transport routes, safety shelters, primary health centers, civil offices etc.) covering up to 50-km radius around each industrial site.

ROCERS includes two ranges of dispersion simulations i) 30-km range providing 24-h chemical plume prognosis



Fig. 1: Release rate estimation in Remote Sensing Enabled Online Chemical Emergency Response System

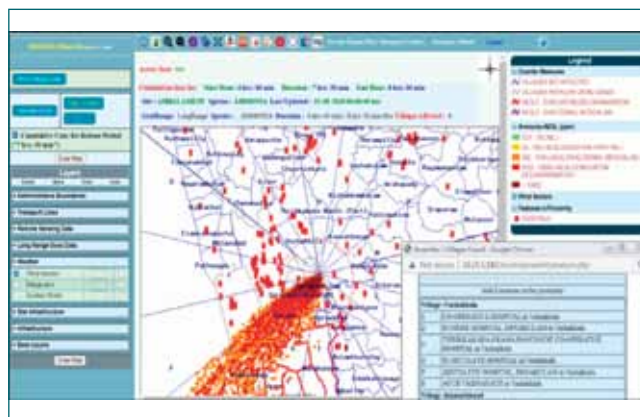


Fig. 1: Chemical impact analysis using ROCERS

using WRF & FLEXPART models for long term ' ≥ 4 h' release. ii) 15-km range providing real-time chemical impact using local scale dispersion model with onsite meteorological data for short term release. Accident source term database for postulated accidents are incorporated in the system for dispersion calculations. In addition, a source term model based on container pressure, temperature, phase etc. is developed in ROCERS which can be used to estimate the release rate (Fig. 1) due to failure of storage tanks or receipt lines. The dispersion model is incorporated with a buoyancy correction scheme to account the effect of buoyancy of releases on the dispersion.

Chemical Impact assessment

The system performs exposure assessment for 6 h or more to initiate protective measures, well in advance, during emergency. It classifies the areas into impact zones as per the national guidelines of emergency exposure threat levels of released substances. In the first phase, ROCERS is developed to cover the three major industrial sites (Ambalamedu, Wellington, Udyogmandal) in Ernakulum district of Kerala for Ammonia, Chlorine, Oium, Hydrogen Sulphide etc. In the next phase, the system will be expanded to other toxic gases and industries under the same common framework. Fig. 2 shows the chemical plume simulation by ROCERS for a hypothetical release of Chlorine from the FACT Cochin complex in Ernakulum district, Kerala. The Web-GIS analysis tools provide the damage distances based on site GIS data and exposure levels.

V.21 A Study on Radon and Thoron Measurements in Glass Fiber Reinforced Gypsum (GFRG) buildings at Kalpakkam

Glass fiber reinforced gypsum (GFRG) wall is a new composite wall product known as Rapid wall/ Gypcrete in the industry. Characterization studies have been done to quantify the radionuclide contents of Phosphogypsum. The results indicate that ^{226}Ra and ^{232}Th are found with concentrations $100\text{--}500\text{ Bq kg}^{-1}$ and $6\text{--}25\text{ Bq kg}^{-1}$ respectively. The present radiation monitoring study is carried out in model GFRG buildings at Edaiyur and Kunnathur army base situated in the Kalpakkam DAE complex. The study includes measurements in two phases of three month duration each. During Phase -1 the buildings were occupied with typical indoor ventilation conditions- a combination of both air conditioned and natural ventilation and in Phase -2, there was no occupancy as well as no ventilation.

Pin-hole dosimeters and Direct Thoron Progeny Sensor (DTPS)/ Direct Radon Progeny Sensor (DRPS) badges designed and developed by BARC were used for the measurement of radon/thoron gases and their progenies. 30 locations were chosen within the rooms of these two buildings and 2 pin hole dosimeters along with 2 DTPS/DRPS badges were deployed in each location for three months at least 2 ft. away from walls. The annual effective inhalation doses are estimated using the dose conversion factors (DCF) reported by UNSCEAR (2000). Annual eff. Dose (radon) = EERC \times DCF \times No. of exposure hours per year

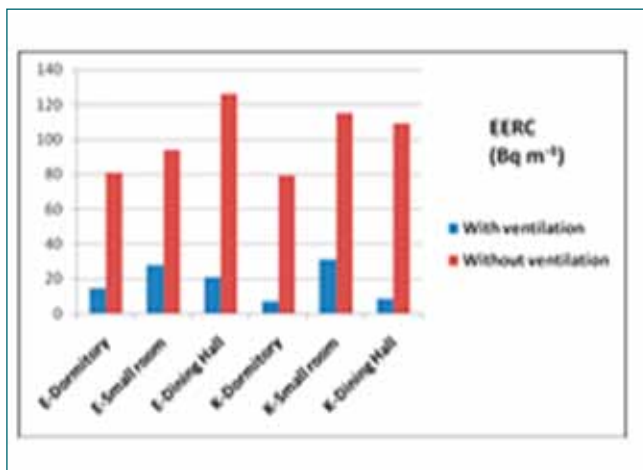


Fig. 1: Comparison of EERC values

One room (Edaiyur Dormitory) was chosen for further analysis. The radon contribution is from the walls and the ceiling. For no ventilation condition, the wall flux was calculated by using the measured indoor radon concentration. With this flux, the ventilation rate of Phase -1 scenario was calculated (Fig.1).

The radon and thoron concentrations in Phase-1 range from 9 ± 1 to $54 \pm 4\text{ Bq m}^{-3}$ and 15 ± 1 to $186 \pm 6\text{ Bq m}^{-3}$ respectively. The radon and thoron concentrations in Phase-2 range from 21 ± 1 to $449 \pm 34\text{ Bq m}^{-3}$ and 22 ± 4 to $188 \pm 24\text{ Bq m}^{-3}$ respectively. The annual effective dose due to inhalation is given in Table 1.

Annual effective dose (mSv) due to inhalation		
Location	Annual effective dose (mSv)	
	Phase -1	Phase -2
Edaiyur		
E-Dormitory	0.87	0.67
E-Small room	0.15	1.26
E-Dining Hall	0.54	0.95
Kunnathur		
K-Dormitory	0.47	0.32
K-Small room	0.45	1.42
K-Dining Hall	0.94	0.39

The annual effective doses due to thoron progeny for the two phases are similar in values whereas the doses due to radon progeny for the two phases show extreme variation.

Thoron progeny with higher deposition rates are independent of ventilation rate. The source (GFRG) radon flux was found to be $1.39 \pm 0.03\text{ Bq m}^{-2}$. The ventilation rate for the Phase -1 exposure condition was found to be 0.12 h^{-1} .

V.22 Lithium Formate – A Tissue equivalent High Level Dosimeter Based on Electron Paramagnetic Resonance

Formation of stable free radicals in irradiated chemicals and their estimation by Electro Paramagnetic Resonance (EPR) spectrometry is an established technique in high dose dosimetry, which is used in the field of radiotherapy, blood irradiation, food preservation and radiation sterilization. RESG, IGCAR is a nodal centre for radiological emergencies and has the mandate of establishing dosimetry facilities for both normal and emergency situations. As part of it, a retrospective dosimetry laboratory using EPR spectrometer has been established at RESG.

This work presents the methodology for dose estimation using tissue equivalent Lithium formate (LiFo) and EPR spectrometer. In this method, EPR Parameters were optimized for irradiated LiFo (Table 1), EPR spectrometer was calibrated using irradiated LiFo, reproducibility and fading characteristics of EPR signal was checked. In addition, LiFo/ EPR dosimetry has been applied to check the spatial dose distribution inside the gamma chamber.

Table 1: Optimized EPR Parameters.

Table 1: Optimized EPR Parameters	
Parameters	LiFo
Microwave power (mW)	19.4 mW
Receiver gain	50
Modulation amplitude (G)	9 G
Time constant (ms)	40.96 s
Conversion time (ms)	40 s
Microwave frequency	9.81 GHz

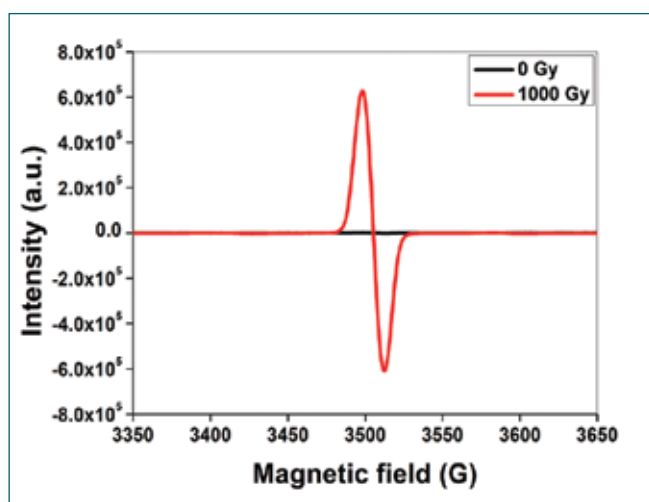


Fig. 1: EPR signal of irradiated and unirradiated LiFo

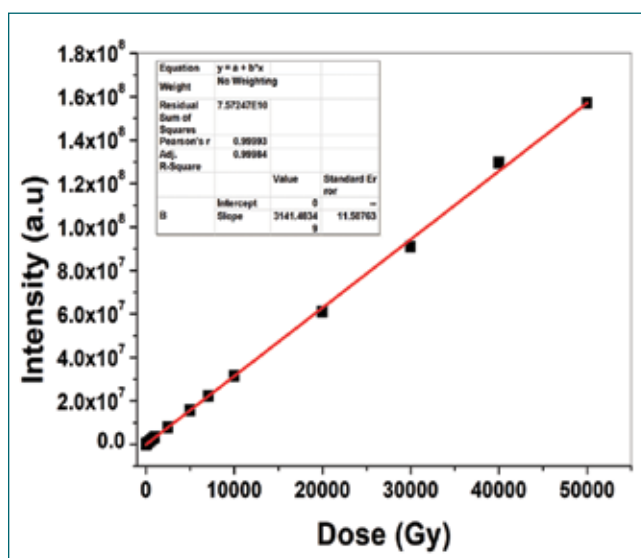


Fig. 2: Dose response of gamma irradiated LiFo

Dose Response

In order to check the gamma dose response of LiFo dosimeter, LiFo (200 mg) was irradiated to doses in the range of 1 Gy to 50 kGy and EPR measurements were carried out. Irradiated LiFo gives one EPR Signal at $g=2.002$ due to carbonate radical and the intensity (peak to peak height) of peak increases with increase in gamma dose and it has linear dose response in the dose range 10 Gy to 50 kGy (Figs. 1 & 2).

Reproducibility and fading studies

EPR signal of irradiated LiFo was checked for reproducibility by measuring EPR spectrum 10 times after irradiation and found to be reproducible. Additionally, negligible fading was observed in the signal after 2 months.

Dose distribution inside gamma chamber

LiFo/EPR dosimetry was used to find out the spatial dose distribution inside the gamma chamber. Dosimeters were placed in different positions along axial and radial directions of gamma chamber and irradiated to 250 Gy gamma dose. It was found that central location of gamma chamber has the average dose value with maximum 17.50 % radial and 15.70 % axial variations from central location, which is matching with the dose distribution values, obtained using alanine dosimeters and EPR spectrometer.

V.23 Site Specific Transfer Factor of ²¹⁰Po from Soil to Rice Crop in the Experimental Field at DAE Site IGCAR

Rice (*Oryzasativa*) is a staple food in India and the soil-to-plant transfer factor of radionuclides present in the environment is an important parameter for estimating the internal radiation dose from food ingestion. In order to assess more precisely and realistically the internal radiation exposure to the public around nuclear facilities during normal operation, site-specific parameters should be taken into account in the area concerned. In the present study, soil to rice transfer factors (TF) for ²¹⁰Po in rice grown in natural field conditions on the East Coast of India are determined. An experimental field (Fig.1) has been developed within Kalpakkam DAE Campus for the radionuclides transfer factor studies in various crops. The objective of the study was to evaluate the soil to rice transfer factors ²¹⁰Po under natural field conditions.

Different parts of the rice plant (root, stem, leaf, different stages of growth of grains) and soil were analyzed (within 15 days of collection) to determine the soil to rice plant transfer factors. Activity concentrations of ²¹⁰Po in soil and different plant parts were analyzed in an alpha spectrometer after auto-deposition of the acid-digested samples. The activity of ²¹⁰Po in soil was 8.5 – 16.67 Bq/Kg (Fig-1). ²¹⁰Po in rice was recorded as 2.32 ± 0.7 Bq/kg in dry weight (dw) whereas, in wet weight (ww) it was observed as 1.76 ± 0.5 Bq/kg. TF for ²¹⁰Po in rice grain and parts are presented in Table 1, for dw and ww. It was observed that root has higher activity followed by

stem leaf and grains. Interestingly, the early stage of the grain was marked with higher activity as compared to the fully grown grains. The observed value of ²¹⁰Po in rice was comparable with other reported values from India. TF of ²¹⁰Po was less in the grains and was followed by the leaf, stem, and root. In dw measurements, it varied between 0.18 – 1.47, whereas, in ww measurements, it varied between 0.13 – 0.43.

Table 1: Activity concentration and site-specific TF of ²¹⁰Po in soil-rice compartment at Kalpakkam

Part of Rice plant (Bq/Kg)	²¹⁰ Po (dw)	²¹⁰ Po (ww)	²¹⁰ Po in Soil	TF (dw)	TF (ww)
Grains (matured)	2.32	1.76	13.19	0.18	0.13
Grains (Early stage)	3.60	2.20	13.19	0.27	0.17
Leaf	4.17	1.08	13.19	0.32	0.08
Stem	10.18	2.85	13.19	0.77	0.22
Root	19.37	5.62	13.19	1.47	0.43

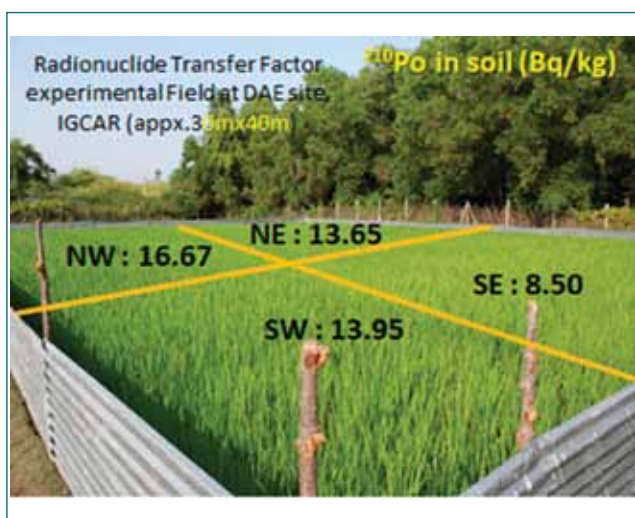


Fig. 1: Radionuclide Transfer Factor experimental Field at DAE site, IGCAR (appx.30 m x 40 m)

The parts of the rice plant that are more in contact with the soil have higher TF. Transpiration of water from the soil plays a significant role in the accumulation of the radionuclide. While the milking grains have more water content and have higher activity, the grown-up grains have less water content and less ²¹⁰Po content. This forms the first information on ²¹⁰Po TF in soil-rice from Kalpakkam.

V.24 Development of Linear Kalman-Filter Technique for Source Term and Dose Rate Estimation

Source term is an important input for dose projections using atmospheric dispersion models during accident condition. Kalman Filter (KF) method is one of most reliable and useful technique in modelling and prediction of environmental data in space time domain.

Linear Kalman Filters

Kalman Filter (KF) is basically a predictor-corrector recursive algorithm for instantaneous state estimation of linear dynamical system from a set of noisy measurements. A Python based in-house Extended Kalman Filter (EKF) algorithm with Gaussian Plume model (GPM) (Dt(qt)) for short range dispersion is developed to compute source term (qt) taking the case of routine release of ⁴¹Ar from Madras Atomic Power Station (MAPS). EKF algorithm is developed based on following equations

$$q_t = q_{t-1} + w(t) \dots\dots\dots(1)$$

$$q_t^+ = q_t^- + K_t[d_t - q_t^- D_t(q_t = 1)]\dots\dots\dots(2)$$

w(t), is the noise associated with time evolution of source term with noise covariance 10¹⁵ Bq².s⁻² which is arrived by innovation technique. Following GPM inversion methodology and gamma detector data, the initial release rate (q0) is estimated to be ~10⁹ Bq/s. In the next time step source term is predicted (q_t⁻) using Eq. 1. Using observed dose rate information (d_t) adjustments are done through Kalman Gain (K_t) and updated source term (q_t⁺) is estimated using Eq. 2. q_t⁺ is used as initial source term for next time step. This algorithm is iteratively used to obtain the time series of release rate.

From literature measurement noise standard deviation is taken as 5% of mean dose rate for each detector. The EKF approach is tested using three Autonomous Gamma Dose Loggers (AGDL) installed in South-West wind sector (plume sector). Data from 50 m meteorological tower for 10 days in February, 2021 is used in EKF model during north-easterly wind flow.

Model Predicted Source Term

EKF model predicted source term for 10 min sampling time is shown in Figure 1. The actual source is taken from daily release value of MAPS reactor which is uniform. The scatter index or normalized root mean square error (NRMSE) for the model estimated source term is ~ 2.01. EKF predicted mean source term is 2.49 times higher compared to MAPS release data with a relative bias ~1.49.

Model Estimated Dose Rate

The observed, GPM predicted and EKF updated dose rates for AGDL-4 are shown in Figure 2. Correlation in GPM predicted dose rate is 0.35 and EKF estimated dose rate is 0.60 which indicates improvement by a factor of 1.8. The RMSE in predicted dose rate is 0.04 μSv/h for EKF and 0.09 μSv/h for GPM suggesting error reduction by a factor of 2 with EKF. Present results show that EKF can be used as alternative method of source term estimation. It is proposed to evaluate its relative performance with simple inversion method for incorporation in the Decision Support System.

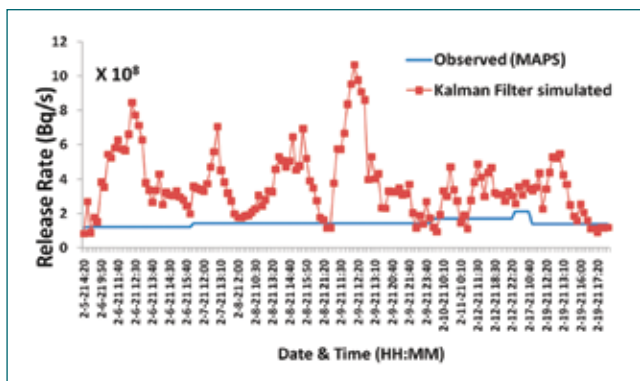


Fig. 1: KF model predicted release rate along with actual release rate

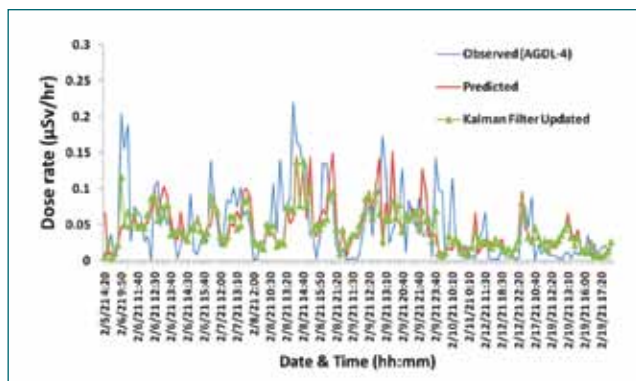


Fig. 2: Observed, model predicted and updated dose rate

V.25 Cytokinesis Block Micronucleus Assay (CBMN) In Gamma Irradiated Blood Samples for Radiation Dose Assessment

Cytogenetic dosimetric techniques involves scoring of chromosomal aberrations in the lymphocytes from the blood samples collected within a few days to few weeks after radiation exposures would reflect the dose received. IAEA 2011 recommends Dicentric assay, Micronucleus assay (MN assay), Premature Chromosome Condensation and Translocation Fluorescent In-Situ Hybridization assays for radiation dose assessment using dose response curve developed for respective dosimetric techniques.

MN assay description

Exposure of blood cells to ionizing radiation causes genetic damages in DNA which results in the formation of small chromosome fragments (micronuclei). Literature studies had also revealed that micronuclei formation is radiation dose dependent and MN scoring in the exposed blood samples could be used for radiation dose assessment purposes. A Dose response curve for MN assay was prepared by irradiating blood samples to different doses of gamma radiation.

Methodology

Aliquots of human blood samples were exposed to gamma radiation, ranging from 0.1Gy to 5 Gy. MN assay was performed as per IAEA 2011 protocol. Briefly, irradiated blood samples were added to culture tubes containing RPMI-1640 supplemented with 20% FBS and PHA-M. Cyt-B was added at 24 h to induce cell division arrest. After a total incubation at 37°C for 72 h, the cells were hypotonically treated with 0.075M KCl and fixed with methanol: acetic acid fixative. Fixed cells were casted on chilled slides and stained with 8% Giemsa for MN analysis by microscopy. Scoring of MN was performed in all irradiated samples and MN frequencies were calculated for dose response curve construction.

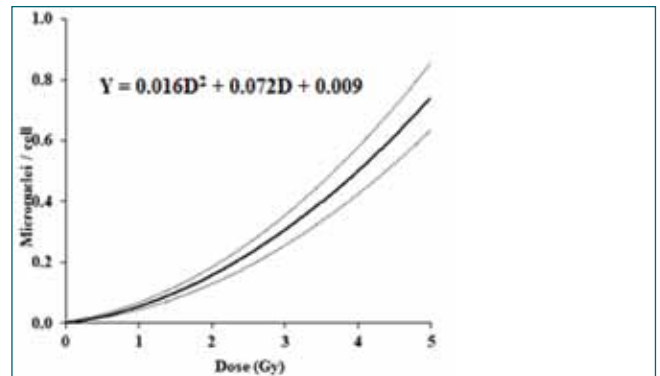


Fig. 2: Dose response curve for MN assay in blood cells irradiated with ^{137}Cs gamma radiation

Dose Response Characteristics

MN frequencies in irradiated blood samples varied between from 0.015 to 0.699. Total of 14050 cells were scored (Fig.1).

A dose response curve based on MN assay in blood lymphocytes irradiated with Cs-137 gamma radiation (dose from 0.1 Gy to 5 Gy) had been established using Polyfit software. A typical dose response curve is shown in Figure 2.

The coefficients of linear and quadratic were 0.072, 0.016 respectively with a background MN frequency of 0.009. The background frequency and coefficients obtained in our lab were comparable with those obtained by other laboratories. Among the IAEA recommended cytogenetic dosimetric assays, MN assay has several advantages over the others, in that, it requires less technical expertise, is more rapid and hence can more rapidly be applied in monitoring large populations during any radiation triage conditions. This technique is applicable for dose assessment in acute and protracted recent exposures.

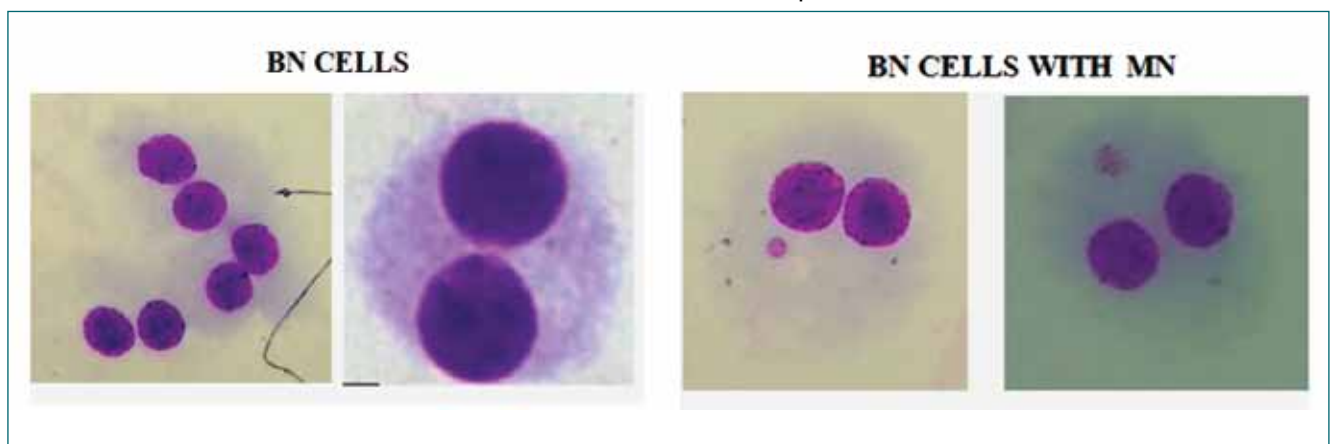


Fig. 1: Micronucleus assay pictures

V.26 Analysis of Extreme Values of Meteorological Parameters at Kalpakkam Site

Meteorological parameters like wind speed, rainfall intensity as well as total rainfall, maximum and minimum temperature, storms, cyclones play a major role in the design of the nuclear facilities from safety considerations. Rainfall forms an important input to other processes like estimation of maximum water level at the site whereas wind speed is necessary to study structural stability particularly of tall structures like cooling towers, stacks, transmission line towers etc. Meteorological parameters at the Kalpakkam site have been measured at Environmental Survey Laboratory (ESL) and the meteorological observation facility at Environmental Assessment Division, IGCAR. Using statistical analysis, a methodology was established for derivation of extreme values of the meteorological parameters at Kalpakkam site at the mean recurrence intervals of 50, 100 and 1000 years.

The long-term (1990-2021) data was collected from for meteorological parameters and quality screening was done. The following parameters are considered : maximum annual temperatures (°C) minimum annual temperatures (°C), annual maximum hourly wind speed at 10 m height (m/s), annual maximum rainfall (mm), annual monthly maximum rainfall (mm), annual daily maximum

rainfall (mm) and annual minimum pressure (mbar). The extreme values of the parameters generally follow one of the two types of distributions: Fisher-Tippet Type I distribution (Gumbel Distribution) & Fisher-Tippet Type II Distribution Frechet Distribution (Frechet Distribution). If x is the parameter value from data set of maximum values in a year, probability P(x) that the value x will not be exceeded is given by

$$P(x) = e^{-e^{-\left(\frac{x-a}{b}\right)^g}} \text{ for Gumbel distribution}$$

$$P(x) = e^{-\left(\frac{x}{b}\right)^g} \text{ for Frechet distribution}$$

where a is the location parameter, b is the scale parameter and g is the shape parameter. Three methods are used to find out the extreme values for the said mean recurrence intervals- i) Graphical method (Least square fitting) ii) Numerical method and iii) MATLAB data fitting.

The data for the maximum annual temperatures, annual wind speeds and annual rainfall for the said time period follow Gumbel distribution. The extremes of these meteorological parameters with 1 σ for the said mean recurrence intervals are shown in Table 1, 2 & 3 respectively. The deviation between the parameters as obtained by three techniques is less than 21%.

Table 1: Extremes of annual maximum temperatures

Mean recurrence interval (y)	Annual maximum temperatures extremes (OC)					
	Graphical technique		Lieble in technique		MATLAB Data fit	
	Mean	Mean+1σ	Mean	Mean+1σ	Mean	Mean+1σ
50	45.44	47.29	45.2	46.26	45.18	47.17
100	46.57	48.42	46.28	47.51	46.26	48.25
1000	50.3	52.16	49.84	51.64	49.83	51.82

Table 2: Extremes of maximum annual wind speeds at 8 m

Mean recurrence interval (y)	Annual maximum temperatures extremes (OC)					
	Graphical technique		Lieble in technique		MATLAB Data fit	
	Mean	Mean+1σ	Mean	Mean+1σ	Mean	Mean+1σ
50	21.78	25.14	20.46	22.22	21.39	25.01
100	23.83	27.19	22.25	24.28	23.36	26.98
1000	30.59	33.95	28.15	31.11	25.02	28.65

Table 3: Extremes of maximum annual rain fall

Mean recurrence interval (y)	Annual maximum temperatures extremes (OC)					
	Graphical technique		Lieble in technique		MATLAB Data fit	
	Mean	Mean+1σ	Mean	Mean+1σ	Mean	Mean+1σ
50	2220.1	2541.3	2051.9	2209.7	2219.6	2576.0
100	2413.3	2734.6	2212.2	2395.0	2413.6	2770.0
1000	3051.9	3373.2	2395.0	3008.5	3054.7	3411.0

V.27 Determination of Angular Dependence Factor for Gamma Radiation Monitoring Instruments

As a part of radiation metrology of gamma radiation monitoring instruments, it is important to understand the degree of variation of the response of the gamma detectors when the radiation falls on them at certain angle of incidence. This study is about determination of angular dependence factor $H^*(10, \alpha)/H^*(10, 0^\circ)$ for the gamma rays of different energies and for different angles between -180° and 180° . The experiment study has been carried out at Regional Calibration Facility (RCF) of RESD using OG-8 gamma irradiator (Fig.1) that houses six gamma radiation sources such as ^{137}Cs sources of 1213 Ci, 30 Ci, 50 mCi, and 10 mCi, ^{241}Am source of strength 1 Ci and ^{60}Co source of strength 20 Ci.

The ambient dose equivalents $H^*(10, \alpha)$ and the relative angular response $H^*(10, \alpha)/H^*(10, 0^\circ)$ measured using handheld Teletector (Automess make) and gamma survey meter (Atomtex make) for 10 mCi ^{137}Cs , 1 Ci ^{241}Am , and 1 Ci ^{60}Co sources at various angles from -180° to 180° in steps of 30° at a distance of 1.5 m from the sources. In case of teletector, the fluctuation in $H^*(10, \alpha)/H^*(10, 0^\circ)$ goes up to 38% for ^{60}Co gamma field, 48% for ^{137}Cs gamma field, and 94% for ^{241}Am gamma field for the angle of incidence from -180° to $+180^\circ$. Similarly, in case of survey meter, the fluctuation



Fig. 1: Photograph of OG-8 Irradiator..

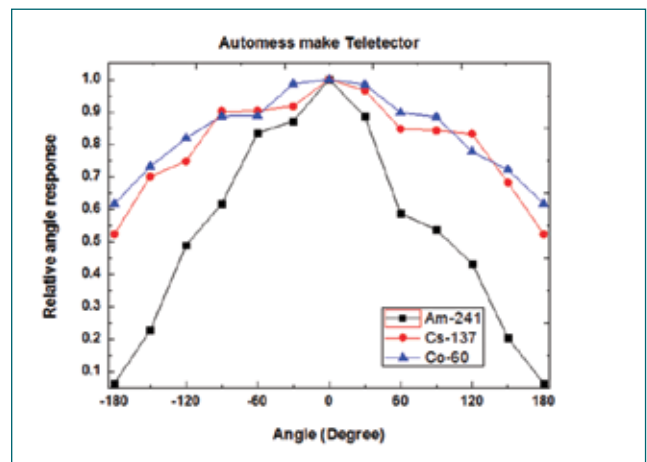


Fig. 2: Angular dependence factor $H^*(10, \alpha)/H^*(10, 0^\circ)$ using Automess make handheld Teletector

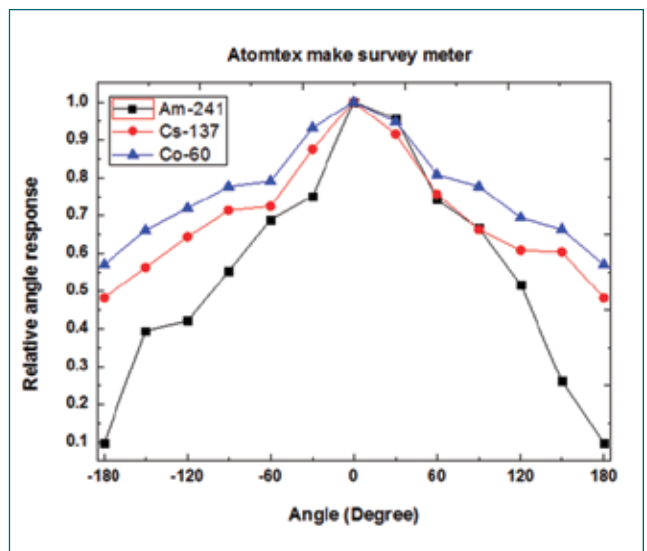


Fig. 3: Angular dependence factor $H^*(10, \alpha)/H^*(10, 0^\circ)$ using Atomtex make survey meter.

goes up to 43% for ^{60}Co gamma field, 52% for ^{137}Cs gamma field, and 90% for ^{241}Am gamma field for the same angle of incidence (Fig. 2&3).

It is observed that the fluctuation in the directional response is higher for low energy gamma radiations of 60 keV from ^{241}Am as compared to high energy gamma radiations of 662 keV and 1250 keV from ^{137}Cs and ^{60}Co respectively. The reason behind the decrease in response with the rotation of the detector is due to the lower effective area of the detectors faced by the radiations. The variation between the teletector and survey meter response may be attributed to the geometry and alignment of the detector inside the instruments and also the calibration factor of the instruments.

V.28 Effective Sampling for Radiocarbon Measurement in the Atmosphere

^{14}C present in atmospheric CO_2 is measured by capturing CO_2 in a suitable chemical substrate and analyzed for ^{14}C activity. The collection of CO_2 from the atmospheric air can be carried out either by active or by passive techniques. The advantage of the passive sampling technique is sampling can be carried anywhere in the vicinity of the plant without use of electrical power requirement. To provide periodic measurements in the open field, pertaining to site-specific condition, it is important to optimize the sampling conditions with respect to type of the sampling carried out. In the passive sampling technique, the net amount of CO_2 absorbed in the passive sampler is dependent on the concentration of the sorbent medium, dimensions of the sampler and duration of the sampling. In this study, optimization of the concentration of sodium hydroxide (NaOH) used and sampling time to get the required amount of CO_2 absorption for the estimation of ^{14}C in the atmospheric air around the nuclear facility and field evaluation is carried out.

Passive Sampling

Atmospheric CO_2 is collected directly by exposing the air to freshly prepared NaOH solution using passive sampler. The passive sampler (PS) is a polyethylene rectangular tray of dimensions 30 cm × 15 cm × 6 cm (length × breadth × height).

Sampling period for passive sample

The absorption capacity of NaOH solutions at different concentrations for CO_2 on different days is studied. The freshly prepared 500 mL of 0.5 N and 1 N NaOH solutions were exposed to atmospheric air for a different number of days. The saturated absorption capacities of 0.5 N and 1 N NaOH solutions are 1.5 g and 3 g of carbon, respectively. The samples were collected in an outdoor atmosphere to a mean temperature of $27 \pm 6^\circ\text{C}$. The amount of carbon absorbed was measured using a TOC analyser.

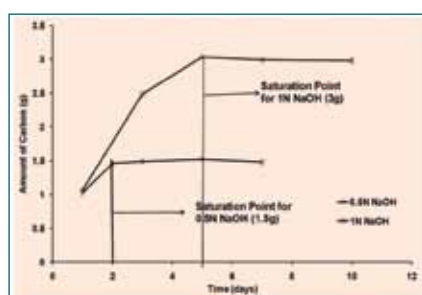


Fig. 1: Mass of the carbon trapped i 0.5 N and 1 N NaOH solutions.

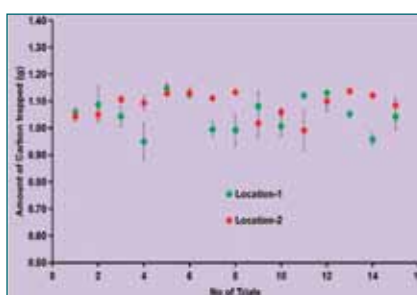


Fig. 2: Mass of the carbon trapped 0.5 N NaOH solution at two different locations

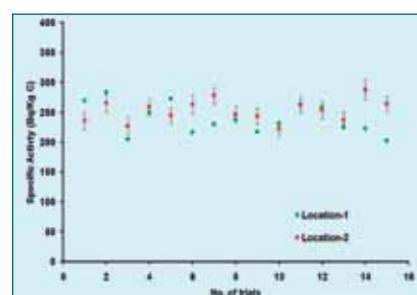


Fig. 3: Measured specific activity of ^{14}C in the atmospheric air.

The amount of carbon absorbed at different sampling duration for 0.5 N and 1 N solutions in passive sampler was shown in the Figure 1. It is observed that 0.5 N NaOH was saturated with atmospheric CO_2 within two days of the sampling duration and whereas 1 N NaOH solution was saturated within 5 days of sampling duration. The minimum amount of amount of carbon needed in the carbon dioxide absorption method for saturation of Carbo-Sorb E is 0.95 g of carbon. The amount of carbon absorbed using 500 ml of 0.5 N NaOH solution is around 1 g of carbon for the sampling duration of one day. Hence the minimum sampling period required for ^{14}C monitoring in the atmosphere is one day using 500 ml of 0.5 N NaOH solution.

Sampling of atmospheric CO_2

15 No.s of atmospheric air samples were collected on successive days to test the consistency of the CO_2 absorption capacity in 0.5 N NaOH solution. Samples are collected for one day from two different locations in the outdoor atmosphere within IGCAR campus. The amount of carbon trapped after completion of sampling was measured and presented in Figure 2. The average amount of carbon trapped in two different locations was 1.05 ± 0.06 g and 1.09 ± 0.05 g, respectively.

The measured specific activities of ^{14}C in two locations for 15 occasions were depicted in Figure 3. The average ^{14}C specific activities in the two different locations were 239.0 ± 25.4 Bq/(kg C) and 242.9 ± 18.2 Bq/(kg C), respectively. The measured specific activity concentrations of ^{14}C were within the statistical fluctuations of the reported activity levels, 228.0 ± 1.5 Bq/kg C with range 226.0–233.4 Bq/kg C. .

The sorbent concentration and sampling periods were optimized to get the required amount of CO_2 absorption such that atmospheric ^{14}C at Kalpakkam site is estimated. The methodology shall be adopted in the plant to determine the ^{14}C release if any and changes in the atmospheric levels.

V.29 A Comparative Study on Residual stress of SS 304L Welds using X-ray Diffraction Technique (XRD)

In Demonstration Fast Reactor Fuel Reprocessing Plant (DFRP), more than 200 Process vessels & 64km length of piping is used for reprocessing of Spent Fast Reactor Fuel. Nitric Acid of varying concentrations, such as 4 to 11.5N in Boiling condition is used as Process Fluid. AISI 304L is the workhorse material due to its excellent corrosion resistance in highly oxidizing atmosphere and better amenable to fabrication. Gas Tungsten Arc Welding (GTAW) is used for welding of process vessels and piping. Commonly used thickness of process vessels in this facility are 6 mm, 12 mm & 16 mm. Gas tungsten Arc Welding (GTAW) is widely used in nuclear industry owing to its better root quality and greater control of weld pool in real time. However, the process is quite slow (75-100 mm/min) compared to other slag based processes. This is a disadvantage especially when thicker sections need to be welded.

Newer welding techniques such as Hybrid Weld (Combination of GTAW & Flux Cored Arc Welding) and Doubler Operator Welding techniques has been attempted to improve the productivity without offsetting the quality requirements. Stress Corrosion Cracking (SCC) is a life limiting factor during service of these process vessels due to synergic presence of residual stress of the weldments in the as-welded condition and Corrosion species. This report mainly discusses on measurement of Weld Residual stress in SS 304L weldments of 6 mm, 12 mm & 16 mm thickness plates, welded by different welding techniques. Surface residual stress is measured using X-ray Diffraction (XRD) technique. The results are discussed in comparison with the conventional GTAW practices.

12 mm & 16 mm thickness SS 304L plates has been welded using Root & Hot pass with GTAW and rest of

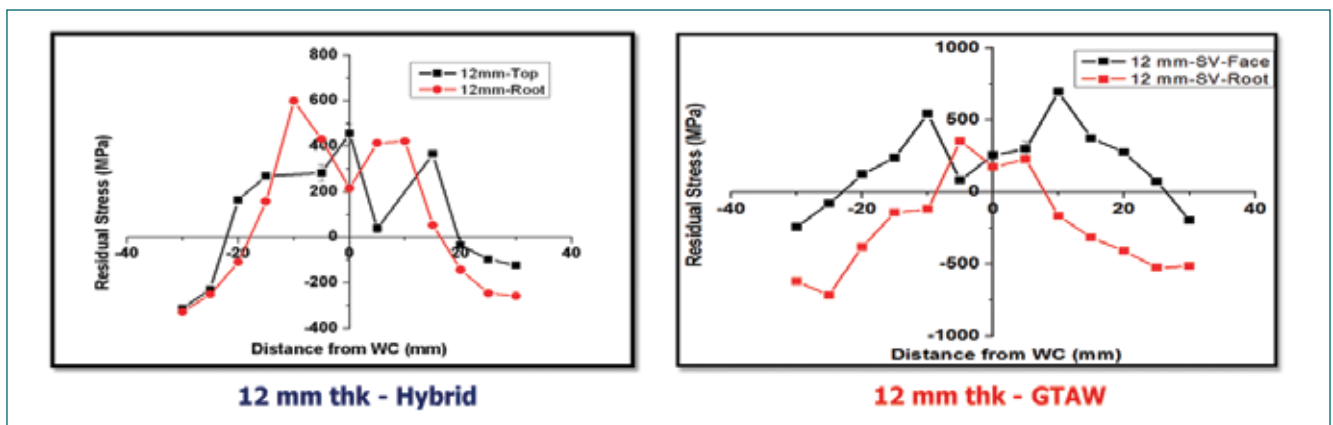


Fig. 1: Residual Stress in 12 mm Hybrid and GTAW weld

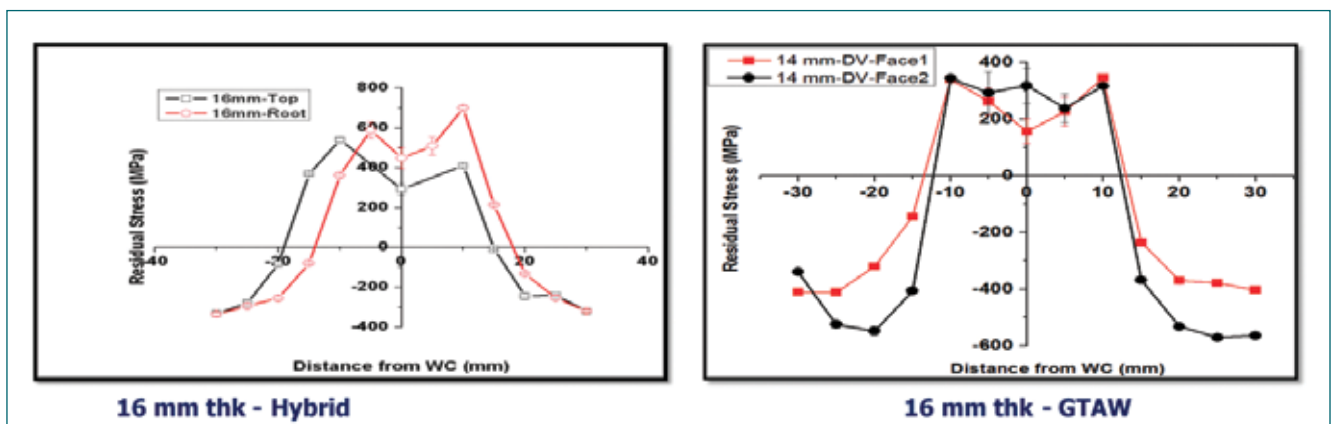


Fig. 2: Residual Stress in 16 mm Hybrid and GTAW weld

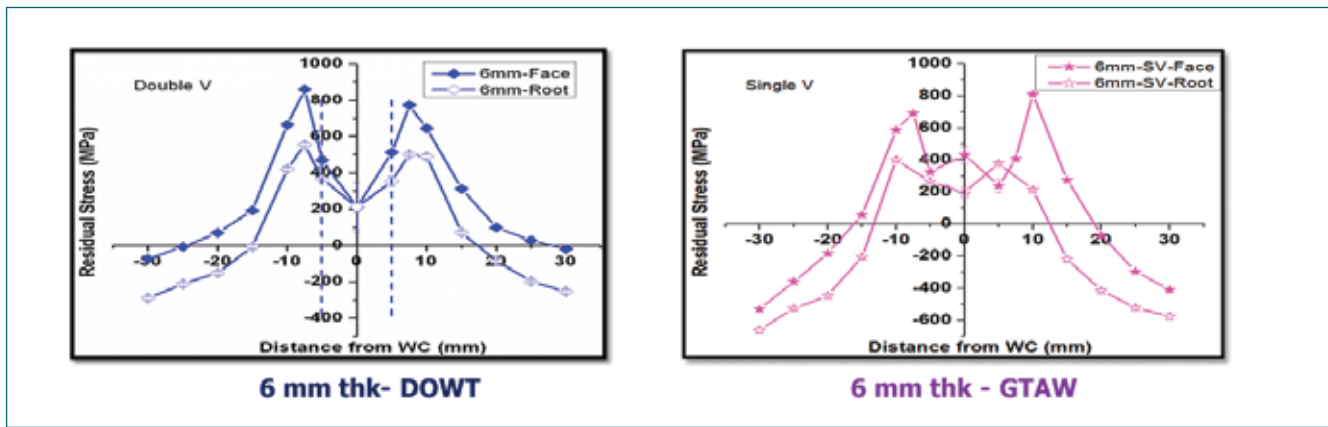


Fig. 3 : Residual Stress in 6 mm DOWT and GTAW weld

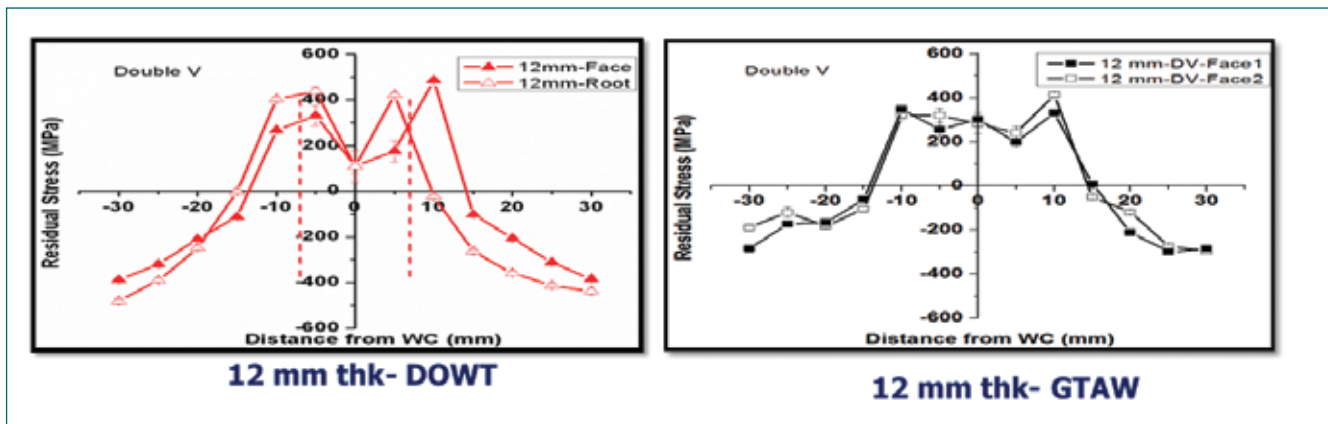


Fig. 4: Residual Stress in 12 mm DOWT and GTAW weld

the fill passes with FCAW (Flux Cored Arc Welding). Single “V” weld joint configuration is used for 12 mm thickness and Double “V” configuration is used for 16mm thickness for Hybrid Weld. 6 mm & 12 mm thickness SS304L coupons are welded using Double Operator Welding Technique (DOWT). In both coupons Double “V” configuration is employed. Simultaneously, 6 mm (Single “V” & Double “V”), 12 mm (Single “V” & Double “V”) & 16 mm thickness (Double “V”) coupons are also welded using GTAW. All these coupons in as welded condition has been experimentally analysed for the presence of Surface residual stress using X ray Diffraction (XRD) technique.

Hybrid Weld is having close to 30% (12 mm thick) & 40% (16 mm thick) saving in Arc on time as compared to that

of GTAW Welds DOWT welds are having close to 36 % (6mm thick) and 33% (12 mm thick) saving in Arc on time as compared to that of GTAW Welds Unsymmetrical “M” curve observed in 12 mm & 16mm thick Hybrid Welds. Peak stress at Weld center is around 200 MPa (R) and 400 MPa (F) in 12 mm thick Hybrid Welds and 500 MPa (R) and 280 MPa (F) in 16 mm thick. Residual stress values in Hybrid welds are seemingly higher than Conventional GTAW Welds due to higher current and voltage used for FCAW welds. Symmetrical “M” curve in 6 mm & 12 mm thick DOWT welds has been observed. Peak stress values in DOWT welds are comparable to that of GTAW welds. However, DOWT Values are closer to GTAW welds in Weld Centre line region. Pictorial comparison of RS values are depicted in Fig.1 to 4.

V.30 Application of machine learning in Ultrasonics for Classification of Annealing Conditions in Austenitic Stainless Steel

Machine learning algorithms were applied on nonlinear ultrasonic signals for classification of the austenitic stainless-steel material subjected to different annealing conditions. The algorithms are trained using the features such as the ratio of harmonic amplitudes, root-mean-square value, and the phase difference between the fundamental and second harmonic components derived from the nonlinear ultrasonic response. The result takes a step forward to the automation of non-destructive testing towards Industrial Revolution 4.0. The results also pointed out the necessity of parameter fusion in non-destructive decision making.

Materials and Methods

The material selected for this study was AISI grade 304 austenitic stainless-steel plate of 12 mm thickness. Specimens of dimension $50 \times 50 \times 12 \text{ mm}^3$ were heat treated in a muffle furnace for different annealing conditions. The nonlinear ultrasonic measurements were performed at multiple locations on these specimens in through-transmission mode.

Nonlinear Ultrasonics

The nonlinear response from the annealed specimens as a function of grain size is shown in Fig. 1. It is obvious that the annealed specimens show only marginal variation in their nonlinear response. In such a situation,

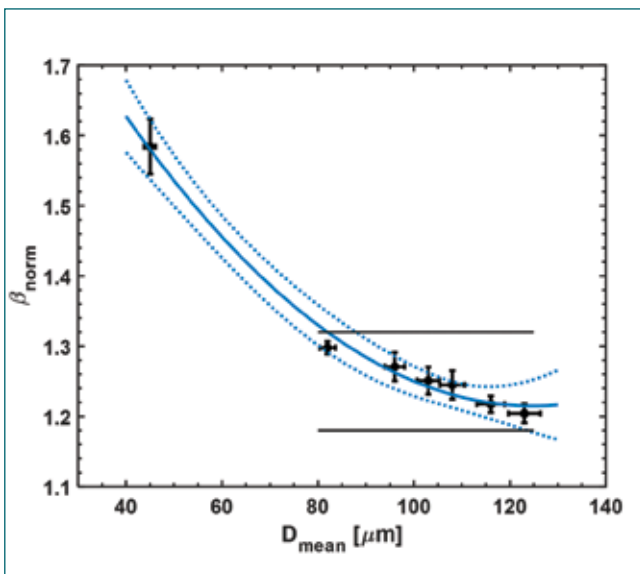


Fig. 1: Nonlinear ultrasonic response as a function of grain size.

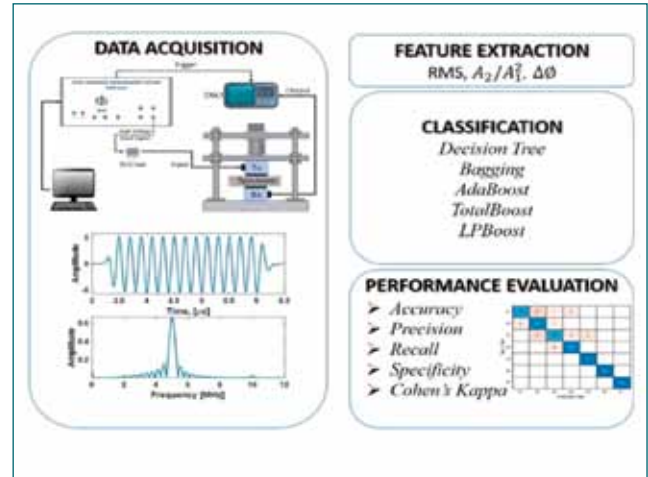


Fig. 2: Classification framework for the proposed ML approach.

classification of materials using the acoustic nonlinearity parameter alone may be erroneous. Though the acoustic nonlinearity can be evaluated from the amplitude ratio of the harmonics, additional features that can be extracted from the received signals include the RMS, and the phase difference between the fundamental and second harmonic components. The ML classification algorithm was developed based on these parameters. Hence, the feasibility of machine learning based algorithms is explored for the classification of such specimens.

Machine Learning

The classification framework adopted in the present study is shown in Fig. 2. Decision tree is one of the most fundamental and simplest predictive modelling algorithms. Most important ensemble modifications to the decision tree are Bagging, Ada Boost, LP Boost and Total Boost. These algorithms were used to classify the specimens from their nonlinear response. On calculation of the classification accuracy using the above parameters, the harmonic ratio is selected to be the root node since the information gain is highest for this feature. The overall performance is significantly better by using the LP Boost ensemble technique, with a classification accuracy of 97 percent. This classifier also has the best recall, specificity, and Kappa scores. The overall results revealed that employing nonlinear ultrasonic data, the LP Boost classifier can effectively classify annealing conditions.

V.31 Numerical Estimation of Efficiency of HPGe Based Actinide Monitor for Various Radionuclides Present in Lungs

HPGe based actinide monitor is used to estimate the internal exposure of actinides by measuring the lung activity. Response of this monitor is estimated experimentally using Lawrence Livermore National Laboratory (LLNL) phantom having different muscle equivalent chest wall thickness (MEQ-CWT). The phantom has individual lung sets with uniform distribution of ^{241}Am and Natural thorium and but many a time it is essential to monitor other actinides, fission products etc which is not present in the LLNL phantom. In order to find the activity of any X-ray or gamma photon emitting radionuclides present in the lungs efficiency curve was established using numerical simulation. The effect of lung size on efficiency was also studied numerically.

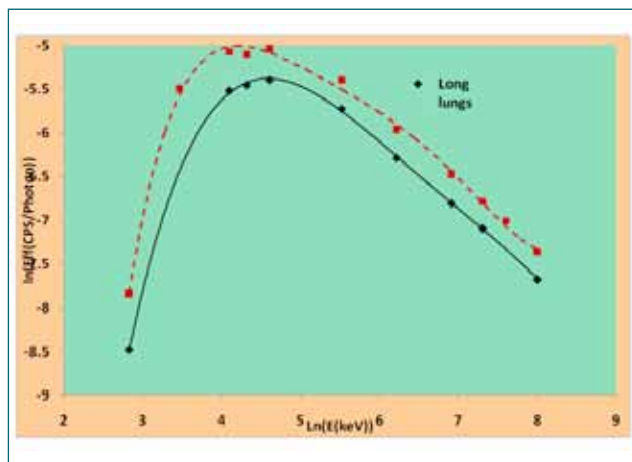


Fig. 2: comparison of efficiency curve for phantoms with short and long lungs

Table 1 Comparison of simulated efficiencies of varies energies for different lung size					
Lung type	Efficiency value (CPS/Bq)				
	^{241}Am	^{239}Pu	Nat U	^{137}Cs	^{40}K
Long (21 cm)	1.44E-03	4.57E-06	2.01E-04	1.28E-03	8.39e-05
Short (11 cm)	2.25E-03	8.62E-06	2.86E-04	1.78E-03	1.16E-04

The actinide monitor is a coaxial HPGE detector of diameter 8.5 cm and thickness 3.03 cm having Be entrance window. This detector was modeled tangential to the sterna notch of the LLNL voxel phantoms [with short (1669.58 & 2220.85 cm³) and long lungs (3110.29 & 4300.40 cm³) having MEQ-CWT of 1.6 cm and parallel to the bed at a distance of 1 cm. MCNP4C

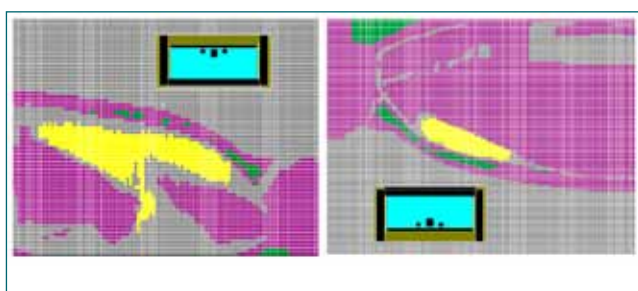


Fig. 1: Simulation of detector over phantom a) with long lungs b) with short lungs

Monte Carlo code was used to estimate the efficiency values. Fig.1 shows the detector modeled above the lungs of LLNL voxel phantom. Pulse height tally along with Gaussian energy broadening was used to estimate the efficiency values. The detector model was validated using experimental point, surface and volume source efficiencies. The LLNL voxel phantom modeling along with the detector was validated with the experimental efficiency of ^{241}Am loaded LLNL phantom with long lungs having a chest wall thickness of 1.6 cm.

The efficiency curves for the two phantoms are compared in Fig. 2. Using these efficiency curves, lung activity of any radionuclide emitting X-rays or gamma photons in the energy range of 10 – 1500 keV can be estimated. The phantom with short lungs has 27- 47% higher efficiency depending on the energy. This is because larger percentage of the lung area is seen by the detector in case of short lungs. In both the cases the efficiency increases and reaches maximum at 100 keV and then decreases. This is due to combined effect of attenuation in the entrance window as well as the dead layer and the interaction cross-section. The efficiencies were fitted using a polynomial logarithmic function of fifth order. The efficiency values estimated using the fitted function are within $\pm 10\%$ of the simulated efficiency. Table 1 gives the efficiency values of the phantoms with two lung sizes for different radionuclides.

V.32 Dimensional Measurement in Gamma Ray CT Imaging using the Shape Phantom

CT has been proven to be an excellent tool for identifying the location and internal features of the complex object. CT helps as a metrological tool for the accurate measurement of the dimensions of the object. Nowadays, CT assists in making 3D computer-aided designs in the field of reverse engineering and in CNC-based 3D printing. While preparing the 3D image by CT scan, it is essential to understand the relationship between the system performance and dimensional accuracy. The CT system performance depends on the spatial resolution and contrast sensitivity of the CT image obtained by the system. An In-house made shape phantom was used to study the dimensional accuracy of the Waste assay system having the CT features.

The Waste assay Computed Tomography WACT (Fig. 1) in HISD, IGCAR is the first generation single source, single detector CT system. It is an indigenously



Fig .1. Photograph of WACT system



Fig .2. Photograph of Shape Phantom

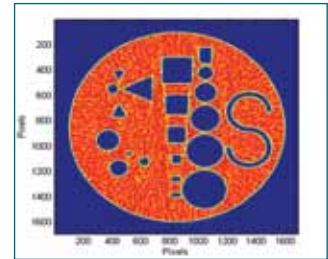


Fig .3. CT image

developed automated system. A two-axis manipulator system is placed between source and the detector to perform the CT movement for a particular layer. The source and detector are collimated, placed in line, facing each other, and can move vertically for each layer scan of the object. The system is mainly intended for the radioactive waste assay of the nuclear waste drum. This system uses in-house developed Convolution-based Filter back-projection algorithms for CT image reconstruction.

The shape phantom (Fig. 2) was fabricated in-house using EDM wire cut at the Central Workshop of CWD, IGCAR. The phantom is a 10 mm thick disk fabricated in aluminium material. The diameter of the disk is 150 mm. The phantom has simple geometric cut-outs of curves-1No., circles-12 Nos., squares- 4 Nos., rectangles-3 Nos. & triangles- 3 Nos. Detailed dimension of all the shapes is given in Table -1. The minimum size of the shape is 1.5 mm circle. A gamma ray CT scan was taken for shape phantom using ¹³⁷Cs (1 Ci) source with the following parameter, Source collimator: 5mm & detector collimator: 5 mm, beam width: 3.5 mm. No of rays per projection: 169 parallel rays (1 mm interval), Total number of projections: 90 (2° interval) and measurement time per ray is 5s.

Reconstructed CT image shows all the shapes in the fabricated phantom (Fig. 3). The Dimensions of the different shapes are measured from the CT image using Matlab regionprops functions. Matlab software was written to identify the shapes and find out the dimensions. The size of different shapes is accurately measured, and compared with the actual dimension measured using the optical coordinate measuring machine. The CT system could reproduce the all the shapes present in the phantom with in 1.0 mm dimensional accuracy.

Shape	Parameter	Measurement (mm)		Error (mm)
		Actual	CT	
Circle	Diameter	150.05	150.16	-0.11
Circle	Diameter	30.01	30.00	0.01
Circle	Diameter	25.01	25.00	0.01
Circle	Diameter	20.01	20.00	0.01
Circle	Diameter	15.02	15.00	0.02
Circle	Diameter	15.01	15.10	-0.09
Circle	Diameter	12.01	12.00	0.01
Circle	Diameter	10.01	10.00	0.02
Circle	Diameter	7.01	6.90	0.11
Circle	Diameter	6.06	5.93	0.13
Circle	Diameter	3.02	2.87	0.15
Circle	Diameter	1.52	0.60	0.92
Square	Length	20.00	20.60	-0.60
Square	Length	15.02	15.60	-0.58
Square	Length	12.02	12.60	-0.58
Square	Length	6.00	6.40	-0.40
Rectangle	Length	12.01	12.10	-0.09
	Width	8.01	8.50	-0.49
Rectangle	Length	6.01	6.30	-0.29
	Width	4.02	4.20	-0.18
Rectangle	Length	6.65	6.50	0.15
	Width	3.01	3.30	-0.29
Triangle	Base	19.99	18.77	1.22
	Height	20.02	19.79	0.23
Triangle	base	10.02	9.20	0.82
	height	10.01	9.30	0.71
Triangle	Base & height	7.49	6.75	0.74
	Height	7.49	6.90	0.59
S-shape	Radius	12.51	12.10	0.41
	Thickness	2.99	2.85	0.14

V.33 Studies on Characteristic Limits for Measuring Ionizing Radiation

In radiation measurements, error in estimation of activity is due to the uncertainties associated with radioactive decay and calibration parameters, which includes systematic variations. The well known Curie's method used in the estimation of characteristic limits of measurement (decision threshold, detection limit and confidence interval) relies on assumption of Gaussian distribution for observed counts and uncertainty in calibration factor (CF) is excluded. This assumption could lead to underestimation of error. The calibration factor, v is defined as, $v = s/A$, where s is signal count and A is activity of the sample. In the international standard on determination of characteristic limits document, ISO11929:2010 (ISO), an attempt is made to include uncertainty of the calibration factor. However, the algorithm given in ISO, significantly overestimates the value of the detection limit or minimum detectable activity (MDA) for high relative uncertainty in the CF, and can produce non-physical results. In case of low background count, which is very common during alpha activity measurements and coincidence counting measurements, the ISO method may produce underestimate of the detection limit. Thus, for low background counts or high uncertainty in CF, Bayesian approach is observed to be more appropriate.

In the present work, an algorithm is developed based on Curie's hypothesis testing approach, which constructs gross count distribution from Bayesian inference. Counting distributions are constructed from underlying Poisson distributions. The Bayesian posterior distribution of inferred mean of the background count from estimated

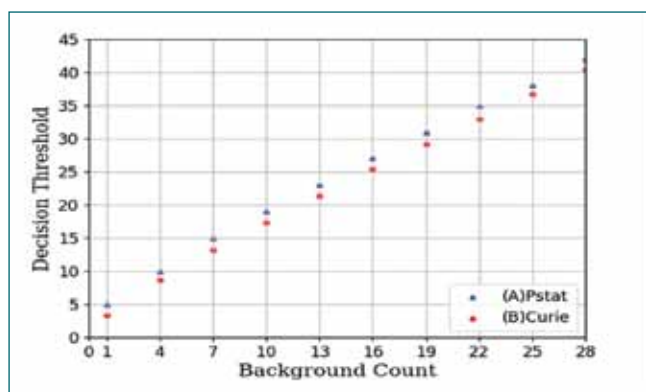


Fig. 1: Decision threshold (95% confidence), (A) Pstat, (B) Curie

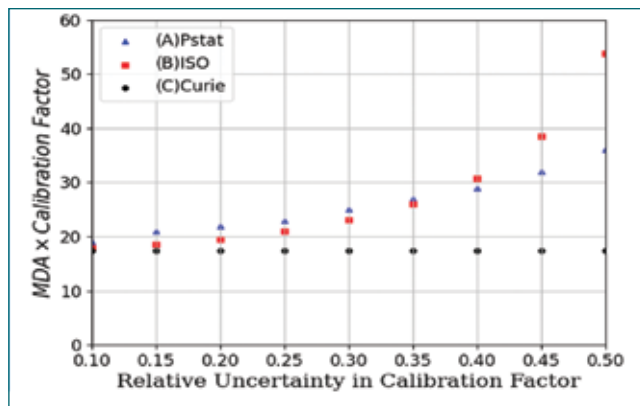


Fig. 2: Product of MDA (95% confidence) and CF (background count = 10, background uncertainty = $\sqrt{10}$): (A) Pstat, (B) ISO, (C) Curie

background count mean and uncertainty, is used to arrive at the background count distribution. The algorithm admits any suitable posterior distribution for the CF from the estimate of its value and uncertainty. Gamma distribution has been chosen as a suitable posterior distribution to model the uncertainty in the true value of the CF as in absence of a more credible model, it is a physically reasonable choice. From the background count distribution, decision threshold can be readily obtained, while varying gross count distribution with respect to sample activity provides detection limit (MDA). The algorithm abbreviated as Pstat, is executed in Python 3.10. The decision threshold (95% confidence) based on Curie's method and Pstat is shown in Fig. 1. The Curie's method slightly underestimates the decision threshold compared to Pstat, but the relative variation in the estimates decreases with increase in background counts. The product of MDA (95% confidence) and CF as a function of the relative uncertainty in the CF at fixed background count (10) and uncertainty ($\sqrt{10}$) is shown in Fig. 2. The ISO tends to give significant overestimate of MDA at higher values of relative uncertainty in CF, while Curie's method does not account for uncertainty in CF and thus gives lower MDA values.

The statistical algorithm provides a better method of evaluation of characteristic limits especially at low background counts and at high relative uncertainty of CF. As the algorithm evaluates the parent distribution, other statistical quantities of interest also could be computed based on requirement.

V.34 Tribocorrosion Behavior and its Mechanisms of Type 304L Stainless Steel in Nitric Acid Media

Tribocorrosion is the material degradation due to the combined effect of wear and corrosion. Tribocorrosion behavior of passive materials is of interest because any destruction of passive film in the material leads to accelerated corrosion. In nuclear reprocessing environment, the tribocorrosion phenomena are encountered in continuous rotary dissolver, solvent extraction apparatus, moving parts, and also some components are subjected to scratches or wear and flow-induced vibrations in the nitric acid medium. The study aimed to provide an understanding of the collective effect of physicochemical and mechanical surface interactions and its degradation mechanisms of type 304L SS in various nitric acid concentrations.

The measured open circuit potential (OCP) values before, during, and after sliding are presented in Figure. 1(a). The shift in OCP to the cathodic potential region over the sliding period indicates the destruction of the passive film in the worn surface, and once the sliding was stopped, the OCP tend to restore to its initial value. The resulting OCP value during sliding was the mixed potential comprised of the active wear track area and unworn passive surface of the sample. The results indicated the degree of cathodic shift in potential decreases with increasing nitric acid concentration. The simultaneous measurement of friction coefficient during the sliding action is illustrated in Fig. 1(b). It could be seen that the COF decreases with increase in nitric acid concentration.

The SEM worn morphology of 304L SS (Fig. 2) revealed that the surface had undergone severe plastic deformation with parallel abrasive grooves. Some pore-like features on the worn surface of 11.5 M HNO₃ (Fig. 2d) are due to localised dissolution of the surface. However, mechanical wear dominates at all nitric acid concentrations. It was inferred from the optical images (Fig. 3) of tribocorrosion tested Al₂O₃ ball that material

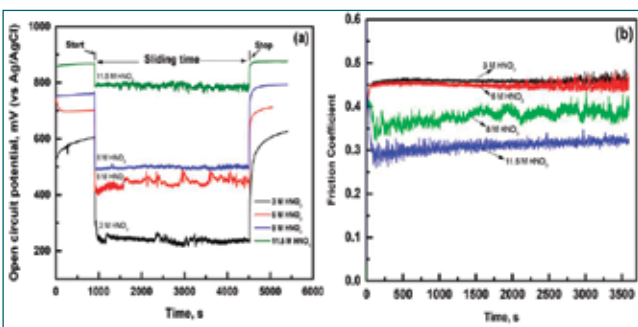


Fig. 1: (a) Open circuit potential sliding test vs time
(b) Friction coefficient vs time

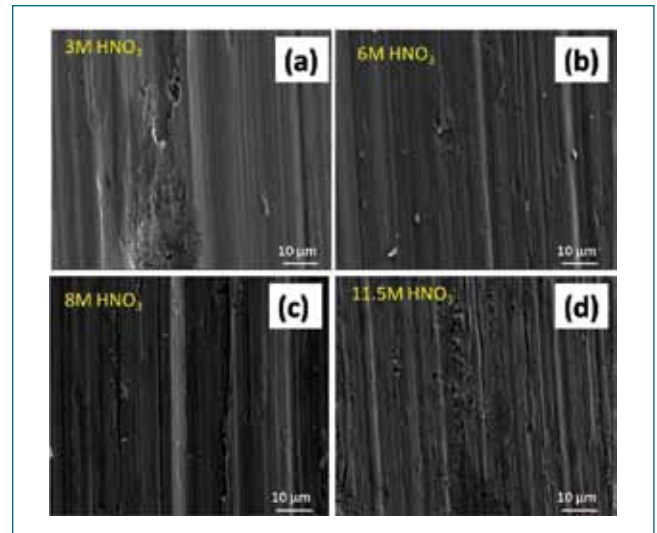


Fig. 2: SEM worn morphology of 304L SS in various nitric acid concentrations

adhesion is higher at 3 M HNO₃ (low concentration) and decreased with increase in nitric acid concentration. The repassivation ability increases as the concentration of nitric acid is increased and adhesive wear reduces due to the regrowth of passive film with contact region. Hence, the wear mechanism of 304L SS in nitric acid is the combined effect of abrasive and adhesive wear. The calculated specific wear rate values of 304L SS are $0.197 \times 10^{-3} \text{ mm}^3/\text{Nm}$, $0.191 \times 10^{-3} \text{ mm}^3/\text{Nm}$, $0.135 \times 10^{-3} \text{ mm}^3/\text{Nm}$ and $0.127 \times 10^{-3} \text{ mm}^3/\text{Nm}$ for 3 M, 6 M, 8 M and 11.5 M HNO₃. The wear rate lowered as the concentration of nitric acid is increased. Tribocorrosion material degradation of 304L SS is a concern in nitric acid medium because both mechanical wear and wear accelerated corrosion are influenced by nitric acid concentration.

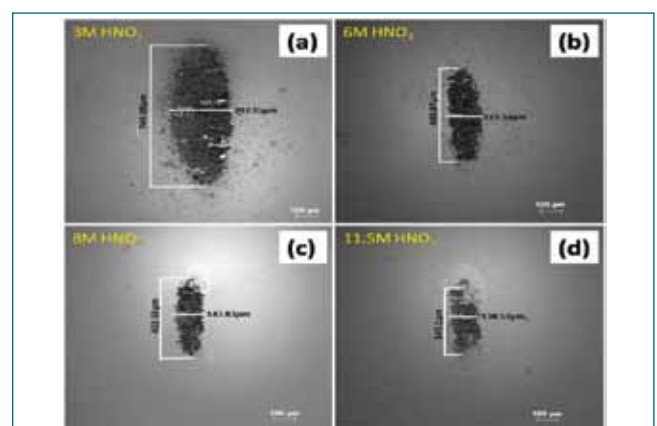


Fig. 3: Optical microscopic grooves present and such features are illustrative of abrasive wear images of the alumina counter body after testing in nitric acid medium

V.35 An AFM Based Study on the Effect of X-ray Exposure on Adhesion Properties of Multi-walled Carbon Nanotube Incorporated Silicone Polymer Nanocomposites

Nano-filler incorporated polymer nanocomposites are being explored as constituents for gloves, aprons, etc., for the shielding of diagnostic X-ray to protect the patients and the operators. Such applications require an understanding of the effect of the ionizing radiation on the adhesion and nano-mechanical properties of the polymer nano-composites for their long-term stability. With this objective, the effect of X-ray irradiation and nanofiller concentrations on the topographic and adhesion properties of multi-walled carbon nanotube (MWCNT) loaded silicone polymer nanocomposites were probed using atomic force microscopy (AFM).

Silicone polymer nanocomposites containing varied concentrations (0.025, 0.25 and 2.5 wt. %) of MWCNT nanofillers were prepared using a room temperature solution casting technique. Two sets of samples were prepared, where only one set was subjected to X-ray irradiation (30-70 keV, 105s, focal spot size ~ 1.5 mm and sample-to-source distance ~ 1000 mm). AFM-based topographic scanning was performed using the semi-contact mode, utilizing a silicon tip of typical bending radius and resonant frequency of ~ 10 nm and 210 kHz, respectively. Adhesion force measurements were performed using a silicon nitride tip of typical bending radius and resonant frequency of ~ 15 nm and ~ 114 kHz, respectively. Topographic measurements indicated ~ 123 % increase in root mean square (RMS) surface roughness of the polymer nanocomposites when the MWCNT concentration was increased to 2.5 wt. %. On the other hand, for a fixed MWCNT concentration, RMS surface roughness increased by ~ 171 % after X-ray irradiation, which was attributed to the X-ray induced polymer degradation that caused isolated aggregation of MWCNT due to poor filler-matrix interaction, leading

to irregular protuberances, as confirmed from the AFM-based topographic imaging of the X-ray exposed polymer nanocomposites (Fig. 1a). Using the force volume method, adhesion force and adhesion energy were estimated from the force-displacement curves. Adhesion energy values were experimentally determined from the areas under the non-contact regions of the force-displacement curves during AFM probe retraction (Fig. 1b). Fig. 1c shows the adhesion force values for the unexposed and exposed polymer nanocomposites. It was observed that adhesion force increased by ~ 118 % with increasing MWCNT concentrations. For a fixed MWCNT concentration of 2.5 wt. %, adhesion force was found to increase by ~ 4 times after X-ray exposure, which was attributed to the increased surface roughness of the X-ray exposed polymer nanocomposites that increased the tip-surface contact area. Experimental results indicated a linear increase in adhesion force with RMS surface roughness. Adhesion energy increased with MWCNT concentration, and after X-ray exposure. Further, the experimental adhesion energy values were found to be in good agreement with the theoretically calculated values, obtained from the Johnson, Kendall and Roberts (JKR) model. Fig. 1d shows the linear increase in adhesion energy with the adhesion force for the X-ray exposed polymer nanocomposites. The experimental findings clearly showed an increase in the surface roughness, adhesion force and adhesion energy for the MWCNT loaded silicone polymer nanocomposites with increasing nanofiller concentration and post X-ray irradiation. The obtained results will be beneficial for optimal design of such polymer nanocomposites for various applications, including the fabrication of lead-free radio-opaque nanocomposites.

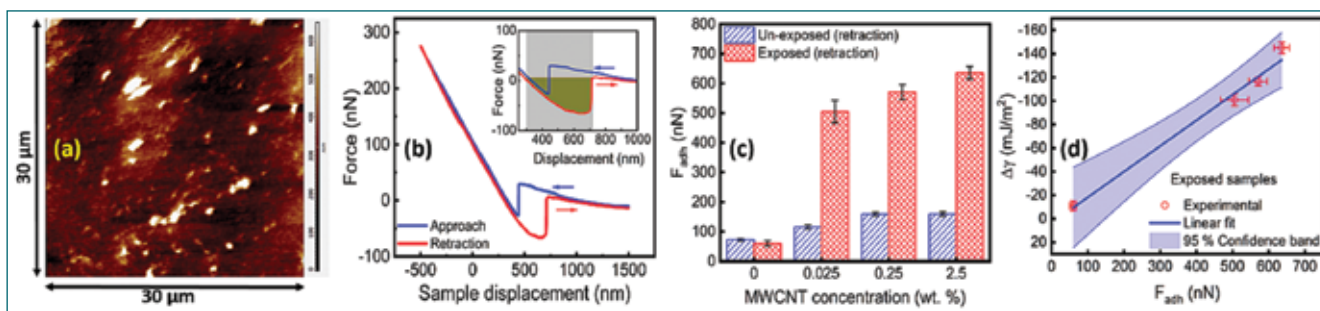


Fig. 1: (a) AFM topographic image of the polymer nanocomposite containing 0.025 wt. % MWCNT, after X-ray irradiation. (b) A typical force-displacement curve during the approach and retraction of the AFM probe. The adhesion force and adhesion energy values are estimated from the non-contact region of the retraction curve. (Inset) Magnified view of the non-contact region, where the shaded area indicates the adhesion energy. (c) A bar-chart showing the adhesion force, as a function of MWCNT concentration for the X-ray exposed and unexposed samples. (d) Linear variation of adhesion energy as a function of adhesion force for the X-ray exposed polymer nanocomposites.

V.36 Effect of Zn Substitution on the AC Magnetic Heating Properties of Zn-Mn Mixed Ferrite Nanoparticles Prepared using Microwave Assisted Synthesis

AC magnetic field induced heating properties of superparamagnetic nanoparticles (MNPs) is being exploited for the development of magnetic fluid hyperthermia (MFH)-based alternate cancer therapeutics. In MFH, a dispersion of MNPs is localized within a cancerous tissue, and thereafter subjected to a radio-frequency alternating magnetic field (RFAMF), which generates heat due to the inherent Neel-Brown relaxation losses. Though Fe_3O_4 is the most widely used candidate for MFH, several other types of ferrite MNPs are being probed with an objective to tune the heating efficiency. The heating efficiency primarily depends on the magneto-structural properties of the MNPs and hence, mixed ferrite MNPs with varied doping exhibits strong variations in MFH properties.

$\text{Zn}_x\text{Mn}_{1-x}\text{Fe}_2\text{O}_4$ ($x = 0.1$ to 0.9) MNPs were synthesized using a microwave assisted coprecipitation technique (temperature $\sim 180^\circ\text{C}$, digestion time ~ 5 min.). Powder X-ray diffraction studies indicated the presence of spinel structure with average crystallite sizes varying from ~ 20 - 8 nm for $x = 0.1$ - 0.9 (Fig. 1a). Due to the lower solubility product of the Zn^{2+} ions, the formation of new nuclei was preferred over grain growth, resulting in the progressive lowering of the crystallite size with increasing Zn concentration. Isothermal DC magnetization studies at 300 K indicated superparamagnetic response of the MNPs with a non-monotonic variation of the saturation magnetization with increasing Zn substitution (Fig. 1b). The saturation magnetization first increased from ~ 46 emu/g to ~ 56 emu/g for $x=0.1$ to 0.5 and then decreased to ~ 19 emu/g at $x = 0.9$. This was attributed to the Yafet-Kittel type triangular spin ordering at higher Zn concentration. Zn^{2+} ions (zero crystal field stabilization energy) preferentially occupy the tetrahedral sites, leading to an increase in collinear Neel type magnetization up to $x = 0.5$. For $x > 0.5$, the spin ordering

in non-collinear due to sub-splitting of the octahedral sites, and the net magnetic moment per formula unit is expressed as: $n_B = M_B \cos \theta_{YK} - M_A$, where M_B , M_A and θ_{YK} indicate the magnetization of the octahedral and tetrahedral sites and the Yafet-Kittel angle, respectively. The higher θ_{YK} values for $x > 0.5$ caused a reduction in the saturation magnetization (Fig. 1b). Temperature dependent magnetization studies indicated the presence of blocking temperature below 300 K, conforming the superparamagnetic response of the prepared MNPs, and the estimated effective anisotropy energy densities varied from ~ 20 - 70 kJ/m³. The variations of the average crystallite sizes, saturation magnetization, and effective anisotropy energy density with increasing Zn substitution significantly influenced the AC induction heating properties. Magneto-calorimetry studies indicated a high specific absorption rate of $\sim 130 \pm 4$ W/g_{Fe} at $x = 0.1$ for RFAMF amplitude and frequency of ~ 33.1 kA/m and ~ 126 kHz, respectively. Fig. 1c shows a bar-chart comparing the experimental SAR values at various conditions. The AC induction heating efficiency did not exhibit any non-monotonicity at $x = 0.5$, and progressively decreased at higher Zn concentration due to the reduction in the average particle size and anisotropy energy density that caused the relaxation dynamics to be Neel-dominated with lower effective relaxation times (Fig. 1d). On the other hand, the dominance of Brownian relaxation at lower Zn concentration was experimentally verified from magneto-calorimetry studies on agar-immobilized MNPs with lower Zn concentration ($x = 0.2$). The experimental findings clearly indicate that saturation magnetization alone does not influence the AC induction heating efficiency, and relaxation dynamics play a significant role. The obtained results are useful for the development of mixed ferrite MNPs with tunable Curie temperature around 42 - 45°C for self-regulated hyperthermia.

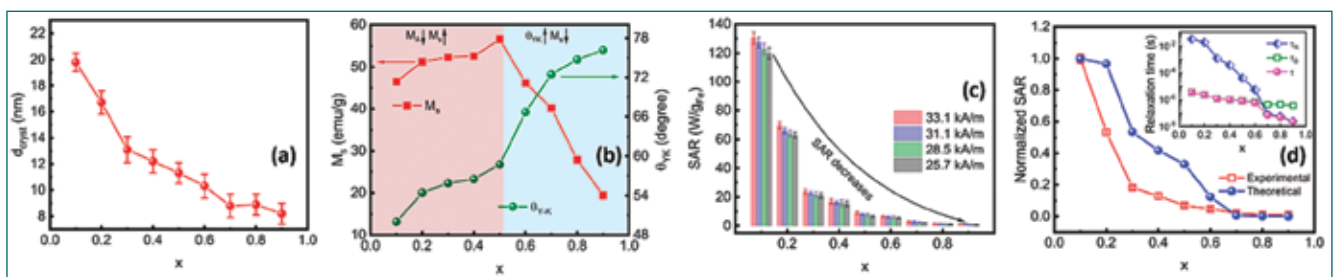


Fig. 1: (a) Variation of crystallite size with increasing Zn substitution. (b) Variation of saturation magnetization and Yafet-Kittel angle with increasing Zn substitution. (c) A bar-chart showing the variations of the experimental SAR values at varied RFAMF amplitudes for different Zn substitutions. (d) Progressively decreasing trend of the experimental and theoretical normalized specific absorption rates with increasing Zn substitution. (Inset) Variation of Neel, Brownian and effective relaxation times with increasing Zn substitution.

V.37 Effect of aging heat treatment on Microstructure, Mechanical Properties, and Lattice Strain of Alloy 617

Alloy 617, a Ni-Cr-Co-Mo alloy is a promising material for high-temperature applications owing to its high temperature strength, reasonable microstructure stability, corrosion and oxidation resistance. Alloy 617 (UNS N06617) is a candidate structural material for Ultra Supercritical Water Reactor (SCWR) and Advanced Ultra Super Critical (AUSC) thermal power plant. In AUSC power plants, live steam parameters are increased to 710-720°C and 310 bar to attain efficiency up to 45%. Alloy 617 is known to precipitate nano-sized spherical γ' -Ni₃(Al, Ti) and grain boundary-M₂₃C₆ precipitates at the operating temperatures of the AUSC power plant, which will have a substantial impact on the mechanical properties. The presence of coherent γ' may produce strain in the alloy. It is critical to investigate these changes in the alloy in order to comprehend its service behaviour. Service exposed material is simulated by subjecting Alloy 617 boiler tubes (52 mm O.D and 11.9 mm W.T) to aging heat treatment at 700°C for 100h, 1000 h and 4000h. The microstructure, mechanical properties, and lattice strain of solution annealed (SA) and aged Alloy 617 were studied.

Microstructure and Mechanical properties

Fig. 1(a) shows the SEM microstructure of Alloy 617 base metal in the as-received solution annealed condition. The microstructure shows the presence of primary Cr- rich M₂₃C₆ and Ti rich-M(C,N) carbides. In addition to primary carbides, the aged Alloy 617 base metal shows δ - Ni₃Mo and formation of more Cr-rich M₂₃C₆ carbides at the grain boundary and γ' -Ni₃(Al, Ti) precipitates within the grains as observed in FESEM micrograph- Fig 1(b). With increase in aging temperature and time, Cr-rich M₂₃C₆ has coarsened and coalesced to form continuous network along grain boundaries. It

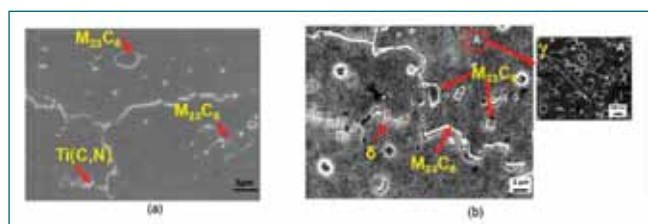


Fig. 1: FESEM micrograph of Alloy 617 in (a) as received, and (b) 700 °C/1000h aged condition

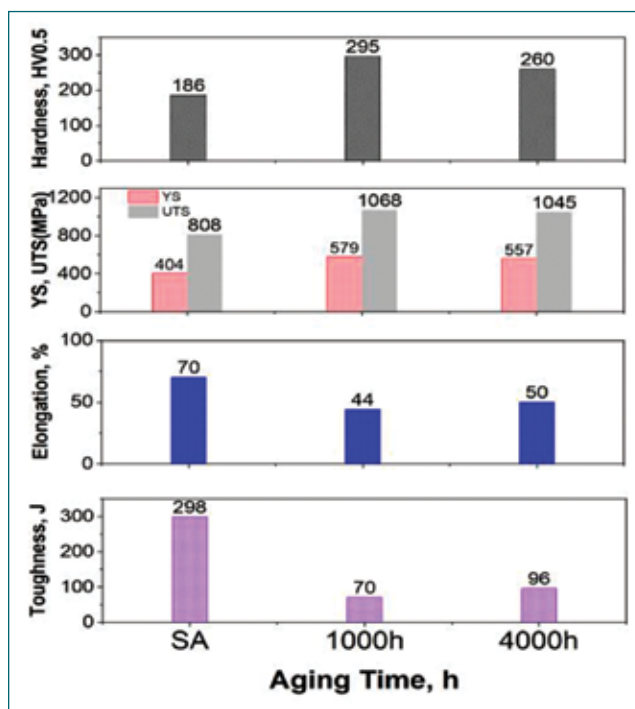


Fig. 2: Mechanical properties of Alloy 617 in solution annealed (SA) and after aging at 700°C.

is found that with increase in ageing time, the volume fraction and size of γ' increased.

The hardness, YS and UTS, % elongation and impact toughness of Alloy 617 in solution annealed condition and aged conditions are evaluated and are presented in Fig 2. The increase in hardness and strength after ageing is due to precipitation of nano sized γ' that forms coherent γ/γ' interface, as both are having an FCC structure and very close lattice parameters, which hinders the active dislocation movement during deformation leading to increase in strength. With further increase in aging time from 1000 h to 4000 h, slight reduction in hardness and strength is observed due to coarsening of γ' precipitates. However, the ductility and Charpy V-notch impact toughness reduced drastically from 295J in the solution annealed condition to 70J after aging for 1000h.

Lattice Strain

X-ray diffraction analysis has been carried out to evaluate the effect of precipitation on lattice strain in the material. The XRD peaks belonging to γ and γ' overlapped in the pattern of aged specimens indicating close lattice parameters. Peak shift is found in the diffraction patterns

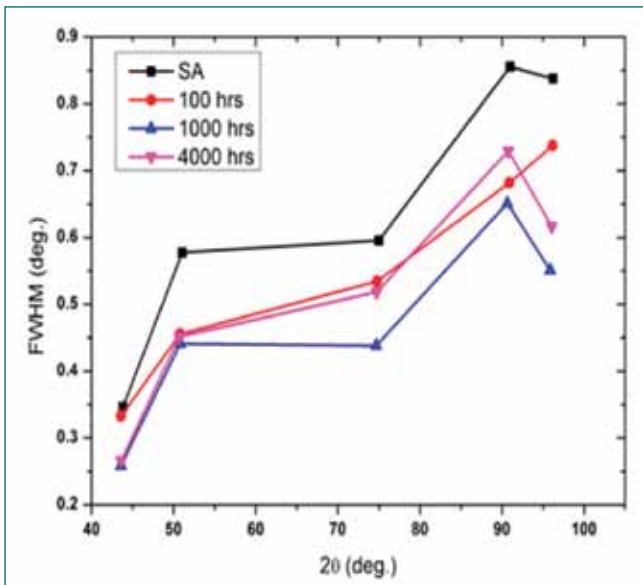


Fig. 3: Full width half maximum of XRD peaks of Alloy 617 in different ageing conditions

of the aged specimen when compared to the solution annealed specimen. The peak broadening of solution annealed and aged specimens are anisotropic as seen in Fig. 3 where, FWHM follows a zig-zag pattern as function of 2θ . The common cause for strain broadening are dislocations or lattice defects with strain field similar to that of dislocations such as stacking faults, grain boundaries, and coherency strains etc.

The anisotropic broadening was modeled using the Rietveld method by implementing Stephen's phenomenological model in GSAS software. Williamson-

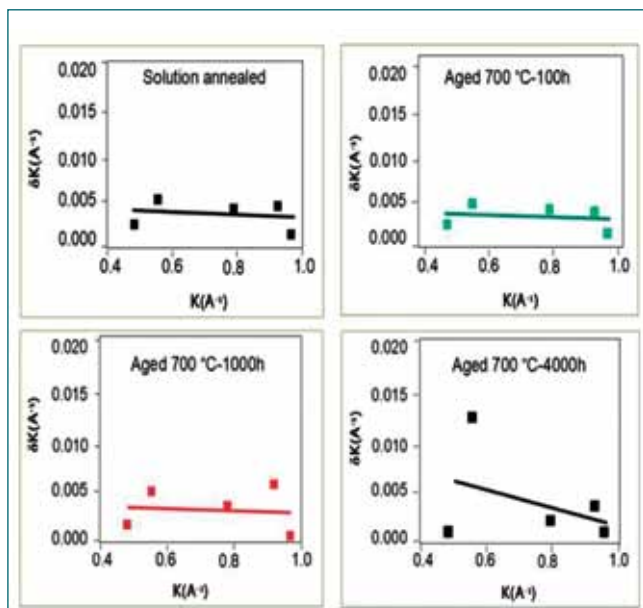


Fig. 4: Williamson-Hall plots for γ matrix in different aged conditions

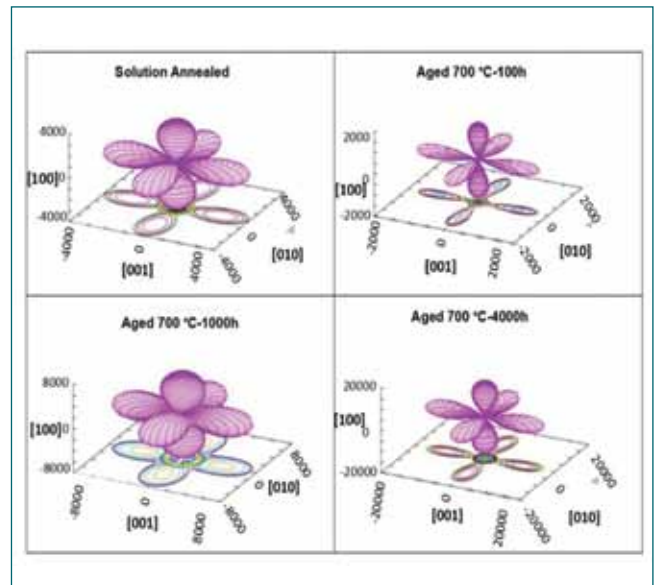


Fig. 5: Three dimensional strain distribution in Alloy 617 in different aging conditions (note the difference in the y axis scales in the plots)

Hall plots of γ and γ' have shown slope variation as a function of ageing time, indicating changes in material lattice strain. While Williamson-Hall plots of γ' revealed isotropic strain on expected lines for intermetallic compounds, Williamson-Hall plots of γ matrix indicated presence of anisotropic strain (Fig. 4).

Stephen's phenomenological model was used to determine the three-dimensional anisotropic strain distribution in the γ -matrix. The three dimensional strain distributions in Alloy 617 at different aging conditions is presented in Fig.5. The strain decreased in 100h aged samples compared to as-received solution annealed samples. This is due to annihilation of defects that contribute to the strain in the material. Upon further aging, the strain in the matrix increased due to formation of γ' precipitate thereby, indicating that the coherency between matrix and precipitate is being maintained even up to 4000h aging.

The yield strength and tensile strength of Alloy 617 base metal after ageing heat treatment increased by 150-200 MPa in comparison to as-received condition. In contrast, the ductility and toughness showed significant reduction after ageing. Three dimensional strain distributions obtained from Stephens phenomenological model indicated that the magnitude of anisotropic strain varied with aging time. This is an indication of evolution of coherency strain in the matrix upon the precipitation of γ' . The change in mechanical properties after simulated ageing heat treatment correlates well with the observed microstructural transformations.

V.38 Molecular Dynamics Simulations on Mechanical Properties and Associated Deformation Mechanisms of Model Materials

The rapid progress of computational capability and the availability of reliable inter-atomic potentials has made the molecular dynamics (MD) simulations a major tool to understand the deformation mechanisms at the atomic scale. In this work, we utilize MD simulations to understand the deformation mechanisms, especially the grain boundary (GB)-GB interactions in model BCC and FCC systems. Fe and Cu were selected as the model systems for BCC and FCC structures, respectively. All simulations were carried out in LAMMPS package employing Mendeleev EAM potential for BCC Fe and Mishin EAM potential for Cu. The deformation was carried out in a displacement-controlled manner at constant strain rate of $1 \times 10^8 \text{ s}^{-1}$ and temperature of 10 K.

Figure 1 shows the formation of new GB due to the interaction of an incoming twin and dislocation with existing $\Sigma 11$ GB in a model BCC Fe. It is observed that initially a twin embryo nucleates from the crack tip and approaches towards the existing GB (Top row in Fig. 1). Once the twin reaches the GB, its penetration and transmission to the next grain gets restricted. Following this, the twin width increases with increasing strain due to the continuous glide of twinning partials along the TBs. In this process of twin growth, the twinning partials interact with existing GB and transform it into a new GB (Top row in Fig. 1). This new GB consist of $\langle 100 \rangle$ immobile dislocations separated by a finite distance. The detailed analysis of misorientation angle indicated that this new GB formation has occurred according to the reaction $\Sigma 3 + \Sigma 11 \rightarrow \Sigma 33$. Figure 1 (bottom row) shows the formation of a new GB due to the interaction of a

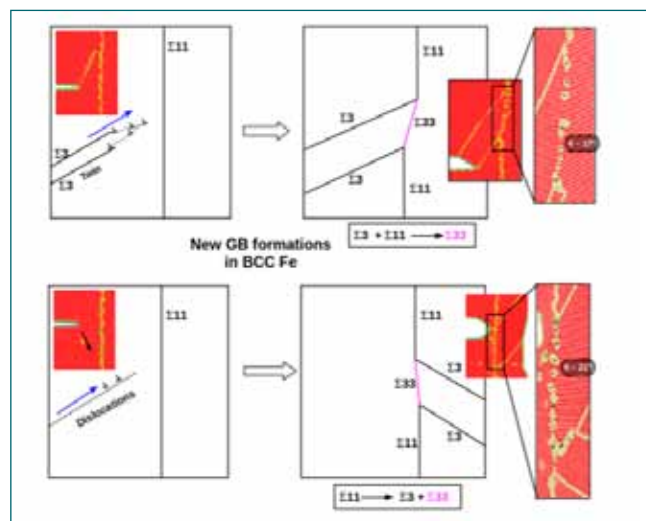


Fig. 1: Formation of new GB due to the interaction of twin and dislocation with existing $\Sigma 11$ GB in a model BCC Fe

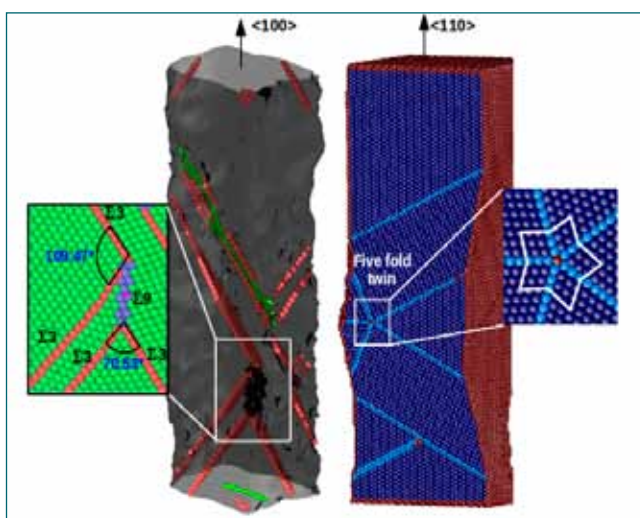


Fig. 2: GB-GB interactions leading to the formation of $\Sigma 9$ GB and five-fold twin in a model FCC Cu system.

dislocation with $\Sigma 11$ GB. Once the incoming dislocation reach close to the boundary, it triggers the nucleation of twin from the GB into the next grain. With increasing strain, more and more dislocations nucleate from the crack tip along with an increase in the twin width. The continuous twin growth leads to the formation of a new GB consisting of a series of $\langle 100 \rangle$ type immobile dislocations. This GB formation has occurred according to the reaction: $\Sigma 11 \rightarrow \Sigma 3 + \Sigma 33$. Figure 2 shows the GB-GB (twin-twin) interactions leading to the formation of $\Sigma 9$ GB and five-fold twin as observed in a model FCC Cu. The formation of $\Sigma 9$ GB occurs due to the repeated interaction of twinning partials on two interacting TBs or $\Sigma 3$ GBs (Fig. 2 left). Each interaction of partials adds one structural unit to the GB and the continuous repetition of this process adds more and more structural units leading to an increase in length of the $\Sigma 9$ GB. In other words, these results suggest that $\Sigma 9$ boundary is an array of $1/6[011]$ type stair-rod dislocations and forms at the intersection of two $\Sigma 3$ GBs. Twin-twin interactions can also lead to the formation of five-fold twin as shown in Fig. 2 (right). This five-fold twin nucleates from the distorted lattice formed close to the corner. Formation of the distorted lattice at the corner is a result of the continuous glide of partial dislocations on the two intersecting TBs. The understandings from this investigation help us to explain how the $\Sigma 9$ boundary takes part in reconfiguring the GB network during the plastic deformation of polycrystalline materials and sheds a new light on the formation mechanism of five-fold twin.

V.39 Electrochemical Preparation of Th_7Ni_3 Intermetallic in CaCl_2 melt by FFC Cambridge Process

Conventionally metals are prepared by chemically reducing the metal halides or oxides with a suitable reducing element based on the Ellingham diagram. Electrochemical reduction of solid metal oxides in a suitable molten salt medium has emerged as an interesting and popular method for the preparation of metals and alloy in recent times. In this high-temperature molten salt electrolysis process, the solid metal oxide cathode is directly converted to respective metal or alloys by electrons or in-situ electro-generated reductant metal, e.g. Ca, Li etc., under application of a constant cell potential or current between the cathode and the platinum or graphite anode. Several important metals and alloys, including actinide metals and alloys, e.g. U, U-Pu, Pu-Fe, U-Ti, U-Mo, U-Nb alloys etc. have been prepared using this method from their respective oxides. FFC (Fray-Farthing-Chen) Cambridge process is one such process, wherein the reduction of metal oxide cathode is effected by electrons. Recently, electro-reduction of solid ThO_2 was attempted in our laboratory in CaCl_2 melt at $900\text{ }^\circ\text{C}$ using FFC Cambridge process. The process was found feasible for Th metal preparation. However, it was observed to be kinetically sluggish due to the high electrical resistivity and thermodynamic stability of ThO_2 . In the study the extent of conversion of ThO_2 to Th was found to be $\sim 93\%$ after conducting the electro-reduction experiment for 96 h. Incorporation of a less stable metal oxide e.g. NiO, in the ThO_2 matrix that leads to the formation of a stable intermetallic

compound e.g. Th_7Ni_3 , might improve the electrical conductivity of the oxide mixture and thereby might lead to faster reduction kinetics. Hence, in the present study feasibility of preparation of Th_7Ni_3 intermetallic from ThO_2 and NiO mixtures (7:3 molar ratio) was investigated in CaCl_2 melt at $900\text{ }^\circ\text{C}$ by FFC Cambridge process. The intermetallic compound Th_7Ni_3 is also known to exhibit superconductivity at $-271.17\text{ }^\circ\text{C}$ (1.98K). In-house prepared ThO_2 [from $\text{Th}(\text{NO}_3)_4 \cdot 5\text{H}_2\text{O}$ by citrate gel-combustion method] and commercially available NiO were taken in 7:3 molar ratio. 3 wt.% PVA (binder) and 1.5 wt.% PEG (plasticizer) solutions were added to metal oxide mixture to form a slurry and it was dried. The dried mixture was ball-milled in a planetary ball mill for 3 h at 150 rpm for homogenization of the mixture. Green pellets (mass = 0.8 g, 12.5 mm dia.) were prepared using a uniaxial pellet press and these were subsequently sintered in air atmosphere at $1200\text{ }^\circ\text{C}$ for 2.5 h. The open porosity of the sintered mixed (Th,Ni) oxide pellets were measured by the water impregnation method using Archimedes' principle and was found to be $\sim 30\%$. The mixed metal oxide preform was characterized by XRD and SEM-EDS. Fig. 1 depicts the X-ray diffraction pattern of the same and the presence of ThO_2 and NiO can be observed in the pattern. SEM image and EDS elemental mapping of the cross-section of the oxide pellet is shown in Fig. 2 and almost uniform distribution of ThO_2 and NiO in the mixed oxide matrix can be visualized. The elemental composition of Th, Ni and O, as obtained from

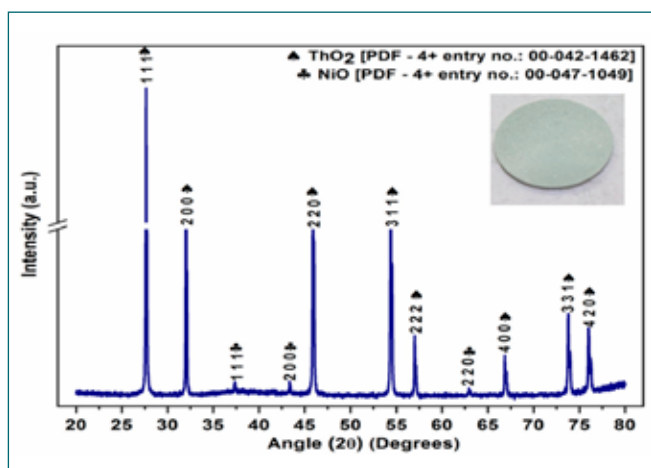


Fig. 1: XRD pattern and photograph of sintered mixed (Th,Ni) oxide pellet

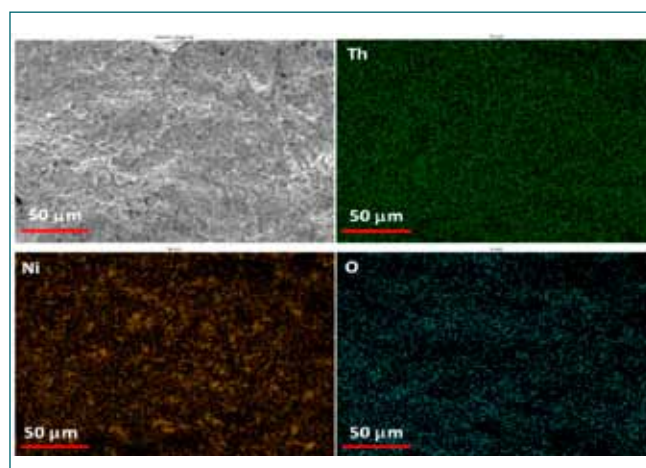


Fig. 2: SEM and EDS elemental mapping of Th, Ni and O in sintered mixed (Th,Ni) oxide pellet (cross-section)

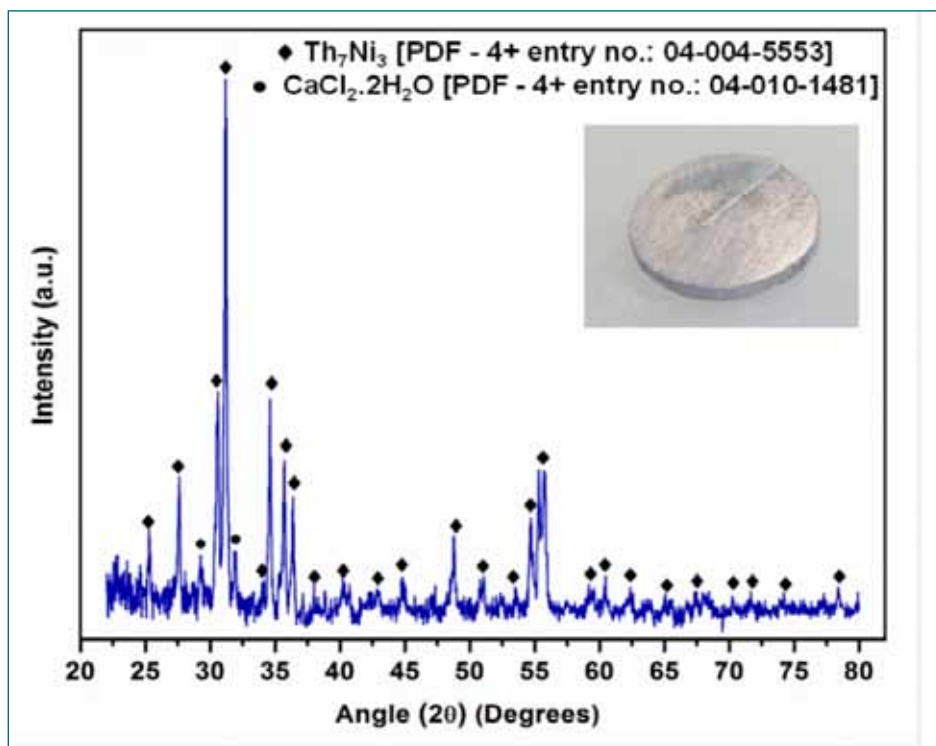


Fig. 3: XRD pattern and photograph of sintered mixed (Th, Ni) oxide pellet (bulk, uniformly ground powder) after electro-reduction experiment conducted for 48 h

EDS map sum spectrum, was 78%, 13.2% and 8.8%, respectively. Anhydrous CaCl_2 electrolyte was prepared by vacuum drying at 200 °C commercially available $\text{CaCl}_2 \cdot 2\text{H}_2\text{O}$ for a prolonged duration for complete removal of crystalline water. Molten salt electrochemical experiments were carried out at 900 °C in a specially designed leak-tight cell made of Inconel 600 containing CaCl_2 electrolyte and the required electrodes under continuous purging of argon.

Cyclic voltammetry studies conducted with Mo metallic cavity electrodes with ThO_2 and NiO revealed that the

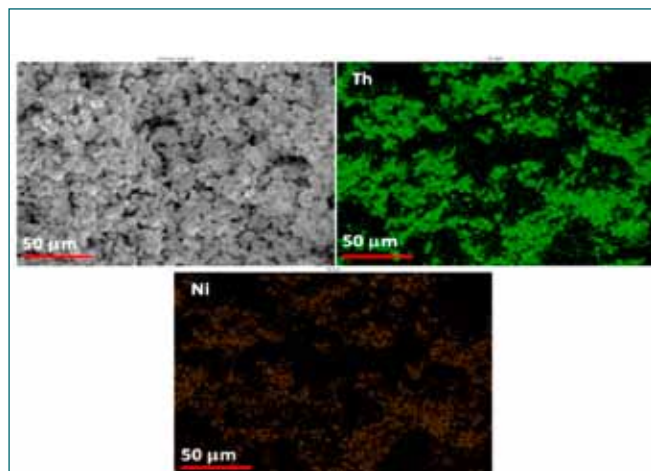


Fig. 4: SEM and EDS elemental mapping of sintered mixed (Th, Ni) oxide pellet (cross-section) after electro-reduction experiment for 48h

electro-reduction of NiO occurs at a less cathodic potential than that of ThO_2 . Constant voltage electrolysis experiments were conducted with sintered mixed (Th, Ni) oxide pellet as cathode and HD graphite as an anode at 3.1 V cell voltage for 6, 12, 24, and 48 h in CaCl_2 melt at 900 °C. The operating voltage (3.1 V) was lower than the decomposition potential of CaCl_2 (3.21 V) at 900 °C. The half-cell potentials were monitored using Ni|NiO reference electrode during electrolysis. The electrolysis commenced with a high current (2.68 A), followed by a gradual

decrease and attained a low value (0.17 A) after 48 h. In the beginning of electrolysis cathode potential was found to be ~ -1.7 V (vs. Ni|NiO), which might attribute to the reduction of NiO to Ni. After that the cathode potential was found to be almost stable at ~ -2.05 V (vs. Ni|NiO), which most probably was due to the formation of the intermetallic Th_7Ni_3 . After electrolysis, the cathode products were ground thoroughly using mortar-pestle and the bulk was analyzed by XRD. The 6 h electrolyzed product showed the presence of Ni and ThO_2 in the XRD pattern. In contrast, in the 12 h electrolyzed product, Th_7Ni_3 and ThO_2 phases were observed. In the 24 h and 48 h electrolyzed product, Th_7Ni_3 phase was solely perceived in the XRD patterns. The presence of $\text{CaCl}_2 \cdot 2\text{H}_2\text{O}$ phase was observed in all the electrolysed products as XRD analysis was carried out without removing the occluded electrolyte. Fig. 3 depicts the photograph and XRD pattern of 48 h electrolyzed product. The SEM image and EDS elemental mapping of the 48 h electrolyzed product cross-section is shown in Fig. 4. The elemental composition of Th and Ni as obtained from EDS map sum spectrum, was 91% and 9%, respectively.

Electrochemical preparation of Th_7Ni_3 intermetallic from mixed (Th, Ni) oxide was demonstrated for the first time using FFC Cambridge process in CaCl_2 melt. The presence of nickel accelerated the reduction kinetics of ThO_2 .

V.40 Li Intercalation in Graphite and Formation of Li_2C_2 in LiCl-KCl Eutectic Melts

Electrodeposition of uranium in LiCl-KCl for pyroprocessing of spent metallic fuels is carried out at SS430 electrode. At high temperatures, the first deposition layer of uranium deposit gets strongly adhered on the steel surface that is difficult to scrap. A very fine layer of metallic uranium remains on the cathode surface that slightly decreases the percentage recovery of deposit in typical electrorefining campaigns. It was long thought that a cathode with self-scraping features would rather help in higher recovery especially in remotely operable systems since scrapping mechanisms may be difficult to design evolve in a confined space. If one compares graphite and steel, graphite is more inert when used as counter electrode and steel is better suited under cathodic polarization conditions at 773 K in LiCl-KCl eutectic melt in absence of any oxide ions. Graphite was explored in this work under cathodic polarization conditions for it to be used as cathode for electrorefining of uranium. Typical cyclic voltammograms of LiCl-KCl eutectic melt at graphite electrode (Fig. 1a) recorded against $\text{Ag}^+|\text{Ag}$ reference at 773 K comprises of a reversible redox couple in potential range -0.50 to -0.40 V and a significantly high current density at -1.10 V and beyond is possibly the cathodic limit potential of LiCl-KCl melt at graphite. This is in contrast to the stability window of melt at metal electrodes where cathodic limit is known to be at around -2.35 V due to $\text{Li}^+|\text{Li}$ couple. This observation confirms that there is a change of about 1.2 V for cathodic stability of Li^+ ions at graphite. A sharp change in current density at -1.10 V (Fig. 1) is due to the accumulation of Li^+ and its reduction on graphite surface that is followed by Li intercalation forming Li-C compounds. Assuming density of graphite at 1.80 g/cm^3 , porosity of 5-10% is expected favouring

the mass transport of Li into the graphite surface, which remains in dynamic equilibrium with Li^+ accumulated around the graphite surface consequently limiting the electrochemical window of LiCl-KCl eutectic melt. Reduction process at -1.10 V can be expressed as

$\text{Li}^+(\text{melt}) + 1e^- \rightarrow \text{Li}(\text{C})$ Redox process in potential range -0.50 to -0.40 V comprises of a reversible soluble-soluble couple that was further explored by cyclic voltammetry. Number of electrons transferred was found to be 2 suggesting that a divalent anion may be involved in the single step oxidation. Potentiostatic electrolysis at -1.25 V at graphite electrode was performed and exposed graphite electrode was characterized by XRD (Refer Fig. 1b) that showed Bragg peaks of Li_2C_2 that can be represented in terms of Li^+ and acetylide ion C_2^{2-} isoelectronic to dinitrogen ion. In LiCl-KCl eutectic melt, Li_2C_2 has limited solubility and it dissociates to the respective Li^+ and C_2^{2-} ions. Oxidation wave at -0.458 V represents the reversible discharge of C_2^{2-} ions to C. Following set of reactions govern the cathodic process at -0.519 V:



Thus, at -0.519 V, cathodic step involves formation of Li_2C_2 (Step 1) that dissociates into Li^+ and C_2^{2-} ions (Step 2). -1.10 V (Fig. 1a) refers to apparent equilibrium potential of $\text{Li}^+|\text{Li}$ couple at graphite. Gibbs energy of formation of Li_2C_2 was estimated from peak potential for formation of Li_2C_2 and apparent equilibrium potential of $\text{Li}^+|\text{Li}$ couple at graphite electrode and was expressed as (in kJ/mol-atom)

$$\Delta_f G_{\text{Li}_2\text{C}_2}^\circ = -76.753 + 5.994 \times 10^{-2} T(\text{K}).$$

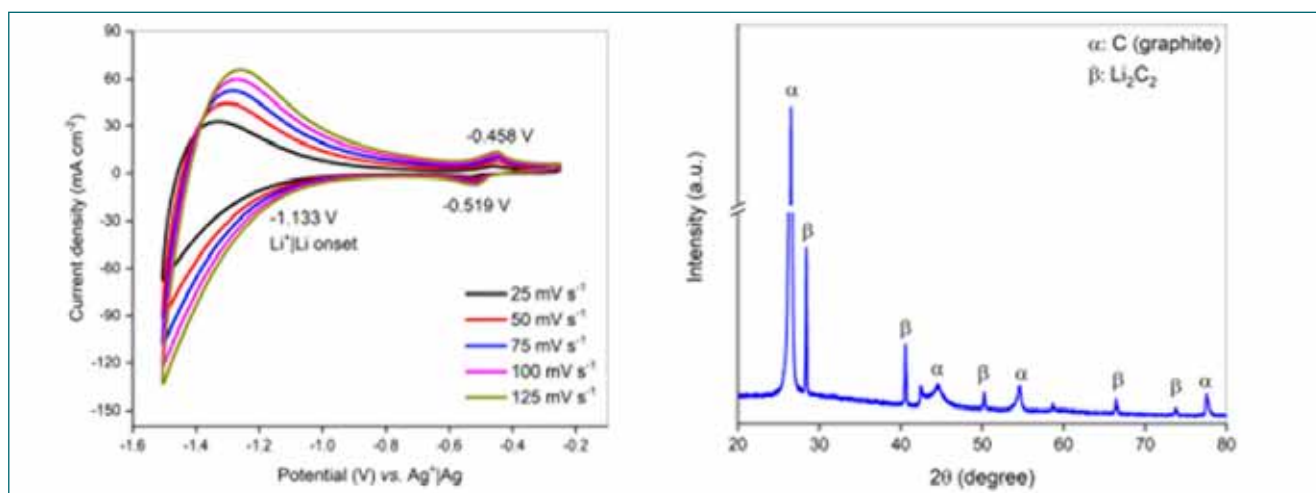


Fig. 1: (a) Cyclic voltammograms of LiCl-KCl eutectic melt at graphite electrode at 773 K. (b). XRD pattern of graphite electrode after electrolysis at -1.25 V.

V.41 Coupled heat and mass transfer simulation of melt crystallization of LiCl-KCl-CsCl mixture

High temperature electrorefining of metal fuel results in the accumulation of heat generating fission products especially Cs-137 in the eutectic salt. These fission products need to be removed from the salt so as to reduce the heat load and contamination. Melt crystallization technique is a simple separation process being pursued for separation of fission products. This involves purification of a substance from a liquid mixture by solidification of the desired component. The crystals are generated by cooling the melt and are formed at a temperature near the pure-component freezing point. The product is collected in its crystal form and the concentrated waste can be separated in liquid state. Numerical modeling of crystallization of LiCl-KCl eutectic mixture containing 5 wt% of CsCl has been carried out using ANSYS Fluent (19.2). Also, the extent of segregation of solute for various cooling rates and crystallizer geometry has been numerically evaluated.

Melt Crystallization model details

During solidification, the salt initially exists in liquid phase with a uniformly distributed solute. When the temperature is lowered, solidification starts near the walls and the solute gets rejected from the solid phase to the liquid phase through an intermittent mushy zone. At the interface, solute transport occurs

by diffusion or micro-segregation. In the LiCl-KCl-CsCl phase diagram, the mixture exists as a ternary eutectic at 260°C containing 57 weight % CsCl and 25, 18% LiCl and KCl respectively and pure LiCl-KCl binary eutectic exists at 355°C. So, a maximum Cesium enrichment of 57 wt% can be obtained if the cooling rate in the crystallizer is tuned to the temperature profile of the phase diagram.

Numerical modeling of the solidification process was carried out to identify the optimal parameters for the separation of CsCl from the LiCl-KCl eutectic salt. Solidification and melting module of ANSYS Fluent (19.2) was used for the simulation. A benchmark (Ammonium chloride–water system) solidification problem was validated initially. The model geometry is an axisymmetrical rectangular domain of size 77mm x 220mm height. Hexahedral mesh of 1mm size with 16940 elements was created. Governing equations for the model includes continuity equation, momentum equation, energy equation and species transport equation. Solidification module of ANSYS-Fluent was activated with Lever rule to simulate micro segregation.

Model results and optimization

Cooling rate and crystallizer surface geometry were considered relatively significant parameters for crystallization of molten salts. Flat, tapered and round bottom were considered as geometrical parameters. Effect of different cooling rates was studied for heat transfer coefficients from 5 to 200W/m².K. Effect of these parameters was studied on the solidification of LiCl-KCl salt, the extent of separation of CsCl from the initial melt and the transient liquid fraction distribution in the crystallizer. The modeling also focused on the cooling time of the crystallizer so as to separate the impure CsCl salt from the pure LiCl-KCl salt mixture.

Tapered bottom crystallizer was found to be suitable for natural and forced cooling. Also, a maximum separation of 54.2 wt% CsCl containing 92% liquid salt can be achieved in 6320s in this geometry. Typical temperature, liquid fraction and CsCl concentration contours for a tapered bottom crystallizer are shown in Fig. 1a, b and c respectively.

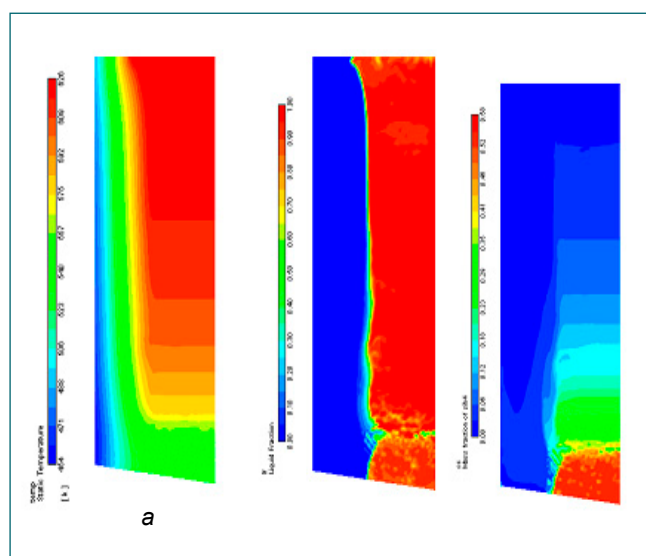


Fig. 1: a) Temperature contour b) Liquid fraction contour c) CsCl concentration contour

V.42 Automatic droplet dispensing system for producing uniform size of microspheres using sol-gel method

The droplet dispensing system is uniquely designed and developed for producing uniform size of microspheres of uranium oxide using sol-gel method in the sphere-pac fuel fabrication route. The solution of uranium oxide for the fuel is prepared, processed and maintained at less than 5 oC to avoid making the gel. The developed system was capable of delivering fuel at a constant flow from a feed tank. As the fuel level falls in the feed tank, the back pressure above the level of fuel changes, which serves as feedback to the pressure regulator and transfers the fuel through a mass flow controller to maintain the constant flow.

The automatic droplet dispensing system consists of various valves & fittings, feed tank, mass flow controller, pressure controller, hardware and software for automation towards production of uniform size of gel by maintaining constant flow of fuel across the nozzle. The schematic of the system requirements is presented in Fig. 1.

A 500 ml volume of stainless steel (SS-316) of feed tank was developed with double wall to maintain the desired low temperature using chiller. The entire system was designed with double wall in such way that during the process, temperature of the solution was maintained below the 5 °C using chiller control mechanism.

The hardware (PIDcontroller-PXF5, signal conditioning, data processing based on 8051 microcontroller, universal process indicator/controller-UT-102, etc.) and software (Human machine interface-standalone) were uniquely developed to control the process & various parameters, display & save the different parameters in a file for the study of microspheres with respect to flow, time, pressure, etc., and have various unique features viz., set the flow rate, chamber pressure, percentage opening of valves, etc. The photograph of developed automatic droplet dispensing system is presented in Fig. 2.

Table. 1. Li concentration (in at.%) in Li-Cd alloys

S. No.	Li concentration in Li-Cd alloy	Li concentration in Li-Cd alloy before annealing	Li concentration in Li- Cd alloy after annealing
1.	25	30	36
2.	50	50	56
3.	75	72	76

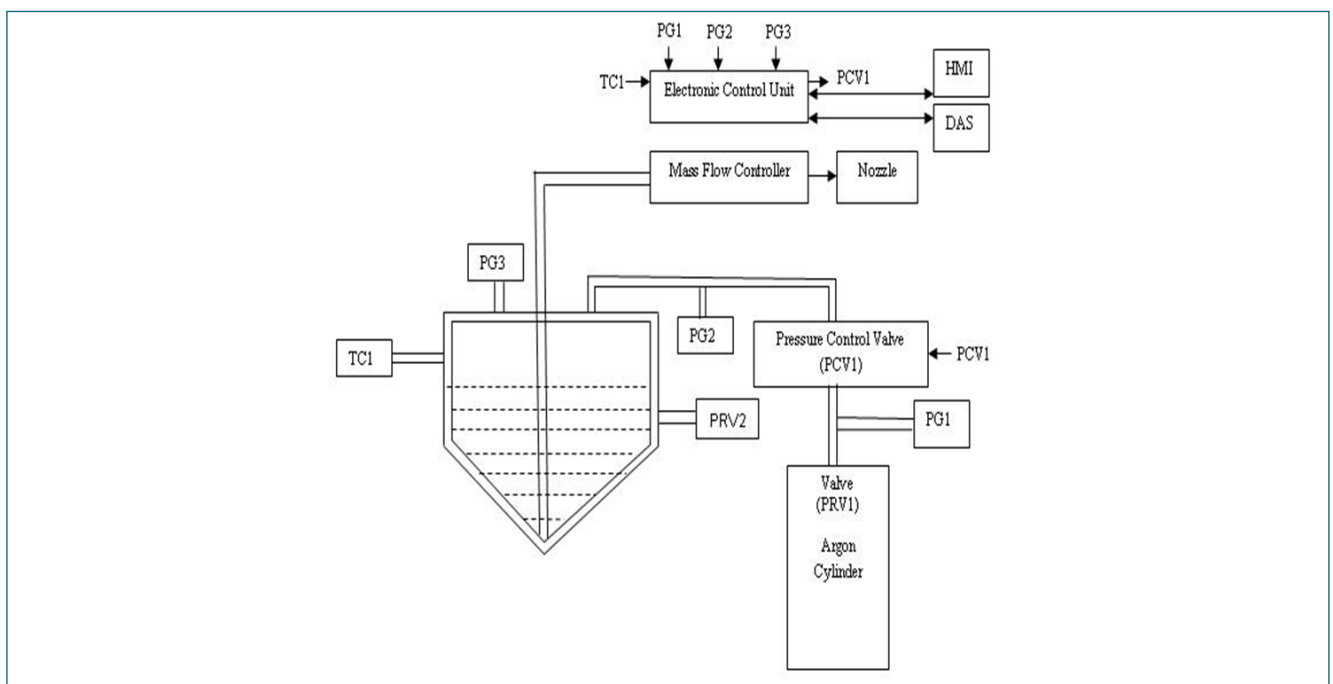


Fig. 1: Block diagram of droplet dispensing system



Fig. 2: Photograph of droplet dispensing system

Typically, the solution, which is required to be transferred (temperature from 1-5 °C, density from 1.6 – 2 g/cc, viscosity from 0.1 to 500 cp, etc.) from feed tank to nozzle by applying argon pressure across the solution of feed tank and maintains the constant flow across the nozzle using feedback pressure of feed tank. Feed tank was pressurized by using argon and the solution is then transferred through a ¼ inch OD tube through mass flow controller (OPTIMASS 3400 - Coriolis low mass flow meter) and further introduced into a 500 – 1200 µm nozzle so that it can fall in silicon oil at 90 °C as a gel for making the micro sphere.

The pressurization and controls in system were carried out at various locations using pressure gauge (OEM Pressure transmitter-JUMO MIDAS S05), pressure relief valve and temperature & pressure control valve (Fuji electric-PXF5/9, Burkert-2863, 8605, 3280, 3285, etc). The temperature of tank was measured using RTD. Mass flow controller (MFC) regulates the desired the flow rate based on feedback pressure of the tank. For production of uniform size of gel, constant flow was required which was set by user. Since, flow rate decreases with time due to pressure drop in the feed tank, hence more pressure



Fig. 3: The Snap shot of droplet system in fume hood

was required in tank to maintain the constant flow. The hardware and software were developed to process the all signals (mass flow controller, feedback pressure, flow, temperature, etc.) and provides more pressure in tank so that constant flow rate will be maintained across the nozzle through mass flow controller. Finally, MFC further regulates the constant flow of solution across the nozzle for precise control. The system was tested with standards inputs (pressure, flow rate, temperature, etc.) and found that results were meeting with an accuracy of 98%.

The dispensing system was installed and integrated with modular glass column in walk-in fume hood and tested with standard inputs and found that all parameters were meeting with standards. The snap shot of droplet dispensing system is presented in Fig. 3 Initially, dispensing system was tested for trail run with water, silicon oil and nitrate solution, etc. and found that desired results were achieved. After the getting the experience, the system will be tested with uranium oxide solution for the fabrication of fuel of mixed uranium oxide microspheres.

V.43 Commissioning of High Purity Argon Glove Box Facility with Process Equipment for DOER Studies

A programme for conversion of metal oxides to metal based on high temperature molten salt electrolysis was taken up in Radiochemistry Laboratory (RCL). The process has been demonstrated for metal preparation from ZrO_2 , UO_2 (200g), etc. in laboratory scale. The U metal thus produced was electrefined and consolidated as an ingot. Now, it is planned to conduct scaled up experiments inside glove box up to 2kg UO_2 per batch. The various process steps include, blending of UO_2 powder, preparation of UO_2 green pellets using rotary pellet press, sintering of green pellets, preparation of molten salt, electrolysis and salt distillation of the cathode product. For this purpose, an inactive laboratory was modified and qualified for handling radioactive materials. Further, an engineering facility consisting of a set of glove boxes, electrolytic cell, blender, rotary pellet press, mini crane etc. were fabricated and commissioned. The salient features are described below.

Glove boxes with process equipments

Glove boxes are normally operated in ambient conditions and so SS-304L (5mm thick) was chosen as the material of construction. As glove boxes were customized in size, extensive trials were carried out and special jigs / fixtures were used to control distortion during fabrication.

This facility housed five glove boxes and the special features are described below. A 3m long glove box (air

box) (Fig.1) was designed and fabricated to house two major equipments i.e blender and the rotary pellet press. Laser cutting was employed for cutting the glove box frames to achieve better control on dimensions and planarity of the glove box. Other glove boxes were inert glove boxes housing the process equipments like electrolytic cell and mini crane. These equipments were designed, fabricated, installed and commissioned in the high purity inert glove boxes. A leak rate of less than 0.05% of box volume/hour, argon purity of 5 ppm of O_2 and moisture was achieved for all inert glove boxes.

Blender

Blending process is highly complicated when a liquid is added to powder. Hence, correct mixing technology was chosen based on the properties of input powder and the output product. Based on these challenges, a customized blender of 1kg capacity was designed, fabricated and installed (Fig.2). Compact scissor jack was specially designed, machined and coupled with DC motor for stirring the powder-liquid mixture. The blades had suitable profile to provide good blending.

Rotary pellet press

An eight station rotary pellet press (Fig.3) has been specially developed for production of about 4000 pellets per batch of $\varnothing 6$ mm with height varying from 5 mm to 15 mm. This unit is primarily employed for



Fig. 1: Special glove box (3m long)

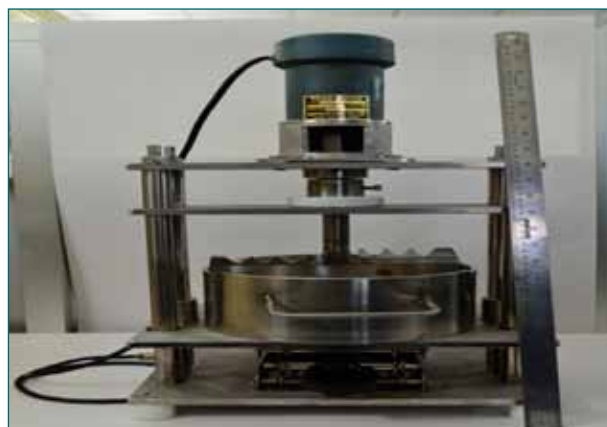


Fig. 2: Blender



Fig. 3: Rotary pellet press in glove box

preparation of green UO_2 pellets. The special features include modular construction to suit installation of a portion of press inside the glove box, rotary sealing arrangement for effective containment of radioactive materials and driver unit outside the glove box for easy maintenance. The press is qualified by operating the system idle for 24 hours and production of pellets using Titanium dioxide and thereafter with UO_2 powder.

Electrolytic cell

An electrolytic cell (Fig.4), loaded with 15 kg of LiCl and 1%Li₂O as the electrolyte, is made out of Inconel-600 (Outer vessel) and SS-316L (Inner main vessel). Upon electrolysis using platinum anodes, the oxygen in the



Fig. 4: Electrolytic cell in glove box



Fig. 5: Mini crane in glove box

metal oxide is stripped off and the metal remains at the cathode. The cell is designed for an operating pressure and temperature of 1bar and 650°C respectively in a highly corrosive and radioactive environment. The salient features of the vessel included leak-tight arrangement for insertion and retrieval of components under inert condition from molten salt and fins / modular cooling water jacket for effective cooling of the top flange.

Mini Crane

In order to handle the heavy components of electrolytic cell in glove box, a modular mini crane (Fig.5) of 50 kg capacity was designed and developed meeting single failure criteria. The crane is designed for a vertical lift of 750 mm and LT travel of 2000 mm.

Conclusion

The laboratory was qualified for radioactive material handling and the glove boxes facility for DOER work were commissioned. Five glove boxes were fabricated, installed, leak tested and commissioned with the process equipments like blender, rotary pellet press, electrolytic cell and mini crane. Secondary HEPA filtration modules were developed. Suitable interlocks and instrumentation were added for flow, temperature and pressure measurement and to ensure safety for the operating personnel and the entire system.

V.44 Design and Development of Power Supply for Electron Bombardment Furnace of KEMS

Knudsen Effusion Mass Spectrometry (KEMS) is a proven vapor pressure measurement technique capable of determining partial pressures at high temperatures. The three distinct parts of the experimental set-up are: (1) molecular beam source (2) ion source and (3) mass spectrometer. A ceramic or alloy sample is placed in a small enclosure with a well-defined orifice known as a Knudsen cell, or effusion cell. The electron-bombardment heating is used to heat the cell placed inside a conductive envelope or block to further reduce thermal gradients. In the cell, near thermodynamic equilibrium conditions which require cell temperature has to be maintained very stable (± 1 K) at desired value to get accurate results. This requires accurate control of filament current, applied accelerating potential, emission current. As an import substitute a power supply to meet the requirement was designed and fabricated in-house. The same was installed and tested and performance was satisfactory.

Power supplies

The KEMS power supply contains two modules (1) High voltage source to apply voltage (600 V to 800 V) between

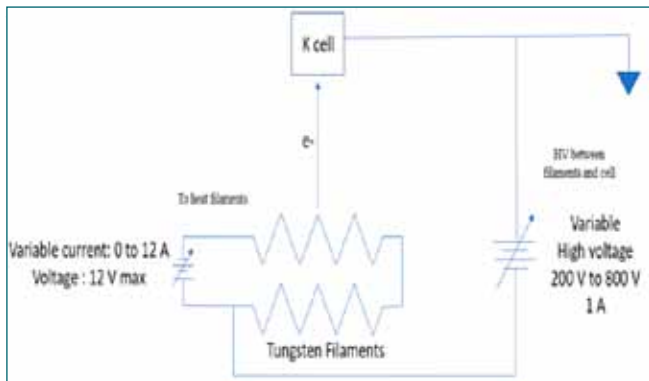


Fig. 1: Simplified line diagram – power supply modules

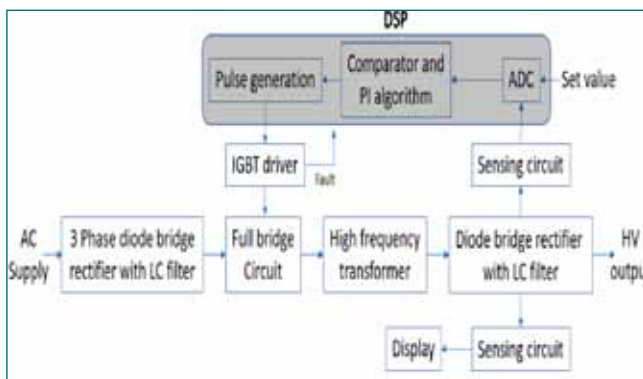


Fig. 2: Block diagram - High voltage module

and (2) Low voltage source to heat tungsten filaments in series to about 2700 K. The simplified line diagram of the system with power supply modules, filaments and cell are shown below in Fig 1.

The HV module maintains the output at desired value irrespective of changes in vacuum, input voltage and emission current. The system utilizes grounded K-type thermocouple for measurement of K-cell temperature. Emission current increases with increase in filament current for fixed acceleration voltage and constant vacuum and the emission current is adjusted automatically by adjusting filament current to maintain the cell temperature at desired value with feedback from thermocouple. The HV module utilizes Phase-Shifted Full Bridge (PFSB) DC/DC Power Converter with Insulated Gate Bipolar Transistor switches that form a full bridge on the primary side of the isolation transformer and diode rectifiers on the secondary side to rectify high frequency quasi square wave to constant DC voltage. Block diagram of high voltage generation module is shown in Fig. 2. Algorithm in Digital Signal Processor ensures the safe operation and the generates the required gate pulses to control of PFSB to maintain the set voltage. For the purpose of exciting filaments, a commercial low voltage power module is used.

Experiments were carried out by measurement partial pressure of silver and tin at different temperatures and the results generated were conforming good temperature stability with a regression factor of 0.9998. Experimental measurements of partial pressure of silver are shown in Fig. 3. The developed power supply maintained acceleration voltage and cell temperature at different user values as required for the experiments.

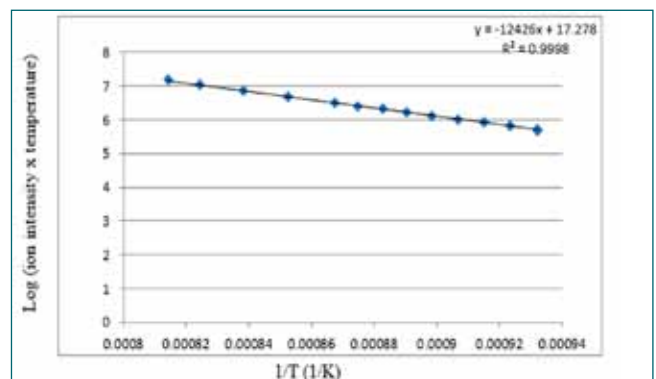


Fig. 3: Measurements of partial pressure of silver

V.45 Removal of Cs⁺ and Sr²⁺ ions from simulated Radioactive Waste Solutions using Zeolites-A Synthesized from Kaolin

Zeolites ($M_{n/p}[Al_pSi_qO_{2(p+q)}].wH_2O$) are framework structured crystalline materials made of silicon (Si), aluminum (Al) and oxygen with cavities and channels inside which cations, water and/or small molecules would be absorbed/occluded.

Zeolite-A was synthesized from kaolin activated at 500°C at relatively lower temperature than the studies reported in the literature. The metakaolin formed at 500°C was used to synthesise zeolite-A by treating with 1-5 M NaOH solutions at 80-100°C for 3-24 h under hydrothermal reaction condition. The XRD patterns of kaolin and meta kaolin are shown in Fig.1.

The zeolite-A was characterized by XRD, FT-IR and

SEM. The percentage of crystallinity and crystallite sizes of the zeolite-A were determined by using Rietveld analysis; the crystal system of zeolite-A was found to be cubic with space group ($Fm\bar{3}cFm\bar{3}c$) (Fig.2).

The ion-exchange property of zeolite-A for Cs⁺ and Sr²⁺ was explored at ambient temperature (25°C) and the results are shown in Table-1.

The adsorption efficiency of zeolite-A is higher for Sr²⁺ than that of Cs⁺; and adsorption capacities for Cs⁺ and Sr²⁺ ions were found to be 91.51% and 99.16 % respectively. Strontium substituted zeolite has higher crystallinity and lattice strain than that of caesium substituted zeolite-A.

Table 1 Concentrations of Cs⁺ and Sr²⁺ ions in the ion exchange medium before and after ion exchanging with zeolite-A.

Type of Ions	Actual concn. of metal ions in 1000 mg/L of initial salt solutions (mg/L)	Concn. of elements present after equilibration with 1000 mg/L CsCl solution (mg/L)	Concn. of elements present after equilibration with 1000 mg/L SrCl ₂ solution (mg/L)
Cs ⁺	789.41	67	Nil
Sr ²⁺	552.70	Nil	4.6
Cl ⁻	210.57 (in CsCl Sol.) 447.76 (in SrCl ₂ Sol.)	153	150
Na ⁺	Nil	141	159
Si ⁴⁺	Nil	50	43
Al ³⁺	Nil	22	36

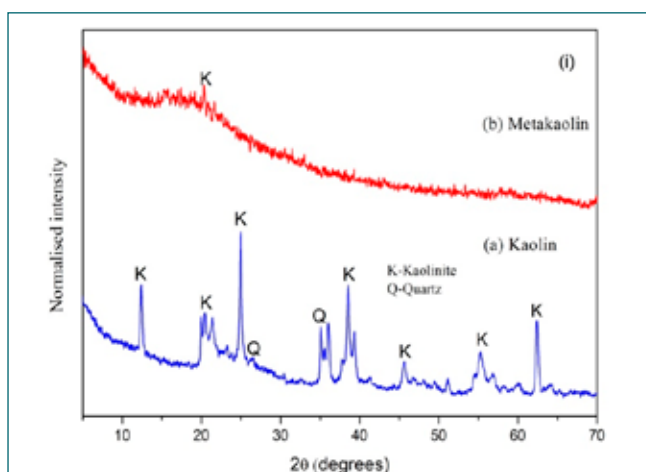


Fig. 1: XRD patterns of Kaolin and meta- kaolin

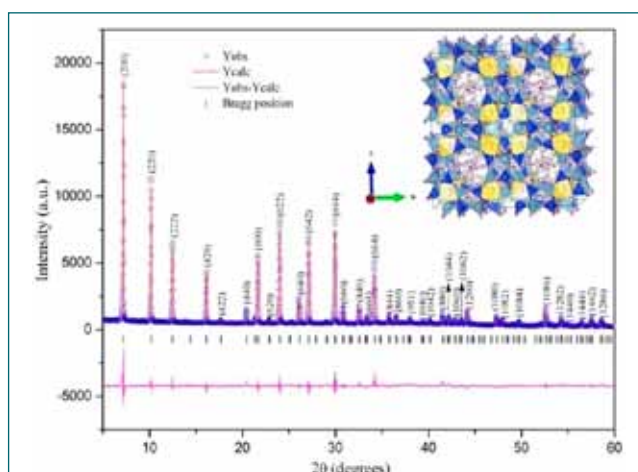


Fig. 2: XRD pattern of zeolite-A synthesized from kaolin

V.46 Electrochemical Studies on Hydride Ion Conducting CaBr₂-CaHBr Solid Electrolyte

Electro-chemical hydrogen meter (ECHM) is used to detect steam leak in secondary sodium circuit of fast reactor. It is an electrode concentration cell. It consists of a hydride ion conducting solid electrolyte whose composition is 60mol% CaBr₂-40mol% CaHBr. It was planned to measure the electrolytic domain boundary of this solid electrolyte from 400°C to 550°C at different low level hydrogen concentrations in liquid sodium fixed by cold trapping method. The electrolytic domain boundary (EDB) measurement consists of the total conductivity measurement of the solid electrolyte by impedance measurement and partial electronic conductivity measurement by DC polarisation technique (Hebbs-Wagner blocking electrode method). Compartment of an EDB cell having a CF-35 flange adaptor was designed and fabricated. Electrolyte thimble and blocking electrode suitable for the cell were machined from pure iron. The schematic of the EDB cell is shown in Fig. 1. Calculated amount of CaBr₂ and Ca were added in the compartment of the EDB Cell. It was heated under flowing hydrogen for the formation of the solid electrolyte, CaHBr at 600°C for 240 h. Blocking electrode was inserted in the molten electrolyte and cooled slowly to achieve pore free solid electrolyte. The cell was installed in a mini sodium loop. Experiments were carried out at 450°C and at dissolved hydrogen concentration of 87±5 ppb corresponding to the partial hydrogen pressure of 6.27 × 10⁻⁷ bar. Total conductivity is a combination of ionic and electronic conductivity.

$$\sigma_{\text{total}} = \sigma_{\text{ion}} + \sigma_{\text{electronic}}$$

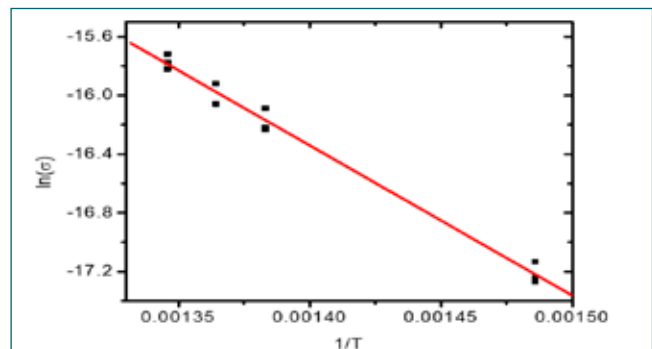


Fig. 2: Conductivity as a function of temperature

It was measured by impedance technique (AC). Partial electronic conductivity was measured by DC polarization technique. D.C. voltage less than the decomposition potential of the electrolyte was applied to the blocking electrode and steady state current was measured. At the steady state, only residual electronic current was present. The total residual current (I_{∞}) is given by $I_{\infty} = I_{\emptyset}(\text{hole}) + I_{\emptyset}(\text{electron})$. Transport number of H⁻ (t_{H^-}) = $\sigma_{\text{H}^-} / \sigma_{\text{total}}$, $\sigma_{\text{total}} = \sigma_{\text{H}^-} + \sigma_{\emptyset} + \sigma_{\ominus}$. σ_{\emptyset} and σ_{\ominus} are determined from the slope and intercept of the plot of the residual

current factor $\frac{I_{\infty}}{1 - e^{-\frac{EF}{RT}}}$ against applied potential factor $\frac{EF}{RT}$. Based on the conductivity measurements of AC and DC methods, t_{H^-} was calculated and found to be 0.91 at 723 K and 0.88 at 743 K. The activation energy for the hydride ion conduction is determined from the $\ln \sigma_{\text{H}^-}$ vs $\frac{1}{T}$ plot shown in Fig. 2 and found to be 85.0 kJmol⁻¹.

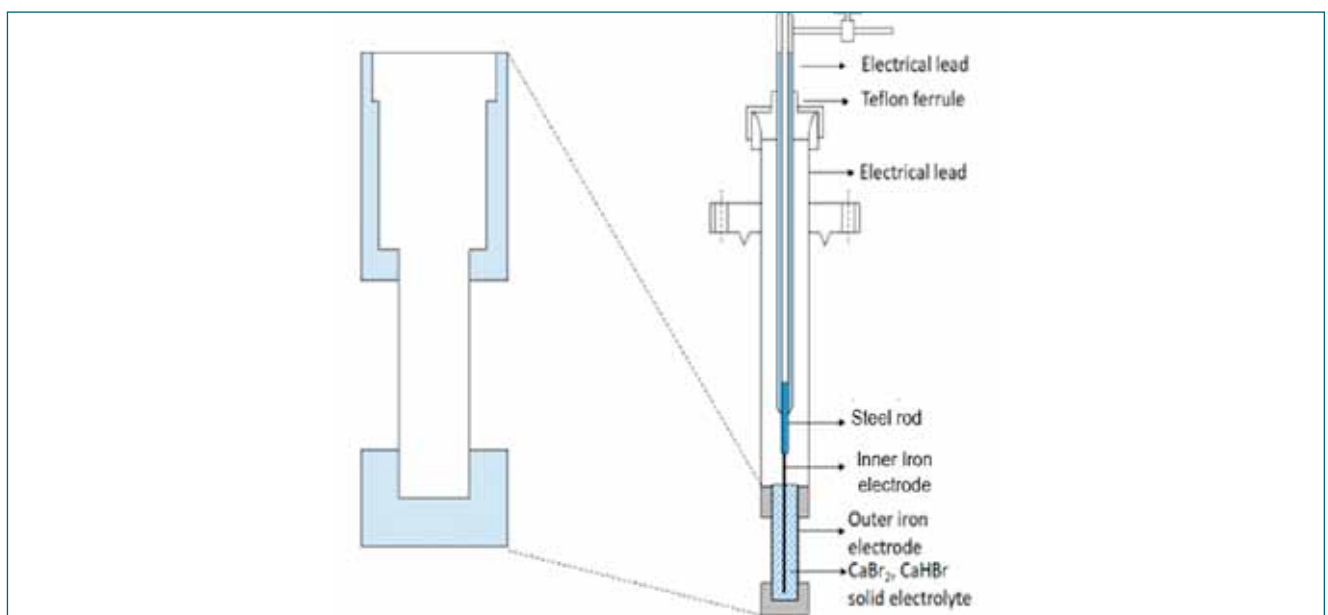


Fig. 1: Schematic of the EDB Cell assembly

V.47 Unraveling the Extraction and Coordination Behavior of U(VI) in Sulphuric Acid Medium by Bi-functional Dialkyl-H-Phosphonates

The estimation of uranium in various stages of the nuclear fuel cycle is required for quantitative estimation. Methods based on potentiometry are routinely employed in most of the radiochemical laboratories for precise and accurate determination of uranium. In this wet chemical method lot of analytical waste is generated which contains uranium in the range of mg/L in sulphuric acid medium (1 M) along with other metallic impurities like Fe, Cr, V, Mo etc. Recovery of uranium from analytical waste is essential because of its reuse as nuclear fuel and also as strategic material. Recovery of U from this waste solution is very much essential before its disposal. Uranium forms a strong complex with sulfate which makes recovery of U from analytical waste a challenging task. Recovery of U by conventional extractants like tri-*n*-butyl phosphate (TBP) is unfavorable due to poor extraction of U by TBP in presence of sulfuric acid. In this context, a solvent extraction method has been developed using dialkylhydrogen phosphonates for the recovery of U from sulphate bearing analytical waste, because of presence of functional groups P-OR, P-H, P=O in the molecule. The present study deals with the extraction of U(VI) from sulfate medium by linear and branched dibutylhydrogen phosphonates. Di-*n*-butylhydrogen phosphonate

(DBHP), di-iso- butylhydrogen phosphonate (DiBHP), & di-sec-butyl hydrogen phosphonate (DsBHP) were synthesized and distribution ratios ($D_{U(VI)}$) for U(VI) were measured by 0.55 M di-alkyl hydrogen phosphonates in *n*-DD from (0.1-6 M) H_2SO_4 . $D_{[U(VI)]}$ vs. $[H_2SO_4]$ was plotted and compared with that of 0.55 M TBP/*n*-DD system, shown in Fig-1(a). The D values for U(VI) by H-phosphonates are found to be significantly higher compared to that of TBP. D values for phosphonates at lower acidity (<1M H_2SO_4) is due to the ion exchange mechanism by enol form of H-phosphonates; whereas at higher acidity the extraction is through solvation. DsBHP shows better extraction compared to its homologues. Density functional theory calculations were performed to understand the electronic structure and complexation energies of U(VI). All calculations were performed using the ORCA version 4.2.1. Geometry optimization was performed by employing BP86 density functional in conjunction with the triple- ζ def2-TZVP basis sets. The resulting stationary points are characterized as energy minima by performing harmonic vibrational frequencies at the same level. Experimental vibrational frequencies, $\nu(P=O)$, are matching with the simulated ones. The lowest-lying electronic structures of DBHP, DiBHP, DsBHP are shown in Fig-1(b-d).

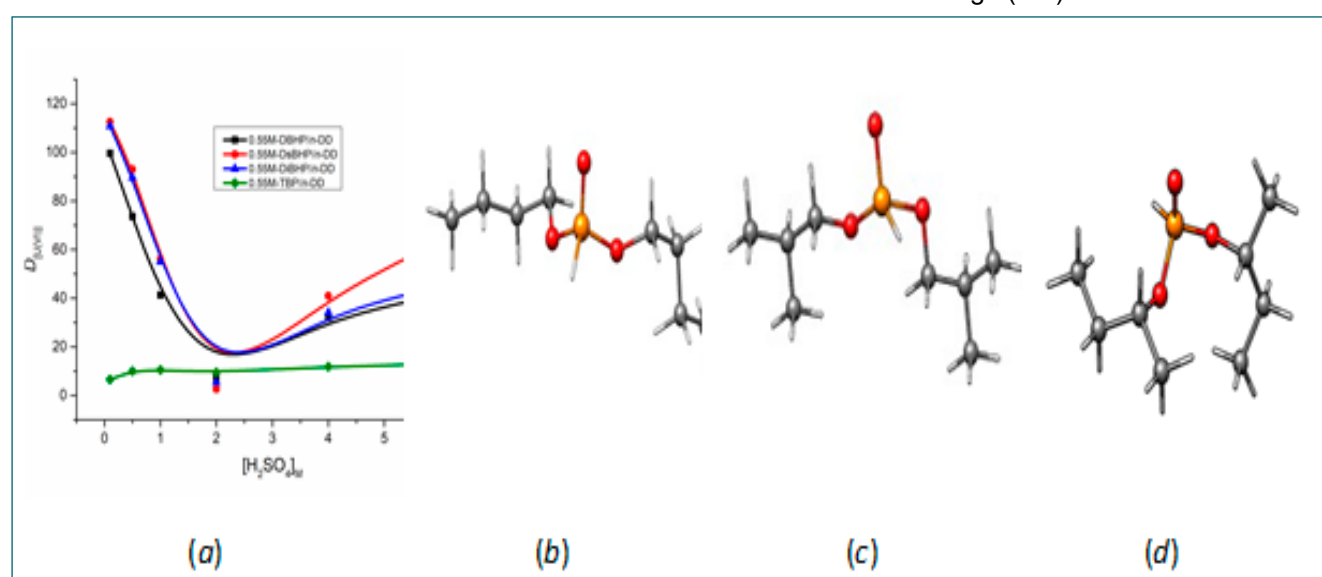


Fig. 1: The plot of (a) $D[U(VI)]$ vs $[H_2SO_4]M$ for the ligands DBHP, DiBHP, DsBHP; optimized geometries of (b) DBHP (c) DiBHP (d) DsBHP at RI-BP86-D3BJ/def2-TZVP level.

V.48 Vaporisation Studies Over <UAl₂(cr)+U(cr)> Two Phase Region of U-Al system

U-Al alloys are used extensively in nuclear reactors as dispersion fuel (metal dispersed in metal) in the form of plates, rods, slugs, or tubes. KAMINI (KAalpakkam MINI) reactor, a special purpose research reactor located at Indira Gandhi Centre for Atomic Research (IGCAR) uses ²³³U (20%)–Al alloy plates as fuel with Al clad. The vaporization behaviour and thermodynamic properties of U-Al binary system are of interest to nuclear technology as these data will serve as inputs for both design and for assessing the performance of fuel during and after irradiation. Thermodynamic properties of these fuel materials are essential to understand their behaviour at high temperatures under normal and in transient conditions. Vaporisation studies over <UAl₂(cr)+U(cr)>two-phase region of U-Al system were performed by Knudsen Effusion Mass Spectrometry.

Samples with compositions χ(U) = 40 & 45 were used for the vaporisation experiments. The alloys were prepared

by arc melting technique by taking appropriate quantities of aluminium and uranium. The vacuum sealed samples were annealed, initially at 900 K for 50 h and then at 1050 K for two weeks and characterised by using X-ray powder diffraction method (XRD) to identify the co-existing phases present. High temperature vaporisation thermodynamic studies over <UAl₂(cr)+U(cr)> two-phase region of U-Al system were carried out by employing Knudsen Effusion Mass Spectrometry in the temperature range of 1146-1327 K.

The vaporisation reaction occurs incongruently and Al(g) was the neutral vapour species observed in the equilibrium vapour. Partial pressure-temperature relation of Al(g) was derived as $\log(p_{Al}/Pa) = (-19809 \pm 209)/T + (12.58 \pm 0.17)$ (Table1). Using the p-T relation, $\Delta_f H_{298.15}^\circ$ of the following reaction: $UAl_2(cr) = 2Al(g) + U(cr)$ was evaluated by second and third law methods. Subsequently, $\Delta_f H_{298.15}^\circ$ and $\Delta_f G_{298.15}^\circ$ of UAl₂(cr) were deduced.

Table 1: p-T relations for Al(g) over <UAl₂(cr)+U(cr)> two phase region

Sample	Run	Temperature range/(K)	$\log(p_{Al}/Pa) = -A/T(K) + B$		$P_{Al(g)} \times 10^4 / Pa$ at T_m
			A	B	
40 at.% U Lot 1	1	1146 - 1276	20028 ± 154	12.80 ± 0.13	4.07
	2	1163 - 1304	20071 ± 138	12.84 ± 0.11	4.12
	3	1174 - 1301	20093 ± 436	12.87 ± 0.35	4.23
40 at.% U Lot 2	4	1167 - 1311	19850 ± 168	12.62 ± 0.14	3.74
	5	1171 - 1288	20141 ± 360	12.94 ± 0.29	4.55
	6	1171 - 1306	20052 ± 210	12.79 ± 0.17	3.80
45 at.% U Lot 1	7	1186 - 1318	20228 ± 438	12.81 ± 0.35	2.87
	8	1183 - 1318	20214 ± 706	12.80 ± 0.56	2.88
	9	1183 - 1318	20078 ± 565	12.71 ± 0.45	3.01
45 at.% U Lot 2	10	1185 - 1327	20012 ± 126	12.79 ± 0.10	4.09
	11	1170 - 1315	20190 ± 203	12.90 ± 0.16	3.79
	12	1179 - 1316	20169 ± 415	12.92 ± 0.33	4.12
Combined	All points	1146 - 1327	19809 ± 209	12.58 ± 0.17	3.68
Pure Aluminum		1115 - 1342	16211	10.92	65.30

V.49 Development of an Indigenous Ion Exchange Based Radionuclides Removal Method for the Routine Laboratory Organic Liquid Waste

The organic liquid waste generated in the radiochemical laboratory poses serious problem due to alpha-emitting radionuclides composed of the different isotopes of americium, curium, neptunium, plutonium and uranium. These wastes are being generated based on the routine laboratory experiments involving batch experiments and mixer settler studies. The radioactivity levels of these wastes (approximately 2,00,000 Bq/mL) was not suitable for the disposal to the Centralized Waste Management Facility (CWMF), who is responsible for the final treatment of the waste. The regulatory body had recommended reducing the radioactivity level due to alpha radionuclides to less than 5000 Bq/mL. The radioactive laboratory organic liquid waste (with the pH mostly varying from 1 to 3) generally comprises different organic solvents, such as tri-n-butylphosphate (with other trialkylphosphates too), amides, phosphine oxides and cocktails contaminated with different radionuclides. In our laboratory, we developed a novel diglycolamic acid anchored cation exchange resin prepared through

chemical modification of the commercially available polystyrene-divinylbenzene resin (PS-DVB-DGAH), to treat the radioactive organic liquid waste through cation exchange mechanism, both by batch and column modes of operation. An excellent decontamination of the radionuclides was accomplished using this PS-DVB-DGAH resin, as disclosed by the gamma spectrometry and liquid scintillation counting. The removal of alpha activity was demonstrated for nearly 1000 mL of the organic waste solution in column mode using this diglycolamic acid anchored resin. The removal efficiency of the process was assayed based on the analysis of the effluent samples using alpha spectrometry. The studies are also underway in developing a miniature lab-scale set-up for the treatment of large volume of radioactive organic waste through automated solid phase extraction methodology. The estimated activity level of organic waste after treatment was less than 5000 Bq/mL. The treated organic waste, which is free from radioactivity, is amenable for further incineration or pyrolysis.

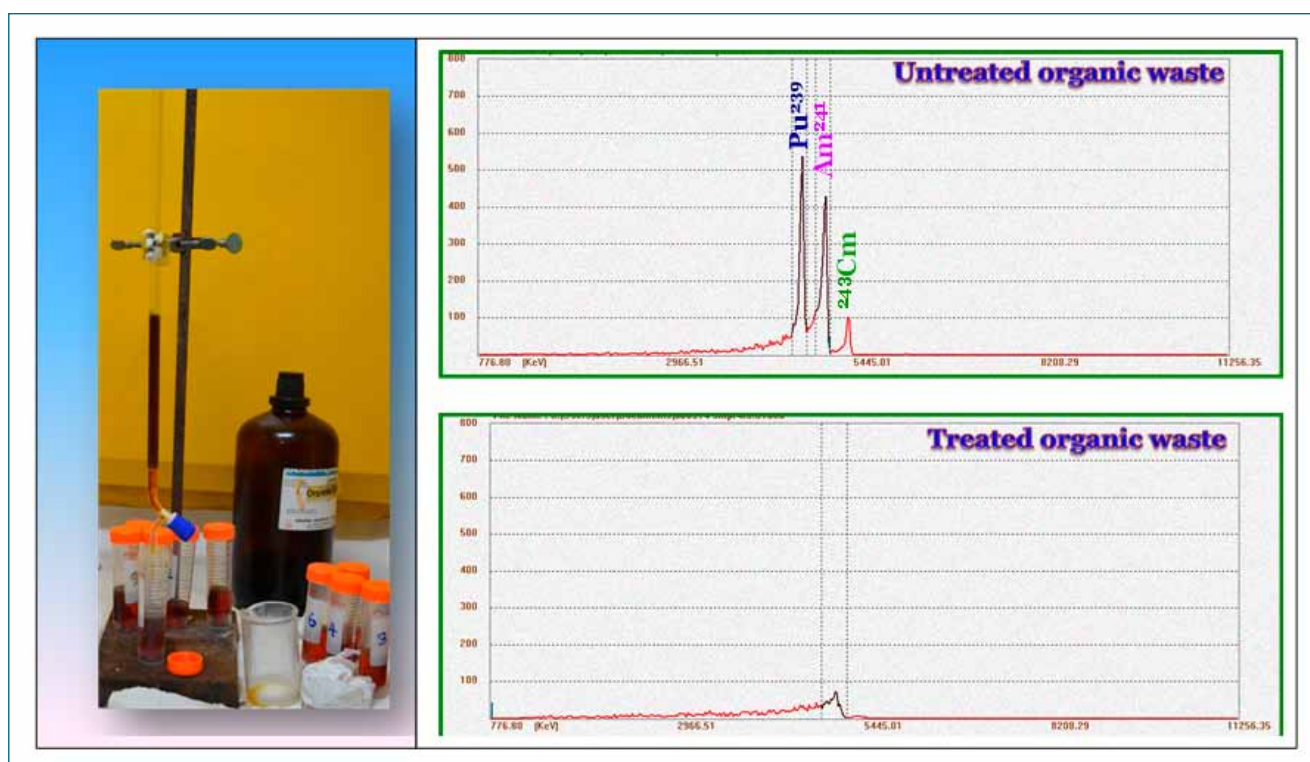


Fig. 1: Column demonstration of the organic waste treatment by PS-DVB-DGAH. Alpha spectra of the untreated and treated organic waste solutions after making planchets.

V.50 In-house Developed Small Volume Calorimeter for Non-Destructive Assay of Plutonium based nuclear fuels

Radioactive calorimetry is a non-destructive technique for quantitative estimation of radionuclides, especially plutonium-containing fuels. The measurement of total heat in terms of power associated with radioactive decay is the basis of this calorimetry technique. This technique is widely used in the nuclear industry to account for plutonium in fuel pellets, powders, and metals. This report describes the in-house design and development of a small volume single cell radioactive calorimeter, and its associated Visual Basic (VB) software developed for data acquisition. The calibration of the calorimeter using thermistor and plutonium standards are discussed. The calorimeter was calibrated by both electrical and plutonium standards. Further, assay of plutonium of known isotopic composition in uranium plutonium oxide pellets (MOX) and U-Pu-Zr metallic alloy fuels are presented and compared with potentiometric method.

A small volume single cell isothermal heat flow radiometric calorimeter developed in-house consists of three nested layers of aluminum sheets forming a nested design with three containers. The six surfaces of the IC were covered with commercially available peltier elements (TEC12706) that could measure the electrical signal (electromotive force, emf) proportional to the heat flow between the IC and the thermostat block (middle container, MC). The IC is surrounded

with sufficient number of peltier elements connected in series. The effective thermo emf was measured using an electrometer (6514 Keithley Instruments).

The outer surface of the MC was coiled with nichrome heating wire. The heating wire was insulated and surrounded by outer aluminum sheet and the temperature of the coil is maintained using a temperature controller (M/s Indfur Superheat Furnaces). The MC consists of only aluminum sheets and rubber foam, which were enveloped alternatively. The temperature of first and second container is monitored using K-type thermocouples. The outer aluminum container was coiled with a copper tube of for chilled water circulation to maintain a constant temperature of 15 °C. This maintains a thermal barrier to overcome not only the room temperature fluctuations but also helps the calorimeter to dissipate the heat produced during measurement.

Fig.1 shows a Photograph of the single cell calorimeter. To acquire and display the experimental data continuously, a computer program with a Graphical User Interface (GUI) was developed in-house using Microsoft Visual Basic 6.0 (VB).

The VB program collects the data from electrometer through a RS232 serial port and sends it to a computer.

Table 1 Comparison of results of plutonium weight obtained by Potentiometry and Calorimetry

MOX Group ID	Weight of Pu by potentiometry (g)	Calorimetry				Error (%)
		Avg Net signal (μV)	RSD (%)	Total Power* (Ps) (mW)	$M_T = P_S/P_{eff}$ # Weight of Pu (g)	
A	0.3218	144 ± 8	2.68	1.585	0.2700	-16.09
B	0.6311	399 ± 4	0.69	4.391	0.7482	18.55
C	0.9936	509 ± 10	0.90	5.601	0.9544	-3.94
D	1.2792	723 ± 6	0.80	7.956	1.3557	5.98
E	1.6341	896 ± 8	0.44	9.860	1.6801	2.81
F	1.9514	996 ± 5	0.43	10.961	1.8676	-4.29
G	2.2822	1280 ± 10	0.67	14.086	2.4001	5.16
H	3.2745	1759 ± 15	0.81	18.807	3.2045	-2.14
I	4.2718	2235 ± 23	0.78	24.596	4.1909	-1.89
J	4.9309	2642 ± 26	0.80	29.075	4.9540	0.47

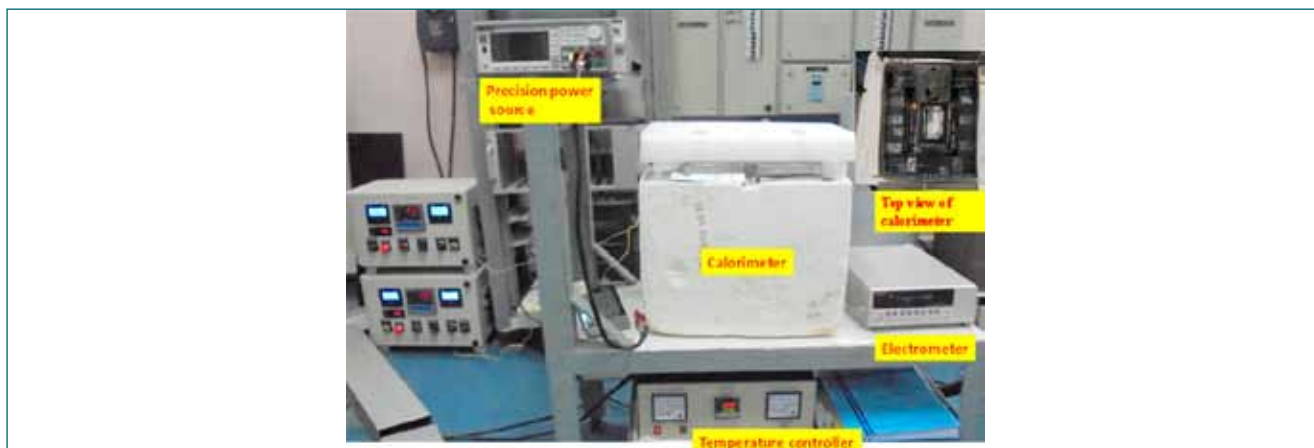


Fig. 1: Photograph of small volume of radioactive calorimeter

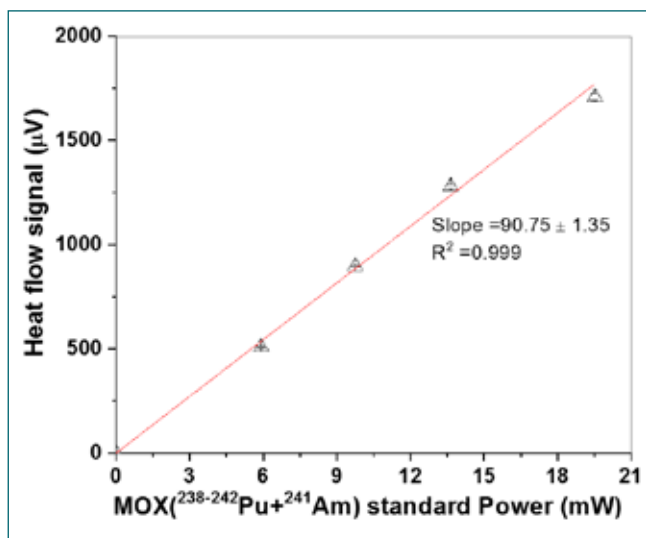


Fig. 2: Electrical calibration performed using 2 kW resistance thermistor

The experimental data from the calorimetry system is acquired by the Remote Command Programming method of the Keithley system.

Electrical calibration (Fig. 2) was performed using 2 kW resistance thermistor by varying the current from 1 mA to 16 mA using a high precision power source through the thermistor positioned inside the inner chamber using a fixture. Similarly, the calibration was also carried out using Pu standards (Fig. 3) of known isotopic compositions. The sensitivity coefficient (S, micro Volt/mW) of the instrument was calculated by both electrical and Pu (MOX) standard and found to be 90.87 ± 0.17 and 90.75 ± 1.35 micro Volt/mW respectively. The difference in sensitivity coefficients obtained from electrical calibration and plutonium standard measurements is $\pm 0.3\%$.

Further, MOX pellets were doubly sealed and loaded inside the calorimeter. The baseline measurement was carried out using an empty cell and the data was collected continuously until the value reached a constant thermal equilibrium. The time taken to attain thermal equilibrium

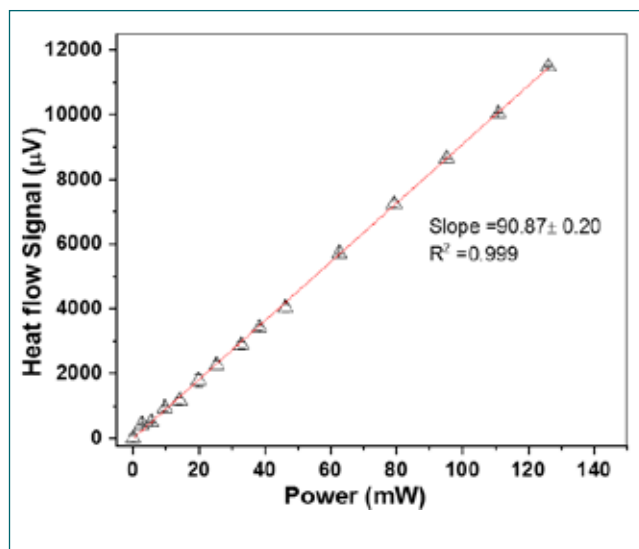


Fig. 3: Calibration using Plutonium (MOX) standard pellets

was ~ 24 h. Similarly, the sample measurement was carried out by loading each group of MOX pellets into the calorimeter and the data was acquired continuously using the software until it reached a constant thermal equilibrium. The amount of Pu in each group is varying from 0.3 to 5.0 g. The total heat output for each group of standards (MOX) was measured by calorimeter. The equilibrium value for the heat output signal was determined using the last 2 h of data that satisfies the condition of relative standard deviation (RSD) in the signal, which is less than 1%. Each MOX standard pellet measurement was carried out

in triplicate and the average heat output signal was considered to estimate the total power.

The total mass of plutonium in the alloy fuel was estimated from the calorimetric total power and effective specific power. The oxide and metallic samples of plutonium were estimated and the results were compared with potentiometric analysis and shown in Table 1. The error is found to $\pm 5\%$ for samples with equivalent to $\text{Pu} \geq 1$ g.

V.51 Highly efficient functionalized Metal Organic Frameworks for the Extraction of Pd(II) from Aqueous Solution

Noble metals like palladium are extensively used for various applications such as catalysis, electronics, pharmaceuticals, etc. Due to its high demand, there is a need to find alternative palladium sources other than natural resources. In this context, the spent nuclear fuel forms a viable source as it contains a significant amount of palladium and other fission products. Various techniques have been reported for the extraction of Pd(II), like liquid phase extraction and ion exchange. Solid-phase extraction has many advantages over the liquid phase extraction techniques, such as greater selectivity, low cost etc.

Therefore, metal-organic frameworks can serve as promising materials for solid-phase extraction of Pd(II) due to their high surface area and porosity. In the present study, the synthesis of two functionalized MOFs, namely UiO-66-Dithizone and UiO-66-Phenylenediamine, are reported for the extraction of Pd(II) from aqueous solution. The pristine MOF UiO-66-NH₂ was synthesized and subjected to post-synthetic modification with dithizone and ortho-phenylene diamine to yield UiO-66-Dithizone and UiO-66-Phenylenediamine. The synthesized MOFs were characterised by powder XRD and FTIR. The post synthetic modification (PSM) and the pristine MOFs were used for the sorption of Pd(II) from aqueous solution within a pH range of 2 to 6. It was found that all the MOFs showed maximum sorption

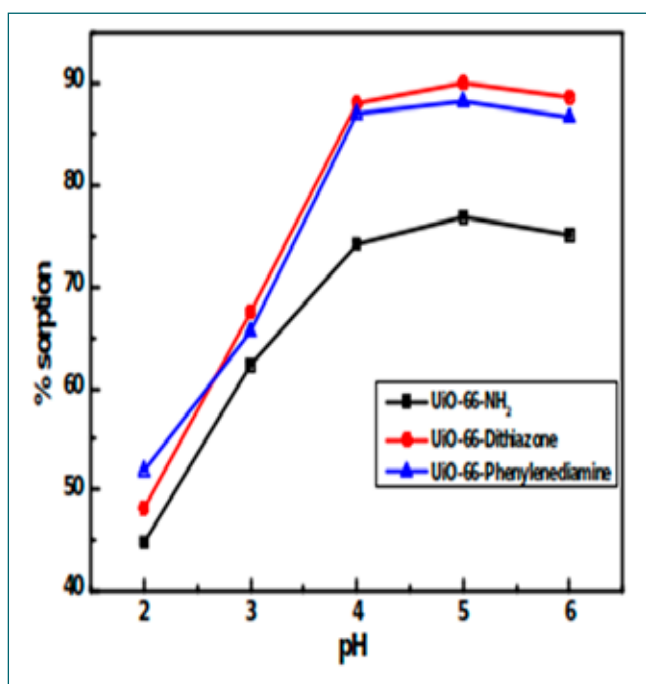


Fig. 1: The variation in sorption (%) of Pd(II)

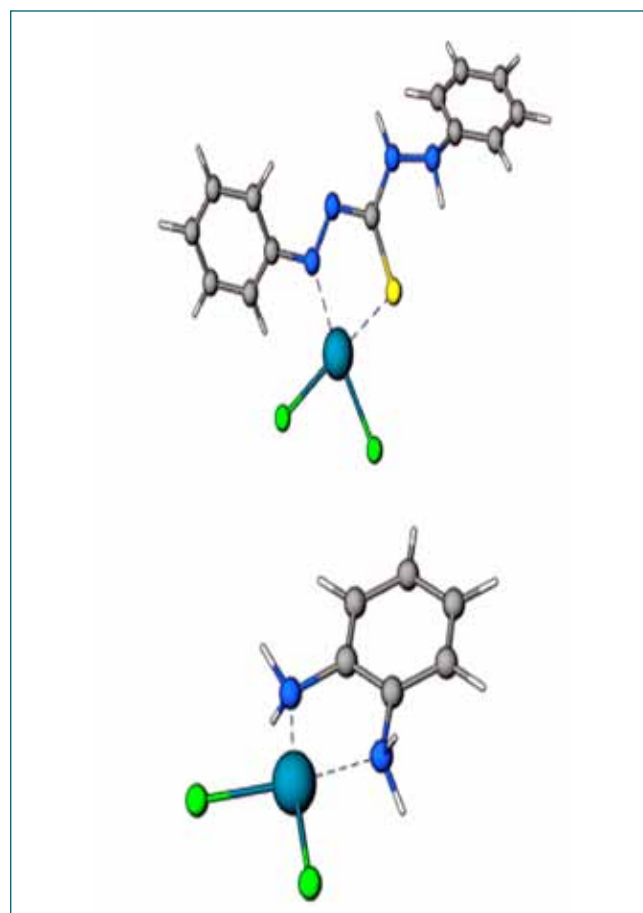


Fig. 2: Optimized geometries of (a) Pd(II)-Dithizone and (b) Pd(II)-Phenylenediamine

percentage at pH 5 beyond which there is a decrease in sorption and the sorption percentage followed the order: UiO-66-Dithizone > UiO-66-Phenylenediamine > UiO-66-NH₂ as shown in Fig. 1. Density functional theory (DFT) was also employed to understand the nature of the interaction of the functionalized MOFs with Pd(II). UiO-66-Dithizone and UiO-66-Phenylenediamine were modeled as dithizone and o-phenylenediamine ligands and their complexes with Pd(II) was subjected to DFT analysis. It was found that the complexation energy for Pd(II)-dithizone complex was the highest which agrees with the experimental results. The greater affinity of UiO-66-Dithizone for Pd(II) can be attributed to the presence of soft S moiety present in dithizone. Hence, the post synthetically modified MOFs were shown to possess a greater affinity for Pd(II) compared to parent MOF UiO-66-NH₂. This can be attributed to functionalized groups in the PSM MOFs, which can bind with the metal in a bidentate fashion, as shown by the DFT calculation (Fig. 2).

V.52 Studies Related to the Aqueous Reprocessing of Metallic Alloy Fuels using Phosphonate based solvents

Metallic alloy fuels, U-Pu-Zr can be reprocessed by aqueous based PUREX process. Tri-*n*-butyl phosphate is being used as an extractant for reprocessing of spent nuclear fuels for last seven decades. In the recent past, Tri-iso-amyl phosphate (TiAP) has been examined as an alternate solvent to TBP for the aqueous reprocessing of metallic alloy fuels, U-Pu-Zr. However, Dialkylalkyl phosphonates were not investigated for the development of flow sheets for the aqueous reprocessing of metallic alloy fuels. In the present study, Dibutylbutyl phosphonate (DBBP) and Diamylamyl phosphonate (DAAP) solvents were examined for the extraction and stripping of metal ions from U-Pu-Zr feed solutions in nitric acid medium. The number of stages required for the extraction and stripping of U and Pu by DBBP and DAAP solvents were evaluated in cross-current mode. Flow sheets for the extraction and stripping of metal ions were investigated in cross-current mode at 303 K. In cross-current experiments, the same aqueous feed (U-Pu-Zr solution in 4 M HNO₃) was contacted with fresh 1.1 M solutions of DBBP and DAAP in *n*-DD during the extraction and vice-versa in stripping of metal ions from loaded organic phase. Quantitative extraction (>99.9%) of U and Pu was observed in four stages by both 1.1 M solutions of DBBP and DAAP in *n*-DD. The extraction stage profiles for U and Pu by 1.1M DBBP and

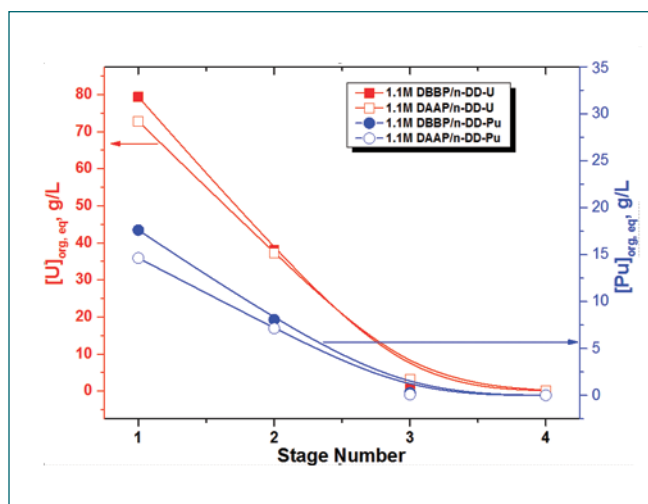


Fig. 1: U and Pu extraction stage profiles by 1.1 M DBBP and 1.1 M DAAP in *n*-DD during the extraction from U-Pu-Zr feed solution

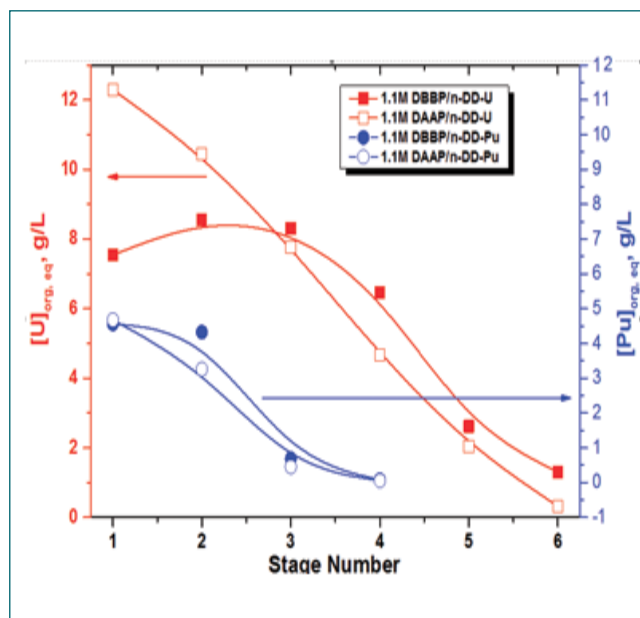


Fig. 2: U and Pu stripping stage profiles during stripping from loaded 1.1 M DBBP and 1.1 M DAAP in *n*-DD

M DAAP in *n*-DD during the extraction from U-Pu-Zr feed solution is shown in Fig. 1. The concentration of U and Pu in the organic phase decreases with stage number indicating that the percentage extraction of U and Pu increases. The concentration of U and Pu in the aqueous phase in 4th stage is found to be below detection limit (2 mg/L). Significant amount of Zr is extracted into the organic phase in all the four stages. Subsequently, stripping of U and Pu from the loaded organic phase was carried out in cross-current mode with 0.01 M HNO₃. The concentrations of U, Pu and Zr was found to be about 50, 10 and 1 g/L, respectively with a nitric acid concentration of ~0.5 M in the organic phase, which is used as organic feed to the strip cycle. The stage profiles for U and Pu during the stripping from organic phase is shown in Fig. 2. The concentration of U and Pu decreases from stage 1 to 4 demonstrate that the recovery of both the metal ions from organic phase. Quantitative stripping (>99.9%) of Pu and Zr was observed in 4 and 2 stages, respectively both in the case of DBBP and DAAP solvents. The stripping of U was found to be >98% indicating that more stages are required for quantitative stripping of U.

V.53 Pyro-processing of Irradiated U-6Zr in Hot Cells

Pyro-processing of spent metal fuels is based on electrochemical recovery of actinides in high temperature molten salts (LiCl-KCl eutectic with 58.5 mol.% LiCl). The flow sheet for the pyro-processing of spent metallic fuel consists of four major steps such as 1) Head end step, 2) Separation, 3) Spent Salt Treatment and 4) Waste disposal and re-fabrication. After the head end steps, the separation step consists of a) Electro-refining (ER) and b) Salt & Cadmium distillation process. In order to demonstrate the remote operation feasibility of the ER process of irradiated U-6Zr inside hot cells and also to study the process parameters, a laboratory scale (100 g scale) pyro process facility was set-up in hot cells of MC&MFCG. For this purpose, the existing hot cell facility was augmented with necessary modifications and customized to the experimental needs.

Electro refining (ER) of irradiated U-Pu-Zr alloy fuel was carried out in the laboratory scale pyro-process augmented hot cell experimental facility of MC&MFCG. About 22.9 g irradiated fuel (with clad) [Figure 1] was loaded with 21 g of fresh U-Pu-Zr alloy in anode basket [Figure 2]. Total weight of U-Pu-Zr alloy loaded inside anode basket was 43.9 g. ER was carried out employing 2.819 kg of LiCl-KCl- UCl_3 (Salt) (3.55 wt% UCl_3) as electrolyte [Figure 3], 10 mm dia SS rod as cathode

and irradiated U-Pu-Zr as anode. Ag wire along with LiCl/KCl/AgCl salt loaded inside a quartz tube which was further inserted in a SS 430 perforated thermo well with Ag wire extension of 10 mm was used as reference electrode.

Before starting the ER runs, potential of cathode (vs. Ag+|Ag ref.) and anode (vs. Ag+|Ag ref.) was measured to be -0.310 and -1.236 V, respectively at 500 °C. ER was carried out at 500 °C in potentiostatic mode by varying the potential at -1.4 V to -1.5 V for 15 hrs. The total cathode deposit recovered is 15.9 g.

The metal deposit [Figure 4] was scrapped from the cathode under hot condition. Three samples of salt solution and two samples of metal deposit were taken using manipulators during the run under hot condition using indigenously fabricated samplers. The samples were taken out of hot cell for characterization. Three salt samples taken in different time durations were analysed for uranium content using spectrophotometric method. The concentration of uranium after electrolysis was found to be about 3.1 wt%. The diluted salt sample was analysed by gamma spectrometry. The radioisotopes ^{134}Cs , ^{137}Cs , ^{144}Ce , ^{154}Eu and ^{155}Eu were found to be present. The cathode deposit was analyzed for uranium and zirconium. Zr contents were found to be < 0.3% in uranium deposit.



Fig. 1: Irradiated U-Zr cut pin sections



Fig. 2: Fuel loaded to anode basket



Fig. 3: Salt and Cd balls loaded to reaction vessel

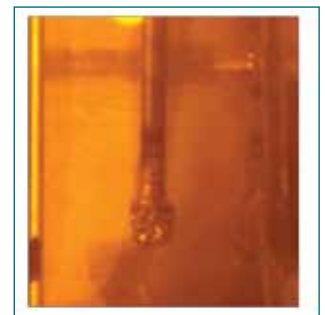


Fig. 4: Uranium metal deposit at SS cathode

V.54 Novel Pulsed Laser Deposition Sampling Methodology for ICPMS Chemical Analysis towards Burn-up Measurements

Post irradiation analysis of nuclear fuel is essential to determine the fuel performance in terms of burn-up measurement, fuel-clad interaction, spatial distribution of fissile atoms and fission products. Among these, burn-up and spatial profiling are the most important parameters. Pulsed laser deposition (PLD) followed by inductively coupled plasma mass spectrometry (ICPMS) analysis is demonstrated for burn-up determination and spatial profiling. PLD is a well-known technique to deposit thin films of complex oxides and other multi-component materials with stoichiometric composition. For such studies, lasers with shorter wavelength (in the UV region), shorter pulse duration (ps or less) and beam shaping optics are employed. PLD-ICPMS is more advantageous because: (i) it can sample with spatial resolution of a few tens of micron spot sizes; (ii) sampling can be done inside a hot-cell or lead shielded mini-cell under a vacuum ($\sim 10^{-3}$ mbar); (iii) only a thin film having minimum radioactivity (compared to an irradiated pellet) needs to be handled during mass analysis, thereby reducing the radiation exposure to a considerable extent; (iv) it will give spatial profile of irradiated pellet more accurately (error $\sim 1\%$) and (v) as the sample for mass analysis is in the form of solution, isotope dilution method can be adopted for accurate concentration measurements.

PLD experiment was performed using Nd:YAG laser of wavelength 1064 nm, pulse width 100 ps, frequency 10 Hz and pulse energy 100 mJ. The laser was focused on the target pellet at an angle of 60° with respect to the surface normal, using a quartz lens of 250 mm focal length. The target was rotated during PLD experiments in order to avoid formation of deeper crater which could lead to larger chip-offs from the target surface.

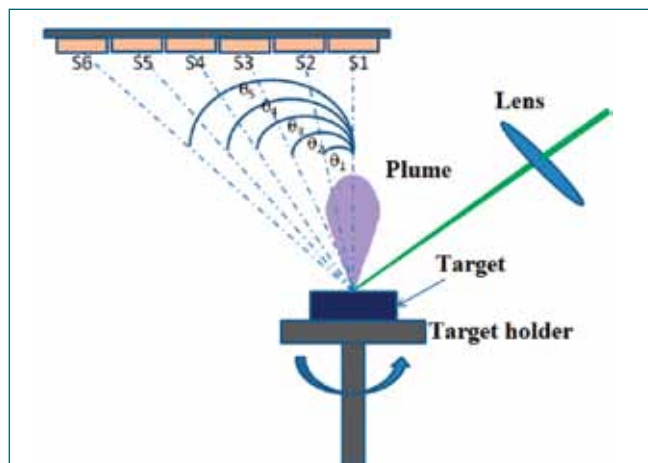


Fig. 1: Schematics of collection angle in PLD

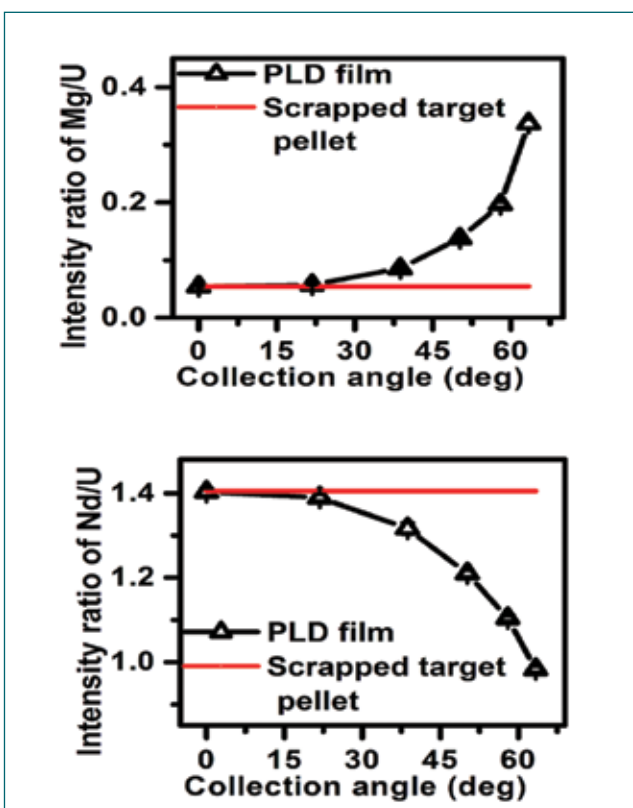


Fig. 2: Effect of mass distribution and collection angle in PLD films from a single target.

Films were deposited on borosilicate glass (Pyrex®, Corning) kept at a distance of 25 mm away from the target surface, for 90 min. All depositions were done at a pressure of $\sim 10^{-3}$ mbar. The deposited films were dissolved separately in 1.6 M quartz distilled HNO_3 and subjected to ICPMS analysis.

A sector field ICP-MS is used as mass analyzer. The mass spectrometer detector enables continuous & simultaneous detection of whole mass range from 6 to 238 amu with a resolution of approximately 500-800 at ^{107}Ag and ^{208}Pb , respectively. PLD thin film samples from target having wide mass range, 24-238 amu (Mg, Ni, La, Nd & U) have been collected at six different angles (0° , 21.8° , 38.7° , 50.2° , 58° & 63.4°) [Fig. 1] with respect to the target surface normal. There is a systematic variation of intensity ratio vs. angle of deposition for different elements [Fig. 2]. The magnitude of variation in intensity ratio depends on the nature of plume species (ions and neutrals), mass number, sublimation energy and ionization energy of the elements, for given laser parameters. However, the intensity ratios only around zero degree angle ($0 \pm 12^\circ$) with respect to target normal at plume centre represent the actual target composition i.e. stoichiometric film.

V.55 Indium Tin Oxide thin-film as Sensor Cum Heater Material

Chemical sensors find their use in various areas not only in the areas of the public domain like agriculture, automobiles, pharmaceuticals, explosive detection but also in more-oriented applications in the programs of nuclear and space. In particular, monitoring any steam leak into the sodium systems of fast breeder reactors made use of semiconducting metal oxide sensors to detect at their inception. Also, chemical gas sensors find their place at the back end of the fuel cycle to monitor the levels of hazardous gases released during the process. Semiconducting metal oxides work at higher temperatures and require a rear-side platinum heater for their operation. Indium Tin Oxide (ITO) is a solid solution of tin oxide in Indium oxide and is known for its usage as a conducting electrode for decades.

The base oxides of indium and tin are n-type semi-conducting oxides and are also well-studied for their gas-sensing applications. The possibility of integrating the functions of the sensing element and the heater by tapping the potential of ITO was explored in the current study. The thin films of ITO were deposited by pulsed laser deposition. The Figure 1 shows the XRD pattern ITO.

Figure 2 is the scanning electron microscopic image of ITO film deposited on alumina substrate. The morphology reveals well grown ITO crystallites with uniform coating. The films were tested towards sensing hydrogen at different power by passing the current accordingly. A typical response toward 130 ppm of hydrogen was shown in Figure 3. This gives a good insight into the development of self-heating sensor films.

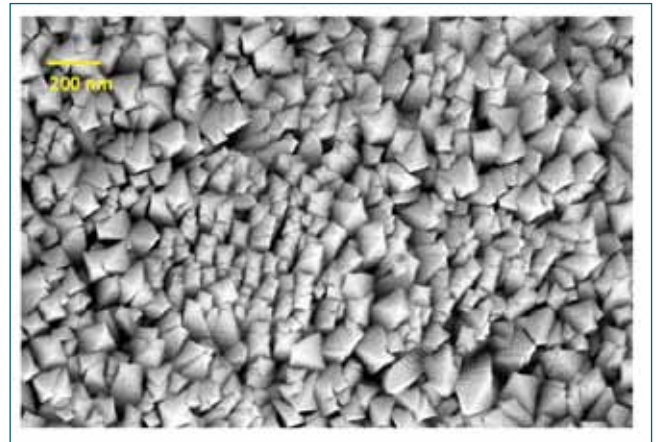


Fig. 2: SEM image of ITO film deposited on alumina substrate.

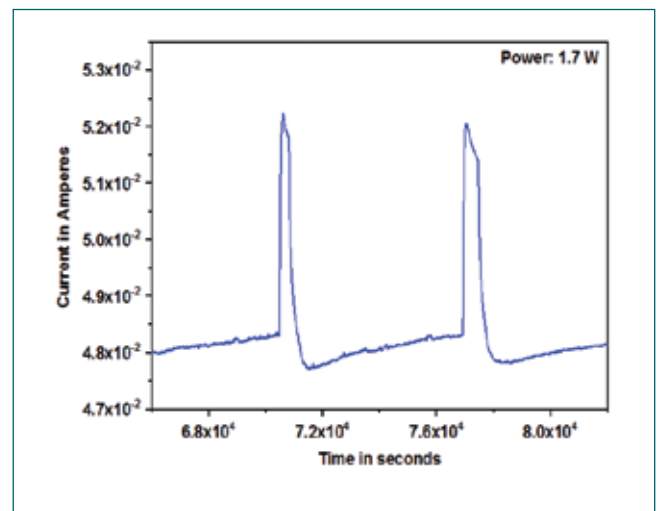


Fig. 3: Response of ITO films towards 133 ppm of H₂ at 1.7 W

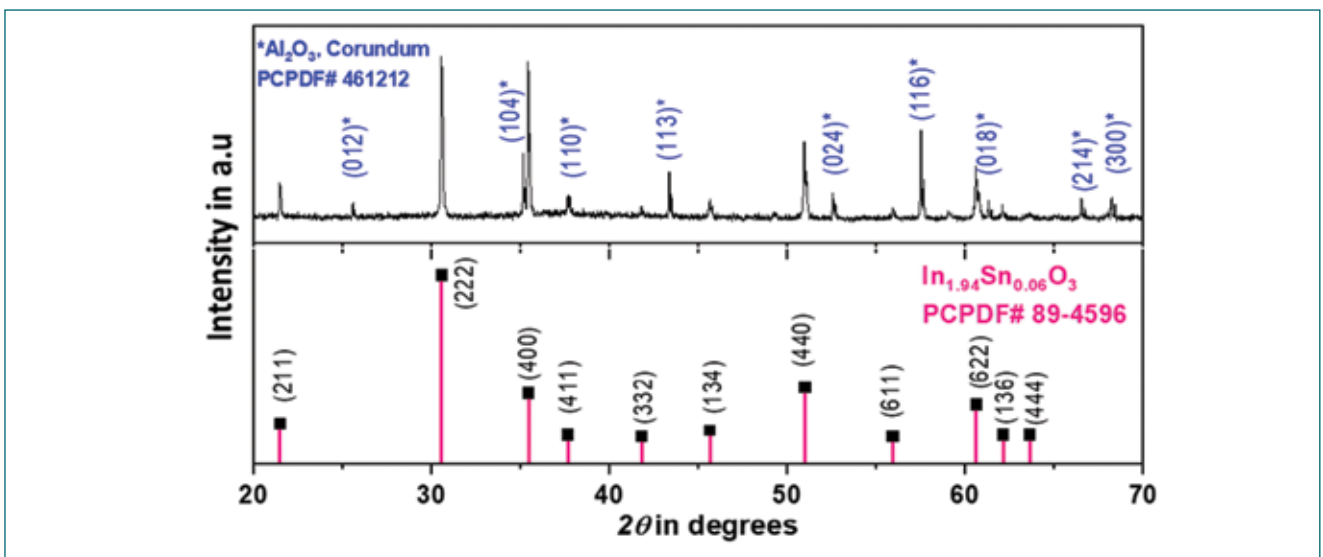


Fig. 1: X-ray diffraction pattern of ITO thin films deposited by PLD

V.56 Experimental Setup for Fatigue Life Testing of Bellows

Standards of Expansion joint manufacturing Association (EJMA) are widely used for the design of bellows which follows “design by rule” approach. Moreover, the weld configurations encountered in bellows are not among the codified configurations and hence, the experimental stress analysis approach is one of the main approaches adopted to get the required codal compliance for nuclear bellows. An experimental setup was developed in-house for fatigue life testing of bellows. Any type of bellows with end flanges can be tested in the setup. The test setup (Fig.1) consists of a hydraulic actuator of 5T capacity connected to an actuating plate through a set of 4 actuating rods. For testing smaller bellows such as bellows in bellow-sealed valves (upto 100NB) buffer tank of a relatively larger volume is used to limit the pressure fluctuation in the bellows while cycling. One of the end flanges of the bellows test specimen is connected to a fixed plate and the other end flange is connected to the actuating plate. For testing larger bellows, the pressure fluctuations during cycling are prevented by providing a compensator bellows. In this method, two identical bellows are connected with a common central flange. The end flanges of the two bellows are connected to the fixed plates of the bellows test setup and the middle common flange of the bellows is connected to the actuating plate. In this arrangement, as one of the bellows gets compressed, other bellows gets extended by the same amount and there will not be any change in internal volume and pressure fluctuations

during cycling. The bellows are subjected to internal pressure through a buffer tank and a header equipped with a pressure gauge. After pressurization, the header is isolated from the air compressor so that the drop in the pressure if any indicates failure of the bellows.

A control panel was used for the actuation of the hydraulic actuator. It had provision for forward/backward movement of actuating plate after taking feedback from reed switches. It has provisions to operate the system both in auto as well as the manual mode and is also equipped with an automatic cycle counter.

Provision of a furnace is also made in the test setup to enable high-temperature testing of bellows. Bellows up to 350 mm in diameter, 500 mm long with an operating pressure upto 5 bar and an operating temperature upto 550°C can be tested in the facility.

Multiply bellows for PFBR Transfer Arm (with a redundant ply approach) are being developed. The free length / internal / external diameters of the bellows are 270 / 38 / 55 mm with 28 convolutions. The bellows were tested at 200°C for a movement of ± 35 mm and internal pressure of 600 mbar. The life of the bellows was found to be around 14000 cycles. A buffer tank of volume 0.5m³ was used during testing to limit pressure fluctuations. Testing of 50NB multiply bellows at 5 bar at room temperature was carried out towards the development of bellows in passive valves of AHWR.

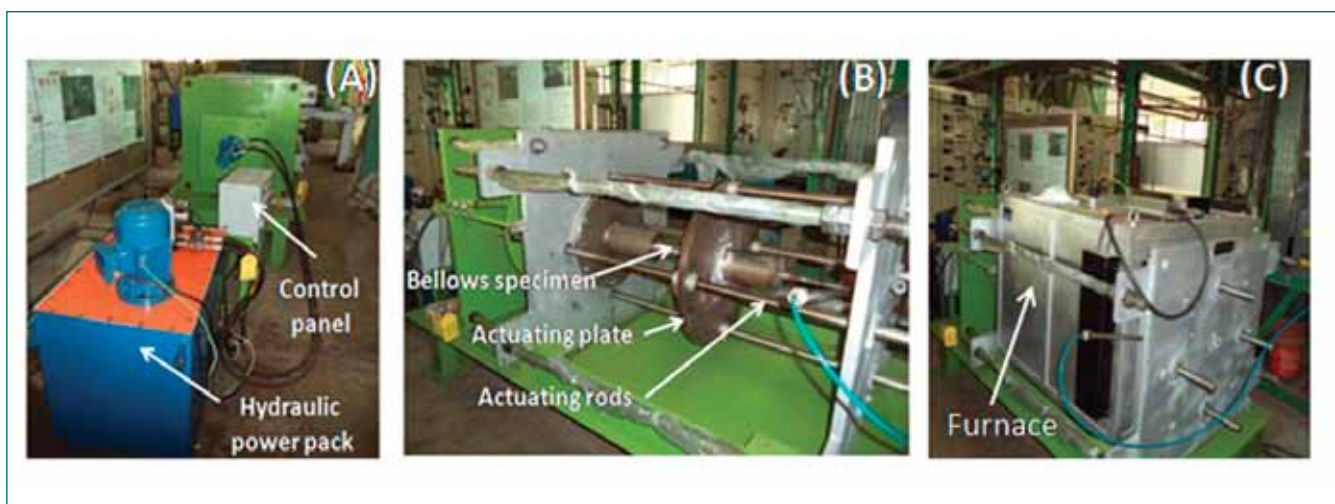


Fig. 1: Below test setup (A) Control panel and hydraulic actuator, (B) Test specimen assembled in the setup and (C) Furnace

V.57 Testing of Ferro-Magnetic Particle Collector in Water

The ferromagnetic particle collector (FPC) is a device designed to remove ferromagnetic particles from primary sodium. The device uses permanent magnets contained in a stainless steel housing to trap the ferromagnetic particles. Four such devices will be located in (i) three DSRDM locations and (ii) Observation port during initial commissioning. An experimental setup simulating the reactor configuration was designed and fabricated. The testing of the FPC was carried out in water to confirm its effectiveness using a full scale prototype.

The test setup includes a test vessel and piping system for water circulation of required flow. The schematic of the test setup is shown in Fig. 1 The test vessel consists of an outer cylindrical shell, a central shell, and a provision for introducing ferromagnetic particles. The central shell is partially perforated with circular holes simulating the shroud tube of the reactor control plug. A water pump is provided along with connecting SS piping to achieve the required flow for testing. Valves are provided to regulate the flow, and rotameters are provided for flow measurement.

During water testing, drag force (33000 LPM) and Reynolds

number (62000 LPM) simulations were ensured. Initially, water was filled up to level corresponding to reactor elevation (+26745 mm). Drag force is simulated when particles are introduced in the circuit. Subsequently, the Reynolds number is simulated after quantifying the effectiveness of FPC to verify the clinging of chips to the device under turbulent flow.

Testing of the ferro particle collector device has been performed in two phases. In the first phase of the experiment, magnetic particles powder (average particle size is 53 μm) is used for drag force and Reynolds number simulation. In the second phase of the experiment, metallic iron chips (10 to 20 mm long, average length 15 mm and 1 mm width) are used for Reynolds number simulation.

Ferro particles (phase 1) and iron chip (phase 2) collected by the device in the experiment are shown in Fig. 2 The FPC is found to be very effective in capturing the ferromagnetic particles reaching its vicinity. Based on experiments conducted, the minimum effectiveness of the device is found 60 % for fine ferromagnetic particles and 50% for metallic chips.

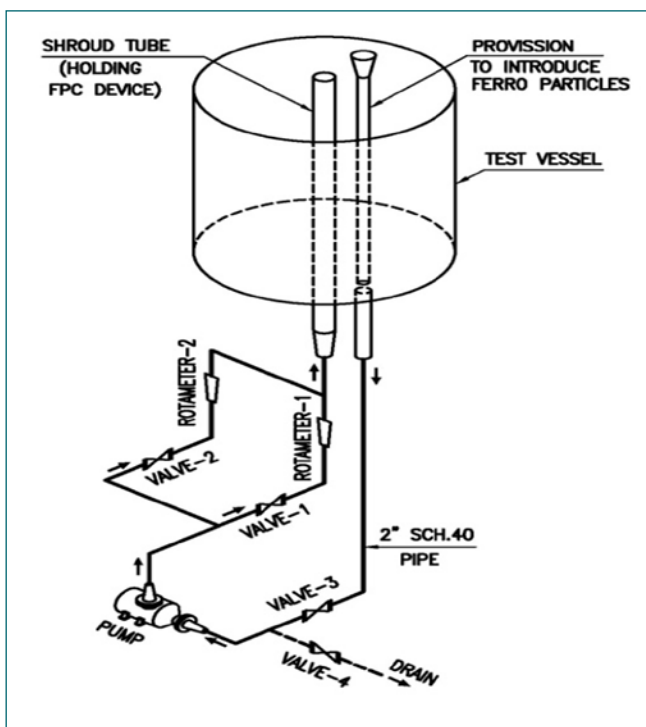


Fig. 1: Schematic of test setup



Fig. 2: Schematic of test setup

V.58 Design, Development and Deployment of Mobile Robotic System for the Pre-Service Inspection (PSI) of DFRP Waste Vault

One of the critical components/areas of the fast breeder reactor (FBR) fuel reprocessing plants identified for in-service inspection (ISI) is the Waste Tank Farm (WTF) of Demonstration FBR fuel Reprocessing Plant (DFRP), where the high-level radioactive waste will be stored for a long time till their half-life is reduced significantly for waste immobilization and safe disposal. Due to high radiation levels, the vault will be inaccessible for any direct inspection and hence, the

established within the vault for online transmission of tele-command (control) and streaming wireless video signals between the mobile robotic system in the vault and the remote user-control station on the surface (Fig. 3). Twelve passive antennas have been installed within the vault for the bi-directional relay of the wireless signals between the mobile robot and the control station. Rigorous testing and qualification of the robot with its deployment tools has been done in the mock-up. Using

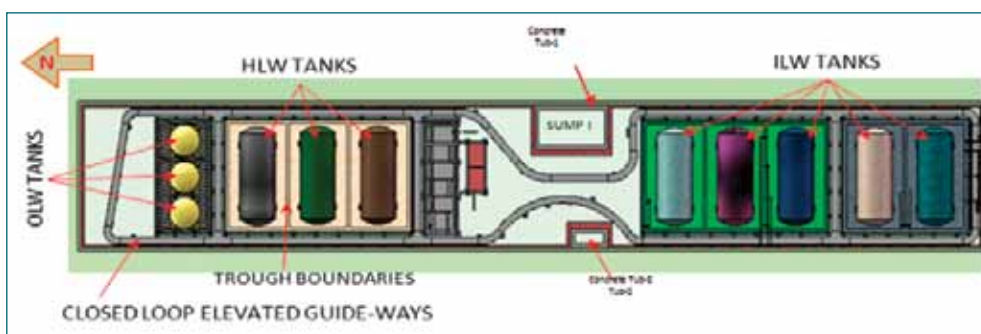


Fig. 1: Plan view of DFRP waste-vault layout showing the track



Fig.2 Mobile Robotic System

ISI of the WTF has to be done remotely through first-person view (FPV) controls. Towards this, a semi-autonomous mobile robotic system has been designed and developed. The 65 m long DFRP waste vault (Fig.1) houses 14 waste tanks inside concrete troughs of height of 1.6 m. An elevated track has been specially designed and built around each tank, for the mobile robot to move around each tank to carry out the inspection of the tanks.

The configuration of the robotic system (Fig.2) uses two driven wheels with individually controlled motors to drive the robot. The wheels are mounted on both sides at the centre of the robot. Four idler spherical wheels are provided at the four corners of the robot. This configuration makes the smallest turning radius, essential for turning properly in the given working space around the sharp cross paths of the track. The speed of the robot can be varied from 1m/min to 3 m/min and differential drive is chosen to steer the robot across the cross paths.

Untethered control is adopted for the mobile robot considering the environment. The robot carries the battery bank and on-board Single Board Computer (SBC) and is equipped with lights, cameras, communication devices, and sensors for navigation of the robot. A fail-safe wireless communication network system has been

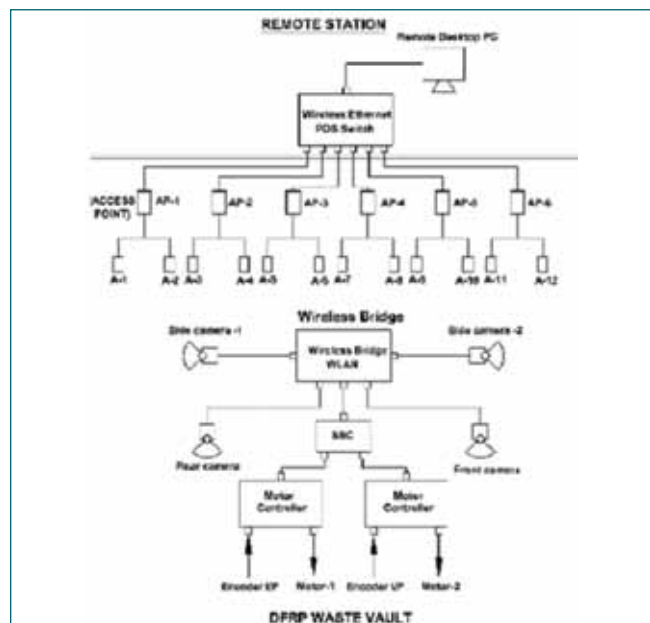


Fig. 3: Mobile Robot communication and Control Schema

the mobile robot with camera, the pre-service inspection (PSI) of the waste vault of DFRP was undertaken and successfully completed. PSI data acquired during the visual inspection of the floor and linear sumps and outer surface, associated sumps and other critical areas of liquid waste storage tanks. This PSI data will be used for assessing the first ISI data and subsequent ISI campaigns. The performance of the mobile robot inside the vault is found to be satisfactory.

V.59 Decay power measurements from P91, SS316L, SS304L and D9 steels: Irradiation experiment in KAMINI

Decay power from P91, SS316L, SS304L and D9 steels were measured using WEAS set-up and compared with ORIGEN2 predictions. The principle of WEAS is to measure the beta and gamma energies that is deposited in the detector simultaneously with detection efficiency close to 100%. The essential part of WEAS set-up is a pair of large bismuth-germanate ($\text{Bi}_4\text{Ge}_3\text{O}_{12}$ BGO) scintillators. An irradiated sample is sandwiched tightly by the BGO scintillators to make 4π geometry.

Fig.1 illustrates a schematic diagram of WEAS along with its associated electronic circuit.

Samples of P91, SS316L, SS304L and D9 steels were irradiated in KAMINI PFTS location for 60 minutes at 20kW reactor power. From this study, it was possible to predict decay powers from P91, SS316L, SS304L and D9 steel samples within $\pm 4\%$, $\pm 8\%$, $\pm 5\%$ and $\pm 8\%$ respectively with respect to measurements. The study also validated the spectrum averaged one group cross section and the neutron flux.

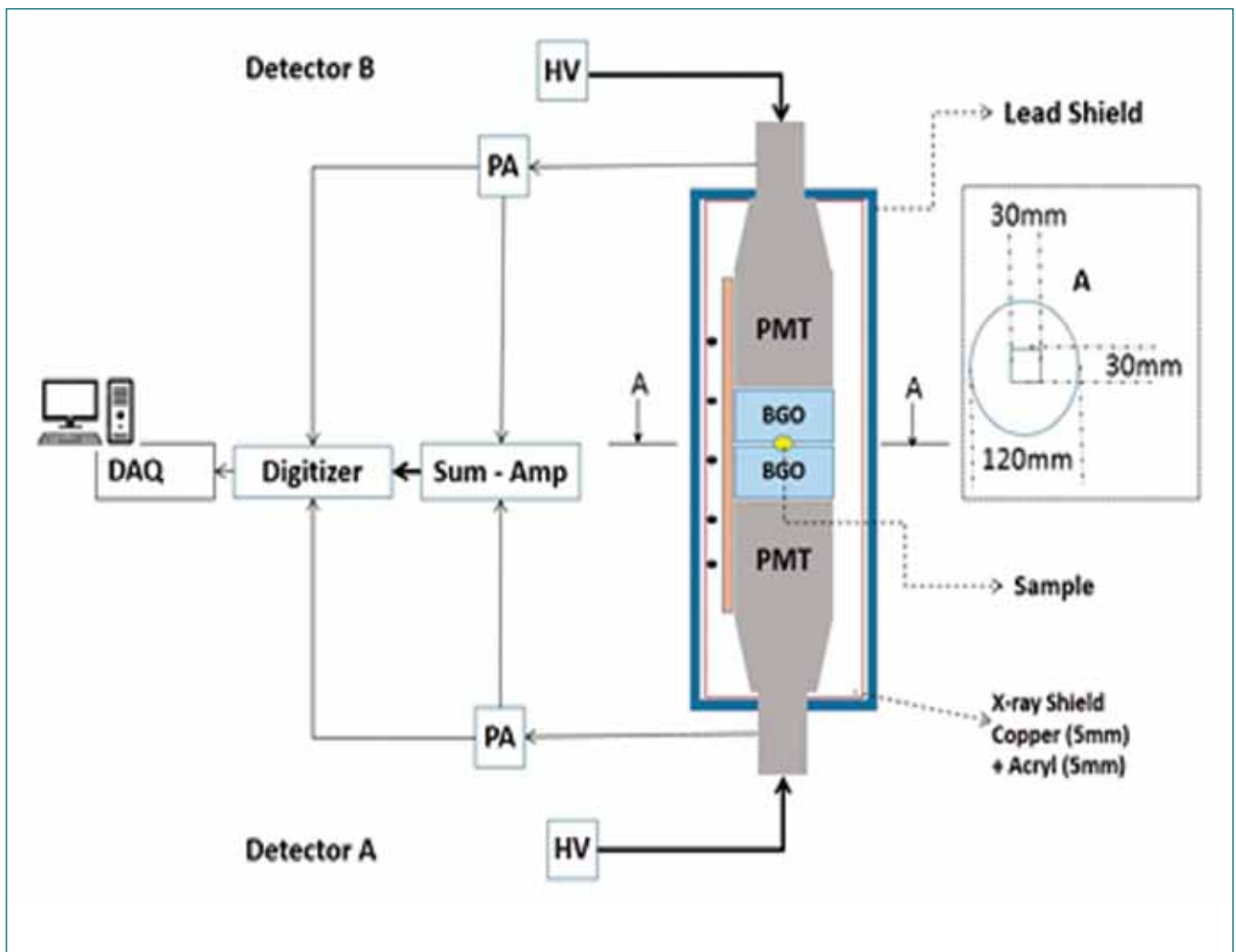


Fig. 1: Schematic diagram of WEAS and Associated Electronic circuit

V.60 Development of a Test Facility for the Multi-Specimen Prototype Pipe Bends for LBB Studies

Leak-Before-Break (LBB) is an essential safety criterion requiring optimisation studies to achieve an economic Fast Breeder Reactor (FBR) piping design without compromising safety. Cyclic bending dominance loading conditions pose challenges in establishing LBB criteria for the FBR piping system, and it is more of a concern for small-diameter piping systems. Hence it is planned to construct an experimental facility to study the crack growth behaviour of small-sized pipe bends (50 NB) to estimate realistic LBB parameters. The designed test facility can undertake simultaneous testing of four-pipe bend specimens. It is planned to test two specimens with a longitudinal notch and two samples with a circumferential notch for pipe bends of size 50 NB.

The test parameters are identified based on 3D finite element analysis. The numerical analysis identifies the critical location to introduce the initial notch and estimates the maximum displacement applied at the top of the pipe bend under cyclic load. Accordingly, the pipe bend, associated straight portions, and rigid end flanges are simulated, and the bottom end of the pipe bend is fixed. The top displacement is applied such that the maximum von Mises stress on the unnotched pipe bend is close to the $3S_m$ limit corresponding to the service conditions (Fig.1). Accordingly, the net dis-

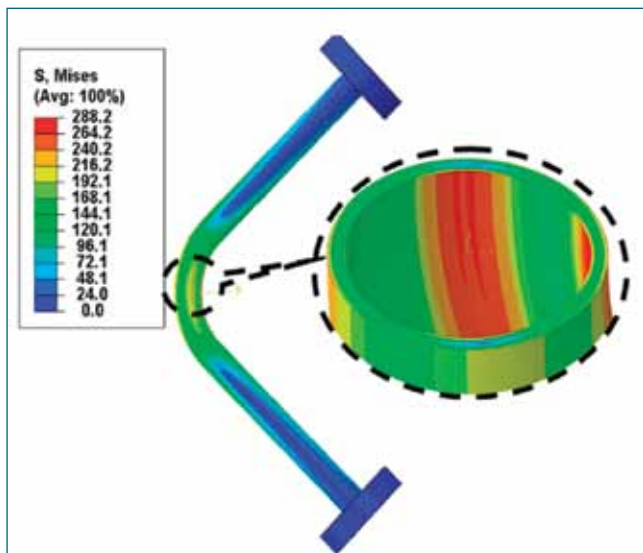


Fig. 1: Von-Mises stress distribution on the 50 NB pipe bend under peak cyclic load

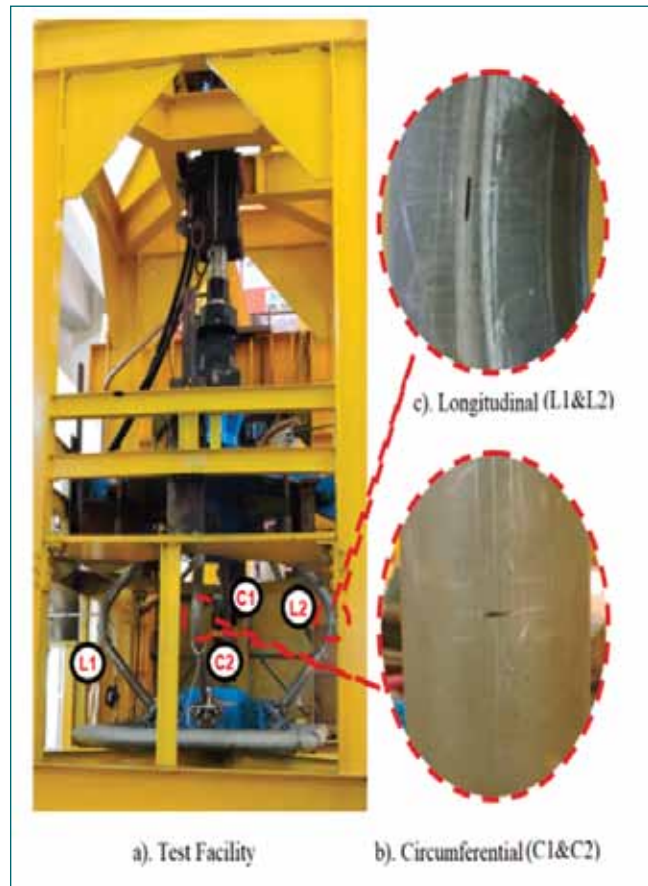


Fig. 2: Photograph of the multi-specimen LBB test facility

placement applied at the top of the pipe bend is 11 mm. The governing stress responsible for the crack initiation in the case of a circumferential notch is longitudinal stress, and that of a longitudinal notch is circumferential stress. The initial notch is identified based on the maximum stress conditions.

Detailed fabrication drawings are prepared based on the input obtained from the numerical analysis to construct a multi-specimen LBB test facility. The photograph of the newly built multi-specimen LBB test facility for pipe bend is shown in Fig.2. All the pipe bends are connected with a common header to apply sustained internal pressure of 0.4 MPa, and the cyclic load is applied with a servo-hydraulic actuator. The presence of an initial notch on the pipe surface will help for early crack initiation (Fig.2). All necessary preliminary experiments on these test specimens are completed, and the results agree with the numerical results.

V.61 Numerical Simulation of Operational Transients of FBR 1&2

Reactor startup and shutdown are planned plant transients that are expected numerous times in the life of FBR1&2. The plant startup comprises of three major activities – 1) Terminating decay heat removal and initiating flow through steam generators (SGs) by the Boiler Feed Pump (BFP), 2) Approach to criticality, and 3) Power raising in the reactor core by raising the control and safety rods (CSRs). Similarly, the plant shutdown comprises of three major activities – 1) Reduction of neutronic power of the reactor to zero by lowering of CSR, 2) Deployment of OGDHRS, and 3) Achievement of cold shutdown condition.

There are various plant design and safety constraints to be met during the execution of these transients 1) the heating/cooling rates of the hot pool should be less than 20 K/h, 2) the total reactivity should be less than pcm, 3) the reactor period should be more than 20 s, and 4) SG cold end $\Delta T < 200$ °C. A “wait and raise” mode for the startup (in which each control rod will be raised for a definite distance after a definite time interval) and a “wait and lower” mode for the shutdown has been adopted

for FBR1&2, similar to that of PFBR. During these transients, primary and secondary loop flow rates shall be maintained at a nominal 100 % flow to avoid thermal stratification issues in the sodium pools. Feedwater flow shall be controlled based on sodium temperature at the SG outlet.

The dynamic analyses for startup and shutdown transients are carried out using in-house plant dynamics code DYANA-P. Two operational parameters, namely, control rod movement distance and waiting time between control rod movements, are optimized as 2.3 mm and 2.75 min, respectively, for the Beginning of Equilibrium Core (BOEC) configuration. The evolution of reactor power and external reactivity during startup is shown in Fig 1. The startup and shutdown durations were both estimated as ~20.5 h each. The design and operational constraints of various plant systems are also satisfied. Parametric studies were also carried out for different core burnups and the control rod stroke and waiting time have been worked out.

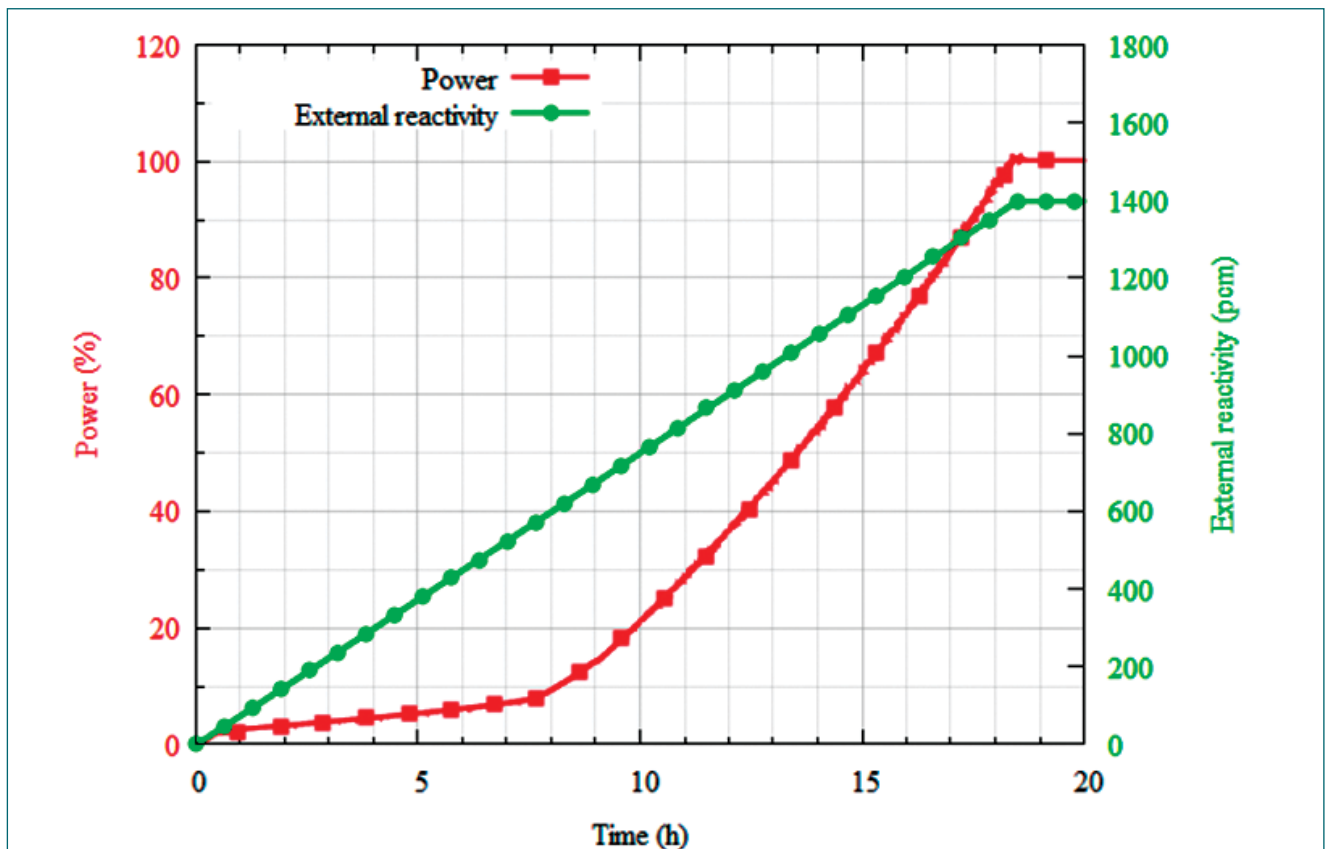


Fig. 1: Evolution of Power and External Reactivity during Startup

V.62 Towards Accurate Computation of Corium Thermal Hydraulics during Fast Reactor Severe Accident

Accidents leading to core meltdown that can release molten corium into reactor pool are rare events with very low probability. However, in the eventuality of an incident that leads to core meltdown and release of molten corium into reactor pool, the transport of the same becomes important and needs to be characterized. Moreover, large volumes of fission gases are also released into reactor pool as well. Accident progression in the fast reactor is expected to be distinct from that in the thermal reactor.

One of the major tasks after release of corium in sodium pool is to avoid clumping (aggregation of fuel fragments) that may result in re-criticality and further large energy release. The focus of the present study is on the movement of corium in liquid state within liquid sodium with resolution of flow structures resulting from two phase instabilities. Towards this, a general use volume of fluid (VOF) based code for analysis of two phase flow physics has been developed. Interface reconstruction is done using a Piecewise Linear Interface Reconstruction (PLIC) method that incorporates a c0 correction step developed during the present work. The add-on template is seen to improve the accuracy of PLIC interface substantially. Sharp interface advection is done using a highly efficient Edge Matched Flux Polygon Algorithm (EMFPA) method. EMFPA is a geometric advection method and allows diffusion free interface advection. Finally, curvature calculations are done using a highly accurate variable stencil Height Functions (HF) method. An improved version of the original HF

method that used a large stencil (3×7 or 7×3), the method allows accurate curvature calculations even for thin (under-resolved) interfaces. Using calculated curvature values, surface tension forces are calculated and incorporated into flow equations using a Continuum Surface Force (CSF) approach. Flow is solved using a force balanced fully implicit projection based solver that ensures minimal surface tension induced parasitic currents. The discretized equations are solved using a pre-conditioned Stabilized Bi-Conjugate gradient (BiCGSTAB) matrix solver. Further the capability of solving energy equation and incorporating density induced buoyancy forces into the computational framework is also developed. All these sub-routines are integrated and incorporated under THYC-MP code (Thermal Hydraulic Code – Multi Phase). The developed code has been validated extensively against benchmark single phase and two phase problems. Two systems of fluids viz. Wood's metal-water and Corium-sodium are studied. The former system is a popular choice as simulant system to study hydraulics of the later. It must be noted that no phase change is considered at present. The evolution of volume fractions of corium (in sodium) and woods metal (in water) as predicted by THYC-MP code is shown in Fig. 1. The computational elements used for the present study are of size 0.5 mm. The total number of elements used is 1.5 lakhs. At present the developed code is further undergoing extension in the form of parallelization of solver that would allow solutions on much finer scales successfully allowing capture of smaller instabilities.

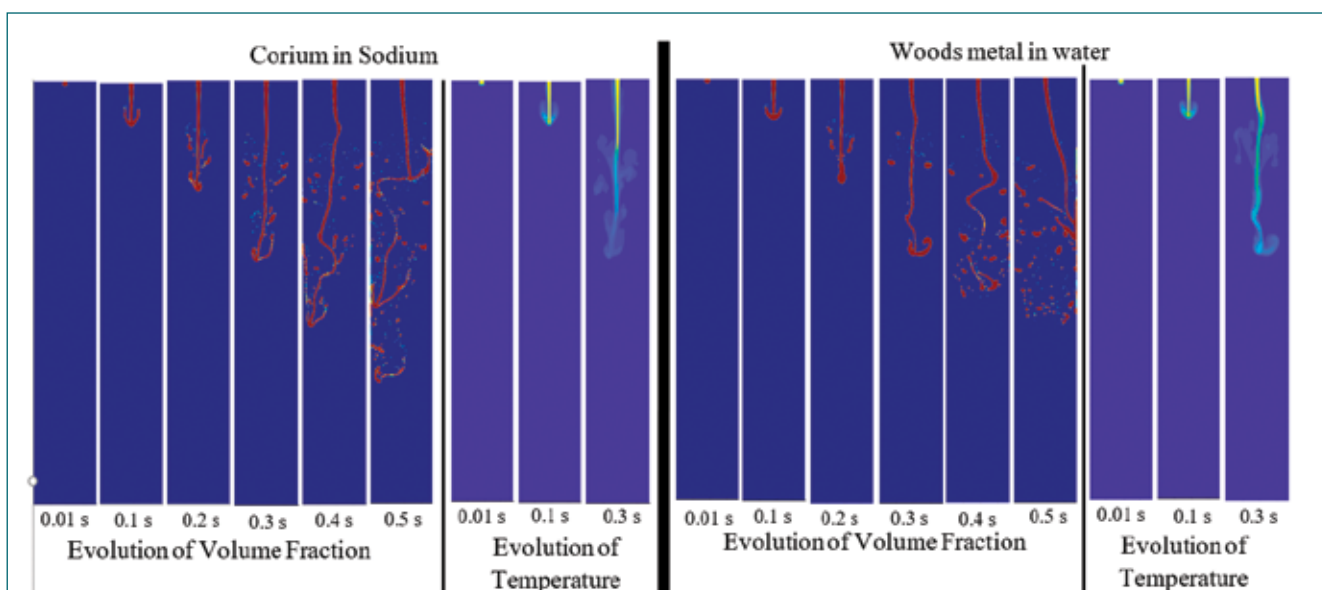


Fig. 1: Evolution of volume fraction and temperature for the two fluid systems studied.

V.63 Numerical Analysis of Sodium Pool Spreading on the Sloped Floor in SFR Cell by Developing Multidimensional Model

Accidental coolant leaks in Sodium-cooled Fast Reactor (SFR) can create pool fire scenario due to spreading of leaked sodium on cell floor surface. Thermal consequences of pool fire depend on the surface area of the pool that can be formed during a leak event. The spreading process increases the surface area of sodium pool exposed to the atmospheric air and hence the amount of sodium burnt and resultant consequences are augmented. In this connection, a 3-D numerical model has been developed based on viscous gravity current equation of shallow layer model to analyze the sodium spreading on the floor (sloped/plane) surface by considering the specific burning characteristics

of sodium pool fire. The model developed has been validated using the benchmark results for the pool spreading process. Further, the validated model has been used to evaluate the transient pool shape and size, pool height profile and maximum pool area for various sodium leak rates and floor slopes. The model predicted results for 36 kg/h sodium leak with different floor slopes are shown in Fig. 1(a-d) The results show that the sloped floor promotes the downward spreading compared to upslope and cross slope directions. This validated spreading model is used with the sodium fire analysis codes.

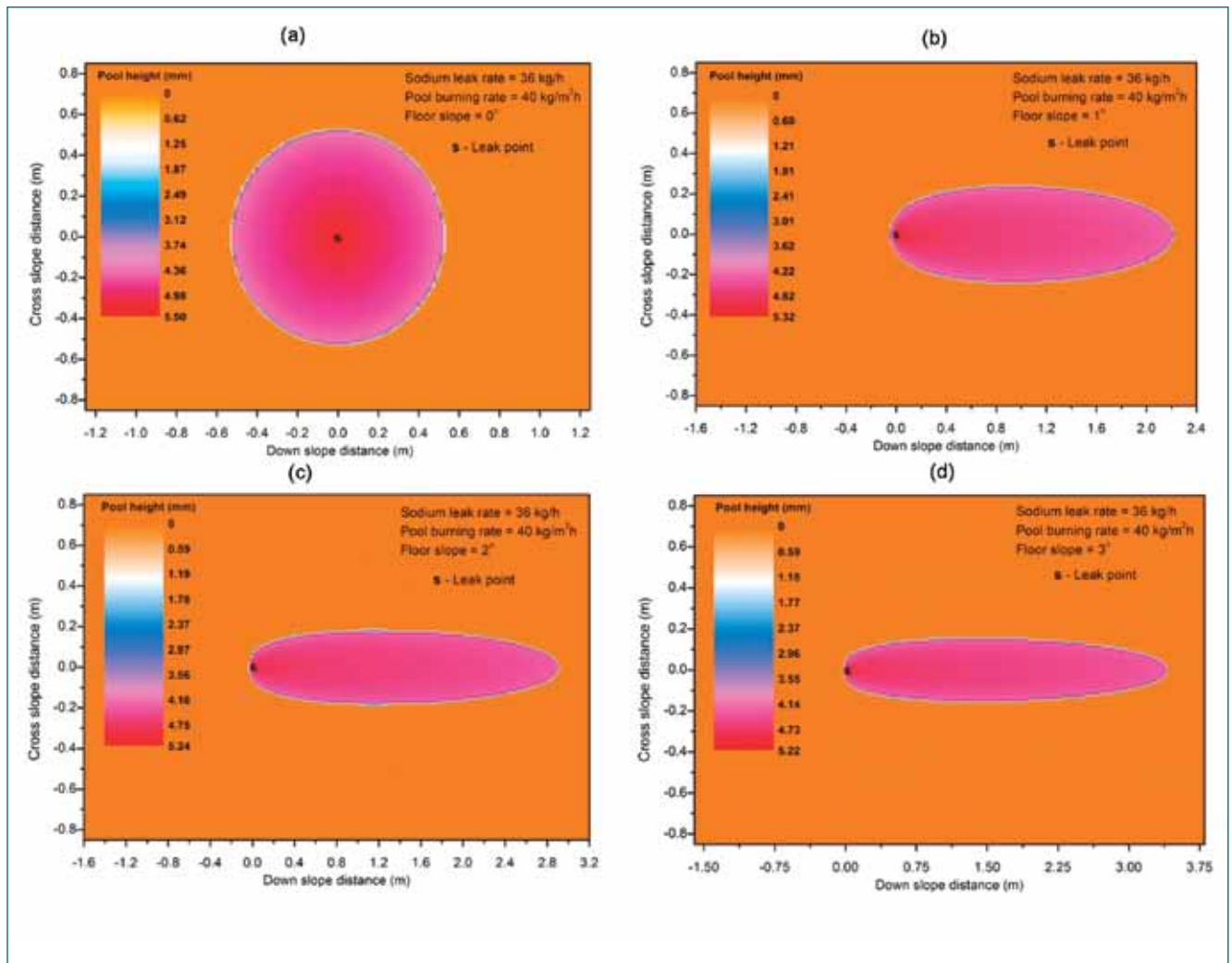


Fig. 1: Equilibrium pool shapes predicted by the model for different floor slopes

V.64 Numerical Analysis of Sodium Flow Boiling in Narrow Sub-Channels of SFR by Developing CFD Based Multiphase Flow Model

Sodium boiling can occur in SFR under hypothetical accident conditions such as large flow blockage in the fuel subassembly flow sub-channels or unprotected loss of flow accident (ULOFA) scenario due to continued mismatch between heat generation and heat removal by the coolant. A CFD based multiphase model for liquid sodium flow boiling under low Peclet number (Pe) flow conditions is developed using finite volume approach (FVM) towards the safety assessment of SFR under such accidental conditions.

The model developed is based on the Eulerian-Eulerian multiphase flow approach (two-fluid model) under near atmospheric pressure conditions and flow boiling of sodium in the narrow sub-channels of SFR. Under such conditions, the sodium vapour bubble formed tends to be larger and the occurrence of high void fraction flow regimes is most likely to occur. Thus the flow regime based modelling is implemented using the flow pattern dependent constitutive correlations for sodium two-phase flow in the framework of Algebraic Interfacial Area Density (AIAD) model. Using this model, sodium boiling from its inception, nucleate boiling, and further

the forced convective vaporization flow regime are predicted numerically.

The benchmark experimental cases are used to validate the model for two-phase flow pressure drop values and also with the empirical correlations available under quasi-steady flow boiling conditions. The model is used to analyze sodium flow boiling in a vertically heated narrow annulus channel ($D_h \sim 3$ mm) under different conditions ($m = 8$ g/s, $q_w = 0.8$ to 1.2 MW/m²) and further implemented to 7-pin bundle geometry for specific flow and wall heat flux conditions to predict the transient boiling. The predictions of void growth behavior along the axial and in the radial direction depict the dominance of dispersed-annular flow boiling regime particularly with low mass flow rates and high wall heat fluxes. The wall heat transfer coefficient in the boiling zone is evaluated from the wall flux partitioning components and compared with the available empirical correlations. Also based on the flow parameters predicted, the possible flow regimes are identified using the available flow pattern maps. The validation for two phase pressure drop (Fig.1) and variation of wall heat flux components (Fig.2) are shown below.

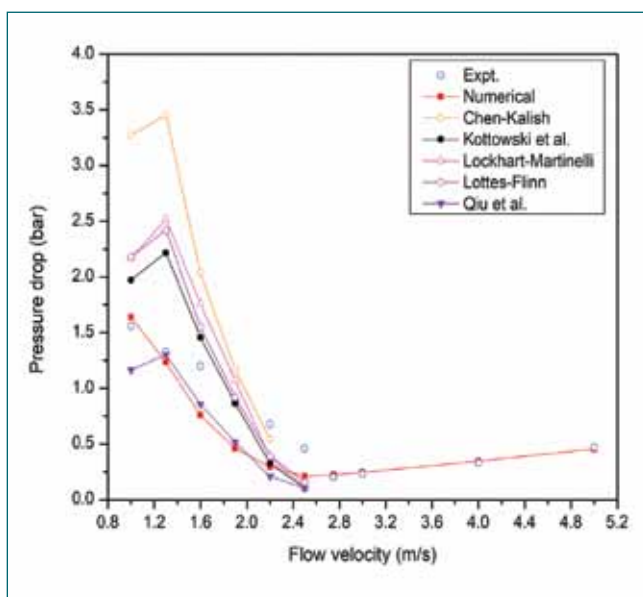


Fig. 1: Variation of pressure drop at various mass flow rates (at $q_w = 1270$ kW/m²)

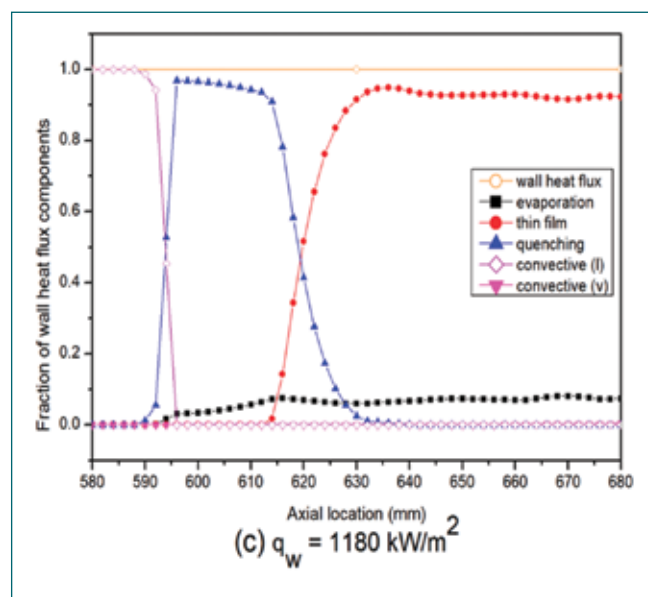


Fig. 2: Variation of wall heat flux components along the end of heated section length

V.65 Analysis of the Criticality Behaviour of FBR Core Debris Bed on the Core Catcher by Developing 2D Diffusion Based Model

Core catcher is a passive safety device provided in a fast breeder reactor (FBR) for collection and long term retention of molten core materials in subcritical and coolable configuration. The criticality potential of core debris for a wide range of debris bed conditions is considered for the safety analysis of the core catcher. So, it is necessary to establish a computational methodology for the reasonably accurate evaluation of the criticality behaviour of disrupted FBR core. For this purpose, an orthogonal cell finite volume method based multi-group neutron diffusion model (2D axi-symmetric) has been developed and validated using fast and thermal reactor criticality benchmarks.

Criticality analysis of the FBR core debris has been carried out for cylindrical and conical shapes of the debris bed with different porosities and various radii of spreading on the core catcher. The results of the study indicate that the compact whole core debris (equivalent to mass of 181 active core subassemblies) settled on the core catcher with radius above 120 cm will be in subcritical condition (Fig. 1). The study also indicates that the critical mass required will increase with increase in debris porosity and the whole core debris with porosity value of higher than 0.3 cannot attain criticality even in optimum geometric configuration.

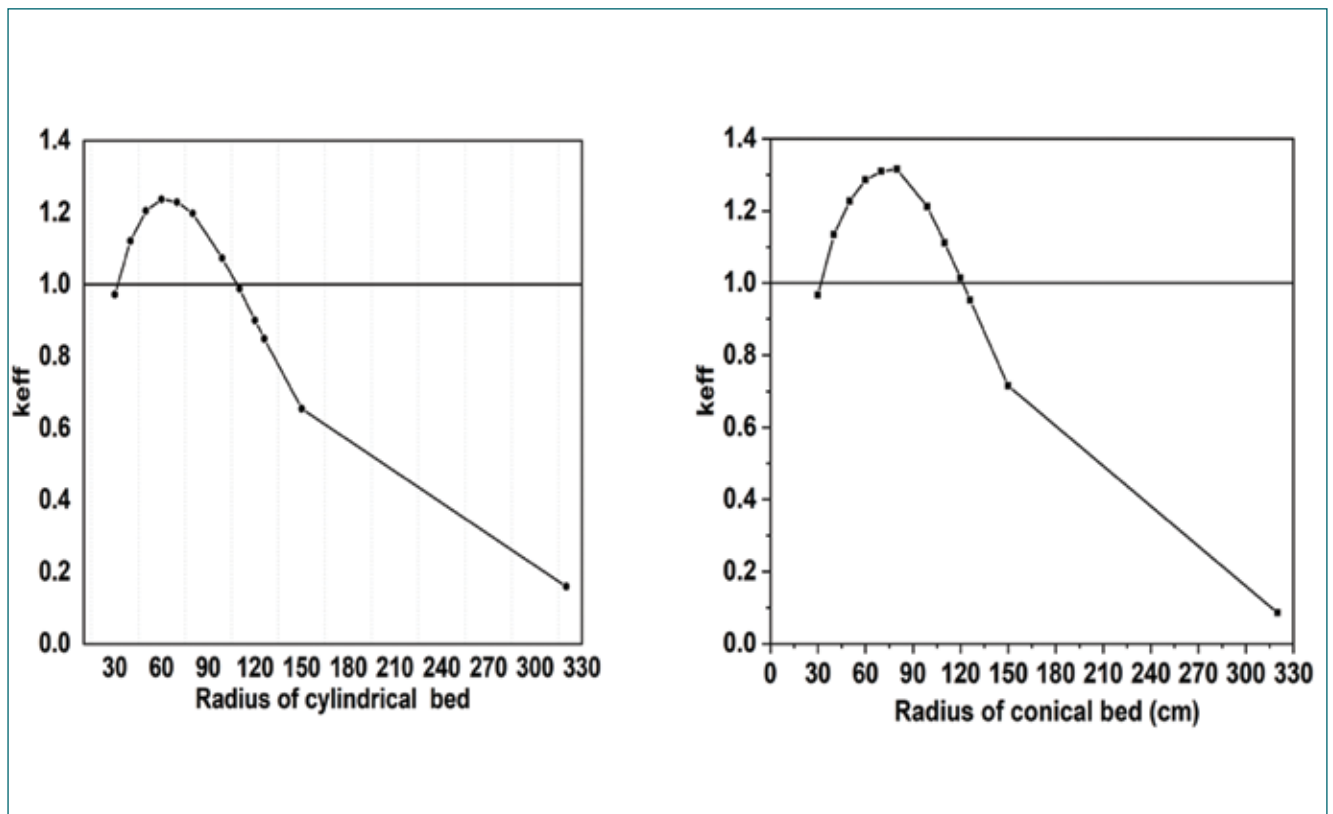


Fig. 1: Criticality behaviour of the whole core debris for cylindrical and conical shaped debris bed

V.66 Development of Sensor for Direct Sodium Pressure Measurement

Conventional pressure sensors are not suitable for direct measurement of the static pressure of flowing liquid sodium due to temperature and chemical affinity of sodium with air and other structural materials. In the light of above, a Sodium Pressure Measurement Device (SPMD) first of its kind has been developed. The newly designed SPMD is compact in size and capable of direct measurement of the static pressure of flowing liquid sodium.

The schematic of SPMD is shown in Fig. 1. The device consists of a disk, stem, strain gauges based force measuring element, bellows, leak detector and finned housing. The force acting on the disk due to sodium pressure is transmitted to the force measuring element through the stem. The bellows is selected as primary leak barrier to prevent the leakage of sodium without interfering with the transmission of force. A spark plug type sodium leak detector is provided to detect any sodium leakage through bellows in case of a failure of the bellows. The finned housing will reduce heat load to the load cell and enhance the leak tightness by providing sodium frozen seal which acts as a secondary seal, in case of sodium leak through bellows. Further a one meter long helically wounded stainless steel un-insulated tube is provided as secondary leak barrier in case of large leak through the bellows. The instrumentation cable of the force measuring element is routed through the tube. The total assembly is provided inside a guard pipe, which can be welded vertically with a suitable standard fitting

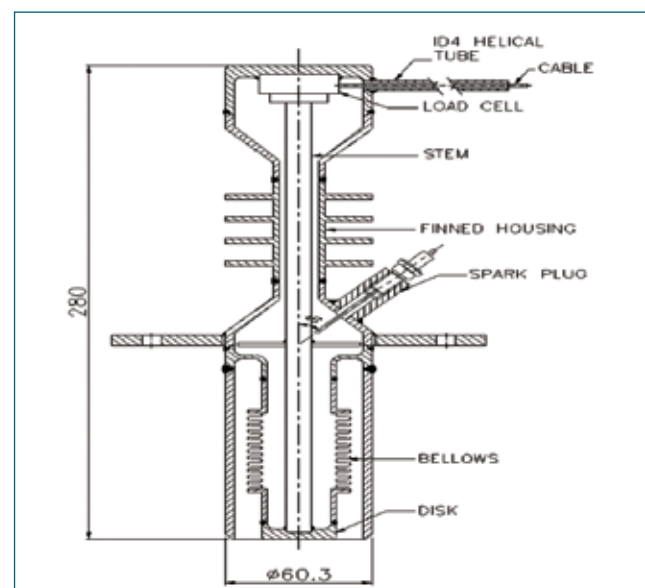


Fig. 1: Schematic of SPMD

to sodium piping. The device will not offer any additional pressure drop to the flowing sodium. The photo of final assembly is shown in Fig 2.

The device has been calibrated in hot air up to 350°C. The result confirms that the device is with good linearity and repeatability. The performance



Fig. 2: Photo of SPMD

of the device is unaffected due to temperature variation as shown in Fig 3. The response time of load sensing element is 60ms and hence it can easily measure the static pressure fluctuation with frequency upto 15 Hz where the pressure fluctuation in a hydraulic system expected range is upto 2 Hz. The capability of the device to measure the pressure fluctuation upto 2Hz was successfully demonstrated in a water facility. Further the device was introduced in a sodium test facility for its functional demonstration in sodium environment and same was confirmed up to operating temperature of 450°C. Now the design has been proposed to be used in sodium system wherever the pressure measurement is required.

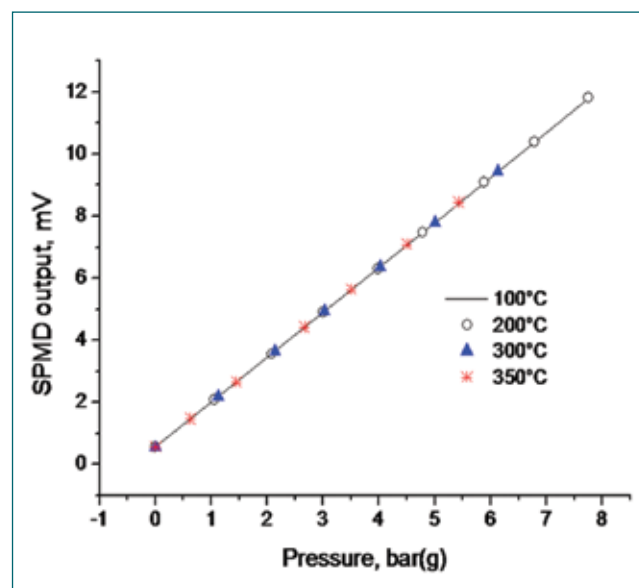


Fig. 3: Results of calibration

V.67 Qualification of Inconel-625H Bellows for Sodium Service Valves

Sodium service valves are different from conventional valves, as it demands stringent leak tightness owing to the chemical reactivity of sodium with air and its constituent moisture. Bellows Sealed Globe Valves (BSGVs) are commonly used for sodium service. BSGVs utilize multi-ply bellows, which acts as primary seal to avoid leakage of sodium to ambient environment. One end of the bellows is welded with valve plug and the other end with the bonnet. It has a mechanism to convert the rotary motion of hand wheel into linear movement of bellows. A secondary seal is also provided by graphite gland packing. The space between primary and secondary seal is continuously monitored by spark plug type sodium leak detector, which will give signal in case of bellows failure. Schematic of BSGV is shown in Fig. 1. Bellows being flexible, accommodates axial movement of stem during valve actuation.

At present, bellows made of SS-316 Ti grade steel is used in sodium service valves up to service temperatures of 600°C. But the material is not fool proof for high temperature application due to probable knife line crack development. Further, the leading valve manufacturers do not provide guarantee for life cycle of bellows for the operating temperature range. Hence, alternative material for bellows construction was explored for high temperature BSGV design. For addressing the issue, it is proposed to use Inconel-625H bellows in high temperature sodium service valves instead of SS-316Ti due to its compatibility with sodium, superior mechanical properties at elevated temperatures, weldability, availability in thin sheets and resistance to SCC and Knife line crack. Qualification of these bellows for sodium service is required before introducing in sodium valves. Six numbers of bellows suited for a 50 NB BSGV were tested in sodium environment. Commercially available

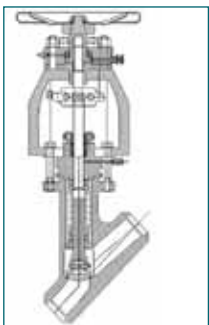


Fig 1: Schematic of Bellows Sealed Globe Valve



Fig. 3: Bellows after removal from test setup



Fig 2: Photograph of bellows test setup with mounting arrangement

Inconel-625 sheets are in low annealed condition; hence bellows after manufacturing are annealed as per ASTM B443

The sodium test setup consisted of six numbers of test mechanisms mounted in series (Fig. 2). Bellows test mechanisms represents replica of a valve without valve body & mating parts. Elongation of bellows as in valve actuation is simulated by a top mounted pneumatic actuator, which generates stroke of 12.5mm on command.

The test study was intended to evaluate performance of indigenously manufactured Inconel-625H double ply bellows. The testing was carried out in sodium at 575°C for 1200 cycles covering duration of sodium exposure for 5000 h. The cyclic operation was automatically controlled by programmed microcontroller based electronic system. The extreme stroke positions were remotely indicated via limit switch mounted on test mechanism.

All the six bellows could withstand the designed creep-fatigue mechanical loading at elevated temperature of 575°C in sodium environment and no leak was observed. After completion of experiment, bellows were removed from test section and it was observed about 50% of bellow length was wetted by sodium and rest of the surface was exposed to Argon space (Fig. 3). Post sodium cleaning, visual testing was performed and no significant defect or physical damage was found. Finally, the bellows were qualified by Helium leak test with leak rate less than 10^{-8} Pa-m³/s. Further metallographic inspection was conducted and its results indicated no change in grain structure or chemical composition in the bellows after the sodium exposure at elevated temperatures. Hence, Indian make Inconel-625 H bellows were successfully qualified for liquid sodium valve applications.

V.68 Design optimization of Core Flow Monitoring Mechanism for Blanket and Storage Subassemblies

The monitoring and measurement of coolant flow rate through the core Sub-assemblies (SA) is essential for operation and safety of the reactor. Any undesirable reduction in coolant, due to blockage in core SA, can lead to many unforeseen critical events. The coolant flow rate through the reactor core sub-assemblies is measured using a device named as Core Flow Monitoring Mechanism (CFMM). It operates during reactor shutdown condition, when sodium flow is reduced to 20% of the nominal flow rate through each sub assembly.

Eddy Current Flow Meter (ECFM) is used as a sensor in CFMM for sodium flow measurement. Two CFMMs of different hydraulic design and geometrical configurations are used to cover the entire core region for sodium flow measurement. CFMM-1 is used to measure the sodium flow rate through Fuel Subassembly (FSA) and CFMM-2 is used to measure the sodium flow rate through Blanket Subassembly (BSA) and Storage Subassembly (SSA). FSA are the major source of heat generation in the reactor, therefore major portion of the coolant is passed through the FSA. The sodium velocity at the sensor (ECFM) region of CFMM plays a crucial role in the accuracy and reliability of the measurement. The sodium velocity in CFMM-1 is high enough, even at fuel handling condition, for obtaining reliable measurement of flow rate. However, the sodium flow rate in BSA and SSA is considerably low during the fuel handling condition. Therefore, the sodium velocity across the sensor region in CFMM-2 is also very low. Hence, it was envisaged to modify the hydraulic design of CFMM-2 so as to increase the sodium velocity in the sensor region for obtaining reliable readings.

Towards the design optimization, various design changes in lower part of CFMM-2 have been studied using numerical tool to arrive an optimized design. The hydraulic design has been optimized in such a way that maximum sodium flow velocity can be achieved at the sensor region for the same range of flow rates in BSA and SSA. The gap between sensor and flow guide has been reduced to increase the velocity. However it results in an increase in pressure drop and thereby reduces the sodium flow through CFMM in a system with multiple parallel flow paths. Therefore, the geometry of

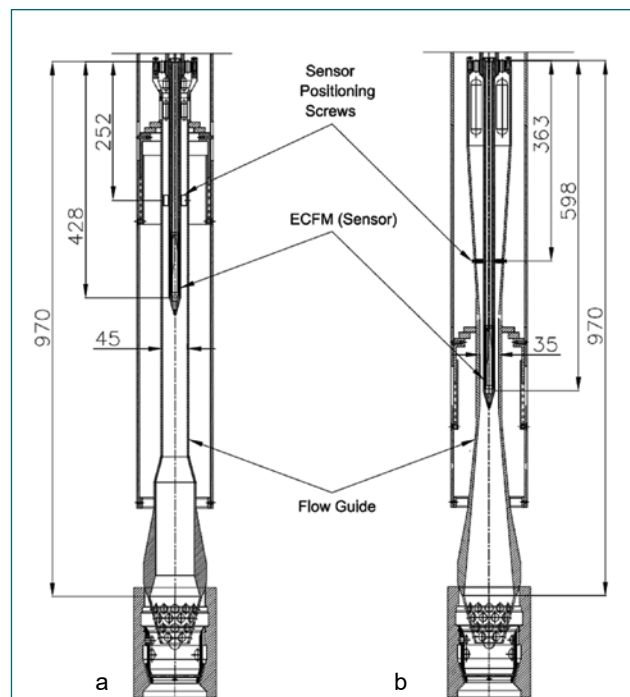


Fig. 1: Schematic of Reference (a) and Optimized (b)

CFMM flow guide is optimized accordingly to reduce the pressure drop. The sudden reduction in flow area was modified to a convergent divergent profile to reduce the pressure drop. The schematic of reference CFMM-2 and modified CFMM-2 designs with SA top are shown in Figure 1 for comparison. The developed optimized design of CFMM-2 was fabricated in 1:1 scale to validate with experimental measurements. The experimental study was conducted in water at 30°C. The experimental results are extrapolated to appropriate reactor conditions using suitable non dimensional numbers. The flow velocity across the sensor region is found to be above 1 m/s, which is increased by 159% with respect to the reference design. The comparison of optimized design and reference design are tabulated in Table 1.

Table 1: Comparison of reference design and optimized design of CFMM-2 for blanket subassembly

Core Flow zone	Sodium Flow rate (kg/s)	Velocity at sensor location of CFMM-2 (m/s)	
		Reference	Optimized
Blanket Zone-8	1.21	0.56	1.44
Blanket Zone-9	1.14	0.52	1.36
Blanket Zone-10	0.86	0.39	1.01
Storage Zone-11	0.50	0.23	0.56
Storage Zone-12	1.00	0.46	1.18

V.69 Development of Compact Hydrogen Meter for Steam Generator Leak Detection System

Steam generator (SG) in Fast Breeder Reactors (FBR) is typically a heat exchanger, in which sodium exchanges the heat produced in reactor with water. SG produces super heated steam to roll the turbine. In SG, sodium flowing at a moderate pressure is physically separated from water/steam at high pressure by a 2.3 mm thick tube wall. In case, one of the tubes becomes defective, steam leaks into sodium, causing sodium-water reaction. It is highly destructive in nature because the instantaneous reaction is exothermic, liberates hydrogen and corrosive NaOH. It is very important to detect SG leak at its incipient stage to minimize the damages. Typically steam leaks initiate with a small magnitude of a few mg/s, which produces hydrogen in small quantities which would be immediately, dissolved in flowing sodium. SG leak detection is by means of on-line measuring hydrogen concentration in sodium at the exit of SG. Any abrupt increase in hydrogen level would be attributed to SG leak. Sputter ion pump (SIP) based hydrogen meters are proven for the purpose. But its main disadvantage is its large size. For Instance, PFBR which has modular type SG requires ten number of hydrogen meters; one for each of the eight modules and one for each of the two sodium headers. More over the meter works at 450 °C that necessitates a separate heater circuit for each of the meter.

Towards development of a compact SGLDS, a Compact Hydrogen Meter (CHS) is conceptualized without compromising its functional & safety requirement. It uses a small size triode SIP with 5 lps capacity, which is developed in Electromagnetic Application & Instrumentation, Division/ BARC and a suitable Nickel diffuser designed and manufactured at IGCAR. Nickel diffuser consists of three thin nickel tubes of 0.3 mm wall thickness placed in a stainless steel shell in the form of a 90°



Fig 1: Nickel diffuser 'U' shaped, once through counter

bend to accommodate the differential thermal expansion between the nickel tube and the SS shell. The nickel diffuser is shown in Fig 1. SIP can be mounted directly on top of the nickel diffuser. The other components of meter section such as sodium economizer, sodium heater and piping are redesigned to an optimum size to make the entire SGLDS compact. Economiser is a

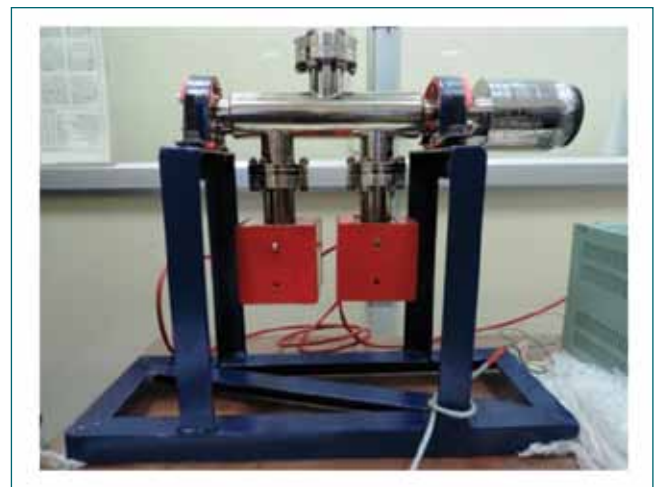


Fig. 3: Dry testing of Compact SIP

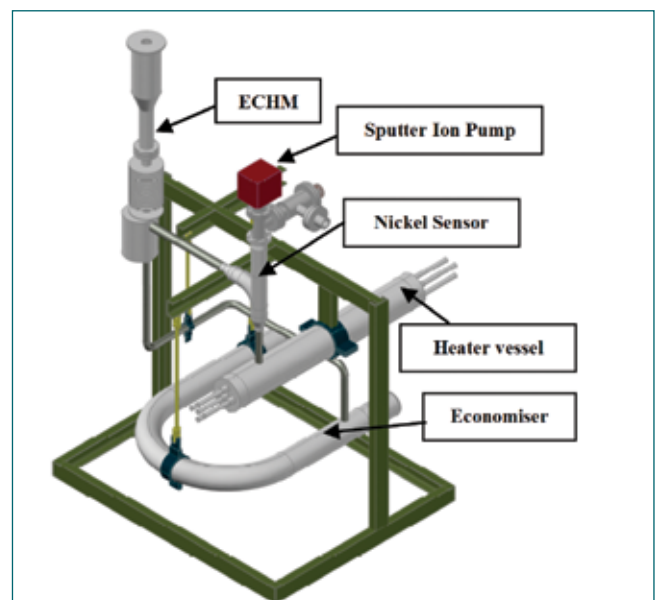


Fig. 2: Compact Steam generator leak detection system

flow shell and tube sodium to sodium heat exchanger. A heater vessel of 16 kW heater capacity is designed to compensate the heat loss through the economiser circuit, for controllability, and to meet uncertainty. New rod type heaters are used to make it still compact. The vacuum system is reduced to a short pipe having a connecting port and isolation valve for a fore pump. The overall space requirement of SGLDS is reduced to 1/5th of the present system. Schematic drawing of the compact SGLDS is shown in fig 2. The SIP was dry tested in a separate vacuum system for one month duration. It is developing 1×10^{-7} mbar steady vacuum. Compact SIPs are shown in Figure 3.

V.70 Optimized Procedure for Regeneration of Secondary Cold Trap

Major impurity expected in secondary sodium circuit of FBR is hydrogen, which is continuously diffused into sodium through the Steam Generator tubes. Hence, the on-line sodium purification system, i.e. secondary cold trap (CT) is designed for trapping hydrogen predominantly. In the CT, sodium would be cooled to a saturation temperature; the dissolved hydrogen in sodium would be crystallized into sodium hydride that would be held within a wire mesh bundle provided at the bottom. Sodium hydride accumulates in the secondary cold trap with time and once it is loaded to its limit, it becomes inoperable. It is estimated that an operation period of 4.5 years is sufficient to fully load the CT in PFBR. It is planned that after every 4.5 years, CT in PFBR would be regenerated in-situ by removing the sodium hydride trapped in the wire mesh for continuing its operation. Vacuum decomposition technique is the proposed scheme for regeneration. It involves gradual heating of the CT up to 400 °C to decompose the NaH into sodium and hydrogen gas in the ambience of vacuum.

A scaled down model of secondary cold trap of PFBR in terms of its volume called Model Secondary Cold Trap (MSCT) was used to demonstrate the regeneration process. Schematic drawing of MSCT is shown in Fig 1. MSCT is a part of SGTF sodium loop, which has facilities to inject known quantity of hydrogen into sodium and a calibrated hydrogen meter in sodium. Objectives of the experiments were to standardize the regeneration procedure and evolve the methodology for accounting and safe management of hydrogen. MSCT was first loaded with a known quantity of NaH. Thereafter, the decomposition by vacuum technique was performed. The evolved hydrogen gas was converted to water vapor by means of a bank of fuel cells.

Proposed mode for heating of CT of PFBR during regeneration is by using immersion heaters installed at the top of CT. In order to heat up the bottom wire mesh loaded with NaH with the immersion heaters at the top, a sodium level at 4.3m would be maintained. MSCT was also heated using immersion heaters fixed at the top, maintaining the sodium column. Three campaigns of regeneration were carried out earlier. In first two campaigns, the total quantity of hydrogen loaded was 0.19 kg and in the third campaign, it was increased to

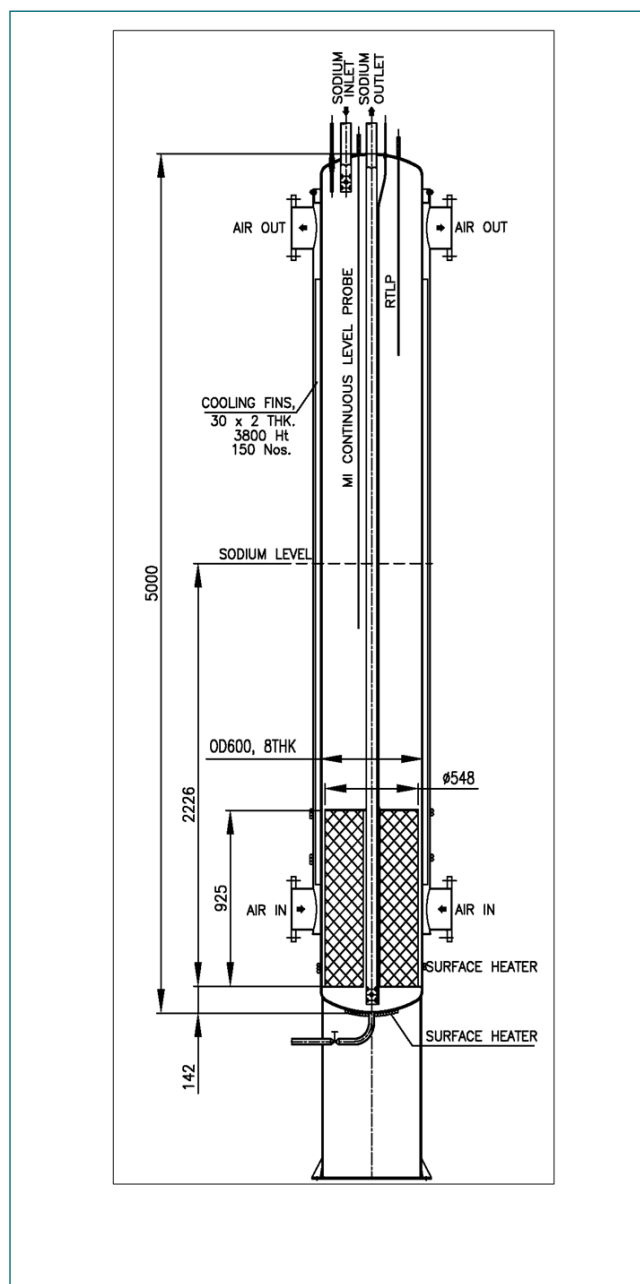


Fig 1: Schematic drawing of MSCT

0.56 kg. In all the campaigns about 70% of the hydrogen loaded could be released in the form of hydrogen gas, which was confirmed with the fuel cell current and a mass flow meter specific to hydrogen. During regeneration, the top part of sodium column was observed to be much hotter such that large temperature gradient of about 100-120 °C existed in axial direction. The hydrogen release rate was also not steady, sudden spikes were observed. It was understood that the top heating is undesirable and accordingly modifications were carried out in the

MSCT. Sufficient surface heaters were provided at the bottom part of MSCT that could provide a uniform temperature profile. In order to map the temperature along the axial length of the CT, additional thermocouples were provided at various axial positions in MSCT. Due to bottom heating, the inventory of sodium just above the wire mesh would only be adequate during regeneration process. A new sodium level probe reaching till the bottom was also introduced.

With the above modification, a fourth campaign of CT regeneration experiment was carried out with a hydrogen load of 0.603 kg. Sodium level was maintained only 2.2m during regeneration. MSCT

was gradually heated to 400°C using only surface heaters. The axial temperature was found uniform. Sustained release

of hydrogen started, when sodium temperature at the bottom crossed above 366°C. The time history of hydrogen release rate and sodium temperature at the bottom wire mesh region of cold trap is shown in Fig. 2. Rate of release of hydrogen gradually increased to a maximum followed by sustained release of hydrogen. The maximum rate of hydrogen release was observed to be 2.5 l/min. The sodium temperature and the static pressure in cold trap cover gas volume during regeneration experiment is shown in Fig. 3. The maximum pressure observed during hydrogen sustained release was around 0.254bar. After 33 hours

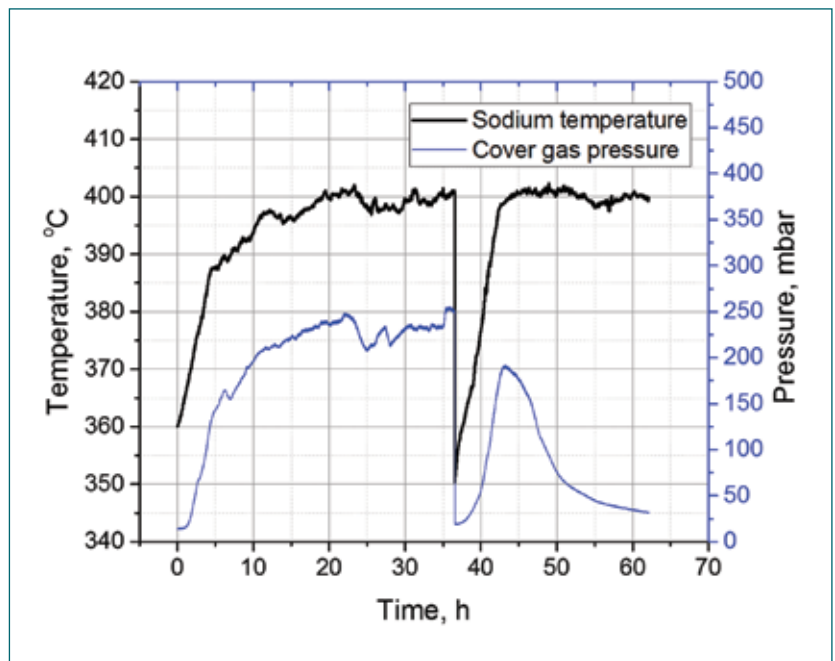


Fig. 3: Pressure developed above cover gas and sodium temperature with respect to time

of regeneration, the experiment was terminated for a short while, for the reasons to replace a degraded fuel cell with a new one. The total volume of hydrogen gas released in this campaign was measured to be 78% of injected hydrogen.

At 400 °C temperature, sodium vapors also would be carried along with hydrogen. A Sodium vapor trap and a sodium vapor condenser are placed in the downstream of hydrogen line to remove sodium from hydrogen incoming to the delicate fuel cell. A part of hydrogen could again react with sodium on its way to

fuel cell. Therefore, remaining hydrogen was expected to be present inside vapor trap or condenser in the form of sodium hydride. The vapor trap and condenser were inspected internally and confirmed the same. Accumulation of sodium hydride was noted.

It could be demonstrated that thermal decomposition of sodium hydride under vacuum is an effective method for regeneration of CT of PFBR. Sustained release of hydrogen was realized by controlled heating, reduced sodium level (2.2m) and maintaining uniform axial temperature across the sodium column. Hydrogen could be disposed safely. Process of In situ regeneration of CT of PFBR is finalized.

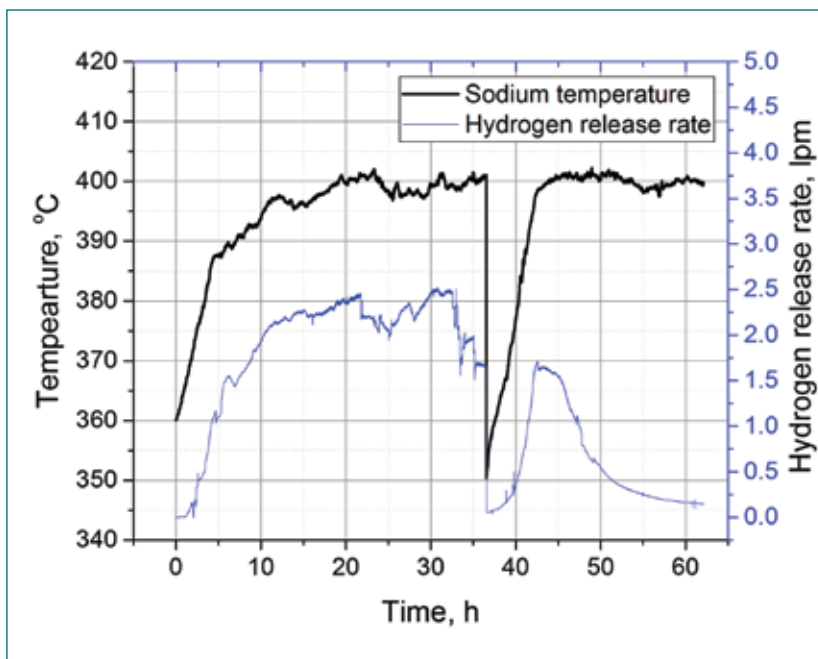


Fig. 2: Hydrogen release rate and sodium temperature of cold trap

V.71 Hydraulic Validation of Hydraulic Suspended Absorber Rods for Future FBRs

The passive means of shutdown plays a significant role in the safety performance of sodium cooled fast reactors. The presence of passive shutdown systems is more critical when active shutdown systems are not actuating on demand. The Anticipated Transients Without SCRAM (ATWS), such as Unprotected Loss of Flow (ULOF) in the primary coolant circuit can lead to coolant boiling and a core melting scenario. Hydraulically Suspended Absorber Rod (HSAR) is a passive reactor shut down device, which can cause shut down of the reactor in case coolant flow drops by definite fraction of the nominal mass flow rate. For future FBRs. In the normal reactor operating condition, sodium mass flow rate of 3.87 kg/s at 400°C is flowing through the HSAR. HSAR contains neutron absorber rods which are kept out of the reactor active core region during normal operation by the drag force generated due to the flowing sodium

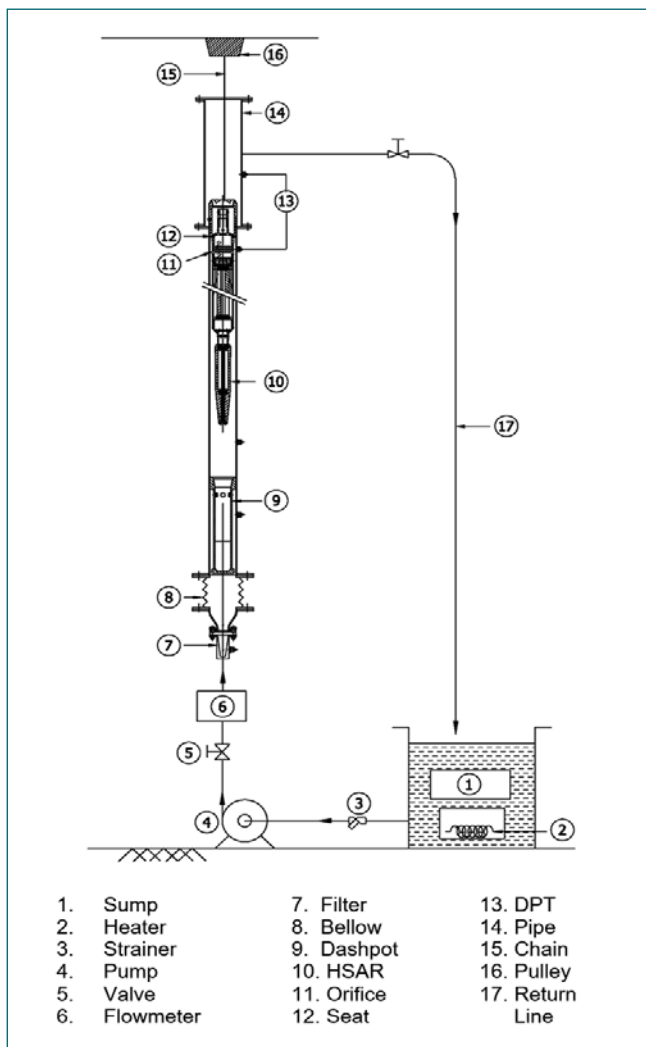


Fig. 1: Schematic of the test loop for hydraulic design validation of HSAR in water

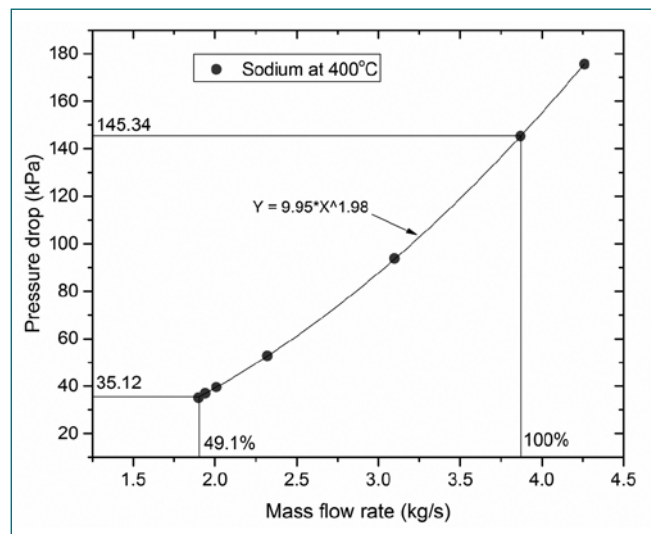


Fig. 2: Pressure drop characteristic in HSAR

across the head assembly at its upper end. It drops by gravity into the reactor core to shut down the reactor, whenever sodium coolant flow rate reduces below 50% of its nominal value.

The pressure drop device and seating interface, provided in the upper end of the HSAR, plays a crucial role in the reliable operation of the HSAR. The drag force is directly proportional to the differential pressure across the pressure drop device provided in the upper end of HSAR and minor increase in leakage from seating interface can reduce the drag force drastically. After successful completion of development and validation of pressure drop device and seating interface, a full-scale integrated HSAR subassembly (HSAR SA) was tested in water for characterization of hydraulic performance and qualification of the hydraulic design. A dummy full scale integrated HSAR SA was fabricated for this purpose. The experiment has been carried out in water using appropriate similitude. The schematic of the test loop is shown in Figure 1. The weight of prototype HSAR is 43.88 kg and apparent weight in sodium at 400°C is estimated as 34.48 kg. The experimental results are extrapolated for reactor conditions and the estimated pressure drop in HSAR for reactor at different mass flow rates of sodium is shown in Figure 2.

It is found that prototype HSAR in sodium at 400°C will detach from its seat at mass flow rate of 1.9 kg/s, which is 49.10% ±2% of nominal mass flow rate. The statistical uncertainty on the sodium flow at which the HSAR will detach is arrived using the experimental data from multiple experiments.

V.72 Development of a Novel Ultrasonic Bath for Centrifugal Extractor Bowl Dechoking

Annular centrifugal contactors are extensively used as solvent extraction equipment in fast reactor spent fuel reprocessing facilities in India. Due to their intricate geometry and small size, the rotating bowls of the centrifugal extractors are prone to choking after repeated runs in the active facilities due to deposition of fines at certain internal locations. Remote operation and maintenance of choked rotating bowl is rather difficult. Hence, a choked bowl might have to be disposed as a solid waste. In the plants that are designed for a higher capacity like DFRP and FRFCF, the size and numbers of the stages of these centrifugal extractors(CE) are considerably higher than those that are being used in CORAL. Hence, the solid waste generation due to choked bowl is a matter of concern. In order to minimize the generation of such solid waste due to choked bowls, a novel ultrasonic de-choking equipment has been designed & fabricated.

The design of equipment for ultrasonic cleaning of the choked CE bowl was decided based on the availability of space and head room at DFRP for remote operation. The de-choking equipment essentially consists of a

stainless-steel bath for housing the choked bowl motor assembly and an ultrasonic resonator probe, suitable for use with the former. Standard commercially available ultrasonic probes were scrutinized: horn type and push pull type resonators were selected for carrying out the experimental studies to validate the design. The bath was designed in such a manner that it can easily be located within the limited reach of the master-slave manipulator and a choked CE rotating bowl along with its drive motor would easily be mounted on top of this bath with minimum efforts.

As shown in figure 1, a cubical ultrasonic bath was fabricated from SS 304L plates. The bath was provided with a hinged top plate to facilitate remote removal of ultrasonic resonator for carrying out maintenance activities. This ultrasonic resonator probe was soldered to a radiation resistant high frequency cable that was housed in an L-shaped SS 304L pipe. An L-bend was provided for safe immersion into the liquid medium in the chamber. The baths were provided with siphoning lines to drain the liquid to the tank. Adequate slope was provided at the drain line to prevent stagnation



Fig. 1: SS Ultrasonic bath with resonator probe and motor bowl assembly.

and choking of lines. The cable was connected to the ultrasonic controller cum generator that was mounted outside the hot cell.

In the typical trial runs, a rotating bowl of a CE was deliberately choked with Zirconium Molybdate slurry. This trial was carried in single stage experimental CE set-up. The weight of the bowl was measured both at the start and end of specified intervals of time. The bowl was allowed to choke up to its flooding condition. The fully choked bowls were cleaned in an ultrasonic bath with different types of probes and with varying concentrations of nitric acid.

After the experimental trials the SS ultrasonic bath was installed in the contactor cells. The Installation and commissioning of this bath involved positioning of the equipment at the hot cell site, welding & joining of the bath at the designated location, routing & welding of lines for the feeding of the bath rotating bowl cleaning solution and draining of the waste solution, calibration of connecting pipelines, calibration of the volume of the bath, testing of instrumentation and electric connections of the resonator probe. Installation and welding of the bath was completed as per standard manufacturing practices, quality control, and quality assurance procedures. Studies pertaining to the total solution holdup, volume calibration and leakage of the equipment and associated systems were performed and validated. Upon choking of the CE rotating bowl, the motor bowl assembly could be removed from the identified stage of the CE bank and then with the help of an in-cell crane, it could be shifted to the bath for de-choking.

The laboratory scale studies were repeated with the equipment setup in DFRP contactor cells. The CE rotating bowls were choked with simulated particles in the laboratory and were cleaned in the bath commissioned in the hot cell. The de-choking experiment

in the bath was performed with 4M nitric acid solution. The solution was fed from an appropriate level from the nitric acid feed point for related contactor cell located in an appropriate area. The temperature of bath was monitored with the help of a K-type thermocouple and was always maintained below 60 °C. These experiments were stopped when the temperature of the bath solution reached 60 °C and was again repeated when the solution cooled down to the ambient temperature. The level inside the bath was measured and maintained in such way that at any point of time the CE bowl would completely be immersed inside the liquid. In all as many as four numbers of rotating bowls were de-choked by using the ultrasonic bath commissioned in contactor cells and the data pertaining to the same are shown in table 1.

Table 1: Observations of experiment conducted in contactor cell-177 for CE rotating bowl de-choking.

Time (min)	Bath temp. (°C)	Weight of the particles remaining in rotating bowl (g)	De-choking (%)	Liquid level in the bath (mm)
0	25	120	0	230
30	33.9	28	7.6	230
70	41.1	7	94.2	230
100	47.5	3	97.5	230
150	50	1	99.2	227
150	50	1	99.2	227

The remote removal and positioning of CE motor bowl assembly in SS bath and remote cleaning of CE bowl with temperature and liquid level control as per actual plant requirement have been successfully demonstrated.

V.73 Uranium extraction and stripping experiments with TiAP solvent in multistage Annular Centrifugal Extractor

PUREX solvent extraction process has been widely used in the nuclear reprocessing industries for more than six decades to separate uranium and plutonium from spent nuclear fuel. 30% TBP in n-Dodecane/NPH (v/v) solvent is a workhorse for the PUREX process. However, despite the overall success of TBP, it has some limitations, such as (i) third phase formation, (ii) aqueous solubility, and (iii) chemical and radiation degradation, etc. The above limitations pose problems in the fast breeder reactor fuel reprocessing. In order to overcome the above limitations, alternate solvents were developed. Among these TiAP is a promising solvent for fast breeder nuclear reprocessing applications. The main advantages of TiAP include (i) low aqueous solubility, (ii) low radiation degradation and (iii) a higher limit for the third phase formation.

Annular Centrifugal Extractors (ACE) are widely used in the fast breeder nuclear reprocessing industries. It has several advantages compared to the pulsed column. These are (i) low residence time, (ii) high throughput, and (iii) compact size (low footprint) etc. In this work, the performance of both TiAP and ACE have been validated with uranium extraction and stripping runs.

The extraction and stripping experiments were conducted in a 16-stage, 25 mm dia ACE (Fig. 1). During the extraction experiment, 36% TiAP in n-dodecane pre-equilibrated with 3N nitric acid was used as the organic phase. Uranium in 4N nitric acid (feed, 77gpl of U) and 3N nitric acid (scrub acid) were used as the aqueous phases. During the stripping experiment, 36% TiAP in

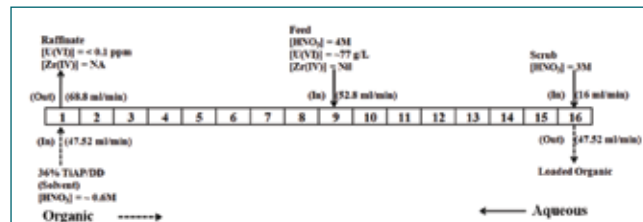


Fig. 2: Aqueous and organic flow rates and its feed location during extraction run

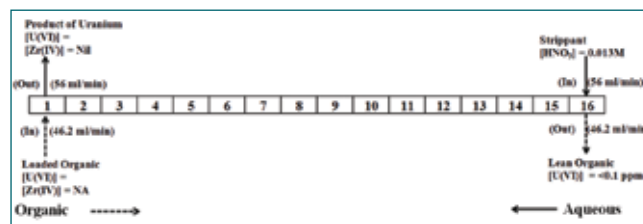


Fig. 3: Aqueous and organic flow rates and its feed location during stripping run

n-dodecane loaded with uranium served as the organic phase, and 0.01 N nitric acid as the aqueous phase. In reprocessing plants, 10% flow fluctuations are allowed during ACE operation due to uncertainties in the auxiliary systems. The details of aqueous and organic flow rates during extraction (with 10% increase in the aqueous feed flow rate and 10% decrease in the organic feed flow rate) and stripping experiment (with 10% decrease in the aqueous flow rate and 10% increase in the organic flow rate) and its feed location in the 16- stages ACE are shown in Fig.2 and 3, respectively.

After reaching the steady-state, the aqueous and organic stage samples from extraction and stripping experiments were collected, and the concentration of uranium was



Fig. 1: Photographic view of 16 stages 25 mm ACE bank inside fume hood.

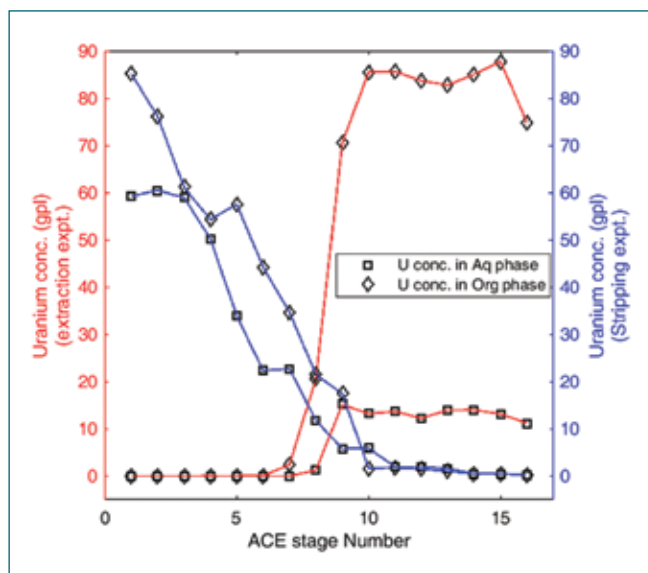


Fig. 4: Uranium concentration in 16 stage ACE

analyzed. The uranium concentration in the 16 stage ACE during extraction and stripping experiments is shown in Fig 4.

From these results, it was concluded that four stages are required in order to complete the extraction of uranium from aqueous phase with flow variation as per plant condition. From the stripping results, it is evident that thirteen stages are required to complete the stripping of uranium from the organic phase with the anticipated flow variation prevailing in the plant. These results reveal that TiAP is a suitable solvent for uranium and plutonium extraction and stripping operation. Sixteen stage-ACE is sufficient to handle the flow fluctuation and complete the extraction and stripping as per plant operating condition. Steam Generator (SG) of FBTR is once through shell and tube type counter flow heat exchanger that generates superheated steam at 125 kg/cm² and 480°C. There are two SG modules in each east and west secondary sodium loops. Out of the total four modules, three modules are made of 21/4Cr-1Mo-Nb stabilized ferritic steel and one module is made of 9Cr-1Mo-Nb stabilized ferritic steel. In each SG module, sodium flows through shell and water/steam flows through the tube.

During 25th irradiation campaign, it was observed that orifice assembly of Tube-E in one east SG module (SGna 500B) had fallen due to stress corrosion cracking (SCC). SCC occurred because of residual tensile stresses developed due to geometrical constraint against thermal shrinkage during welding of orifice holder tube and orifice assembly. The existing water sub-headers of three SG modules have welded type orifice assemblies made up of SS 316 and are susceptible for

premature failure due to SCC. The SG module made up of 9Cr-1Mo-Nb stabilized ferritic steel has bayonet type orifice assembly which is also likely to dislocate from its position due to depressurization cycles. Hence, it was decided to replace all existing water sub-headers with newly fabricated water sub-headers made up of Alloy 800 as it is a superior material compared to SS 316. All works related to water sub-header replacement was carried out inside SG casing itself. This work was taken up prior to 31st irradiation campaign.

Before starting the replacement work, welding procedure sequence and welder performance qualification were carried out for meeting FBTR specifications. As FBTR steam generator modules were fabricated with different materials for steam header and water header of individual modules, separate procedure and performance qualifications were carried out.

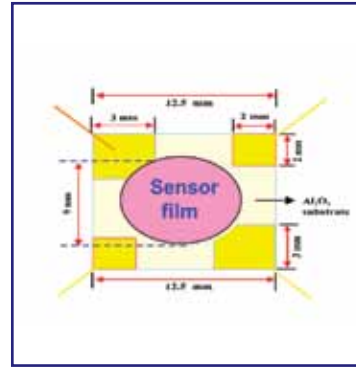
After successfully completing the qualification requirement, mock-up trials were conducted for weld configurations simulating the congested locations to obtain experience by the working personnel.

After successful completion of mock-up trials, cutting locations were marked in the water sub-headers and tubes and then they were cut (Fig. 1) after obtaining clearance from Quality Assurance authorities. Water sub-headers of all the four SG modules were cut and replaced one after another.

Gas Tungsten Arc Welding (GTAW) process with argon gas purging was used for welding. Every day, before commencing the actual job, trial pieces were welded to establish consistent performance of welders. Tube internal areas were inspected visually with videoscope before fit-up and weld edges were also inspected visually to avoid any abnormalities before fit-up. Liquid Penetrant Test (LPT) was carried out on weld edges to detect any surface defect.

In SGna 500B, the blanked Tube-D was made through at both water and steam headers and expansion bend segment of Tube-E at water header was also normalized. After successful completion of all the welding works (Fig.2&3), Post Weld Heat Treatment (PWHT), LPT, Radiography Test (RT) and Helium Leak Test (HLT) were carried out for all the weld joints. Finally, hydro testing of SG at 135 bar was carried out and all weld joints were qualified successfully.

After replacement of SG water headers, reactor was operated at 40 MWt in 31st irradiation campaign.



CHAPTER VI

Infrastructure,
Resource Management
& Biodiversity

VI.01 Commissioning of an Emergency Backup Evacuation System in RML

Radio-Metallurgy Laboratory (RML) nitrogen environment (inert) hot cells and air environment hot cells are maintained at pressures respectively in the ranges of (-)20 to (-)30 mm WC and (-)12 to (-)19 mm WC with respect to operating area to avoid any spread of contamination the surroundings. A closed loop Inert Gas Recirculation System (IGRS) is provided in RML for the ventilation of 4nos. of inert environment hot cells. Since hot cells are maintained at negative pressure with respect to the surroundings, air leaks into these cells from surrounding areas through the micro-cracks formed over the years in the walls and gasketed joints on their surfaces. Therefore high purity nitrogen is fed to the IGRS loop @ 25 Nm³/hr, to improve the quality of nitrogen inside these hot cells. Three automatic venting lines are provided between the IGRS loop and Exhaust System-III (ES-III) header to vent out the excess air and nitrogen for maintaining desired negative pressures inside the hot cells. ES-III header is maintained at a significantly low pressure of (-) 160 mm WC with respect to the basement area. When the cell pressures reach set upper limit, the controllers of automatic venting lines open the electro-pneumatic valves and start the evacuation of cells. As the cell pressures reach set lower limit, they close the valves and thus maintains required negative pressure inside the hot cells. The air

environment hot cells are connected to upper isolation area (UIA) and ES-III header for ventilation. The pressure differential exists between them draws air from the UIA through the air environment hot cells to ES-III header and establishes once through ventilation in air hot cells.

Non-availability of ES-III due to power outage or component failure can lead to pressure rise in the hot cells due to the leakage of air into them from surroundings. This rise in pressure inside the hot cells can cause leakage of radio-active particles to operating area, lower isolation area and upper isolation area during pressure transients.

A new ventilation system called Emergency Backup Evacuation System (EBES) has been developed in RML for the ventilation of hot cells during absence of ES-III. This is a redundant system, which does not use the components of the existing ventilation systems for its operation, to increase the reliability of hot cell ventilation. In case ES-III fails, immediately EBES automatically starts and isolates the hot cells. EBES consists of blowers, EBES header, manual and automatic valves, HEPA filters, activated charcoal beds, associated piping and PLC system. Fig.1 and Fig.2 show the schematic diagrams of the inert and air environment hot cell ventilation arrangements.

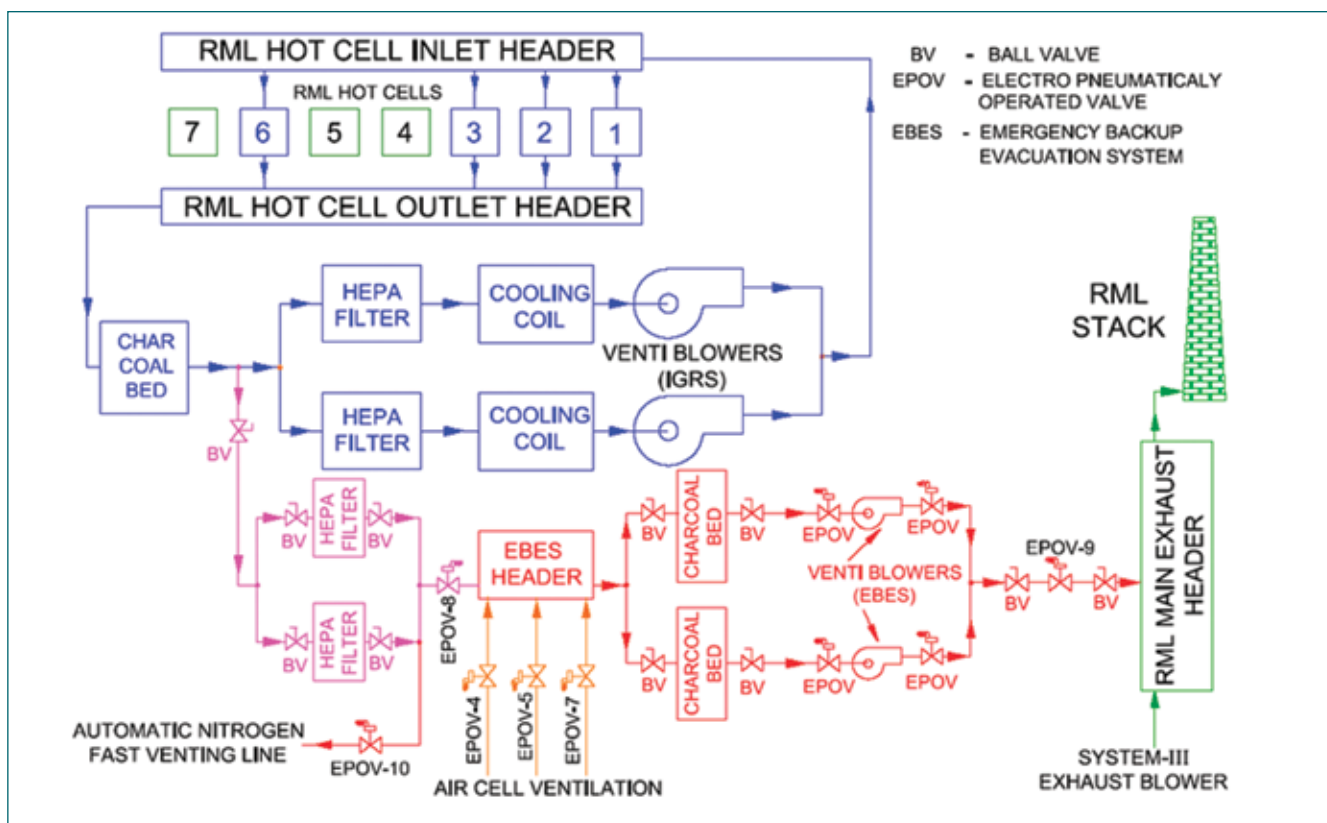


Fig. 1: Schematic of Inert hot cell ventilation of EBES

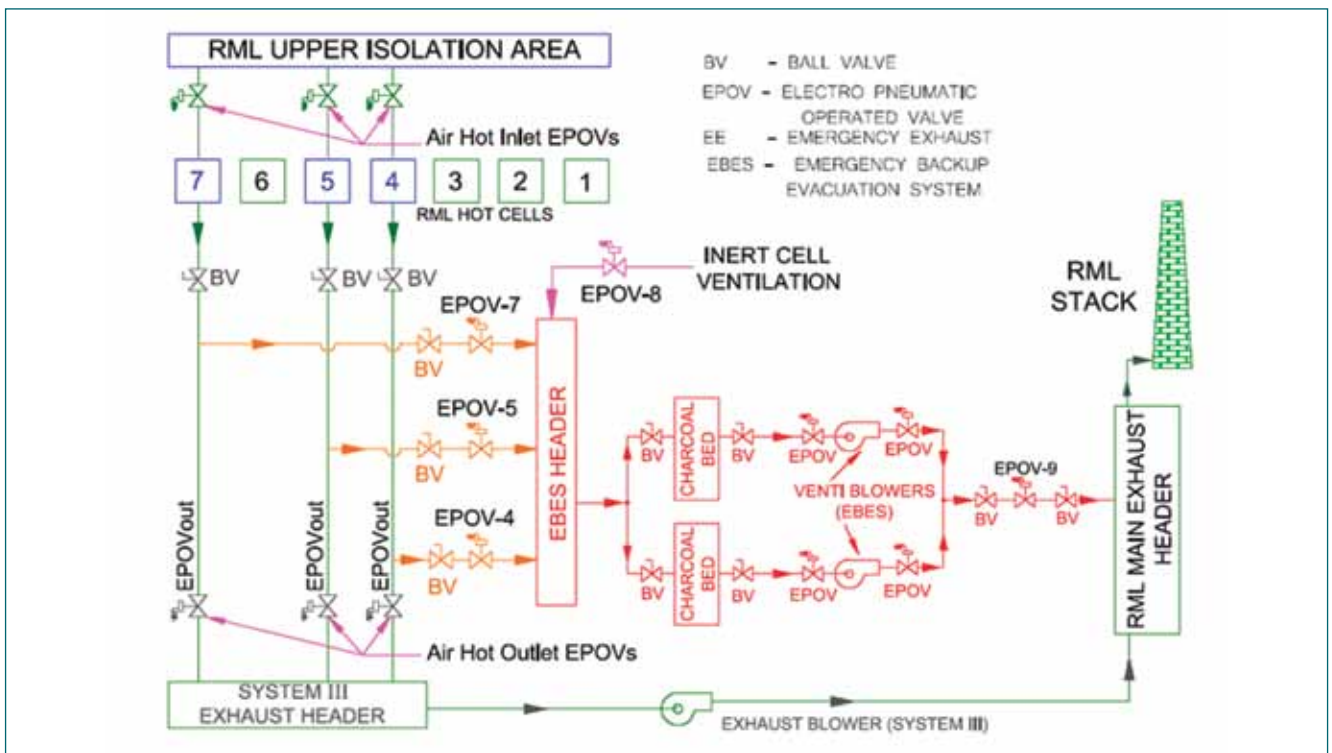


Fig. 2: Schematic of Air hot cell ventilation of EBES

EBES control unit continuously monitors the pressure inside the basement exhaust header to ensure the healthiness of ES-III. If header pressure goes above (-) 100 mm of WC, the control unit isolates the IGRS loop and air hot cells from ES-III by closing the electro-pneumatic valves between them and switch on its blowers to start evacuation of EBES header. EBES maintains pressures inside the hot cells using the following methods:

- i Inert hot cells - when the IGRS loop exhaust header pressure rises above (-) 20mm WC, EBES control unit opens the valves in the automatic venting lines (3 nos.) and starts evacuation of IGRS supply/exhaust headers until the internal pressure reaches (-) 30mm WC and then closes the valves. Pressures inside the hot cells follow the pressures in the headers. The valves remain closed until exhaust header pressure reaches (-) 20mm WC and then the process repeats, and
- ii Air hot cells - when pressure inside any of the air cells rises above (-) 12mm WC, the EBES control unit opens the valves in the pipe spool connecting the particular hot cell with EBES header and starts evacuation of the cell. The evacuation continues until the cell pressure reaches (-) 19mm WC and then closes the valves. The valves remain closed until the hot cell pressure reaches (-) 12 mm WC and then the process repeats.

As the ES-III header pressure returns to -150mm WC, the EBES control unit closes all the valves, stops its motors and reinstates the normal hot cell ventilation.

The mechanical system of EBES is installed in the basement area room #BC6 and its control and instrumentation panel is installed in room #BC-7. The control and instrumentation panel has Human-Machine Interface (HMI) with password protection. Also a duplicate HMI of the system is installed in the RML control room. After installation, the system performance was evaluated by simulating various failure scenarios. The following are the simulation events used during the commissioning trials of EBES.

- i Simulation of above (-)100mm WC in the ES-III header by switching off the running ES-III blower,
- ii Simulation of pressure in air environment hot cells above (-)12mm WC by adjusting control signals, and
- ii Simulation of pressure in nitrogen environment hot cells above (-) 20mm WC by feed adjustments and also adjusting control signals.

Presently, the EB ES is powered by Class IV electric supply with provision (automated) for Class III (DG set) supply. Also work has been initiated to provide class II (UPS) power supply for the system.

EBES was commissioned after the successful completion of comprehensive testing of functionalities of the system. It is observed that during the planned changeover of ES-III blower in every fortnight and power failures, EBES automatically spring into action and maintains the pressure in the hot cells within allowable limits.

VI.02 Restoration of RML High Bay 20/5T Electric Overhead Travelling Crane Clutch Plate.

The 20/5T capacity electric overhead travelling (EOT) crane installed in Radio-metallurgy Laboratory (RML) high bay is in service for more than three decades. It is installed at an elevation of 12.5m from high bay floor. Recently during trial run of fuel transfer operation to another laboratory of IGCAR, a threaded stud from its carriage fell to the floor. Since all safety precautions were strictly adhered during the operation, no accidents happened due to this incident. Immediately the trial run cancelled and suspended all crane operations.

A team was formed to find out the root cause for the incident and started investigation. Team members climbed up and examined the crane. They found that the threaded stud was detached and fallen from the clutch assembly between the main motor and micro motor cum gearbox assembly in the crane hoist. The clutch assembly consists of a Magnetic unit holder, friction disc, friction disc holder with studs and springs. The friction disc holder has four threaded studs as shown Fig.1. These studs are screwed to the friction disc holder and immobilized by tack welding as shown in Fig.2.

The components of clutch assembly are shown in Fig.3. Detailed examination of the clutch assembly revealed that, three out of the four threaded studs have loosened and detached from the friction disc holder due to the failure of immobilizing tack welds and thread damages. One of them fell to the high bay floor and the other two found lying on the crane carriage floor. The suspected reason for the failure is the vibrations during the hoist operation.

The clutch assembly was dismantled from the crane and brought to shop floor for repair work. It was dismantled and examined thoroughly. Severe damages were noticed on the external threads of the studs and internal threads of friction disc holder. Since spare clutch was not available and the fabrication of a new clutch assembly may lead to longer downtime, it was decided to repair and restore the same clutch assembly. During the repair work, new studs were machined and a special bonding procedure was adopted for fixing the friction disc on the friction disc holder.



Fig. 1: The clutch assembly in the crane



Fig. 2: Tack welds in the friction disc holder

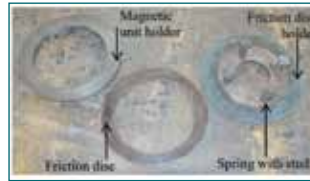


Fig. 3: Components of clutch assembly



Fig. 4: Clamping arrangement for uniform pressure application

After the removal of the friction disc from the friction disc holder, the bonding compound present on their surfaces were removed by applying acetone and scrubbing with wire brush. Emery sheets were used for obtaining matt finish on the surfaces. Synthetic resin based brake shoe bonding adhesive Anabond 230 paste was then applied evenly on the friction disc holder and friction disc at the surfaces to be joined. They were then dried in an induction furnace at 70°C for 40 minutes. Subsequently, they were assembled together using C-clamps by applying uniform pressure as shown in Fig .4.

The assembly was then heat treated at 190° C +/- 5 °C for 60 minutes in an induction furnace followed by air cooling to room temperature outside the furnace. The clutch after repair was integrated with the main motor flange using spring-loaded studs as shown in figure 1. The magnetic unit holder was adjusted to maintain a uniform gap of 3mm between the faces of the friction disc and magnetic unit holder.

A stainless steel guard was provided around the clutch assembly as shown in Figure 5, as additional safety measure, to prevent the falling of studs to the high bay floor, even if they got detached from the friction disc holder in the future. After the restoration of the clutch assembly, trial operations of the crane were carried out. Subsequently competent authority has tested the crane and issued fitness certificate.



Fig. 5: Image of clutch assembly with stainless steel guard

VI.03 Operating Performance and Sustained Quality of Permeate at 2 MIGD Desalination Plant at IGCAR

To meet the growing need of potable water for all DAE units including IGCAR, BHAVINI, NRB, BARCF at Kalpakkam, Sea water Reverse Osmosis desalination plant (SWRO) was constructed in 2015 with a capacity of 2 Million Imperial Gallons per Day (2 MIGD). The 2 MIGD plant is designed With state of the art Reverse Osmosis Technology. Figure 1 shows RO stage I in the palnt. For operation of the plant, the inlet sea water is received from the discharge point of Auxiliary Seawater System (ASW) of BHAVINI.

The permeate water quality is maintained conforming to potable water as per IS 10500. The final permeate water is delivered to the IGCAR reservoir, from where all DAE units draw potable water based on their requirement.

The major part of the plant energy consumption is by the high pressure pumps. The high pressure pumps have to develop up to 60 bar pressure to extract the permeate water from the seawater through a specially rolled polyamide Reverse Osmosis (RO) Membrane. The design Specific Energy Consumption (SEC) is 3.18 kWh/cu.m. Presently, the plant delivers the permeate water within the design limit.

The Reverse Osmosis process discharge brine is diluted in the BHAVINI discharge canal and delivered to the sea via MAPS outfall canal after monitoring conductivity, pH and temperature.

Predictive and preventive maintenance are being carried out to ensure the availability of the plant. Few notable modifications are also made to improve the quality and life of the filter media inside the pretreatment section of the desalination process. Multimedia Filter (MMF) outlet header nozzles modification work has been carried out for all four skids. The base plate nozzle type is converted to individual pipe nozzle type header for better first



Fig. 1: Reverse Osmosis Stage 1



Fig. 2: Aerial view of new Mini-Laboratory

stage filtration of intake seawater. The Filter media is also renewed.

Indigenous Ultra Filtration (UF) membranes are used in the plant for the first time in January 2022. The performance of the indigenous UF membranes is competitive to the imported membranes till date.

The life of RO membranes is heavily impacted by the “Silt Density Index” (SDI) of the Ultra Filtered seawater input. The SDI has to be controlled within the designed limit of less than 5. The SDI is being tested and monitored periodically by newly installed Automatic SDI Analyser. The actual SDI is presently observed as 1.2-2.8.

Routine timely backwash and structured Chemical Enhanced Backwash (CEB) will ensure the SDI within limited value. This is being measured and monitored on regular basis.

The critical parameters of permeate is being tested regularly in accredited third party laboratory. Further, a mini water testing laboratory (Figure 2) is established for testing quality of inlet Seawater/ In-Process water / final permeate potable water. Since the age of the plant has crossed 6 years, it is essential to monitor the process parameters of the plant intensely and direct the plant operators to operate the plant accordingly.

The quality parameters like pH, TDS, Conductivity, Turbidity, residual Chlorine are monitored at various stages to ensure the effectiveness of the each stage of filtration process. The above in-process quality parameters will indicate the failure of the individual stage instantly for taking shop floor corrective actions. This step will make the process rectified immediately ensuring deliverables and extending the life of the plant components including life of UF & RO membranes.

The technical upgradation and controls will ensure the quality of final permeate delivered to IGCAR reservoir. It also extends the healthiness & life of all filter media of the desalination plant.

VI.04 Restoration of an Aged Building Through Strategic Repair

Ageing is an inherent feature of nature and hence of materials, structures and systems. The topic is gaining lot of attention due to the financial implication to the nation. Management of ageing is possible through identification of driving forces contributing to the ageing at appropriate time and the strategic measures. In light of the principles of the circular economy, demolishing damaged reinforced concrete (RC) structures is not desirable. And application of an appropriate repair method for the occurred damage is important to ensure the intended service life extension.

The building considered for ageing restoration was assessed for identification of cause of distress based on condition survey as indicated in Figure 1. The slender reinforced concrete columns were cracking from synergistic effects of ageing related stiffness degradation, presence of chloride and carbonation. Hence the repair methodology had to encompass all the three stressors. The CPWD handbook, ACI 562 and EN 1504 gives general guidelines towards repair and restoration.

Major guidelines were taken from EN1504, where the repair options are elaborated for repair of damage in concrete as well as reinforcement corrosion.

Repair work started with chipping of the existing



Fig. 1: Damaged RC column and condition survey



Fig. 2: Restoration of RC columns & monitoring

delaminated concrete till the sound concrete surface is reached in the distressed columns. The reinforcement bars were cleaned thoroughly to remove any rust etc. from the surface by wire brush and the diameter of the bars was checked. Then rust converter was applied and wherever the diameter of the bar was found to be reduced then additional reinforcement bars were provided and welded with the existing bars as per IS 9471. Couple of coats of corrosion protection treatment of zinc primer was applied over the surface of the old and new reinforcement bars. Shear keys 8mm diameter were fixed by drilling holes in staggered manner to a depth of 75mm-100mm on the sound existing concrete member with a two component polyester based resin grout plugging the hole. Additional skin reinforcement bars of 16 mm diameter were inserted and grouted to the foundation. Epoxy resin based bonding agent was applied over the old concrete surface to receive the 75mm thick micro concrete around the column. For additional strength to counter the buckling effect carbon fiber reinforced polymer wrapping was provided around the effected column with an epoxy adhesive.

The building has been restored as indicated in Fig .2 and made functional with an extended service life and is being monitored on regular basis with encouraging results.

VI.05 Formation of 33 kV Ring Main System for Improved Reliability

When the infrastructure development for north plant site was taken up, the site was identified as an evolving major load centre. IGCAR receives power at 33 kV level through radial feeders. After detailed internal deliberations, it was decided to form 33 kV ring main system (RMS) with 1 No. 33 kV (NCSS-3) substation at north plant site as the 3rd node. Such ring will ensure dual feed at all the 3 nodes thus improving the reliability. The 3rd node NCSS3 is designed to meet upto 25 MVA power demand for facilities in North Plant site. RMS that enables two way feed for the 33 kV substations ensures high degree of reliability. The 33 kV ring main feeder links north plant site to 33 kV CSS at IGCAR and 33 kV NCSS-2 near desalination plant. (CSS: Central Switching Station and NCSS: New Central Switching Station). Ring main consists of 2 runs of 33 kV, 400 sq.mm XLPE cables. Capacity of the ring feeder is in the order of 35 MVA. At present the ring is formed with one number 400 sq.mm cable and second run will be added in the next phase.

Figure 1 shows the block diagram of the 33kV ring main system formed to improve system reliability between CSS, NCSS-2 and NCSS-3.

33kV Cables of length 4.5 km from NCSS-2 to north plant substation (NCSS-3), 3.65 km from CSS to NCSS-3 and 2km between CSS and NCSS-2 are installed to form the 33kV Ring main system with 3 nodes.

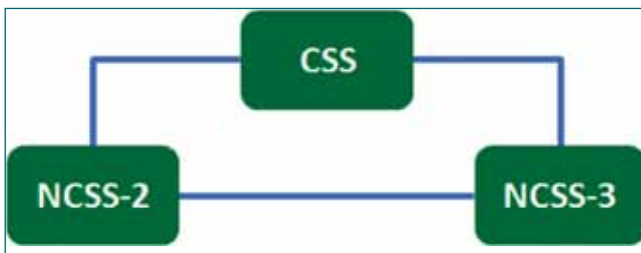


Fig. 1: Block diagram of the ring main system



Fig. 2: OFC cable and 33kV Cable 2 runs from NCSS-2 to NCSS-3 and cable between NCSS-3 and CSS



Fig. 3: 33kV cable from NCSS-3 to CSS in trench

Cable route between NCSS-3 and NCSS-2 comprises 2.35 km of cable laid underground and 2.15 km of built-in trench (part RCC Trench & part over ground structure). 33kV cable run 1 is laid along the entire route to form the ring. Additionally run 2 cable of length 2.5 km is laid along the route, which will be extended in future. Figure 2 shows the above said two runs and the cable between NCSS-3 and CSS.

Cable route between NCSS-3 and CSS comprises 2 km of cable in built-in-trench and 1.65 km of cable underground. Figure 3 shows the above said feeder between NCSS-3 and CSS laid in RCC built in trench.

To increase the reliability, major part of the 33 kV RMS is installed either in RCC built-in-trench or in over ground structure. This arrangement will ensure that any future construction or maintenance related works of other services will not interfere with the Ring Main System.

Figure 4 shows cables from NCSS-3 to CSS and NCSS-2 on Edaiyur bridge cable support structure along with water pipe lines to north plant.

Total of 10.65 km of 33kV cables was laid to complete the 33 kV Ring Main system.



Fig. 4: 33kV Cable over Edaiyur Bridge

VI.06 Increased Reliability of Central Chilled Water Supply and Revamping of Air Handling Units for ACV services of IGCAR

Air-conditioning and ventilation services of radioactive facilities and other facilities of IGCAR are primarily met by Central Water Chilling Plant (CWCP-1) since 1978. The plant supplies chilled water at $8.5 \pm 1^\circ\text{C}$ and it is circulated to various buildings of IGCAR through underground insulated pipelines. In each building, air handling units circulates air through the chilled water cooling coil to produce the required air-conditioning and ventilation effect to the facilities.

With the expansion of the centre in the last 4 decades, the AC loads on CWCP-1 attained saturation and new standalone chiller units and unitary systems were also installed parallel to meet the additional air-conditioning demands of the centre. Fig:1 shows the AC load distribution among various systems in IGCAR as in December 2022..

At present, the total operating AC load of IGCAR is about 5000 Tons of Refrigeration (TR). CWCP-II was established near IGCAR gate to gradually phase out the high Global Warming Potential (GWP) Refrigerant, R-22 based energy intensive package units and unitary ACs like window/split ACs with energy efficient, more reliable central AC system and to reduce on O & M cost. Fig 2: shows the newly established CWCP-II near IGCAR

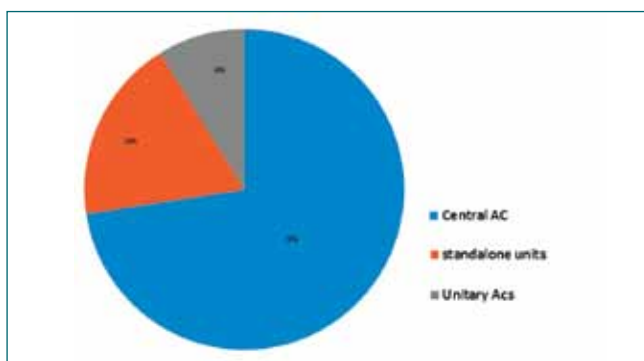


Fig. 1: AC load distribution in IGCAR



Fig. 2: CWCP-II established near IGCAR gate.

gate with 2 nos. of 750 TR capacity, eco friendly R134a refrigerant based water cooled centrifugal chillers and 2 nos of 375 TR air cooled screw chillers. CWCP may be expanded for another 200 TR capacity in future. Table - 1 shows the present AC load distribution of CWCP - I & II.

Table – 1 AC load distribution of CWCP - I & II			
CWCP-1 Building	Load (TR)	CWCP-II Building	Load (TR)
ESG PH -I	32	CDO	200
ESG PH -II	48	TS&TC	280
RCL	400	ENGG Hall IV	40
RCL Annex	128	RELab	40
BORON Plant	108	EID- I & II	136
RDL	288	PIF- I & II	64
RDL Ph - II	40	CMPL	144
FBR	48	MSL Ph I & II	120
RGAS	32	MDL	160
FBTR	280	INSOT & MTD	80
RML	208	SGTF & Hall-III	80
DFMF	36	ADMIN	84
HBB Ph II	192	CIVIL & CWD	120
DIGITAL LIB	40	HBB Ph I	88
CAFETERIA	40	CC & SML	136
TOTAL LOAD	1920	TOTAL LOAD	1772

Both the plants are looped in two ring main headers with interconnected valves to operate in standalone mode or parallel mode, providing flexibility and reliability of chilled water supply from any plant to any facility.

On the building side, 10 nos of air handling units that are more than 20 years old and less performing, were replaced with new ones with energy efficient fans, cooling coils and ultraviolet germicidal irradiation (UVGI) lamps for sterilization of circulating air and improving indoor air quality. Fig: 3 shows new air-handling units installed at HASL building with UVGI lamps.



Fig. 3: AHUs revamped at HASL building

VI.07 Commissioning of 11 kV PDC XI Substation

Facilities at North side of IGCAR main campus was being fed from PDC II (Power Distribution Centre – II) located near SGTF facility. In recent years many additional laboratory infrastructure are being built in this location. Prominent among them are WSCD Phase II of BARCF, Gamma irradiation facility and other facilities of SED.

Considering the establishment of additional facilities, an assessment of load growth was carried out. The study concluded the requirement of one 11 kV substation with 4 MVA capacity. At that time a decision was taken to locate WSCD Phase II building in the extended campus further North of WSCD Phase I. Hence it was decided to locate the new substation also in the extended land.

The substation was named PDC XI and the design was completed. Construction of this substation was included in ESG vision proposal.

11 kV PDC XI is designed as a part of ring main system (RMS) with Central Switching Station & 11 kV substation PDC IV. RMS that enables two way feed for the 11 kV substations ensure high degree of reliability in an economic way. As part of the ring the substation has 2 incomers, (each with 3C x 400 Sq.mm UG cable) one from CSS and other from PDC IV Substation at 11 kV level.

In the substation, 11 kV supply is stepped down to 415 V level and distributed further to various facilities.

Considering the saline environment, indoor substation is selected. In addition Indoor substation occupies less space and requires less maintenance. An indoor electrical substation layout with the prospective loads



Fig. 1: 11kV Switch board at PDC XI substation



Fig. 2: LT Switch board with Bus-duct at PDC XI substation

has been worked out.

The substation equipment are listed below:

- 11 kV switchboard with 7 circuits (fig. 1)
- 415 V switchboard with 22 circuits (Fig. 2)
- 3 transformers of 2 MVA, 11/0.415kV Oil cooled with two working and one standby configuration. (Fig. 3)
- 415 V bus-ducts.
- 415 LT switchboard to feed substation loads
- Class I battery system for substation control supply

HT and LT switchboards are provided with numerical relays for advanced protection and fault recording. HT switchboard is provided with arc flash detection system and rear cover safety lock system for improved personal safety.

Complete system is installed, tested and commissioned. The switchboard is energised after approval from Central Electricity Authority". Energisation of this feeder will strengthen the power source capability for all DAE facilities at north side of IGCAR campus.



Fig. 3: 2 MVA transformers of 11/0.415kV Oil type

VI.08 Building for Development & Testing Facility for Advance Study on High Temperature Material

IGCAR has taken the responsibility to provide R&D support for indigenous development of high temperature materials like nickel based super alloy, austenitic stainless steels and ferritic martensitic steels for Advance Ultra Super Critical (AUSC) Technology. The material development needs step by step characterization of composition and the properties such as workability and weld ability required for fabrication of components, creep, fatigue, fracture, fire and steam corrosion properties required for better in-service life. This characterization needs dedicated testing machines, equipment and microscopes.

The laboratory is constructed at Northern Plant site of DAE Kalpakkam. This building is designed with area of 2386 sq.m in ground floors & 2462sq.m in first floor area with labs and high bay with all services. It comprises three reinforced concrete framed structures, viz a high bay frame 36.0 m x 21.0 m of height 10.325 m, an another Bay Frame 16.0 m x 48.0 m of height 8.55 m and 15.0 m x 45.0 m of height 8.55 m with one floor future extension. The ground floor and first floor comprises Laboratory Room, Electrical Panel Room, AHU Room, Server Room and services. This building is designed based on NBC 2016 as it is in the mixed category of Business and industrial building. Provision for different laboratory are adopted in modular grids for flexible design. Freight lift is provided for men / equipment movement. In this building as per AC service requirement of 8 Hours and 24 hours Labs are grouped together on energy conservation. Main axis of Building is in E-W direction to avoid direct sunlight and to reduce HVAC load. Finishing material are sustainable and green building materials such as vitrified tiles, mineral wool false ceiling, engineered wood Flooring and ACP cladding for Front elevation as indicated in Fig. 1. For electrical panel & AHU rooms IPS & high bay hardonite flooring are provided.



Fig. 1: Sketch showing Front elevation of the Building

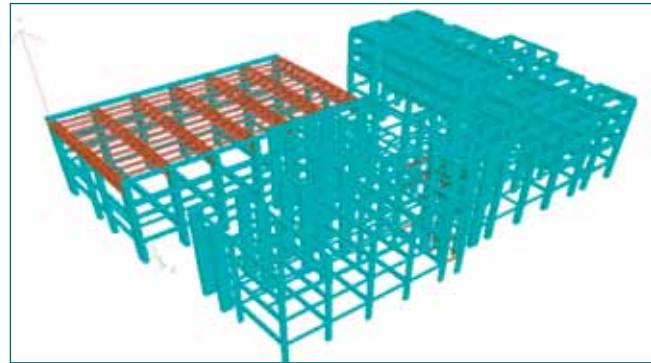


Fig. 2: 3-D Rendered View of FE Model

The framed structure of AUSC (High Bay and Low bay I and Low bay II) is idealized using Finite Element (FE) beam element as indicated in Fig. 2.

The FE model was structurally analyzed and designed using linear elastic analysis as per Indian standard for Dead Load, live Load and earthquake load. Design earthquake is considered as per Indian Standard IS 1893:2016 with the following parameters: Zone III, Importance factor, I is 1.5 and Response reduction factor, R is 5. Ductile detailing is followed as per IS13920:2016. There are 97 footings which consist of isolated footings, combined footings and 116 no. of column of various sizes are located in this building. Columns are designed on the basis of strong column-weak beam concept as per IS13920:2016 so that in unlikely event plastic hinges will be formed in beams rather than column. The foundation is taken to minimum depth of 2.5m from existing ground level where Safe bearing capacity of soil is not less than 150kN/m².

In modal analysis, the predominant natural frequencies of High bay observed at 0.954 Hz, 1.105 Hz and 16.75 Hz with mass participation 48.448 %, 65.417% and 14.747% in X, Z and Y direction respectively and natural frequencies of Low bay I at 0.64Hz, 0.663 Hz and 12.132 Hz with mass participation of 79.423%, 96.896% and

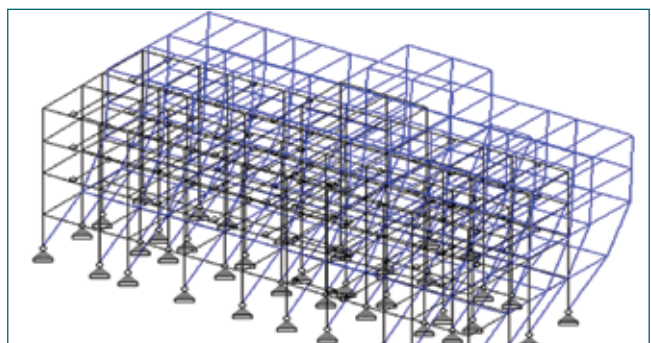


Fig. 3: Mode Shape 1 (Low bay-I1)

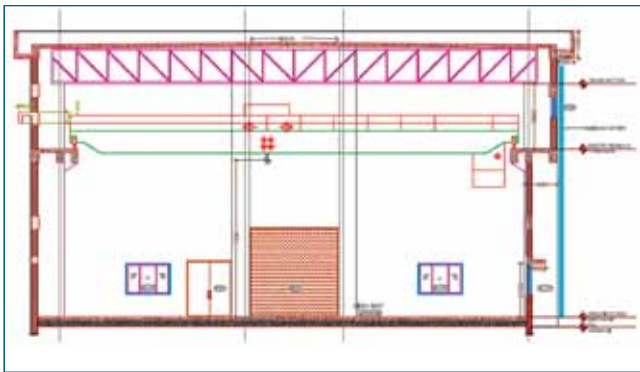


Fig 4: Crane 20Ton capacity (High bay)

60.096 % in X, Z and Y direction respectively and of low bay II at 0.652 Hz, 0.673 Hz and 12.526Hz with mass participation of 96.917%, 95.973% and 85.616% in X, Z and Y direction respectively. Fig.3 indicates one of those mode shapes.

The base shear (expressed as % weight of structure) is as follows:

S.No.	Description	EQX	EQY	EQZ
1	High bay	5.91	1.22	4.98
2	Low bay I	1.96	2.54	2.45
3	Low Bay II	3.96	2.10	3.99

The maximum displacement is found to be 26 mm in Low bay. Since the low bay building is having length 70 m, so an expansion gap of 150 mm is provided at length of 48 m between Low bay 1 and Low bay 2. The expansion gap is calculated as Per IS1893 (Part 1):2016. The two low bays, with expansion gap between them, is required to be separated by R times floor displacements of that two low bay. Thus the expansion gap is calculated as $=R \cdot \Delta_1 + R \cdot \Delta_2$ (where Δ_1, Δ_2 are max. displacements) $=5 \cdot 14 + 5 \cdot 15 = 145 \text{ mm}$ So 150 mm expansion gap was provided between High Bay and Low bay 1, Low bay 1 and Low bay 2.



Fig 5: Truss (High bay)

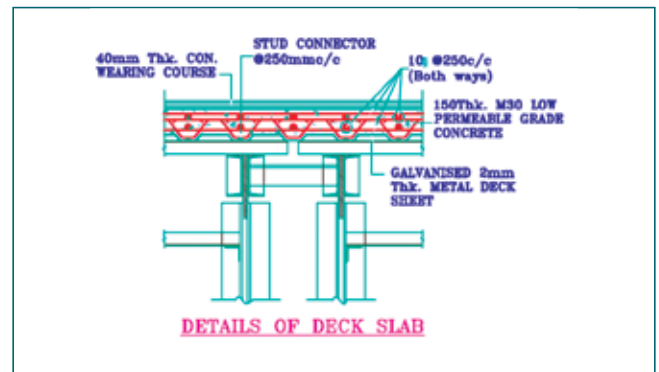


Fig 6: Decking slab (High bay)

In high bay indicated in Fig.4, 20T capacity crane is provided. The crane is supported on Gantry beam, which is analyzed with moving load concept to find the critical position.

In the low bay area of this building, plinth beams at -0.60m ground floor slabs at +4.50m level and First floor slab at +8.55m level and in the High Bay area of the building, plinth beams at -0.60m level, the working platform in steel and RCC at +4.5 m level, Gantry beams at +7.50 m level, RCC brackets for truss fixing at +10.40 m level, Tie beams at +10.325 m level and roof beams at +12.465 m level have been constructed using conventional technique.

At top of High bay deck slab is provided with left-in shuttering supported on purlins & trusses shown in Fig.5. Left-in shuttering is provided with trapezoidal decking of mild steel sheet (min. thickness 2.0 mm) for faster construction of high bay roof slab.

The metal decking slab is connected to purlin with stud connector indicated in Fig.6. Due to stud connector, integral and composite action between decking slab and metal deck sheet is achieved. Metal decking is painted with two coats of 250 micron DFT epoxy paint on exposed surface. Fig. 7 shows view after completion of construction of the building.



Fig 7: View of Complete Building

VI.09 Establishment of Hydraulic Pressure Test Facility for Portable Fire Extinguishers and Self Contained Breathing Apparatus (SCBA) Filling Facility in IGCAR

In IGCAR there are around 3500 nos. of various type & capacity portable fire extinguishers are installed. Out of which 1500 nos. (Water type, Mechanical foam type and Dry Chemical Powder type fire extinguishers) can be hydro tested in house as per IS 2190:2010. Each fire extinguisher (gas cartridge) installed in IGCAR campus shall be hydraulically pressure tested as per the schedule given in Table 1.

Industrial & Fire Safety Section has established hydraulic pressure test facility to meet the statutory requirements as well as to ensure the healthiness of the portable fire extinguisher. The hydraulic pump (Fig. 1) is electric motor driven having pressure set valve to fix the required test pressure and also a pressure relief valve to release the stored pressure after every test. The main function of a hydraulic test is to ensure that the fire extinguisher can still withstand its pressure rating. When a fire extinguisher undergoes hydraulic pressure testing, it is filled above its pressure rating with water. At that point, the technician monitors the fire extinguisher, looking for any drop in pressure. A drop in pressure during the test indicates that the fire extinguisher has a leak, and should be permanently removed from service. Extinguisher, which fails during the pressure testing, shall be replaced.

The hydraulic pressure testing will be carried out such that at least one third (1/3) of the extinguishers are tested every year and the pressure testing cycle of all extinguishers are completed every three years.

S.No.	Type of Extinguisher	Test Interval Year	Test Pressure kg/cm ²	Pressure Maintained for Min
1.	Water type	3	35	2.5
2.	Mechanical foam	3	35	2.5
3.	Dry powder type	3	35	2.5

A self-contained breathing apparatus (SCBA) enables a person to remain in irrespirable and poisonous atmosphere for a specified period of time, if required. It is also known as a rescue apparatus or gas mask. In this type of SCBA, compressed air carried in cylinders is fed through a demand valve and breathing tube to a full face-piece. These cylinders require refilling after every usage during rescue operations, entry in confined spaces and training to the employees.

Industrial & Fire Safety Section has established Self Contained Breathing Apparatus (SCBA) cylinder filling facility to meet the requirement of filling cylinders in house. This compressor (Fig. 2) will be used to refill the high pressure cylinders at 200 bar & 300 bar with breathing air at charging rate greater than 240 Liters Per Minute. Filling station comprises of breathing air compressor and safe filling containment chamber (Fig.3) and it can accommodate two cylinders at a time during refilling. This two cylinder SCBA filling enclosure is complied with NFPA 1901 requirements and it also has safety automatic interlock which requires no actuation of secondary latching mechanism from outside during filling.



Fig. 1: Hydraulic pressure testing facility



Fig. 2: Self Contained Breathing Apparatus (SCBA) cylinder filling compressor



Fig. 3: Cylinder safe filling containment chamber

VI-10 Industrial, Fire and First Aid Training Program to Meet AERB Regulation

As per the AERB guidelines, Industrial Safety, Fire Safety and First Aid training programmes have to be conducted every year for IGCAR employees and workers. The programme consists of series of lectures from various experts from IGCAR. Safety induction training, one day safety seminar for workers training by workers and first aid training were scheduled and conducted for the year 2022. Among them some of the important programmes are briefly given in this report.

As per AERB guidelines employees and contract workers are to be trained in industrial and fire safety and also in first-aid training every year. A two day Industrial and fire safety training was organized to enhance the awareness of safety among officers/engineers, supervisors of IGCAR during Jan-2022, Mar- 2022, June- 2022 and Augt-2022 Total 235 participants were attended for this training programme. First-aid training programme was conducted on 02 occasions Feb, July-2022 for 111 employees. All the contract workers (772 nos.) were given safety induction training before inducting them into work and Height-pass test & training was conducted for 436 nos. of workers who are working at height. One day “Safety Seminar” for workers by workers was been conducted during Mar-2022 at RFG. A total of 49 employees were attended the programme and lectures were delivered by respective participants of their group.

Industrial & Fire Safety Training (IFST)

Total five IFST programmes were organized and conducted to enhance the awareness of safety among officers/engineers, supervisors of IGCAR.

Live demonstration of various types of fire extinguishers used to put off the different type of fire scenarios were conducted with the co-ordination of NPCIL Fire officers & CISF Fire Wing during the IFST programme.



Fig. 2: Fire Safety Training by CISF Fire Wing



Fig. 3: First Aid Training - CPR demonstration

Table1: IFST programmes organized during 2022

Programme	Date	Participants
IFST-1	04 th & 05 th – Jan 22	60
IFST-2	29 th & 30 th – Mar 22	60
IFST-3	28 th & 29 th – June 22	63
IFST-4	24 th & 25 th – Aug 22	52
IFST-5	09 th & 10 th – Nov 22	60

First Aid Training (FAT)

Total three FAT programmes were conducted by doctor’s team from Apollo Hospitals, Chennai at IGCAR campus.

Table 2: FAT programmes organized during 2022

Programme	Date	Participants
FAT-1	25 th Feb 22	46
FAT-2	27 th July 22	65
FAT-3	30 th Nov 22	51



Fig. 1: Industrial Safety Training

At the end of each FAT programme, theory and practical examination were conducted. First Aid Training Certificates are distributed to the successful employees.

VI.11 Human Resource Management – Induction of Junior Research Fellows in IGCAR

IGCAR is a constituent institution of Homi Bhabha National Institute, that provides the link between academia and industry in the Department of Atomic Energy. Homi Bhabha National Institute offers doctorate degrees to young research scholars. The process of selection is through open advertisement followed by screening through written test and selecting based on personal interviews.

During November 2022, a drive for selection of research scholars in about 15 disciplines viz., physical sciences, chemical sciences and engineering sciences was initiated. This process was to conclude quickly to match with the requirement of having the scholars in position by January 2023 so as to facilitate their registration in the January session with HBNI.

The selection had to be across varied educational qualifications and eligibility criteria. There were some major subjects that were not eligible under each of the disciplines and also some of the disciplines had different types of degrees. Apart from these, a set of scholars who had valid scores through all-India competitive examinations like GATE, JEST, UGC-CSIR-NET had to be considered under different criteria.

Taking into consideration, the need for reinstating the scholars quickly after the screening, conduct of written examinations and interview and the availability of limited staff members to coordinate the process, it was decided to develop a portal for receipt of applications

online, screening the applications based on eligibility criteria and to short-list the applications for written test and direct-interview, including issue of call letters. The selection process was to conclude with declaration of result of written examination and interview.

The online portal was developed and hosted using open source web technologies. A domain name was registered to host online services for registration of applicants. This portal provided following functionalities to the applicants and coordinating staff members.

- i) Secure email based authentication
 - ii) Hosting advertisement material for reference
 - iii) Online filling of application form
 - iv) Printing of duly filled in application form
 - v) Update screening result by the screening committee
 - vi) Download admit card (for written test / interview)
- VI) Hosting of results of written examination and automated email alerts to applicants

The portal was developed and hosted in a very short period in order to comply with the time schedule of recruitment. Subsequently the written examination was held at Chennai on December 4, 2022 followed by interviews spanning December 5 to 9, 2022 at Kalpakkam and the whole process of induction was concluded as planned and executed in a mission mode and the scholars would be joining the Centre in January 2023.

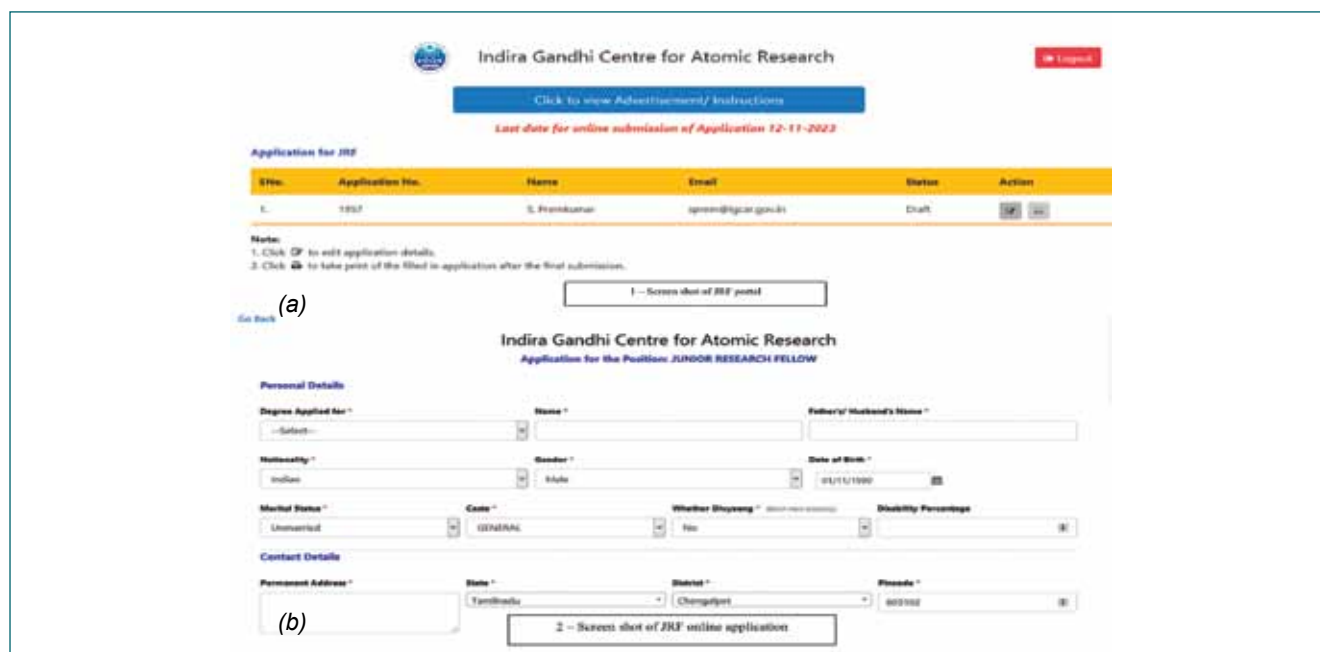


Fig. 1: Screen shot of JRF portal, (b) Screen shot of JRF online application

VI.12 Development of Budget Automation System (DAEBAS) v2.0 for DAE Units

The budget proposals are called for from respective DAE units by Budget Planning Office, DAE. This includes Revised Estimate (RE) for current financial year and Budget Estimates (BE) for next financial year under Capital & Revenue Budgets.

Towards automation of the budget process, software called DAE Budget Automation system (DAEBAS) was developed at IGCAR and is in use since July 2017. The budget data is collected from DAE units and the system compiles the information and generates various reports for submission to Chairman AEC, Member(Finance) AEC and to Ministry of Finance for obtaining approval of the Parliament. This system has been implemented over ANUNET.

Salient features of DAEBAS

This system automates the entire budget cycle

- (1) Online submission of Budget proposals by Units and report generation
- (2) Compilation & generation of various MIS reports for submission to authorities for review and approval
- (3) Generation of Statement of Expenditure Budget (SBEs) reports for submission to Ministry of Finance
- (4) Generation of excess/savings reports at sub-head level for approval of Secretary, DAE/ Member(Finance), AEC / Ministry of Finance
- (5) Generation of reports for Re-appropriation (re allocation of savings / surrenders to different Units / different Head of Accounts under both Capital / Revenue section)
- (6) Generation of reports for "Surrenders" (list of items under which unspent funds are surrendered to Ministry of Finance)
- (7) Incorporation of Unit wise / Head of Account wise approved allocations / ceilings at DAE for intimating

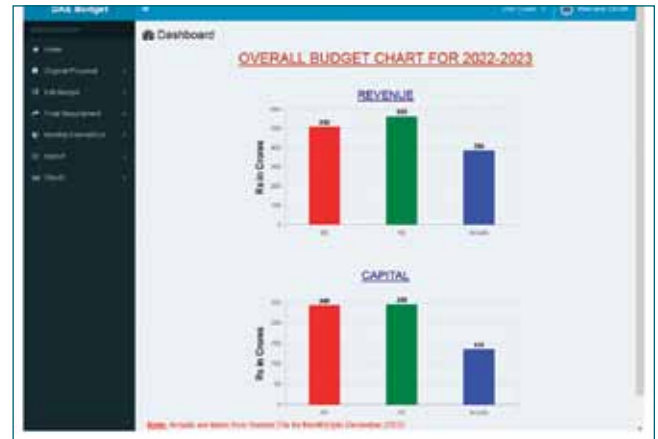


Fig. 2: Dashboard for Administrator of IGCAR

to all Units for submission of revised break up for approved RE / BE

- (8) Preparation of Detailed Demands for Grants (DDG) along with annexure in the prescribed format for printing and submission to the Parliament for its approval
- Online data collection eliminates the need for repeated data entry
 - This is a role-based system, means each user can access only the data / information they are authorized to
 - Automatic validation of data prevent errors, thus re-checking of data is avoided
 - Uniform formula for Salary Budget enables more accurate calculation of required funds
 - Automatic closure of entry provision after the cut-off date.
 - Units can be asked to rework the provisions sought by enabling "edit option"
 - Monitoring of data-entry activity by the units is possible

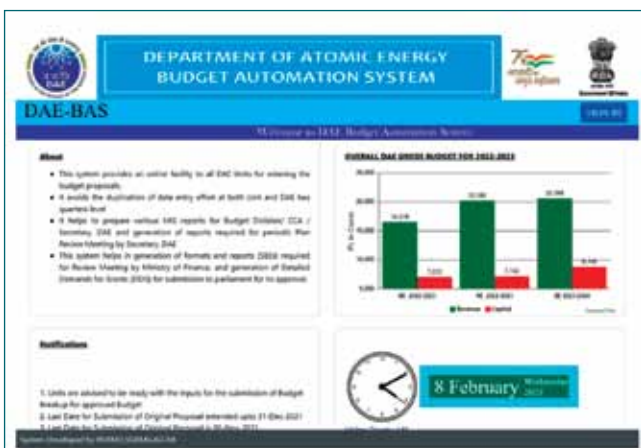


Fig. 1: Home page of DAEBAS 2.0



Fig. 3: Establishment data entry screen

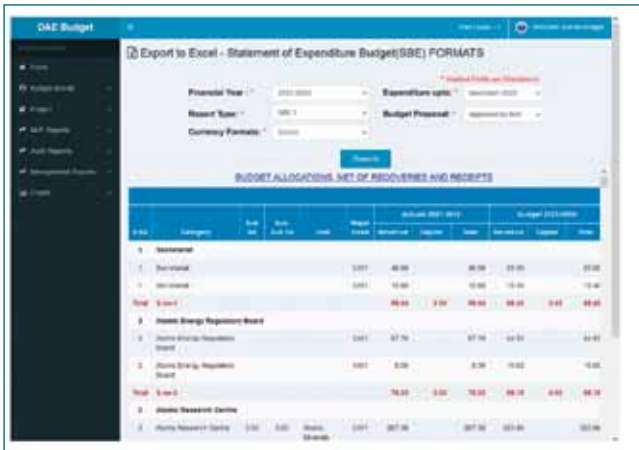


Fig. 4: Statement of Expenditure Budget (SBEs) report

Further,

- The system will allow only authorized users with valid credentials
- Within IGCAR, access is restricted based on the IP address
- The database is being backed up periodically to avoid data loss

The need for re-development of DAEBAS

The current version of the system has been developed with a focus on providing solution to the user requirement as primary objective. The subsequent security audits on the system emphasized the following:

- Usage of latest version of Windows OS – which involve procurement of newer version of the licenced proprietary software
- Keeping the PHP / MySQL / Apache web server updated to its latest version
- Avoidance of SQL injection
- Avoidance of Cross site scripting

While most of the above recommendations have been complied, implementing the remaining aspects of the security audit resulted in complete re-development of the system, due to which the process initiated for DAEBAS version 2.0

Towards redevelopment of DAEBAS, the following hardware / software were used

- MVC architecture is implemented using Code Igniter framework for developing the web pages and it provides for code reuse
- Open source Operating System Viz. Linux instead of proprietary OS to avoid frequent re-licensing
- A high-end server with latest configuration to enable high availability, maximum throughput, increased speed and minimize down-time.

Hence, the redevelopment of DAEBAS was taken up and completed. The process to deploy the new server through Anunet & user testing is in progress.

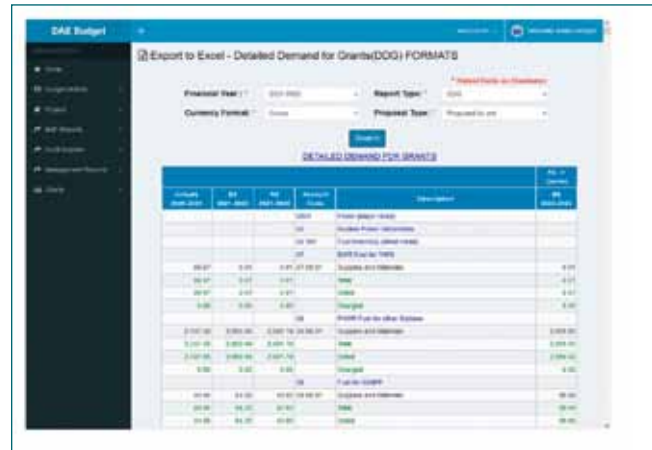


Fig. 5: Detailed Demands for Grants (DDG) report

Benefits of the new system (DAEBAS 2.0):

- The new system complies with computer security audit requirements
- It provides improved user experience through enhanced look & feel and easy to use menus
- Additional reports provided for budget monitoring purpose
- Facility to export the reports in pdf format in addition to MS-excel
- Representation of data through Graphs / Charts
- Enhanced facility for user / administrator roles
- Provision made for changing the user password & forgot password
- User-friendly messages on data mismatch etc.
- Latest server hardware for increased speed
- Open source, free & more secure Operating System

System Maintenance:

The frequent requests for additional modules, changes in the existing modules have always been incorporated. The changes in the master data like HoA are incorporated as and when required.

- Twice, the rationalized Head of Account has been changed completely. All the program modules and reports have been modified so that the system would serve data for both old as well as the new heads.
- The recent order on new object heads was incorporated.

Further Development:

A new requirement for Pension and Receipt budget module has been received from DAE. A study on the development of the same is in progress.

Screens from the DAEBAS system:

The automation of Budget process at DAE by implementation of DAEBAS has resulted in the elimination of data re-entry at DAE, improved accuracy of information, aided quick decision making, avoided manual checking & validation of voluminous data submitted by various Units and has enabled adherence to timelines fixed by Ministry of Finance, etc.

VI.13 Aazadi ka Amrit Mahotsav and DAE Iconic Week

Azadi ka Amrut Mahaotsav Anu Yatra (AKAM AnuYatra)

As a part of Azadi ka Amrit Mahotsav celebrations, IGCAR has organised a sequence of awareness programs to showcase and celebrate the technology development carried out and transfer of certain technology in the application of societal benefits by Department of Atomic Energy for the past 75 years after independence. The program is organised in association with A.P.J. Abdul Kalam International Foundation, Rameswaram, The Tamil Nadu Ariviyal Sangam and Indian Association for Radiation Protection. The program is started with curtain raiser event at Kalpakkam on 23th July' 2022 and culminated at Kudankulam on 12th Aug' 2022 covering 1100 km in 10 nodal institutions. The sequential venues (colleges) along with event dates and the route map of the program is given in Fig. 1.

The program is a two days event in each nodal institutions comprising of various competitions and exhibition. The nodal institutions were asked to coordinate with schools and colleges in their educational divisions to participate in the program. The nodal institutions are identified with the help of Tamil Nadu Ariviyal Sangam. The program is organized in each institution by inviting a nodal personality as a chief guest of their choice and AD/GD

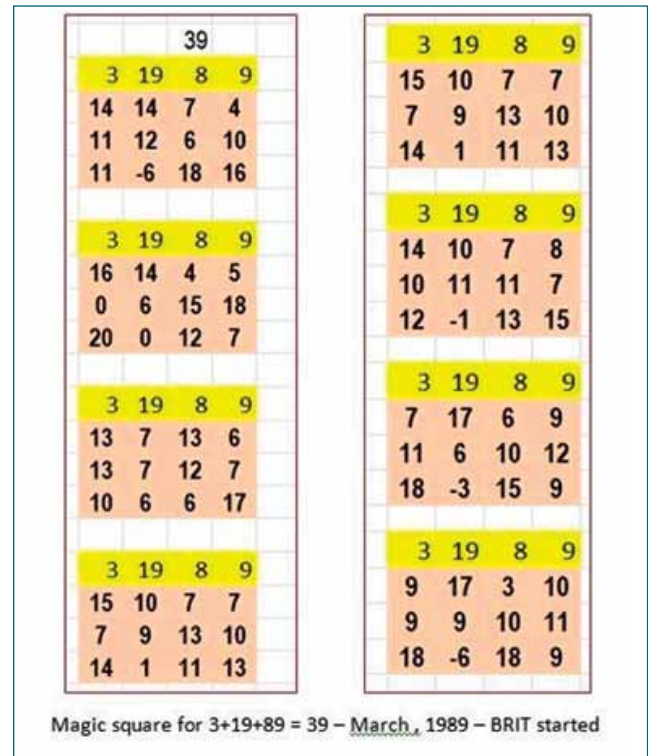


Fig. 2: Magic square.

level officials of IGCAR along with a crew of officers for the conduction of events and interactions. The overall footfall for the events would be 20,000.

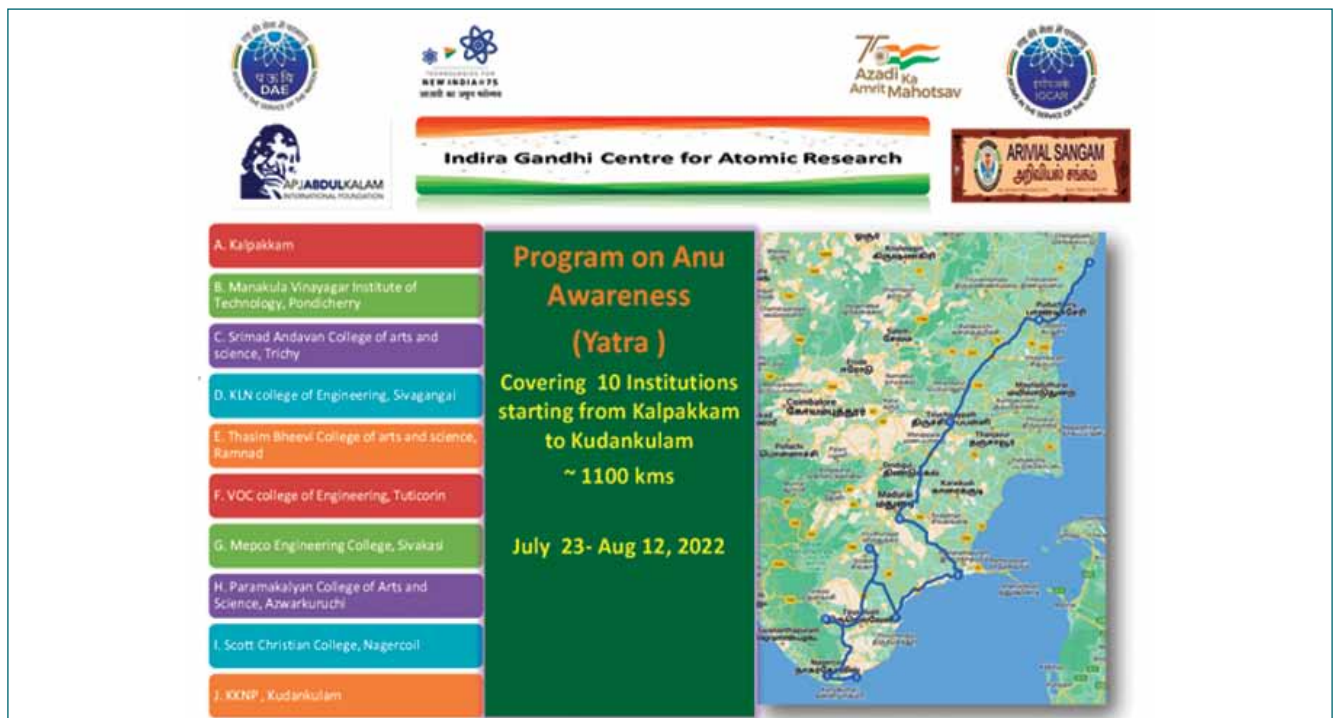


Fig. 1: DAE ICONIC Week celebrations

Generation of Magic Square - 750 Squares using 75 iconic dates of DAE with 75 Students

IGCAR has organized one day event on “Generation of Magic Squares” of 750 squares with 75 students from nearby eight Govt. Higher Secondary Schools of Kalpakkam, using 75 important dates of milestone activities of different units of DAE. The event is conducted on 22nd Aug’ 2022, in Higher Sec School, Sadurangapattinam. The program is conducted by a mathematician Shri. Jothi Lingam, Retd., Station Master, Indian Railway. In this event 4 x 4 matrices were created using month and year of the milestone dates. Eg. Aug 1948–AEET Established- 8+19+4+8=39 (magic square with sum 39) as shown in Fig. 2. A Tamil Song about Atoms in the service of Nation was composed by a Tamil Teacher from Pavalaru Tamil School, Kalpakkam and sung by the same school Children of 1st standard.

Sand art sculpture

As a part of Azadi ka Amrit Mahotsov (AKAM) -DAE ICONIC week Celebrations, IGCAR and GSO, have organized a sand art sculpture in the Kalpakkam beach during 27th -28th Aug, 2022 depicting various technologies of DAE applied to the societal benefits, highlighting contribution to power sector, agriculture, health and technology development. The sculpture was inaugurated by RDO, Chengalpattu Smt. Shajeevana IAS in the presence of President of Pudupattinam Panchayat, Senior Commandant, CISF and officials of IGCAR & GSO, Principals and students of AECS and KVs. Flood light arrangements were made. Wide publicity was given. There were more than 20000 foot falls from the residents of DAE Townships, Pudupattinam and Sadurangapattinam villages (Fig. 3).



Fig. 3: Sand sculpture of various technologies of DAE.



Fig. 4: Anu Walkathon at Elliot's Beach, Chennai.

ANU Walkathon of AKAM

During DAE’s Iconic Week celebrations from 27th -28th Aug, 2022, various activities were executed by the Centre to popularize the activities of the Department. Anu Walkathon was one of the activities conducted at Rajaji Bhavan and Elliot’s beach, Chennai on 28th August 2022 (Fig. 4).

DAE exhibition during 88th Annual Meeting of the Indian Academy of Sciences

DAE Exhibitions were held at SRM University - AP during 3rd - 6th November 2022 on the occasion of the 88th Annual Meeting of the Indian Academy of Sciences. 21,455 students from different Schools, ITIs, Polytechnics and Colleges from the districts of Krishna and Guntur visited the Exhibitions. Further, the event received excellent media publicity covered in 52 regional and national dailies / TV Broadcasts.

Upgradation of the Information Centre

IGCAR DAE Information Centre is being set up at Shastri Bhavan, Chennai, which houses around 65 Central government offices. The primary objective of the centre is to provide a facility to the general public that highlights various accomplishments of the Department of Atomic Energy. The exhibits and audio visual displays at this Centre would help the visitors to understand the seminal contributions made by the Department of Atomic Energy in deploying radio isotopes to agricultural and industrial applications besides the key attributes of nuclear technology. Currently this centre houses many displays which include both textual narrations as well as interactive working models with audio descriptions on Nuclear Reactor systems and many key components that were indigenously developed by various units of the Department of Atomic Energy including BARC and IGCAR.

VI.14 Incubation and Transfer of IGCAR Technologies

DAE Incubation Centre, IGCAR (IC-IGCAR) was inaugurated on 30th October 2020 on the occasion of 111th birth anniversary of Dr. Homi Jehangir Bhabha by Shri. K.N. Vyas, Secretary, Department of Atomic Energy (DAE). IC-IGCAR has a mandate of taking forward Government of India's mission of Atma Nirbhar Bharat and incubate/transfer various DAE technologies to encourage start-ups and commercialise the technologies.

Technology Transfers

Pulsating sensor based conductivity meter is a high performance instrument developed at EIG(Fig. 1).

This device is suitable for real-time monitoring of electrical conductivity of aqueous solutions in plants and field applications apart from its usage in chemical laboratories for analysis and quality control. Performance of this device has been validated with many applications in IGCAR and found to be robust even in demanding environments. The technology has been transferred to two start ups: one in Bengaluru and another in Udaipur (Rajasthan).

A portable high volume air sampler (HVAS) has been developed at SQRMG. It is a light-weight device, made of Fiber Reinforced Plastic (FRP) and has an in built embedded controller to start, stop, log and to calculate the total volume of air sampled. This is employed to collect airborne particulates in a filter paper medium at desired flow rates up to 2800 lpm. HVAS is used in nuclear installations for the collection of air samples to estimate air-borne radioactivity levels. This technology has been transferred to a Bengaluru based start up (Fig. 2).

Autonomous Gamma Dose Logger (AGDL) is a radiation monitor developed at SQRMG to measure environmental radiation in a wide range of 100 nGy/hr to 5 Gy/hr. Currently ~28 numbers of in-house made AGDL systems are operating successfully at DAE Kalpakkam site and connected to the Decision Support System for real-time radiation field inputs. This technology has been transferred to a Chennai based start up as well as to a Hyderabad based industry.

Incubation of Technologies

IC-IGCAR has signed a collaborative incubation agreement with a Mumbai based private manufacturer to complete development of the technology "Replaceable Feed-through Connectors for Glove Boxes". This is IGCAR's first technology incubation agreement with private sector following the DAE Incubation Policy (2021).

Another collaborative incubation agreement has been signed between IC-IGCAR and a start-up company based in IIT (Madras) for developing "Hydrogen Sensor" technology. This partnership with the start-up is expected to accelerate development of this IGCAR technology from its current technology readiness level (TRL) of '4' to TRL '8' or '9', suitable for commercialisation, during the incubation period of ~18-24 months (Fig. 3).

IC-IGCAR will continue to play a role of providing the start-ups with necessary guidance, technical support, networking, and facilitating a host of other resources that may be required for them to sustain and scale up.



Fig. 1: Conductivity meter



Fig. 2: Portable Air Volume Sampler

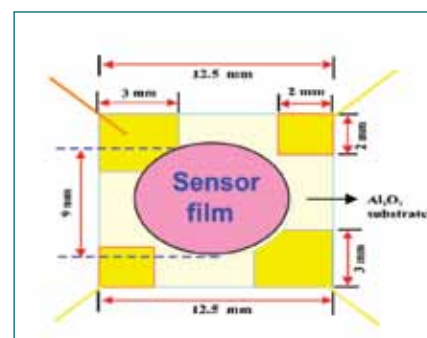


Fig. 3 Schematic of Hydrogen Sensor

VI.15 Advanced Digital Library & Services

Scientific Information Resource Division (SIRD) is a research library that provides a comprehensive platform to access resources across the IGCAR Campus and uses the latest technologies to offer information services on a 24x7 basis.

SIRD has created an instance for IGCAR in Indian Research Information Network System (IRINS) <https://igcar.irins.org/>. The IRINS is the premier database of profiles of scientists, researchers and other faculty members working at leading academic institutions and other R & D organizations in India. The database would be instrumental in the selection of panels of experts for various committees and taskforce established by the Ministries / Government establishments for monitoring and evaluation purposes. It is a powerful tool to increase the exposure of Indian research to the International community.

A book titled "Butterflies of Kalpakkam" (Fig. 1) was published in 2022 by SIRD with information on butterflies like Common name, Scientific name, Family, Larval host plant, Wingspan, and Spotted area. Seventy-eight butterfly species are covered in this book. The book was published on the Foundation Day Celebrations on April 30, 2022 by former Director, Dr. S.A.V. Satya Murty.

Foundation Day of IGCAR was celebrated on April 30, 2022. For the foundation day, a video on DFRP fuel chopping and a short film on Butterflies of Kalpakkam was filmed by SIRD. On that occasion, few books were released by former Directors of IGCAR. SIRD edited and printed the booklet on Hindi, FBTR ahead, and the Butterfly book. The video and photo shoot of the entire event inauguration of Integrated Radiation Monitoring Facility (IRMF) covered by SIRD. SIRD also designed the display on the video wall erected for the foundation day.

SIRD regularly provides IGCAR Publication data and other metrics to NAAC, Audit and PRIS Committees. The Publications of IGCAR in peer-reviewed journals during 2022 is 445 plus; the H-index is 126 in Google Scholar, 116 in Scopus and 109 in Web of Science. As part of such activity, SIRD subscribes to Scispace (formerly known as Typeset) tool used for scientific

proof reading of research articles, citation databases Scopus and Sci-Finder and research assistance tools like Grammarly, and Ithenticate. Further resource subscriptions include Springer LB materials database, ICDD, IEEE/IEL databases and 450 journals pertaining to 70 publishers belonging to the core area of research at IGCAR. SIRD has 65,000 books. This year we have added 400 more books to our collection. Stock verification was done in the Chemistry discipline using RFID gadgets.

The video streaming infrastructure (Fig. 2) of Sarabhai Auditorium was upgraded to latest streaming facility with HD-cameras, option to connect HDMI output to virtual platform and enhanced storage & networking facilities. The security gadgets to SIRD were enhanced by the commissioning of IP based CCTV system with 60 number of fixed dome camera, 6 bullet cameras and 3 PTZ cameras covering the entire SIRD premises. 12 KW cooling rack with more advanced features like automotive gaseous fire suppression, finger print based authentication and automatic alert was added to our Datacenter.

This year, ASTM International (Fig. 3) honored SIRD for the extensive usage of its databases. IGCAR is the first Library in DAE to be honored this way by ASTM International.

SIRD was awarded the Certificate of Appreciation under Best Office Premises during the Swatchatha campaign in 2022.

Video coverage is an activity of SIRD that includes dignitaries visits, every event, selection committee skill tests, awareness programs for Journalists visit, Foundation day, Amrit ka Mahotsav Anu Yatra at Chennai, etc.

In-house publication activity includes editing to printing the IGC newsletters, IGC Reports, IGC annual reports, brochures, booklets, etc.

Preprints server, Auditorium facility, interlibrary loans, archiving IGCAR publications, news clips on FBRs, digitizing old print copy standards, content creation activities are other value added services from SIRD.

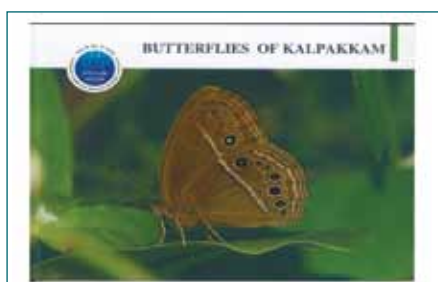


Fig. 1: Butterflies of Kalpakkam



Fig. 2: Video streaming Facility



Fig. 3: ASTM International Honour to IGCAR

VI.16 Biodiversity at DAE Kalpakkam complex

DAE Kalpakkam complex is a favourite destination for birds due to the presence of many water bodies like freshwater ponds, backwater areas, mangrove vegetation and seashore. Many wetland and wetland-associated birds are present in Edaiyur Backwater, Sadras Backwater, WIP Marsh, and FBTR Backwater, Kokilamedu Lake, and M.S. Swaminathan research plant. The water bodies are secluded and it attracts many migrant birds. More than 186 species of Birds were recorded in the DAE Kalpakkam complex.

The freshwater ponds like WIP Marsh, and FBTR Marsh attract many water birds like grebes, cormorants, egrets, herons, dabbling ducks, moorhen, swamp hen, water hen, lapwings, stilts, sandpipers, plovers, terns, pelicans, storks, etc. Rare migratory birds visit every year between November and February.

During this year some of the rare and uncommon bird species that were documented are Western Reef Egret, Great Grey Shrike, Common Greenshanks flocks, Snipes, Barn Owl, Collared Dove, Albino Myna, Jungle Prinia, Grey headed lapwing, Yellow headed lapwing, Oriental Honey Buzzard, A flock of Marsh sandpipers and Red Necked Falcon. These avian species were found near WIP marsh and Kunnathur gate (Fig. 1).

Thousands of migratory species Rosy Starling were



Fig. 2: Rosy Starling

documented this year in the township and DAE Kalpakkam campus (Fig. 2).

This year's special capture is Flying foxes. Hundreds of Flying foxes visit DAE complex to roost between July and December in casuarina trees. Flying foxes are seen in large numbers in nights in search of food in both the DAE township parks, the Fire station mango tree, ESL lab, etc (Fig. 3).

The biodiversity documentation time and again indicates that the DAE complex at Kalpakkam is buzzing with activities with avian migratory visitors and residents. It reiterates that nuclear energy is environment friendly.

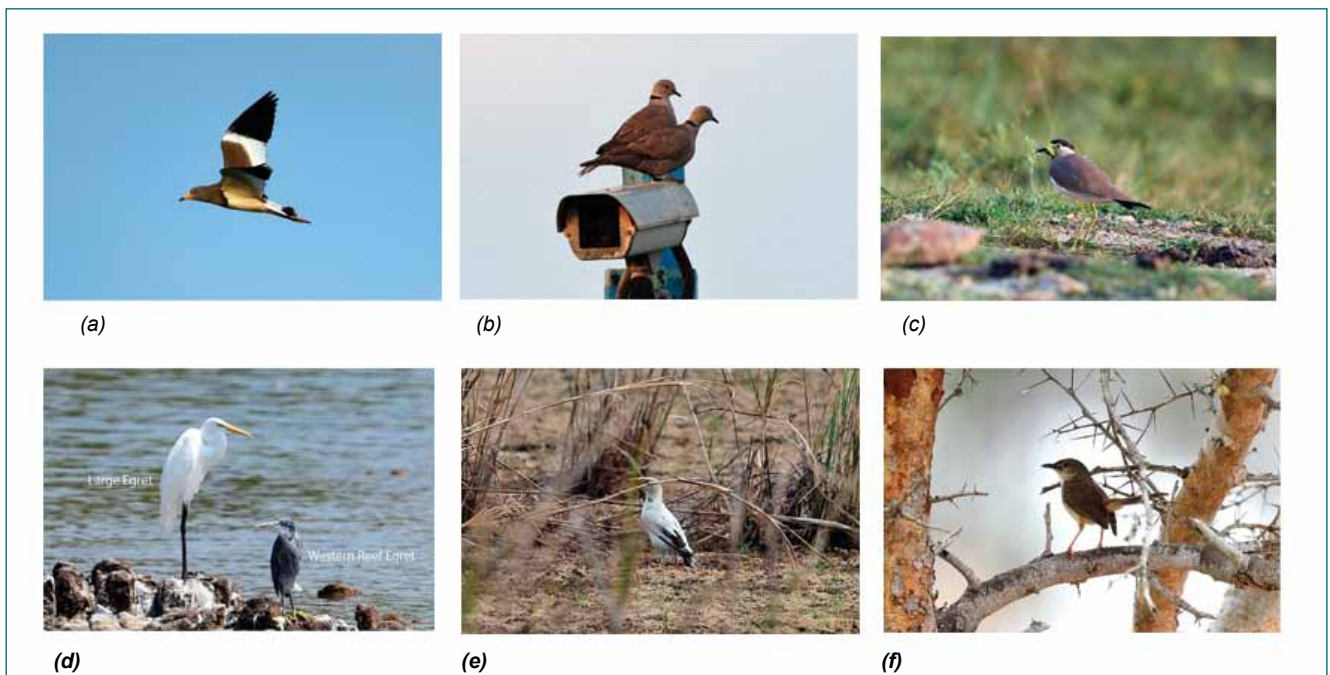


Fig. 1: (a) Grey Headed Lapwing, (b) Collard Dove, (c) Yellow Wattled Lapwing, (d) Large Egret & Western Reef Egret, (e) Albino Myna and (f) Jungle Prinia



Fig. 3: Flying Fox



CHAPTER
VII

Awards / Publications /
Events / Organisation

Awards & Honours

Dr. B.Venkataraman and Dr. John Philip have been conferred the Honorary Fellowships of the Indian Society of Analytical Scientists, Mumbai.

Dr. John Philip has been appointed as Associate Editor of International Journal of Ceramic Engineering and Science, American Ceramic Society, Wiley Publishers

Ms. Geethi Jena, CSTD, MMG has been awarded "NACE Foundation India Scholarship" of Rs.1,50,000/- by the NACE Foundation (USA)

Mr. Paulson Varghese, CSTD, MMG has been awarded "NACE Foundation India Scholarship" of Rs.1,50,000/- by the NACE Foundation (USA)

Dr. John Philip has been appointed as Associate Editor of Frontiers in Nanotechnology (Nanomaterials), Frontiers Publishing, UK

Dr. John Philip has been selected as an Editorial board member of Smart Materials in Medicine, Elsevier, Netherland

Dr. John Philip has been selected as an Editorial board member, Materials Futures, Institute of Physics(IOP), UK

Dr. John Philip and Dr. Vasudevan featured in the world's top 2% Scientist list in the career-long category with 128,190, and 255,412 ranks, respectively published by Elsevier and Standford university in 2022.

Dr. John Philip, Dr. Vasudevan and Dr. B. B. Lahiri featured in the world's top 2% Scientist list in the single-year category with 46,826, 100,534 and 215,992 ranks, respectively published by Elsevier and Standford university in 2022.

Ms. Manali Nandi, SMARTS, MCG received the Best PhD Research Award (Physics) 2022 of Dr. K. V. Rao Scientific Society, Hyderabad for the thesis "Inter-droplet force measurement between gamma alumina Stabilized Pickering nanoemulsion droplets: role of electrostatic and electric dipolar interactions"

Dr. Geetisubhra Jena, CSTD, MCG, received the Best thesis award by NACE International India Section – during CORCON 2022, 19 – 22 September, Udaipur, India for her thesis titled "Development of graphene oxide based composite coating with improved corrosion resistance and antibacterial properties".

Dr. John Philip has been appointed as Associate Editor of Hybrid advances of Elsevier Publishers.

Dr. M. Vasudevan has been selected for Fellow of Indian Institute of Metals (FIIM).

Dr. M. Vasudevan is selected as an Editorial Board Member of Engineering Failure Analysis Journal of Elsevier Publishers.

Shri E. Premkumar, SIRD, IGCAR won the Bronze medal on Uganda Para-badminton International tournament held during 13-18 September, 2022 in both Men's Singles and Men's Doubles categories represented from India.

Smt. S. Rajeswari, SIRD, IGCAR honoured for dedicated commitment and exceptional contribution to ASTM standards by ASTM International, 2022.

Smt. S. Rajeswari, SIRD, IGCAR is selected as a member of Library Advisory Board of Institute of Physics Publishing, UK, IOPP from 2022.

Best Paper Awards

K. K. Madapu, C. Abinash Bhuyan, S. K. Srivastava, S. Dhara

The novel mechanism in understanding a strong enhancement of photoluminescence quantum yield in large-area monolayer MoS₂ grown by CVD. J. Mater. Chem. C 9 (2021) 3578

Reshma. T. S, Sourav Pan and Arindam Das

Selective Adsorption and Fast Photocatalytic Degradation of Mixture of dyes by Uncapped SnO₂ QDs. International Conference on Frontiers for Technological Applications (FIMTA 2022) (Gold Medal)

Dr. Anandkumar, Surdharshan, T. Nandakumar, Ravishankar and J. Philip

CSTD received the Best Poster Award of CORCON 2022 held during Sept 19-22, 2022 for the poster titled "Development of silane-based epoxy hybrid coating on water transporting pipeline materials for enhanced microbiologically influenced corrosion protection performance"

Ram Kumar Maity, T. Sudararajan, K. Velusamy

“An enhanced piecewise linear interface construction template based on c0 correction”

Proceedings of the 48th National conference on Fluid Mechanics and Fluid Power (FMFP), December 27-29, 2021, BITS Pilani, Pilani Campus, RJ, India

Dr. B. B. Lahiri,

Young Achiever Award in the 66th DAE Solid State Physics Symposium (DAE-SSPS 2022).

M. Vasudevan along with co-authors (D. K. Dwivedi of IIT Roorkee and Anup Kulkarni of Pratt and Whitney) received the W. H. Hobart Memorial Award 2021 of the American National Welding Society for the paper titled “A functionally graded joint between P91 steel and AISI 316L SS”

Best Poster Awards

S. Murugan, S. Sathees Kumar, M. Krishnamoorthy, V. Praveen Kumar, B.S. Ramesh Babu, Utpal Borah, Mohd Sabih, Alka Kumari, G. Ramesh and M.V. Kuppusamy from Central Workshop Division (CWD) and Quality Assurance Division (QAD), IGCAR.

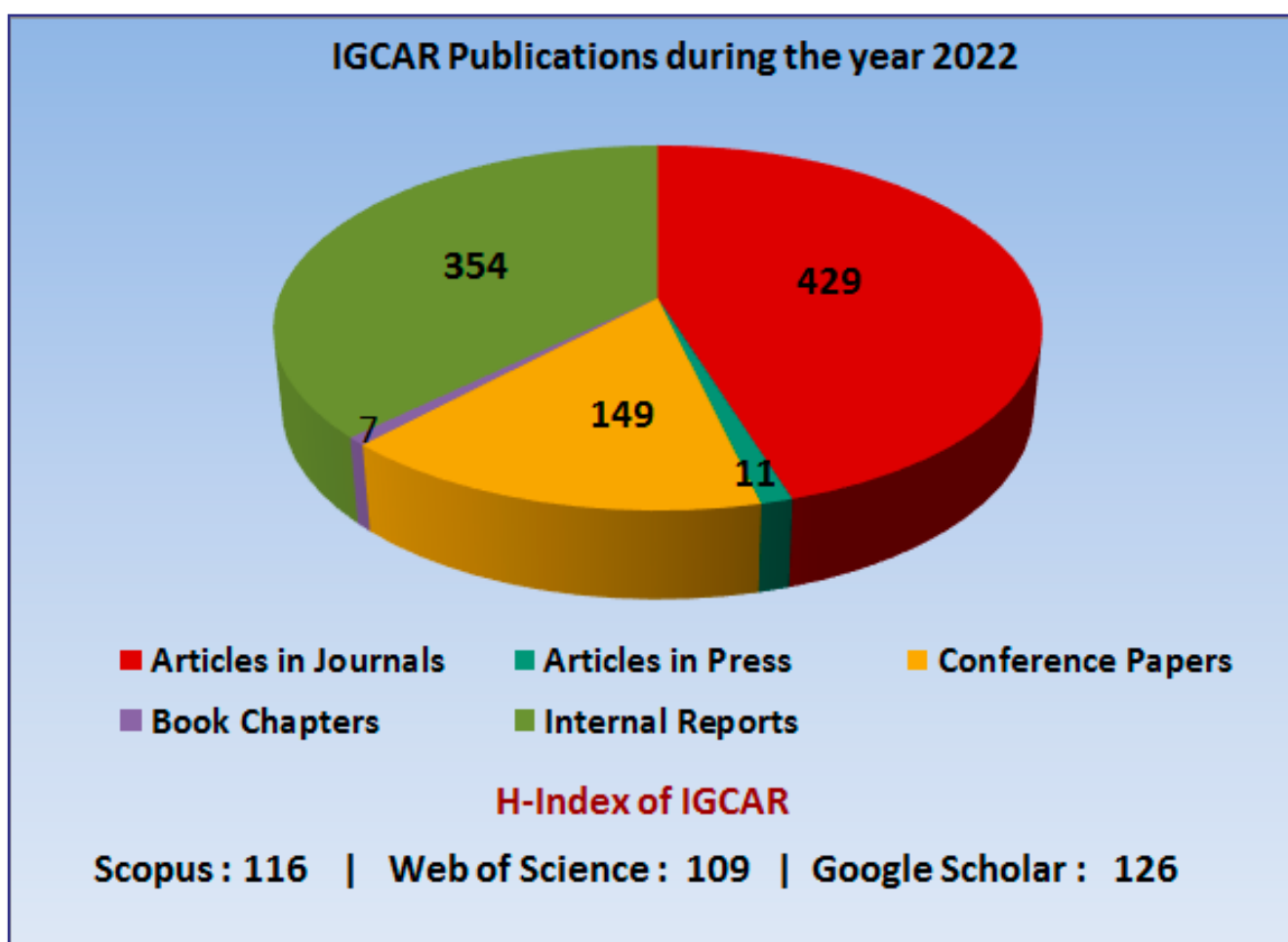
“Manufacturing experience of Large Austenetic Stainless Steel Inner Vessels (I&II) for Sodium Technology Complex”. Venus Wires Award 2022 for the Best Paper in Stainless Steel Application by The Indian Institute of Welding.

Seminars, Workshops, Webinars and Meetings

- Seminars, Workshops, Webinars and Meetings
- “The story of Chicago pile” by Dr. P.R. Vasudeva Rao, Vice Chancellor HBNI by IANCAS-SRC at Sarabhai Auditorium on January 6, 2022.
- “Applications of Radiation and Nuclear Technologies for societal benefits” National Hindi webinar at Sarabhai Auditorium on January 10-11, 2022.
- “RTI Act 2005” conducted as Online Training Programme by ATI, Mumbai at Raja Ramanna Auditorium on January 13, 2022.
- Awareness Programme by Internal Compliants committee, women cell at Raja Ramanna Auditorium on February 25, 2022.
- “Sexual harassment of women employess by constitution of CCSHWE” Awareness Programme at Sarabhai Auditorium on February 25, 2022.
- Science day celebration by Indian Women Scientists Association at Raja Ramanna Auditorium on February 28, 2022.
- Swatchchta Pakwada, by Admin at Sarabhai Auditorium on March 2, 2022.
- “ Working place stress management by natural way of life” by Healer A. Pattammal and “Vinnum Pennum” by Smt. Sumathy Kumaravel, Chennai conducted as Awareness Programme at Sarabhai Auditorium on March 8,2022.
- National Conference on Urjavarana 2022 “Disha dialogues In sustainable HVAC and Architecture” by ISHARE at Sarabhai Auditorium on March 9-10, 2022.
- “Orientation workshop for contract labourers” by Admin at Raja Ramanna Auditorium on March 10,2022.
- “Hindi Fortnight Prize Distribution Function” by Hindi section at Sarabhai Auditorium on March 24, 2022.
- “Our Biosphere and Water futures pathways for sustainable Development” by S. Janakarajan Former Professor, MIDS, Chennai, President South asia Consortium for Interdisciplenary Water Resoures studies saci waters, Hyderabad, Water day celebration by AARCO at Sarabhai Auditorium on March 28, 2022.
- “Women are pearls of the nation” talk by Dr. R.Rajammal, women's day celebration by AARCO at Sarabhai Auditorium on March 28, 2022.
- “Acoustic Monitoring of the Oceans and Applications” by Dr. G. Latha, Scientist and Group Head, Ocean Acoustics, NIOT, Chennai and “Journey of a Scientist to an Entrepreneur” by Dr. Rachna Dave, Entrepreneur- Micro Go, Chennai, women's day celebration by IWSA at Sarabhai Auditorium on April 7,2022.

- Baldevraj Memorial lecture - "Additional Challenges before Nuclear Energy in a Net Zero World" by Dr. Anil Kakodkar Chancellor Homi Bhabha National Institute, Mumbai, Chairman, Rajiv Gandhi Science & Technology Commission, Former Chairman AEC & Secretary, DAE by IIM kalpakkam chapter at Sarabhai Auditorium on April 09, 2022.
- "Nuclear Materials & Associated Technology" IIM Course at Sarabhai Auditorium on April 19-20, 2022.
- "IPR and Technology Transfer" Awareness Programme by DAE IPR Cell at Sarabhai Auditorium on April 26, 2022.
- "Pension & Retirement Benefits, Life Management post retirement" training programme by ATI Mumbai at Raja Ramanna Auditorium on May 18 - 19, 2022.
- "Awareness Camp for Contractor Employees" by Enforcement Officer, EFPO at Raja Ramanna Auditorium on May 27, 2022.
- "Yoga for Humanity" by Sr.Prof. K.R. Munirathinam, WCSC Chennai, celebration of Inter Nat. Yoga day at Sarabhai Auditorium on June 21, 2022.
- Inter-Department Meeting between IGCAR and RRCAT collaborative projects at Sarabhai Auditorium on June 23 - 24, 2022.
- Azadi Ka Amrit Mahotsav lecture series - "The Science of Climate Change" by Dr. M. Rajeevan, MoES, Distinguished Scientist, National Centre for Earth Science Studies (NCESS), Kerala & Former Secretary, Ministry of Earth Sciences, Government of India at Sarabhai Auditorium on June 27, 2022.
- "Usage of Spoken Hindi in OL Implementation" and "OL Policy and Noting & Drafting" by Hindi section at Raja Ramanna Auditorium on June 28, 2022.
- "Advancement of Non-oxide Technical Ceramics Towards India's Strategic Self-reliance" by Dr. Abha Bharti, Co-founder, Advisor-Hydrogen & Fuel cell CeraTattva InnoTech IITM Research Park, Taramani, Chennai, IWSA technical talk at Raja Ramanna Auditorium on June 30, 2022.
- Seaborg Memorial Lecture – "Recovery of radio-ruthenium from radioactive feeds - Challenges and strategies" by Dr.P. K.Mohapatra, OS, Head, RCD, BARC at Sarabhai Auditorium on August 16, 2022.
- Azadi Ka Amrit Mahotsav lecture series - "The legend lives – The story of Bhabha" by Dr.G.Amarendra Raja Ramanna Fellow, NFC, Hyderabad, Former Director, MSG & MMG, IGCAR at Sarabhai Auditorium on August 25, 2022
- "Works Procedure and Contract Management" Training Programme by ATI, Mumbai at Raja Ramanna Auditorium on August 25, 2022.
- "National Pension Scheme – II" training programme by ATI, Mumbai at Raja Ramanna Auditorium on August 26, 2022.
- "Acts & Codes" Training Programme by ATI, Mumbai at Raja Ramanna Auditorium on August 29, 2022.
- Azadi Ka Amrit Mahotsav lecture series - "Ocean Science for the Society: Success of Sustained Real-Time Observations of Oceans" by Dr.R.Venkatesan, Former Head, Ocean Observation Systems, National Institute of Ocean Technology, Chennai at Sarabhai Auditorium on August 30, 2022.
- Prof. Brahm Prakash Memorial Materials Quiz (BPMMQ-2022) by IIM kalpakkam chapter at Sarabhai Auditorium on September 09, 2022.
- Celebration of Hindi Fortnight in IGCAR by Hindi Section at Sarabhai and Raja Ramanna Auditorium on September 22-29, 2022.
- 55th Engineer's day celebration - " Smart Engineering for Better World" by Dr.N. Anandavalli, Director CSIR-SERC, SERC campus Tharamani Chennai at Sarabhai Auditorium on September 23, 2022.
- "Sub Conventional Aerial Threats" awareness Programme by Air force official at Sarabhai Auditorium on October 14, 2022.
- Graduation day 16th batch (OCES-2021) BARC training school IGCAR campus at Sarabhai Auditorium on October 26, 2022.
- Cyber Security Awareness Workshop by Computer Division at Sarabhai Auditorium on October 31, 2022.
- Vigilance Awareness week by Admin at Sarabhai and Raja Ramanna Auditorium on November 01-04, 2022.
- "Corruption free India for a developed Nation" by Shri M. Sundaravel ,ADSP, Anti-Corruption Branch, CBI, Chennai, Vigilance Awareness week at Sarabhai Auditorium by Admin on November 2,2022.

- Azadi Ka Amrit Mahotsav lecture series - “Advanced Materials and Processing: Challenges and Opportunities” by Dr. Dinesh Srivastava, Distinguished Scientist, Chief Executive, Nuclear Fuel Complex at Sarabhai Auditorium on November 21, 2022.
- Prof. C. V. Sundaram Memorial Lecture - “Nuclear Safety and Need for Nuclear Energy for Future Survival” by Shri G. Srinivasan, Former Director, Reactor Operations and Maintenance Group, Indira Gandhi Centre for Atomic Research at Sarabhai Auditorium on November 22, 2022.
- “Anti Tobacco Awareness” by Dr. B. Dakshinamurthy, Assistant Professor, Department of Respiratory Diseases, Government Omandurar Medical College, Chennai and “Diabetes-The New Epidemic” by Dr. P. Jayaganesh, Professor of Pathology, Saveetha Medical College, Chennai Health Awareness Programme at Sarabhai Auditorium on November 29, 2022.
- One day Hindi workshop by Hindi section at Raja Ramanna Auditorium on November 30, 2022.
- “Pension & Retirement Benefits, Life Management post retirement” training programme by ATI Mumbai at Raja Ramanna Auditorium on December 12 - 13, 2022.



EVENTS

National Hindi Scientific Seminar (NHSS-2022)

January 10, 2022



Director, IGCAR along with OLIC members releasing the abstract volume of NHSS-2022

On the occasion of World Hindi Day (10th January, 2022), the Official Language Implementation Committee (OLIC) of IGCAR & GSO jointly organized a two day National Hindi Scientific Seminar (NHSS-2022) on the theme of "SAMAJ-KALYAAN MEIN VIKIRAN EVAM NABHIKIYA PROUDYOGIKI KE ANUPRAYOG" (Applications of Radiation and Nuclear Technology for Societal Benefits) in hybrid mode on January 9-10, 2022. The seminar was conducted in Vikram Sarabhai Auditorium, IGCAR with more than 75 participants from IGCAR, GSO and other DAE Units at Kalpakkam attending it physically. About 35 outstation participants joined virtually through Webex online platform mainly comprising Scientific & Technical Officers, Doctors and Researchers from various DAE units and other prestigious institutions, from different parts of the country. The objective of the seminar was to facilitate exchange and dissemination of information regarding the benefits of radiation and nuclear technologies and also to encourage the use of official language Hindi in scientific and technical presentations.

The seminar was inaugurated by Shri S. A. Bhardwaj, Former Chairman, AERB, Mumbai in online mode. In his inaugural address Shri Bhardwaj impressed upon the participants to make conscious efforts to increase the use of Hindi language in writing reports and other forms of official work. He also delivered a plenary talk titled 'SAMAJ KALYAAN EVAM VIKIRAN' (Societal Benefits of Radiation Technologies) in the first technical session, that followed the inaugural function. Dr. B. Venkatraman, Director, IGCAR & Chairman, OLIC delivered presidential address. He highlighted the contributions of DAE and its constituent units in various fields of science and technology and said that we are also successfully eliminating tons of carbon emissions, annually, by producing electricity through nuclear energy which is a clean and green energy. Dr. B. K. Nashine, Group Director, ESG, & Alternate Chairman, OLIC, IGCAR also shared the dais as a guest of honour. In his address, Dr. Nashine expressed happiness over holding of the Hindi Seminar at a time when the country is celebrating Azadi Ka Amrit Mahotsav to commemorate its 75th year of independence and said that we should take pride in propagating our scientific achievements among the masses through the medium of our own languages. Earlier, the inaugural function started with welcome address by Dr. Awadhesh Mani, SO/H & Convener, NHSS-2022 who also presented brief details of the seminar. The inaugural session concluded with vote of thanks by Dr. Vani Shankar, SO/G & Co-convener, NHSS-2022.

During this two-day seminar, a total of 29 technical presentations highlighting various applications of radiation in different fields like agriculture, energy, food preservation, health, industry, medicine, research & development and technology transfer were made in four technical sessions including 1 plenary lecture, 5 keynote addresses, 7 invited talks and 16 contributory presentations. The guests lecturers, contributory presenters and other participants hailed from different units like AIIMS, JAMIU (New Delhi); AERB, BARC, DAE, TMC (Mumbai); NPCIL (Rawatbhata), IPR (Gandhi Nagar), RMP (Mysore), ECIL (Hyderabad), RRCAT (Indore), IREL (Manavalakuruchi), MSME_DI (Chennai), IGCAR, GSO, BHAVINI, BARC-F, SRI/AERB (Kalpakkam). The technical sessions were chaired by Dr. B. K. Nashine, Director, ESG, Shri Tanmay Vasal, Head, PPCD/RDTG, Dr. N.V. Chandra Sekhar, Associate Director, MSG and Dr. Sekhar Kumar, Head, RPOD/RpG who also conducted the valedictory session in which the outcomes of the seminar was discussed and feedback obtained from the participants. NHSS-2022 successfully concluded with the vote of thanks by the Convener, followed by national anthem and group photography of physical participants, chairpersons and members of the organising committee.

*Reported by
Dr. B. K. Nashine, Director, ESG*

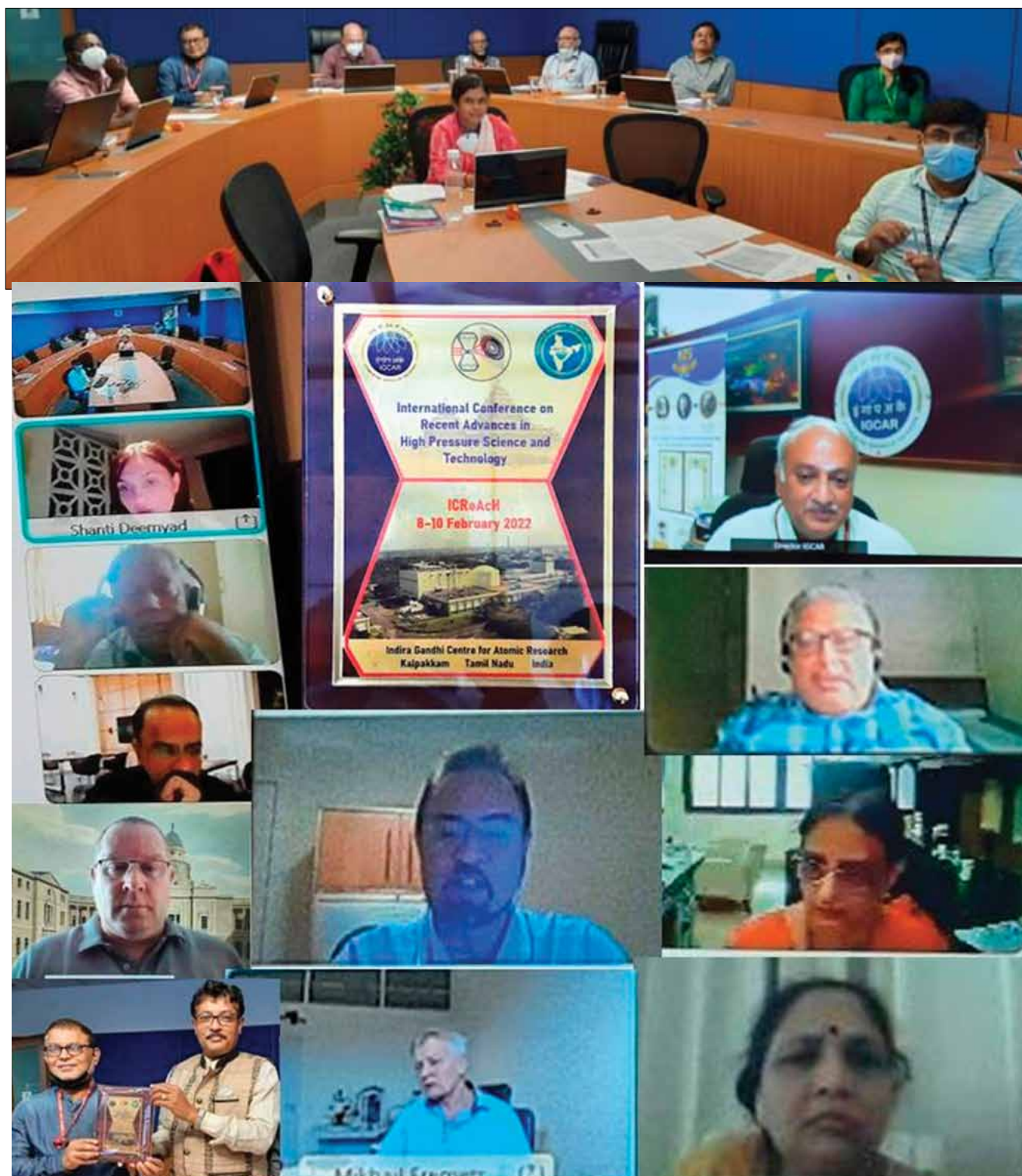
International Conference on Recent Advances in High Pressure Science and Technology (ICReAch-2022)

8-10 February 2022



Release of souvenir at the ICReAch-2022 conference

An International Conference on Recent Advances in High Pressure Science and Technology (ICReAch-2022) in online mode was held by IGCAR during 8-10 February 2022 from the Blue Room, Homi Bhabha Building. After the Welcome address by the Convener of the Conference Dr. N. V. Chandra Shekar, Associate Director, MSG, an overview of the Conference was given by the Chairman Dr. S. Raju, Director, Materials Science Group. The Conference was inaugurated by Dr. B. Venkatraman, Director, IGCAR, who released the Conference Abstracts book and delivered his Inaugural address. Dr. Venkatraman recalled the pioneering and seminal contributions of Nobel Laureate Percy William Bridgman to this field of research, and discussed the importance and relevance of high pressure research to DAE. In this Conference there were 3 Plenary Lectures, 23 Invited Talks, 28 Oral and 22 Flash Presentations, out of which 15 were from abroad (9 Europe, 5 US, 1 Japan). There were talks on high pressure studies on multiferroics, phase transformations, first principles computations, crystallography, thermodynamics of alloying, high temperature superconductivity, plastic strain induced phase transformations using rotational diamond anvil cell, high pressure synthesis of super hard materials, among other things. The technical sessions started with a Plenary Lecture by Professor Gautam Dev Mukherjee from IISER, Kolkata on Pressure induced re-entrant multiferroic/ferroic behaviour in certain oxide systems such as $\text{Fe}_4\text{Nb}_2\text{O}_9$. This was followed by an invited talk by Prof. A. Sundaresan from JNCASR, Bengaluru, on HP Synthesis of doubly ordered perovskites NaYMnO_6 and NaNiO_6 , and their multiferroic properties. Dr. Ranjan Mittal gave a detailed presentation of phase transition mechanism of hexagonal graphite to hexagonal and cubic diamond using ab-initio calculations. Prof. Chris Pickard from the University of Cambridge, UK, described his new approach to map the complex chemistry of dense matter, and ab-initio random structure searching using data-driven, machine learning algorithms. Prof. Shanti Deemyad from the University of Utah talked on her research on quantum effects that affect the structural phase transitions of lithium at low temperature. Prof. Ganapathy Vaitheeswaran from the University of Hyderabad presented the results of his ab-initio calculations on pressure induce metallization of solid iodanyl ($\text{C}_6\text{I}_4\text{O}_2$), that becomes a metal at ~ 22 GPa. Prof. Leonid Dubrovinsky from Bayreuth University spoke on their development of a portable laser heating system with which they have studied a number of oxides, silicates and carbonates that are of geophysical importance. Dr. Subramanian Raju, Director, Materials Science Group and Metallurgy and Materials Group, IGCAR, presented an analysis of thermodynamics of materials under pressure, and stressed on the importance of high pressure calorimetric measurements that are scant in the literature. Dr. Mikhail Erements from Max Plank Institute for Chemistry, Germany, reviewed the status of research on superconductivity near room temperature, including his group's work on metal hydrides and pure hydrogen. Prof. Malcolm McMahon from the University of Edinburgh, spoke of the high pressure "collapsed" phases of lanthanide elements that were reported to be monoclinic. However, the diffraction data from these phases are not well fitted by the monoclinic structure. The collapsed phases of Tb, Gd, Dy, Ho, Er and Tm have a 16-atom orthorhombic structure (oF16) not previously seen in the element. Dr. Alexander Goncharov talked on the synthesis and properties of novel polyhydride and polynitride materials at high pressure and high temperature; these materials are potentially ultrahard, energetic or superconducting. Prof. Valery Levitas gave a detailed presentation of his group's work on plastic strain induced phase transformations under high pressure using rotational diamond anvil cell, and how plastic shear reduced graphite to diamond



The webinar was attended by senior scientists and engineers

phase transition pressure drastically from 70 GPa to 0.7 GPa. In the concluding session, Dr. S. Raju and Dr. N. V. Chandra Shekar, and General Secretary Dr. Awadhesh Mani shared their thoughts on the Proceedings, and hoped that this Conference will not be a one-off event, and other active Groups will take up organizing this periodically. Dr. T. R. Ravindran summarized the talks given in the Conference, giving a snapshot of the Proceedings. After this, winners of five Best Oral Presentations and five Best Flash Presentations in the Conference were announced by Dr. Raju. Evaluation was based on the clarity of presentation and quality of research content as adjudged by a panel of eminent scientists; Certificates and mementos were sent to the Winners by regular mail. The Conference concluded with Vote of Thanks by Dr. N. R. Sanjay Kumar.

*Reported by
Dr. Awadhesh Mani , Material Science Group*

Theme Meeting on Computational Modelling of Nuclear Reactor Materials

March 10, 2022



Few photographs of the online meeting on Computational Modelling of Nuclear Reactor Materials

A theme meeting on “Computational Modelling of Nuclear Reactor Materials” was held on 10th March, 2022 virtually at IGCAR. The meeting was inaugurated by Dr. N. V. Chandra Shekar, Associate Director, MSG, while Dr. R. Govindaraj, Head, DDS, MSG briefed about the theme of the meeting. The objective of the theme meeting was twofold, firstly to explore areas of challenges in treating the nuclear materials computationally and the way forward and secondly to explore areas of possible collaboration in these areas. The theme meeting concentrated on techniques like the modelling of the properties the density functional theory (DFT), molecular dynamics (MD), Monte-Carlo and numerical simulations. The speakers, from BARC, IITD and IGCAR, made presentations on their work. Dr. Ashok Arya, BARC Mumbai talked on thermal behaviour of (U,Np)O₂ and (Th,Np)O₂ mixed oxides using DFT and MD. Dr. Manoj Warriar, BARC Vizag, talked about characterising extended defects like dislocations and dislocation loops that formed under ion irradiation using MD. Dr. Sharat Chandra gave an overview of the computational activities in MSG, IGCAR and Dr. J Christopher presented the numerical modelling of stress in steels while subjected to deformation and damage. Dr. C Ravi spoke about the thermodynamics of point defects in bcc Uranium, while Dr. Gurpreet Kaur talked about her work on phase stability of Uranium, Uranium compounds and intermetallics using DFT. Prof. Anoop Krishnan, IIT Delhi, covered the use of AI/ML in design of glasses of required composition and properties and generation of relational scientific database using the materials-aware language model, MatSciBERT. Dr. G. Gopakumar, talked about modelling the actinide separation and recovery processes in nuclear fuel cycle using quantum chemical methods. Mr. Shakti Singh talked about using Monte-Carlo methods to obtain accurate atomistic descriptions of silica and iron phosphate glasses, while Dr. Manan Dholakia presented his work on modelling the damage in many oxides which are used in ODS steels and for waste immobilization using MD. All the talks held in two sessions chaired by Dr. N. V. Chandra Shekar, AD, MSG and Dr. R. Divakar, AD, PMG respectively were followed by quite enlightening discussions from the present speakers and audience. Many important possibilities of collaboration emerged from these discussions. The meeting concluded with the vote of thanks by Dr. Sharat Chandra, Head, MMS, DDS. Thus the whole gamut of the nuclear fuel cycle, from structural materials like steels, nuclear fuel materials, separation and recovery of actinides during reprocessing and materials for waste immobilisation was covered during the meeting.

Reported by

*Dr. R. Govindaraj and Dr. Sharat Chandra,
Materials Science Group*

5th National Conference URJAVARAN – 2022

March 10, 2022



Release of souvenir during inaugural function: Shri T. V. Maran; Shri Biswanath Sen, Convener; Dr. B. K. Nashine, OS & Director - ESG; Shri S. Raghupathy, DS & Director - RDTG & EIG; Prof. Dr. Dhiman Chatterjee, IIT Madras; Shri S. Vijaybhaskaran, RD, ISHRAE HQ; and Shri V. Suresh Kumar, Organizing Secretary

Air-Conditioning & Ventilation System Division (AC&VSD), IGCAR organized the 5th National Conference URJAVARAN – 2022 in association with Indian Society of Heating Refrigerating & Air-conditioning Engineers (ISHRAE) - Kalpakkam Chapter at Sarabhai Auditorium on 10th March, 2022. The theme of the conference was “Dialogues In Sustainable HVAC and Architecture (DISHA)”. About two hundred and sixty delegates from various DAE units, academic institutions, industries and leading consultants attended the conference.

The conference started with the warm welcome address by convener Shri Biswanath Sen. The inaugural function was presided over by Shri S Raghupathy, Distinguished Scientist and Director, RTDG & EIG. In his presidential address, Shri Raghupathy emphasized on reduction of CO₂ emission, implementation of climate policy and contribution of FBRs towards clean & green energy. He also stressed upon time limit for implementing the climate guidelines. Dr. B. K. Nashine, Outstanding Scientist & Director, ESG delivered the inaugural address and highlighted the significance of energy conservation for a sustainable environment. He has coined a new acronym “ACARA - Air-Conditioning As Reasonable as Achievable” and requested all to follow. Prof. Dr. Dhiman Chatterjee of IIT, Madras delivered the keynote address on “Vapor-liquid, two phase flow and phase change”. The address was interesting, intriguing and very relevant to the theme of the conference.

The Conference souvenir was released by Shri S. Vijaybhaskaran, Regional Director, South-II, ISHRAE HQ. Shri V. Suresh Kumar, Organizing Secretary proposed the vote of thanks. Shri A. Jyothish Kumar, OS & Director (Operations), BHAVINI and Dr. N. Sivaraman, OS & Director, MC&MFCG have inaugurated the exhibition stalls of exhibitors & industrial partners. Various industries, from the field of Heating Ventilation & Air Conditioning (HVAC) system and component design, showcased their products at the venue and shared specific features of their products.

The conference deliberated on the latest technologies, products and ongoing research on sustainable air conditioning and ventilation of buildings. Four invited talks were delivered by eminent speakers from academia, industries, R&D organizations, leading architects and consultants. Eighteen contributed papers from DAE units (IGCAR, BARCF, GSO), educational institutions and industries were presented covering wide spectrum like green building, automobile air-conditioning, concrete wall penetration cooling system, high temperature piping, including eleven posters. Shri J. K. Gayen, GM-Operations (BARCF), Dr. Kitheri Joseph, AD, MFRG, Shri S. Vijaybhaskaran, RD, ISHRAE HQ evaluated the posters. Product presentations from reputed industries were also a part of the conference. The conference facilitated good interaction among the delegates and experts in the area of sustainable HVAC.

During the valedictory function, Shri T.V. Prabhu, Convener, Technical Committee, summed up the one-day conference. Dr. K. Ananthasivan, OS & Director, RpG delivered the valedictory address. In his address he described the nuclear energy as green energy and emphasized on exploring energy conservation in air-conditioning & ventilation systems. Shri M. Ravi, President Elect., ISHRAE Kalpakkam proposed the vote of thanks.

Reported by

*Shri Biswanath Sen, Convener, URJAVARAN – 2022
Engineering Services Group*

2nd Foundation Day of Indira Gandhi Centre for Atomic Research, Kalpakkam

April 30, 2022



Shri G. Nageswara Rao, Chairman, AERB releasing the booklet "Journey of FBTR - Reaching Further Heights" during the 2nd Foundation Day of IGCAR along with Shri S. Raghupathy, Director, RDTG & EIG, Dr. Shankar V. Nakhe, Director, RRCAT, Dr. B. Venkatraman, Director, IGCAR Dr. P. R. Vasudeva Rao, Vice Chancellor, HBNI, Dr. D. K. Sinha, Director, AMD, K. R. Sethuraman, CAO, IGCAR

Organizational set up for Reactor Research Centre, now renamed as Indira Gandhi Centre for Atomic Research (IGCAR), was approved by Dr. Vikram Sarabhai, the then Secretary, DAE, & Chairman, Atomic Energy Commission, on 30th April 1971. Foundation Day is an important occasion to reflect on the beginning of the Organization, recalling the fond memories, the wisdom, courage, commitment, the enormous challenges faced by our seniors and the significant scientific and technological contributions made by them in developing indigenous technologies, the privilege we had of sharing their expertise and work ethics even while expressing our gratitude to them.

Indira Gandhi Centre for Atomic Research celebrated its 2nd Foundation day on 30th April 2022 with great fervour. This year was very significant because our Organization completed 51 years since its inception, 50 years after the first ground breaking of our flagship Fast Breeder Test Reactor, which also attained its designed capacity of 40 MWt on 07th March 2022.

Shri G. Nageswara Rao, Chairman, Atomic Energy Regulatory Board, Mumbai, Dr. P. R. Vasudeva Rao, Vice Chancellor, Homi Bhabha National Institute, Mumbai, Dr. D. K. Sinha, Director, Atomic Minerals Directorate for Exploration and Research, Hyderabad, Dr. Shankar V. Nakhe, Director, Raja Ramanna Centre for Advanced Technology, Indore, were our Guests of Honour, on this grand occasion.

Programme Highlights

Shri S. Raghupathy, Director, Reactor Design & Technology Group and Electronics & Instrumentation Group, IGCAR, delivered the Welcome Address. Dr. B. Venkatraman, Director, IGCAR, made a presentation on the activities of IGCAR. Dr. D. K. Sinha, Director, AMD, delivered a talk on the exploration activities and the contributions of AMD to the Nuclear Power Programme. Dr. Sinha released a Hindi booklet titled "दुरुत ररिक्टर प्ररुदुयुगकि के कुषुेकुतुर डुडु 51 वरुषुु डुडु डुडुतुरा: डुडु डुडुलक".

Dr. P. R. Vasudeva Rao, Vice Chancellor, HBNI, delivered a talk on the importance of metallic fuel for the future of the nuclear power programme. Dr. Vasudeva Rao distributed the awards for best Ph.D./M.Sc. (Engg.)/M. Tech thesis nominations for the last three years. Dr. Shankar V. Nakhe, Director, RRCAT, delivered a talk on the Laser and Electron Beam technologies and its societal benefits. Dr. Shankar V. Nakhe released a book titled "Butterflies of Kalpakkam" and distributed Certificate of Appreciation for Ph.D./M.Sc. (Engg.)/M.Tech thesis. Shri G. Nageswara Rao, Chairman, AERB, delivered a talk on the role of regulatory authorities and the use of radiation technologies for societal benefits. Shri Nageswara Rao inaugurated the "Integrated Radiation Monitoring Facility" building at Anupuram Township and remotely inaugurated "Chopping of Uranium Oxide pins at Demonstration Fuel Reprocessing Plant". Shri Nageswara also released a document titled "Journey of FBTR - Reaching Further Heights". Views, thoughts and opinions expressed by the distinguished dignitaries radiated a source of energy and set a perfect platform for the occasion. Shri K. R. Sethuraman, Chief Administrative Officer, proposed the vote of thanks.

*Reported by
K. R. Sethuraman, Chief Administrative Officer*

Inauguration of Integrated Radiation Monitoring Facility

April 30, 2022



Shri G. Nageswara Rao, Chairman, AERB, along with Dr. B. Venkatraman, Director, IGCAR and senior colleague while Inaugurating IRMF building at Anupuram

Integrated radiation monitoring facility consisting of in-vivo & in-vitro monitoring laboratories and a decontamination centre, meeting the latest NDMA and AERB guidelines is established at Anupuram hospital complex. The facility is designed to cater to the entire Kalpakkam complex to provide monitoring service both under normal as well as radiological emergency conditions. The facility was inaugurated by Shri G. Nageswara Rao, Chairman, Atomic Energy Regulatory Board on April 30, 2022.



Integrated Radiation Monitoring Facility building at Anupuram

Reported by

Dr. D. Ponraju, AD, HSEG & Head, HISD

Azadi ka Amrit Mahotsav
Indira Gandhi Centre for Atomic Research
Program on Anu Awareness – a brief report
 July 23 – August 12, 2022

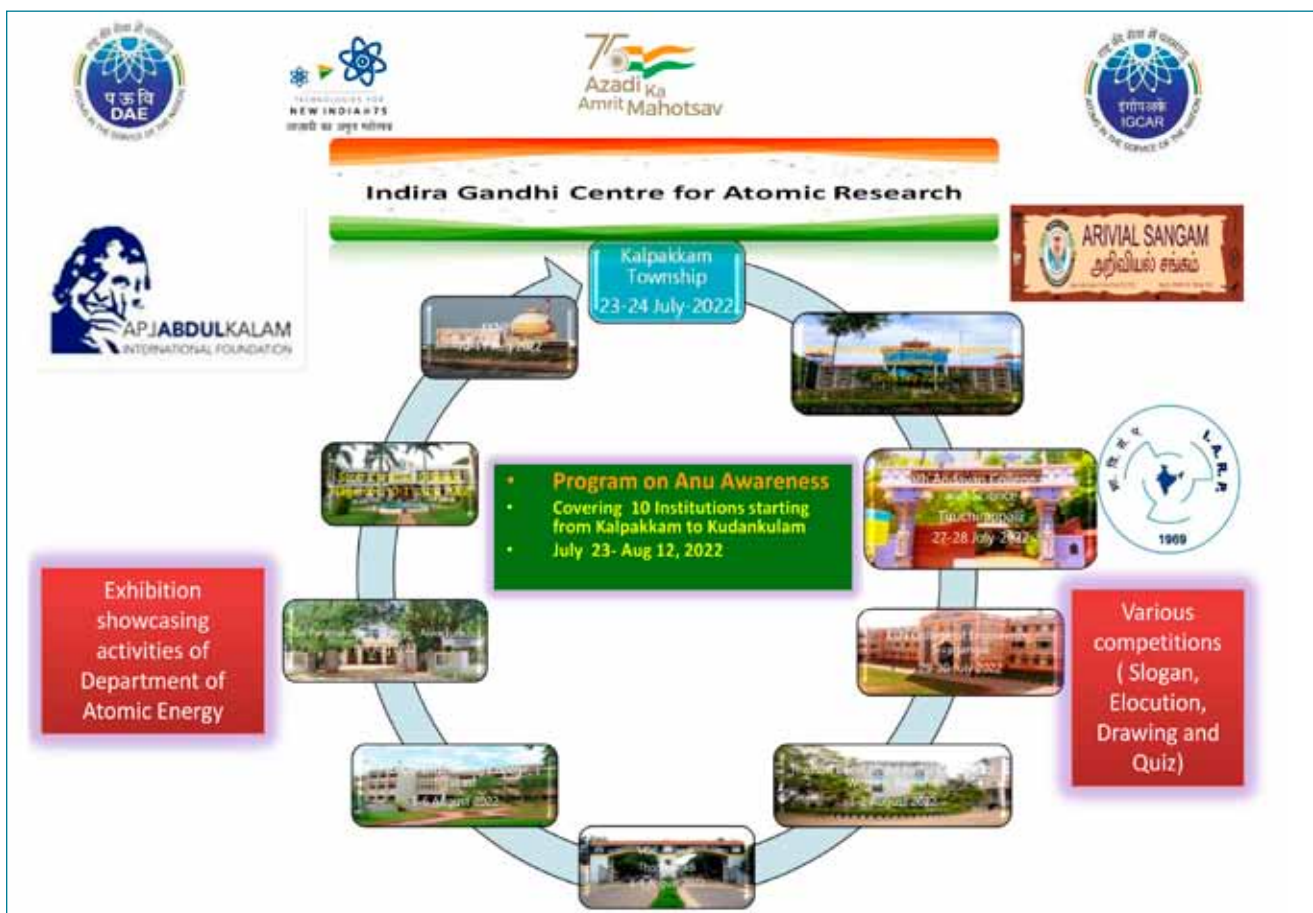


Figure 1: The nodal college venues

As a part of Azadi ka Amrit Mahotsav celebration, IGCAR has organised a sequence of awareness program to showcase and celebrate the technology development carried out and transfer of certain technology in the application of societal benefits by Department of Atomic Energy for the past 75 years after independence. The program is organised in association with A. P. J. Abdul Kalam International Foundation, Rameswaram, The Tamil Nadu Ariviyal Sangam and Indian Association for Radiation Protection. The program is started with curtain raiser event at Kalpakkam on 23-July-2022 and culminated at Kudankulam on 12-Aug-2022 covering 1100 kms in 10 nodal institutions. The sequential venues (colleges) along with event dates and the route map of the program is given in Figure 1 and Figure 2, respectively. The program is a two days event in each nodal institutions comprising of various competitions and exhibition. The nodal institutions were asked to coordinate with schools and colleges in their educational division to participate in the program.



Figure 2: The route map of Anu Awareness Program

The nodal institutions are identified with the help of Tamil Nadu Ariviyal Sangam. The program is organised in each institutions by inviting a nodal personality as a chief guest of their choice and AD/GD level officials of IGCAR along with a crew of officers for the conduction of events and interactions.

About the event: Each event is highlighted with foot fall of about 2000 students. The detailed list of institutions, their places, chief guests of the respective events, number of foot falls for the events are given in Table

Table 1: The details of each event viz. venue, officers from IGCAR, Chief guests and foot falls.

Dates	Place	Institution	SQRMG Officers: Dr/ Shri/Ms	Chief Guest (GDs)/ Top officials*	Guest of Honors	Foot fall
23-24, July 2022	Kalpakkam	KV-1,2 and AECS-1,2,3 HSS, Pudukottam and Sadras Kalpakkam	V. Subramanian and S. Chandrasekaran	Director, IGCAR. CS, MAPS, Facility Director, INRPK Director, GSO CAO, IGCAR CAO, GSO	Shri A.P.J Salim Founder Dr.A.P.J Abdul Kalam International Trust Shri Gopal Parthasarathy, Secretary Tamil Nadu Ariviyal Sangam	1300 students
25-26, July 2022	Puducherry	Sri Manakkula Vinayagar Eng College, Pondicherry	Jalaja Madhanmohan, Vijaya Gopal, Krishnan Hemnath Dr. Kannan Ramu	Dr. B. K. Nashine Director, ESG and GSO	Shri Arun Nagalingam, VIBHA, Tamil Nadu Ariviyal Sangam	2500 students
27-28, July 2022	Tiruchirappalli	Srimad Andavan College, Tiruchirappalli.	Dr. Ponraju Mathiarasu Jalaja Madhanmohan, Hemnath Dr. Ganesan Ramu	Dr. Ponraju AD, HSEG, SQRMG	Dr. Mani Pragpathy, Joint Secretary, VIBHA	1800 students
29-30, July 2022	Sivagangai (Madurai)	K L N Eng Collge Pottapalayam, Sivagangai.	Dr. Ponraju Mathiarasu Jalaja Madhanmohan, Hemnath Dr. Ganesan Ramu	Dr. Ponraju AD, HSEG, SQRMG	Dr. Jeyakanthan State Trustee, Tamil Nadu Ariviyal Sangam	2000 students
01-02, Aug 2022	Ramanathapuram	Thassim Beevi Abdul Kader College for Women Ramanathapuram	O. Annalakshmi Madurai Meenachi Dr. Prabhakaran Parthipan Dr. Kannan	Dr. S. Ananthasivan Director, RpG	Madam. APJM Mazima Marakkayar, Trustee, A. P. J Abdul Kalam International Foundation	1500 students
03-04, Aug 2022	Tuticorin	V O Chidambaram College Thoothukudi	O. Annalakshmi Madurai Meenachi Dr. Prabhakaran Parthipan	Shri T. K. Ramachandiran, IAS, CEO, VOC Port Trust, Tuticorin	Shri Gopal Parthasarathy – Participated with teachers	2000 students
05-06, Aug 2022	Sivakasi	MEPCO Schlenk Eng. College, Sivakasi	M. Manohari R. Ramar Dr. Prabhakaran Parthipan	Shri S. Athmalingham Former , Associate Director RESG, SQRMG	Dr. Mani Pragpathy, Joint Secretary, VIBHA	3500+ students
08-09, Aug 2022	Alwarkuruchi	Sri Paramakalyani College, Alwarkuruchi	CAO, IGCAR EO, GSO Jalaja Madhanmohan Parthipan Ramu	Shri S. A. Murugasan, IAS, IFA	Dr. V. Parthasarathy, Vice President, Tamil Nadu Ariviyal Sangam	1800 students including about 80 Students from Hearing and speech impaired.
10-11, Aug 2022	Nagercoil	Scott Christian college Nagercoil]	Chandrasekar Bramha Jalaja Madhanmohan Ramu	Dr. James R Daniel General secretary, Kanyakumari Academy of Science & Arts		3000 students
12 Aug 2022	KKNPP Kudankulam	Community hall, kknpp township	Dr. V. Subramanian Chandrasekar Bramha Jalaja Madhanmohan Ramu	Director IGCAR, SD, KKNP 1&2, CEE, KKNP 5&6	Shri A. P. J. Salim Founder Dr. A. P. J Abdul Kalam International Trust Dr. Umaiorubhagan, President, Tamil Nadu State Ariviyal Sangam	500 students

1. The competitions include, Elocution, Slogan writing, Drawing and Quiz. The competitions are held in two categories viz. up to school level students and college students comprising of about 250 students in each category. The general topic for all the competitions is “Science Development in India for the past 75 years after independence”. The exhibits cover the working models of three stage reactors, Bhabhatron and Gamma Irradiation Chamber along with panels on DAE

technologies to the application of societal benefits. In addition to the above, a tree plantation event of about 100 saplings is organised in each institutions towards environmental care. The tree plantation event is organised in association with APJ Abdul Kalam International Trust.

Reported by
V. Subramanian, SQRMG

DAE-ICONIC Week Celebration Indira Gandhi Centre for Atomic Research

August 22-28, 2022

SAND ART Sculpture



Inauguration of Sand Art Sculpture at Kalpakkam Beach by Tmt. R. V. Shajeevana, IAS, RDO, Chengalpattu along with Dr. B. Venkatraman, Distinguished Scientist, Director, IGCAR

As a part of Azadi ka Amrit Mahotsov (AKAM) -DAE ICONIC week Celebrations, IGCAR and GSO, have organised a sand art sculpture in the Kalpakkam beach during August 27-28,2022 depicting various technologies of DAE applied to the societal benefits, highlighting contribution to power sector, agriculture, health and technology development.

The sculpture was inaugurated by RDO, Chengalpattu Smt. Shajeevana, IAS, in the presence of President of Pudupattinam Panchayat, Senior Commandant, CISF and officials of IGCAR & GSO, Principals and students of AECS and KVs. Flood light arrangements were made. Wide publicity was given. There were more than 20000 foot falls from the residents of DAE Townships, Pudupattinam and Sadurangapatinum villages.

*Reported by
V. Subramanian, SQRMG*


DAE-ICONIC Week Celebration Indira Gandhi Centre for Atomic Research

August 22-28, 2022

Generation of Magic Square-750 Squares using 75 iconic dates of DAE with 75 Students

As a part of Azadi ka Amrit Mahotsov and DAE ICONIC week Celebrations during August 22-28, 2022, IGCAR has organised one day event on 22-08-2022, in the Higher Secondary School, Sadurangapattinam. The event was planned as "Generation of Magic Squares" of 750 squares with 75 students from nearby Higher Secondary Schools (State board) of Kalpakkam in the Chenglepet Educational District, to commemorate 75 years of Independence 75 numbers of important milestone dates of Department of Atomic Energy. The program was conducted by a mathematician Shri Jothi Lingam, Retd., Station Master, Indian Railway.

The School	Number of Students
Government Higher Sec School, Sadurangapattinam	12
Government Higher Sec School, Pudupattinam	09
Government Higher Sec School, Vayalur	09
Government Higher Sec School for Girls, Thirukkazukundam	09
Government Higher Sec School, for Boys, Thirukkazukundam	09
Government Higher Sec School, Vengambakkam	09
Adi Dravidar Welfare Government Higher Sec School, Manamai	09
Government Higher Sec School, Mamallapuram	09





Indira Gandhi Centre for Atomic Research, Kalpakkam

Organizing

Department of Atomic Energy: Iconic Week Programs -
22-28, Aug 2022

Generation of 750 Magic Squares with 75 students
using 75 milestone dates of DAE





Place : GHSS, Sadras 25 8-1962 Date : 22.08.2022

8	19	6	2
16	2	16	1
1	7	10	17
10	7	3	15

8	19	6	2
13	10	10	2
1	10	5	19
13	-4	11	12

8	19	6	2
2	10	20	3
15	3	2	15
10	3	7	15

8	19	6	2
1	10	20	4
16	3	2	11
10	3	7	15

Name: Yugesh - C

School: Government H.S. School, Mamallapuram

The details of the school:

The program started with Tamil Thai Vazhthu by school students of Sadurangapattinam followed by lighting of lamp. The program was inaugurated with a self composed Tamil Song about Atoms in the service of Nation sung by Nursery School Children of Pavalaru Tamil School, Kalpakkam. The welcome address was given by Head Mistress, Sadurangapattinam. The program was presided by President, Panchayat Board, Sadurangapattinam. The chief guest of the program was Dr. B. Venkatraman, Director, IGCAR.

The generation of magic square was carried out with iconic dates of DAE. A booklet on the compilation of 750 magic square has been prepared. The sample work sheet is shown in Figure 1. The participation certificate is issued to all the students and mementoes for the teachers.

Reported by
V. Subramanian, SQRMG

Figure 1: Generation of magic square

DAE-ICONIC Week Celebration Indira Gandhi Centre for Atomic Research

August 22-28, 2022

Anu Walkathon - 2 km stretch with 150 Students

As part of the Azadi Ka Amrit Mahotsav and DAE Iconic Week Celebrations, a series of programmes were organised by IGCAR, Kalpakkam during 22-08-2022 to 28-08-2022.

Anu Walkathon was organized on August 28 2022 by IGCAR at Elliot's beach Chennai. Dr. B. Venkaraman, Director, IGCAR welcomed the gathering and Shri S. Raghupathy, Director, RD&TG and Director, EIG briefed the participants about DAE and its activities. The walkathon was flagged off by Shri R. K. Kaushal Special Director General, CPWD and Dr. G. A. Ramadass, Director NIOT from Rajaji Bhavan, Besant Nagar. The Anu Walkathon team proceeded to the Elliot's beach, Besant Nagar with necessary Police support covering a 2 km stretch. 150 students from various city colleges and 100 public including DAE employees both serving and retired, participated in the walk for nuclear energy - Atoms in the Service of Nation. The participants were addressed by all senior officers from CPWD, NIOT, Madras University, Ariviyal Sangam and IGCAR. The walkathon concluded by returning back to Rajaji Bhavan. All police personnel, NSS coordinators and the eminent guests from other departments were facilitated. The student



Senior officers from CPWD, NIOT, Madras University, Ariviyal Sangam and IGCAR.

participants pledged their support for Nuclear Energy and there was a much appreciation by all the participants for such an event. IGCAR acknowledge the support of Ministry of Youth Affairs & Sports, CPWD and Tamilnadu Police department for the success of the event.

*Reported by
V. Subramanian, SQRMG*

Technology Incubation Activities

October -18, 2022.

Technology Incubation Activities: DAE Incubation Centre, IGCAR signed a collaborative incubation agreement on 18.10.22 with a Mumbai based private manufacturer to complete development of the technology “Replaceable Feed-through Connectors for Glove Boxes” within a period of 10-12 months. This is IGCAR’s first technology incubation agreement with private sector following the DAE Incubation Policy (2021).



Incubation agreement for “Replaceable Feed-through Connectors for Glove Boxes” technology. Inset is a photograph of the signing of the agreement.

Technology Incubation Activities

November - 01, 2022.

A collaborative incubation agreement, as per DAE Incubation Policy (2021), has been signed on 01.11.2022 between DAE Incubation Centre-IGCAR and a start-up company based in IIT(Madras) for developing “Hydrogen Sensor” technology. This partnership with the start-up is expected to accelerate development of this IGCAR technology from its current technology readiness level (TRL) of ‘4’ to TRL ‘8’ or ‘9’, suitable for commercialisation, during the incubation period of ~18-24 months. Developers of this IGCAR technology work in the Materials Chemistry and Metal Fuel Cycle Group.



Incubation agreement for “Hydrogen Sensor” technology. Inset (Right): Presentation on the technology by a MC&MFCG colleague prior to signing the agreement on 01.11.22 (Left): Photograph of the signing of the agreement.

Internal review meeting on 'Role of Defects in Condensed Matter - Vistas from Materials Science Group'

November 16-17, 2022.



Participants while meeting being conducted at (a, b) e-learning studio and (c) CMPL meeting room. (d) Group photograph in front of CMPL building.

A two-day internal review meeting on 'Role of Defects in Condensed Matter- Vistas from Materials Science Group' was conducted during 16-17 November 2022 in hybrid mode. Dr. N. V. Chandra Shekar, Associate Director, MSG, delivered the welcome address. He highlighted both positive and negative impact of defects on material properties and emphasized the seminal contributions on defects-studies related to reactor materials from MSG. The inaugural address was given by Dr. R. Divakar, Director, Materials Science Group. He discussed significance and relevance of research on defects in nuclear structural materials and its implication to DAE.

The review meeting comprised of an introductory lecture by Dr. R Govindaraj and 10 invited review talks by members of MSG. Dr. Govindaraj recalled the pioneering achievements from MSG on experimental and modelling studies on various fuel and reactor materials. He reviewed the current status of research on defects in condensed matter. The first review talk was delivered by Dr. B. Sundaravel who gave a detailed overview on creating defects in a controlled manner by utilizing 1.7 MV tandetron accelerator, 150 keV and 400 keV accelerators. He also brought out the scope and utility of recently developed dual ion beam line for co-implantation studies. In addition, he also discussed a detailed introduction to the physics of the ion beam implantation and gave a flavor of various ion beam implantation-based experimental techniques to study and characterize defects. These techniques include RBS, ion channeling, NRA, ERDA, PIXE, EELS etc. In specific, he elucidated the work carried out on D9 steels to study the void swelling behaviour using a combination of step height, positron beam based Doppler broadening measurements, the results of which

were corroborated from TEM measurements. The characterization of defects was further carried forward by Dr. S. Abhaya. She highlighted the concepts of characterizing various defects by utilizing positron annihilation spectroscopy. She focused on the recent research works carried out in the lab bringing out the sensitivity and selectivity of positrons to vacancy defects starting from Indian Reduced Activation Ferritic Martensitic steels to nano-porous gold to topological insulators to polymer blends and finally to the iron phosphate glasses. The review then moved onto discussion on defects in nuclear materials. Dr. S. Amirthapandian focused on this and gave a complete overview of the radiation resistance in oxide dispersed strengthened steels giving supporting evidence for the nature of dispersoids present and their kinetics using high resolution TEM images, selected area diffraction etc. The afternoon session was fully dedicated to computer simulations of defects on different scales. First talk by Dr. Gurpreet Kaur gave insights to the solute atoms interactions and binding in Y-Ti, Al and Zr-based ODS steels from first-principles density functional theory (DFT). Dr Ravi Chinnapan talked about the importance of defect calculations from DFT and gave an overview of solute and defect energies in bcc Fe and U. The last talk of the day was delivered by Dr. Manan Dholakia. He gave a review of molecular dynamics simulations of different defects and study of cascade in single crystal, bicrystal and nanocluster embedded in a matrix of bcc Fe. The second day started with a detailed presentation by Dr. R. M. Sarguna on bulk synthesis and defect mitigation in technologically important bulk single crystals for radiation detector applications. Dr. Edward Prabu highlighted the role of defects and disorder in superconductors and topological insulators with emphasis on magnetotransport properties. Dr. Kishore Madapu presented a thorough review on defects in 2D semiconducting materials with respect to their role in tuning electronic, optical and magnetic properties. The final presentation of the meeting was by Dr. K. Gururaj who spoke about quantum computers and importance of decoherence time of quantum states and research towards Nitrogen vacancy centers in diamond for usage as qubits. Dr. N. V. Chandra Shekar summarized the talks delivered in the review meeting and concluded by thanking the speakers and the participants.

*Reported by
Dr. N. V. Chandra Shekar,
Materials Science Group*

IGC COUNCIL



Chairman

Dr. B. Venkatraman

Distinguished Scientist & Director, IGCAR

Dr. B. Venkatraman, is from the 27th batch of Bhabha Atomic Research Centre Training School. With a research career spanning 38 years, he has specialised in application of ionizing and non ionizing radiations for non-destructive evaluation of materials and processes. During the last ten years, he has focused on enhancing, existing and establishing newer facilities as part of broad based radiation and environmental research programs at IGCAR.

He is a Member of AERB, SARCAR Committee and Convenor of BIS CHD 30 Sub Committee on Radiation Protection. He was a visiting scientist at Fraunhofer Institute of NDT Saarbrucken, Germany 2006-2007, has served as an expert for IAEA in Digital Radiology. He has more than 200 publications, is the recipient of Homi Bhabha Science and Technology Award 2007, INS Gold Medal 2005, seven Group Achievement Awards of DAE, D & H Schereon Award of IIW 1993, ISNT-NDT Man of the Year Award (R & D) 2001, IIW sharp tools award 2011, ISNT international recognition award 2013, and has won more than 10 best paper awards. He has been invited to deliver keynote, plenary and invited talks in international and national conferences . He is the Honorary Fellow of Indian Society of NDT and Fellow of Chennai Academy of Sciences. He is the President of Indian Society for NDT (ISNT) and President, Indian Association for Radiation Protection (IARP). He has guided about 6 students for their Ph D and is presently guiding 6 students. He is presently Distinguished Scientist and Director, IGCAR, GSO, and Safety, Quality and Resource Management Group.

Members



Dr. A. K. Mohanty, born in 1959 at Odisha is a well-known nuclear physicist, completed his Bachelor's degree in 1979 from MPC College, Baripada and Master's degree in Physics in 1981 from Ravensshaw College, Cuttack which was at that time under Utkal University, Bhubaneswar. Dr. Mohanty graduated from the 26th batch of the BARC Training School and joined Nuclear Physics Division of Bhabha Atomic Research Centre in 1983 and got his PhD degree from Bombay University later on. He has taken over as Director, BARC on 12th March 2019. Before his appointment as Director, BARC, Dr. Mohanty has held the position of Director of Saha Institute of Nuclear Physics, Kolkata from June

2015. During the past 38 years, Dr. Mohanty has worked in several areas of nuclear physics covering collision energy from sub-Coulomb barrier to relativistic regime. It includes experiment using Pelletron accelerator at TIFR, PHENIX and CMS experiments at Brookhaven National Laboratory (BNL), USA and CERN, Geneva respectively. Dr. Mohanty has held several honorary positions. To name a few, he served as Secretary and Member Secretary of BRNS Basic Science Committee from 2004-2010, General Secretary of India Physics Association (IPA) 2012-2016 and later on President of IPA 2018-2020, India-CMS Spokesperson (CMS Experiment at CERN Geneva) 2013-2015, Dean, Academic, Physical & Mathematical Sciences,

BARC, Homi Bhabha National Institute. Dr. Mohanty has been recipient of several awards and recognitions during his illustrious career. Some of Dr. Mohanty's awards and recognitions are: Gold Medal in Graduation (1979, Radha Gobinda Trust, Mayurbhanj), Young Scientists Award of Indian Physical Society (IPS, Kolkata, 1988), Young Physicist Award by Indian National Science Academy (INSA, New Delhi 1991) and DAE Homi Bhabha Science & Technology Award (2001) by Department of Atomic Energy, Mumbai. He was also conferred the CERN Scientific Associate position at CERN, Geneva from 2002-2004 and thereafter again from 2010-2011.



Shri S. Raghupathy, is currently heading Reactor Design & Technology Group and Electronics & Instrumentation Group as Group Director. He is a mechanical engineer and had graduated from A.C. College of Engineering & Technology, Karaikudi. After graduation, he joined the 29th batch of BARC Training School and completed the Nuclear Engineering course in 1985. He joined IGCAR in 1986 and was associated with the design of reactor assembly components and later with the design of fuel handling systems for PFBR & future FBRs. He is one of the Directors on the Board of BHAVINI and a member of several task forces for design, development and testing of fast reactor components. He has several national & international publications to his credit. He has received the DAE Science Technical Excellence Award and several group achievement awards. He has participated in many IAEA meetings & international conferences on FBRs. His field of interest include design of pressure vessels, regulatory codes & standards, heat & mass transfer, in-service inspection, non-destructive testing and reactor safety & economics.



Dr. N. Sivaraman, Joined Indira Gandhi Centre for Atomic Research (IGCAR), Kalpakkam in the year 1987. He is from the 30th Batch of BARC Training school. His area of research interest includes actinide chemistry, fuel chemistry, pyrochemical process, lanthanide separations, sodium chemistry & sensors, solvent extraction of heavy metals, high performance liquid chromatographic separation of radioactive species, burn-up measurements on nuclear reactor fuels, Supercritical fluid extraction of actinide complexes and development of extraction chromatographic techniques for recovery of actinides, etc.

He is recipient of INSA-Royal Society, UK Fellowship (1997), Indian Nuclear Society Medal (2007) & Homi Bhabha Science and Technology Excellence Award (2008). He is also Professor of HBNI and supervising PhD scholars. He is presently Outstanding Scientist and Director, Materials Chemistry & Metal Fuel Cycle Group.



Dr. B. K. Nashine, FNAE, an Outstanding Scientist is B.E. in Electrical Engineering from GCE&T, Raipur, M.E. from VJTI, Bombay University, Ph.D from HBNI, Mumbai. He is from 31st batch of BARC Training School and presently Director Engineering Services Group and Associate Director Sodium Facility Group, RDTG. His research career spans for 34 years and he has specialized in the design of electromagnetic pumps, power system for Sodium loop and sodium loop operation for conducting experiments in support of R&D for sodium cooled Fast Reactors. The electromagnetic pumps designed by him have been tested successfully and employed in the Prototype Fast Breeder Reactor (500 MWe). He has developed sodium

submersible electromagnetic pump which can withstand 550°C ambient temperature without any external cooling. He has served as Secretary in professional body like Institution of Engineers, Kalpakkam chapter, Indian Society for Non Destructive Testing, Kalpakkam chapter and Indian Nuclear Society, Kalpakkam chapter.



Shri K. V. Suresh Kumar is a graduate in Chemical Engineering and joined Department of Atomic Energy at BARC Training School in Mumbai as a trainee (29th batch) in 1985. After successful completion of one year training, he joined in FBTR operation in 1986. Initially he was involved in the commissioning of various system of FBTR such as Sodium heated Steam Generators, Steam & Water system and Turbo-Generator. He was involved in the first raising of reactor power and carried out physics & engineering tests for validating the assumptions made in the design. He has got vast experience in Reactor operation, operation of sodium systems, steam and water system, turbine & its auxiliaries and all other auxiliary systems in FBTR. He was instrumental in carrying out many plant modifications and contributed in improving the availability factor of the plant. He shouldered many responsibilities in the plant and was Director, Reactor Facilities Group from March 2016 to November 2022 and was responsible for operation of FBTR, KAMINI Reactor and PFBR Fuel Fabrication Facility. During his tenure, FBTR power was raised to its design power level of 40 MWt feeding electricity to the grid. In addition to his responsibility in Reactor Facilities Group, he was also involved in the review of commissioning procedures / reports and Technical specifications for PFBR Operation. He was the chairman of Project Design Safety Committee (PDSC) constituted by Atomic Energy Regulatory Board (AERB) for issuing stage wise clearance for commissioning of PFBR. He is a Distinguished Scientist and on 2nd December, he took over as Chairman and Managing Director (CMD), BHAVINI.



Dr. T. V. Krishna Mohan is born in 1966. He graduated in Chemical Engineering from Osmania University and pursued his Masters in Business Administration (MBA) from the same university. He got his PhD degree from Homi Bhabha National Institute in 2016. He is from 34th batch of BARC training school and presently Facility Director, BARC Facilities, and Head, Water and Steam Chemistry Division. His field of specialisation is Design, Procurement, Installation, Commissioning, and Operation of Simulated Engineering loops to carry out water chemistry, biology and heat transfer experiments. His contributions are towards Bioremediation, Flow Accelerated Corrosion, Biological Denitrification, Aerobic Granulation, Wastewater Engineering. He is recipient of DAE Group Achievement Awards. He has more than 100 publications and one patent to his credit.



Dr. T. S Lakshmi Narasimhan is from 31st batch of BARC Training School and joined IGCAR in 1988. He completed his Ph.D. from University of Madras in the year 2001 and did his post doctoral research at Forschungszentrum, Juelich Germany (2004-2006) under Indo-German collaboration. His main area of research has been in the field of high temperature mass spectrometry which include fuel-clad chemical interaction studies related to fast reactors, vaporization thermodynamic studies on U-Pu-Zr, Metal- tellurium and Metal –tellurium- oxygen systems, alloys, boron, fullerenes etc., He has also been associated with Burn up measurements of thermal and fast reactor fuels. He has delivered many invited lectures in India and abroad and has about 55 Scientific publications in reputed International journals and about 70 papers in national and international conferences.

In July 2017 he became Associate Director, Resource Management Group. He served as Dean, Student Affairs under Homi Bhabha National Institute, a deemed university. He also served as Professor in the same University and guided two Ph.D. Students. He was heading the Technology transfer cell of IGCAR and coordinated the filing of patents and technology transfers and in October 2020 was designated as CEO of Incubation Centre at IGCAR to look after incubation and technology transfer activities. He is a mentor for the INSPIRE program of Department of Science and Technology for School Students and also actively involved himself in the spread of scientific awareness amongst educational institutions. Currently he is the Regional Director of Madras Regional Purchase Unit (MRPU), DPS which caters to the purchase and stores activities of IGCAR and other DAE units at Kalpakkam, HWP, Tuticorin and NFC, Pazhayakayal.



Ms. Sushma Taishete joined as Joint Secretary in the Department of Atomic Energy, Government of India on 08-04-2020. She is a post graduate in Medical Microbiology from Haffkine Institute, Parel, Mumbai. She is the In-charge of Research and Development wing of the DAE handling Bhabha Atomic Research Centre (BARC), VECC, Kolkata, RRCAT, Indore, IGCAR, Kalpakkam and all aided institutions (eleven) in the Department. International Projects such as, ITER, LiGO, also fall under R & D Division. She has served in various capacities in Ministry of Defence, Ministry of Health & Family Welfare, National Health Systems Resource Centre, Ministry of Petroleum and Natural Gas and Department of Justice, Ministry of Law & Justice, Government of India during 1991 - 2020.



Shri S. A. Murugesan, IAS, Uttarakhand cadre -2005 Batch. Currently on deputation to Department of Atomic Energy serving as Internal Financial Advisor (IFA) in IGCAR and GSO.



Shri K. R. Sethuraman joined the Department on 02/02/1988 with a degree in commerce from Bangalore University. After joining the Department, he was sponsored by the Department for Diploma in Public Policy and Management course from the Management Development Institute, Gurgaon (2010-2012). He has completed 34 years of service in the Department serving in various capacities in different Units like AMDER, DAE Secretariat, BARC Facilities, RRCAT, BRIT and IGCAR thus gaining vast experience in all matters relating to administration. He is holding the post of Chief Administrative Officer from 15/02/2018.

As administrative head of the Unit his mandate for administration is to provide service, advice and support with the highest level of professionalism valuing rules and procedures as a tool to achieve the objectives of the Organization and the desired outcome, contribute towards smooth internal functioning of the organization through dissemination of information, extensive use of automation and information technology, updating and simplifying procedures and instructions to the changing environment, proper record and data management systems, developing standard process sheets to ensure procedural compliance, periodical training of Officers and staff to enhance the knowledge and skill, secure better focus and ownership of task and increase their yield, monitoring delays, identifying bottlenecks and implementing remedial measures, promoting transparency and accountability in decision making process, mentor subordinates and build teams, promote harmonious relations and secure maximum amount of cooperation from the employees.

Organisation and Activities of Various Groups

Electronics and Instrumentation Group



Shri S. Raghupathy
Director, EIG



Dr. D. Thirugnanamurthy
AD, E&CG



Shri R. Jehadeesan
Head, CD



Shri N. Sridhar
Head, ED



Shri M. Sakthivel
Head, I&CD



Shri R. P. Behera
Head, RTSD

Electronics and Instrumentation Group is focused on design and development of indigenous technology in the areas of Electronic Instrumentation & Control systems for fast breeder reactors and reprocessing plants that include Development of Distributed Digital Control System, Safety Critical and Safety Related Systems, Safe & Secure PLC, Virtual Control Panel based Control Room, Full-scope Operator Training Simulator, 3D modeling, animation & visualization of FBR subsystems and VR walkthrough of structures, Cyber Security Management for IT and I&C systems. Design and Development of advanced equipment and technology such as, indigenous Wireless Sensor Networks for nuclear facilities, strategic and societal applications, Time Domain Electromagnetic for Deep Seated Atomic Minerals Exploration, Plutonium Condition Air Monitoring System for reprocessing plants, Test Instrument for Steam Generator Tube Inspection, Radar Level Probe for Liquid Sodium Level Measurement, radiation resistance MEMS based sensor for nuclear applications and innovative sensors and instruments for nuclear facilities have been completed. Considerable expertise exists in designing, building and maintaining state-of-the-art high-performance supercomputing facility that continues to meet large scale compute- and data-intensive requirements in multi-disciplinary domains. Implementation of IT-enabled Nuclear Knowledge Management system for Fast Reactors and associated domains, computational intelligence systems, cryptography, cyber security solutions, knowledge management and development and deployment of modern security systems for access control and physical protection of nuclear complexes are initiated.

Engineering Services Group



Dr. B. K. Nashine
Director, ESG



Shri N. Suresh
AD, CEG & Head, CED



Shri K.P. Kesavan Nair
AD, TSG



Shri Sudipta Chattopadhyaya
Head, CM&MWD, A&SED



Shri Biswanath Sen
Head, AC&VSD



Shri Utpal Borah
Head, CWD



Shri L. Subramanyam
Head, ESD

The Engineering Services Group (ESG) has a very important mandate of infrastructure development for all units of the Department of Atomic Energy located at Kalpakkam. It spans from planning, design, engineering, execution, testing and commissioning of Civil, Electrical, Mechanical, Air-conditioning and Ventilation works for the Laboratories, Township including housing, schools, hospitals, hostels, roadways and various public infrastructure, utilities and facilities. This Group was also responsible for commissioning, operation and maintenance of various services for the Atomic Energy installations at Kalpakkam. Over a period of time when the facilities are grown, the responsibilities are limited mainly for IGCAR infrastructure. ESG comprises of two sub-groups: Civil Engineering Group (CEG) and Technical Services Group (TSG).

Civil Engineering Group (CEG) is primarily created with the intention of developing all the required infrastructures for mission of IGCAR. Mandate of CEG is design & construction of several laboratories, buildings and services beginning with the conceptual design to construction and its associated maintenance, for IGCAR's mission of 'Fast reactor development and its associated fuel cycles'. CEG undertakes in-house and collaborative research projects in civil engineering aspects of Fast Breeder Reactor (FBR). CEG has been keeping pace with progress in engineering, design and construction with technical advances. Engineering, analysis and design have undergone remarkable changes with computer codes developed by the group to solve complex problems. Concrete production and delivery systems have been improved, with automated mixing plants and stringent quality control. Apart from durable concrete, special types of concretes have been developed and now the group has proved itself in providing technical support in design of major projects like PFBR and associated fuel cycle facilities. The group has developed expertise in characterization of site for safety related structures including geotechnical investigation, flood level studies. As the plant site has crossed 50 years, CEG has undertaken a mandate of conducting condition survey, assessment and formulating repair methodologies of Reinforced Concrete Structures of existing radiological facilities, major laboratories, infrastructure buildings at IGACR including IMSc, Chennai.

The present mandate of CEG is to sustain the present infrastructure as envisaged in the present Vision -3 and augment it during coming plan periods, continue the support for coordination and commissioning of PFBR related civil works, focus in the preparation of DPR of next Vision-3 consisting of civil works from different user group, IGCAR Infrastructure and carrying out in-house architectural & structural design, execution and quality control of civil infrastructure works for other unit works in DAE Kalpakkam along with development of the associated township works. With IGCAR South Plant site getting saturated, the focus is in developing north plant site for non-radiological facilities - Doppler Weather Radar, Mid Tropospheric Radar Facility Building, RHIDS & SHIDS etc. to mention a few, and associated service corridor considering future requirements. CEG has recently completed Seismic Margin Assessment studies for RC structures of DFRP and associated safety buildings & structures. The tasks are being steered by a team of senior civil engineers. The Group has major plans of providing an aesthetic and sustainable green environment at the project site and also intends to introduce efficient water management scheme by recycling treated water for usage of makeup water for refrigeration and in development & maintenance of garden & lawn at IGCAR.

Technical Services Group (TSG) was established to take care of non-civil services of IGCAR. TSG comprises of three divisions: Air Conditioning and Ventilation Systems Division, Central Workshop Division and Electrical Services Division.

Air-conditioning and Ventilation Systems Division (AC&VSD) has a mandate of providing air conditioning and ventilation service to radioactive facilities and research laboratories of IGCAR. Presently, IGCAR has a total air-conditioning load of about 4500 TR, which is met by 2 Central water chilling plant (CWCP I & CWCP - II) and standalone AC systems like package units (PAC), variable refrigerant flow (VRF) units, window and split air-conditioners. In view of increase of facilities at IGCAR and in order to sustain reliable air-conditioning services to the centre, a 2000 TR central Air-conditioning plant is (CWCP 2) established near IGCAR gate as part of vision 3. The building is constructed and chillers of 2250 TR capacity have been commissioned. The division is also responsible for design, execution, testing and commissioning of material handling equipment like Electric overhead travelling (EOT) cranes, Electric wire rope (EWR) hoists for new facilities of IGCAR. Later, AC&VSD was entrusted with the responsibility of operation and maintaining of sea water desalination plant to provide potable water to IGCAR, BARCF and BHAVINI. All skids of the plant is capable of being operated at full capacity and required quality as per IS 10500. It also looks after water purifiers for the facilities within IGCAR. The plant was commissioned in 2015. Since then, the plant is continuously supplying potable water to IGCAR reservoir as per the demand.

The need for dedicated workshop facilities was felt right during the days of conceptual formation of Reactor Research Centre (RRC). The Zonal Workshop at Hall-1 was established initially to meet the immediate requirements. Later, to meet the growing demand of manufacturing activities at RRC complex, Central Workshop Division (CWD) was established with the state of the art machines and became operational in 1975. CWD, specializing in machining, cold plate rolling, welding, fabrication and inspection, is a centralized manufacturing facility of IGCAR and undertakes in-house manufacturing of various products, which are technically challenging, commercially unviable, and needed urgently to meet the project schedules. CWD carries out multiple manufacturing activities for Prototype Fast Breeder Reactor (PFBR), Fast Breeder Test Reactor (FBTR), Kalpakkam Mini Reactor (KAMINI), Reprocessing Facilities, Post-Irradiation Examination (PIE) Facilities, R&D Projects and Infrastructure Development apart from operation and maintenance requirements. The welding procedure for the PFBR Sub-Assembly (SA) in 2G position was developed by CWD welders and the first batch of Fuel/ Blanket SAs was welded at CWD successfully. Recently two notable major works were successfully carried out for PFBR and FBTR, namely, modification of 731 dummy SAs of PFBR on site at reactor containment building (RCB) within the specified time schedule and manufacturing of modified water sub-headers of FBTR Steam Generator, which were integrated with the FBTR to raise its power level to rated 40MWth.. CWD maintains the highest precision and quality standards to conform to the stringent specifications and functional requirements under various codes, viz. ASME, ASTM, RCC-MR and ISO. CWD processes nearly 400 work orders on average every year to meet the demands of various users/projects. Recently, a few major machining, cutting, heat treatment and inspection facilities were commissioned at CWD to augment its capabilities and capacity. DAE has conferred many meritorious service awards and Group Achievement Awards to CWD officials for their excellence in machining, fabrication, inspection and maintenance fields.

Electrical Services Division (ESD) has a mandate to provide adequate, high quality, reliable and uninterrupted power required for various needs of the research activities and the infrastructural requirements of the centre. To meet this Electrical Services Division designs, construct, operate, maintain and upgrade Electrical distribution system keeping in mind the system reliability & safety. The division is also responsible for providing state of the art intercom telecommunication services to the plant site as well as for Energy conservation in the Electrical sphere through auditing and implementing various energy conservation measures. At present the Electrical demand is 29 MVA and which is catered by Electrical distribution network consisting of two numbers of 33 kV substations and 14 numbers 11 kV substations.

Thanks to the foresight of the earlier planners, MAPS has been providing adequate, safe, reliable and quality power to IGCAR, BARC Facilities and GSO till date. Starting from an operating load of about 1.5 MVA during 1977 fed by one number 33 kV substation and five number of 11 kV substations, the load on the power system has grown to a level of 29 MVA fed by two number 33 kV substations and 14 number 11 kV substations. The projections indicate that the load would grow to about 60 MVA by 2028. To meet the growing demand third power source with 230 kV/33 kV/11 kV, 50 MVA transformer at BHAVINI switchyard was commissioned in 2012. To evacuate this power along with this 33kV Indoor sub-station NCSS-2 was also commissioned in 2012. Main source for FRFCF is from NCSS-2. The electrical power system of FRFCF is conceived to meet the power requirements for the present phase as well as the envisaged expansion in the future. Moving further the transformer in the Second IGCAR feeder at MAPS was upgraded to 35 MVA in 2019 to meet the growing power demand.

ESD has taken up many Energy Conservation activities over the years. One of the major activities being taken up under this is to establish a 2.2MWp grid connected solar plant in the newly developed parking area in front of IGCAR new gate. In line with the GOI policy of promoting Green Energy, added 333.64 kWp of generating capacity. The total solar generation capacity in IGCAR is increased to 833kWp and this is expected to save 16 Lakhs units of electricity annually. Energy Conservation is a continuing activity and many innovative ideas are being implemented in the journey. ESD as a team is well set to take on the challenges pertaining to sustenance, augmentation and establishment of power systems at new projects of IGCAR. With a proactive approach all along, the division has initiated several augmentation measures at source end, receiving end and associated networks. With the steps that are being initiated, ESD will be able to meet the projected power requirements and is moving ahead with an objective to sustain the path of excellence.

Materials Chemistry & Metal Fuel Cycle Group



Dr. N. Sivaraman
Director, MC&MFCG



Dr. Kitheri Joseph
AD, MFRG



Dr. V. Jayaraman
AD, FMCG



Shri T. V. Prabhu
Head, CFED



Dr. S. Ghosh
Head, MFPD



Shri B. Muralidharan
Head, PPEd



Ms. S. Vijayalakshmi
Head, ACSd



Dr. A. Suresh
Head, FChD



Dr. Rajesh Ganesan
Head, MCD

The Materials Chemistry and Metal Fuel Cycle Group (MC&MFCG) is involved in Research and Development studies relating to metal fuel program, establishing pyrochemical processing of metal fuel, development of aqueous reprocessing methods, including reprocessing of metal fuels, sodium chemistry and development of novel chemical

sensors for detection of hydrogen, ammonia, NO_x etc. Some important current activities include installation of injection casting system for casting U-Zr slugs, augmentation of 10 kg injection casting system for the fabrication of U-6Zr slugs; fabrication and characterization of slugs for Delayed Neutron Detection (DND) applications for PFBR, Integrated operation of Argon Pressure Control System (APCS), temperature and attaining purity by Argon Recirculation and Purification System (ARPS), establishing the purity of 500m³ containment box for its purity and the requisite purity of O₂ and moisture (below 50 ppm each) in engineering test scale of pyroprocessing, pyroprocessing of irradiated U-Zr in hotcells at lab scale, direct oxide reduction of oxides of uranium to uranium metal, optimization of process parameters towards oxidation of metal fuel prior to its dissolution in nitric acid medium followed with extraction of heavy metals using TBP/n-DD, thermochemical properties and phase diagram studies on fuel materials and materials of interest for pyroprocessing, development of non-destructive methods for assay of plutonium, studies on the development of synthetic inorganic matrices for immobilization of waste from fast reactor fuel reprocessing, production of ⁸⁹Sr for societal applications, etc. Other important activity includes development of metal organic framework for sorption of actinides from aqueous medium, supercritical extraction and recovery of heavy metal ions; development of extraction chromatographic methods for recovery of actinides from lean aqueous waste streams, recovery of zirconium from aqueous waste and computational study on the structural aspects of actinide complexes. MC&MFCG also provides expert Analytical support and Radioanalytical services to various programmes in the Centre and for other DAE units. Some of these are development of analytical methods for assay of metal fuel and samples originating from pyrochemical process, measuring isotopic composition of boron and heavy metal ions e.g. actinides from reprocessing samples, assay of primary sodium samples for actinides and fission products. Besides these activities, some basic R&D studies are also undertaken for exploring intermolecular interactions using matrix isolation spectroscopy technique for the extractants of interest towards reprocessing application.

Materials Science Group



Dr. R. Divakar
Director, MSG



Dr. N. V. Chandra Shekar
AD, MSG



Dr. R. Govindaraj
Head, D&DSD



Dr. Sandip Kumar Dhara
Head, S&SSD



Dr. Nagendran
Head, S&DTD



Dr. Awadhesh Mani
Head, CMPD

The Materials Science Group (MSG) comprises of Defects and Damage Studies Division, Condensed Matter Physics Division, SQUID & Detector Technology Division and Surface & Sensors Studies Division. Scientists of MSG work on research problems spanning from the studies of irradiated defects in nuclear materials, developing thin film coatings for tribological applications, high pressure and temperature induced phase transitions in condensed matter systems and SQUID based MEG applications. Details of the research activities are as follows.

Defects and Damage Studies Division (DDSD) focuses on studies on defects, defect-impurity interactions in reactor structural materials, supplemented by computations. Ion beam radiation damage studies are carried

out using a 1.7 MV tandem accelerator and a 400 keV in-house built linear accelerator either in single or dual ion beam modes of irradiation to study defects and radiation response in materials of relevance for fusion and fission reactors. Defects, in particular open volume defects such as vacancies and their clusters are studied using positron annihilation spectroscopy. Positron beam based Doppler broadening studies have been used mainly for depth resolved defects studies in irradiated materials. Ion beam based characterization techniques such as high resolution RBS, channeling are being used extensively in addition to ion beam induced luminescence studies. Irradiation creep studies are being planned with proton beam of energy 2-3 MeV and high beam current. Various experimental results related to defects are analyzed using detailed computations with a variety of simulation and ab-initio codes. High speed cluster computers at IGCAR are being extensively utilized for computation of materials properties.

Surface & Sensors Studies Division (SSSD) focuses on studies of monolithic and multilayered thin films and nanostructures using a variety of techniques such as secondary ion mass spectrometry, nanomechanical testing, Focused Ion Beam (FIB) based nanostructuring and nanopatterning, Scanning Probe Microscopy based characterization of various electrical and mechanical properties at nanoscale, nanospectroscopy with tip enhanced Raman spectroscopy (TERS) and Nanoscopy with near-field scanning optical microscopy (NSOM) imaging at sub-diffraction limit using polarized light. The division also specializes in high temperature tribological studies of structural materials as well as novel nano- and micro-crystalline diamond thin films. Furthermore, development of novel nanomaterials of 0D transition metal oxide (TMO), 1D noble metals and nitrides, 2D TMOs, and transition metal dichalcogenides (TMDs) for advanced sensor applications is being carried out. Research activities relating to sensors based on micromachined cantilevers are also being pursued.

Condensed Matter Physics Division (CMPD) pursues several theme based research programs: investigation of structure and physical properties of materials under extreme conditions such as high pressures, low temperatures, high temperatures and high magnetic fields. Further, over the years various facilities for the synthesis of novel, superhard materials have been established including a Laser Heated Diamond Anvil Cell (LHDAC) facility. The systems under investigation encompass nuclear materials, superconductors, strongly correlated systems, magnetocaloric materials, topological insulators, multiferroics, energetic materials, frustrated systems, f-electron based intermetallics and oxides, glasses and super hard transition metal borides. Research is also pursued to investigate emergent phenomena and proximity effects in heterostructures. Dynamic light scattering and confocal microscopy are utilized for studies on soft condensed matter. Optical trapping and manipulation of mesoscopic particles using holographic optical tweezers (HOTs) to study inter-particle interactions in colloidal suspensions/biological systems are being pursued. Besides there is also an intense effort towards quantum metrology based research studies using entangled photons.

SQUID & Detector Technology Division (SDTD) focuses mainly on using SQUID based systems for applications. Magneto-Cardiography (MCG) and Magneto-Encephalography (MEG) have been successfully designed, assembled, standardized and used for clinical studies. Further, SQUID based measuring systems such as high field SQUID magnetometer, SQUID VSM, SQUID based set-up for Non-Destructive Evaluation (NDE) have been developed. SDTD also carries out intense research activities related to using SQUID based time domain electromagnetic measurements (TDEM) and geophysical explorations using TDEM. Another major thrust research area of this division is the development of gamma irradiation detectors. Towards this the researchers have grown highly resistive CdTe single crystals and developed a gamma detector for pulse height spectroscopic studies. This research activity is being actively pursued to develop compact semiconductor based detectors with enhanced efficiency, and technologically important single crystals for detector applications.

Metallurgy and Materials Group



Dr. R. Divakar
Director, MMG



Dr. John Philip
AD, MCG



Dr. M. Vasudevan
AD, MD&TG



Shri Shaji Kurien
Head, PIED



Dr. Anish Kumar
Head, NDED



Dr. Arup Dasgupta
Head, PMD



Dr. S. Ningshen
Head, CS&TD



Dr. A. Nagesha
Head, MMD



Dr. A. Moitra
Head, MJ&MMD



Dr. V. Karthik
Head, HMTD

The Metallurgy and Materials Group (MMG) of IGCAR, is pursuing a vibrant research and development programme targeted to generate comprehensive knowledge-based solutions to a variety of materials related issues of critical importance to India's fast reactor and associated fuel cycle programmes. In addition, in the recent past, the Group has contributed significantly to the development of high temperature materials and related technologies for India's Advanced Ultra Supercritical power plant and fusion energy harnessing initiatives. Accordingly, the R&D activities of MMG are manifold. In scope, they encompass the design, indigenisation and accelerated field realisation of new and indigenous material choices and process modifications mandated by emerging demands on high design reliability. Amidst such a setting, MMG has been spearheading a mix of basic and directed cross-disciplinary research activities under various themes. The current portfolio of MMG includes:

- (i) Nuclear and high-temperature materials design, testing consultancy and production through industry,
- (ii) Advanced microstructure, physical and mechanical property characterization,
- (iii) Novel component manufacturing initiatives for current and future FBR's, including advanced materials fabrication and joining methods, special nuclear materials fabrication, Coatings and surface modification technologies for FBR and fuel reprocessing programs,
- (iv) Development and implementation of non-destructive testing, inspection and qualification technologies,
- (v) Post-irradiation examination for performance assessment and research on new FR materials, and component failure analysis,
- (vi) Research and development on corrosion mitigation and materials protection solutions for FR fuel cycle facilities

The human resource expertise of MMG supporting the above activities is a diverse blend of experienced and energetic workforce, spanning nearly all domains of materials engineering. It may be added that owing to the availability of quality technical expertise in combination with a wide range of advanced characterization tools, MMG has contributed to the development of three generations of nuclear structural materials aimed at withstanding severe operating environmental conditions, typical of high flux fast reactors. Thanks to the Internationally acclaimed expertise, MMG hosts many young scholars to pursue their research and post-doctoral research at IGCAR, under the banner of Homi Bhabha National Institute (HBNI).

Reactor Design & Technology Group



Shri S. Raghupathy
Director, RDTG



Dr. B. K. Nashine
AD, SFG



Shri Jose Varghese
Head, CH&MD



Shri Sriramachandra Aithal
Head, RC&AD



Dr. K. Devan
Head, RND



Dr. A. John Arul
Head, RS&DD



Shri U. Parthasarathy
Head, SHTD



Dr. B. Babu
Head, DD&RSD



Shri V. A. Suresh Kumar
Head, RIOD & SGTF



Shri V. Vinod
Head, ETHD



Shri Joseph Winston
Head, RH&IED



Dr. B. K. Sreedhar
Head, SE&HD



Dr. K. Natesan
Head, THD

Reactor Design & Technology Group (RDTG) is responsible for the design, structural & thermal hydraulics analysis, core safety & plant dynamics analysis, structural mechanics including seismic testing, manufacturing technology development, engineering development, testing and qualification of Fast Breeder Reactor (FBR) components/systems. In addition, the responsibility of RDTG includes: Development of In service inspection devices & remote handling equipment for FBRs & FBR fuel reprocessing plants, Development of sensors & devices for sodium applications, Planning of irradiation experiments for testing of various fuel, structural and shielding materials

in FBTR, Design, development & fabrication of various irradiation devices for experiments in FBTR, Out-of-pile testing, precision machining and welding of miniature components and planning & execution of Shielding / Foil Activation experiments in KAMINI reactor. RDTG has expertise in design & engineering development of various systems/components of FBRs covering the Nuclear Steam Supply Systems (NSSS) and Balance of Plant (BoP) systems viz. Reactor Physics & Core Engineering, Reactor Assembly, Absorber Rod and Component Handling Mechanisms operating in sodium, Primary & Secondary Sodium Heat Transport Systems, Decay Heat Removal systems, Tertiary Steam Water Systems, Various Plant Auxiliary Systems, Electrical Power Systems, Plant Layout, Sodium Pumps, Electromagnetic Pumps, Cold Trap and Ultrasonic devices for use in sodium. RDTG has indigenously developed the design of Prototype Fast Breeder Reactor (PFBR) of 500 MWe capacity based on its design & analysis expertise, R&D program, technology development exercise and with the support from and in association with various other groups of IGCAR. The group is extending its technical support and design expertise to the PFBR project which is under commissioning by BHAVINI and is responsible for getting design safety clearances for PFBR from the Atomic Energy Regulatory Board (AERB). It also provides analytical support to other groups in the Centre. RDTG constantly provides the design and analytical expertise for the continuous enhancement of fuel & core performance of the Fast Breeder Test Reactor (FBTR) and operation at higher powers and higher operating temperatures focusing on the core engineering design, plant dynamics and core safety analysis. RDTG also plays a major role in the development of future Metallic fuel and has designed the metal fuel pins of different designs and fuel compositions for irradiation testing.

Design validation of critical components of FBRs are achieved through testing in sodium and in water using scaled down/full scale models. RDTG has acquired expertise in the development of sensors and devices for sodium applications, such as electromagnetic flow meters, level probes and leak detectors. Expertise has also been developed in handling of sodium and in the design, construction, commissioning & operation of various high temperature sodium test loops/facilities. The major sodium test facilities of RDTG include 5.5 MWt Steam Generator Test Facility (SGTF) for testing model steam generators of FBRs, SADHANA loop for experimentally demonstrating natural convection based safety grade decay heat removal system, Large Component Test Rig (LCTR) for testing critical full scale components, In Sodium Test facility (INSOT) for creep and fatigue testing of advanced materials, Sodium Water Reaction Test (SOWART) facility to study self wastage & impingement wastage of Steam Generator tubes and a state-of-art Sodium Facility for Component Testing (SFCT) for testing small and medium sized components and sensors. To meet the requirements of future FBRs, a new facility called Sodium Technology Complex is under execution.

Recent achievements of RDTG: Compression & flexure testing of enriched B4C pellets for FBTR poison rods, Hydraulic validation of Poison subassembly for FBTR, Decay heat measurements of structural material in KAMINI, Technical support towards rectification of LRP bearing, Evaluation of rotor dynamic coefficients of sodium pumps through CFD analysis, Simulation of pressure transient under turbine trip event, Performance and endurance testing of 50 m³/h Annular linear induction pump, Design and manufacture of additional nickel detectors for steam generator tube leak detection system of PFBR, Experimental verification of methodology in simulating neutron count rates with 0.1 cps/nv HTFC during initial fuel loading of PFBR, Seismic PSA study for PFBR, Study on the effect of orientation of PFBR fuel subassembly on response of gamma detector in FIZID system, Estimation of guard pipe compartment bellows, Vibration analysis of IHX downcomer, Stability analysis of secondary sodium pump, Vibration limits for ALIP in secondary sodium fill & drain circuit, Design and thermal hydraulic analysis of secondary sodium based decay heat removal system for FBR 1&2, Improved severe accident analysis in SFRs using slug-ejection model, Integrated steady and transient pool hydraulic analysis of primary sodium circuit, Numerical methodology for estimation of asymptotic crack size and comparison with A16 master curve prediction, Numerical analysis of hydrostatic bearing of large sodium pump using ARMD software, Numerical analysis of dynamic seals used in CSRDM, Testing of large sized bellows in sodium environment, Parametric studies to assess the bonding quality of sodium compatible ultrasonic transducers, Sensitivity evaluation of 100 NB permanent magnet flowmeters in sodium, Development and manufacture of 200 NB sidewall permanent magnet flow meter, Development of non-return valves for sodium service, Improvements in regeneration of sodium cold trap by altering geometry of wire mesh top plate, Simulation of gas entrainment phenomena inside FFLM, Finalisation of calibration scheme for eddy current flow meter of primary sodium pump, Performance evaluation of wire type leak detector layout for dished end test section in LEENA facility, Design & development of Reactor core viewing system (RCVS), Design, analysis and development of pressure decay method leak measurement system using mems based pressure sensor and Transfer & safe transportation of 3T of indigenously manufactured sodium from Baroda to Kalpakkam.

Besides providing technical support to PFBR, RDTG is currently engaged, in the development of future FBRs incorporating enhanced safety and improved economy. It has finalised the conceptual design of the future FBR and is currently undertaking the development of key systems and components and detailed engineering. Further, RDTG has evolved the preliminary conceptual design of a metal fuelled 100 MWt test reactor, planned to be

launched after FBTR. These apart, it has a modern design office with many advanced modeling and analysis softwares, experimental facility for testing major Reactor Assembly systems, Structural Mechanics Laboratory (SML) having state-of-the-art facilities for carrying out tests at component level to verify structural integrity at high temperature and a 100 t shake table with six degrees-of-freedom for seismic tests. The shake table is extensively used for the design validation of reactor systems and components of Nuclear Power Plants of NPCIL and other research projects undertaken by BARC.

RDTG also plays a major role in developing highly competent human resources by undertaking academic courses for the various science and engineering disciplines through the BARC Training Schools located at Mumbai, at IGCAR, Kalpakkam and at NFC, Hyderabad and provide guidance to many employees / students / JRF & SRF in their Post graduate, Ph.D and Research Programs.

Reactor Facilities Group



Shri S. Raghupathy
Director, RFG



Shri G. Shanmugam
SD, RF



Shri N. Manimaran
AD, O&MG



Shri M. S.Chandrasekar
Head, ROD



Shri K. G. Subramanian
Head, QA&ISD



Shri K. Bhanumurthy
Head, RMD



Shri A. Suriyanarayanan
Head, THRDD



Shri S. Rama Rao
Head, TSD

Reactor Facilities Group (RFG) is responsible for safe operation of Fast Breeder Test Reactor (FBTR), KAMINI Reactor and Interim Fuel Storage Building (IFSB). FBTR has been operating at design power level of 40 MWt with 68 Mark-I subassemblies and 4 poison subassemblies (to maintain the required shutdown margin) in the core and completed two successful irradiation campaigns at 40 MWt with turbine- generator generating ~10 MWe connected to the grid. Utilizing the reactor for irradiation of advanced fuels and structural materials for fast reactors and conducting safety related experiments form major goals of FBTR. FBTR is also used for the production of Strontium-89 isotope for medical application. KAMINI Reactor has been extensively used for neutron radiography, activation studies and testing of indigenously developed neutron detectors. RFG is also responsible for fabrication and safe storage of fuel, blanket, source and control subassemblies for PFBR. All the required number of assemblies for the first core of PFBR have already been fabricated and stored safely in IFSB with all security surveillance measures and safeguards. The training division of the group is responsible for training the O&M staff of FBTR, PFBR and future FBRs. RFG has also taken part in the operational safety review of PFBR project.

Reprocessing Group



Dr. K. Ananthasivan
Director, RpG



Shri Shekhar Kumar
AD, FRPPCG



Shri K. Rajan
AD, RPPOG



Dr. R. V. Subba Rao
Head, PRCD



Shri M.S. Gopi Krishna
Technical Audit (TA)



Shri T. Selvaraj
Head, ED&AD



Shri J. Kodandaraman
Head, PDTS&TD



Dr. K. A. Venkatesan
Head, PRCRRDD



Shri M. Geo Mathews
Head, RpMD-E



Shri M. Dhananjeyakumar
Head, RpMD-M



Shri Surajit Halder
Head, RPOD

The Reprocessing Group at IGCAR has the primary mandate to establish the technology for the reprocessing of advanced fast reactor fuel. The major activities in progress include, design, construction, commissioning and operation of the fast reactor fuel reprocessing plants, development of novel processes & equipment and carrying out the R&D associated with the same. This group comprises the CORAL (Compact facility for Reprocessing Advanced fuels in Lead cells) facility, the Demonstration fast reactor Fuel Reprocessing Plant (DFRP), divisions for providing support in chemical characterisation, mechanical engineering electrical, electronics and instrumentation control engineering and a research facility for carrying out advanced research on fast reactor fuel reprocessing. The CORAL facility was commissioned in 2003 and continues to operate successfully, processing the mixed carbide spent fuel from FBTR. The facility continues to serve as a test bed and has provided valuable feedback for the design and construction of future reprocessing plants. CORAL has completed its original mandate of reprocessing of FBTR fuel sub-assemblies and closing the fast reactor fuel cycle and has been further relicensed by the regulatory body, after up gradation of the safety systems. The DFRP, whose mandate is to demonstrate the reprocessing of FBTR spent fuel at a plant scale and the initial spent fuel subassemblies of PFBR, has been cold commissioned with uranium processing and is awaiting the approval of AERB for hot commissioning. The commercial scale plant, Fuel Reprocessing Plant (FRP), for processing the fuel discharged from PFBR is being constructed at the Fast Reactor Fuel Cycle Facility (FRFCF). The responsibility of providing design inputs for establishing the FRP rests with RpG. In addition, this group also lends its expertise in procurement of long delivery items such as the optical glass slabs for radiation shielding windows, various types of master slave manipulators, lead bricks etc, for the FRFCF project. Concurrently focused R&D is being pursued to develop equipment, alternate processes and aqueous processing of metallic fuel.

Safety, Quality & Resource Management Group



Dr. B. Venkatraman
Director, SQRMG



Dr. D. Ponraju
AD, H&SEG



Dr. Vidya Sundararajan
Head, P&HRMD



Ms. S. Rajeswari
Head, SIRD



Dr. C. V. Srinivas
Head, EAD



Dr. V. Subramanian
HEAD, RESD



Shri Sanjay Kumar Das
HEAD, SED



Shri Vimal Kumar
HEAD, TC&QMD



Dr. N. Subramanian
Head, Incubation Centre

Safety, Quality & Resource Management Group (SQRMG) is responsible for Health Physics, Radiation Safety and Quality Assurance services, studies on Environment Impact Assessment, Severe Accident & Sodium Fire and management of resources like Financial (Budget), Human, Scientific Information services and conduct Academic Programmes of BARC Training School at IGCAR. Health and Safety Engineering Group (HSEG) comprises of Health & Industrial Safety Division (HISD) and Safety Engineering Division (SED). Radiological & Environmental Safety Group (RESG) comprises of Radiological & Environmental Safety Division (RESD), Environment Assessment Division (EAD), Quality Assurance Division (QAD) Planning and Human Resource Management Division (PHRMD) and Scientific Information Resource Division (SIRD).

HISD provides radiological protection and surveillance to all active plants, Bio assay and Whole body accounting services to all the occupational workers of the Centre and industrial and occupational health safety services to meet the mandatory requirements of AERB. HISD organizes training and awareness programmes on industrial, radiation and fire safety to occupational workers.

SED is carrying out studies on Severe Accident and Sodium Fire Safety. The major experimental facilities are THEME and SOFI for Molten Fuel Coolant Interaction studies, PATH facility for post accident heat removal studies, MINA and SOCA facilities for sodium fire studies and SFEF for large scale sodium fire and severe accident studies.

RESD focuses on R&D activities in the areas of sodium aerosol science and technology, radiation safety through modeling & simulation and societal applications of ionizing and non-ionizing radiations. RESD organizes public awareness programmes on radiation safety and nuclear energy. Technical Co-ordination & Quality Management

Section (TC&QMS) is primarily responsible for quality control of several critical equipment for IGCAR manufactured in the western region of the country and provides technical co-ordination services for the centre with BARC as well as the DAE, Mumbai. TC&QMS also participates in R&D activities which are being carried out at BARC towards meeting the mandate of IGCAR, FRFCF/NRB and PFBR.

EAD is responsible for providing radiation safety services such as TLD personal monitoring, luminescence dosimetry, retrospective dosimetry, bio dosimetry and focuses on R&D activities on atmospheric dispersion and modelling.

QAD is primarily responsible for catering quality assurance, inspection, Non-Destructive Testing (NDT) and quality audit activities during fabrication, construction & erection of System, Structure & Equipment for various Groups of our Centre in order to establish and implement an effective quality management system. QAD also extends its expertise to other DAE units and other strategic sectors.

The significant activities of PHRMD are planning and human resource management, conducting the academic programmes of BARC Training school at IGCAR and stipendiary trainees, formulating and monitoring capital projects towards budget planning and management, facilitating induction of Research Scholars, Research Associates and Visiting Scientists, coordinating the visits of important dignitaries and delegations to the Centre, formulating and facilitating collaborations and MoU including patents and piloting the activities relating to technology transfer.

Scientific Information Resource Division (SIRD) is the second-largest research library in DAE, with about 65,000 books, 50,000 back volumes, 540 journals, 15,000 standards, and two lakh technical reports. SIRD caters to the needs of more than 5000 scientists, engineers, research scholars, and students of various DAE Units at Kalpakkam. SIRD maintains the centralized institutional repository, the preprint server, and the RFID-based Library Resources databases. Dissemination of resources is through WebOpac, and remote access is through a mobile app. SIRD provides various services like photography, videography, reprography, content creation, auditorium, desktop design, and publication assistance. SIRD has played a vital role in documenting the biodiversity.

An Incubation Centre has been set up at IGCAR to promote and incubate the spin-off technologies from IGCAR. A team has been formed to meet the objectives, set up the necessary infrastructure and to interface with various Groups at IGCAR.

Administration & Accounts



Shri K.R. Sethuraman
CAO



Shri S. A. Murugesan
IFA



Shri P.T. Mani
AO-III (E & V)

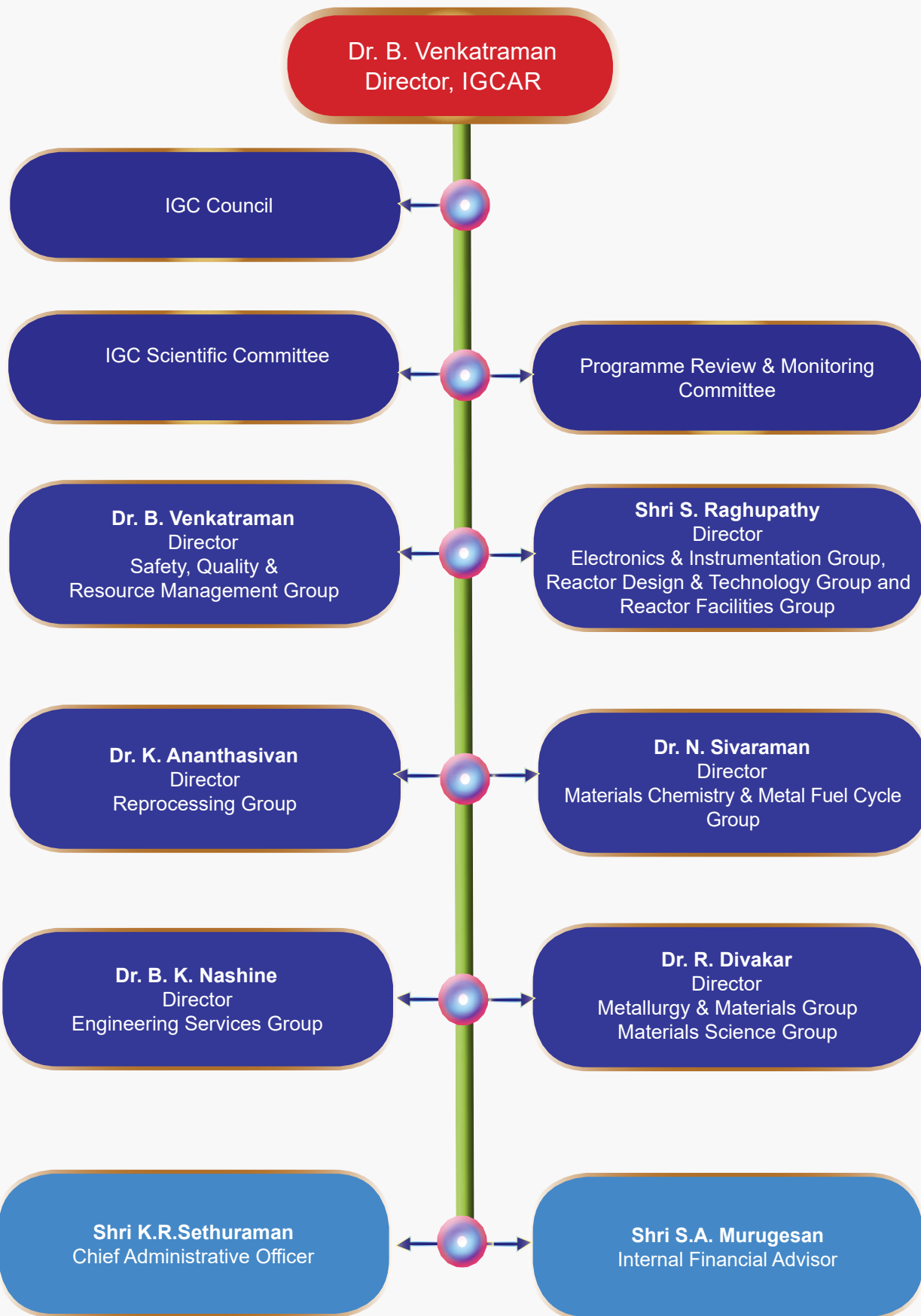


Smt Jussy Jacob
AO (L, G&R)

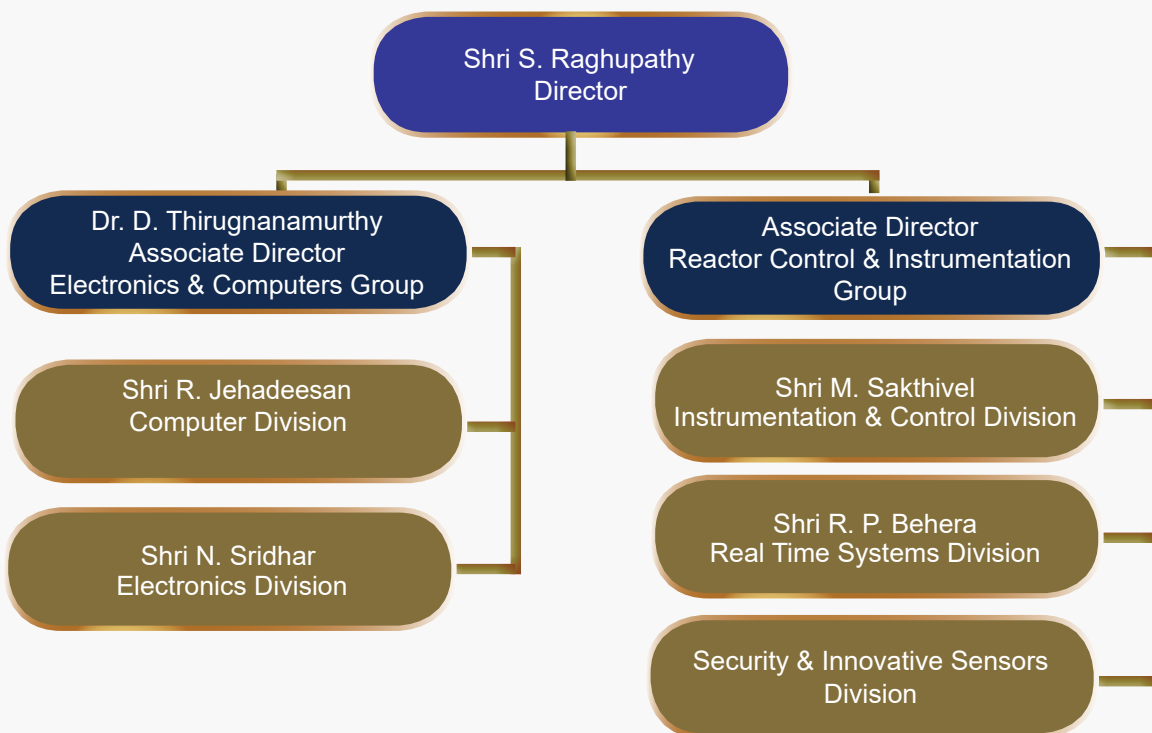


Smt Radhika Saikannan
DCA

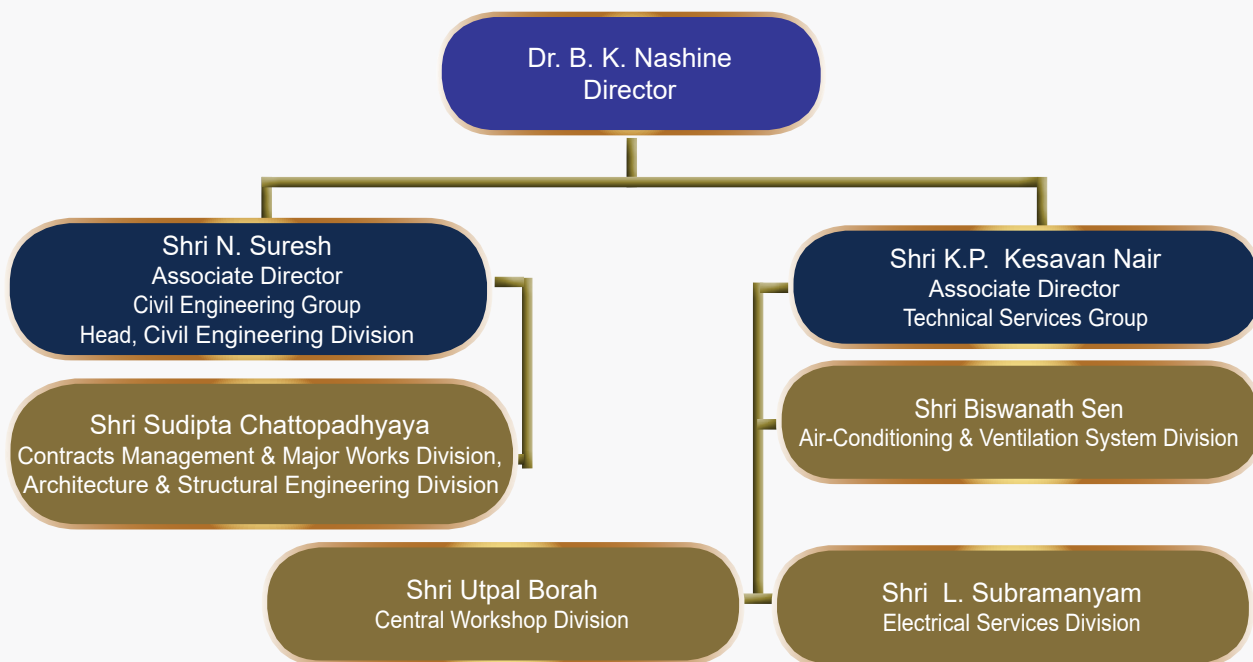
Organisation Chart - IGCAR



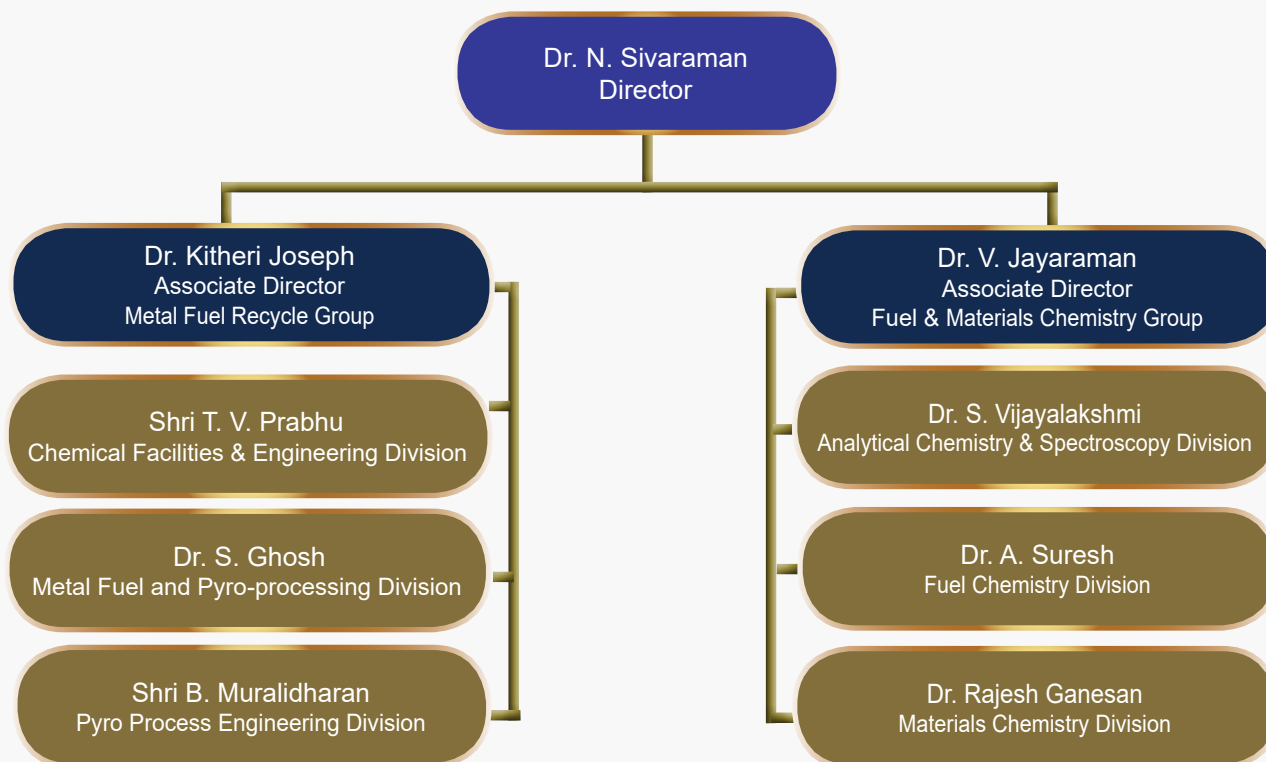
Electronics & Instrumentation Group



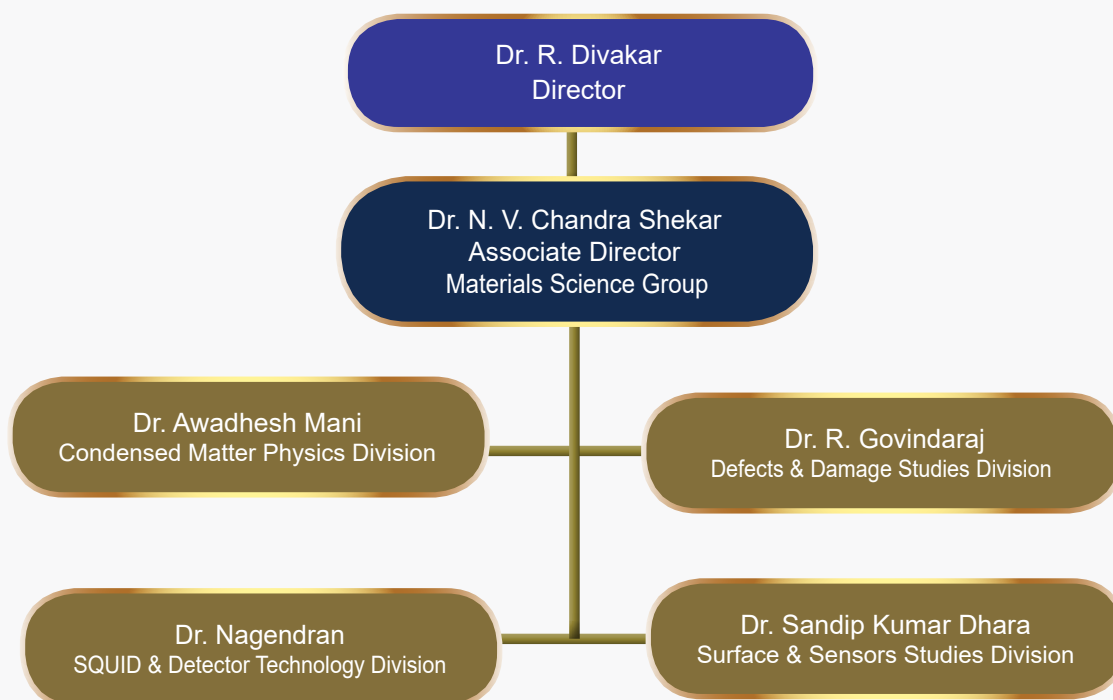
Engineering Services Group



Materials Chemistry & Metal Fuel Cycle Group



Materials Science Group



Metallurgy & Materials Group

Dr. R. Divakar
Director

Dr. M. Vasudevan
Associate Director
Materials Development & Technology Group

Dr. V. Karthik
High-temperature Materials Technology Division

Dr. A. Moitra
Materials Joining & Materials Mechanics Division

Dr. A. Nagesha
Mechanical Metallurgy Division

Dr. John Philip
Associate Director
Materials Characterization Group

Dr. S. Ningshen
Corrosion Science & Technology Division

Dr. Anish Kumar
Non-Destructive Evaluation Division

Dr. Arup Dasgupta
Physical Metallurgy Division

Shri Shaji Kurien
Post Irradiation Examination Division

Reactor Design & Technology Group

Shri S. Raghupathy
Director

Shri Jose Varghese
Component Handling & Mechanisms Division

Shri Sriramachandra Aithal
Reactor Core & Assembly Division

Dr. K. Devan
Reactor Neutronics Division

Dr. A. John Arul
Reactor Shielding and Data Division

Shri U. Parthasarathy
Sodium Heat Transport Division

Dr. B. K. Nashine
Associate Director
Sodium Facility Group

Dr. B. Babu
Device Development & Rig Services Division

Shri V. A. Suresh Kumar
Rig Operations Division & SGTF

Shri S. Raghupathy
Structural Mechanics Division

Shri V. Vinod
Experimental Thermal Hydraulics Division

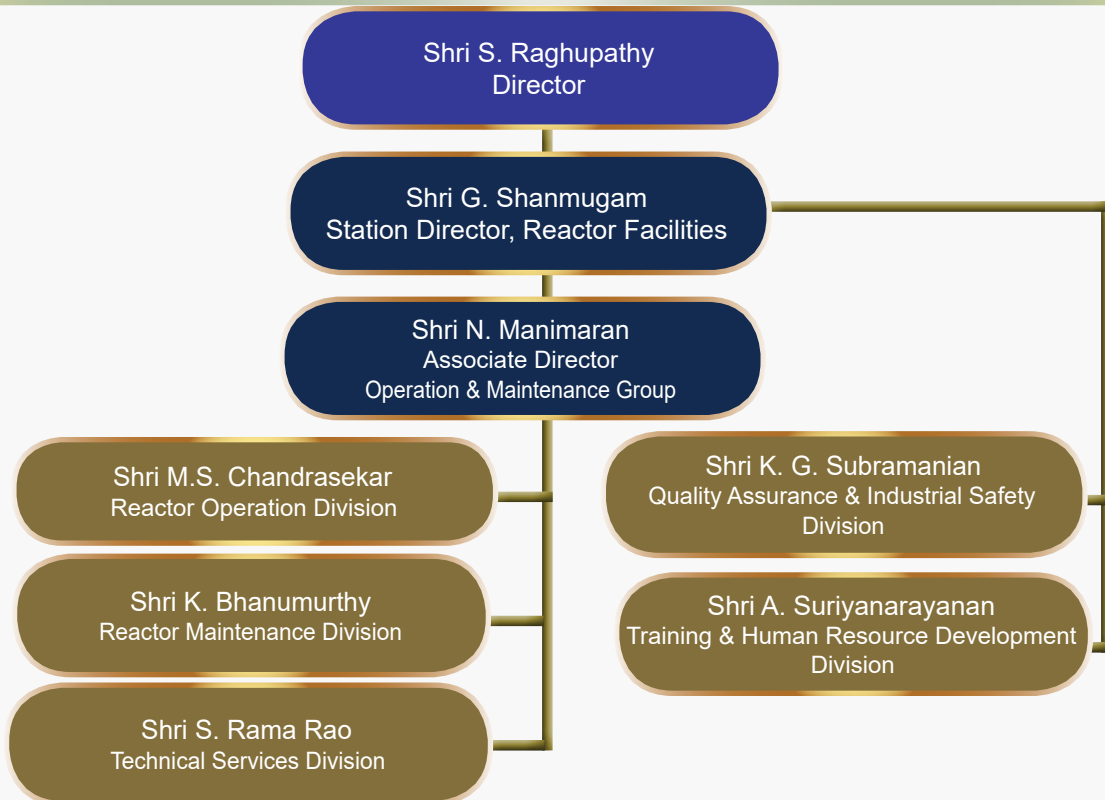
Shri Joseph Winston
Remote Handling & Irradiation Experiments Division

Shri B. K. Sreedhar
Sodium Experiments & Hydraulics Division

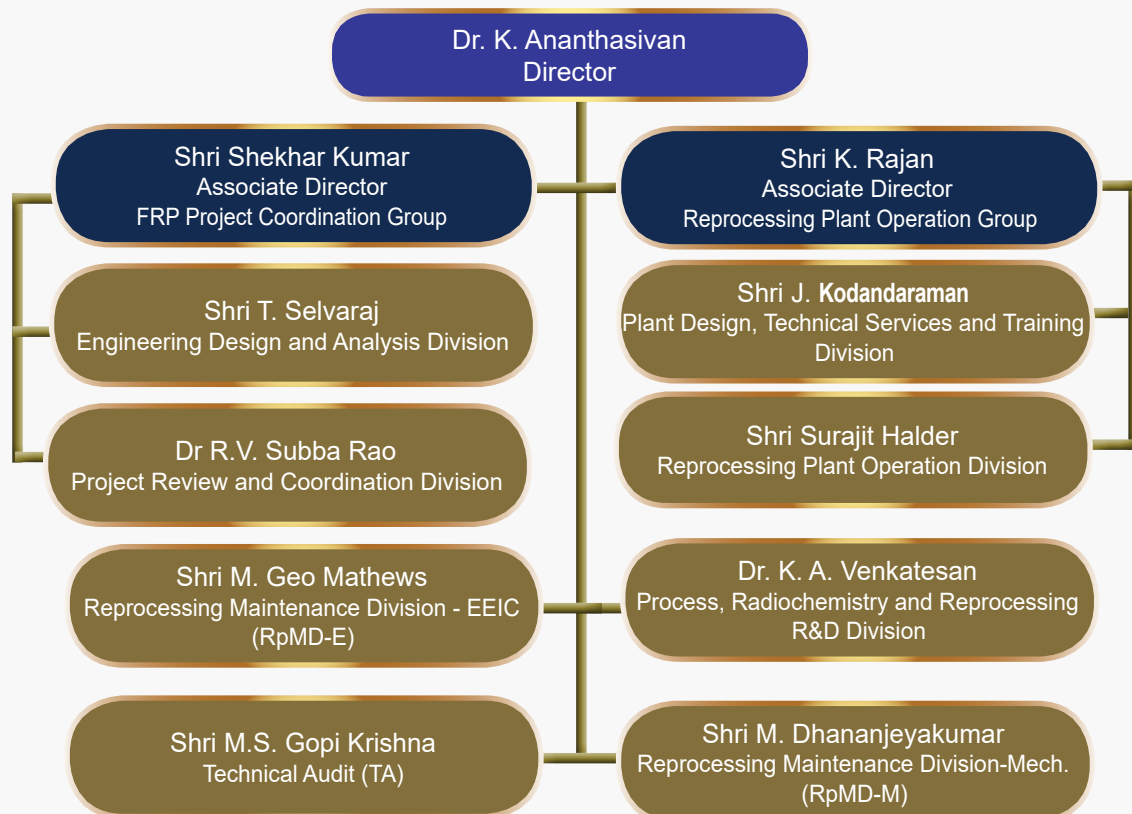
Shri K. Natesan
Thermal Hydraulics Division

Shri S. Raghupathy
Power Plant Control Division

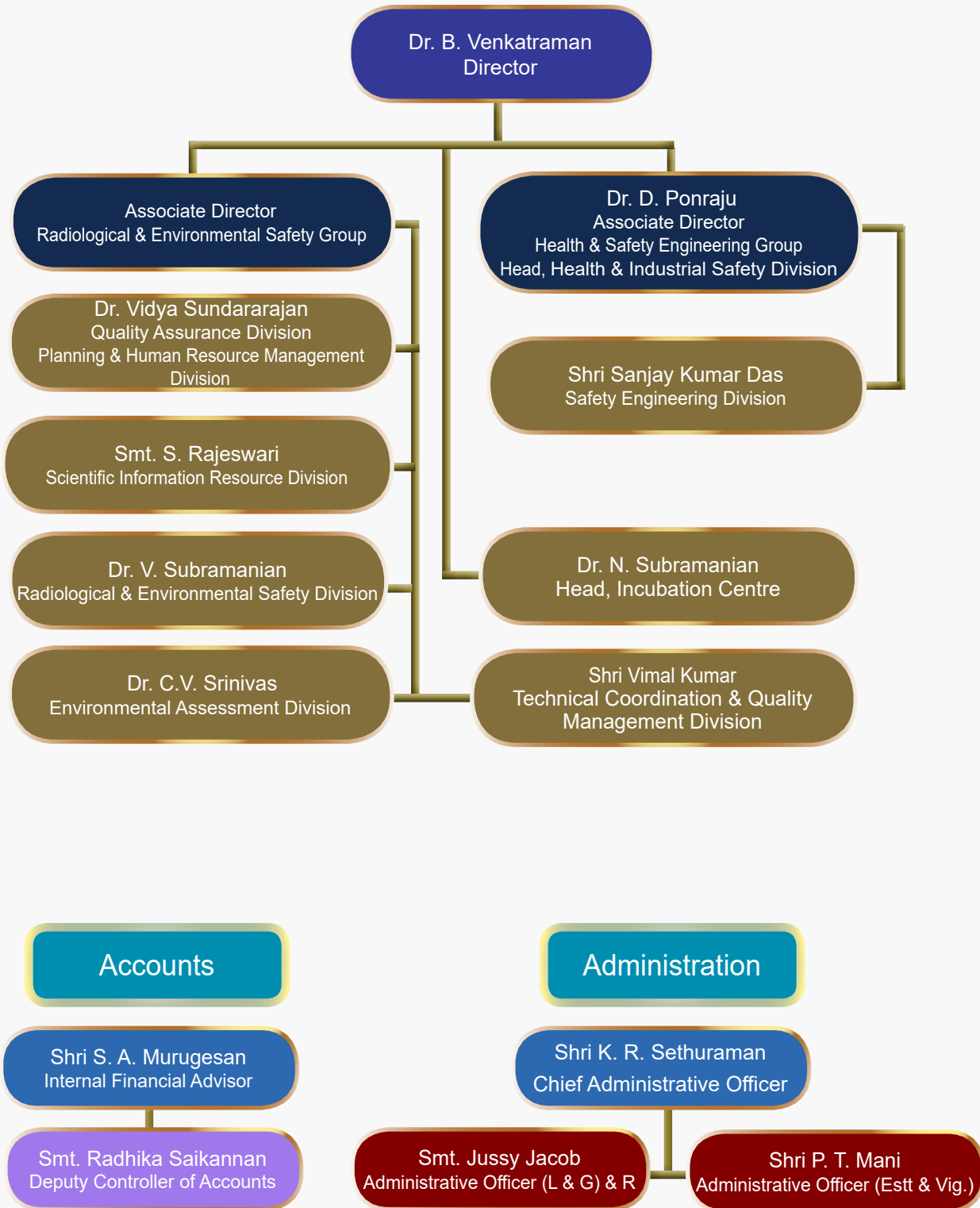
Reactor Facilities Group



Reprocessing Group



Safety, Quality & Resource Management Group



LIST OF IMPORTANT ABBREVIATIONS

AC&VSD	Air Conditioning and Ventilation System Division	MMG	Metallurgy and Materials Group
AERB	Atomic Energy Regulatory Board	MPD	Materials Physics Division
A&SED	Architecture & Structural Engineering Division	MRPU	Madras Regional Purchase Unit
BARC	Bhabha Atomic Research Centre	MSG	Materials Science Group
BARCF	Bhabha Atomic Research Centre Facilities	NDED	Non-Destructive Evaluation Division
BHAVINI	Bharatiya Nabhikiya Vidyut Nigam Limited	NFC	Nuclear Fuel Complex
CD	Computer Division	NICB	Nuclear Island Connected Building
CED	Civil Engineering Division	NPCIL	Nuclear Power Corporation of India Ltd.
CEG	Civil Engineering Group	NSDG	Nuclear Systems Design Group
CF&ED	Chemical Facilities & Engineering Division	OMG	Operation & Maintenance Group
CH&MD	Components Handling & Mechanism Division	PFBR	Prototype Fast Breeder Reactor
CMPD	Condensed Matter Physics Division	P&HRMD	Planning & Human Resource Management Division
C&MWD	Contracts & Major Works Division	PHWR	Pressurized Heavy Water Reactor
CORAL	Compact facility for Reprocessing Advanced fuels in Lead cell	PIED	Post Irradiation Examination Division
CSTD	Corrosion Science & Technology Division	PMD	Physical Metallurgy Division
CWD	Central Workshop Division	PPCD	Power Plant Control Division
DDSD	Defects & Damage Studies Division	PPED	Pyro Process Engineering Division
DDRSD	Device Development and Rig Services Division	QAD	Quality Assurance Division
DFRFRPD	Demonstration Fast Reactor Fuel Reprocessing Plant Division	QA&ISD	Quality Assurance & Industrial Safety Division
DFRP	Demonstration Fuel Reprocessing Plant	RCAD	Reactor Core & Assembly Division
ED	Electronics Division	RD&TG	Reactor Design & Technology Group
EIG	Electronics and Instrumentation Group	R&ESD	Radiological & Environmental Safety Division
ESD	Electrical Services Division	RESG	Radiological & Environmental Safety Group
ESG	Engineering Services Group	RH&IED	Remote Handling & Irradiation experiments Division
ETHD	Experimental Thermal Hydraulics Division	RMD	Reactor Maintenance Division
FBTR	Fast Breeder Test Reactor	RND	Reactor Neutronics Division
F&MCG	Fuel & Materials Chemistry Group	ROD	Reactor Operation Division
FChD	Fuel Chemistry Division	RFG	Reactor Facilities Group
FRFCF	Fast Reactor Fuel Cycle Facility	RpMD	Reprocessing Maintenance Division
HISD	Health & Industrial Safety Division	RpG	Reprocessing Group
HSEG	Health, Safety & Environment Group	RpOD	Reprocessing Operation Division
GSO	General Services Organisation	RRDD	Reprocessing Research and Development Division
IAEA	International Atomic Energy Agency	RSDD	Reactor Shielding and Data Division
IIT	Indian Institute of Technology	RTSD	Real Time Systems Division
IMSc	Institute of Mathematical Sciences	RC&IG	Reactor Control & Instrumentation Group
I&CD	Instrumentation & Control Division	SDTD	SQUIDS & Detector Technology Division
MAPS	Madras Atomic Power Station	SED	Safety Engineering Division
MCG	Materials Characterization Group	SE&HD	Sodium Experiments & Hydraulics Division
MC&MFCG	Materials Chemistry & Metal Fuel Cycle Group	SFG	Sodium Facility Group
MCD	Materials Chemistry Division	SHTD	Sodium Heat Transport Division
MDTG	Materials Development & Technology Group	SDTD	SQUID & Detector Technology Division
MJMMD	Materials Joining & Materials Mechanics Division	SIRD	Scientific Information Resource Division
MFFD	Metal Fuel Fabrication Division	SISD	Security and Innovative Sensors Division
MFPG	Metal Fuel and Pyroprocessing Division	SMD	Structural Mechanics Division
MMD	Mechanical Metallurgy Division	SSSD	Surface & Sensors Studies Division
MMTD	Materials Development & Technology Group	SQRMG	Safety, Quality & Resource Management Group
	Materials Development & Technology Group	THD	Thermal Hydraulics Division
		THRDD	Training & Human Resource Development Division
		TSD	Technical Services Division
		TSG	Technical Services Group

Editorial Team



Smt. S. Rajeswari
Chairman



Dr. John Philip



Dr. T. R. Ravindran



Shri A. Suriyanarayanan



Shri Biswanath Sen



Dr. C. V. S. Brahmananda Rao



Shri G. Venkat Kishore



Shri M. Rajendra Kumar



Shri S. Kishore



Dr. N. Desigan



Ms. P. N. Sujatha



Shri P. Vijaya Gopal
Secretary



Shri K. Varathan

